

AFRL-SN-RS-TR-2004-115
Final Technical Report
May 2004



RESONANT ENHANCED MODULATORS

Sarnoff Corporation

APPROVED FOR PUBLIC RELEASE; DISTRIBUTION UNLIMITED.

**AIR FORCE RESEARCH LABORATORY
SENSORS DIRECTORATE
ROME RESEARCH SITE
ROME, NEW YORK**

STINFO FINAL REPORT

This report has been reviewed by the Air Force Research Laboratory, Information Directorate, Public Affairs Office (IFOIPA) and is releasable to the National Technical Information Service (NTIS). At NTIS it will be releasable to the general public, including foreign nations.

AFRL-SN-RS-TR-2004-115 has been reviewed and is approved for publication

APPROVED: /s/
JAMES NICTHER
Project Engineer

FOR THE DIRECTOR: /s/
RICHARD G. SHAUGHNESSY, Lt Col, USAF
Chief, Rome Operations Office
Sensors Directorate

REPORT DOCUMENTATION PAGE

Form Approved
OMB No. 074-0188

Public reporting burden for this collection of information is estimated to average 1 hour per response, including the time for reviewing instructions, searching existing data sources, gathering and maintaining the data needed, and completing and reviewing this collection of information. Send comments regarding this burden estimate or any other aspect of this collection of information, including suggestions for reducing this burden to Washington Headquarters Services, Directorate for Information Operations and Reports, 1215 Jefferson Davis Highway, Suite 1204, Arlington, VA 22202-4302, and to the Office of Management and Budget, Paperwork Reduction Project (0704-0188), Washington, DC 20503

1. AGENCY USE ONLY (Leave blank)	2. REPORT DATE MAY 2004	3. REPORT TYPE AND DATES COVERED FINAL Jun 00 – Jun 03
4. TITLE AND SUBTITLE RESONANT ENHANCED MODULATORS		5. FUNDING NUMBERS C - F30602-00-C-0116 PE - 63739E PR - J811 TA - 00 WU - 01
6. AUTHOR(S) J. H. Abeles, A. N. Lepore, M. H. Kwakernaak, H. Mohseni, G. A. Pajer, G. Griffel, D. Bechtle, A. F. Ulmer, Z. A. Shellenbarger, H. An, I. Adesida, S. Rommel, J-W. Bae, J-H Jang, W. Zhao		8. PERFORMING ORGANIZATION REPORT NUMBER N/A
7. PERFORMING ORGANIZATION NAME(S) AND ADDRESS(ES) Sarnoff Corporation 201 Washington Road Princeton NJ 08540		9. SPONSORING / MONITORING AGENCY NAME(S) AND ADDRESS(ES) AFRL/SNDP 26 Electronic Parkway Rome NY 13441-4514
11. SUPPLEMENTARY NOTES AFRL Project Engineer: James Nichter/SNDP/(315) 330-7423		10. SPONSORING / MONITORING AGENCY REPORT NUMBER AFRL-SN-RS-TR-2004-115
12a. DISTRIBUTION / AVAILABILITY STATEMENT APPROVED FOR PUBLIC RELEASE; DISTRIBUTION UNLIMITED.		12b. DISTRIBUTION CODE
We developed fabrication technology, advanced materials and design techniques to realize resonance enhanced modulators with ring-resonators. The devices are based on a lateral geometry with deeply etched waveguides in InP. ICP etching techniques and masks were developed to obtain sub-micrometer deep etched waveguides with nanometer residual sidewall roughness for low optical loss and high quality resonators. Ultra compact multi-mode interference (MMI) couplers are designed and fabricated for coupling of the ring-resonators with superior reproducibility and low excess loss. Design and test procedures were established for ring-resonators and resonance enhanced modulators. We developed three-step quantum wells in GaInAsP/InP for enhanced electro-optic coefficients. Measured electro-optic coefficient of the three-step quantum wells is nearly three times higher than the conventional rectangular quantum well at 1.55μm. The enhanced electro-optic effect, combined with a low optical absorption coefficient $\alpha < 1 \text{ cm}^{-1}$ increases a modulator figure of merit by nearly 36 times, and decreases the power consumption by nearly one order of magnitude compared with a conventional quantum well design. MMI-coupled electro-refractive ring resonators have been fabricated using deeply etched InGaAsP/InP waveguides. We demonstrated the first electro-refractive ring-resonator modulators. RF-modulation with the ring resonator is demonstrated. Resonance enhanced modulation efficiency with the ring-resonance was confirmed.		
14. SUBJECT TERMS Resonance enhanced modulator, Microresonator, Ring resonator, Modulator, Quantum well modulator, Stepped quantum wells, MMI couplers, Plasma etching		15. NUMBER OF PAGES 453
		16. PRICE CODE
17. SECURITY CLASSIFICATION OF REPORT UNCLASSIFIED	18. SECURITY CLASSIFICATION OF THIS PAGE UNCLASSIFIED	19. SECURITY CLASSIFICATION OF ABSTRACT UNCLASSIFIED
20. LIMITATION OF ABSTRACT UL		

Table of Contents

1.	Summary	1
1.1.	Introduction	1
1.2.	Device Concept as Proposed	2
1.2.1.	Requirements for Low- V_π Resonant Enhanced Modulator	2
1.3.	Status of Resonant Enhanced Modulator Development.....	2
1.4.	Summary of Accomplishments by Year	4
1.4.1.	Program Timeline.....	4
1.4.2.	Key Accomplishments.....	4
1.4.3.	Key Personnel.....	5
1.5.	Resource Issues During the Program	5
1.6.	Recommendations for Further Work.....	6
2.	Methods, Assumptions and Procedures	7
2.1.	Micro-Ring Optical Resonators.....	7
2.1.1.	Marcatili Proposal	7
2.1.2.	Microspheres	7
2.1.3.	Summary of Other Work (post 1996).....	7
2.2.	Micro-Ring Resonator Modulators	7
2.2.1.	Governing Principles	7
3.	Results and Discussion	14
3.1.	Laterally Coupled Resonant Enhanced Modulators.....	14
3.1.1.	Anisotropic Patterning and Etching.....	14
3.1.2.	Low-Loss Waveguides & Couplers.....	22
3.1.3.	Couplers.....	24
3.1.4.	Modulator Materials	27
3.1.5.	Low-Capacitance Planarization.....	37
3.1.6.	Electrode Design	39
3.1.7.	Chip-Level Characterization Set-Up	41
3.1.8.	Packaging Design	44
3.1.9.	Passive Ring Characterization.....	45
3.1.10.	Active Ring Characterization.....	45
3.1.11.	Issues with RF Modulation Response.....	46
3.2.	Impact of REM Technology beyond RFLICs	50

3.2.1. DARPA/MTO CS-WDM Program	50
3.2.2. DARPA/MTO SWAODL Program.....	52
3.2.3. DARPA/MTO AOSP-PAWG Subcontract to UCF-CREOL.....	53
4. Conclusions.....	57
5. References.....	58
APPENDICES	60
Appendix A: Viewgraph Presentations	
• REM Kickoff Arlington August 2000	62
• REM Site Visit Sarnoff February 2001	80
• REM Site Visit Sarnoff February 2002	105
• REM GOMAC Monterrey March 2002.....	202
• REM Site Visit Sarnoff October 2002.....	232
• REM PI Review Reno 2003.....	323
• REM Site Visit Sarnoff March 2003	393
Appendix B: Publications	
• JVST B 2002 Rommel	422
• CLEO 2003 Kwakernaak.....	426
• EIPBN 2003 Bae.....	428
• APL 2003 Jang.....	430
• JVST B 2004 Bae.....	433
• APL 2004 Mohseni	437

List of Figures

Figure 1. Schematic of Resonant Enhanced Modulator. From left to right, optical signal enters, is split in a coupler, interacts with several ring resonators, recombines in a second coupler, and exits. The RF modulation signal is push-pull modulated on the upper and lower array of ring resonators, which are electro-optically modulated. The RF propagation delays denoted by serpentine RF electrode patterns are matched to the optical delay in the ring resonators, where light circulates multiple times on average.....	1
Figure 2. Nature of resonant enhancement is low capacitance.....	1
Figure 3. (Figure 13 From Proposal) Transfer Curves for Resonant Enhanced MZ Modulator, 95% reflectivity. Modulator consists of Mach-Zehnder structure with 8 resonant micro-optical phase shifters coupled to each arm and is driven push-pull. Photon lifetime is 9x the round-trip time for each resonator. Electro-refractive coefficient is taken from Zucker et al.....	4
Figure 4. Schematic of multi ring- resonator Mach-Zehnder modulator.....	8
Figure 5. Schematic of single ring-resonator.....	8
Figure 6. Calculated power transmission, phase response and group delay of ring-resonator.....	10
Figure 7. Modulation sidebands in the ring-resonator.....	11
Figure 8. Calculated modulation response.....	11
Figure 9. Finesse, Transmission, and ring-enhancement of ring resonator as a function of loss per roundtrip and coupling.....	13
Figure 10. Process flow for the fabrication of sub- μ m deeply etched InP/InGaAsP waveguides.....	14
Figure 11. SEM images of etched sidewall.....	15
Figure 12. SEM image of ring-resonator waveguide. The NiCr/ SiO ₂ mask has not been removed.....	15
Figure 13. Scanning electron micrograph of a InP/InGaAsP epitaxial layer etched with 110 W RF power, 900 W inductive power, -215 V DC Bias, Cl ₂ /Ar/H ₂ = 6 sccm/ 9 sccm/ 0 sccm, 1.5 mT, and 225°C. These layers exhibit a large undercut of the etch mask, which is still in place.....	17
Figure 14. Scanning electron micrograph of a InP/InGaAsP epitaxial layer etched with 110 W RF power, 900 W inductive power, -215 V DC Bias, Cl ₂ /Ar/H ₂ = 6 sccm/ 9 sccm/ 6 sccm, 1.5 mT, and 225°C. The width of the etched segments is 0.7 μ m, the gap is 0.275 μ m. The etch depth is 4 μ m.....	18
Figure 15. Scanning electron micrograph of a InP/InGaAsP epitaxial layer etched with 110 W RF power, 900 W inductive power, 215 V DC Bias, Cl ₂ /Ar/H ₂ = 6 sccm/ 9 sccm/ 9 sccm, 1.5 mT, and 225°C. InP layers show large undercuts whereas InGaAsP layers show little lateral etching.....	18

Figure 16. SEM micrograph of a InP/InGaAsP race-track resonator. The ridge is etched to a depth of 5 μm , and has a width of 0.9 μm and gap of 0.275 μm	19
Figure 17. (a) General schematic for test pattern showing staggered segments 200 μm long and staggered by 4 μm . (b) Perpendicular measurement of the sidewall is performed on the cleaved sample thereby preserving the z-directional movement of the AFM tip.....	20
Figure 18. A SEM micrograph of deep-etched InP/InGaAsP waveguide heterostructures using an ICP-RIE system. 1- μm wide lines were etched to a depth of 10.7 μm . Waveguide sidewall is on the x - y plane where x is the direction of light propagation. The z -axis is normal to the waveguide sidewall.....	20
Figure 19. (a) AFM and SEM micrographs of waveguide sidewall etched up to 4 μm . Sampled profile in x - and y -direction is displayed. (b) 3 dimensional view of sidewall profile measured with AFM. (c) An AFM scan image of a cleaved InP substrate used to create the sample is included as reference.....	21
Figure 20. Distribution of SWR for the etched sidewall (a) $\text{SWR}_{(x_i)}$ and (b) $\text{SWR}_{(y_j)}$	21
Figure 21. SiO_2 masking process to reduce the sidewall roughness as a result of the line edge roughness of the NiCr metal mask.....	22
Figure 22. Illustration of the sources of loss in waveguides.....	22
Figure 23 Measured losses of deeply etched InP/InGaAsP waveguides.....	24
Figure 24. Coupling length of evanescent couplers calculated for various ridge widths and waveguide separations.....	25
Figure 25. Calculated field intensity in the MMI (left).Excess loss calculations (right). The width and length of the MMI are 2.74 μm and 34.5 μm respectively. The input and output waveguide widths are 0.8 μm	26
Figure 26. Design details of ring-resonator with MMI's smooth bending and mode-matched interfaces.....	27
Figure 27. Developed software flowchart and important specification.....	29
Figure 28. Simulated optical absorption coefficient, and change of index spectra.....	30
Figure 29. Energy-band structure and the quasi-Fermi levels of a modulator at V=-1 volts.....	30
Figure 30. Calculated change of index versus measured change of index by Zucker et ala around 1.3 mm and 1.5 mm.....	31
Figure 31. Photoluminescence is used for Material quality (Intensity, FWHM), Effective Bandgap (Peak wavelength), Macroscopic uniformity (PL mapping), and • Growth calibration.....	32
Figure 32. X-ray diffraction and simulation are used to assess Material quality (Intensity, FWHM), Strain (Relative peak position), Composition and thickness of the layers (Simulation), and Growth calibration.....	32

Figure 33. Transmission Electron Microscopy is used to assess Material thickness, Microscopic uniformity, and Interface abruptness.	33
Figure 34. Schematic of the measurement setup.	33
Figure 35. (a) Change of index versus wavelength for different voltage bias, and (b) Change of index versus voltage bias for different wavelengths.	34
Figure 36. Comparison of experimental and theoretical data. Adjustable parameters for the model were: Structure (from x-ray simulation), Linewidth broadening and band edge (from measured loss), Internal field (from device modeling).	35
Figure 37. Stepped Quantum Well performance compared with a standard quantum well.	35
Figure 38. Performance of the stepped QW compared to the published data.	36
Figure 39. Schematic of completed device with Cytop planarization.	37
Figure 40. BCB Sidewall delamination after planarization etch.	37
Figure 41. Process flow for planarization with Cytop.	38
Figure 42. SEM image of sub- μ m waveguide planarization with Cytop dielectric.	38
Figure 43. SEM image of sample with Cytop planarization and metal contact.	39
Figure 44. Three-ring modulator structure.....	40
Figure 45. Initial electromagnetic simulation of three-ring modulator. Phase delays between adjacent rings. Overall delay is 42 ps +/- 2 ps across band.	41
Figure 46. Calculated transmission (amplitude and phase) of a simple ring-resonator with one access waveguide. The coupler have a splitting ratio of 0.5:0.5 (left) and 0.05:0.95 (right). The excess loss of the resonators are 0.05 (left) and 0.5 (right) per single roundtrip of the light through the ring.	42
Figure 47. Setup to measure transmission and group delay.....	42
Figure 48. Measured transmission and group delay of two ring-resonators. Left: under-coupled resonator (negative group delay at resonance). Right: over-coupled resonator (positive group delay at resonance). Solid: measured; Dashed: calculation.	43
Figure 49. Transmission and group delay of a ring-resonator close to critical coupling. Variations of coupling and/or loss across the measured wavelength span turn the ring from under-coupled at short wavelengths (negative group delay) into over-coupled at long wavelengths (positive group delay).	43
Figure 50. Device layout.....	44
Figure 51. Package design.	44
Figure 52. Transmission a) and group delay b) of a single ring resonator (see Figure 53a). Solid: measured data; Dotted: calculation.	45
Figure 53. Ring resonator in a Mach Zehnder configuration.....	46
Figure 54. a) Transmission of a Mach-Zehnder interferometer with a ring-resonator in one arm . b) Modulation gain (i.e. modulation efficiency as compared to that	

of a straight waveguide of length equal to the ring circumference). Solid: measured data; Dotted: calculation.....	46
Figure 55. (a) The active region is immune from the surface accumulation in a shallow mesa structure. In deep etch mesas however; the effect depends on the mesa width. For a deep and wide mesa (b) the effect is not as significant as for a deep and narrow mesa (c).	47
Figure 56. Energy band structure of (a) $3\text{ }\mu\text{m}$ wide and (b) $0.8\text{ }\mu\text{m}$ wide InP layer with surface charge density of $10^{11}\text{ electron/cm}^2$ and background doping level of $10^{16}/\text{cm}^3$	47
Figure 57. Modeling of the electric field intensity and vector of a deeply etch p-i-n modulator structure (a) without surface accumulation and (b) with surface accumulation.....	48
Figure 58. Modulation frequency response of a modulator.....	49
Figure 59. Infrared micrograph of a forward biased device.	50
Figure 60. a) Device structure b) Schematic of the modified MMI-coupler.	51
Figure 61. a) Transmission of a ring-resonator, b) Coupling and loss extracted from transmission measurements from ring-resonators for various MMI joint angles.	52
Figure 62. a) Tuning of the resonance in 1Volt steps. b) Eye diagram of a link with a ring-resonator modulator.	52
Figure 63. Measured Transmission through ring-resonator with a circumference of 1.1 mm and a modified MMI-coupler. The quality factor is 90,000. The finesse is 34 and the optical bandwidth of the resonance is 2.25GHz.....	53
Figure 64. Fabry-Perot oscillation shift in a 2 mm long phase modulator for different bias values.	55
Figure 65. Measured change of index versus reverse bias voltage at different wavelengths.....	55
Figure 66. Change of index versus bias for a linearized phase modulator compared to a conventional phase modulator at $\lambda=1.56\text{ }\mu\text{m}$ and for TE polarization.	56

List of Tables

Table 1. Resonant Enhanced Modulator Component Technologies and Status	2
Table 2. Design Principles for Low- V_π Resonant Enhanced Modulators.....	3
Table 3. Summary of key ring-resonator properties with formulas.....	9
Table 4. Comparison of evanescent couplers and MMI couplers.....	26

Forward

In the early 1990s, the U.S. Department of Defense recognized that the advent of newly commercially available components for optical telecommunications constituted an opportunity to bring the advantages of fiber optics to analog functions such as communications, remoting, and signal processing.

On February 15 and 16th, 1996, Sarnoff Corporation participated in an ARPA workshop entitled *R-FLICS*, organized by Brian Hendrickson and Robert Leheny.¹ In the resulting program, Sarnoff in 1997 demonstrated narrow-linewidth (200 kHz), low relative-intensity-noise (RIN < -152 dBc/Hz over 0-10 GHz), high-power (200 mW) distributed feedback lasers and, additionally, a mode-locked laser. These components were delivered under subcontract to Uniphase for photonic synthesis as part of the first R-FLICS program. Sarnoff presented two papers reporting these results on January 13th-15th, 1998 at the *Eight Annual DARPA Symposium on Photonic Systems for Antenna Applications* (PSAA-8), at the Naval Postgraduate School in Monterey, CA. (Session Three).

The importance to RF-photonics of high-efficiency, i.e., “low- V_π ”, modulators was stressed at several PSAA meetings. Coincidentally, Sarnoff had initiated research activities on semiconductor ring lasers and passive resonators. At PSAA, Sarnoff suggested to one government organization the benefits of introducing ring resonators to modulators. It was speculated that recirculating light beneath a single ring resonator electrode could provide higher modulation efficiency compared to a standard lumped-element modulator in which light passes beneath the electrode only once. This particular speculation eventually proved incorrect because the dwell time of photons beneath a given electrode determines both modulation depth and modulation efficiency regardless of the recirculation effect.²

During January 26th-27th, 1999, Sarnoff Corporation participated in a second workshop organized by Robert Leheny.³ He led a discussion concerning performance requirements for lasers, modulators, and photodetectors to enable the transport of RF signals over fiber optic links at performance levels attractive to RF system engineers. Of the three components, lasers and photodetectors in 1999 were already at or near the necessary level of performance. Modulators were not: the voltage necessary to obtain a given degree of optical modulation, denoted by V_π ,⁴ was excessive. For example, Northrop-Grumman⁵ stated that noise figures below 5 dB for a 10 GHz link using 20 mW optical power required $V_\pi < 138$ mV. However commercial modulators at 10 GHz have V_π of at least 10 times larger than this value (i.e., several volts). Northrop-

¹ ARPA/ETO RF-Lightwave Integrated Circuits (R-FLICS) Workshop held at Booz-Allen Hamilton in Crystal City, VA

² This point was independently recognized by R.C. Williamson of MIT Lincoln Labs who discussed it with Sarnoff at the October, 2000 DARPA/MTO Optoelectronics Review in Cincinnati, OH and may have published this as a theoretical work.

³ DARPA/ETO Workshop on R-FLICS held at the Hyatt Regency in Crystal City, VA.

⁴ For a Mach-Zehnder modulator V_π is the voltage swing required to alter from the fully transmissive to fully opaque states. The notation refers to the π required phase shift.

⁵ Dr. Akis Goutzoulis, *Microwave Photonics Needs for Future Communication Phased Array Antennas*

Grumman further discussed other system architectures that required V_{π} as low as ~ 100 μ V. The workshop highlighted the need for a high-efficiency, low-insertion-loss, ≥ 10 GHz electro-optic modulator device.

Several months later, Sarnoff proposed a traveling-wave implementation comprising multiple ring resonators. The new principle contained in this proposal was the use of a discretized traveling wave geometry, the benefit of which is reducing electrode capacitance for a given V_{π} as compared to a conventional traveling wave electro-optic modulator. The resulting DARPA R-FLICS *Resonant Enhanced Modulator* program had as its purpose the exploitation of micro-optical ring resonators to obtain dramatic performance improvements for electro-optic modulators.

Preface

The three-year DARPA R-FLICS *Resonant Enhanced Modulator* program concentrated on designing and demonstrating micro-ring resonator waveguides, waveguide couplers, high-performance indium phosphide modulator materials, nanofabrication techniques (to create low-loss micro-resonators), processing techniques (to create suitable RF transmission lines and electrodes for 10 GHz operation), and integrating these demonstrations to create a modulator of $V_\pi < 250$ mV. Sarnoff was to deliver 12 REM devices after three years. The University of Illinois at Urbana-Champaign (UIUC), under Prof. I. Adesida, was to provide nanofabrication expertise and resources, which were lacking at Sarnoff. The program was initially proposed to DARPA/MTO in July 1999, and began in June 2000. The contracting officer's representative was James Nicther, U.S. Air Force Research Laboratory, Rome, NY. Owing to unique resource limitations described below, the program ended without reaching its goal of demonstrating low- V_π resonant enhanced modulators.

The purpose of this report is to provide detailed information on the successful demonstration activities listed above.

Acknowledgments

Performed for

U.S. Air Force Research Laboratory, Rome, NY,
James Nichter, Contracting Officer's Representative

Funded by Defense Advanced Research Projects Administration, Microsystems Technology Office, Program Manager, Radio Frequency Lightwave Integrated Circuits Program:

DARPA/MTO R-FLICS Program Managers:

David A. Honey (inception – 12/00);
William Schneider (1/01 – 3/03);
John Zolper (3/03 – 5/03);
James D. Murphy (5/03 – present).

Army Research Laboratories, Adelphi, MD, provided Sarnoff with access to its e-beam writer under the supervision of Dr. Alma Wickenden. A CRADA was established for this purpose. The ARL e-beam writer was used extensively in the development of the micro-ring resonator technology reported here. Dr. Allen N. Lepore, who departed ARL to join Sarnoff in May 2001, facilitated the interaction.

1. Summary

1.1. Introduction

The Resonant Enhanced Modulator (REM) program had as its purpose exploiting micro-optical ring resonators to obtain dramatic performance improvements for electro-optic modulators.

The REM (Figure 1) has the advantage of providing dramatically lower capacitance than a conventional traveling wave modulator (Figure 2). Significantly less reactive loading is introduced by the electro-optic ring modulators as compared to a conventional traveling wave modulator of the same V_π . For a traveling wave modulator, V_π , inversely, and the waveguide propagation loss component of insertion loss directly, are proportional to optical propagation delay through the modulator.

For any modulator, performance is limited by electro-optic coefficient, RF electrode loss, and optical waveguide propagation loss. Where the losses of RF electrodes dominate, specifically those in contact with the semiconductor, the REM offers significant advantages over a conventional traveling wave modulator.⁶ This typically arises for low-optical-propagation-loss waveguides. The explanation is that the capacitance of the ring modulator electrode is inversely proportional to the enhancement factor of the ring, defined as the photon lifetime in the coupled ring divided by the propagation time for a single circuit around the ring.

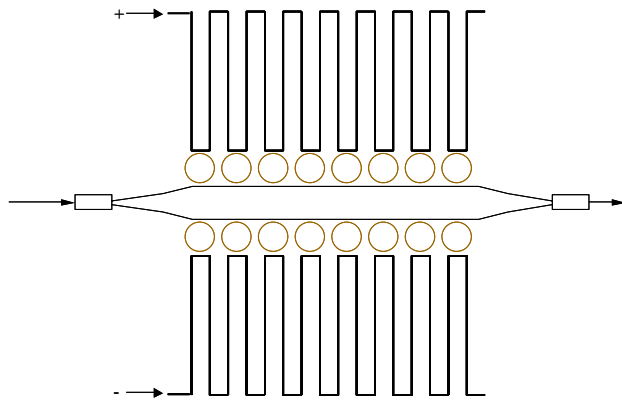


Figure 1. Schematic of Resonant Enhanced Modulator. From left to right, optical signal enters, is split in a coupler, interacts with several ring resonators, recombines in a second coupler, and exits. The RF modulation signal is push-pull modulated on the upper and lower array of ring resonators, which are electro-optically modulated. The RF propagation delays denoted by serpentine RF electrode patterns are matched to the optical delay in the ring resonators, where light circulates multiple times on average.

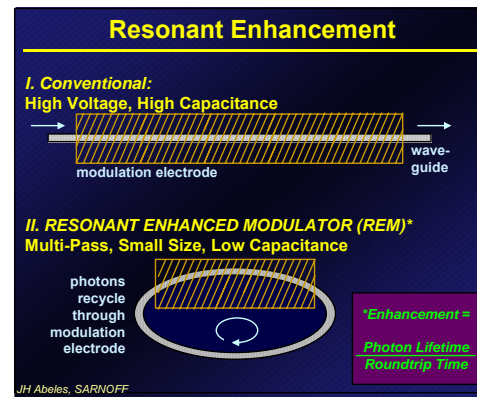


Figure 2. Nature of resonant enhancement is low capacitance.

⁶ Alternatively, in the case where the RF electrode loss is not a limitation, the REM may not offer an advantage over a conventional traveling wave design.

1.2. Device Concept as Proposed

1.2.1. Requirements for Low- V_π Resonant Enhanced Modulator

The REM relies upon high quality indium-phosphide-based ring resonators and an RF electrode able to supply properly phased RF signals to each modulator. The rings must exhibit low bending losses. The photon lifetime in the rings must be small compared to the inverse of the modulation frequency.

Table 1. Resonant Enhanced Modulator Component Technologies and Status

	Component Technology	Status at Program End
1	Low-loss deeply etched InP-based waveguides	Complete Demonstrated excellent sidewall verticality and smoothness
2	High-modulation-efficiency InP-based material	Complete Achieved ~3x better electro-refractive coefficient material than ever reported before.
3	Low-loss input/output ring/waveguide couplers	Complete Developed first low-loss multi-mode interference (MMI) couplers suitable for micro-ring resonators
4	Low-capacitance processing	Complete Developed self-aligned contact scheme allowing electrical contact to the top of a ~1 μ m ring waveguide
5	Planarization	Complete Developed planarization technique relying on Cytop dielectric to permit encapsulation of micro-ring resonators without separation from ring sidewalls, and allowing low-capacitance electrical contacts and RF waveguides to be integrated.
6	Packaging	Complete Carried out detailed mechanical/thermal/optical design of butterfly package for REM modulator
7	RF waveguide	Complete Carried out detailed design for REM RF waveguide
8	High-speed ring modulation	Incomplete <i>Modulation speed for a single ring not achieved. Surface states and/or leakage across the p-n junction, (exposed during deep etching of the InP-based waveguide) are responsible. Limitation of funds prevented Sarnoff from implementing solutions for this problem which has been addressed by others in the field.</i>

1.3. Status of Resonant Enhanced Modulator Development

Table 2 summarizes the statuses of the component technologies to realize a working low voltage ($V_\pi = 0.25$ V) resonant enhanced modulator. Most of REM component technologies were completely developed during the program.

At the conclusion of the program, Sarnoff had demonstrated all component technologies necessary to realize a REM with the exception of high-speed modulated large-index-contrast

waveguides. Such waveguides have been demonstrated by other groups and reported in the literature, but owing to limited funds could not be demonstrated under the present program. Accordingly, there was also no opportunity to verify that the RF electrode structure could be correctly fabricated.

During the program certain limiting cases for modulators were recognized:

Table 2. Design Cases for Low- V_π Resonant Enhanced Modulators

Limiting factor	Consequence
1 Insertion Loss of On-Chip RF Electrodes	<p>A multiple-ring Resonant-Enhanced Modulator geometry combined with low-loss RF electrodes is an effective solution.</p> <p>The conventional high-loss RF electrode/waveguides are replaced by low-loss RF waveguides situated on a planarized Cytop layer above the modulator waveguide. The lower capacitance of the micro-resonator elements allows sufficient RF design flexibility, freeing the RF waveguide design from meeting the requirements of an electrode (i.e., freeing the design from conventional limitations of typical on-chip metalization).</p>
2 Propagation Velocity Mismatch between Optical Waveguide and On-Chip RF Waveguide/Electrode	<p>Properly designed multiple-ring RF waveguide and micro-resonator modular designs can reduce velocity mismatch to negligible levels.</p> <p>As above, separation of the RF waveguide function from the electrode functions</p>
3 Optical Waveguide Loss	<p>It is a general principle that, for a given insertion loss, the maximum modulation will be limited by the optical waveguide propagation loss. This is also the case for a resonant enhanced modulator. There is no advantage, with respect to modulation index for a given insertion loss, to re-circulating photons within the resonator.</p> <p>However, the benefit of resonant enhancement is the reduction of electrical loading by electrodes in contact with the electro-optic waveguide. Using this benefit, the limitations of conventional electro-optic modulators due to optical propagation loss can be surpassed using resonant enhancement.</p> <p>Resonant enhancement provides a higher input impedance as presented to the RF signal. Therefore, dramatically lower V_π can be achieved using an RF transformer to “step-up” the input voltage. This would <i>not</i> be possible for a conventional electro-optic modulator because of the capacitive loading of the electrodes is too great (capacitance is reduced by a factor of 10, for a given modulation, when photons circulate 10 times on average in the resonator).</p> <p>Sarnoff has demonstrated deeply etched waveguides of exceptionally low loss (0.1 cm^{-1})</p>
4 Modulation Bandwidth	<p>The maximum frequency of modulation determines the maximum <i>finesse</i> (i.e., resonant enhancement) that can be usefully employed for a ring of a given diameter. For higher modulation bandwidths, the ring circumference must be smaller and more rings must be used to achieve a given V_π performance.</p>
5 Coupler Loss	<p>The optical loss present in the couplers between micro-resonators and input/output waveguides limits the number of resonators that can usefully be cascaded while maintaining adequate insertion loss.</p> <p>Sarnoff has obtained MMI coupler loss under 10%. Lower coupler losses are possible in further work.</p>

1.4. Summary of Accomplishments by Year

1.4.1. Program Timeline

Year 1:

- Demonstrated high-quality ring fabrication
- Demonstrated high-Q ring resonators (13,000)

Year 2:

- Demonstrated high-performance indium-phosphide-based stepped quantum well modulator material
- Implemented nanofabrication at Army Research Laboratory

Year 3:

- Demonstrated planarization processing using Cytop dielectric
- Demonstrated MMI couplers

1.4.2. Key Accomplishments

- Sarnoff demonstrated indium-phosphide-based stepped quantum well materials having about 3x lower modulation voltage than the best previously reported materials.
- Sarnoff developed new nanofabrication techniques to define and etch high-refractive-index-contrast waveguides and process them into electro-optic modulators.
- Sarnoff demonstrated the first multi-mode-interference-coupled ring resonators, the first laterally-coupled indium-phosphide-based ring resonators, and the first electro-optically modulated semiconductor ring resonators.
- Sarnoff designed and created mask designs for REM modulators.
- UIUC demonstrated detailed characterization of deeply anisotropically etched nanofabricated waveguide ridges.

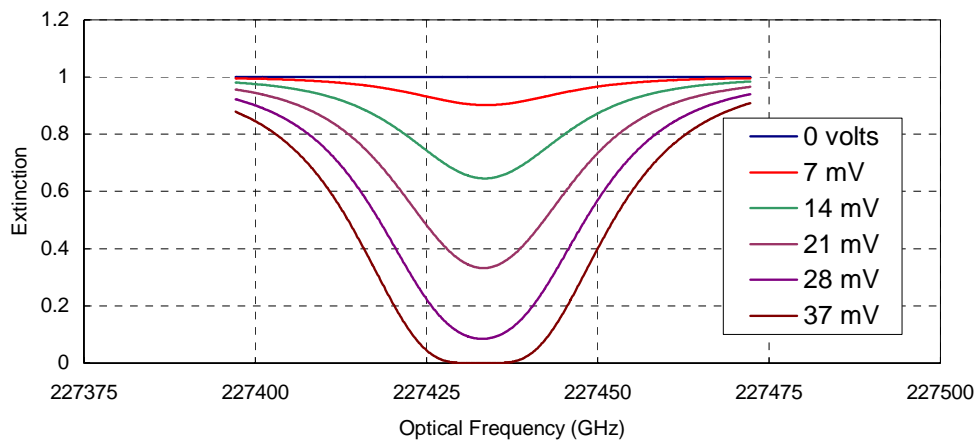


Figure 3. (Figure 13 From Original Proposal, Appendix A) Transfer Curves for Resonant Enhanced MZ Modulator, 95% reflectivity. Modulator consists of Mach-Zehnder structure with 8 resonant micro-optical phase shifters coupled to each arm and is driven push-pull. Photon lifetime is 9x the round-trip time for each resonator. Electro-refractive coefficient is taken from Zucker et al.¹

1.4.3. Key Personnel

Sarnoff Corporation

Joseph H. Abeles – Principal Investigator

Martin H. Kwakernaak – Modulator and Ring Resonator Design and Testing

Hooman Mohseni – Modulator material design and characterization

Alan. N. Lepore – Advanced nanofabrication and advanced process development

Giora Griffel – Ring resonator concept

Daniel W. Bechtle – RF electrode design

University of Illinois at Urbana-Champaign

Ilesanmi Adesida – Professor

Sean Rommel – Postdoctoral Associate (now Assistant Professor at Rochester Institute of Technology)

Jae-Hyung Jang – Postdoctoral Associate (now Assistant Professor, Kwangju Institute of Science and Technology, Korea)

Jeong-Woon Bae – Postdoctoral Associate

Weifeng Zhao – Graduate Research Assistant

1.5. Resource Issues During the Program

Four significant resource issues arose during this program:

Attainment of micro-ring resonators during Year 1:

The program was proposed based on the use of UIUC electron beam lithography for patterning. Similarly, the proposal relied upon the use of UIUC inductively coupled plasma etching facilities. It was expected that this could be accomplished in a few months using existing technology UIUC had published and for which it was known. In fact, however, after one year it was recognized that the program had incurred a significant delay owing to the need to train a new postdoctoral student at UIUC and the limited availability of access to the lithography and etching capabilities at UIUC. In addition, the UIUC principal investigator had been appointed director of a large microelectronics laboratory at UIUC, limiting his availability to support the REM program.

During the entire first year, the Sarnoff team was unable to make adequate progress owing to the absence of samples from UIUC. Until just before the PI review at the end of the first year (in summer, 2001 at the LAX Embassy Suites South), Sarnoff had not received a useful ring resonator sample from UIUC.

At the same time, Sarnoff hired A. N. Lepore, who was departing Army Research Laboratories. Dr. Lepore is a world expert in electron beam lithography and associated semiconductor processing issues. With Dr. Lepore on our staff, Army Research Labs was willing to allow

Sarnoff access to its facilities in Adelphi, MD. Dr. Lepore began a weekly trip to ARL to perform e-beam writing. In exchange for granting access to Sarnoff, ARL required Dr. Lepore to provide support services for which he was eminently qualified, having worked with that equipment for years and possessing more know-how than anyone else at ARL.

Three other factors affected the resources available for this program:

During the latter portion of the program, Sarnoff sought to end the UIUC contract, thereby saving approximately \$75K in program costs needed to complete it. According to UIUC, financial resources representing this amount were unspent as of November 2002. However after receiving Sarnoff's official instruction to terminate, UIUC characterized all its authorized funds as having been spent. This jeopardized, and in fact prevented, completing the program. It is important to note that Sarnoff was expending effort in microfabrication that was to have been performed by UIUC, and as a consequence incurred extra costs beyond the original plan.

In addition, DARPA removed approximately \$50K from the program as compared to the originally proposed cost.

Finally, during the period from 1999, when the REM program was originally proposed, until 2003 when it was to have ended, business conditions for Sarnoff necessitated an increase in our rates, such as those for overhead and for general and administrative costs. The impact to the program can be estimated to be similar to the above numbers.

In sum, resources originally expected to be sufficient to complete the REM program were perhaps \$200K to \$400K less than needed as a result of all the previously noted factors that could not have been anticipated.

1.6. Recommendations for Further Work

Sarnoff has made significant advances towards demonstrating a Low V_π modulator. The REM program should be continued. In addition, conventional Mach-Zehnder modulators should be built from the superior materials demonstrated and developed at Sarnoff during this program.

Finally, mode-converters need to be integrated to attain low insertion loss. The total amount of work to accomplish these items is significant in terms of the originally planned REM program, ranging from 15% to 30% additional funding.

2. Methods, Assumptions and Procedures

2.1. Micro-Ring Optical Resonators

2.1.1. Marcatili Proposal

E. Marcatili in the Bell System Technical Journal first proposed photonic ring resonators approximately 30 years ago. Integrated photonic ring resonators were not aggressively pursued for many years. One of the limitations was the absence of a technology for high-index-contrast waveguides capable of low bending loss. To bend waveguides with radii of 100 μm or less, high index contrast is required. Conventional ridge waveguides in indium phosphide or gallium arsenide materials provide only relatively small index contrasts in the range of 0.02 or less. To attain proper bending in planar waveguides required introducing advanced lithography and etching capabilities.

Ring resonators are different from Fabry-Perot resonators because they provide four ports instead of two, and can be integrated in large quantities on a planar substrate.

2.1.2. Microspheres

Before introducing excellent planar ring resonators, experiments were conducted in glass microspheres by Giora Griffel (then at Polytechnic University) and other workers. Extremely high quality factors (Q 's) could be attained. Griffel brought his interest in microspheres to the planar micro-ring resonators at Sarnoff.

2.1.3. Summary of Other Work (post 1996)

Around 1996, a workshop was held at Crested Butte to discuss micro-ring resonators, co-organized by Griffel. The workshop sparked further interest. Since then several groups became active in this field. Northwestern University demonstrated extremely tight radius microresonators and small couplers. Caltech demonstrated further advances in microspheres. The University of Maryland collaborated with MIT to demonstrate high quality planar resonators in both semiconductor and glass, and the University of Maryland demonstrated nonlinear properties of microresonators in semiconductors. USC demonstrated vertically coupled indium phosphide based microdisk resonators based on a wafer bonding technique. Sarnoff developed vertical-coupled microresonator techniques that were transferred to spin-off Princeton Lightwave, Inc. and USC.

2.2. Micro-Ring Resonator Modulators

2.2.1. Governing Principles

Figure 4 shows a schematic of a multi-ring resonator modulator. The optical light travels through a Mach-Zehnder interferometer. Modulation of the refractive index in the ring-resonators results in a phase modulation of the light in the interferometer arms, which translates into amplitude modulation at the output. The design of the RF delay line and the optical waveguides and resonators ensures that the RF and the optical delay from ring to ring are identical.

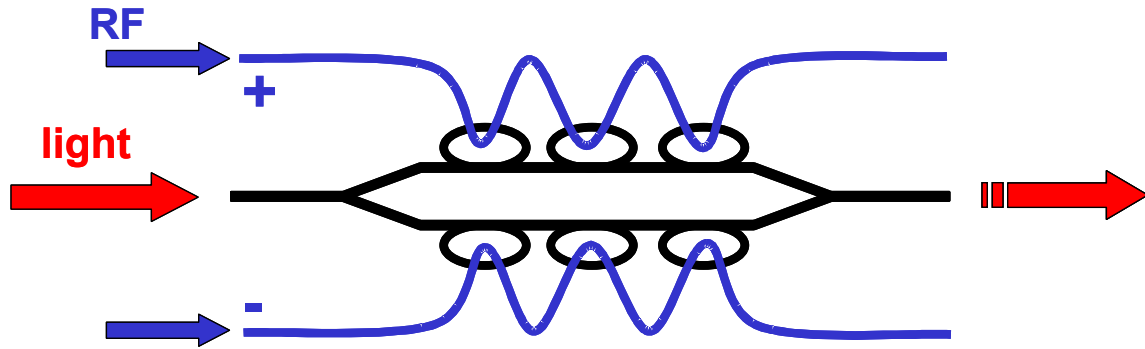


Figure 4. Schematic of multi ring- resonator Mach-Zehnder modulator.

This device is an assembled ring resonator. A schematic of a single ring resonator is shown in figure Figure 5. It consists of a coupler and a ring-waveguide. The most basic parameters of this resonator are ring-circumference, coupling and loss. All resonator properties can be derived from these values as summarized in table Table 3.

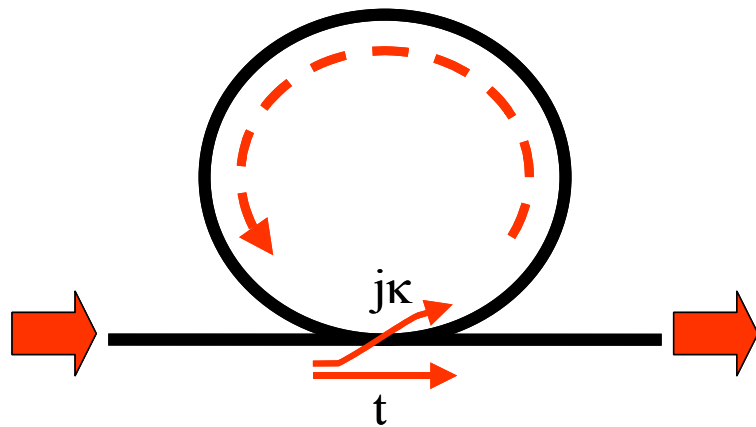


Figure 5. Schematic of single ring-resonator.

Table 3. Summary of key ring-resonator properties with formulas.

Transmission	$T = \frac{t - a e^{(j2\pi ln_{eff}/\lambda)}}{1 - t a e^{(j2\pi ln_{eff}/\lambda)}} \text{ (complex transmission)}$ $ T ^2 = \left(\frac{t - a}{1 - t a} \right)^2 \text{ (power transmission at resonance)}$
Group delay	$\tau_g = \frac{ln_g}{c} \Re \left\{ \frac{a \kappa^2 e^{(j2\pi ln_{eff}/\lambda)}}{\left(1 - t a e^{(j2\pi ln_{eff}/\lambda)}\right) \left(t - a e^{(j2\pi ln_{eff}/\lambda)}\right)} \right\}$ $\tau_g = \frac{ln_g}{c} \frac{(t^2 - 1)a}{(1 - t a)(t - a)} \text{ (at resonance)}$
Free spectral range	$FSR_\lambda = \frac{\lambda^2}{n_g l} \text{ (in units wavelength)}$ $FSR_f = \frac{c}{n_g l} \text{ (in units frequency)}$
Finesse	$finesse = \frac{FSR}{optical\ bandwidth} = \frac{\pi}{\cos^{-1} \left(\frac{2at}{1 + a^2 t^2} \right)}$
Quality factor	$Q = \frac{\lambda}{\lambda_{fwhm}} = \frac{\pi n_g l}{\lambda \cos^{-1} \left(\frac{2at}{1 + a^2 t^2} \right)}$
Optical Bandwidth	$\lambda_{fwhm} = \frac{\lambda^2}{\pi n_g l} \cos^{-1} \left(\frac{2at}{1 + a^2 t^2} \right) \text{ (in units wavelength)}$ $f_{fwhm} = \frac{c}{\pi n_g l} \cos^{-1} \left(\frac{2a\kappa}{1 + a^2 \kappa^2} \right) \text{ (in units frequency)}$
RF Bandwidth	$f_{3dB} = \frac{1}{2} f_{fwhm} \text{ (optical wavelength at resonance)}$
	Ring circumference l Coupler: coupling κ Coupler: through transmission $t = \sqrt{1 - \kappa^2}$ Ring round trip loss $a = \exp(-\alpha/2l)$ Waveguide loss α Wavelength λ Effective index n_{eff} Group index n_g

Figure 6 shows the calculated transmission, phase response, and group delay of a resonator with indications of some of the key properties.

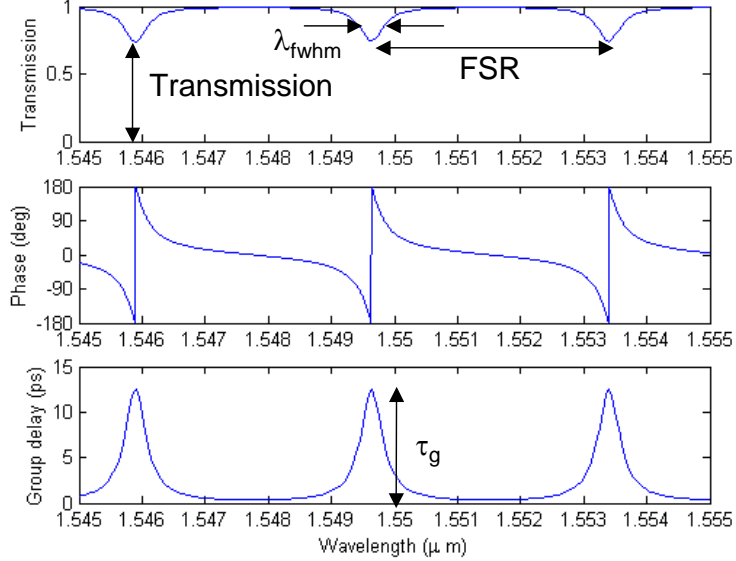


Figure 6. Calculated power transmission, phase response and group delay of ring-resonator.

The phase response to refractive index modulation of a ring resonator can be expressed in a general form:

$$\frac{d\phi}{dn} = \tau_g \frac{2\pi c}{\lambda n}$$

This derives from the fact that an index change has the same effect on the phase as a wavelength change in a waveguide-type device. From this we can define an enhancement of the phase modulation to be the phase response of the resonator divided by the phase response of the waveguide alone.

$$\tau_g = \underbrace{\frac{(t^2 - 1)a}{(1 - ta)(t - a)}}_{\text{Ring enhancement}} \underbrace{\frac{ln_g}{c}}_{\text{Group delay of one roundtrip}}$$

The ring-resonator phase modulation is only enhanced at the resonance. The useful optical bandwidth to obtain phase modulation is the resonance bandwidth.

The RF-modulation bandwidth is limited in a ring-resonator due to the dwell-time of the light in the ring. Modulation of the index in the ring-resonator creates sidebands in the optical spectrum in the ring. (See Figure 7). All relevant sidebands need to be inside the resonator's optical bandwidth to obtain the full modulation.

A small-signal model modeled the modulation frequency response. The model solves the equations for the ring-resonator for the three significant optical components involved (see Figure 7). Simultaneously the coupling of these components as a result of the index-modulation of the ring-waveguide is taken into account. Figure 8 shows the calculated modulation response for a ring-resonator with the wavelength tuned to several positions close to the resonance. The modulation gain is defined as signal amplitude obtained with the ring-modulator divided by the signal modulation obtained with a straight phase modulator of a length, which is equal to the ring-circumference.

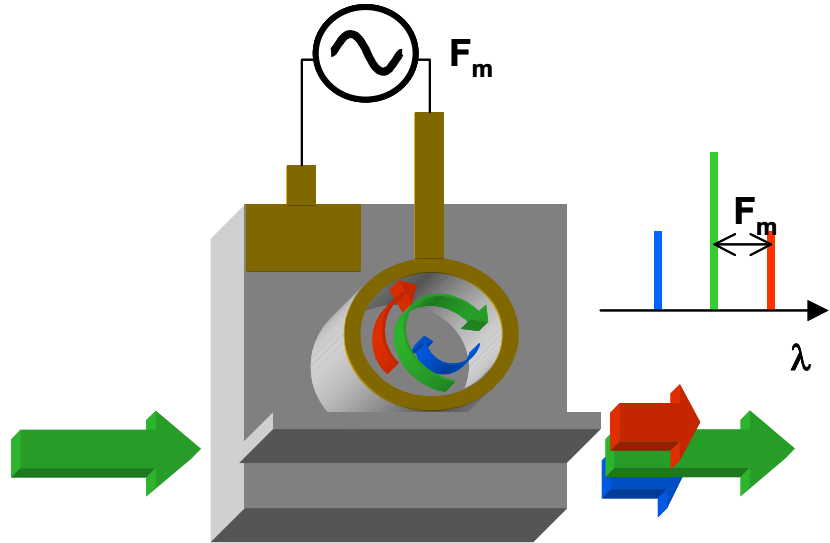


Figure 7. Modulation sidebands in the ring-resonator.

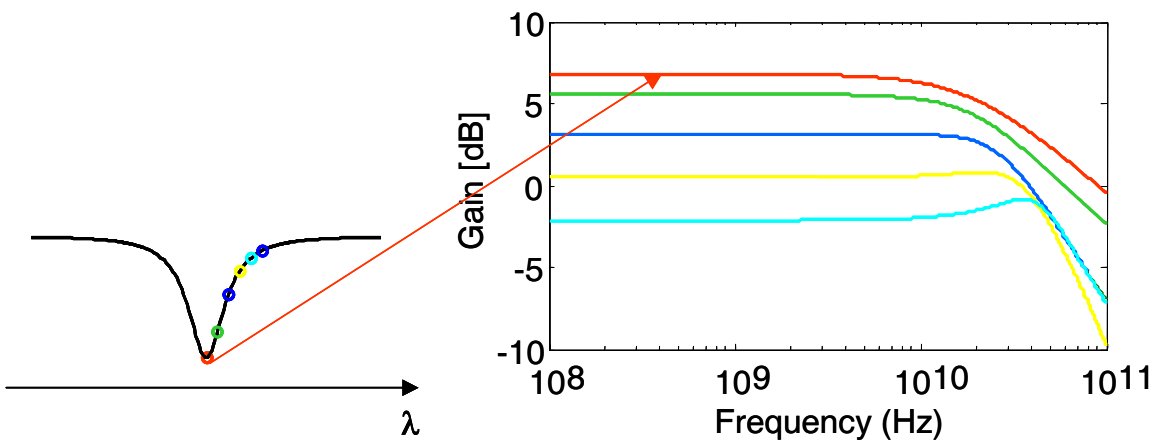


Figure 8. Calculated modulation response.

With this model the 3dB RF modulation bandwidth could be verified to be twice the optical bandwidth of the resonance with the wavelength at resonance.

In addition to the optical cavity bandwidth limitation there is, of course, a bandwidth limit from electrical parasitics. The narrow waveguides and choice of a small ring size pushes the RC frequency limit to large values.

For designing a ring resonator phase modulator, the following strategy was pursued:

- Choose a design with high optical transmission at resonance (to allow for cascading the rings).
- Choose a ring resonator with high enhancement (to obtain maximum modulation at a minimum electrode size).
- The RF-bandwidth requirement (10GHz) limits the Q of the optical resonator.
- Choose a design with an optical group delay, which is not sensitive to fabrication tolerance. This is important since not being able to reproduce the optical group delay makes it impossible to match the RF-delay with the optical delay in multi-ring device.

Specifically one must make a choice of what coupling to choose and what size the ring should be. Figure 9 shows the finesse, the transmission at resonance, and the enhancement of ring-resonators as a function of coupling value and loss in the ring-resonator. The loss is defined as the loss of the light in one pass through the ring waveguide. This includes waveguide loss and excess loss in the coupler, not including the light that escapes the ring through the coupler. The plot in Figure 9 is independent of the ring-size. This graph can be used to choose an operation regime and design of the ring. Losses are to be minimized.

Given a certain loss value that can be achieved, we chose a coupling value where the transmission is high, the enhancement is high, the enhancement is insensitive to the loss (enhancement and group delay are proportional), and where we can fabricate highly reproducible coupling.

We chose a design with 50:50% coupling. This fulfills the above requirements:

- By using MMI couplers we can accurately reproduce 50:50% coupling ratios.
- At a one-pass waveguide loss of < 0.3 the enhancement and group delay is insensitive to loss. 0.3 is practically achievable loss.
- The enhancement is ~ 6 . This yields a reduction of the electrode size by a factor of 6 to obtain the same phase modulation when compared to a straight phase modulator.

The size of the ring is then chosen based on the required bandwidth and parasitic capacitance constraints.

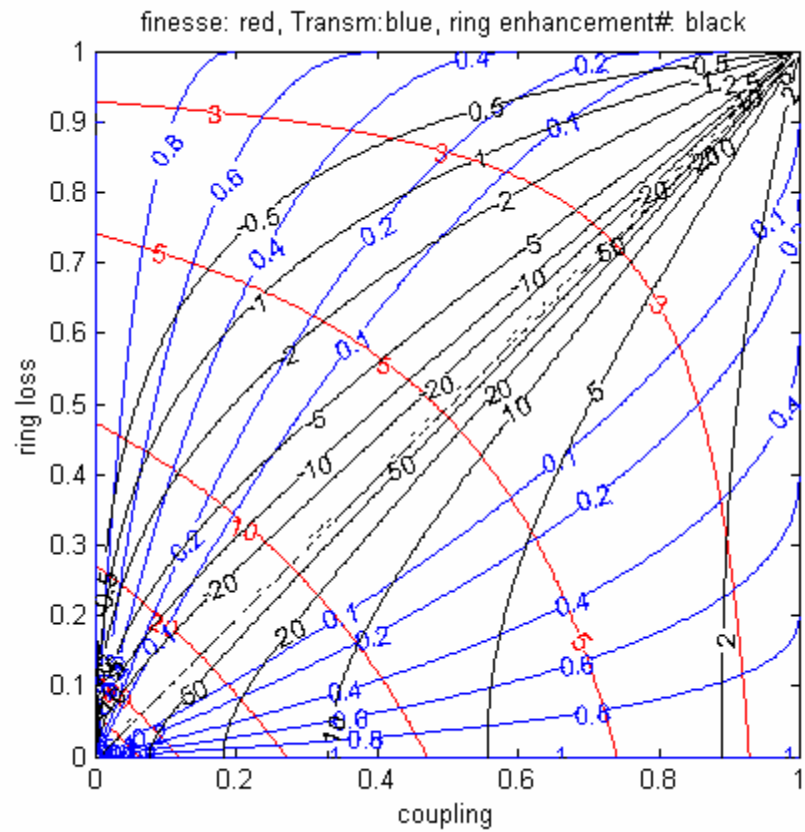


Figure 9. Finesse, Transmission, and ring-enhancement of ring resonator as a function of loss per roundtrip and coupling.

3. Results and Discussion

3.1. Laterally Coupled Resonant Enhanced Modulators

3.1.1. Anisotropic Patterning and Etching

3.1.1.1. Dual Layer Resist

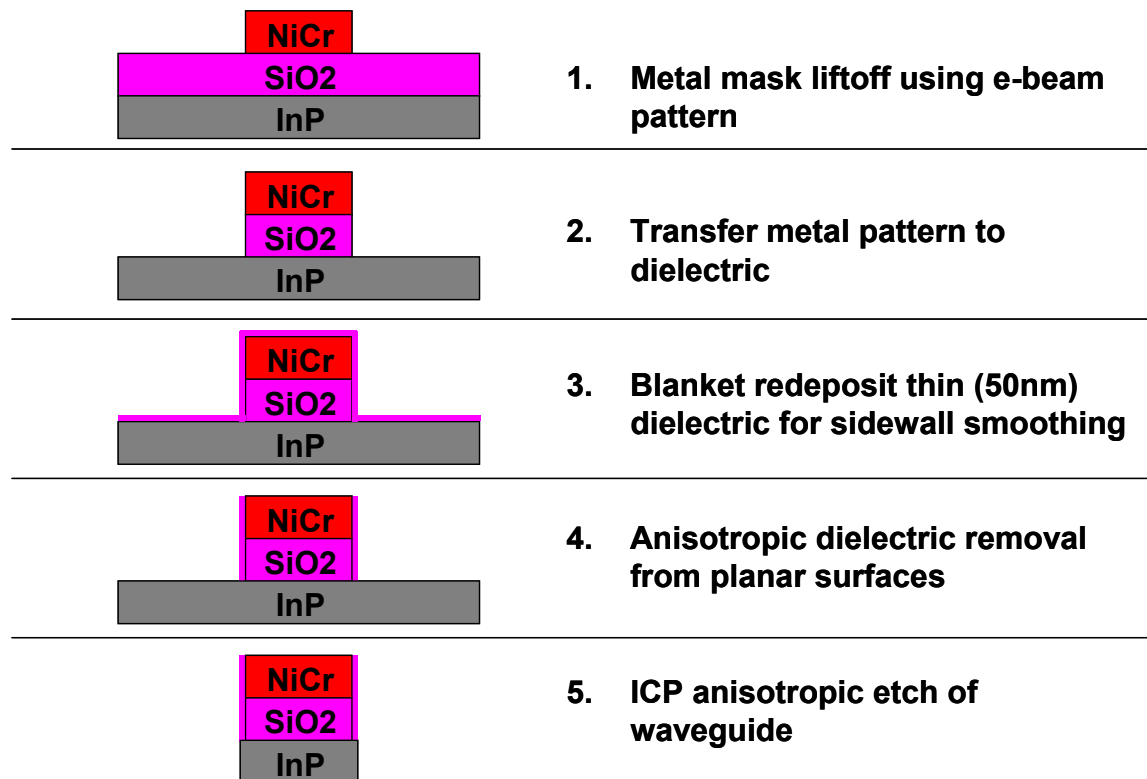


Figure 10. Process flow for the fabrication of sub- μ m deeply etched InP/InGaAsP waveguides.

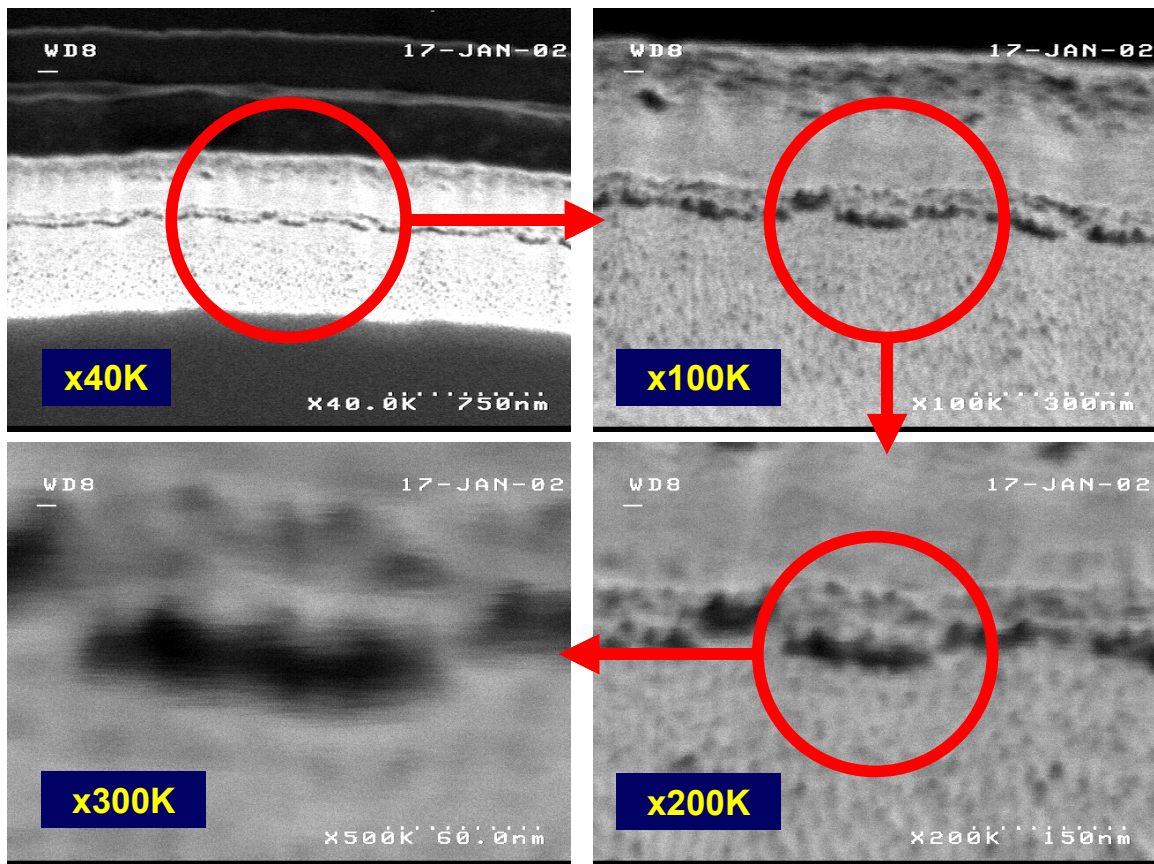


Figure 11. SEM images of etched sidewall.

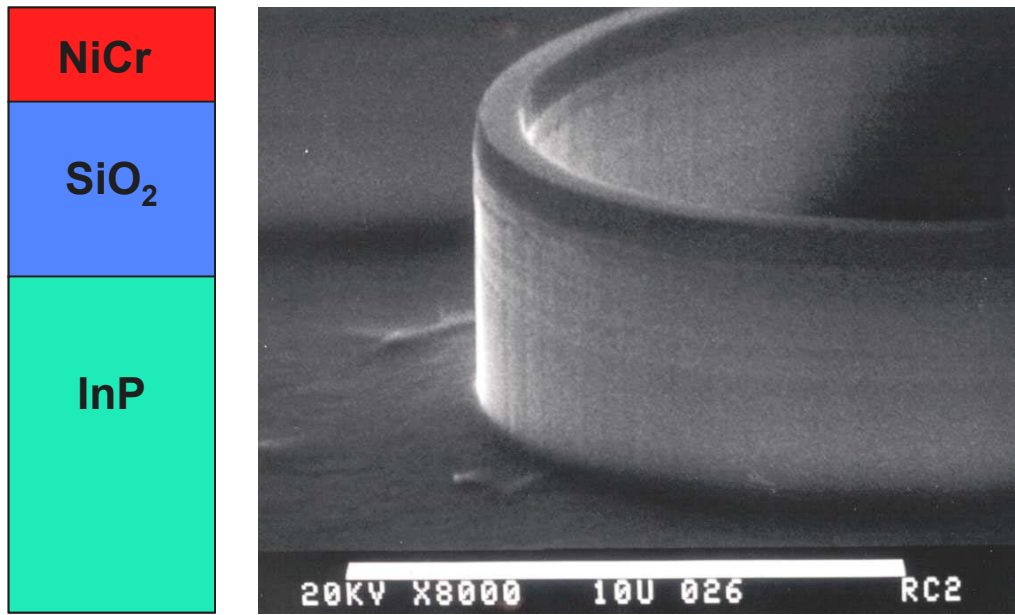


Figure 12. SEM image of ring-resonator waveguide. The NiCr/ SiO_2 mask has not been removed.

3.1.1.2. Edge Acuity

A ring resonator — a fundamental building block of planar lightwave integrated circuits (PLCs) — consists of a straight waveguide segment adjacent to a ring waveguide separated by a narrow air gap. An input signal launched into the straight waveguide segment couples into the ring resonator via the air gap if it is narrow enough to allow a wavefunction overlap (i.e., a spacing < 300 nm). It is desirable to make the ridge waveguide narrow so the structure supports only a single transverse mode, and the tail of the Eigen mode “leaks out” of the ridge to ensure coupling to the resonator. This basic structure acts as a notch filter. When the wavelength is on-resonance, the signal ideally propagates only in the ring; when the transmission is off-resonance, the signal is only transmitted through the straight waveguide.

The key to realizing these structures is developing precision lithographic and dry etching processes, which can produce highly anisotropic structures with high edge acuity and smooth surface morphology. Striations on the edge of the deep-etched waveguides may cause deleterious optical scattering loss and must be minimized. The significant role of sidewall roughness (SWR) in waveguides calls for a thorough quantitative study of their evolution during fabrication. Contributions to SWR engendered by lithography derive from line edge roughness (LER) of the developed resists. In turn, the contributions to LER by the lithography process emanate from its components of resist materials, development process, resist thickness, lithography tool, and exposure strategy. In aggregate terms, the LER can impose itself on mask edge roughness in cases where masks are required to transfer the defined patterns into the waveguide materials. In many cases, metals or dielectrics are utilized as masks. During the process of mask deposition and or etching, the LER of the resist is transferred to mask edge roughness. This is further translated to SWR during the etching of the waveguides. Important parameters in etching such as ion energy have the potential to contribute to SWR through mask edge erosion. Therefore, we emphasize again that the control of lithography and etching processes are essential to the realization of waveguides with minimal SWR.

In our work, we utilized electron beam lithography (EBL) for pattern definition. The high resolution achievable with this technique and the multiple-pass electron beam exposure strategy was utilized in order to minimize LER. For pattern transfer, we developed an etching process based on inductively coupled plasma-reactive ion etching (ICP-RIE) to transfer patterns into InP/InGaAsP heterostructures for waveguide applications. Extensive characterizations of the SWR of the waveguides were performed using atomic force microscopy.

3.1.1.2.1. Waveguide Fabrication

Detailed experimental work was carried out on EBL for pattern definition. Gaps between waveguides in ring resonator structures can be as small or even smaller than 0.25 μm . Therefore, resist process optimizations are needed to achieve these small gaps and minimal LERs. In our experiments with waveguide fabrication, we utilized the JEOL 6000FS electron beam nanowriter with the properties of 50 keV beam energy and 5 nm beam diameter. For etching InP/InGaAsP heterostructures, silicon dioxide deposited by plasma-enhanced chemical vapor deposition (PECVD) was utilized masking purposes. For mask patterning, PMMA-P(MMA-MAA) bilayer electron beam resist system was used for the lift-off of 60 nm-thick NiCr metal mask. The metal mask was used to etch the silicon dioxide in a conventional RIE system with CHF_3 plasma. The

resulting NiCr/SiO₂ was then used as a mask to etch the waveguide heterostructures using Cl₂/Ar/H₂ gas mixtures in an inductively coupled plasma-reactive ion etching (ICP-RIE) system.

3.1.1.2.2. Anisotropic Etching

Etch rates of InP, InGaAs, and various concentrations of InGaAsP were studied in a Unaxis SLR 770 ICP-RIE system in Cl₂/Ar/H₂ gas mixtures. The reactor conditions were 110 W rf power, 900 W coil power, 1.5-mT chamber pressure, and 225 °C substrate temperature. The gas mixture of Cl₂:Ar was fixed at 2:3 and H₂ was varied as a parameter to study its influence on etch profiles. It was determined that H₂ has a strong influence on the etch rates and the profiles of these materials⁷. Three distinct regions of influence were noted with the most important being the region of moderate H₂ flow (i.e. where the composition ratio of Cl₂/Ar/H₂ was between 2/3/1 and 2/3/2) where the chemical etching mechanism of Cl₂/H₂ is balanced by the physical etching mechanism of Ar. This region showed the highest degree of anisotropy in etched profiles in InP structures. Overall, the information derived from the etch rates and profiles was then used to study the etch profiles of waveguide heterostructures. A specific heterostructure designed for waveguiding consisting of .051 μm In_{0.53}Ga_{0.47}As, 1.41 μm InP, 0.3 μm In_{0.86}Ga_{0.14}As_{0.32}P_{0.68}, 0.09 μm In_{0.75}Ga_{0.25}As_{0.54}P_{0.46}, 0.3 μm In_{0.86}Ga_{0.14}As_{0.32}P_{0.68}, and 1.5 μm of InP on a semi-insulating InP substrate was used in the study. A 500 nm-thick SiO₂ mask was deposited on the surface of the sample by plasma enhanced chemical vapor. Submicron waveguides were then patterned by electron beam lithography on the SiO₂ mask and etched in CHF₃. The heterostructure was then etched to determine the resulting profile as a function of H₂ concentration.

The profile in the Cl₂-dominated region exhibits a large undercut. Figure 13 shows a scanning electron microscope micrograph for the extreme case of Cl₂/Ar/H₂ ratios of 2/3/0. As the percentage of H₂ was increased it was observed that the undercut simultaneously decreased. The transition between InP and the InGaAsP layers is not evident in the micrograph. This indicates that the epitaxial layers are etched at approximately the same rates. Highly anisotropic etching occurred for a Cl₂/Ar/H₂ ratio of 2/3/2, in the balanced etching regime. Figure 14 illustrates a section of a racetrack resonator-type structure etched under these conditions. The structure has a linewidth of 0.7 μm, and a gap of 0.275 μm

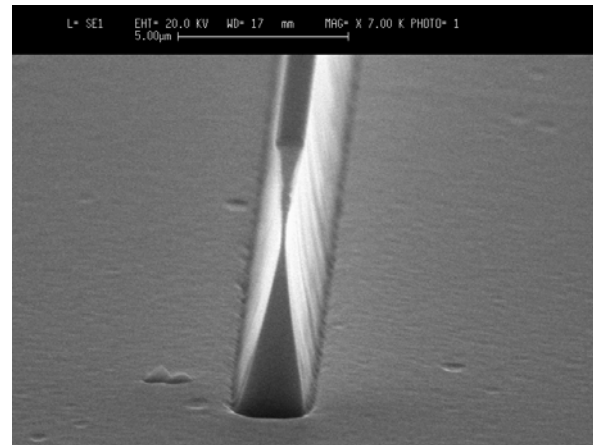


Figure 13. Scanning electron micrograph of a InP/InGaAsP epitaxial layer etched with 110 W RF power, 900 W inductive power, -215 V DC Bias, Cl₂/Ar/H₂ = 6 sccm/ 9 sccm/ 0 sccm, 1.5 mT, and 225°C. These layers exhibit a large undercut of the etch mask, which is still in place.

⁷ S. L. Rommel, J.H. Jang, W. Lu, G. Cueva, L. Zhou, I. Adesida, G. Pajer, R. Whaley, A. Lepore, Z. Schellenbarger, and J. H. Abeles, "Effect of H₂ on the Etch Profile of InP/InGaAsP Alloys in Cl₂/Ar/H₂ Inductively-Coupled-Plasma Reactive Ion Etching Chemistries for Photonic Device Fabrication," *Journal of Vacuum Science and Technology* **B20**, 1327-1330 (2002).

between the line and racetrack. The sidewalls of the structure are very smooth and show little surface roughness as determined by scanning electron microscopy. The gap between the lines appears completely etched. Again, it is difficult to discern the positions of the various epitaxial layers in the micrograph, suggesting that the layers have etched at nearly the same rate. Clearly, this chemistry is optimal for fabricating highly anisotropic waveguides. In the third region (H_2 -dominated, i.e., $Cl_2/Ar/H_2$ ratio of 2/3/3), the etch profiles show a distinct behavior, illustrated in Figure 15. Once again, InP layers suffer from a 0.15 μm undercut. However, it is evident that the addition of H_2 causes InP and InGaAsP/InGaAs epitaxial layers to etch at different rates. Furthermore, InGaAsP epitaxial layers of varying composition are observed to etch at different rates as the etch rate data suggested. Three distinct stripes, corresponding to the 0.3 μm $In_{0.543}Ga_{0.457}As_{0.33}P_{0.67}$, 0.09 μm $In_{0.539}Ga_{0.461}As_{0.55}P_{0.45}$, and 0.3 μm $In_{0.543}Ga_{0.457}As_{0.33}P_{0.67}$ waveguiding region are evident in the center of the micrograph. This regime of etching is unique for revealing the heterostructure's compositional details.

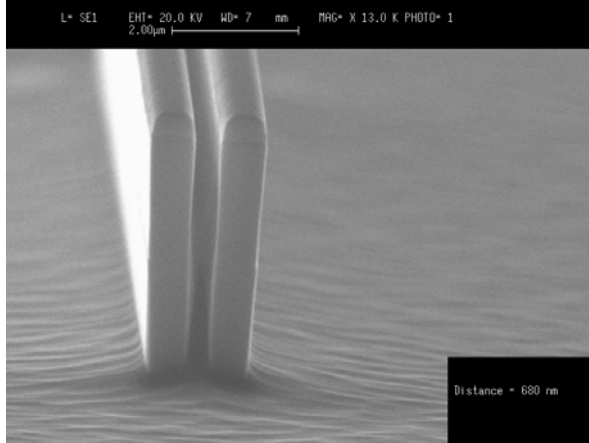


Figure 14. Scanning electron micrograph of a InP/InGaAsP epitaxial layer etched with 110 W RF power, 900 W inductive power, -215 V DC Bias, $Cl_2/Ar/H_2$ = 6 sccm/ 9 sccm/ 6 sccm, 1.5 mT, and 225°C. The width of the etched segments is 0.7 μm , the gap is 0.275 μm . The etch depth is 4 μm .

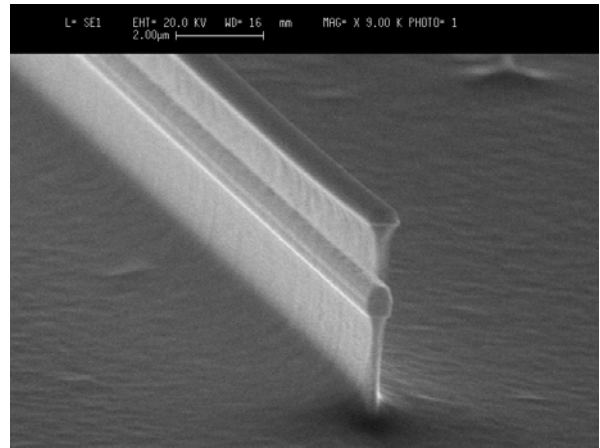


Figure 15. Scanning electron micrograph of a InP/InGaAsP epitaxial layer etched with 110 W RF power, 900 W inductive power, 215 V DC Bias, $Cl_2/Ar/H_2$ = 6 sccm/ 9 sccm/ 9 sccm, 1.5 mT, and 225°C. InP layers show large undercuts whereas InGaAsP layers show little lateral etching.

For waveguiding applications, the highly anisotropic etching regime is the most appropriate for realizing devices. A ring resonator device fabricated in the same heterostructure using the etching method described above is shown in Figure 16. In this design, a straight segment length of 90 μm is used to enhance the coupling between the straight guide and the ring. The ridge width was $\sim 0.9 \mu m$, and the air gap had a width of 0.275 μm . A radius of 15 μm was used in the curved regions. The structure was etched with the optimized $Cl_2/Ar/H_2$ etch to a depth of 4 μm .

3.1.1.2.3. Sidewall Roughness

Sidewall roughness contributes significantly to waveguide optical scattering losses. For an accurate estimation of scattering losses, it is cardinal to obtain quantitative SWR measurements.

Although attempts have been made using various techniques such as scanning electron microscopy (SEM) and transmission electron microscopy (TEM) to measure SWR, these techniques, at best, have utilized indirect means of estimating SWR. Some measurements translate the edge acuity realized from lithography reflected in the LER of resist or mask as being the SWR of waveguides. This is especially untrue for deep-etched waveguides. In our work, we have utilized atomic force microscopy (AFM) to directly characterize SWR of large areas of the sidewalls of deep-etched high-mesa InP/InGaAsP structures⁸.

A specially designed line pattern, schematically shown in Figure 17 (a), is delineated in parallel with the crystal orientation of InP by electron beam lithography. The staircase patterns allowed the cleavage of the sample to result in at least one segment of the waveguides being very close to the cleaved wafer edges so an AFM tip can easily access the sidewalls of the waveguides in the direction perpendicular to the sidewall (see Figure 17 (b)). With the AFM tip normal to the etched sidewall, the feedback loop of the z -directional movement of the AFM tip is still effective and needs no modification in the control loop. The resolution of the AFM is highest in the direction of the surface normal. Therefore, this configuration allows an AFM tip full access to the sidewall, resulting in full high resolution imaging of the sidewall. Of course, this is a destructive measurement; therefore, a test wafer must be utilized for this purpose.

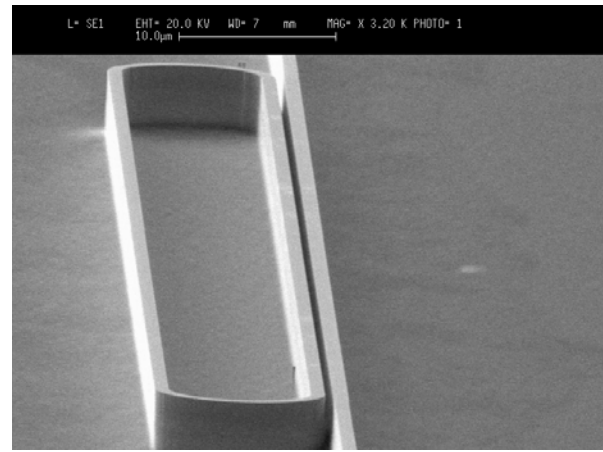
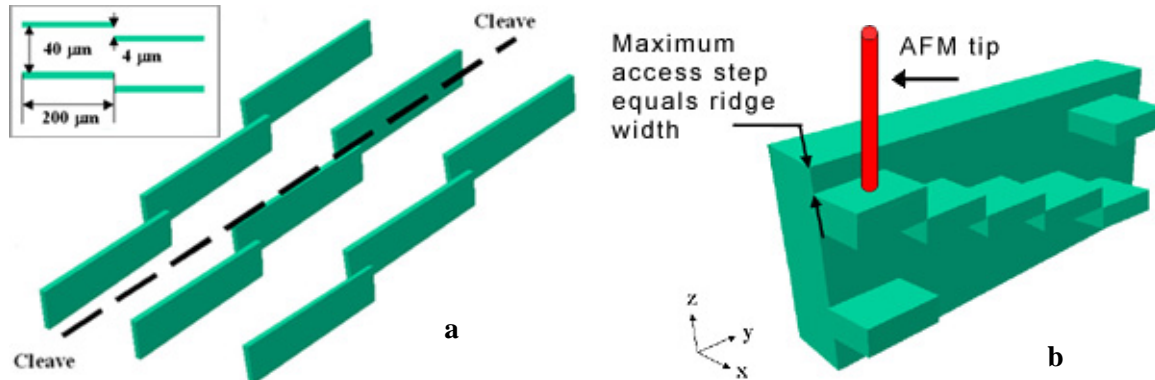


Figure 16. SEM micrograph of an InP/InGaAsP race-track resonator. The ridge is etched to a depth of 5 μm , and has a width of 0.9 μm and gap of 0.275 μm .

⁸ J.-H. Jang, W. Zhao, J.-W. Bae, D. Selvanathan, S. L. Rommel, I. Adesida, A. Lepore, M. Kwakernaak, and J. H. Abeles, "Direct measurement of nanoscale sidewall roughness of optical waveguides using an atomic force microscope," *Applied Physics Letters* **83**, 4116-4118 (2003).

Figure 17. (a) General schematic for test pattern showing staggered segments 200 μm long and staggered by 4 μm . (b) Perpendicular measurement of the sidewall is performed on the cleaved sample thereby preserving the z-directional movement of the AFM tip.

Figure 18 shows the specially designed lines, as illustrated in Figure 17 (a), which have been defined and etched in InP/InGaAsP. An ultra-sharp AFM tip (typical diameter of curvature was ~ 10 nm both silicon nitride and carbon nanotube tips) was utilized to carry out high fidelity sidewall profiling. Figure 19 (a) and (b) show typical SEM and AFM images of the sidewalls of waveguides etched up to 4 μm deep and Figure 19 (c) shows an AFM image of the sidewall of the InP substrate cleaved along the (100) crystal orientation. In the AFM images of the waveguide sidewalls, vertical striations on the sidewall are clearly visible. The striations begin at the top of SiO_2 mask layer and are transferred down to the bottom of the scanned sidewall. The origin of the vertical striations is ascribed to the line edge roughness (LER) of the etch mask. It is expected that mask erosion caused by ion-bombardment during ICP-RIE etching adds to the LER of an etch mask. The SEM image in Figure 19 (a) shows the eroded mask at the top. Two sampled sidewall profiles in the x - and y -directions are also illustrated at the bottom and the left-hand sides of the AFM micrograph in Figure 19 (a).

$$\text{SWR}_x(x_n) = \sqrt{\frac{\sum_m (z(x_n, y_m) - z_{ave, x_n})^2}{M}}, \quad z_{ave, x_n} = \frac{1}{M} \sum_m z(x_n, y_m) \quad (1a)$$

$$\text{SWR}_y(y_m) = \sqrt{\frac{\sum_n (z(x_n, y_m) - z_{ave, y_m})^2}{N}}, \quad z_{ave, y_m} = \frac{1}{N} \sum_n z(x_n, y_m) \quad (1b)$$

The RMS roughness values in the x and y directions are displayed in Figure 20. The SWR's were calculated with the following equations (1),

where $z(x_n, y_m)$ is a $N \times M$ matrix that contains roughness amplitude information. The RMS roughness ranged from 2 to 6 nm. The RMS roughness in the y -direction, SWR_y , is highest in the InP region beneath the InGaAsP waveguiding layer and is shown in Figure 19 (a) and (b), and Figure 20 (b). As the etching process proceeds from the top downwards, the material difference gives rise to additional roughness when it crosses the heterointerface between InGaAsP and InP. The etch rate of InGaAsP was about half the etch rate of InP for the etching conditions used. The different etch rates of these distinct materials resulted in the different

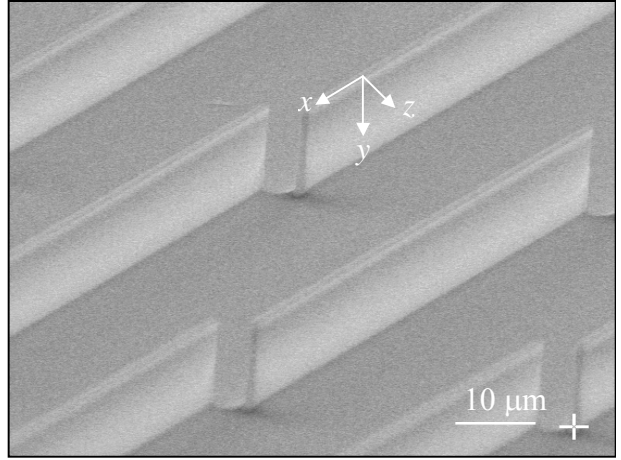


Figure 18. A SEM micrograph of deep-etched InP/InGaAsP waveguide heterostructures using an ICP-RIE system. 1- μm wide lines were etched to a depth of 10.7 μm . Waveguide sidewall is on the x - y plane where x is the direction of light propagation. The z -axis is normal to the waveguide sidewall.

Figure 19 (a) and (b) show typical SEM and AFM images of the sidewalls of waveguides etched up to 4 μm deep and Figure 19 (c) shows an AFM image of the sidewall of the InP substrate cleaved along the (100) crystal orientation. In the AFM images of the waveguide sidewalls, vertical striations on the sidewall are clearly visible. The striations begin at the top of SiO_2 mask layer and are transferred down to the bottom of the scanned sidewall. The origin of the vertical striations is ascribed to the line edge roughness (LER) of the etch mask. It is expected that mask erosion caused by ion-bombardment during ICP-RIE etching adds to the LER of an etch mask. The SEM image in Figure 19 (a) shows the eroded mask at the top. Two sampled sidewall profiles in the x - and y -directions are also illustrated at the bottom and the left-hand sides of the AFM micrograph in Figure 19 (a).

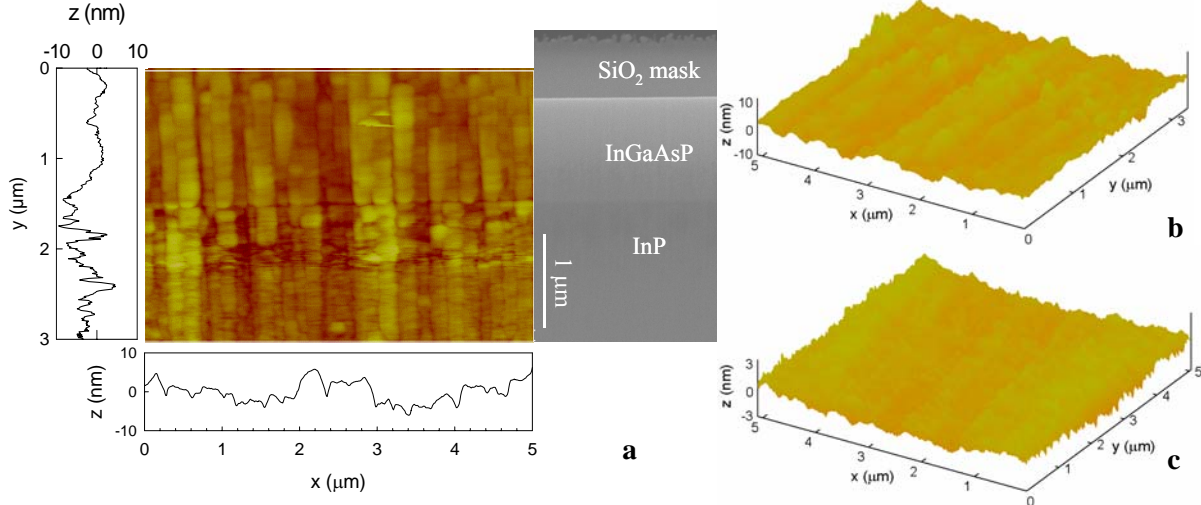
$$\text{SWR}_x(x_n) = \sqrt{\frac{\sum_m (z(x_n, y_m) - z_{ave, x_n})^2}{M}}, \quad z_{ave, x_n} = \frac{1}{M} \sum_m z(x_n, y_m) \quad (1a)$$

$$\text{SWR}_y(y_m) = \sqrt{\frac{\sum_n (z(x_n, y_m) - z_{ave, y_m})^2}{N}}, \quad z_{ave, y_m} = \frac{1}{N} \sum_n z(x_n, y_m) \quad (1b)$$

The RMS roughness values in the x and y directions are displayed in Figure 20. The SWR's were calculated with the following equations (1),

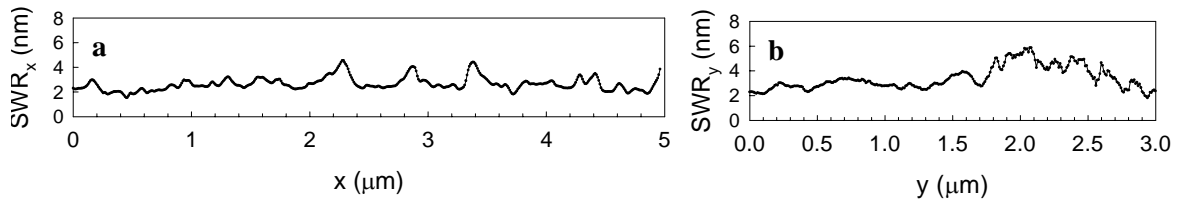
where $z(x_n, y_m)$ is a $N \times M$ matrix that contains roughness amplitude information. The RMS roughness ranged from 2 to 6 nm. The RMS roughness in the y -direction, SWR_y , is highest in the InP region beneath the InGaAsP waveguiding layer and is shown in Figure 19 (a) and (b), and Figure 20 (b). As the etching process proceeds from the top downwards, the material difference gives rise to additional roughness when it crosses the heterointerface between InGaAsP and InP. The etch rate of InGaAsP was about half the etch rate of InP for the etching conditions used. The different etch rates of these distinct materials resulted in the different

textures on the etched sidewall as shown in Figure 19 (a) and (b). For reference, the sidewall of the cleaved InP substrate was also scanned in the same configuration. The AFM scan image is shown in Figure 19 (c). No significant striations were detected for the cleaved sidewall of InP



substrate. The RMS roughness measured on the cleaved sidewall of InP substrate was 0.75 nm and the peak to valley height difference was ~ 4.5 nm.

Figure 19. (a) AFM and SEM micrographs of waveguide sidewall etched up to 4 μ m. Sampled profile in x - and y -



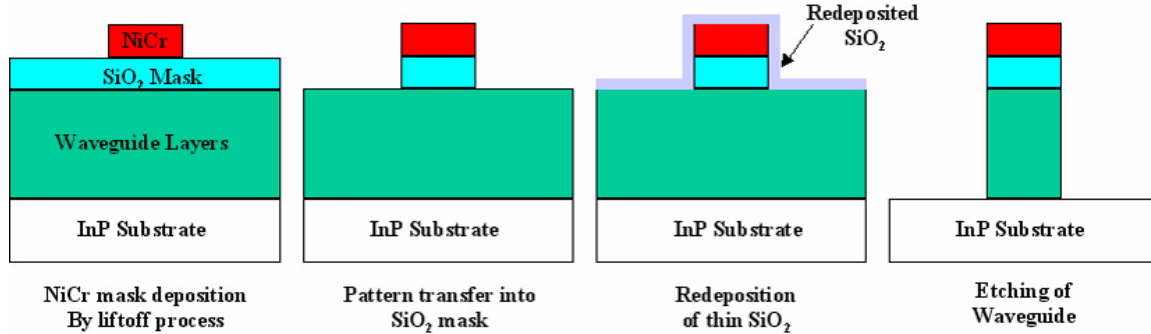
direction is displayed. (b) 3 dimensional view of sidewall profile measured with AFM. (c) An AFM scan image of a cleaved InP substrate used to create the sample is included as reference.

Figure 20. Distribution of SWR for the etched sidewall (a) $SWR(x_i)$ and (b) $SWR(y_j)$.

Based on SWR measurements and autocovariance SWR analysis, the rms roughness values were 3.4 and 2.7 nm in the x and y directions, respectively. These are highly smooth sidewalls. In investigating the nature of mask formation on the resulting sidewall roughness, we have compared the performances of NiCr/SiO₂ mask and SiO₂/NiCr/SiO₂ composite mask⁹. In the latter mask, a 50 nm SiO₂ remasking was deposited on the initial NiCr/SiO₂ to smoothen any etch striations or roughness in the mask itself before pattern transfer into InP/InGaAsP. The

⁹ J.-W. Bae, W. Zhao, J.-H. Jang, I. Adesida, A. Lepore, M. Kwakernaak, and J. H. Abeles, "Characterization of sidewall roughness of InP/InGaAsP etched using inductively-coupled-plasma for low loss optical waveguide applications," *Journal of Vacuum Science and Technology B21* (6), 2888-2891 (2003).

masking sequence is shown in Figure 21. The results indeed showed that SWRs obtained using $\text{SiO}_2/\text{NiCr}/\text{SiO}_2$ mask were lower than corresponding SWRs obtained using NiCr/SiO_2 mask.



Also, we have found that SWRs increase with etch depth due to continuous mask erosion and faceting.

Figure 21. SiO_2 masking process to reduce the sidewall roughness as a result of the line edge roughness of the NiCr metal mask.

3.1.2. Low-Loss Waveguides & Couplers

Waveguide losses and excess optical losses at the couplers are key issues for the development of the proposed ring-modulators. The sources of loss in waveguides and waveguide bends are:

- Absorption loss
- Radiation leakage loss in the bends
- Scattering loss due to roughness
- Leakage of the light through the substrate in the bends.

Figure 22 illustrates the sources of loss of the waveguides.

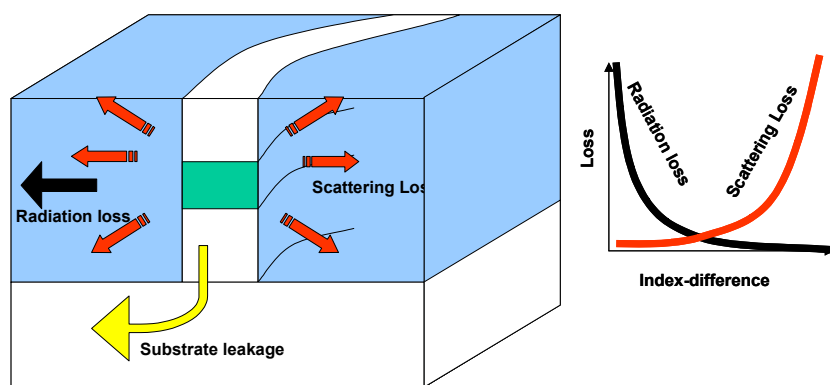


Figure 22. Illustration of the sources of loss in waveguides.

Absorption loss of the InGaAsP/InP waveguides is determined mainly by the choice of the bandgap of the quantum wells. It is a design trade-off between electro-optic response (dn/dV) and absorption loss (See separate chapter).

The ring resonators require tight bends, which cannot be accommodated by traditional ridge type or buried waveguides. We chose to use deeply etched waveguides to enable tight bending radii. The deeply etched semiconductor waveguides with an index of ~ 3.3 and air or a dielectrics surrounding with an index below 2 allow bending with negligible radiation loss to radii as small as $4\mu\text{m}$.

Increasing the etch depth beyond the guiding core can eliminate leaks into the substrate at the bends.

Deeply etched waveguides can provide a platform for extremely compact photonic circuits due to the tight bending radii, which can be obtained with negligible optical loss. However, in this case the large index difference with the semiconductor results in high scattering losses at the waveguide-dielectric interface in the presence of sidewall roughness. The scattering loss scales approximately with Δn^2 . Δn is the difference between the semiconductor index and the surrounding dielectric. The ability to turn the light around tight bends increases the requirements on smooth etching substantially.

Calculations following ¹⁰ and ¹¹ show that the scattering loss due to roughness:

- Depends on the index-step
- Depend on RMS roughness value
- Depends on statistics of roughness
- Increases with narrower waveguides (for strongly guiding waveguides).

Figure 23 shows the losses measured for straight deeply etched waveguides without dielectric encapsulation. In qualitative agreement to scattering loss theory the loss increases with decreasing waveguide widths. Roughness of these particular waveguides has been estimated to be ~ 5 nm RMS by evaluating SEM images.

¹⁰ D. Marcuse, *Bell Syst. Tech. J.*, vol. 48, pp. 3187-3215.

¹¹ J.P.R. Lacey and F. P. Payne, *IEE Proc.*, vol. 137, pp. 282-288, 1990.

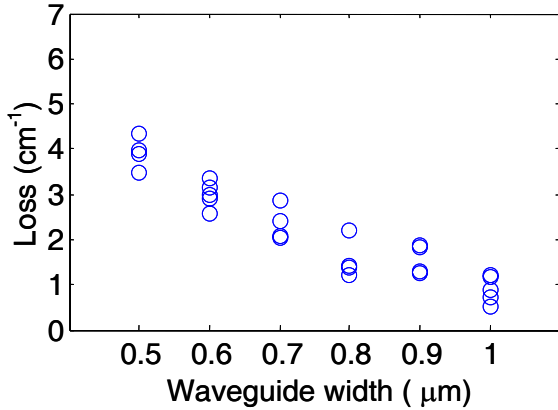


Figure 23 Measured losses of deeply etched InP/InGaAsP waveguides.

3.1.3. Couplers

3.1.3.1. Evanescent Couplers

Evanescent couplers provide a way to couple light from one waveguide theoretically with no excess loss. Figure 24 shows calculated coupling lengths for evanescent couplers of various ridge widths and gaps. The coupling length is defined to be the length required to obtain complete coupling. The power coupling for other lengths is $|\kappa|^2 = \sin^2(\pi/2 \cdot L/L_c)$. As Figure 24 shows, to obtain large coupling values it is necessary to use very narrow waveguides to squeeze the mode out of the semiconductor, very small gaps to increase the modal overlap, or long couplers for increase the interaction length.

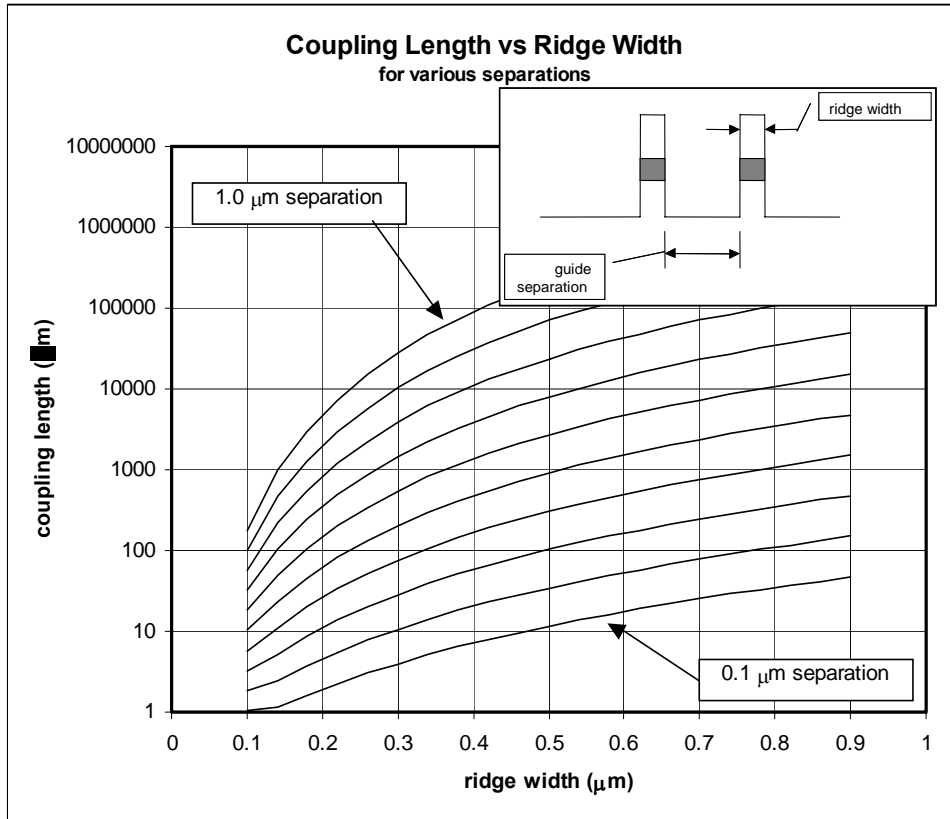


Figure 24. Coupling length of evanescent couplers calculated for various ridge widths and waveguide separations.

The disadvantage of these measures is:

- Narrow waveguides: Result in higher waveguide loss due to roughness induced scattering
- Small gaps: Difficult to fabricate. Proximity effects reduce the etch-rates in the gaps.
- Long couplers: Increases ring resonator size

The sensitivity of the coupling to the gap-width also makes control of the coupling values extremely difficult.

3.1.3.2. Multimode Interference Couplers

Coupling of the light in an access waveguide to ring-resonators is critical and determines key characteristics such as filter function and quality factor. In order to build advanced ring-resonator-based optical circuits, the design of the coupling coefficient in a reliable and repeatable fashion is required. This is particularly important in the multi-ring resonator modulator where optical delay and RF-delays must be matched. Popular ways to couple light into ring-resonators in lateral as well as in vertical coupling schemes is evanescent coupling. In the lateral arrangement the requirements on size and therefore bend-radius demand deep-etched high index-contrast waveguides. This geometry however results in extremely narrow gaps between access

waveguides and ring-waveguides, which are difficult to fabricate and need to be extremely well controlled. Vertical coupling schemes result in epitaxially defined waveguide spacing but require elaborate processes such as wafer bonding as well as accurate lithographical alignment. Multi-mode interference (MMI) couplers are widely used to provide 50% coupling in lateral geometries.

Using the MMI couplers with ring resonators require extremely low excess losses. The MMI width, length and input and output waveguide positions are optimized for low loss. The remaining loss is a result of not ideal modal dispersion in the MMI waveguide and an incomplete matching of input/output waveguide modes with the superposition of MMI modes. This loss depends in the optimized layout also on the ratio of waveguide width and MMI width. With the use of very narrow waveguides ($0.8 \mu\text{m}$) the low loss regime is achieved with couplers of small dimensions as well. This makes them useful for use in ring-resonators. Figure 25 shows the calculated field in the MMI and the excess loss in the optimized design.

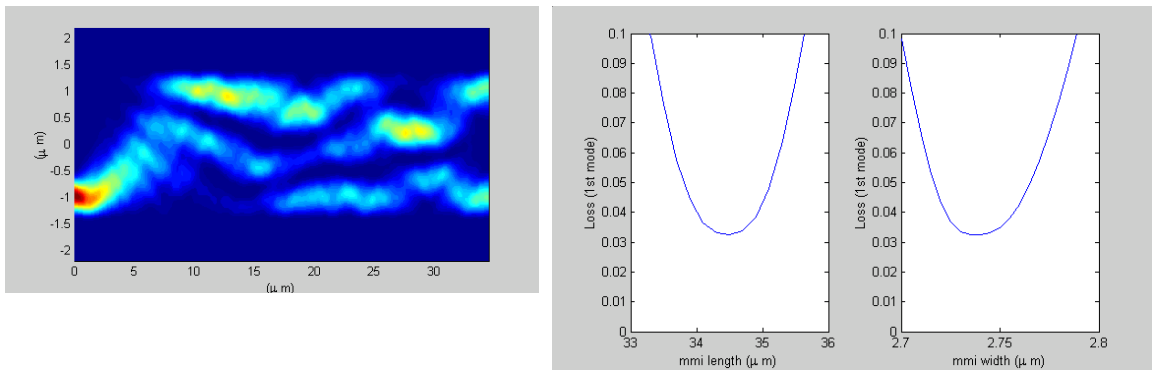


Figure 25. Calculated field intensity in the MMI (left). Excess loss calculations (right). The width and length of the MMI are $2.74 \mu\text{m}$ and $34.5 \mu\text{m}$ respectively. The input and output waveguide widths are $0.8 \mu\text{m}$.

In comparison with evanescent couplers, the main advantage of MMI couplers are their reproducibility (see Table 4).

Table 4. Comparison of evanescent couplers and MMI couplers.

Evanescent Couplers	Multi-mode interference couplers
<ul style="list-style-type: none"> Require extremely narrow gap ($0.3\text{-}0.4\text{mm}$). Depend critically on gap width. \rightarrow difficult to control coupling ratio. Arbitrary coupling ratios. Size scales with coupling ratio; high coupling is 	<ul style="list-style-type: none"> No small features. 50:50 coupling. Minimum size is limited. Excess loss due to modal mismatch of MMI region and waveguides.

difficult if small devices are required.

- Excess loss at waveguide-coupler transitions.

Figure 26 shows the design details of the ring-resonators layout with MMI coupler. Modal displacement in the curved waveguide can result in losses when two waveguides of different curvatures are joined. The curved waveguide entering has been offset to compensate for the curvature change. As opposed to using a racetrack waveguide with straight segments and curved segments the waveguide curvature varies continuously to avoid any curvature discontinuities.

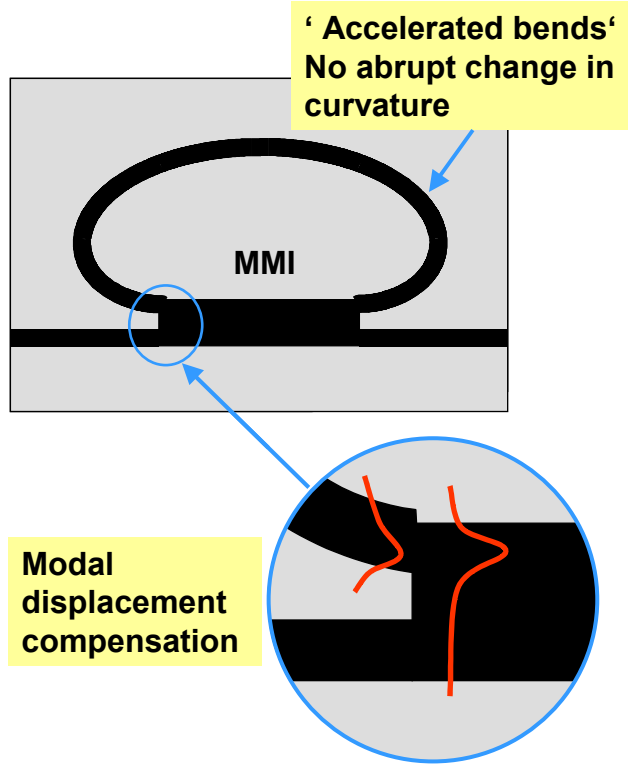


Figure 26. Design details of ring-resonator with MMI's smooth bending and mode-matched interfaces.

3.1.4. Modulator Materials

3.1.4.1. Background

High-speed optical modulators are essential parts of most photonic systems. These devices are based either on electrorefraction (ER) or electroabsorption (EA). The former can be used for amplitude and phase modulation, while the latter can only be used for amplitude modulation. An inherent advantage of electrorefraction compared to electroabsorption is that the linear loss can be maintained very low. This leads to two important consequences. First, a low optical absorption means low electron-hole pair generation as well as low heat generation. Therefore, electrorefractive modulators can handle a much higher optical power densities compared to their electroabsorptive counterparts due to the absence of bleaching and overheating. High optical

power densities are extremely desirable for radio frequency (RF) photonic and long haul optical fiber communication systems. Second, a low optical absorption provides the possibility of using Fabry-Perot or ring resonator to form the so-called “slow-wave” modulation¹², where the modulation efficiency can be enhanced by orders of magnitude due to the enhanced interaction time.

Currently, the commonly used materials for high-speed phase modulators are lithium niobate (LN), III-V compound semiconductors, and polymers. Modulators based on LN have the most mature technology, since the material has been extensively studied for other commercial applications such as acoustic-wave filters for mobile phones. Traveling-wave LN modulators have achieved high bandwidths exceeding 100GHz¹³. Unfortunately, LN modulators cannot be integrated with III-V active components due to the material incompatibility. Monolithic integration is long sought for realization of low-cost photonic subsystems with high functionality and speed. Moreover, the inherently low electrooptic coefficient of lithium niobate ($r_{33} \sim 30 \text{ pm/V}$) leads to a high operating voltage ($V_{\pi}L = 40$ to 80 Vmm) and hence long device size and high power consumption.

Recently, polymeric modulators have been studied extensively. The main advantage of this type of modulators is their relatively easy fabrication process and a high modulation bandwidth exceeding 110 GHz¹⁴. However, they have low electrooptic coefficients in the 10 to 70 pm/V range. Combined with their low refractive index their sensitivity becomes similar to LN ($V_{\pi}L = 30$ to 200 Vmm). Other drawbacks of polymeric modulators include unproven lifetime and stability as well as limited maximum optical power density and operating temperature.

Although optical modulators based on III-V quantum wells have a higher sensitivity ($V_{\pi}L = 10$ to 20 Vmm) compared to LN and polymeric modulators, they are difficult to couple to fiber optics and hence are not as suitable for discrete devices. However, they are excellent choices for monolithic integration with other III-V active components. Power consumption becomes a much more important issue for an integrated device, since power generation and transfer as well as heat dissipation are significantly restricted in a closely packed integrated subsystem. Thus, there have been significant efforts to enhance material sensitivity, since modulator power consumption is inversely proportional to the square of the material sensitivity.

Theoretically, more than one order of magnitude enhancement of sensitivity has been predicted for symmetric¹⁵ and asymmetric^{16,17,18,19} coupled quantum wells. Experimental results however,

¹² H. Teylor, J. of Lightwave Technol. **17**, 1875 (1999).

¹³ K. Noguchi, O. Mitomi, and H. Miyawaza, J. Lightwave Technol. **16**, 615 (1998).

¹⁴ D. Chen, H. Fetterman, A. Chen, W. Steier, L. Dalton, W. Wang, and Y. Shi, Appl. Phys. Lett **70**, 3335 (1997).

¹⁵ Y. Chan, and K. Tada, IEEE J. of Quantum Elect. **27**, 702 (1991).

¹⁶ H. Feng, J. Pang, K. Tada, and Y. Nakano, IEEE Photonic Technol. **9**, 639 (1997).

¹⁷ C. Thirstrup, IEEE J. of Quantum Elect. **31**, 988 (1995).

¹⁸ Y. Huang, Y. Chen, and C. Lien, Appl. Phys. Lett. **67**, 2603 (1995).

¹⁹ Y. Chen, H. Li, Z. Zhou, and K. Wang, J. Appl. Phys. **76**, 4903 (1994).

have shown enhancements approaching a factor of five²⁰ in GaAs/AlGaAs material system. Unfortunately, such improvements have not been demonstrated for the InP based modulators, which are especially attractive for telecommunication applications.

3.1.4.2. Software for Modeling

We calculated optical absorption spectrum of the quantum wells using an effective mass approach. The excitonic effect was calculated based on a variational method¹⁷, and change of index was calculated from the Kramers-Kronig relationship. Figure 27 shows the program flowchart for the developed software, as well as its important specifications. Figure 28 illustrates the simulated optical absorption coefficient, and change of index spectra for a quantum well structure.

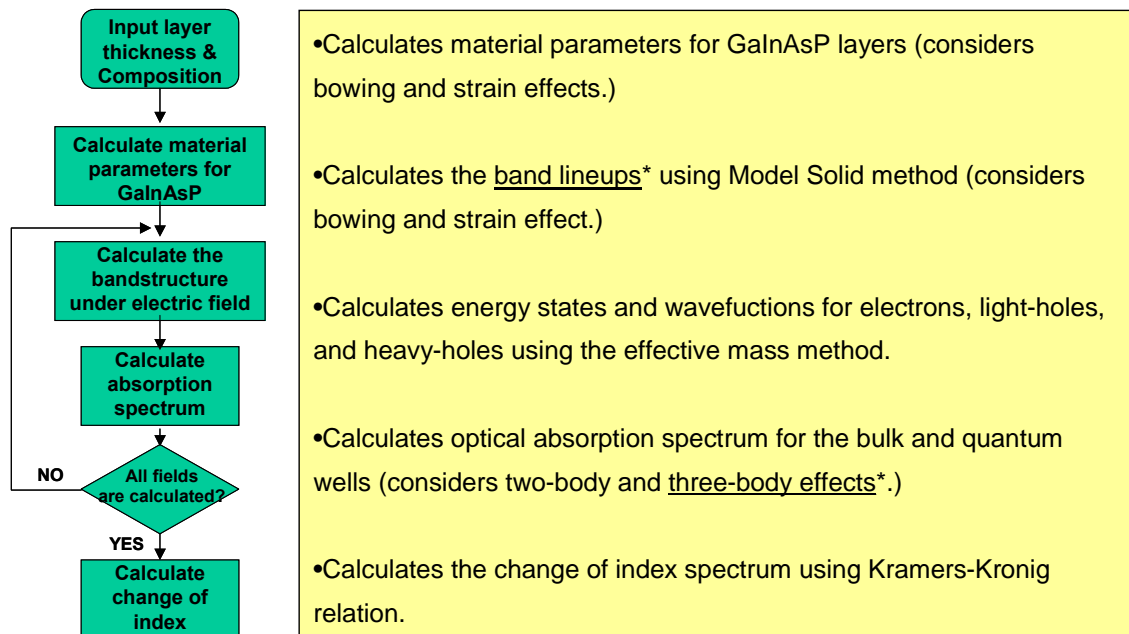


Figure 27. Developed software flowchart and important specification.

²⁰ H. Feng, J. Pang, M. Sugiyama, K. Tada, and Y. Nakano, IEEE J. of Quantum. Elec. **34**, 1197 (1998).

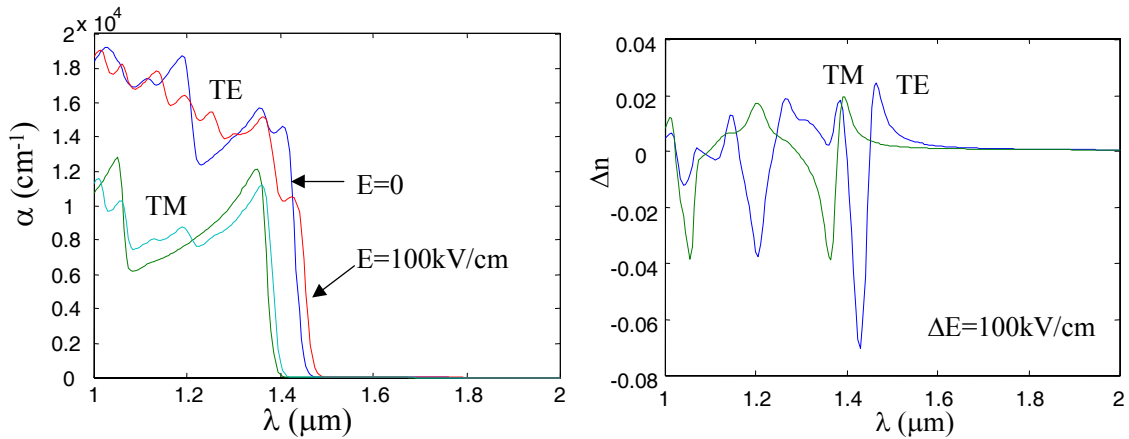


Figure 28. Simulated optical absorption coefficient, and change of index spectra.

The electric field inside the active region was calculated using diffusion-drift and Poisson's equation. Figure 29 shows the energy-band structure and the quasi-Fermi levels of a modulator at $V=-1$ volts. We optimized the thickness and composition of the layers of the quantum well to maximize change of index per change of voltage $\Delta n/\Delta V$, while keeping the absorption coefficient $\alpha=1 \text{ cm}^{-1}$ at $\lambda \sim 1550 \text{ nm}$.

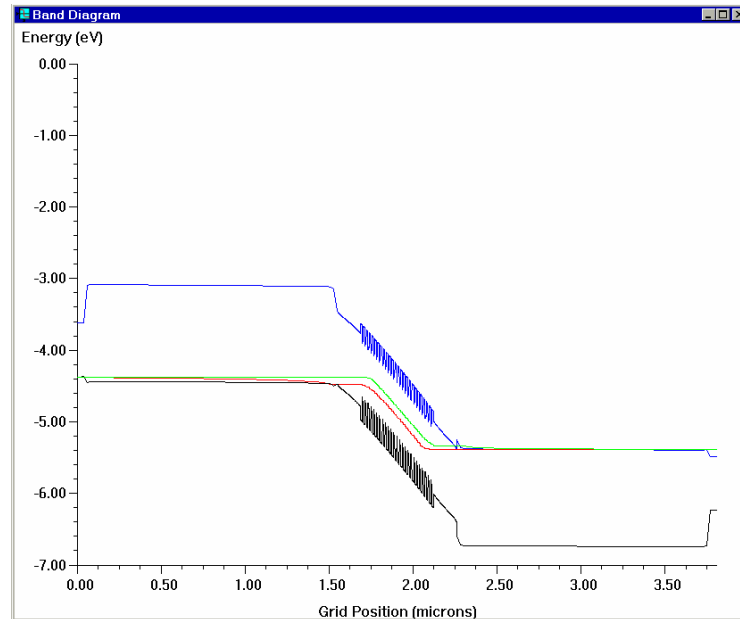


Figure 29. Energy-band structure and the quasi-Fermi levels of a modulator at $V=-1$ volts.

The accuracy of the program was evaluated by comparing the simulation data with the published experimental data. Figure 30 shows the calculated change of index versus measured change of index by Zucker et al. around 1.3 μm and 1.5 μm .

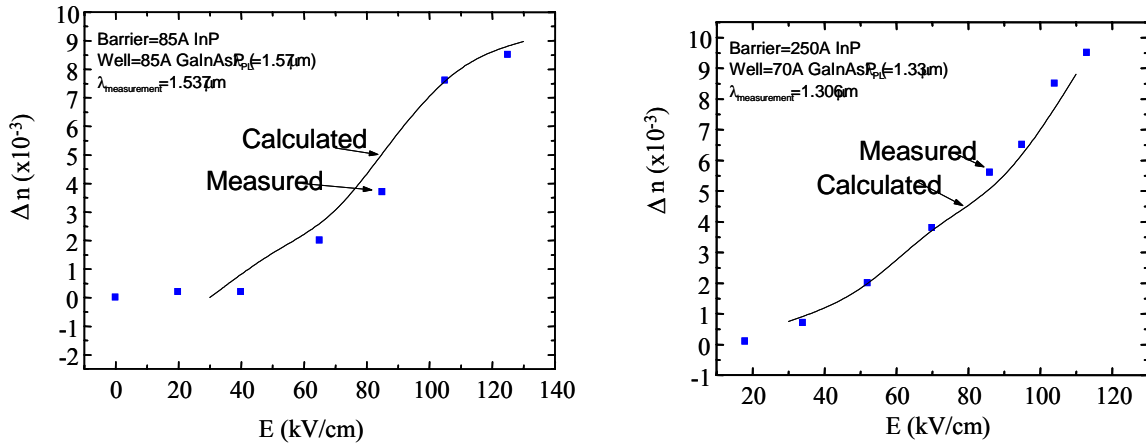


Figure 30. Calculated change of index versus measured change of index by Zucker et ala around 1.3 mm and 1.5 mm.

3.1.4.3. Stepped Quantum Well Material

Quantum well structures were grown by low-pressure metal organic vapor phase epitaxy (MOVPE) on n-type InP substrates. The thickness of the active region in all of the designs is kept at $\sim 0.4 \mu\text{m}$ by adjusting the number of quantum wells. This region is sandwiched between 1.5 μm thick n and p-type InP cladding layers, and the device is terminated with a 50 nm thick, highly doped InGaAs cap layer

3.1.4.4. Optimization Procedure

We used several characterization methods to ensure that high material quality as well as the correct layer thickness and composition. These include photoluminescence, high-resolution x-ray diffraction, and Transmission Electron Microscopy. Photoluminescence is used for material quality (intensity, FWHM), effective bandgap (peak wavelength), macroscopic uniformity (PL mapping), and growth calibration (see Figure 31). X-ray diffraction and simulation are used to assess material quality (intensity, FWHM), strain (relative peak position), composition and thickness of the layers (simulation), and growth calibration (see Figure 32). Transmission Electron Microscopy is used to assess material thickness, microscopic uniformity, and Interface abruptness (Figure 33).

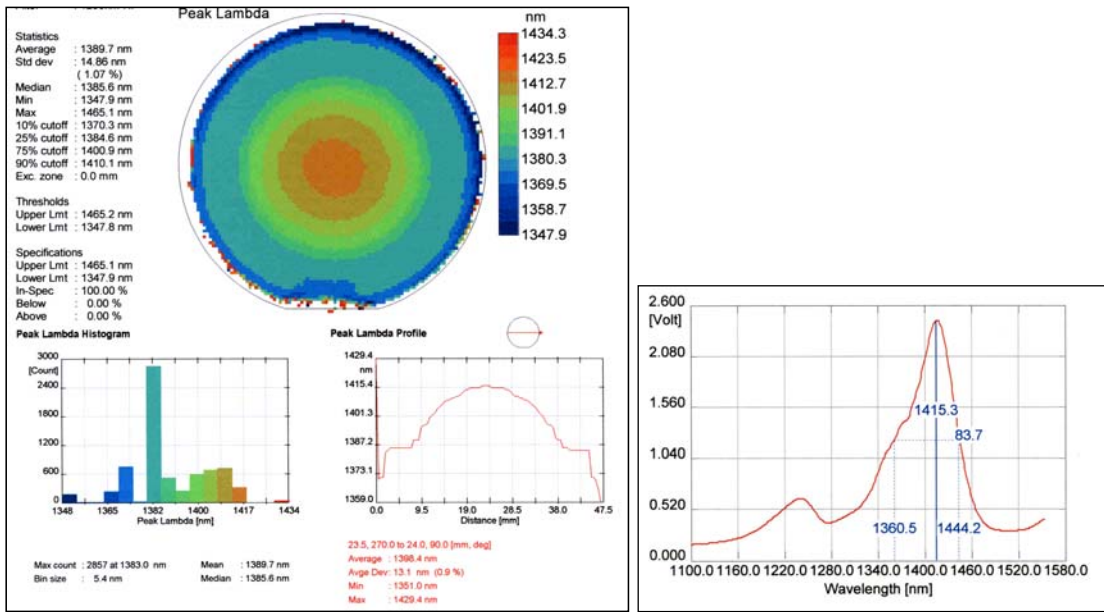


Figure 31. Photoluminescence is used for Material quality (Intensity, FWHM), Effective Bandgap (Peak wavelength), Macroscopic uniformity (PL mapping), and • Growth calibration.

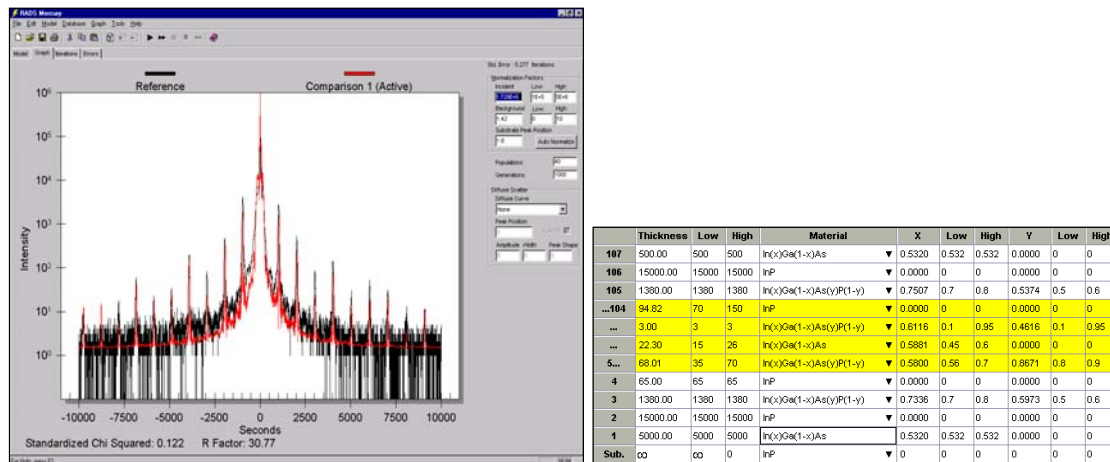


Figure 32. X-ray diffraction and simulation are used to assess Material quality (Intensity, FWHM), Strain (Relative peak position), Composition and thickness of the layers (Simulation), and Growth calibration.

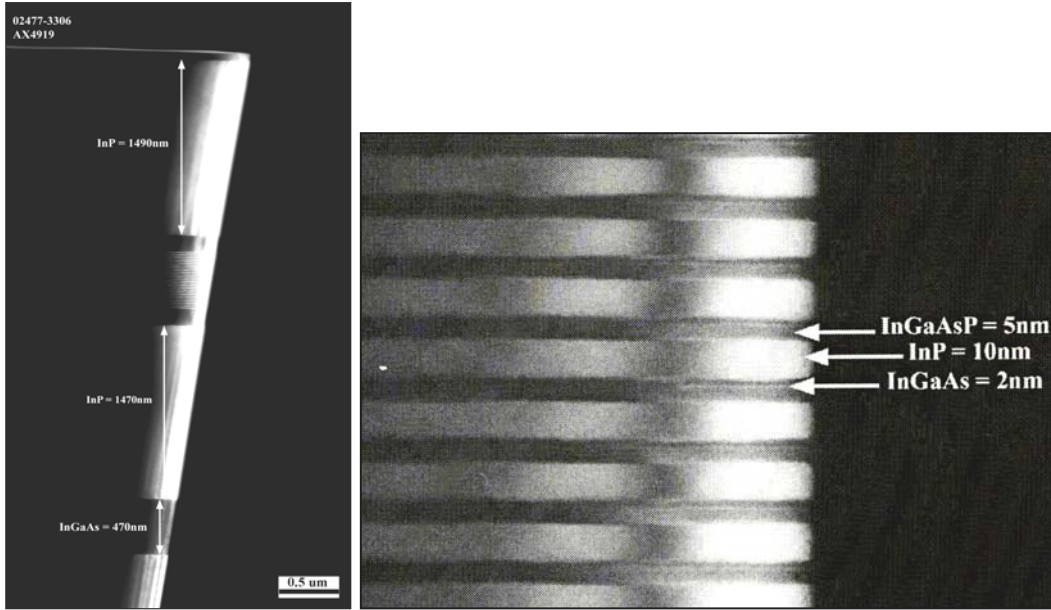


Figure 33. Transmission Electron Microscopy is used to assess Material thickness, Microscopic uniformity, and Interface abruptness.

3.1.4.5. DC Electro-Refractive Characterization Method

The material is processed into single mode ridge waveguides through standard photolithography and CH_4/H_2 based reactive ion etching (RIE). We measured optical absorption coefficient and change of index of the modulators by measuring Fabry-Perot oscillation²¹, optical transmission, and the modulator photoresponse (see Figure 34). Leakage currents were significantly lower than values that could cause heat-induced change of index.

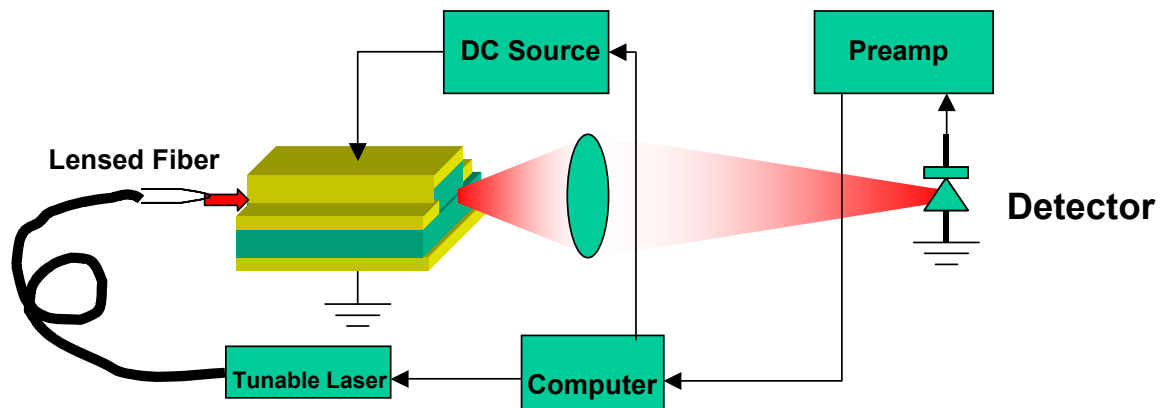


Figure 34. Schematic of the measurement setup.

²¹ T. R. Walker, Electron. Lett. **21**, 581 (1985).

3.1.4.6. Experimental Results

Figure 35 (a) and (b) show the measured change of index versus wavelength for different voltage bias, and the change of index versus voltage bias for different wavelengths for a modulator.

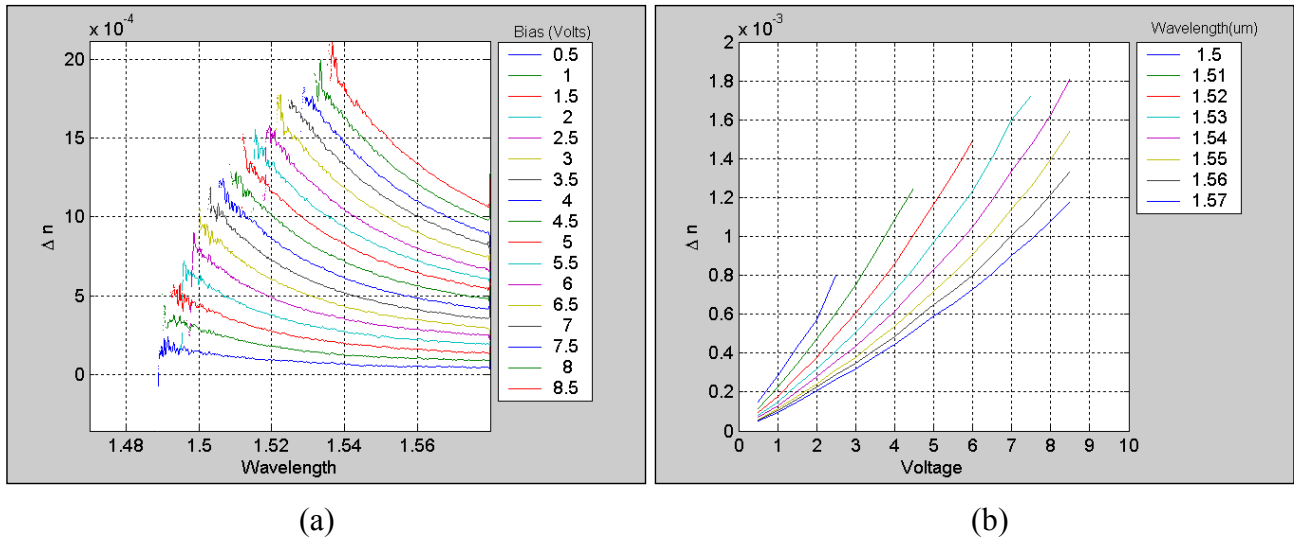


Figure 35. (a) Change of index versus wavelength for different voltage bias, and (b) Change of index versus voltage bias for different wavelengths.

In general, the simulated data showed good agreement with the measured data. Figure 36 compares the experimental and theoretical data for a modulator. Adjustable parameters for the model were: a) Structure obtained from x-ray simulation, b) Linewidth broadening and band edge obtained from measured loss, and c) Internal field obtained from device modeling.

We systematically compared the performance of stepped quantum well (SQW) and rectangular quantum well (RQW). Since the detuning from the energy gap of the devices has a significant effect on the measurement, we only compared devices with similar bandgap energies. Also, plotting α versus $\Delta n/\Delta V$, and eliminating their wavelength dependency, reduced the detuning effect in our comparison. Figure 37 compares the performance of a modulator with 2SQW and 3SQW active region to a modulator with a conventional RQW at $\lambda=1.550 \mu\text{m}$ and TE polarization. The material figure of merit $V_\pi L$ shows three times enhancement in the SQW compared with the conventional RQWs.

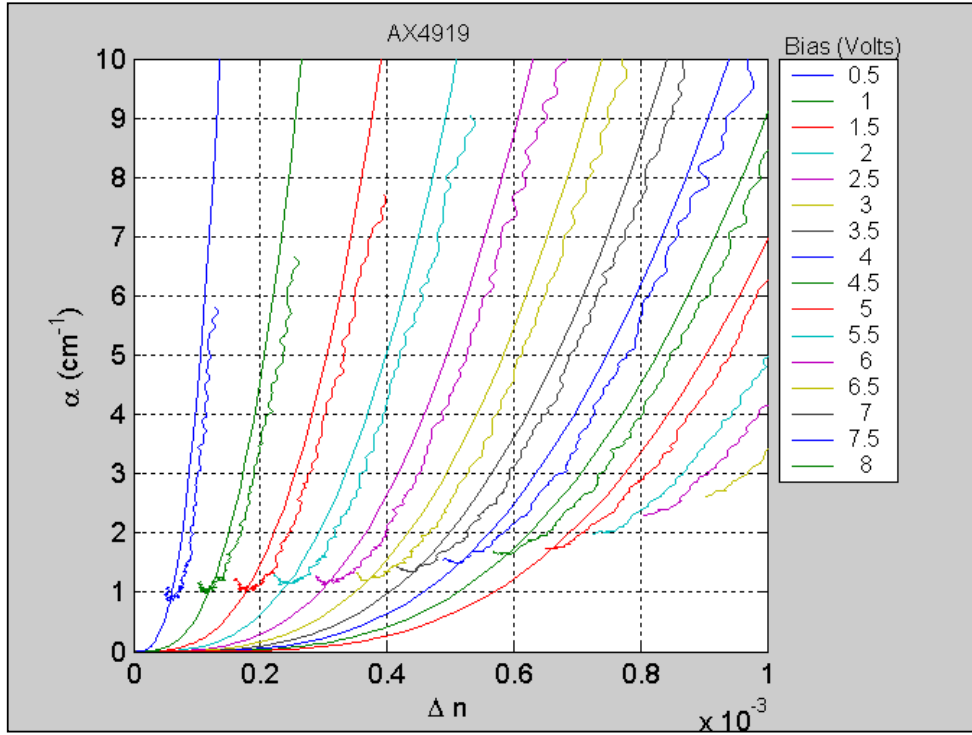


Figure 36. Comparison of experimental and theoretical data. Adjustable parameters for the model were: Structure (from x-ray simulation), Linewidth broadening and band edge (from measured loss), Internal field (from device modeling).

Sample #	$\Delta n/\Delta V @ \alpha=1 \text{ cm}^{-1}$	$V_z L (\text{V.mm})$ (Push-Pull)	DC Bias (V)	Type	Potential Profile
AX4922	$\sim 1 \times 10^{-4}$	~ 3.8	1	Regular QW	
AX4919	$\sim 1.3 \times 10^{-4}$	~ 2.9	1	2-step Asym.	
AX4966	$\sim 3 \times 10^{-4}$	~ 1.29	1	3-step Asym.	

Figure 37. Stepped Quantum Well performance compared with a standard quantum well.

The importance of a low optical loss can be better understood by considering the gain of an impedance matched analog RF photonic link²²:

²² See for example S. Hamilton, D. Yankelevich, A. Knobles, R. Weverka, and R. Hill, IEEE Transactions on Microwave Theory and Techniques **47**, 1184 (1999).

$$G = \left(\frac{e^{-\alpha L}}{V_\pi} \cdot \frac{\pi 10^{-l/10} R r_d P}{4} \right)^2 \quad \text{Equation 1}$$

where α is the optical absorption coefficient, L is the length of the modulator, and V_π is the voltage required for a π phase shift, R is the detector responsivity, r_d is the detector resistance, P is the laser power, and l is the total loss from the interconnects and fiber optics in decibel. Retaining the relevant parameter to the modulator, one can define modulator figure of merit as $M = (\exp(-\alpha L)/V_\pi)^2$. Assuming a small change of index, the value of V_π can be calculated as $V_\pi = \lambda/[2L(\Delta n/\Delta V)]$. Here λ is the laser wavelength and $\Delta n/\Delta V$ is the change of index versus change of bias in the modulator. Therefore, the optimum length of the modulator required to maximize M can be calculated as $L_{opt} = 1/\alpha$, and the figure of merit of a modulator with the optimum length becomes:

$$M_{opt} = 4e^{-2} \left(\frac{\Delta n/\Delta V}{\alpha \lambda} \right)^2 \quad \text{Equation 2}$$

Inserting the measured values of optical absorption coefficient and change of index for bias values of 2 volts into Equation 2, one obtains $M_{opt} \sim 0.10 \text{ V}^{-2}$ for the RQW and $M_{opt} \sim 3.60 \text{ V}^{-2}$ for 3SQW. This means that replacing the conventional RQW with the 3SQW can improve the gain of an analog RF link by 15.5 dB. Figure 38 compares the overall performance of the stepped QW with the published data.

Material (Barrier-Well)	λ μm	$V_\pi L$ V.mm	α cm^{-1}	(P_{opt_RF}/P_{elec_RF}) $\propto 1/(V_\pi L \alpha)^2$
InP-GaInAsP (This work)	1.55	2.6	1	14.8
InP-GaInAsP ¹	1.54	~2.5	~12	~0.1
InP-GaInAsP ²	1.3	6.1	~10	~0.03
InAlAs-InGaAs ³	1.55 1.60	0.75 1.65	11.5 7.6	1.34 0.64
InP-InGaAs ⁴	1.55	2.7	7.6	0.24
InAlAs-InGaAlAs ⁵	1.55	0.84	27.5	0.18

Figure 38. Performance of the stepped QW compared to the published data.

3.1.5. Low-Capacitance Planarization

Providing contacts to the rib waveguides.

Figure 39 shows a schematic of a deeply etched waveguide with Cytop dielectric planarization and metal P-contacts to the top of the waveguide and N-contacts next to the waveguide.

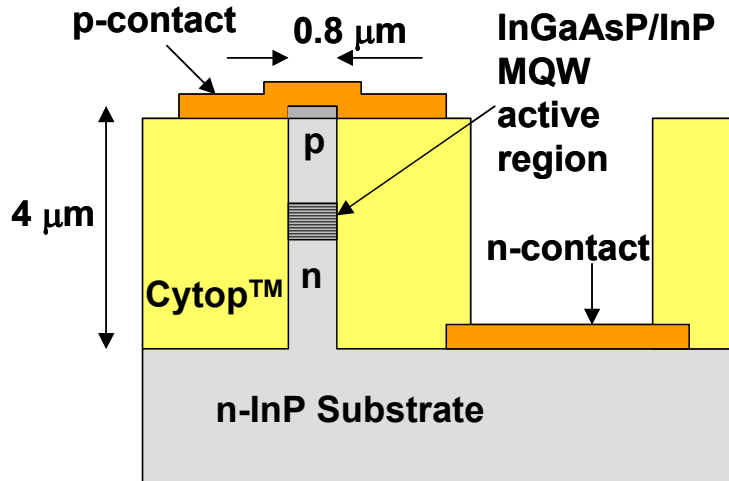


Figure 39. Schematic of completed device with Cytop planarization.

3.1.5.1. BCB

Initially BCB has been used for planarization. BCB has excellent optical and electrical RF-properties. However during the curing process BCB shrinks substantially. As a result of this and the exceptionally smooth sidewalls the BCB pulls back and delaminates from the etched waveguide sidewalls (See SEM, Figure 40). Subsequent metal evaporation entering the gap between BCB and waveguide short-circuits the device and/or results in excessive optical losses due to the proximity of the metal with the optical mode. BCB was dropped because of this drawback.

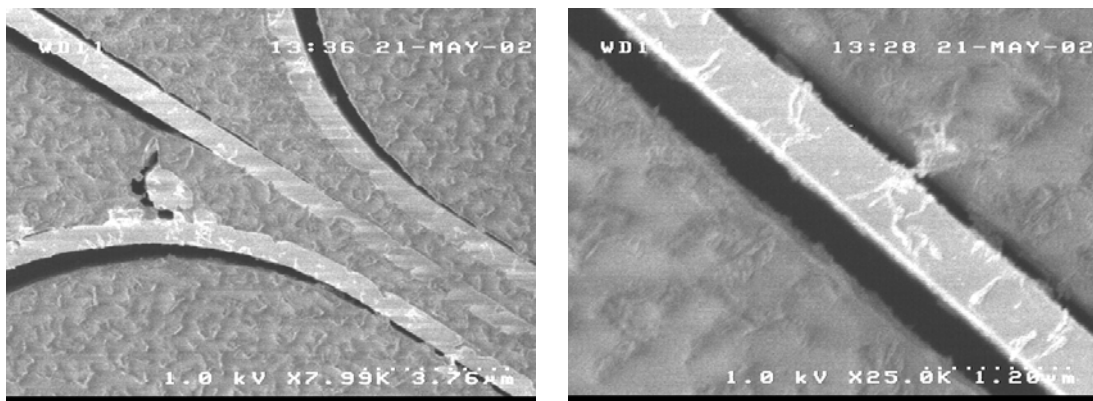


Figure 40. BCB Sidewall delamination after planarization etch.

3.1.5.2. Cytop planarization

Figure 41 shows the process flow for planarization with Cytop.

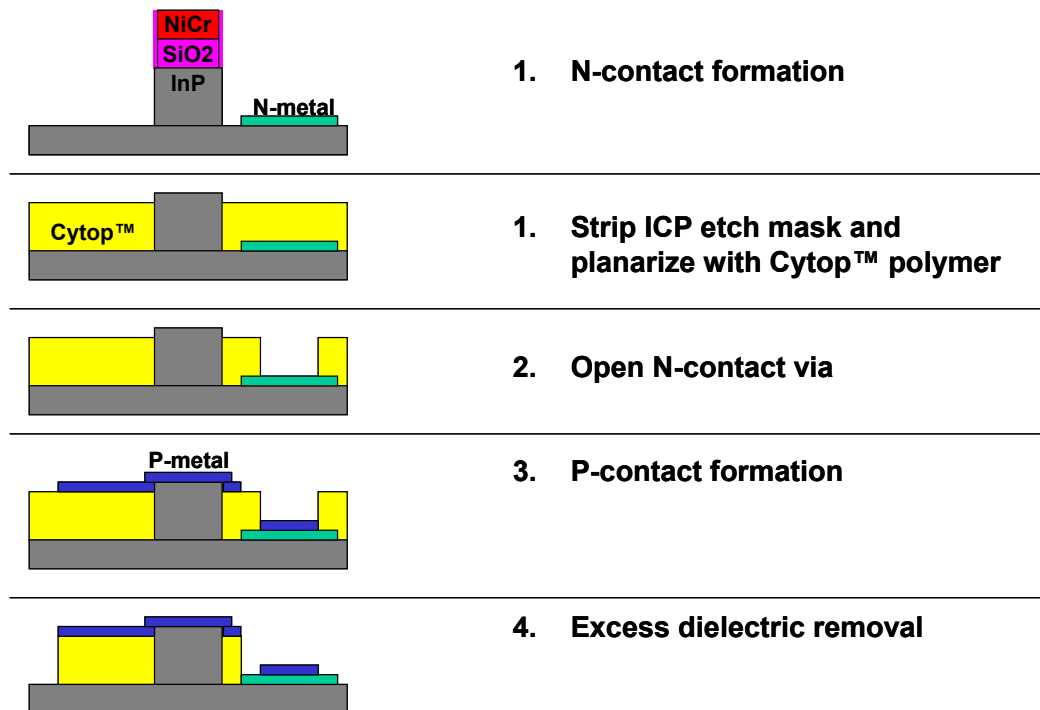


Figure 41. Process flow for planarization with Cytop.

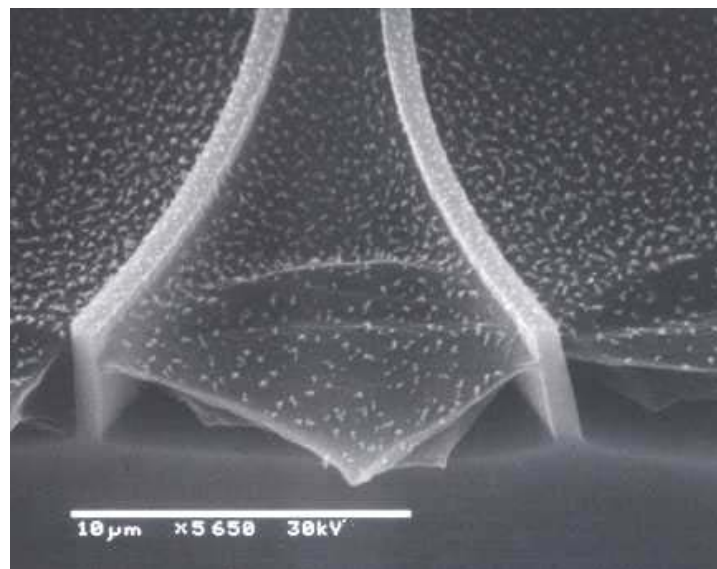


Figure 42. SEM image of sub-μm waveguide planarization with Cytop dielectric.

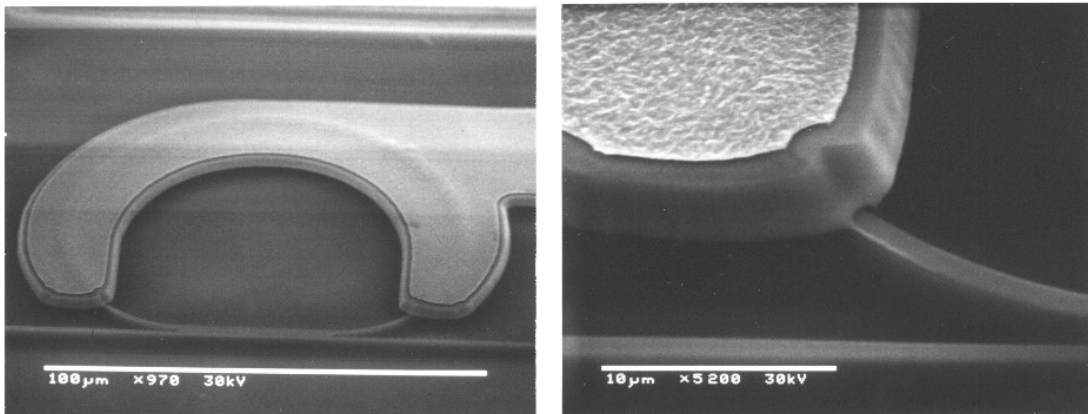


Figure 43. SEM image of sample with Cytop planarization and metal contact.

3.1.6. Electrode Design

The electrode design has two main objectives:

- Phase-match the microwave propagation to the optical propagation.
- Minimize stray reactance in the ring contact area.

In a conventional semiconductor Mach-Zehnder traveling-wave modulator, the microwave phase velocity tends to be much smaller than the optical group velocity. As the modulating signal travels down the modulator structure it becomes increasingly out of phase with the optical signal. Since the modulating signal propagates along the optical waveguide the electrode structure also has a high impedance (yielding high losses) and is limited by the capacitance across the optical waveguide.

The cascaded ring resonator modulator has a significant advantage over the straight modulator: Due to the optical delay in the rings, the average optical group velocity is slower than the microwave phase velocity. This makes it possible to phase-match the signals by delaying the modulating signal between resonators. In addition RF losses are reduced because the microwave delay lines are in the lower loss Cytop-covered field

The ring structure with a delay-line electroding is shown in Figure 44. A layer of Cytop nominally 4 μm thick planarizes the ring. A contact metal and a plated metal form the contact to the conductive top of the ring, a narrow lead, and the delay-line structure. In the ring the conductive layers are separated by approximately 1 μm . The ring and the narrow lead form a reactive load to the delayed transmission line on top of the 4 μm thick Cytop. The line was designed for impedances between twenty ohms and fifty ohms. Since the modulation depends on voltage rather than power a lower impedance line is advantageous. Twenty-ohm impedance represents a lower limit to the line width in the current geometry, while fifty-ohm impedance is conventional signal impedance. Operationally, the 10 GHz modulating signal would be transformed to 20 ohms in a microstripline interface to the modulator chip.

The final geometry and lengths of the RF-delay lines to match the group velocity of the optical signal depend on optical group delay of the ring, and the separation between adjacent rings. The analyses included separate electromagnetic simulation of the rings and of the delay structures. The electromagnetic simulations were necessary to include cross-coupling effects between adjacent delay line segments. The analysis where the effective delay between rings 200 μm apart was 21 ps at 10 GHz yielded 4800 μm long fifty-ohm delay lines. The lines are essentially hairpin shaped, occupying a 200 μm by 2300 μm area.

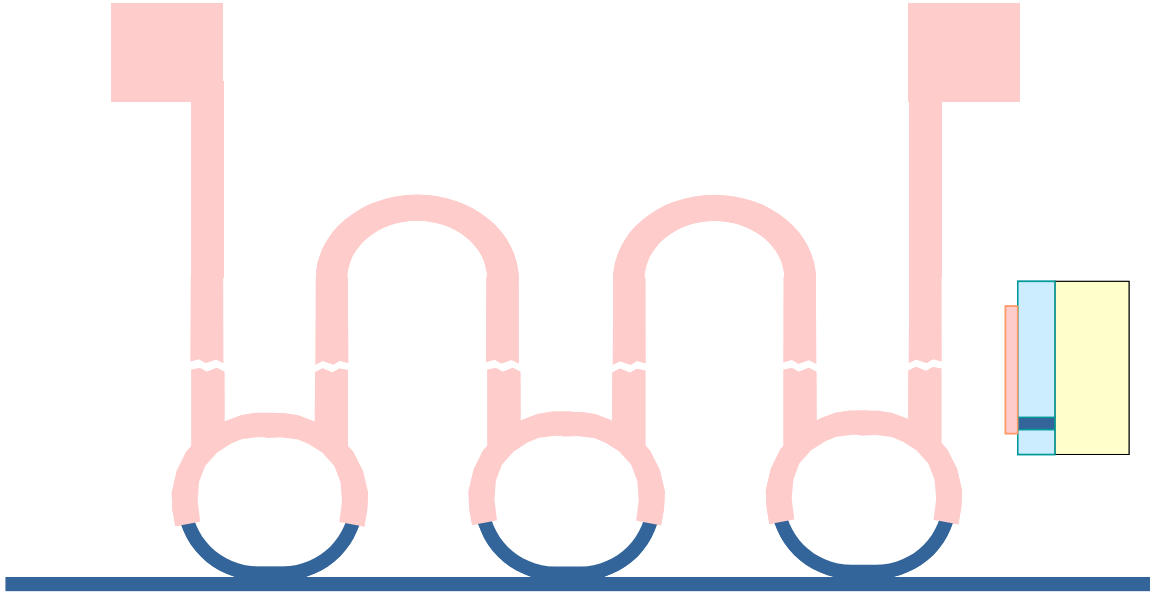


Figure 44. Three-ring modulator structure.

The initial electromagnetic simulations of a three-ring modulator yielded delays between adjacent rings of 19 ps to 25 ps from 1 GHz to 20 GHz, with 22 ps \pm 1 ps near 10 GHz, as shown in Figure 45. The maximum difference in delays between the three rings is 5 ps at 13 GHz. The difference at 10 GHz is 2 ps, corresponding to 7° in phase. Further refinement in the analysis and structure can be expected to give a maximum difference of 2 ps to above 20 GHz and less than 1 ps at 10 GHz (3.6°). In contrast, an equivalent delay of 42 ps on a straight modulator would lead to a difference of 10 ps, or 36° in phase at 10 GHz, from one end to the other. This difference comes from the differences in optical group velocity in InP ($c/3.5 = 0.286*c$) and electrical group velocity ($0.381*c$ for 50 ohm impedance) for a straight modulator.

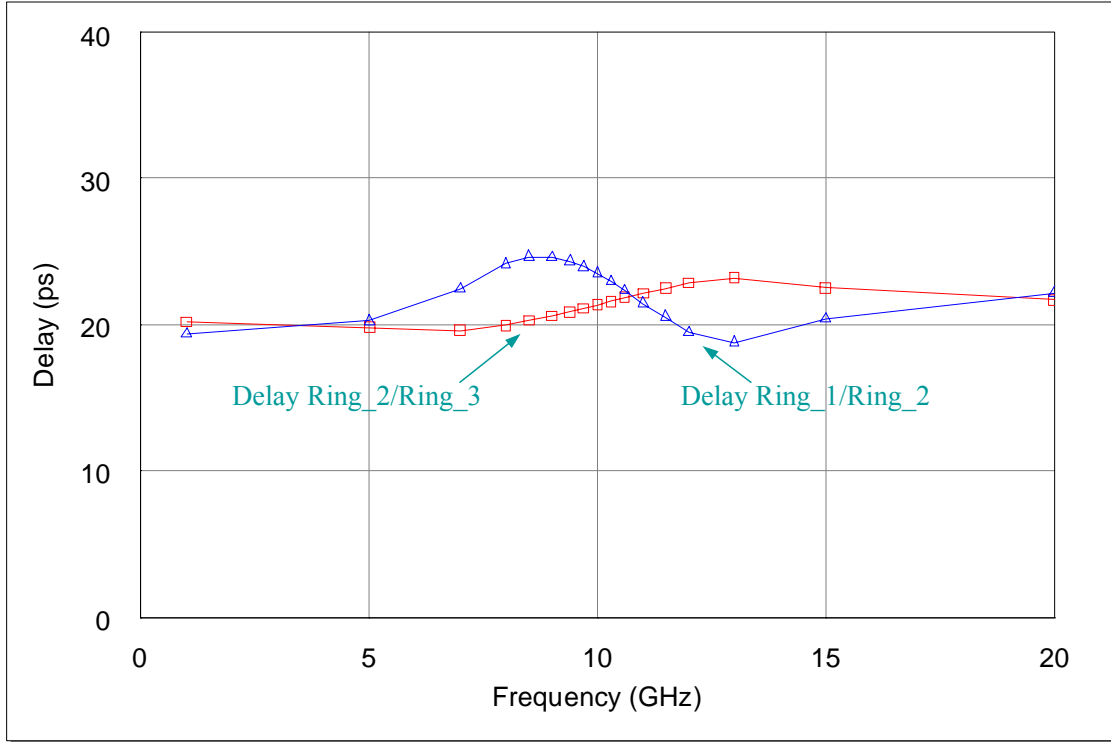
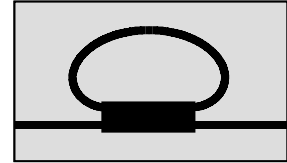


Figure 45. Initial electromagnetic simulation of three-ring modulator. Phase delays between adjacent rings. Overall delay is 42 ps +/- 2 ps across band.

3.1.7. Chip-Level Characterization Set-Up

The characterization of the ring-resonators is a central part in this project. Besides the determination of overall characteristics such as quality factor, finesse and free spectral range the extraction of ring-loss and coupling values of the access waveguides to the rings are essential for understanding and optimization of the fabricated devices. The standard technique is to measure the transmission through a device with a tunable laser. However the determination of the properties of most simple devices, a ring-resonator with one access waveguide, is not unambiguous from a transmission measurement alone. This is illustrated with the calculated transmissions of two different devices shown in figure Figure 46. The power transmission through the two devices is identical. However, the phase response is substantially different. While one device shows a 2π phase change across the resonance, the other device has only a small phase change at resonance. The over-coupled device (with 2π phase change) with a small transmission dip is desired for creating a phase-modulator. The under-coupled device is less useful.



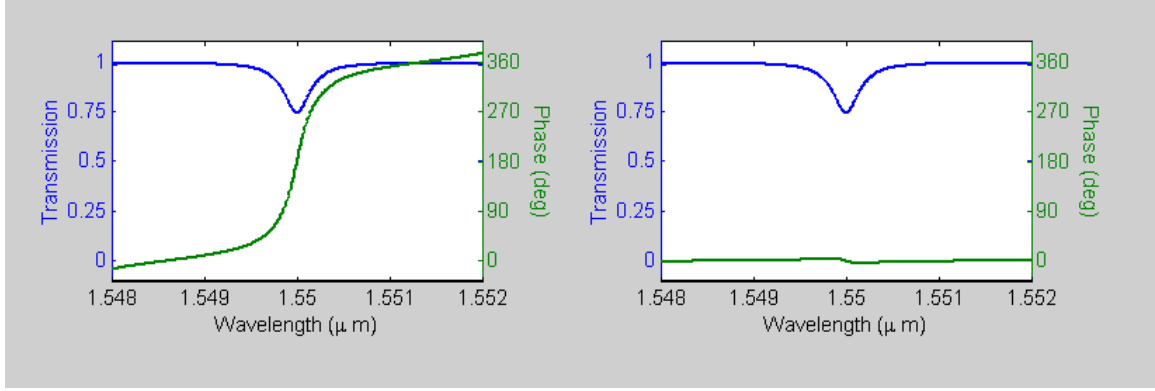


Figure 46. Calculated transmission (amplitude and phase) of a simple ring-resonator with one access waveguide. The coupler have a splitting ratio of 0.5:0.5 (left) and 0.05:0.95 (right). The excess loss of the resonators are 0.05 (left) and 0.5 (right) per single roundtrip of the light through the ring.

Amplitude and phase characteristics of the devices have been measured with a modulation phase shift method. The setup is shown in figure Figure 47. The modulator at the input is used to create sidebands in the optical spectrum at an offset to the carrier wavelength, which corresponds to the modulation frequency. Dispersion of the device causes the different wavelength components entering the device to experience different delays. The beating of these tones in the detector results in an electrical signal phase, which is determined by the difference phase of the optical tones. The lock-in amplifier yields both amplitude and phase of this electrical signal. The group delay τ_g of the light through the tested device is directly related to detected electrical signal phase $\Delta\phi$ by $\tau_g = \frac{1}{2\pi} \frac{d\phi}{df} \approx \frac{\Delta\phi}{2\pi f_0}$. f_0 is the modulation frequency and ϕ is the phase of the optical signal.

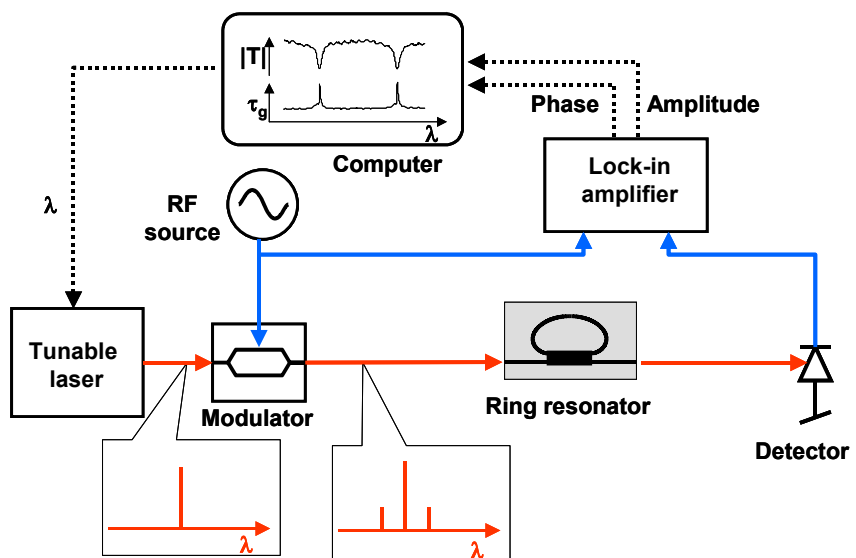


Figure 47. Setup to measure transmission and group delay.

Figure 48 shows the measurement of transmission and group delay of two ring-resonator devices. One is over-coupled and the other under-coupled, signified by the opposing sign of the group delay at resonance. Figure 49 shows a device close to critical coupling.

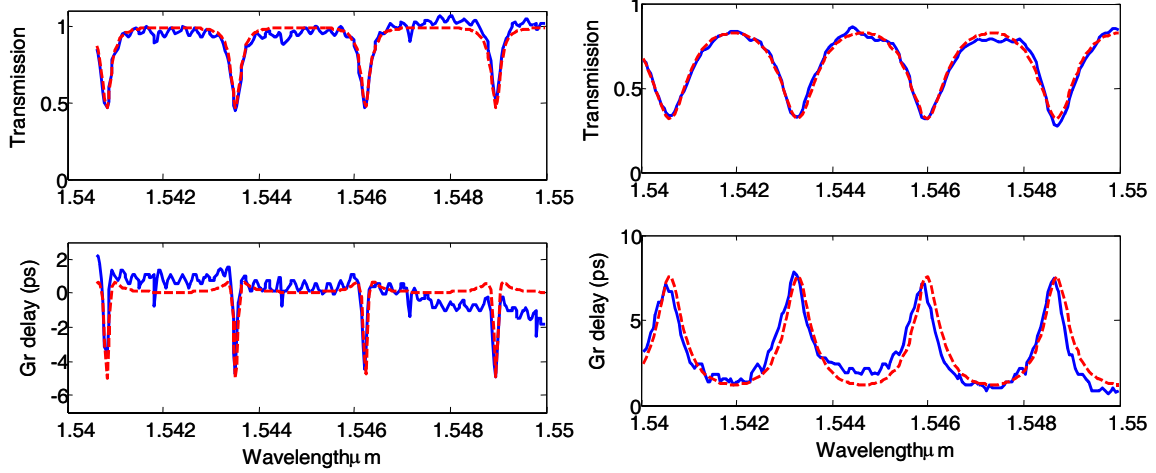


Figure 48. Measured transmission and group delay of two ring-resonators. Left: under-coupled resonator (negative group delay at resonance). Right: over-coupled resonator (positive group delay at resonance). Solid: measured; Dashed: calculation.

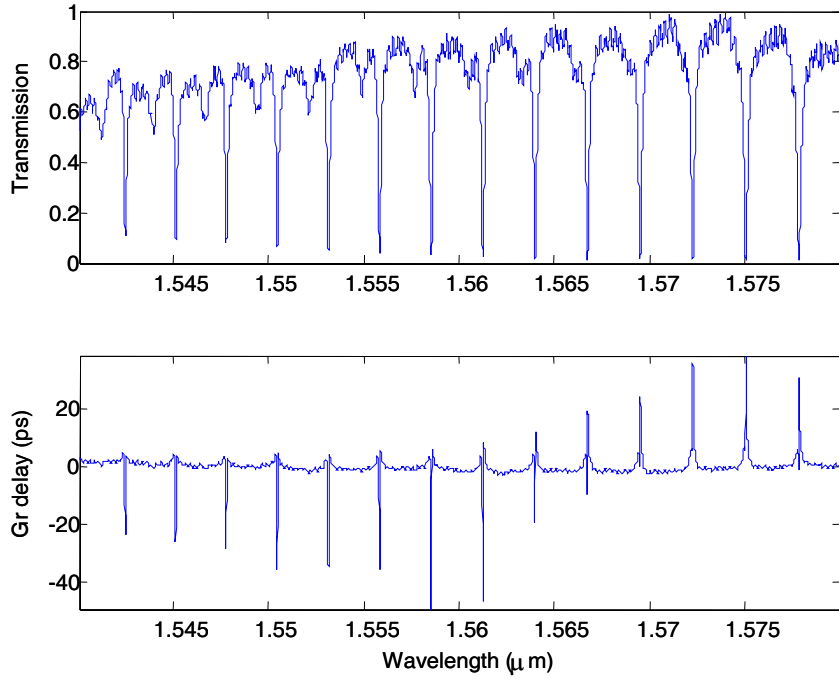


Figure 49. Transmission and group delay of a ring-resonator close to critical coupling. Variations of coupling and/or loss across the measured wavelength span turn the ring from under-coupled at short wavelengths (negative group delay) into over-coupled at long wavelengths (positive group delay).

3.1.8. Packaging Design

Figure 50 shows a schematic of the full device including six ring resonators and the RF delay lines. A package design for this device is shown in Figure 51.

The package was designed to allow optical access via optical fibers to both facets of the device. The fibers were lensed to optimize coupling efficiency, and coated with an anti-reflective coating to minimize reflections. Additionally, the package allowed for high-speed connections via GPO connectors on each side capable of 40 GHz transmissions. The signal was taken from the GPO connector via wire bonds to a ceramic submount patterned with high-speed striplines and carried to the device contacts. Temperature control was provided externally.

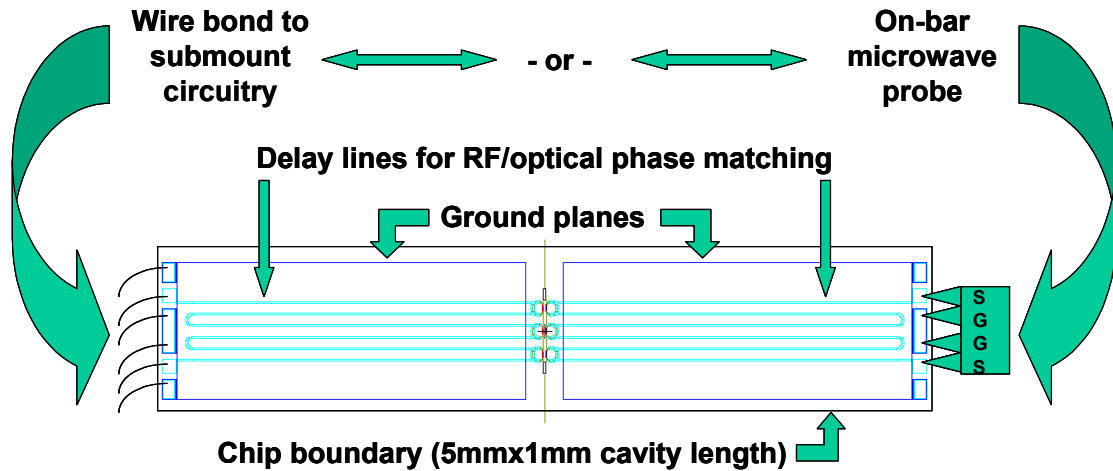


Figure 50. Device layout.

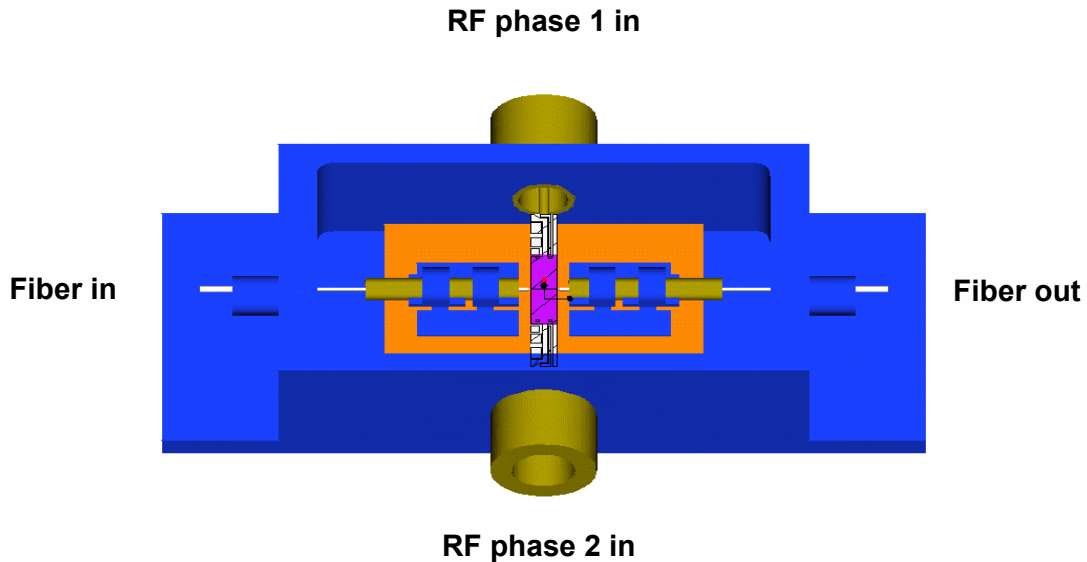


Figure 51. Package design.

3.1.9. Passive Ring Characterization

Figure 52 shows the measured transmission and group delay of a ring resonator. Transmission has been measured with a tunable laser and the group delay extracted with a modulation phase shift method. Dashed curves are calculations fit to the measured data. The resonator quality factor Q is 4500. The transmission and group-delay data allows unambiguous determination of coupling and loss, which are respectively 51% and 8.5% (0.4 dB) per ring revolution. In this (over-coupled) regime the ring resonator Q is determined by the coupling coefficient rather than the loss, and is thus defined by the design.

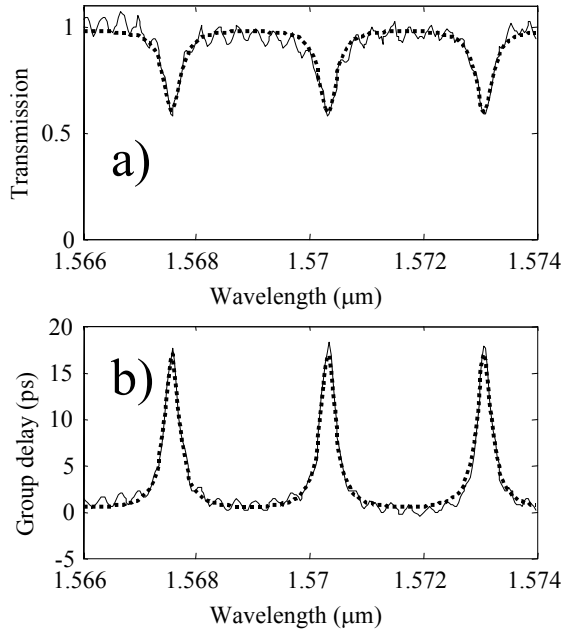


Figure 52. Transmission a) and group delay b) of a single ring resonator (see Figure 53a). Solid: measured data; Dotted: calculation.

3.1.10. Active Ring Characterization

3.1.10.1. RF response

Figure 54a shows the transmission of an interferometer with a ring resonator in one arm. Ring resonator index modulation of the results in an enhanced phase modulation of one interferometer arm. The measured modulation response of the configuration is displayed in Figure 54b. In this measurement the ring resonator is reverse-biased, and a 1 GHz sine-signal is applied. The modulation depth of the signal is retrieved with a network analyzer, while the wavelength is scanned.

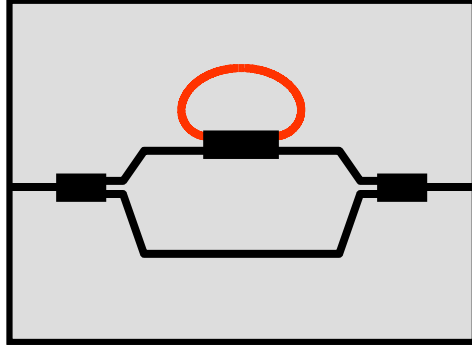


Figure 53. Ring resonator in a Mach-Zehnder configuration.

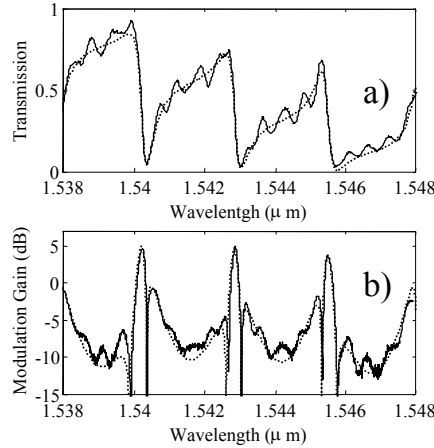


Figure 54. a) Transmission of a Mach-Zehnder interferometer with a ring-resonator in one arm . b) Modulation gain (i.e. modulation efficiency as compared to that of a straight waveguide of length equal to the ring circumference). Solid: measured data; Dotted: calculation.

3.1.11. Issues with RF Modulation Response

Fast recombination rate at the surface of semiconductors is a well-known phenomenon leading to a high dark current in semiconductor detectors and high leakage current in mesa transistors. This effect becomes far more significant for devices with a large edge-to-area ratio. The submicron width of the etched ridges in these ring resonators leads to an extremely high edge-to-area ratio compared with a standard semiconductor device. In fact, our experimental data for the ring resonators shows a very high leakage current density compared to the theoretically predicted values. The general belief is that the termination of the periodic potential of the semiconductor crystal at the surface and formation of the so-called dangling bonds lead to formation of energy states inside the bandgap of the semiconductor. If the density of such states is high they effectively produce a semi-metallic surface that can pin the Fermi level and cause a surface accumulation. Unfortunately, the accumulation is deeper in the undoped active area of the device (see Figure 55.)

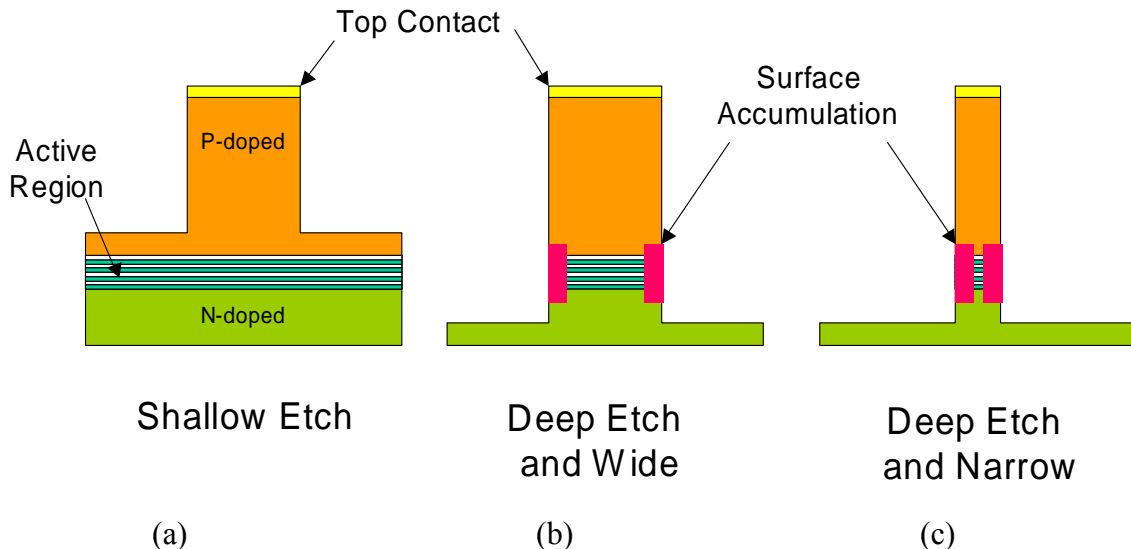


Figure 55. (a) The active region is immune from the surface accumulation in a shallow mesa structure. In deep etch mesas however; the effect depends on the mesa width. For a deep and wide mesa (b) the effect is not as significant as for a deep and narrow mesa (c).

Numerical calculation shows that even a small surface charge density can produce deep accumulation layers in low-doped layers. Figure 56 compares the conduction and valence band energy profiles for $3\text{ }\mu\text{m}$ and $0.8\text{ }\mu\text{m}$ wide ridges with surface charge density of $10^{11}\text{ electron/cm}^2$ and background doping of 10^{16} cm^{-3} . The accumulation layer clearly covers a large volumetric fraction of the $0.8\text{ }\mu\text{m}$ wide ridge.

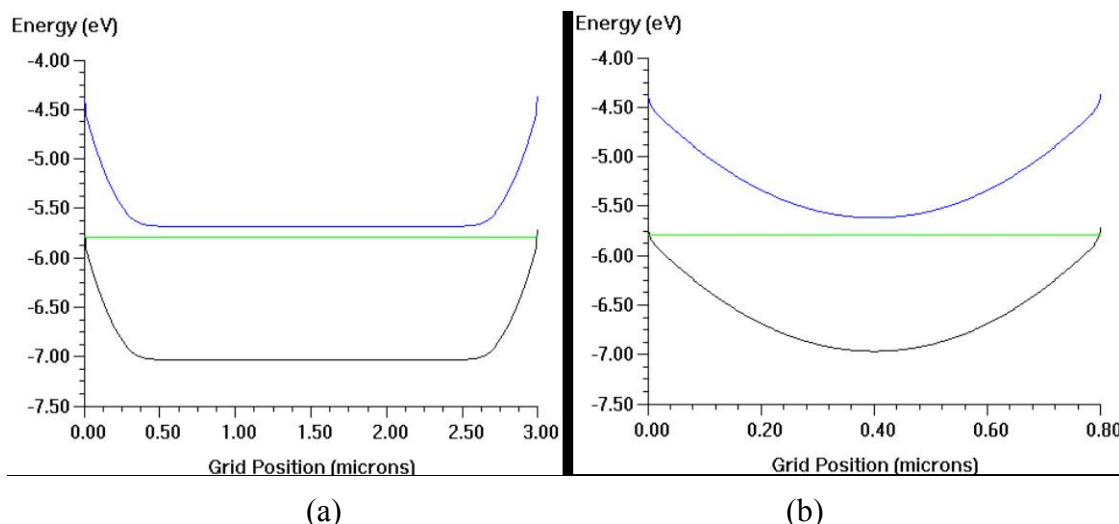


Figure 56. Energy band structure of (a) 3 μm wide and (b) 0.8 μm wide InP layer with surface charge density of 10^{11} electron/cm 2 and background doping level of $10^{16}/\text{cm}^3$.

A two-dimensional modeling was carried on using finite element method (FEM) to study the effect of surface accumulation on the electric field inside a narrow ridge. Figure 57 compares the simulated electric field (intensity and vector) in a $0.8 \mu\text{m}$ wide deeply etched modulator structure without (a) and with (b) the accumulation layers. It shows that the accumulation layer not only reduces the intensity of the field inside the active region, but it also diverts the vertical electric field vectors to a direction not effective for the electrorefraction effect.

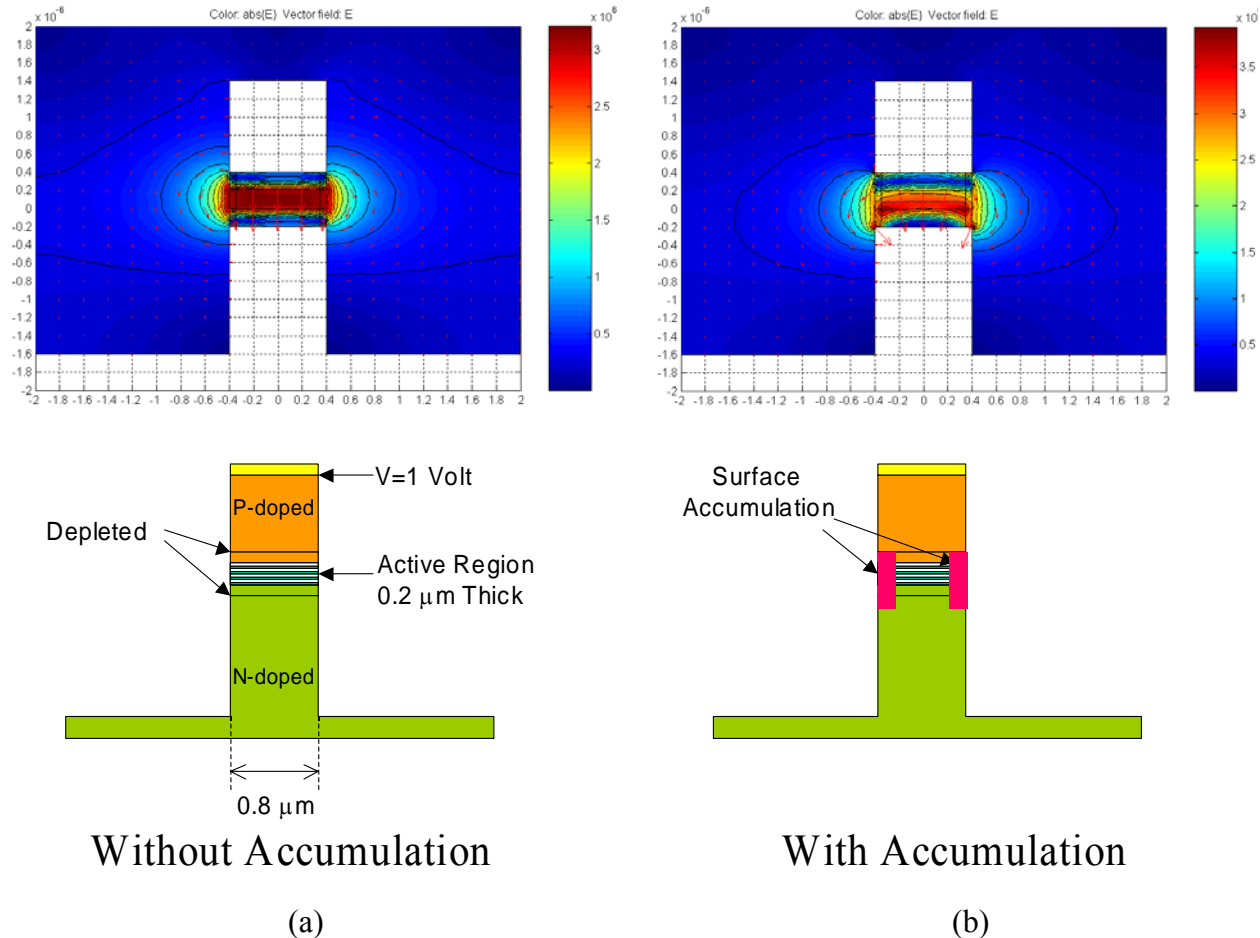


Figure 57. Modeling of the electric field intensity and vector of a deeply etched p-i-n modulator structure (a) without surface accumulation and (b) with surface accumulation.

Our measured data for deeply etched modulators shows that their modulation efficiency is about 50% lower than the shallow-etched modulators processed from the same wafers. We compared the modulation efficiency of the devices with different surface coating. Samples coated with Cytop showed $\Delta n/\Delta V \sim 0.5 \times 10^{-4}$ (1/volts) compared to a $\Delta n/\Delta V \sim 3 \times 10^{-4}$ for the shallow etched (without any exposed surface at the active layers) devices. However, samples coated with a-Si showed $\Delta n/\Delta V \sim 1 \times 10^{-4}$, a factor of two better efficiency than the devices coated with Cytop.

Also, high frequency measurements of the modulation response of the rings show an unusually low cutoff frequency (~ 4 GHz) that could not be explained by an RC model indicating at least a 10 GHz cutoff frequency (see Figure 58). Our speculation is that the deep energy states at the surface behave like deep level charge traps that cause a slow frequency response.

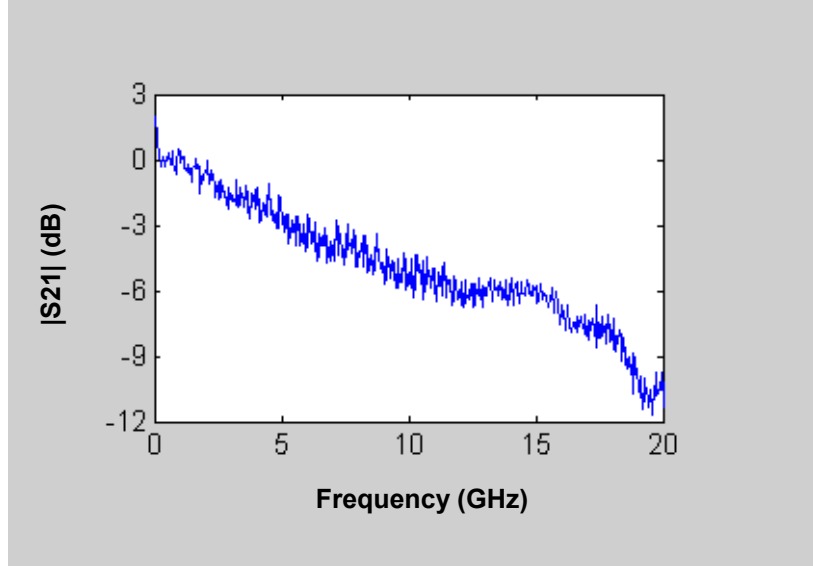


Figure 58. Modulation frequency response of a modulator.

High density of the surface states should also lead to a high recombination rate at the surface. Since the radiative recombination rate is constant, a faster surface recombination rate (non-radiative) means that the majority of the carriers will not go through the radiative recombination channel. This means that if carriers are injected to the active layer by forward biasing the modulator, one should see a lower radiation for narrow ridges compared to the wide ridges. We verified this behavior experimentally as shown in Figure 59. The MMI in the forward biased device is ~ 3 μm wide, while the waveguide sections are ~ 0.8 μm wide. The metal contacts are on the narrow waveguides only, so the current injection level is highest at the narrow waveguide area. However, infrared microscope image shows that the emission intensity is significantly higher in the wider MMI area due to the lower edge-to-area ratio in this section.

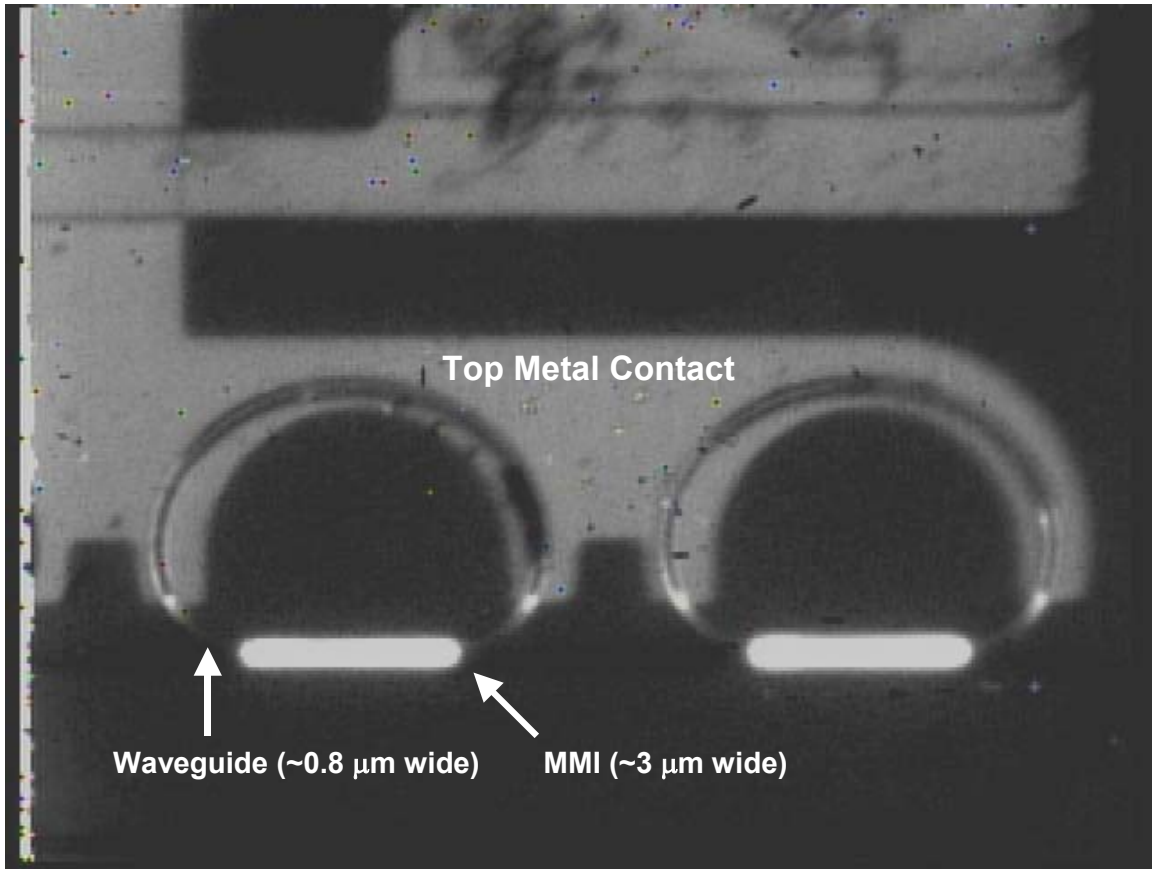


Figure 59. Infrared micrograph of a forward biased device.

3.2. Impact of REM Technology beyond RFLICs

3.2.1. DARPA/MTO CS-WDM Program

The Sarnoff ring-modulator activity was continued under the CS-WDM DARPA project. Here we are taking advantage of the wavelength selective nature of the ring-modulators. Ring-resonators are further optimized and new coupling schemes were introduced to accommodate for the requirements to achieve wavelength selective modulators.

Electro-refractive InP/InGaAsP ring-resonators with quality factors of up to 20,000 are demonstrated. A novel modified MMI-coupler provides reproducible low coupling to the access waveguide. We demonstrate modulation and the first link experiments²³.

²³ M. H. Kwakernaak, A. N. Lepore, H. Mohseni, N. Maley, H. An, Z. Shellenbarger, A. M. Braun, W. Chan, J. H. Abeles, J. W. Bae, J. H. Jang, I. Adesida, "Wavelength Selective Electro Optic Modulator with High-Q Ring Resonators in Deeply Etched InP/InGaAsP Waveguides", Conference on Lasers and Electrooptics CThH, 2004.

Ring-resonator modulator arrays for WDM applications can enable a dramatic reduction in size, power consumption and cost. The resonant cavity of the ring resonator results in a substantial decrease of the V_π of the modulator for a given electrode length. As a consequence compact devices with low electrical parasitics can be used for efficient modulation. The wavelength-selective nature of the resonators allows modulation at one or multiple, specific wavelengths without using filtering devices such as AWG's.

The fabricated ring-resonators are based on deeply etched 1- μm -wide waveguides on InGaAsP/InP. Smoothly, highly vertical etched sidewalls enable low optical losses²⁴ and an advanced quantum-well active region design results in a high dn/dV ²⁵.

Accurate control over the coupling value to the access waveguide is essential for device designs involving multiple rings to obtain specific filter functions or multi-wavelength resonator arrays. The coupler we use consists of two cascaded MMI sections, which join at a small angle (Figure 60b). Each section is a 2x2 MMI with a coupling ratio of 14.6%:85.4%. The coupling ratio of the combined coupler can be selected by the angle at the joint. This MMI scheme results in much more reproducible coupling ratios than directional couplers and does not involve the elaborate processing required for vertical coupling schemes^{26 27}.

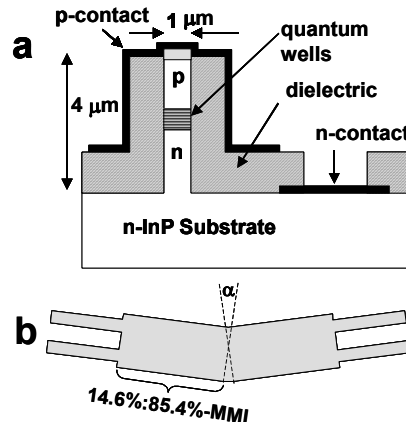


Figure 60. a) Device structure b) Schematic of the modified MMI-coupler.

²⁴ J. H. Jang, W. Zhao, J. W. Bae, D. Selvanathan, S. L. Rommel, I. Adesida, A. Lepore, M. Kwakernaak, J. H. Abeles, "Direct measurement of nanoscale sidewall roughness of optical waveguides using atomic force microscope", *Applied Physics Letters* 83(20), 4116 (2003).

²⁵ H. Mohseni, H. An, Z. A. Shellenbarger, M. H. Kwakernaak, and J. H. Abeles, "Enhanced electro-optic effect in GaInAsP-InP three-step quantum wells" *Applied Physics Letters* 84(11), 1823-1825, 2004.

²⁶ V. Van, P.P. Absil, J.V. Hrymiewicz, P.-T. Ho, "Propagation loss in single-mode GaAs-AlGaAs microring resonators: measurement and model", *IEEE J. Lightwave Technol.* 19, 1734 (2001).

²⁷ K. Djordjev, C. Seung-June, C. Sang-Jun, P.D. Dapkus, "Vertically coupled InP microdisk switching devices with electroabsorptive active regions", *IEEE Photon Technol. Lett.* 14, 1115 (2002).

Figure 61a shows the optical transmission of ring resonators with a quality factor of 20,000 and a finesse of 36. The ring circumference is 200 μm and the coupling to the access waveguide is 7%. Values for the coupling and resonator losses extracted from transmission measurements are shown in Figure 61b. Resonator losses, which include one pass waveguide loss and excess coupler loss, are 10%.

Figure 62a shows the electro-optic response of a ring resonator with a reverse bias from 0 to 10 V. A tuning coefficient df/dV of 6 GHz/V is obtained. With appropriate biasing the close to critically coupled ring-resonator acts as a modulator with an equivalent V_π of 2 V. An eye diagram at 1 Gb/s in a link with this ring modulator is shown in Figure 62b.

Support by DARPA/MTO under contract number DAAD17-02-C-0094 is acknowledged.

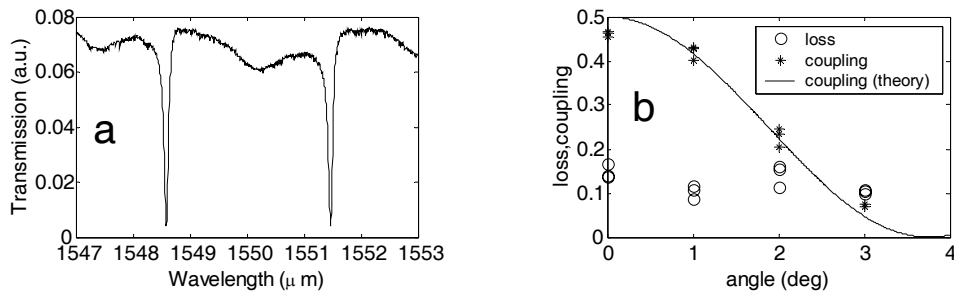


Figure 61. a) Transmission of a ring-resonator, b) Coupling and loss extracted from transmission measurements from ring-resonators for various MMI joint angles.

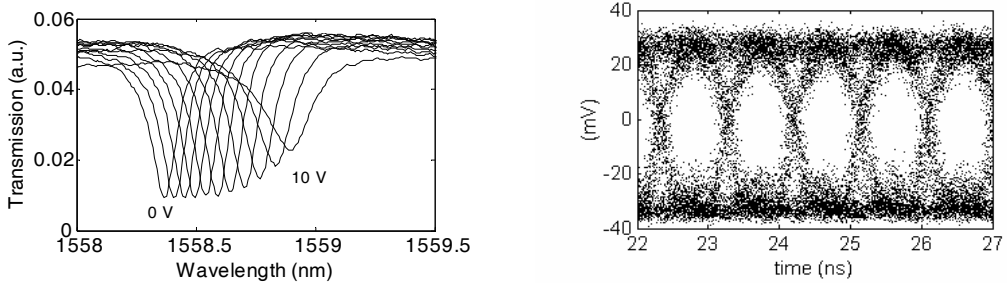


Figure 62. a) Tuning of the resonance in 1 Volt steps. b) Eye diagram of a link with a ring-resonator modulator.

3.2.2. DARPA/MTO SWAODL Program

Under the AOSP DARPA project the ring-resonator work was continued and ring-resonators were optimized for high Q. Values of 90,000 were obtained (See Figure 63).

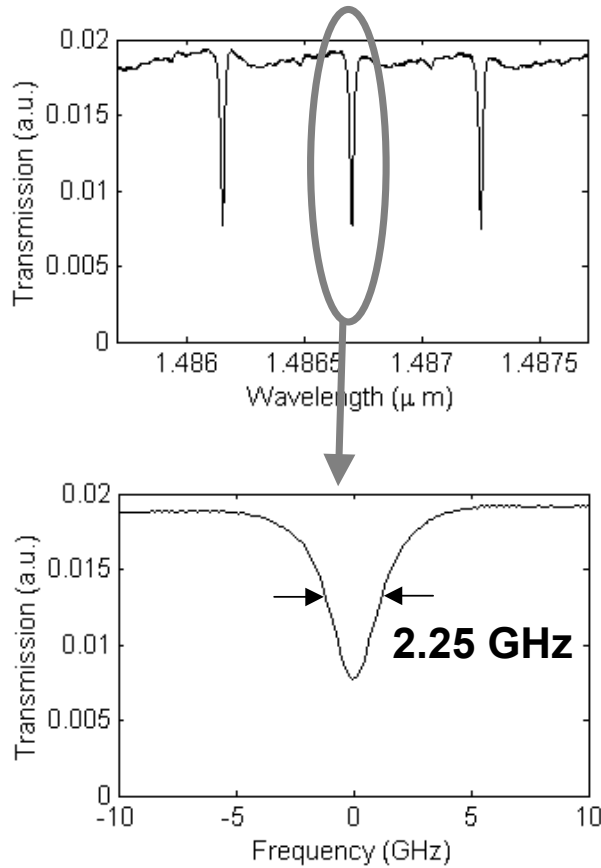


Figure 63. Measured Transmission through ring-resonator with a circumference of 1.1 mm and a modified MMI-coupler. The quality factor is 90,000. The finesse is 34 and the optical bandwidth of the resonance is 2.25GHz.

3.2.3. DARPA/MTO AOSP-PAWG Subcontract to UCF-CREOL

As part of the AOSP DARPA project Sarnoff realized modulator materials with a highly linear phase response. These materials are based on stepped quantum wells, having been developed under RFLICS to obtain very efficient modulation while being optimized for linearity.

Highly linear and efficient InGaAsP phase modulators are presented. These devices show an order of magnitude higher linearity than bulk or quantum well phase modulators, while their efficiency is comparable to the best reported values²⁸.

Highly linear optical phase modulators are attractive for many applications including laser gyroscopes, multi-wavelength laser sources, beam steering, and photonic arbitrary waveform

²⁸ H. Mohseni, H. An, Z. A. Shellenbarger, M. H. Kwakernaak, A. N. Lepore, J. H. Abeles, P. J. Delfyett, Jr, "Highly linear and efficient GaInAsP-InP phase modulators" Conference on Lasers and Electrooptics CWI4, 2004.

generators²⁹. Although commonly used phase modulators based on lithium niobate have an inherent high linearity, they cannot provide the degree of integration required for applications such as high-speed optical NxN switches³⁰, where hundreds of closely spaced modulators are needed. In contrast, semiconductor-based phase modulators can provide a high degree of integration, but they are inherently non-linear. The main sources of non-linearity in the semiconductor phase modulators are quadratic electrooptic (QEO) effects. Although using bulk semiconductors, instead of quantum wells, active layers can reduce these effects, and would also reduce the modulation efficiency significantly. Here, we present linearized phase modulators based on GaInAsP/InP quantum wells. Modulator linearity is more than one order of magnitude higher than bulk GaAs and GaInAsP, while modulation efficiency is comparable to the best low-loss quantum well modulators.

The active layer of our modulators is based on GaInAsP stepped quantum wells. The absorption spectrum of the quantum wells was modeled using an effective mass approach, and the excitonic effect was modeled with a variational method. The change of index was then calculated from the Kramers-Kronig relationship. Thickness and composition of the quantum well layers were optimized for high linearity, while keeping the absorption coefficient below $\sim 1 \text{ cm}^{-1}$.

Modulator structures are grown by low-pressure metal organic vapor phase epitaxy (MOVPE) on n-type InP substrates. The doping profile in the cladding layer was designed to further improve the phase linearity. Conventional phase modulators with square quantum well active layers were also grown as references. The material was then processed into shallow-etched waveguides for optical and electrical measurements.

Optical absorption coefficient and change of index of the modulators are measured using Fabry-Perot oscillation shifts. Figure 64 shows an example of the measured Fabry-Perot oscillation shift in a 2 mm-long modulator versus the modulator bias at $\lambda \sim 1550 \text{ nm}$. Figure 65 shows the measured change of index versus the applied reverse bias at different wavelengths for a linearized phase modulator. Change of index versus bias is linear over the measured wavelength range of 1500 to 1570 nm. In order to compare the quadratic and linear electrooptic effects, we fit a second order polynomial $\Delta n = A_0 + A_1 V + A_2 V^2$ to the measured data points, and use A_1/A_2 ratio as a measure of linearity. Figure 66 compares the change of index versus bias of a linearized modulator to a conventional modulator at $\lambda = 1560 \text{ nm}$ for TE polarization. Linearized modulator shows A_1/A_2 ratio of ~ 640 , while the modulator with a conventional design shows A_1/A_2 ratio of ~ 10 . The linearized modulator shows higher linearity than the modulators based on bulk semiconductors. For instance, calculated A_1/A_2 ratio for GaAs and InP at $\lambda \sim 1550 \text{ nm}$ is

²⁹ T. Yilmaz, C. M. Christopher, M. DePriest, T. Turpin, J. H. Abeles, and P. J. Delfyett, "Towards a Photonic Arbitrary Waveform Generator Using a Modelocked External Cavity Semiconductor Laser," *IEEE Photon. Technol. Lett.* **14**, 1608 (2002).

³⁰ E. Shekel, D. Majer, G. Matmon, A. Krauss, S. Ruschin, T. McDermott, M. Birk, M. Boroditsky, "Broadband testing of a 64/spl times/64 nanosecond optical switch," *Lasers and Electro-Optics Society, 2002. LEOS 2002. The 15th Annual Meeting of the IEEE*, Volume: 2, 10-14 Nov. 2002 Page(s): 371 -372 vol.2.

about 75 and 20 respectively³¹. The modulation efficiency of the linearized modulator is about $48^\circ/\text{mm.V}$ with a maximum loss of $\sim 1 \text{ cm}^{-1}$, which is more than three times better than the efficiency of bulk-based modulators³¹.

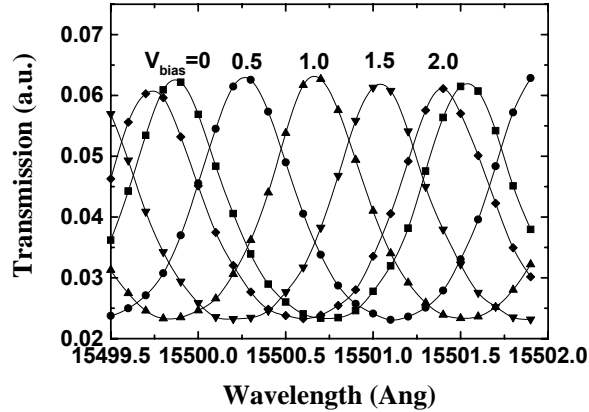


Figure 64. Fabry-Perot oscillation shift in a 2 mm long phase modulator for different bias values.

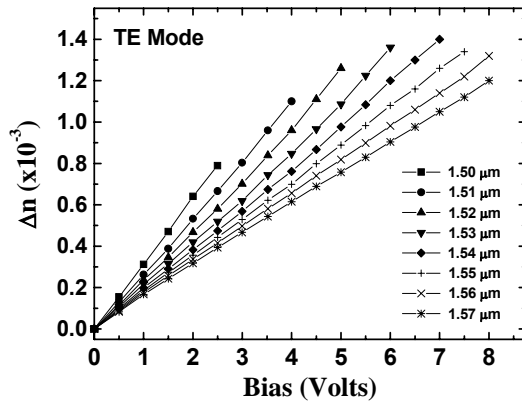


Figure 65. Measured change of index versus reverse bias voltage at different wavelengths.

³¹ S. Lee, R. Ramaswamy, V. Sundaram, "Analysis and Design of High-speed High-efficiency GaAs-AlGaAs Double-Heterostructure Waveguide Phase Modulators," IEEE J. of Quantum Elect. **27**, 726 (1991).

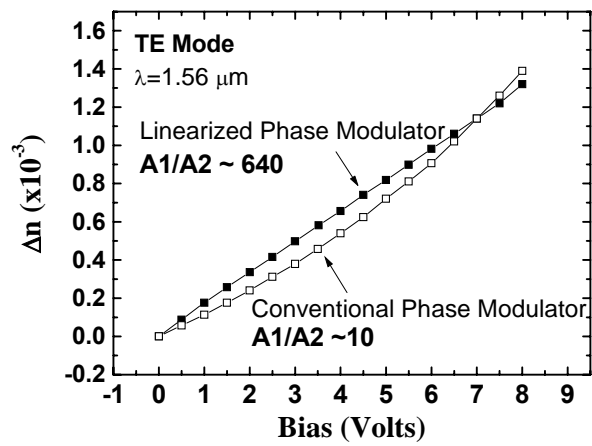


Figure 66. Change of index versus bias for a linearized phase modulator compared to a conventional phase modulator at $\lambda=1.56 \mu\text{m}$ and for TE polarization.

4. Conclusions

Summarized below are the most important conclusions drawn from this project.

Materials:

- The quantum well performance can be modeled accurately.
- High-resolution x-ray diffraction and photo luminescence must be used routinely to monitor the crystal quality of the epitaxial layers as well as their thickness and composition.
- Stepped quantum wells have superior performance compared to the conventional square quantum wells for low-loss phase modulators.
- We showed that the stepped quantum wells, unlike the coupled quantum wells, could be grown with conventional growth methods, and achieve the predicted superior performance routinely.

Design:

- In lateral waveguide geometry MMI couplers are superior over evanescent couplers as they can be fabricated with predictable properties.
- Predictable coupler properties are essential to obtain predictable ring properties such as group delay, Q, and RF-bandwidth.
- Careful design of the ring-resonator with gradual change in curvature as opposed to a racetrack design and careful mode matching to the coupler can result in good ring-resonator properties even if the waveguides are not strictly single-mode.
- The optical ring Quality factor limits the RF modulation bandwidth. However the rings can be designed to meet the required modulation bandwidth requirement. The V_{pi} obtained with single rings will be limited as well but can be further reduced with multiple rings.
- Ring resonators can alleviate the velocity mismatch limitations in traditional modulators since RF and optical delays can be designed more independently.
- The ultimate limitation to the modulation signal amplitude at the output is the optical loss. With loss less waveguides and couplers it is possible to design multiple ring-modulators with arbitrary low V_{pi} operating up to the desired RF bandwidth.

Processing:

- Extremely smooth etching is required to obtain acceptable waveguide loss and ring-properties due to the large index contrast needed for the tight bends.
- ICP etching of InGaAsP/InP waveguides with a NiCr – SiO_2 etch mask and SiO_2 remasking can result in deeply etched waveguides with RMS roughness as low as 3 nm.
- We found electrical surface issues to be extremely important for a high-speed and efficient REM device.

5. References

- [7] S. L. Rommel, J.H. Jang, W. Lu, G. Cueva, L. Zhou, I. Adesida, G. Pajer, R. Whaley, A. Lepore, Z. Schellenbarger, and J. H. Abeles, "Effect of H₂ on the Etch Profile of InP/InGaAsP Alloys in Cl₂/Ar/H₂ Inductively-Coupled-Plasma Reactive Ion Etching Chemistries for Photonic Device Fabrication," *Journal of Vacuum Science and Technology* **B20**, 1327-1330 (2002).
- [8] J.-H. Jang, W. Zhao, J.-W. Bae, D. Selvanathan, S. L. Rommel, I. Adesida, A. Lepore, M. Kwakernaak, and J. H. Abeles, "Direct measurement of nanoscale sidewall roughness of optical waveguides using an atomic force microscope," *Applied Physics Letters* **83**, 4116-4118 (2003).
- [9] J.-W. Bae, W. Zhao, J.-H. Jang, I. Adesida, A. Lepore, M. Kwakernaak, and J. H. Abeles, "Characterization of sidewall roughness of InP/InGaAsP etched using inductively-coupled-plasma for low loss optical waveguide applications," *Journal of Vacuum Science and Technology* **B21** (6), 2888-2891 (2003).
- [10] D. Marcuse, *Bell Syst. Tech. J.*, vol. 48, pp. 3187-3215.
- [11] J.P.R. Lacey and F. P. Payne, *IEE Proc.*, vol. 137, pp. 282-288, 1990.
- [12] H. Teylor, *J. of Lightwave Technol.* **17**, 1875 (1999).
- [13] K. Noguchi, O. Mitomi, and H. Miyawaza, *J. Lightwave Technol.* **16**, 615 (1998).
- [14] D. Chen, H. Fetterman, A. Chen, W. Steier, L. Dalton, W. Wang, and Y. Shi, *Appl. Phys. Lett.* **70**, 3335 (1997).
- [15] Y. Chan, and K. Tada, *IEEE J. of Quantum Elect.* **27**, 702 (1991).
- [16] H. Feng, J. Pang, K. Tada, and Y. Nakano, *IEEE Photonic Technol.* **9**, 639 (1997).
- [17] C. Thirstrup, *IEEE J. of Quantum Elect.* **31**, 988 (1995).
- [18] Y. Huang, Y. Chen, and C. Lien, *Appl. Phys. Lett.* **67**, 2603 (1995).
- [19] Y. Chen, H. Li, Z. Zhou, and K. Wang, *J. Appl. Phys.* **76**, 4903 (1994).
- [20] H. Feng, J. Pang, M. Sugiyama, K. Tada, and Y. Nakano, *IEEE J. of Quantum. Elec.* **34**, 1197 (1998).
- [21] T. R. Walker, *Electron. Lett.* **21**, 581 (1985).
- [22] See for example S. Hamilton, D. Yankelevich, A. Knoesen, R. Weverka, and R. Hill, *IEEE Transactions on Microwave Theory and Techniques* **47**, 1184 (1999).
- [23] M. H. Kwakernaak, A. N. Lepore, H. Mohseni, N. Maley, H. An, Z. Shellenbarger, A. M. Braun, W. Chan, J. H. Abeles, J. W. Bae, J. H. Jang, I. Adesida, "Wavelength Selective Electro Optic Modulator with High-Q Ring Resonators in Deeply Etched InP/InGaAsP Waveguides", Conference on Lasers and Electrooptics CThH, 2004.

- [24] J. H. Jang, W. Zhao, J. W. Bae, D. Selvanathan, S. L. Rommel, I. Adesida, A. Lepore, M. Kwakernaak, J. H. Abeles, “Direct measurement of nanoscale sidewall roughness of optical waveguides using atomic force microscope”, *Applied Physics Letters* 83(20), 4116 (2003).
- [25] H. Mohseni, H. An, Z. A. Shellenbarger, M. H. Kwakernaak, and J. H. Abeles, “Enhanced electro-optic effect in GaInAsP-InP three-step quantum wells” *Applied Physics Letters* 84(11), 1823-1825, 2004.
- [26] V. Van, P.P. Absil, J.V. Hrynewicz, P.-T. Ho, “Propagation loss in single-mode GaAs-AlGaAs microring resonators: measurement and model”, *IEEE J. Lightwave Technol.* 19, 1734 (2001).
- [27] K. Djordjev, C. Seung-June, C. Sang-Jun, P.D. Dapkus , “Vertically coupled InP microdisk switching devices with electroabsorptive active regions”, *IEEE Photon Technol. Lett.* 14, 1115 (2002).
- [28] H. Mohseni, H. An, Z. A. Shellenbarger, M. H. Kwakernaak, A. N. Lepore, J. H. Abeles, P. J. Delfyett, Jr, “Highly linear and efficient GaInAsP-InP phase modulators” *Conference on Lasers and Electrooptics CWI4*, 2004.
- [29] T. Yilmaz, C. M. Christopher, M. DePriest, T. Turpin, J. H. Abeles, and P. J. Delfyett, “Towards a Photonic Arbitrary Waveform Generator Using a Modelocked External Cavity Semiconductor Laser,” *IEEE Photon. Technol. Lett.* **14**, 1608 (2002).
- [30] E. Shekel, D. Majer, G. Matmon, A. Krauss, S. Ruschin, T. McDermott, M. Birk, M. Boroditsky, “Broadband testing of a 64/spl times/64 nanosecond optical switch,” *Lasers and Electro-Optics Society, 2002. LEOS 2002. The 15th Annual Meeting of the IEEE* , Volume: 2 , 10-14 Nov. 2002 Page(s): 371 -372 vol.2.
- [31] S. Lee, R. Ramaswamy, V. Sundaram, “Analysis and Design of High-speed High-efficiency GaAs-AlGaAs Double-Heterostructure Waveguide Phase Modulators,” *IEEE J. of Quantum Elect.* **27**, 726 (1991).

APPENDICES

Appendix A: Viewgraph Presentations

- **REM Kickoff Arlington August 2000**
- **REM Site Visit Sarnoff February 2001**
- **REM Site Visit Sarnoff February 2002**
- **REM GOMAC Monterrey March 2002**
- **REM Site Visit Sarnoff October 2002**
- **REM PI Review Reno 2003**
- **REM Site Visit Sarnoff March 2003**

Appendix B: Publications

• **JVST B 2002 Rommel**

S. L. Rommel, J-H Jang, W. Lu, G. Cueva, L. Zhou, I. Adesida , G. Pajer, R. Whaley, A. Lepore, Z. Shellenbarger, J. Abeles, "The effect of H₂ on the etch profile of InP/InGaAsP alloys in Cl₂/Ar/H₂ inductively coupled plasma-reactive ion etching chemistries for photonic device fabrication.", J. of Vacuum Science and Technology B, 20, 1327 (2002).

• **CLEO 2003 Kwakernaak**

M.H. Kwakernaak, A. Lepore, H. Mohseni, H. An, Z. Shellenbarger, J.H. Abeles, J.-O. Bae, S. L. Rommel, I. Adesida, "Electro-Optic Low Loss MMI-Coupled Ring Resonators", Conf. on Lasers and Electro-Optics, CtuW, 2003.

• **EIPBN 2003 Bae**

J.W. Bae, W. Zhao, J. H. Jang, I. Adesida, A. Lepore, M. Kwakernaak, J. H. Abeles "Characterization of sidewall roughness of InP/InGaAsP etched using inductively coupled plasma for low loss optical waveguide applications", International Conference on Electron, Ion, Photon Beam Technology and Nanofabrication, PH 9, 2003.

• **APL 2003 Jang**

J. H. Jang, W. Zhao, J. W. Bae, D. Selvanathan, S. L. Rommel, I. Adesida, A. Lepore, M. Kwakernaak, J. H. Abeles, "Direct measurement of nanoscale sidewall roughness of optical waveguides using atomic force microscope", Applied Physics Letters 83(20), 4116-4118, 2003.

• **JVST B 2004 Bae**

J.W. Bae W. Zhao, J. H. Jang, and I. Adesida A. Lepore, M. Kwakernaak, and J. H. Abeles, “Characterization of sidewall roughness of InP/InGaAsP etched using inductively coupled plasma for low loss optical waveguide applications”, *J. Vac. Sci. Technol. B* **21**, 2888 (2003).

- **APL 2004 Mohseni**

H. Mohseni, H. An, Z. A. Shellenbarger, M. H. Kwakernaak, and J. H. Abeles, “Enhanced electro-optic effect in GaInAsP–InP three-step quantum wells” *Applied Physics Letters* 84(11), 1823-1825, 2004.

Resonant Enhanced Modulator Development

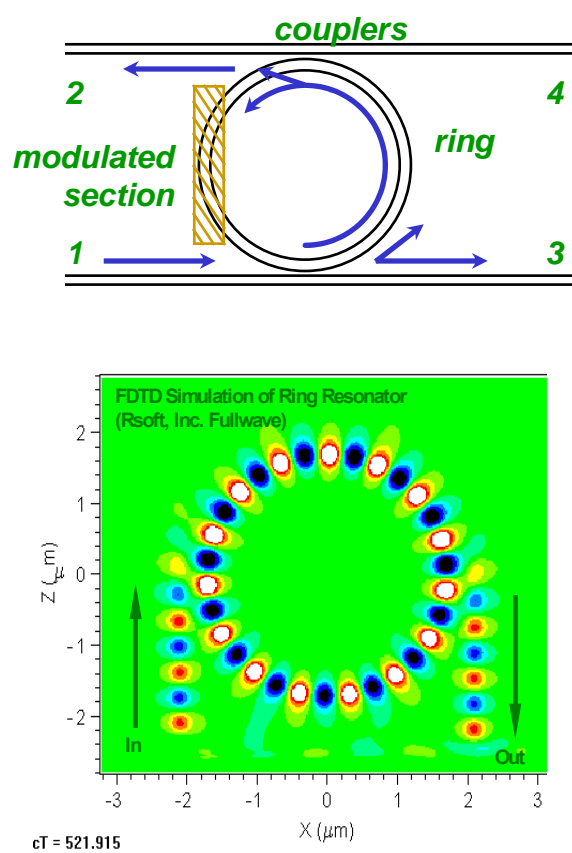
J.H. Abeles
Sarnoff Corporation

DARPA/MTO R-FLICs Program: Kickoff Meeting

Hilton Arlington & Towers, Arlington, VA
August 16, 2000

- Requirements for V_π Under 1 Volt
 - RF Photonics
 - High Dynamic Range
 - High Speed/Frequency/Bandwidth
 - $CV^2\Delta f$ Prohibitive Switching Power
 - Direct Connection to Antenna
 - Arrays
- Current Technology Inadequate (>1 Volt at ~ 10 GHz)
 - LiNbO₃
 - Electroabsorption
 - Polymer
- **Need: V_π in mV's, not Volts**

Double-Coupled Resonators



$$\left| \frac{\bar{E}_2}{\bar{E}_1} \right|^2 = \frac{k_1 k_2}{t_1^2 t_2^2 A^2 + 1 - 2t_1 t_2 A \cos \phi_R}$$

$$\phi_{21} = \tan^{-1} \left(\frac{-t_1 t_2 A \sin \phi_R}{t_1 t_2 A \cos \phi_R - 1} \right)$$

$$\phi_R = (\beta + \Delta\beta)L$$

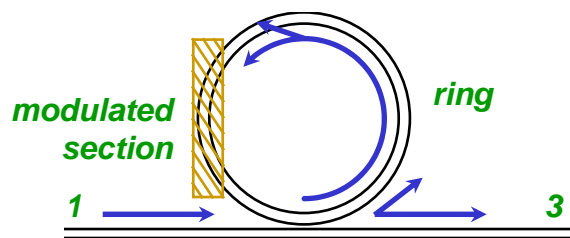
$$\beta = \frac{\omega}{c} \Delta n; \Delta\beta = \frac{\omega}{c} \Delta n$$

$$A = \exp^{-\alpha_{ampl} L}$$

$$k_{1,2} = power-coupling$$

Single-Coupled Resonators

$$\left| \frac{\bar{E}_3}{\bar{E}_1} \right|^2 = \frac{t^2 + A^2 - 2At \cos(\phi_R)}{t^2 A^2 + 1 - 2At \cos \phi_R}$$



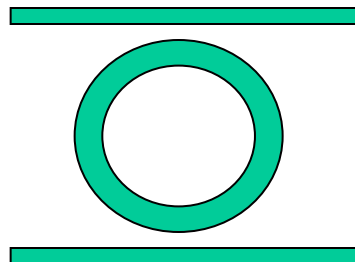
$$\phi_{31} = \tan^{-1} \left(\frac{A(t^2 - 1) \sin \phi_R}{t(A^2 + 1) - A(t^2 + 1) \cos \phi_R} \right)$$

$$\phi_R = (\beta + \Delta\beta)L$$

$$\beta = \frac{\omega}{c}n; \Delta\beta = \frac{\omega}{c}\Delta n$$

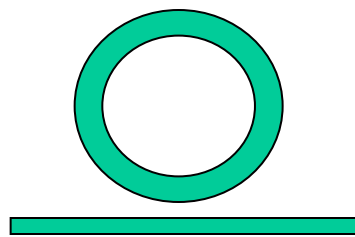
$$A = \exp^{-\alpha_{amp}L}$$

$$t = \sqrt{1 - (power_coupling)}$$



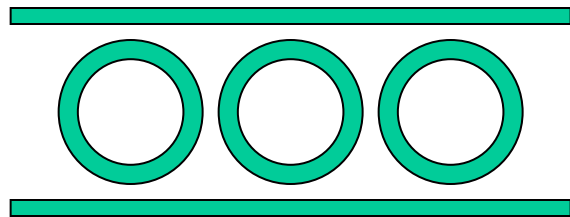
Double-Waveguide Coupled
Ring Resonator

- Tunable Filters
- WDM Add-Drop Multiplexers
- Ring Lasers



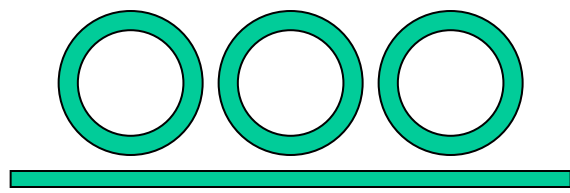
Single-Waveguide Coupled
Ring Resonator

- Frequency selective variable attenuators
- Frequency selective amplitude modulators
- Frequency selective phase modulators



Double-Waveguide Coupled
Multiple Ring Resonator

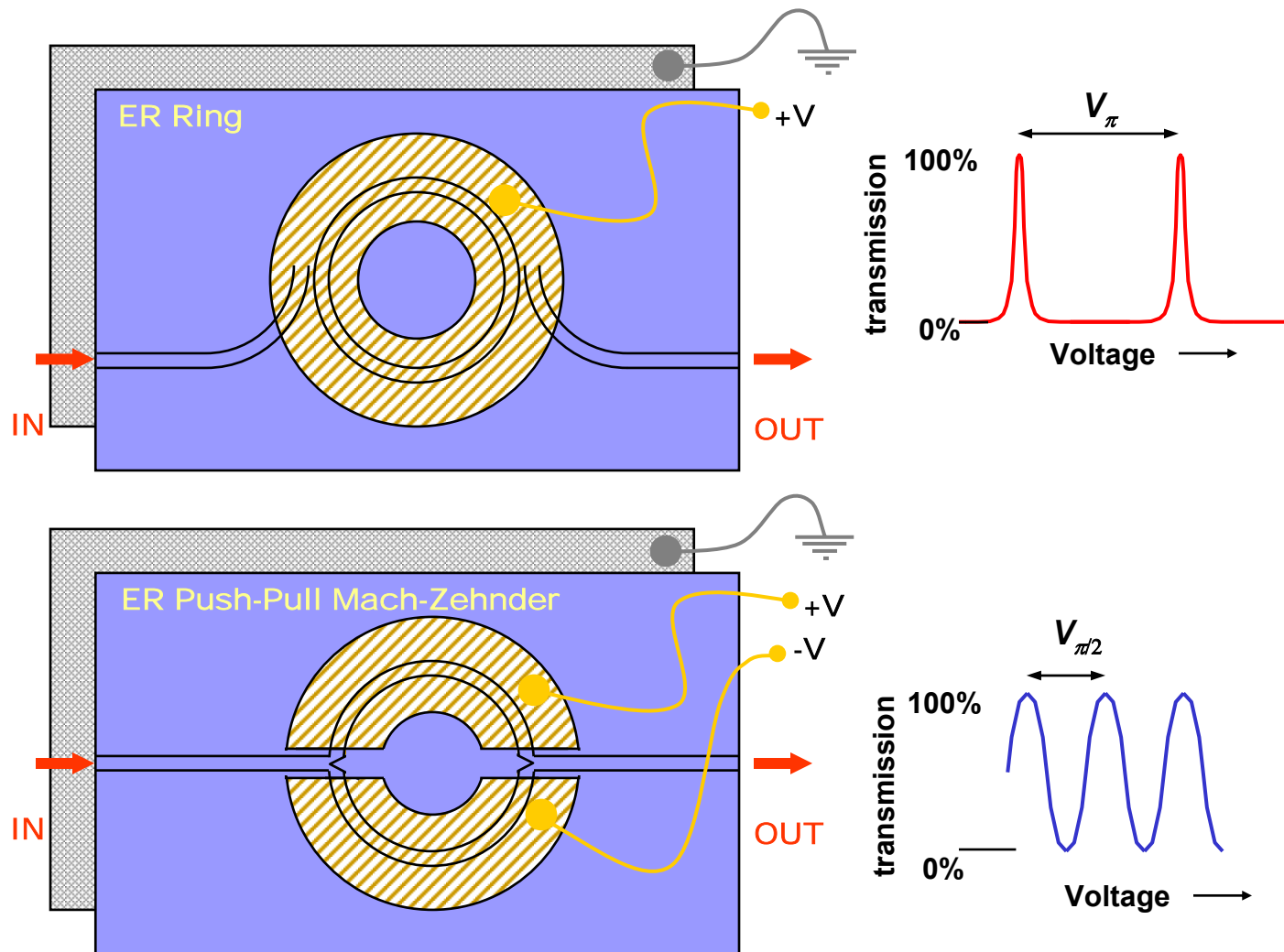
- Flat-top Tunable Filters
- Flat-top WDM Add-Drop Multiplexers



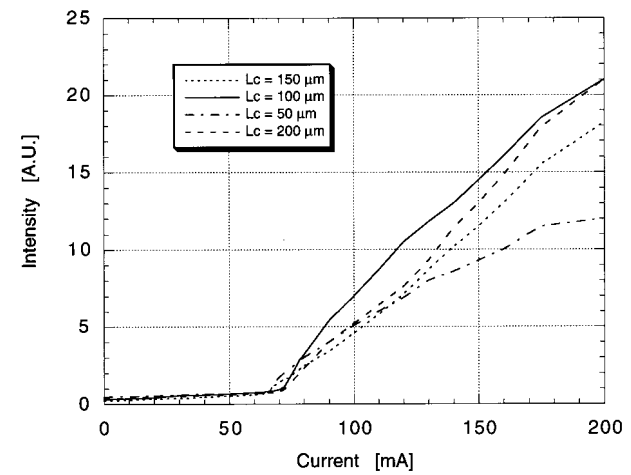
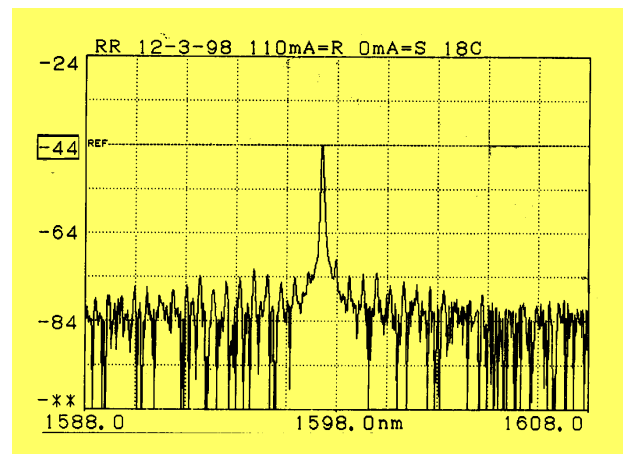
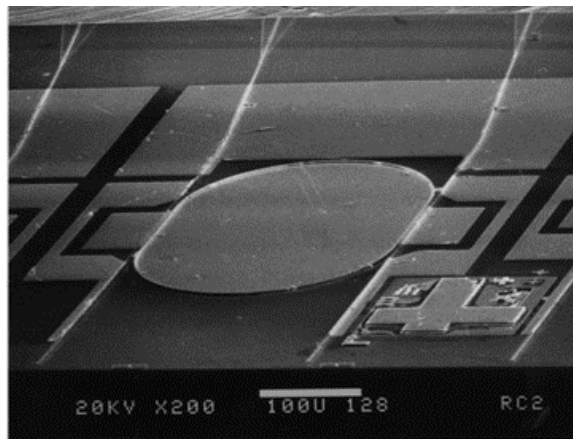
Single-Waveguide Coupled
Multiple Ring Resonator

- Multi-wavelength variable attenuators
- Amplifier gain equalizers
- Dispersion compensators

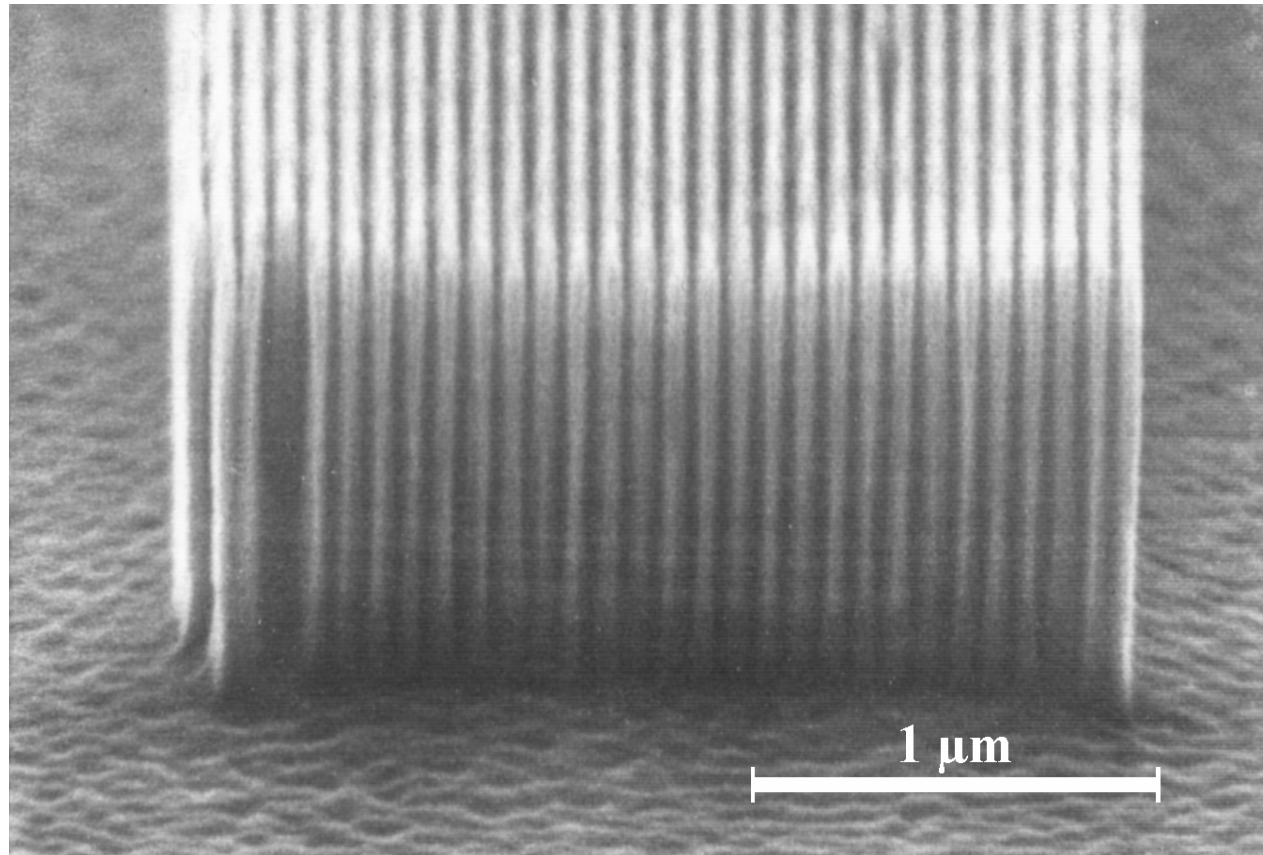
Ring Resonator vs. Mach-Zehnder



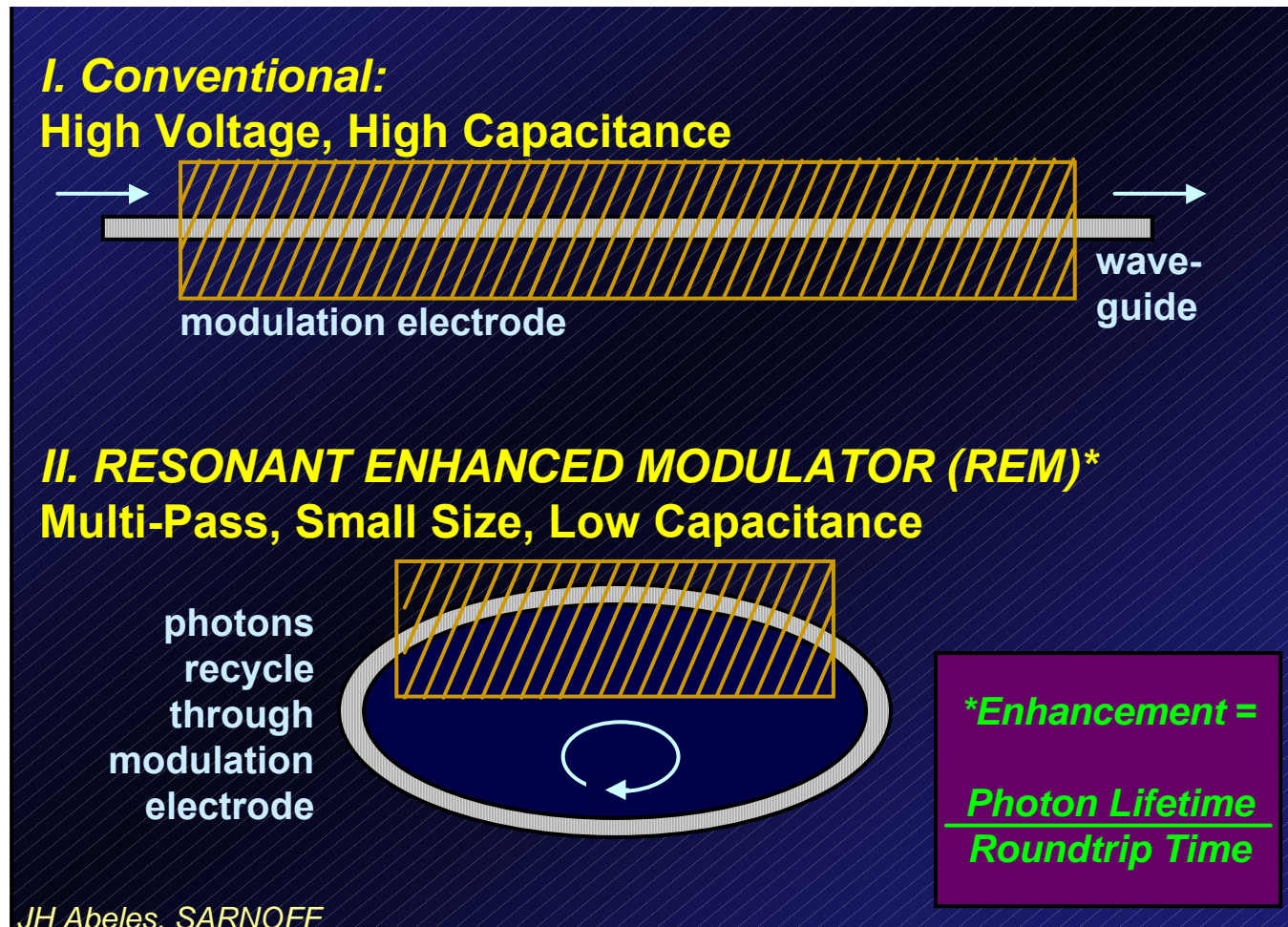
Record Low Threshold Ring Lasers



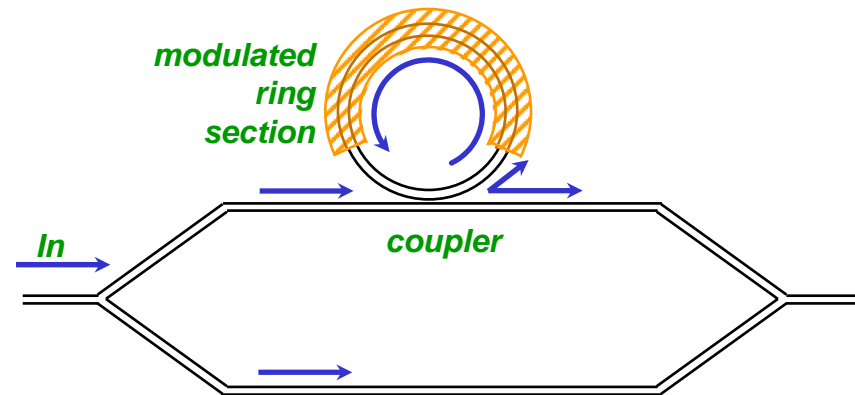
- $60 \text{ mA} = I_{th}$
- 1550 nm



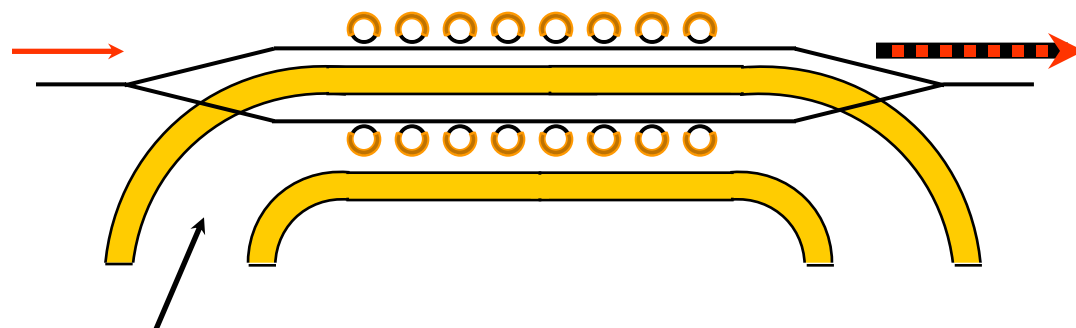
- $\text{CH}_4\text{-H}_2$ based
- 700 nm period



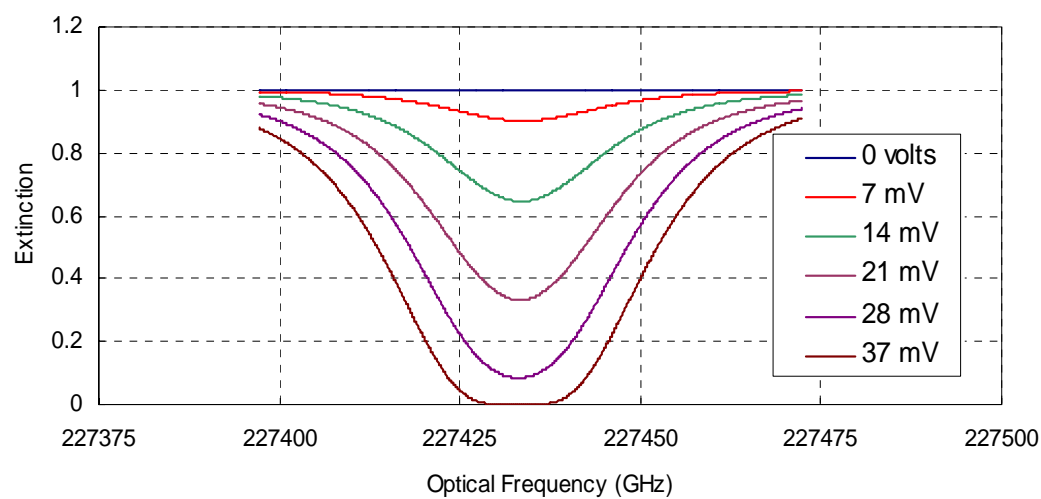
- Phase modulation due to coupled resonators
- Combine multiple resonators to achieve performance enhancement



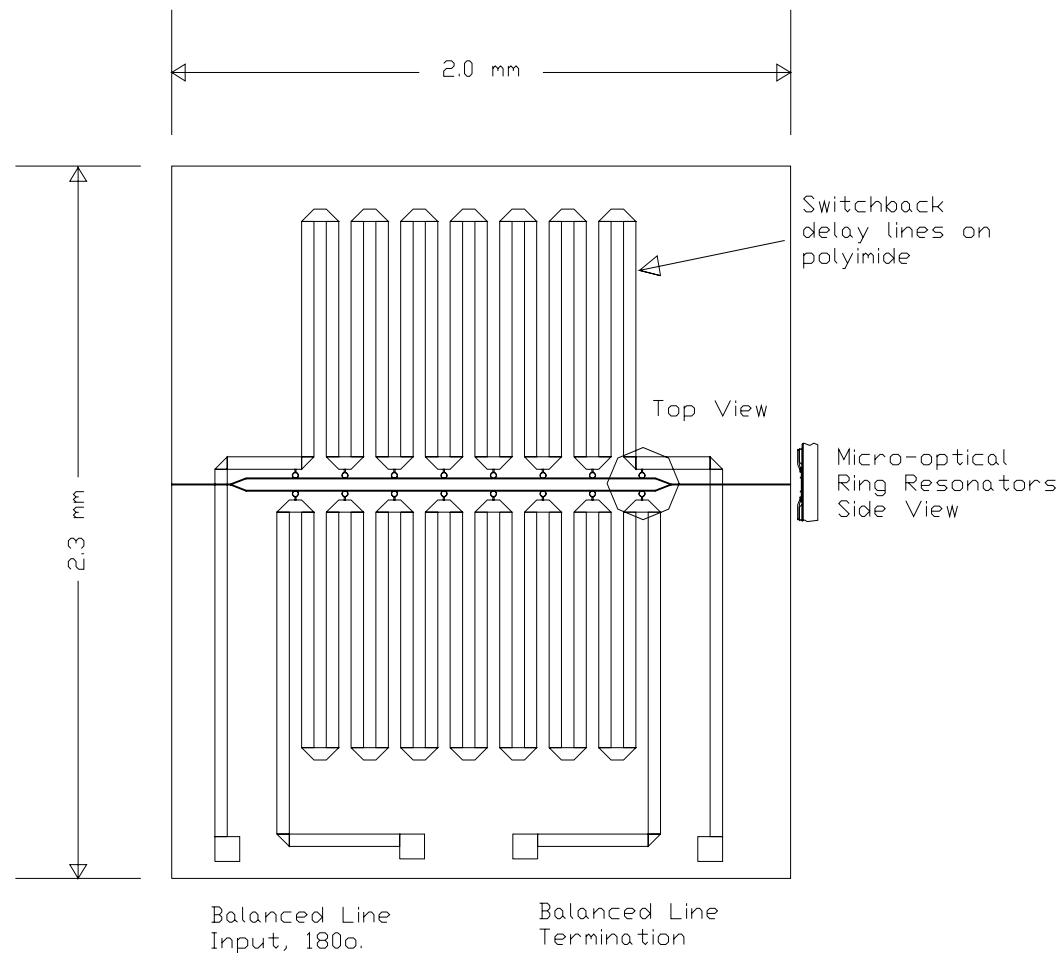
diameter (um)	FSR (GHz)	Passband (GHz)			Photon Lifetime (psec)		
		Finesse= 3	Finesse= 10	Finesse= 30	Finesse= 3	Finesse= 10	Finesse= 30
5	5968	1989	597	199	0.1	0.3	0.8
10	2984	995	298	99	0.2	0.5	1.6
20	1492	497	149	50	0.3	1.1	3.2
50	597	199	60	20	0.8	2.7	8.0
100	298	99	30	10	1.6	5.3	16.0



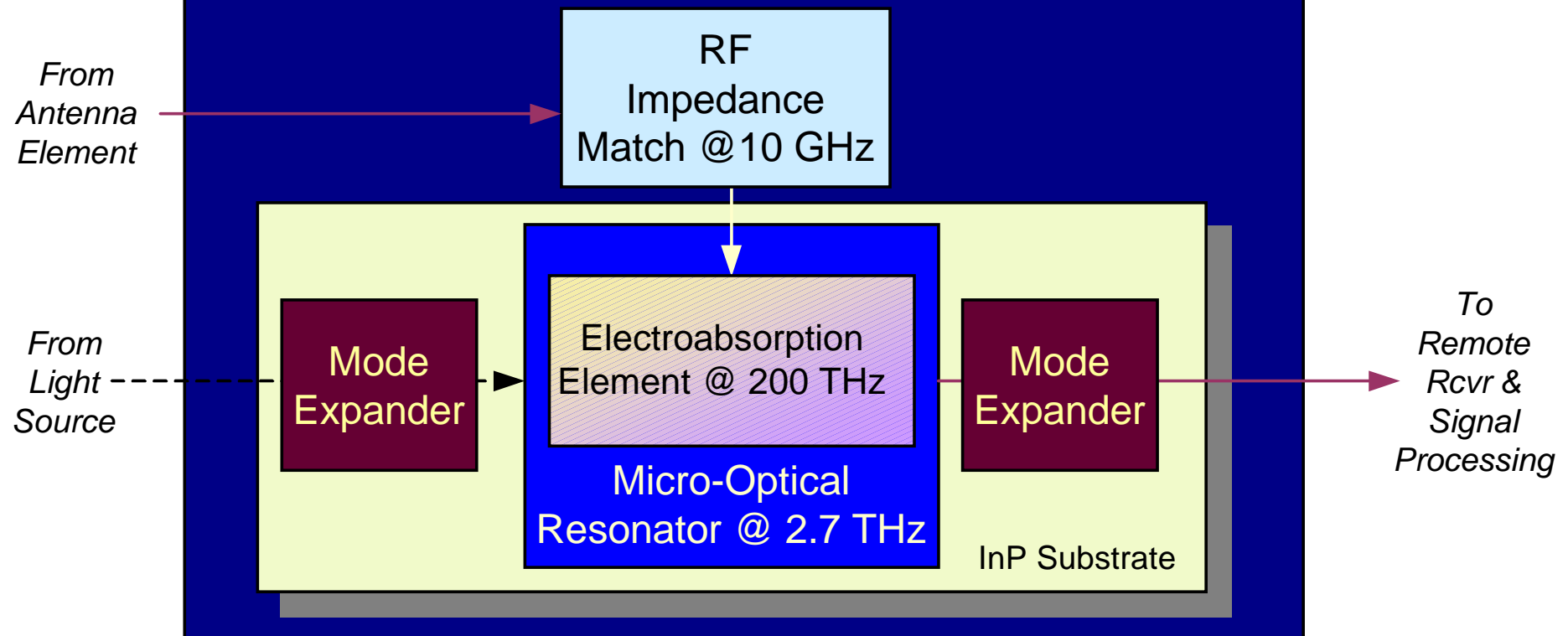
- Push-Pull Config'n
- $37 \text{ mV} = V_\pi$
- 10 GHz Operation



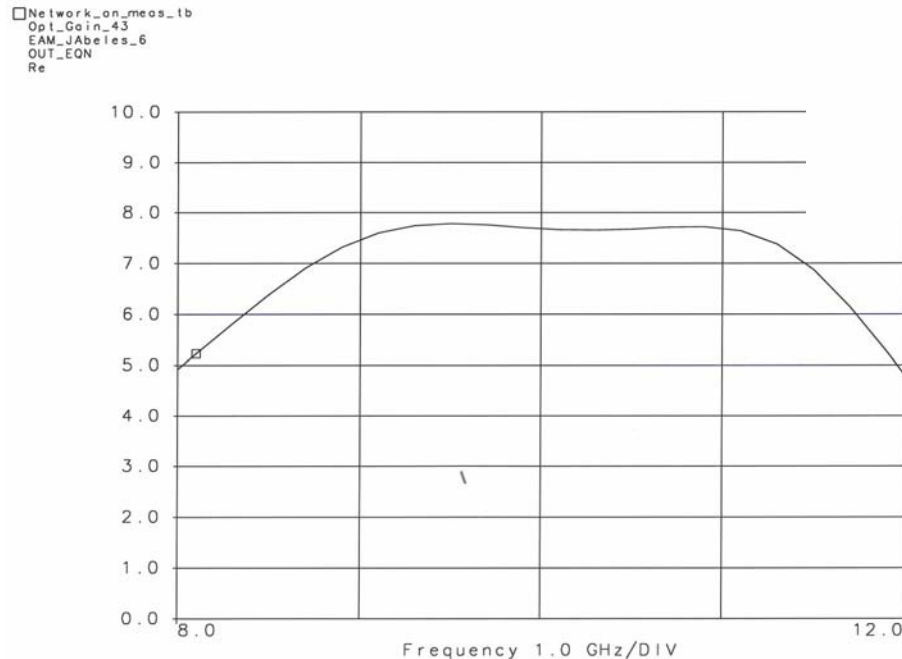
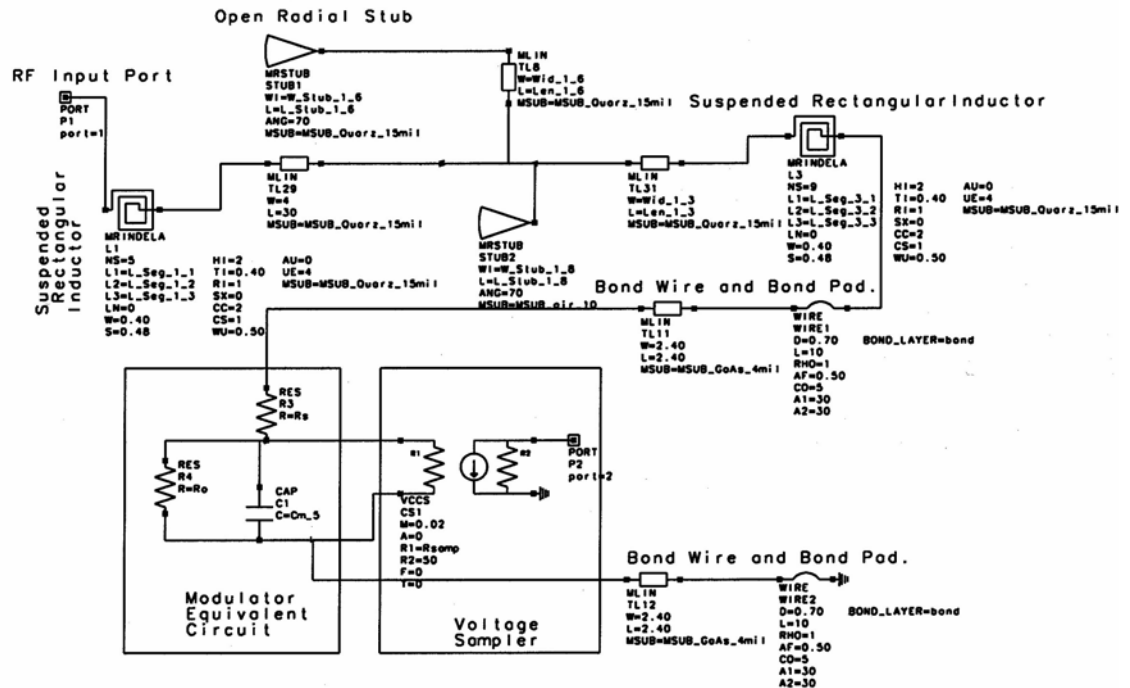
RF Delay Line Structure



Resonant Enhanced Modulator: Triply Resonant

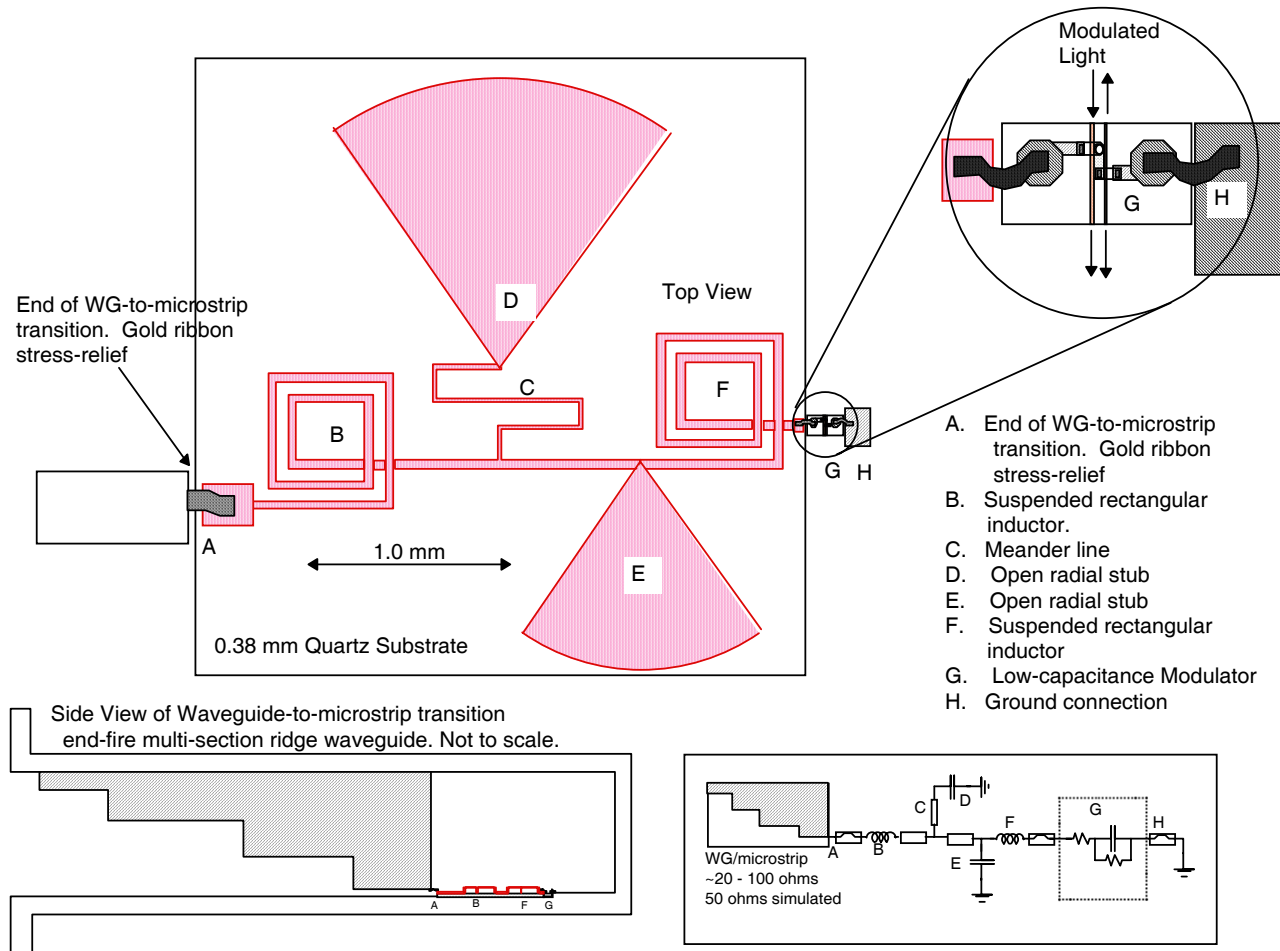


8 dB Gain



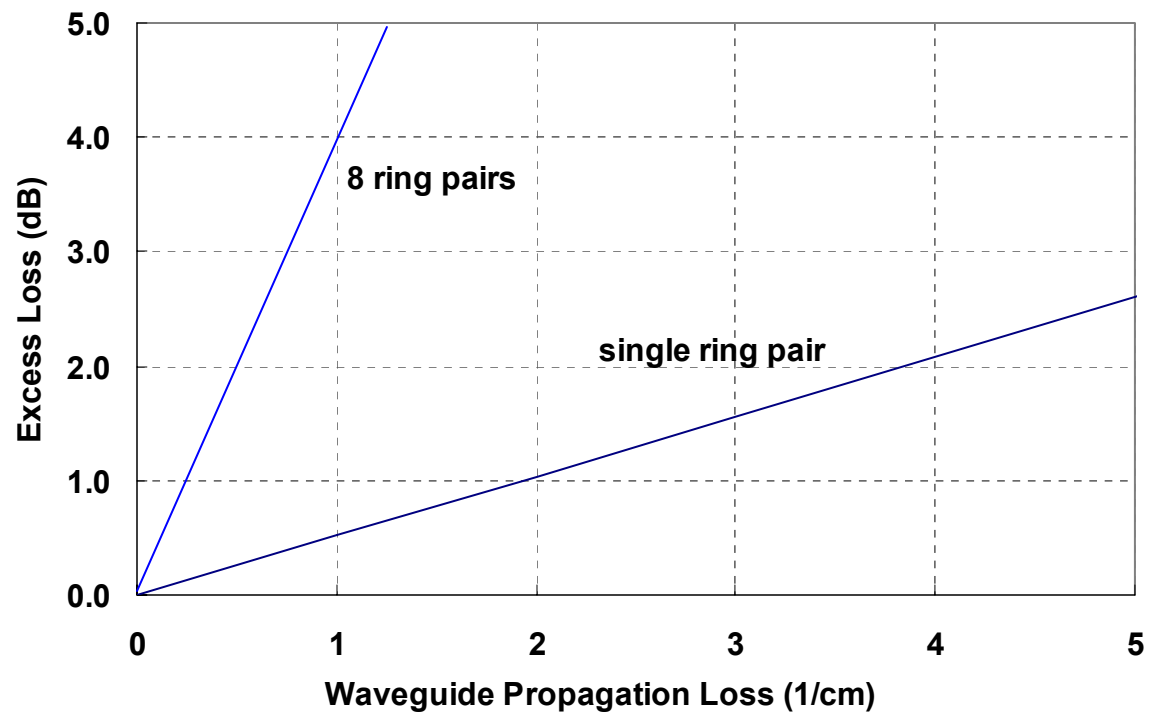
Simulated Optical Gain

Example Design Layout



Propagation Loss Effects

- Propagation losses
 $\sim 1 \text{ cm}^{-1}$
- Consistent with 3 dB excess loss

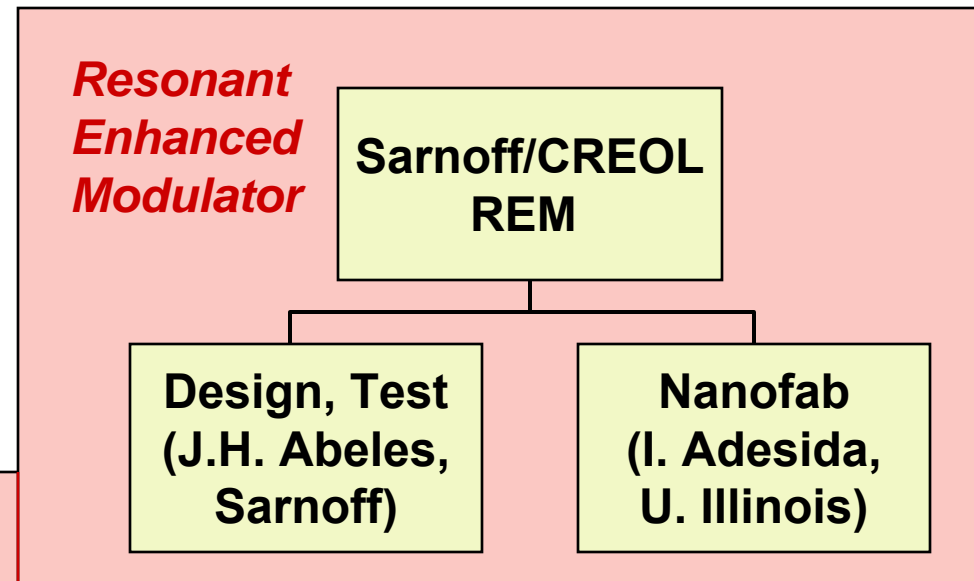


Sarnoff:

G. Pajer, A. Braun,
 R. Menna, J. Abeles (PI)

UIUC:

S. Rommel, I. Adesida (PI)



KEY GOALS:

• V_π	0.025 V
• RF Frequency	10 GHz
• RF Bandwidth	4 GHz
• Insertion Loss	6 dB

Resonant Enhanced Modulator Development

J.H. Abeles, G. Pajer, R. Whaley, A. Braun, D. Bechtle, J. Krishnan
Sarnoff Corporation

I. Adesida, S. Rommel
University of Illinois, Urbana-Champaign

DARPA/MTO RFLICs Site Visit

Sarnoff Corporation
Princeton, New Jersey
February 16, 2001

Objectives

- Objective: A Low V_π Modulator (< 100 mV)
- Approach: Laterally Coupled InP Based Microring Resonators
- Program Started 6/13/00; to End 6/13/03
- Milestones
 - 24 mos ... Prototype REM
 - 30 mos ... Optimized REM
 - 36 mos ... 12 Deployable REMs

Accomplishments, 10/00

- Demonstrated Smooth Anisotropic ICP Etching
- Analyzed Loss Requirements for Microrings
- Designed Delay Line Microwave Circuit

Accomplishments, 2/01

- Fabricated Test Structures
- Began Characterizing Test Structures
- Engineering Design Begun

Key Milestones Coming Year

- Fabricate Prototype Structure (4/01)
- Characterize Modulated Ring Properties (6/13)

Tech Transition

- Supply Deployable REMs to Systems Organization
- Production by Sarnoff

Lateral Ring Technology (LRT)
Approach

- DARPA RFLICs *Resonant Enhanced Modulator Program*

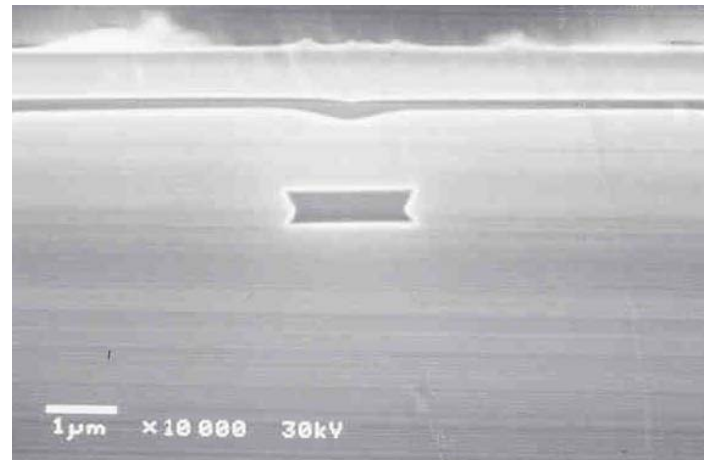
- NRO *Low V_π Modulator Program* Vertical Ring Technology (VRT)
Approach
- Princeton Lightwave, Inc. *Vertical Ring Technology Program*

Princeton Lightwave, Inc., a spin-off company from Sarnoff Corp, has begin to pursue interests in meso-optics at Sarnoff.

Two PLI staff members participate in the PLI program at Sarnoff:

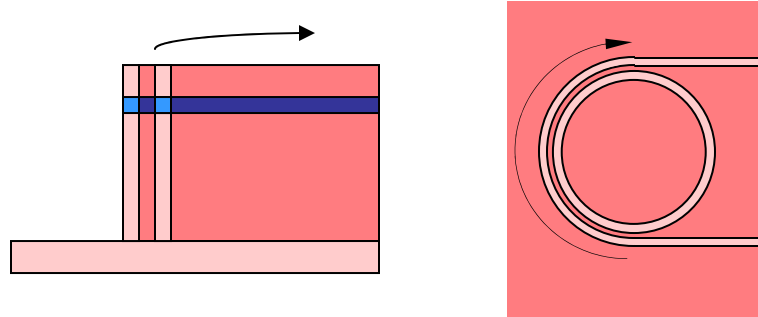
G. Griffel
S. Park

Vertical Ring Technology

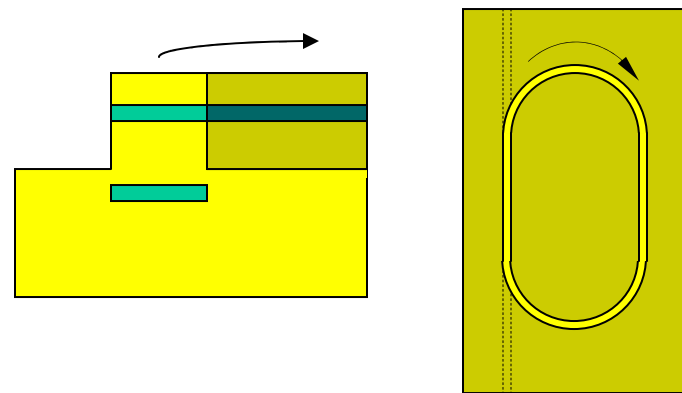


**Buried Waveguide by 3-Step OMCVD
under NRO Low V_π Modulator Program**

- **Lateral Ring Technology**
 - + Few lithography steps
 - + Coupling strength high
 - + High-index-contrast submicron waveguides

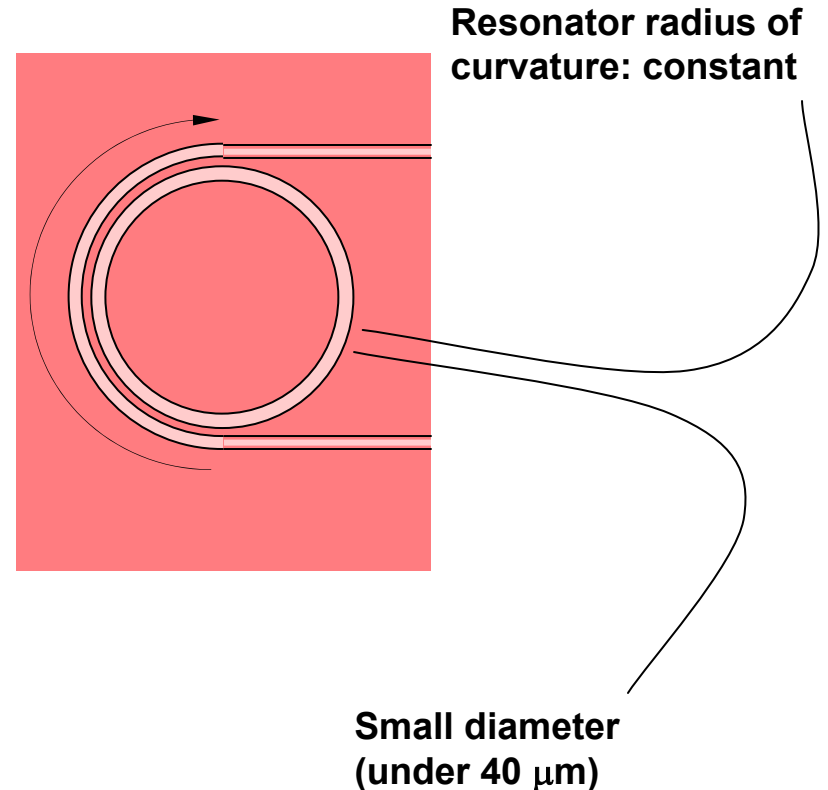
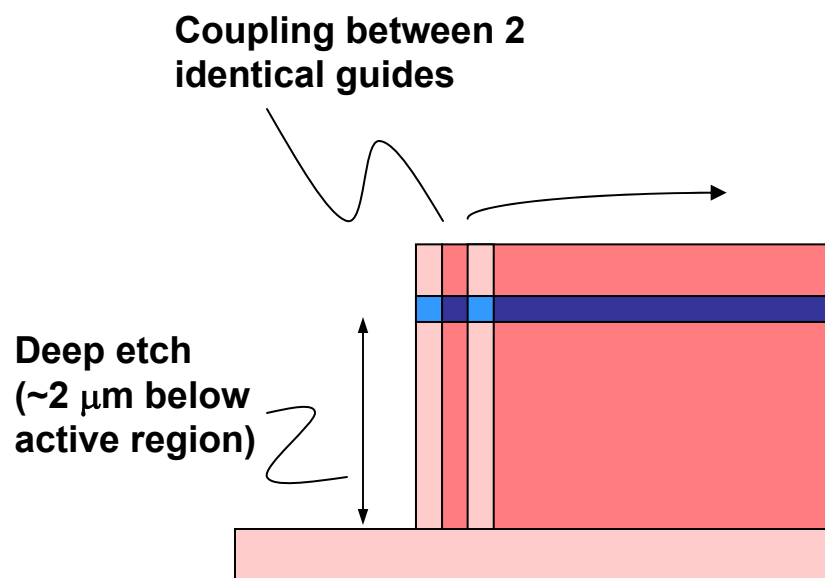


- **Vertical Ring Technology**
 - Complex fabrication
 - Coupling too weak, except with:
 - High bend losses (or submicron rings)
 - High waveguide transition losses
 - High-index-contrast lower guides



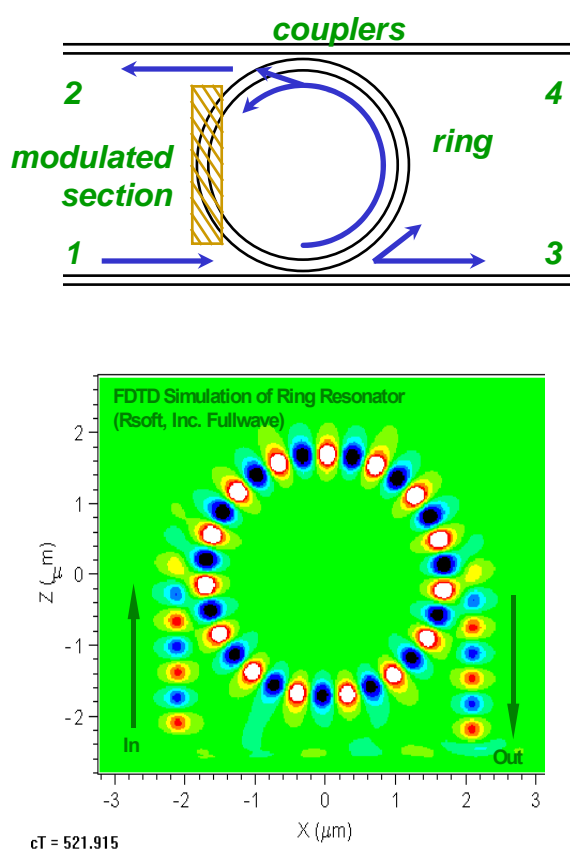
- Submicron lithography
- Uniformity requirements
- + Coupling mediated by epitaxy
- + Active/passive integration easy
- + Optical lithography

Prefer LRT for RF applications (<40 μm dia. rings)



- Enhanced sensitivity of REM depends on microring cascadability
- For absorption modulation (EA):
 - ring frequency response narrows, progressively, with # of rings
- For phase modulation (ER)
 - frequency response is unchanged with # of rings

- Requirements for V_π Under 1 Volt
 - RF Photonics
 - High Dynamic Range
 - High Speed/Frequency/Bandwidth
 - $CV^2\Delta f$ Prohibitive Switching Power
 - Direct Connection to Antenna
 - Arrays
- Current Technology Inadequate (>1 Volt at ~ 10 GHz)
 - LiNbO₃
 - Electroabsorption
 - Polymer
- **Need: V_π in mV's, not Volts**



$$\left| \frac{\bar{E}_2}{\bar{E}_1} \right|^2 = \frac{k_1 k_2}{t_1^2 t_2^2 A^2 + 1 - 2t_1 t_2 A \cos \phi_R}$$

$$\phi_{21} = \tan^{-1} \left(\frac{-t_1 t_2 A \sin \phi_R}{t_1 t_2 A \cos \phi_R - 1} \right)$$

$$\phi_R = (\beta + \Delta\beta)L$$

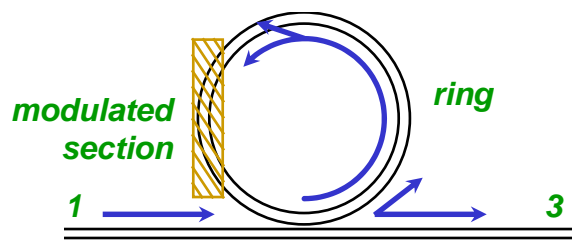
$$\beta = \frac{\omega}{c} \Delta n; \Delta\beta = \frac{\omega}{c} \Delta n$$

$$A = \exp^{-\alpha_{ampl} L}$$

$$k_{1,2} = power-coupling$$

Single-Coupled Resonators

$$\left| \frac{\bar{E}_3}{\bar{E}_1} \right|^2 = \frac{t^2 + A^2 - 2At \cos(\phi_R)}{t^2 A^2 + 1 - 2At \cos \phi_R}$$



$$\phi_{31} = \tan^{-1} \left(\frac{A(t^2 - 1) \sin \phi_R}{t(A^2 + 1) - A(t^2 + 1) \cos \phi_R} \right)$$

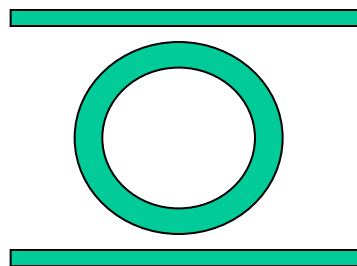
$$\phi_R = (\beta + \Delta\beta)L$$

$$\beta = \frac{\omega}{c}n; \Delta\beta = \frac{\omega}{c}\Delta n$$

$$A = \exp^{-\alpha_{amp}L}$$

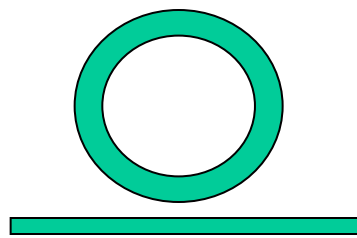
$$t = \sqrt{1 - (power_coupling)}$$

Ring Resonator Applications



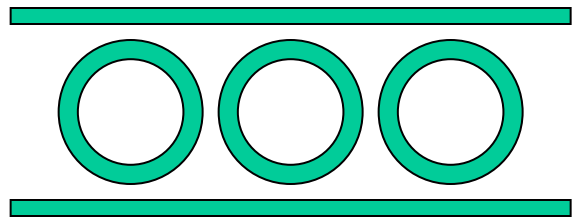
Double-Waveguide Coupled
Ring Resonator

- Tunable Filters
- WDM Add-Drop Multiplexers
- Ring Lasers
- Transversal Filters
- Switchable Delay Lines



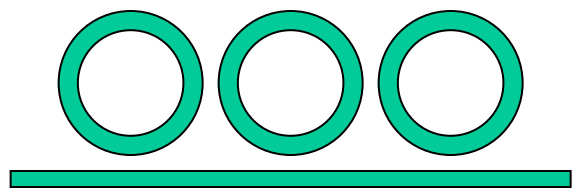
Single-Waveguide Coupled
Ring Resonator

- Frequency selective variable attenuators
- Frequency selective amplitude modulators
- Frequency selective phase modulators



Double-Waveguide Coupled
Multiple Ring Resonator

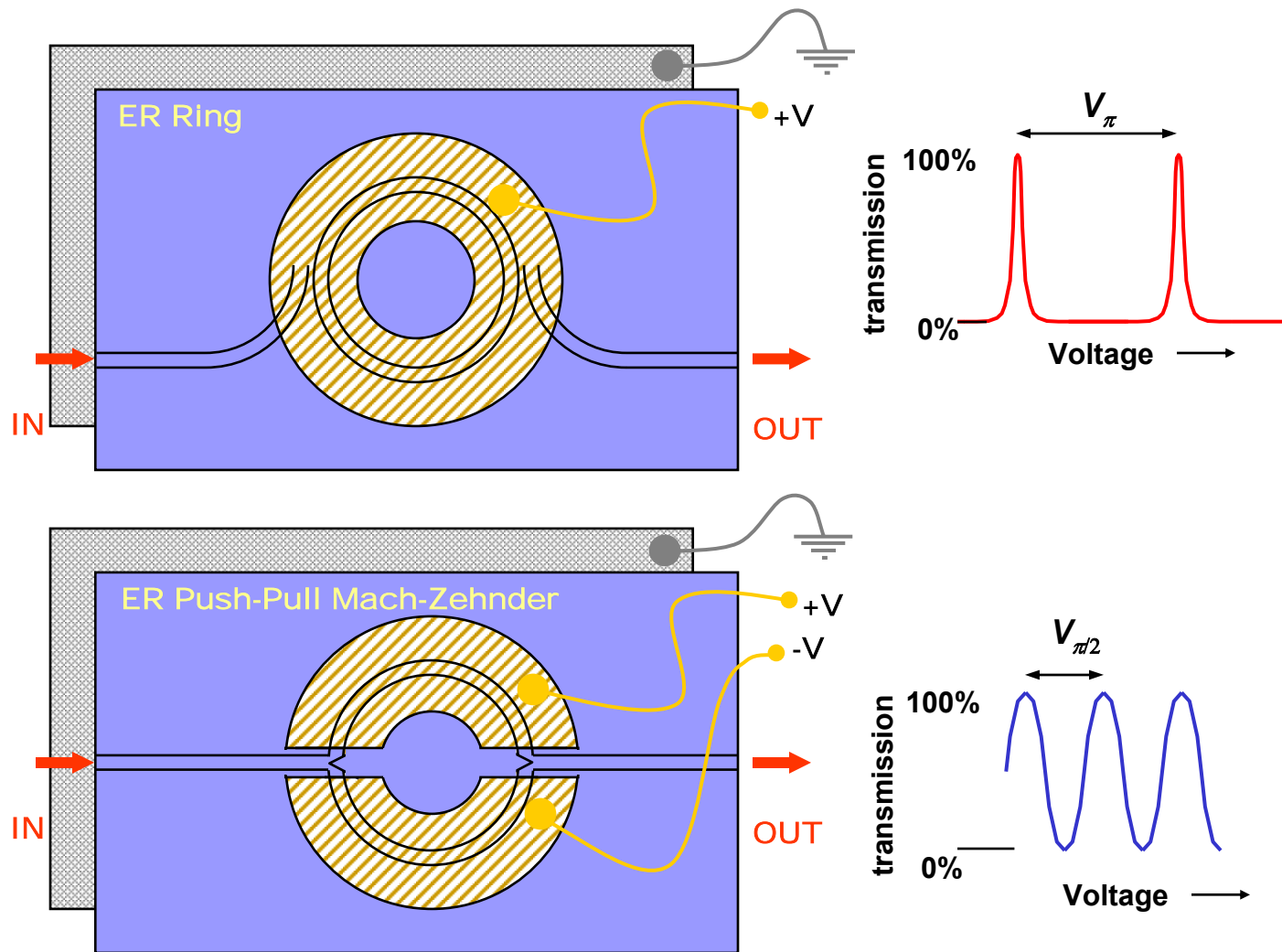
- Flat-top Tunable Filters
- Flat-top WDM Add-Drop Multiplexers



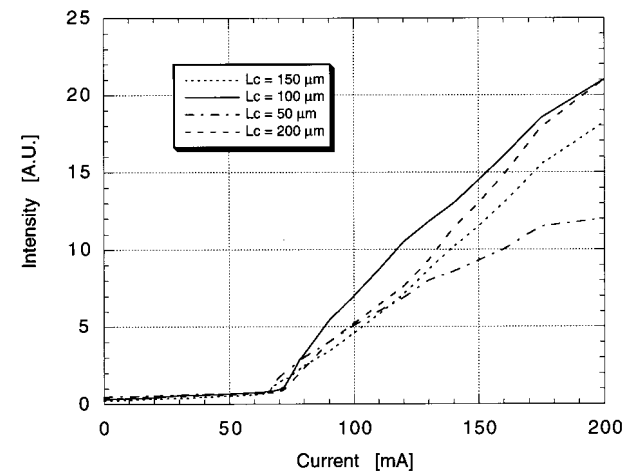
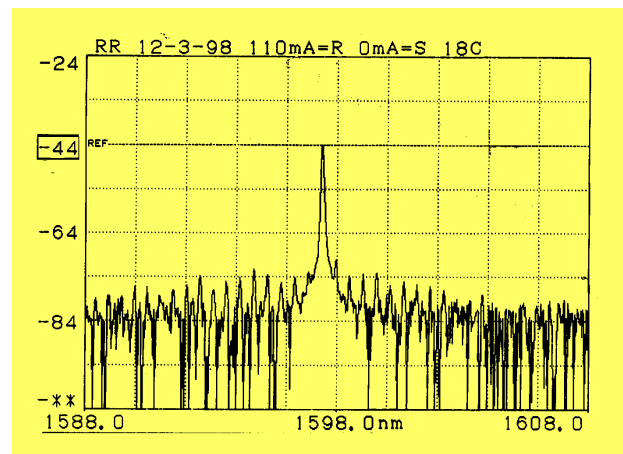
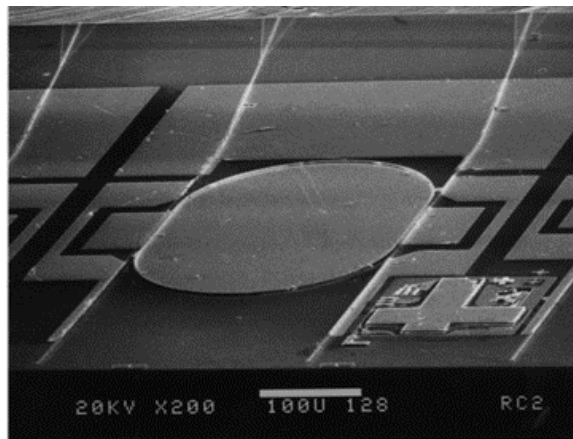
Single-Waveguide Coupled
Multiple Ring Resonator

- Multi-wavelength variable attenuators
- Amplifier gain equalizers
- Dispersion compensators

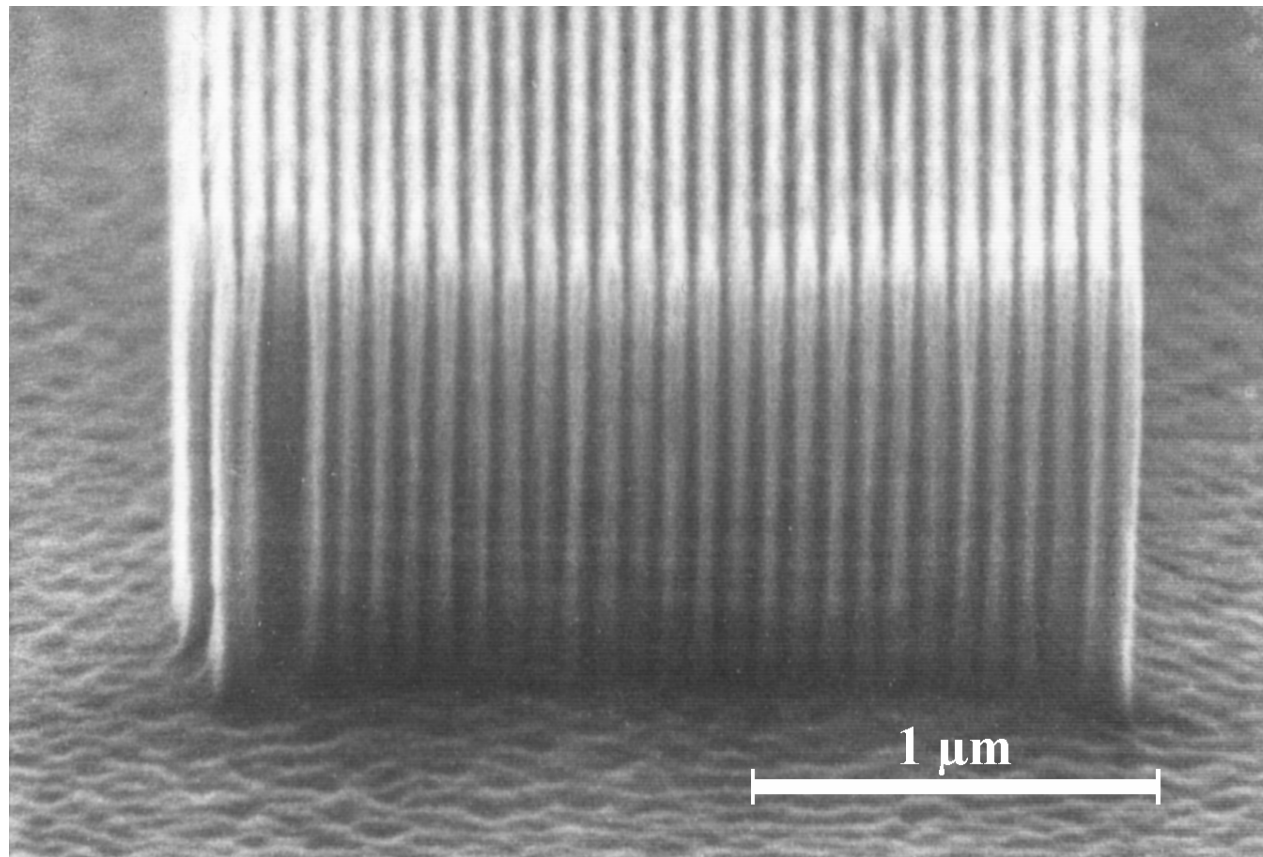
Ring Resonator vs. Mach-Zehnder



Record Low Threshold Ring Lasers

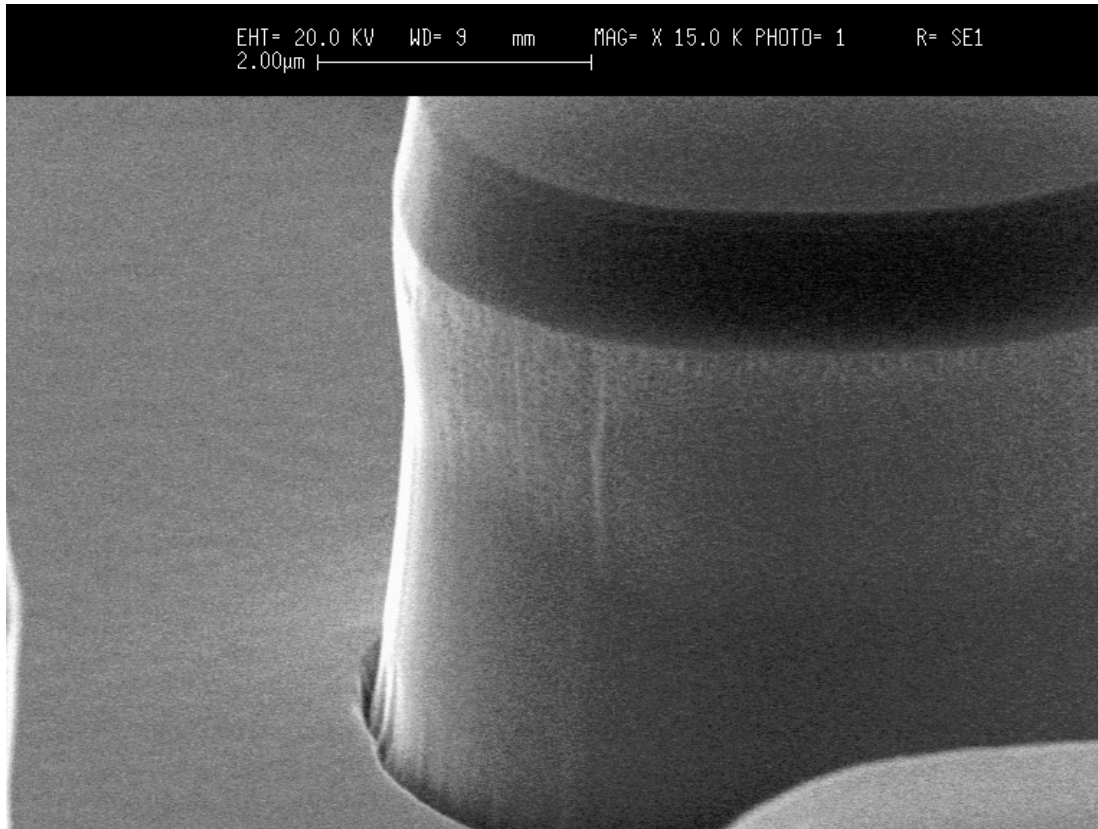


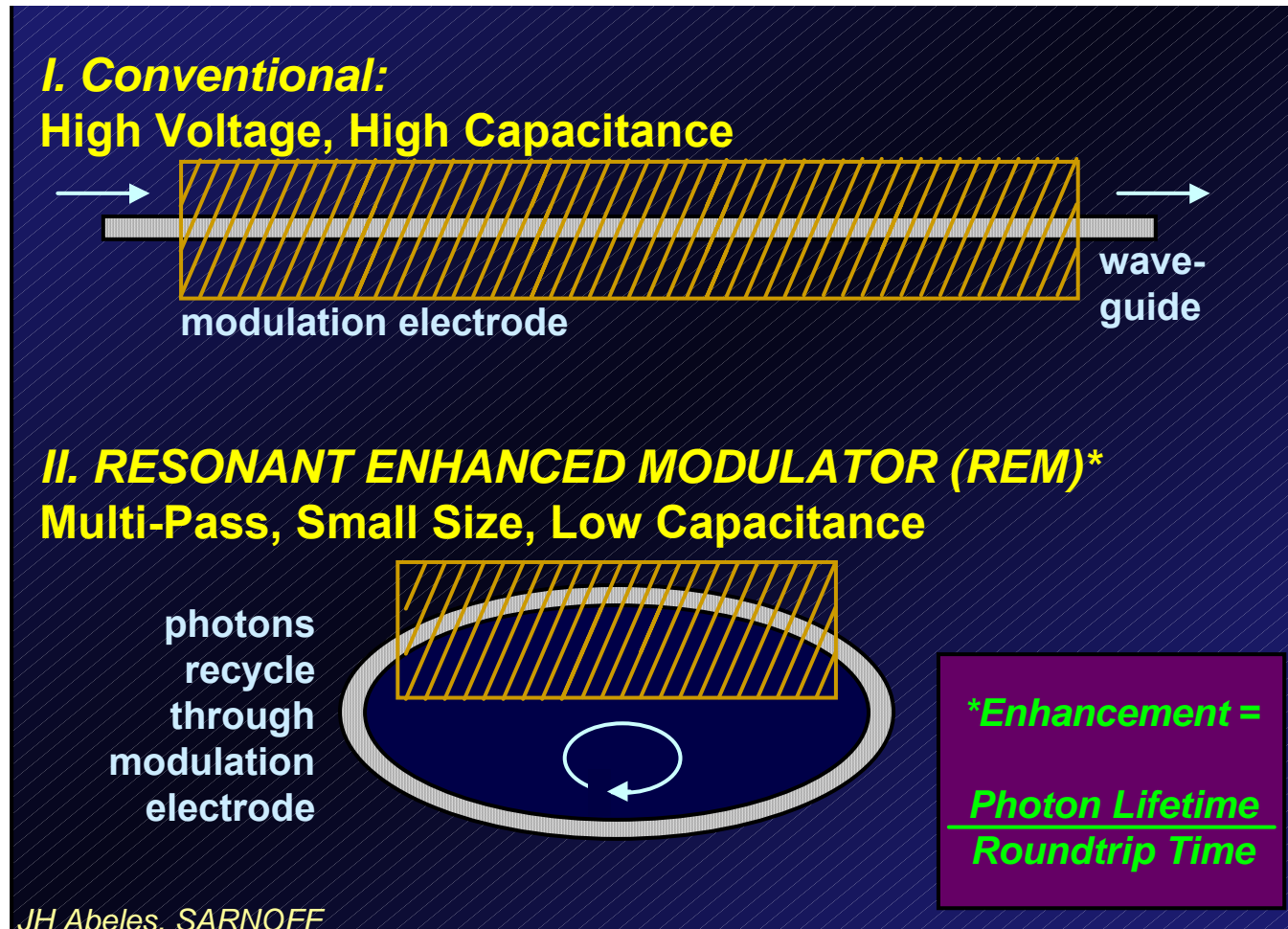
- $60 \text{ mA} = I_{th}$
- 1550 nm



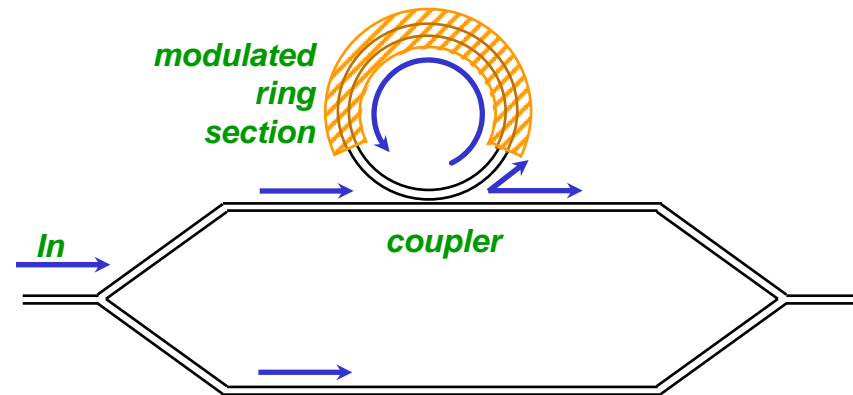
- $\text{CH}_4\text{-H}_2$ based
- 700 nm period

Inductively Coupled Plasma Etching of InP at UIUC



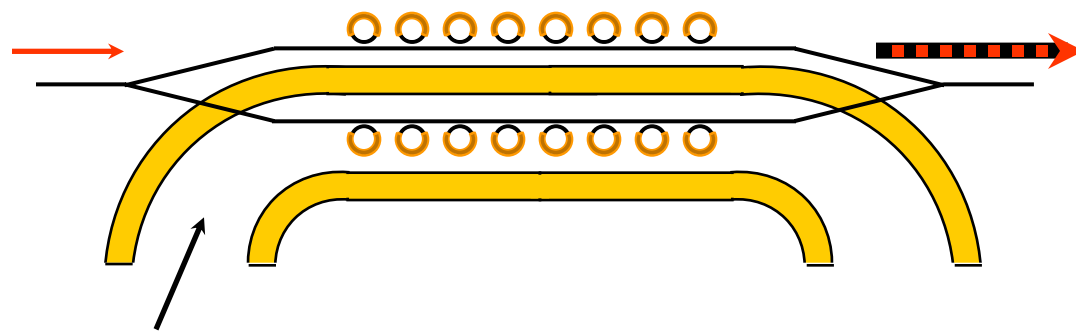


- Phase modulation due to coupled resonators
- Combine multiple resonators to achieve performance enhancement

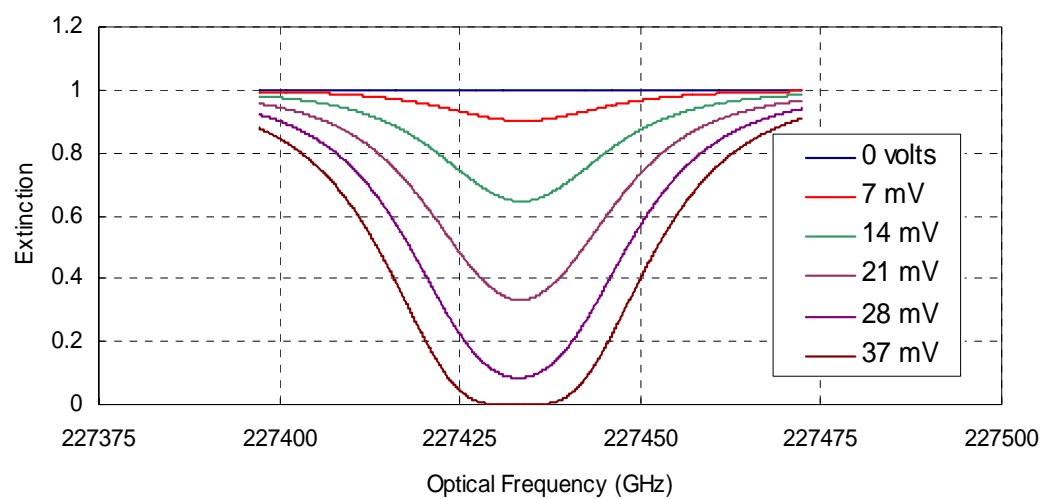


diameter (um)	FSR (GHz)	Passband (GHz)			Photon Lifetime (psec)		
		Finesse= 3	Finesse= 10	Finesse= 30	Finesse= 3	Finesse= 10	Finesse= 30
5	5968	1989	597	199	0.1	0.3	0.8
10	2984	995	298	99	0.2	0.5	1.6
20	1492	497	149	50	0.3	1.1	3.2
50	597	199	60	20	0.8	2.7	8.0
100	298	99	30	10	1.6	5.3	16.0

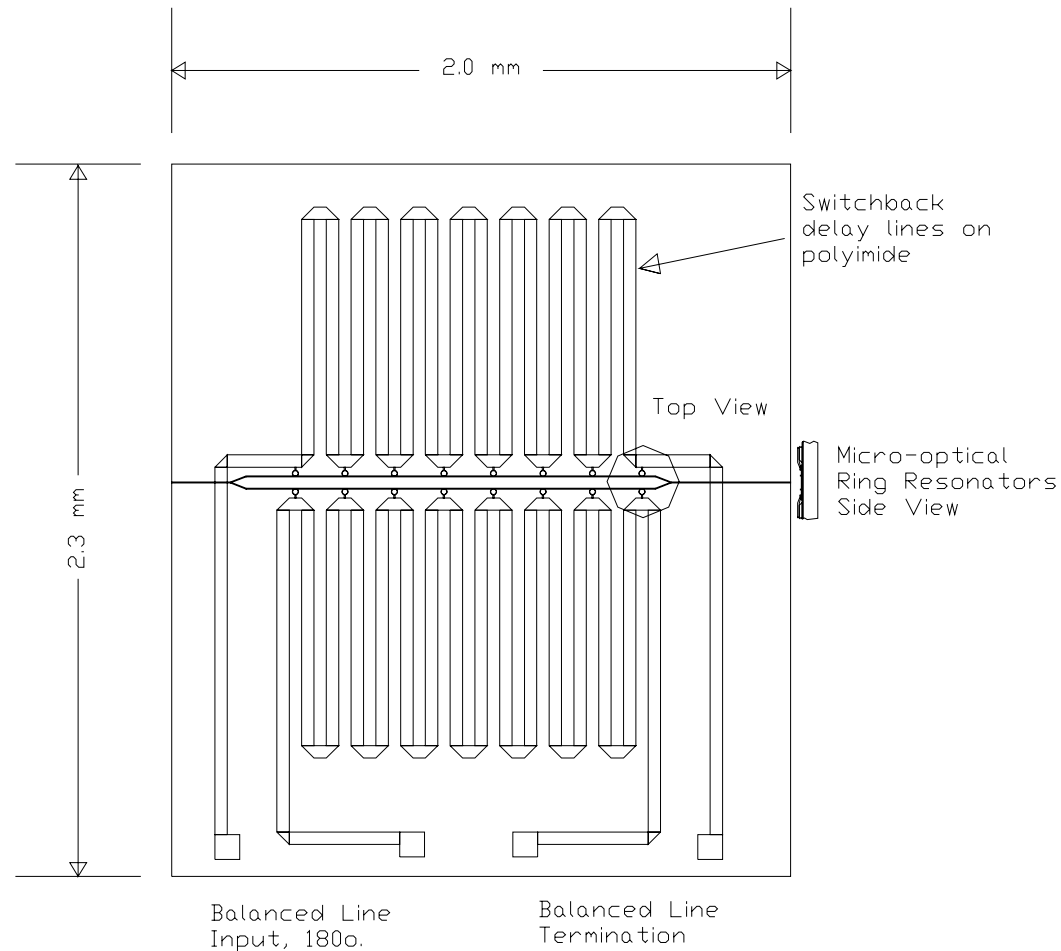
Sixteen-Ring Modulator



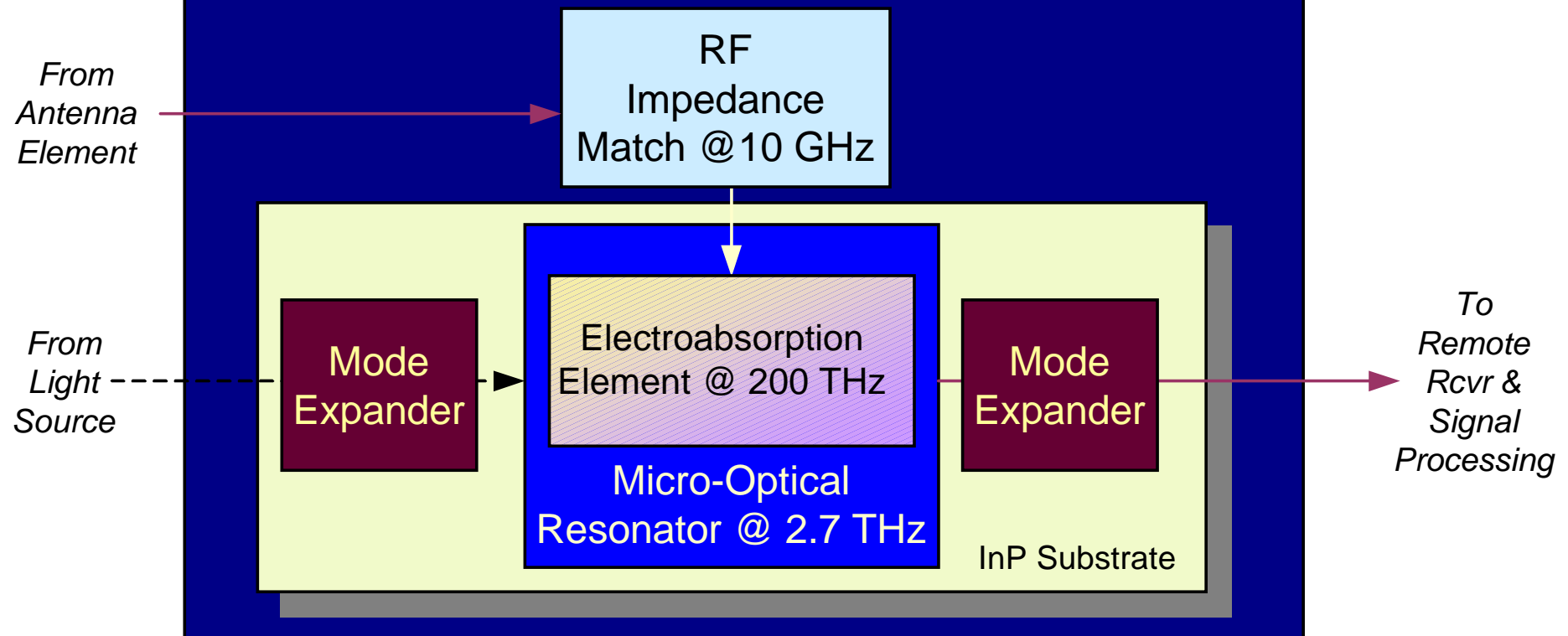
- Push-Pull Config'n
- $37 \text{ mV} = V_\pi$
- 10 GHz Operation



RF Delay Line Structure

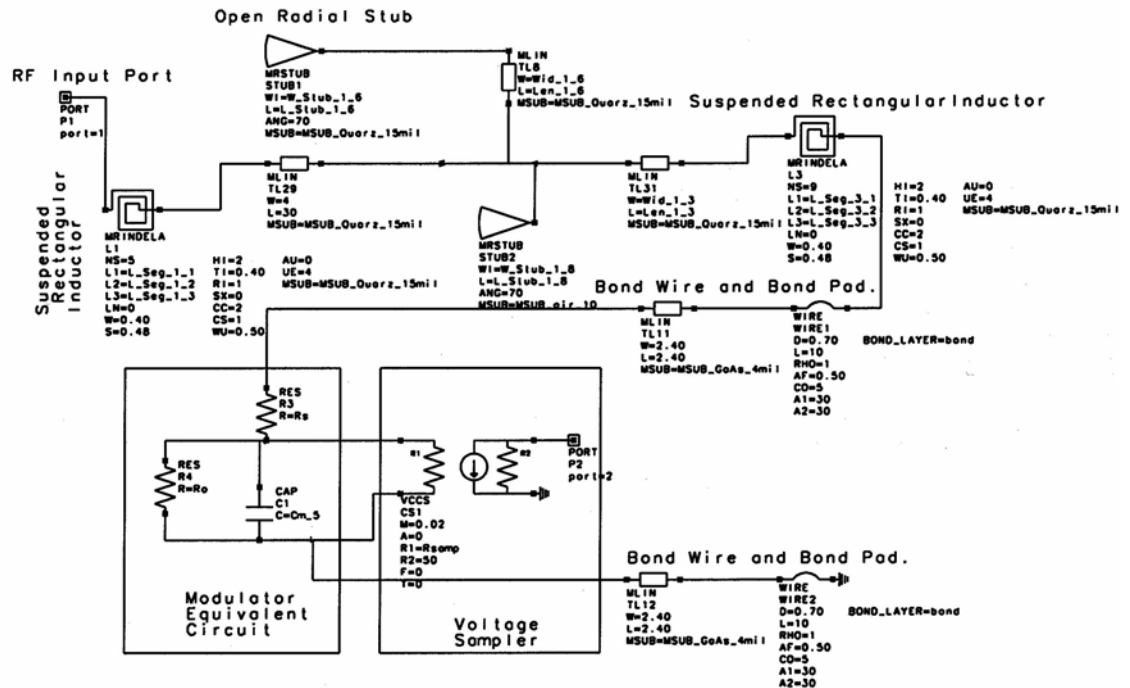


Resonant Enhanced Modulator: Triply Resonant

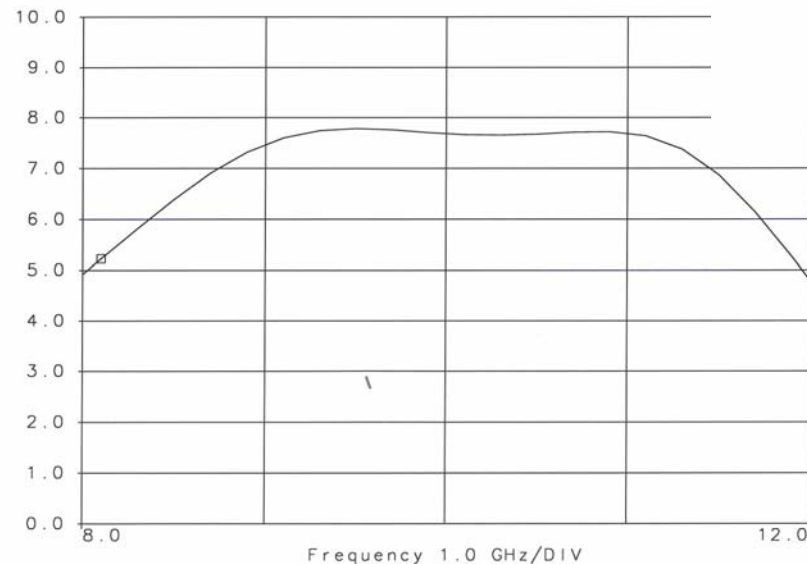


Microwave Impedance Transformer

8 dB Gain

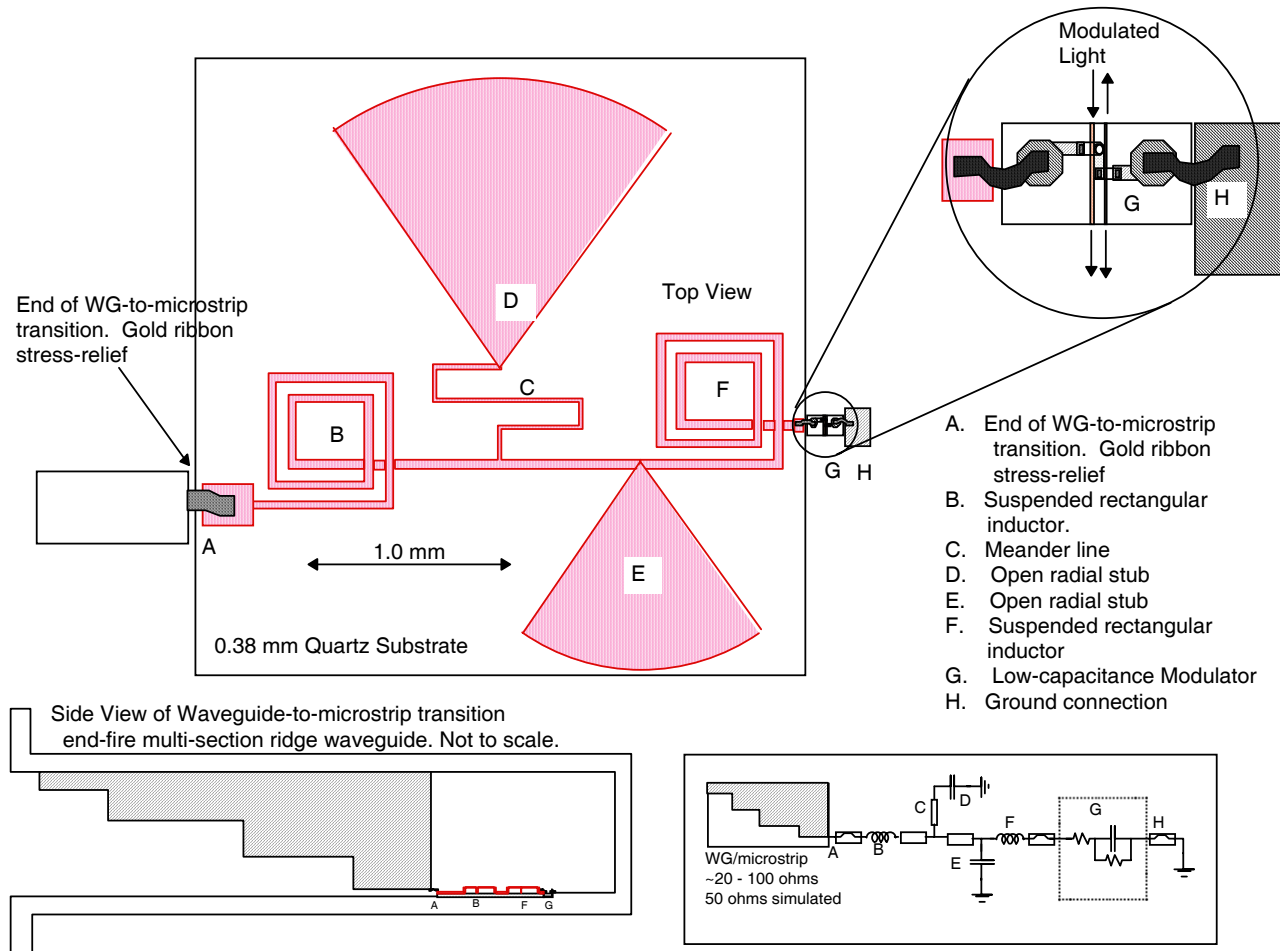


Network_on_meas_tb
 Opt_Gain_43
 EAM_JAbeles_6
 OUT_EQN
 Re



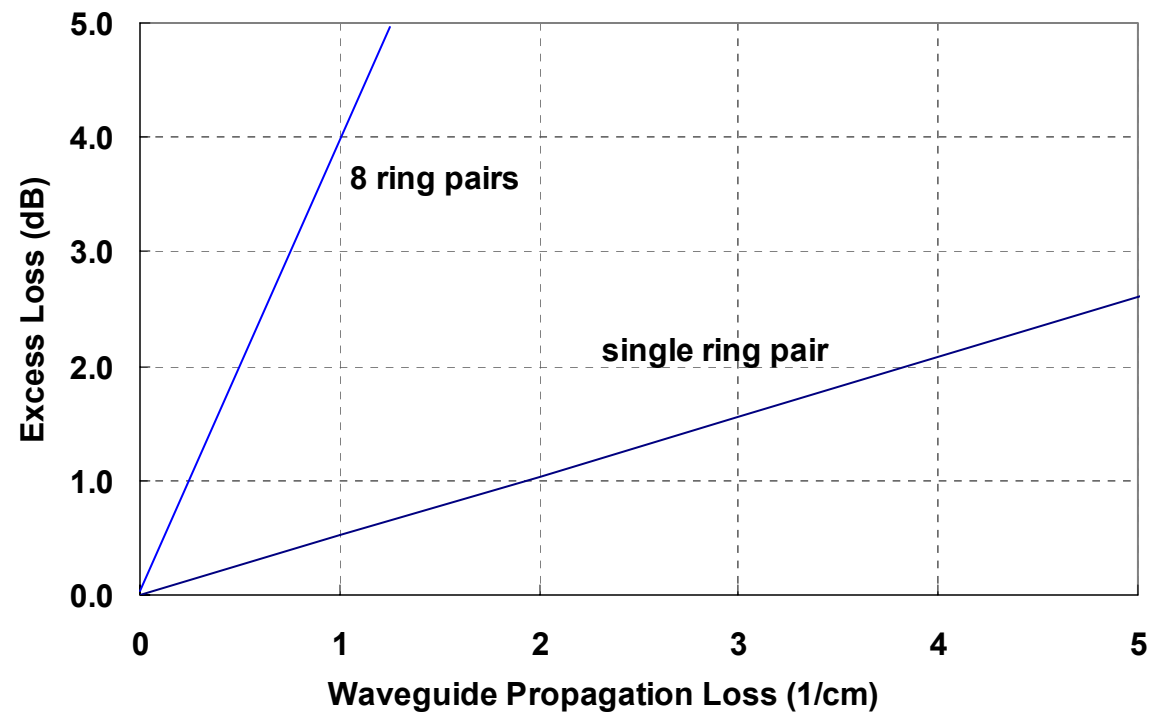
Simulated Optical Gain

Example Design Layout



Propagation Loss Effects

- Propagation losses
 $\sim 1 \text{ cm}^{-1}$
- Consistent with 3 dB excess loss

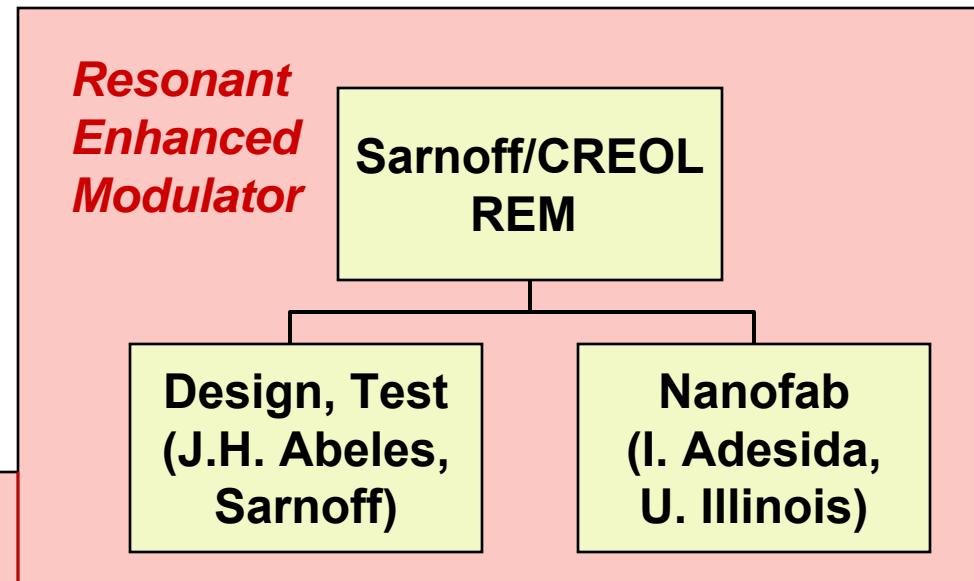


Sarnoff:

G. Pajer, A. Braun, R. Whaley
T.P. Lee, J. Abeles (PI)

UIUC:

S. Rommel, I. Adesida (PI)



KEY GOALS:

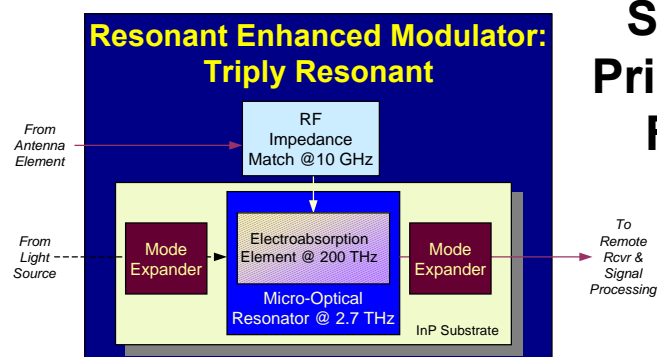
• V_π	0.025 V
• RF Frequency	10 GHz
• RF Bandwidth	4 GHz
• Insertion Loss	6 dB

Resonant Enhanced Modulator Development

J.H. Abeles (PI), A. Lepore (PM), M. Kwakernaak, H. Mohseni, D. Bechtle
Sarnoff Corporation

I. Adesida, S. Rommel
University of Illinois, Urbana-Champaign

DARPA/MTO RFLICs Site Visit



Sarnoff Corporation
Princeton, New Jersey
February 20, 2002

Agenda

February 20, 2002



• Introduction/Overview	0800 - 0825h	J. Abeles
• Program Review	0825 - 0845h	A. Lepore
• Financial Status Review	0845 - 0900h	A. Grupper
• Ring Physics & Performance	0900 - 0920h	M. Kwakernaak
• Coupler Physics & Perf.	0920 - 0935h	M. Kwakernaak
• Waveguide Loss	0935 - 0955h	M. Kwakernaak
• Nanolithography	0955 - 1015h	A. Lepore
• Nanoscience Review	1015 - 1035h	I. Adesida, UIUC
• Anisotropic Etching	1035 - 1055h	S. Rommel, UIUC
• Coupled QW Modulators	1055 - 1125h	H. Mohseni
• Q & A	1125 - 1140h	J. Abeles
• Tour	1140 - 1215h	A. Lepore
• Lunch	1215 - 1315h	(invitees)
• Departure	1315h	
• <i>Arrival Princeton E-Quad</i>	1335h	

REM Fabrication Activities (from 1st Annual Review)

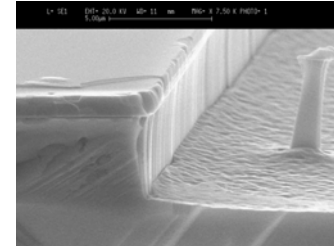
Fabrication:

June, 2000

Program Start

ICP Characterization

Leica/Cambridge e-beam initial use



October, 2000

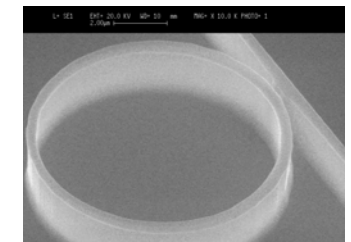
Ring nanostructures reported by UIUC

Resist development

Etching condition studies

Leica/Cambridge e-beam dosage studies

Etching of coupling region



February, 2000

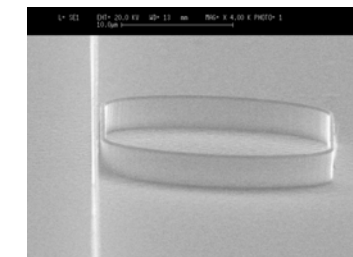
Sample microrings delivered to Sarnoff

Resist quality development (cont'd)

Pattern interchange (Sarnoff-UIUC)

Sample handling

Stitching issues



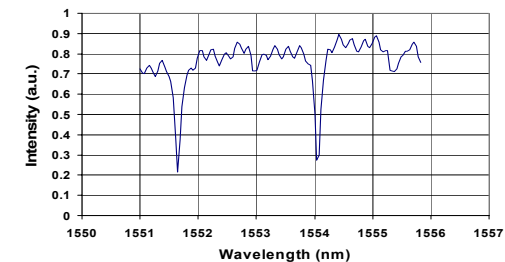
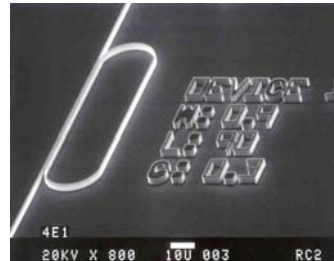
May, 2000

Routine characterization of microrings structures at Sarnoff

Resist development (cont'd)

Switch to new JEOL e-beam tool

Switch to larger rings for diagnostics



Introduction/Overview

J. Abeles

Resonant Enhanced Modulator Program



- **Nanofabrication issues**
 - **Gap etching**
- **University of Illinois**
 - **Partner vs. supplier**
- **Second source of e-beam tool and expertise**
 - **Army Research Lab, Adelphi, MD**
 - **Brought on board: Dr. Allen N. Lepore**
- **Re-staffing of program between 12 and 16 months**
 - **Dr. A.N. Lepore, Program Manager**
 - **Dr. M. H. Kwakernaak, Microring Physics and Characterization**
 - **Dr. H. Mohseni, Electrorefractive Physics and Epistructures**
- **Re-planning of program**

DARPA-Requested Status



1. Most significant accomplishments

- Characterization of group delays in rings
- Design of high-coupling REM
- Demonstration of MMI coupler
- Electrically modulated structure
- Replan of program

2. Most recent experimental data (prototype hardware) or when will the first prototype will be tested:

- September 2002 (see plan in A. Lepore presentation)

DARPA-Requested Status (cont'd)



3. What is the plan to meet the program objectives in the final half of the program with hardware fabrication schedules.

-- See A. Lepore presentation

4. Upcoming challenges.

-- Waveguide loss of 1 cm^{-1} (April '02)

-- Low loss rings (April '02)

5. Financial status

-- On track with a linear spend rate (see A. Grupper presentation)

Program Roadmap



- **Year 2**
 - Obtain electrorefractive ring modulator (24 months)
 - Demonstrate electrorefractive ring modulator REM (24 months)
- **Year 3**
 - Demonstrate 10 GHz electrorefractive ring modulator
 - Demonstrate 100 millivolt class V_π modulator (30 months)
 - Deliver 12 REM devices to DARPA (36 months)

Program Review

A. Lepore

Overview



- **Waveguide Losses**
 - Edge acuity
- **Evanescence lateral couplers**
 - UIUC deep etching (~5 μm)
 - Selected to facilitate patterning of coupling “gap”
 - Results in poor edge acuity
 - Other approaches
 - Dual step
- **Multimode lateral coupling**
 - “MMI” coupler
 - High coupling ratios (i.e., 50/50)
 - Necessitates redesign of ring
- **New ring design**
- **Alternative modulator design**

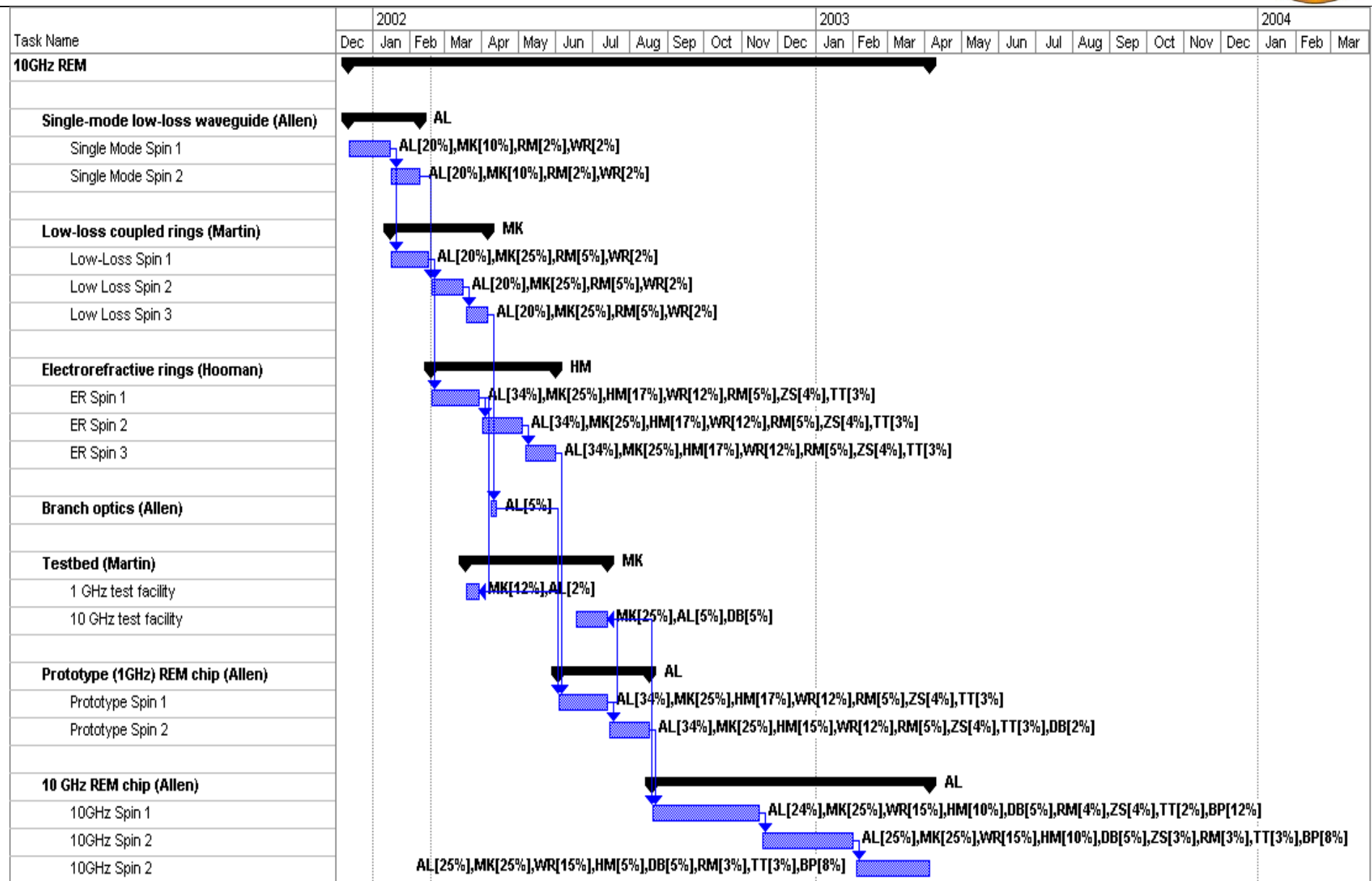
Key Technical Accomplishments



- **Demonstrated MMI-coupled rings**
- **Identified multimode behavior issues with resonance and coupling**
- **Developed understanding of coupler design space**
- **Configured testbed for phase measurement**
- **Established and verified modeling software for layer structure design**
- **Electron-beam lithography: established redundant patterning capability, increased throughput, reduced stitch impact***
- **Established high-resolution imaging (500k magnification)***
- **Dramatic reduction in waveguide breakage during processing**
- **Increased process/test throughput via pattern layout redesigns**
- **Demonstrated metal mask patterns w/ 100kV positive-tone resist**

* Army Research Laboratory, Sensors and Electronic Devices Directorate

Revised Program Plan

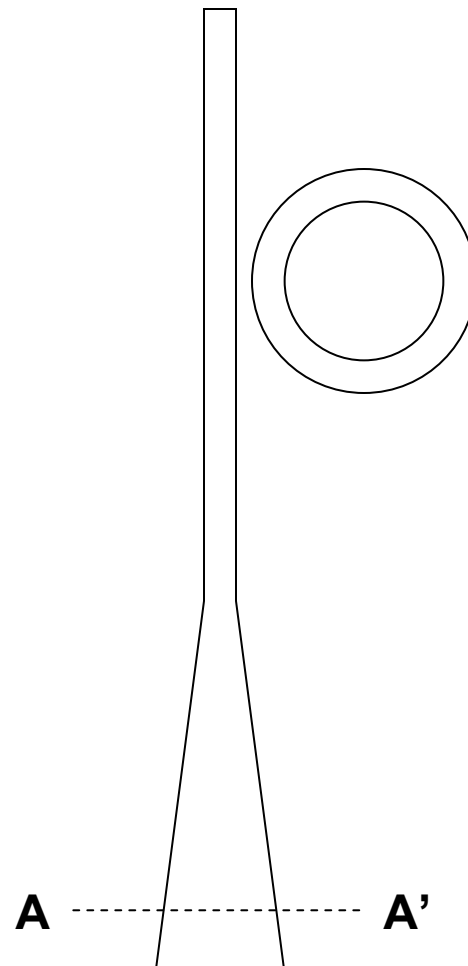


BCB Encapsulation of Ridge

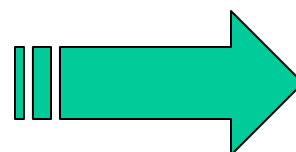
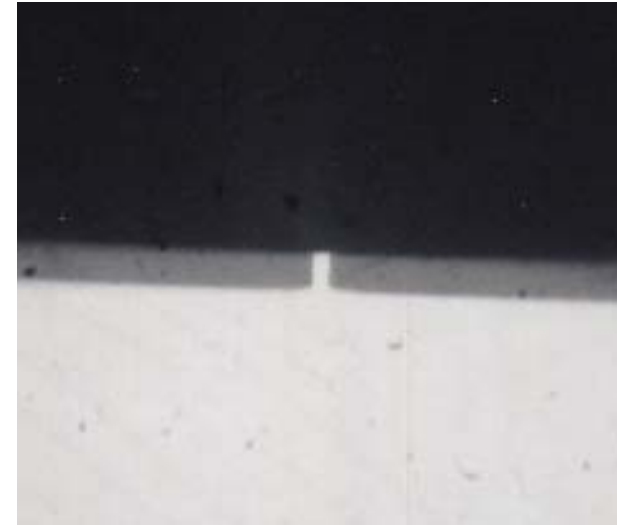
... to improve yield of cleaved facets ...



Plan view of waveguide cross-section

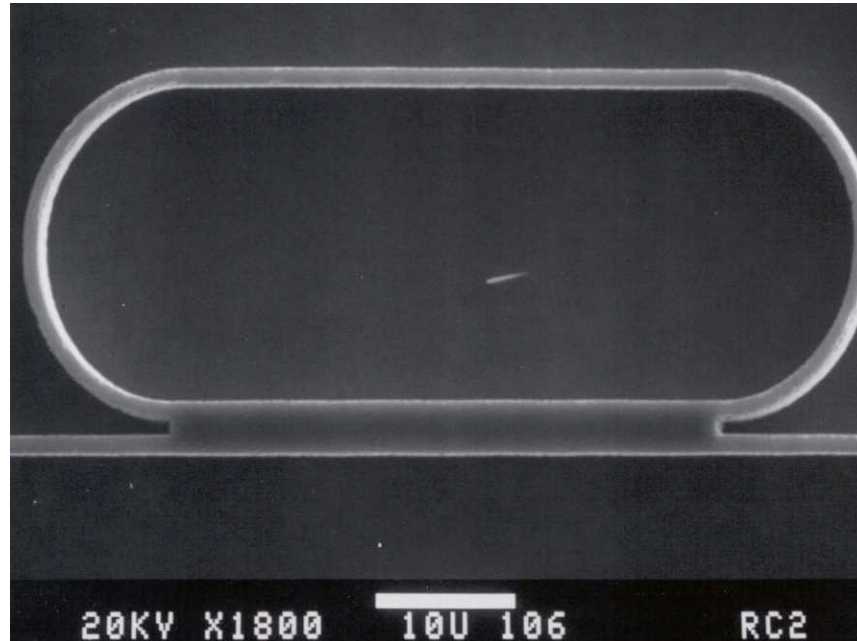


Cross-sectional view of BCB-planarized ridge waveguide



- Excellent damage protection
- Excellent planarization

MMI Coupler



Example of fabricated mmi-coupled ring

Accelerate Electrical Device Spins



- **Program plan incorporates electrical device designs in low-loss waveguide spins, for parallel evaluation**

Electrical process steps as follows:

- ***Utilize additional process developments from another Sarnoff (commercial) program involving BCB, for electrical contacts***
- ***Employ simplified process during initial material evaluation***
- ***High interaction/support for UIUC nanofab.***

Key Schedule Issues



- **UIUC ICP etch process transfer to new post-doctoral student**
- **Introduction of improved anisotropic etching procedures**
 - E.g., Two-step etching depth
- **Characterization of CH_4/H_2 etching**
- **Equipment access: schedule insertion time, downtime (planned ARL lab renovation)**

Risk Areas



Risks:

- **Waveguide loss**
- **Prediction of coupling for gap-coupled devices (non-linear)**
- **Low-leakage epitaxial structure**

Risk reduction:

- **MMI coupler: eliminate gap sensitivity, reduce anisotropy requirement, reduced etch depth and associated roughness**
- **Redundant etch capability with metal mask and mmi-coupler: CH_4/H_2**
- **Two step etch process- shallow straight sections for lowest loss, deeper etch only where needed at bends**

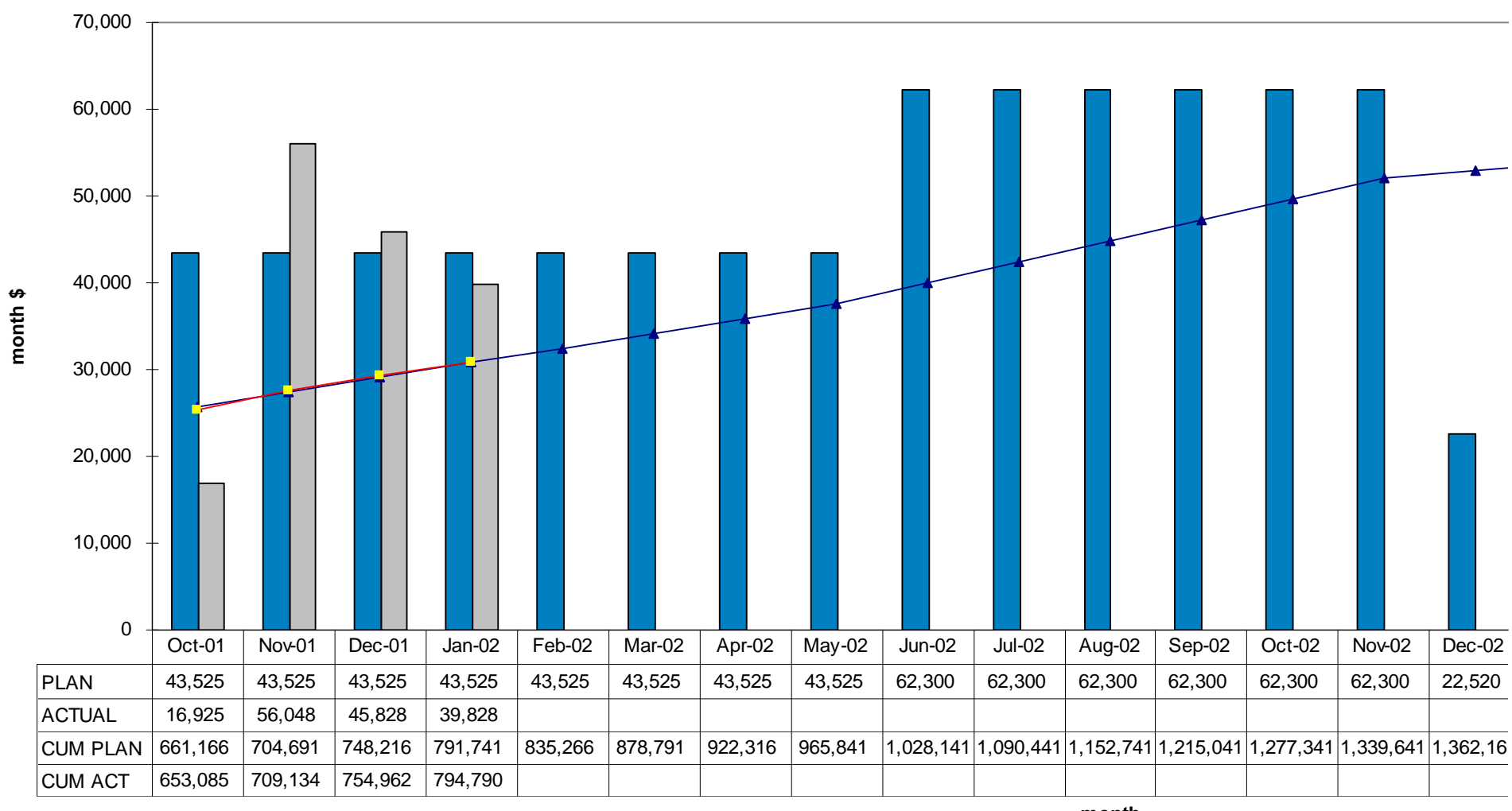
Financial Status Review

A. Grupper

Spending



Resonant Enhanced Modulator



CFSR



CONTRACT FUNDS STATUS REPORT (DOLLARS IN <u>0</u>)																						
1 CONTRACT NUMBER			3 CONTRACT FUNDING		5 PREVIOUS REPORT DATE		7 SARNOFF CORPORATION			9 INITIAL CONTRACT PRICE												
F30602-00-C-0116			INC		AS OF <u>12/31/2001</u>		CN5300, PRINCETON NJ, 08543-5300			TARGET <u>\$1,590,874</u>												
MOD P00002			FOR FY <u>2000</u>							CEILING N/A												
2 CONTRACT TYPE			4 APPROPRIATION		6 CURRENT REPORT DATE		8 PROGRAM			10 ADJUSTED CONTRACT PRICE												
CPFF					AS OF <u>01/31/2002</u>		Resonant Enhanced Modulator (REM)			TARGET <u>\$89,540</u>												
11			FUNDING INFORMATION																			
LINE ITEM/WBS ELEMENT	APPROPR. IDENTIFI- CATION	FUNDING AUTH TO DATE	ACCRUED EXPEND.	CONTRACT WORK AUTHORIZED				FORECAST			TOTAL REQUIRE- MENTS	FUNDS CARRY OVER	NET FUNDS REQUIRED									
				PLUS OPEN COMMIT.	DEFINITIZED	NOT DEFINITIZED	SUBTOTAL	NOT YET AUTHORIZED	ALL OTHER WORK	SUBTOTAL												
a	b	c	d	e	f	g	h	i	j	k	l	m										
TOTAL												\$1,301,665	\$822,852	\$1,301,665	\$0	\$1,301,665	\$289,209	\$0	\$289,209	\$1,590,874	\$0	\$1,590,874
12			01/31/2002 CONTRACT WORK AUTHORIZED (WITH FEE/PROFIT) ACTUAL OR PROJECTED																			
			ACTUAL TO DATE									AT COMPLETION										
a.	OPEN COMMITMENTS		\$28,062	\$14,031	\$96,000	\$85,291	\$74,582	\$63,872	\$53,163	\$42,453	\$31,744	\$74,581	\$0									
b.	ACCRUED EXPENDITURES		\$794,790	\$835,266	\$878,791	\$922,316	\$965,841	\$1,028,141	\$1,090,441	\$1,152,741	\$1,215,041	\$1,362,161	\$1,590,874									
c.	TOTAL		\$822,852	\$849,297	\$974,791	\$1,007,607	\$1,040,423	\$1,092,013	\$1,143,604	\$1,195,194	\$1,246,785	\$1,436,742	\$1,590,874									
13	FORECAST OF BILLINGS																					
	TO THE GOVERNMENT-Non Cumulative		\$753,305	\$41,485	\$40,476	\$43,525	\$43,525	\$43,525	\$62,300	\$62,300	\$162,300	\$162,300	\$1,590,874									
14	ESTIMATED TERMINATION COSTS																					
	Non Cumulative		\$79,979	\$110,391	\$207,002	\$198,192	\$185,876	\$195,152	\$204,427	\$307,111	\$409,795	\$548,413	\$0									
REMARKS			MOD P00002 provides funding thru 11/1/2002																			

Ring Physics & Performance

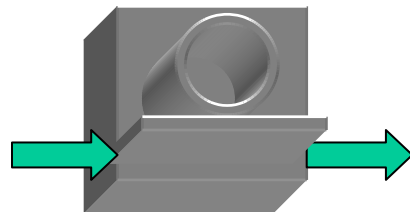
M. Kwakernaak

Ring Physics and Performance

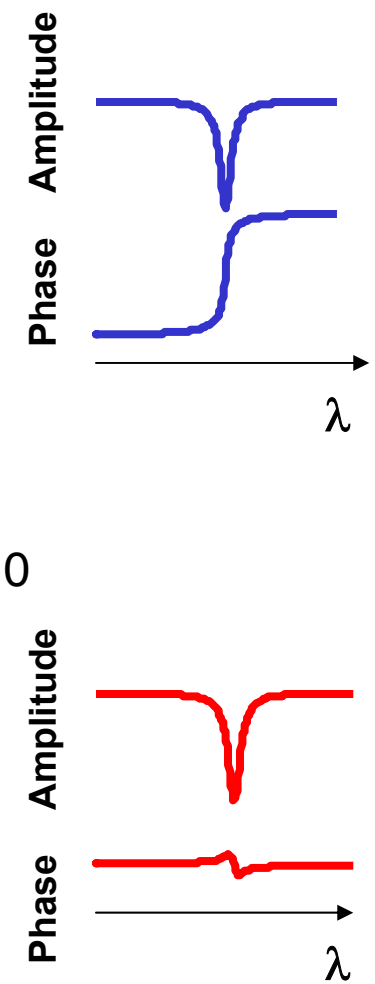
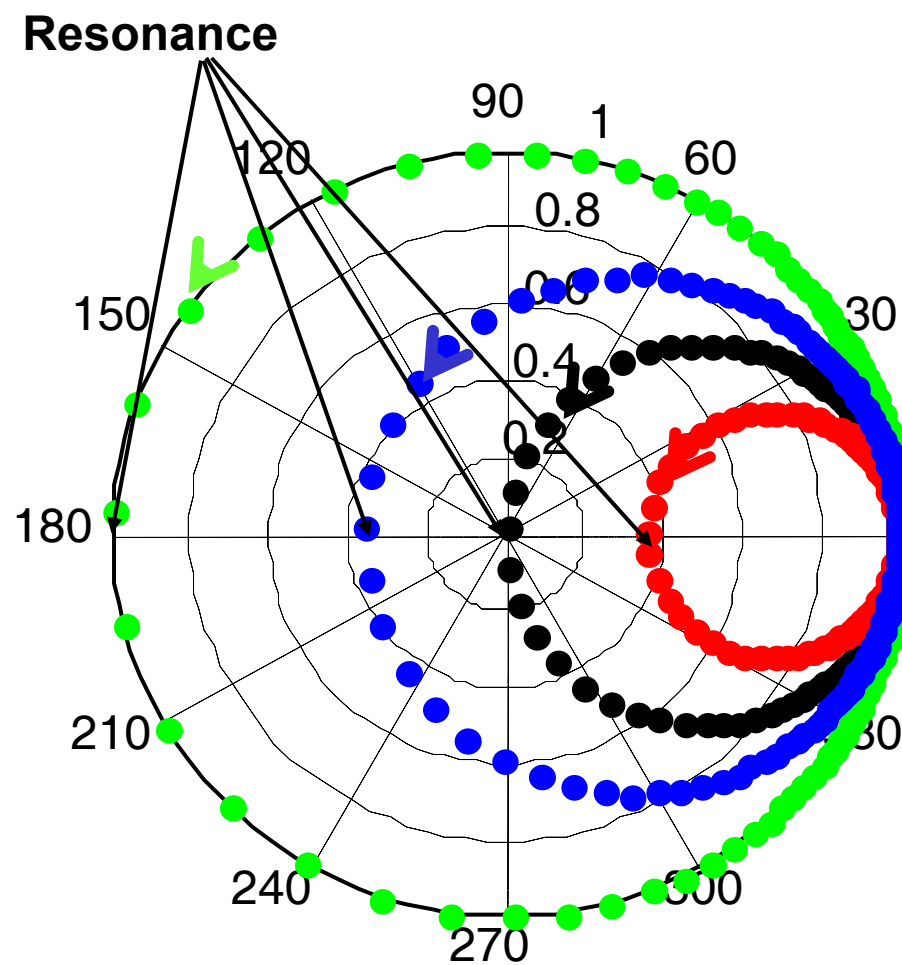


- **Ring physics**
- **Phase diagrams**
- **Group delay measurements**
- **Bandwidth and REM design**
- **Loss requirements**

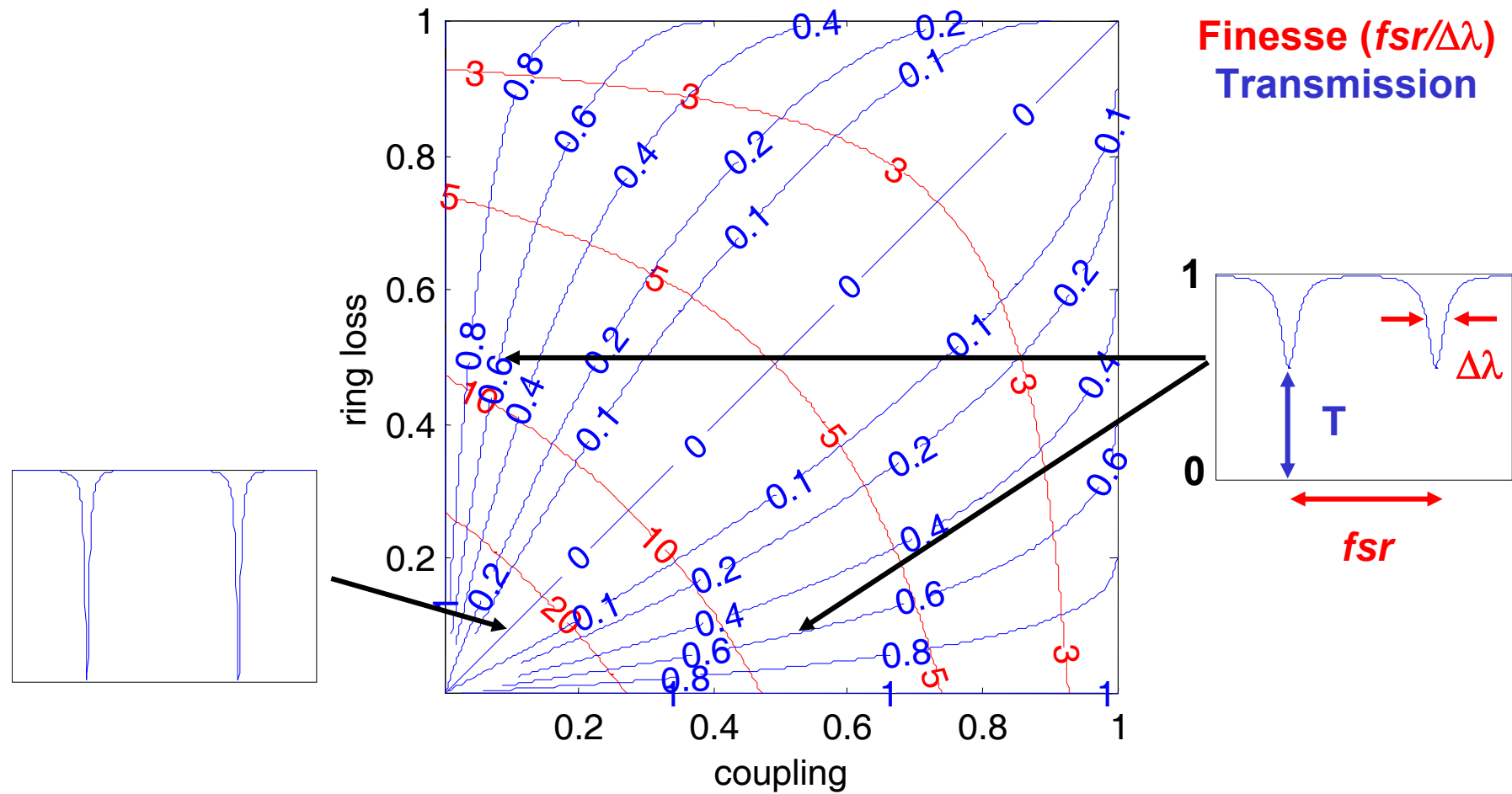
Ring Transmission, Complex Space



- No Loss
- Coupling > Loss
- Coupling = Loss
- Coupling < Loss



Phase Diagram



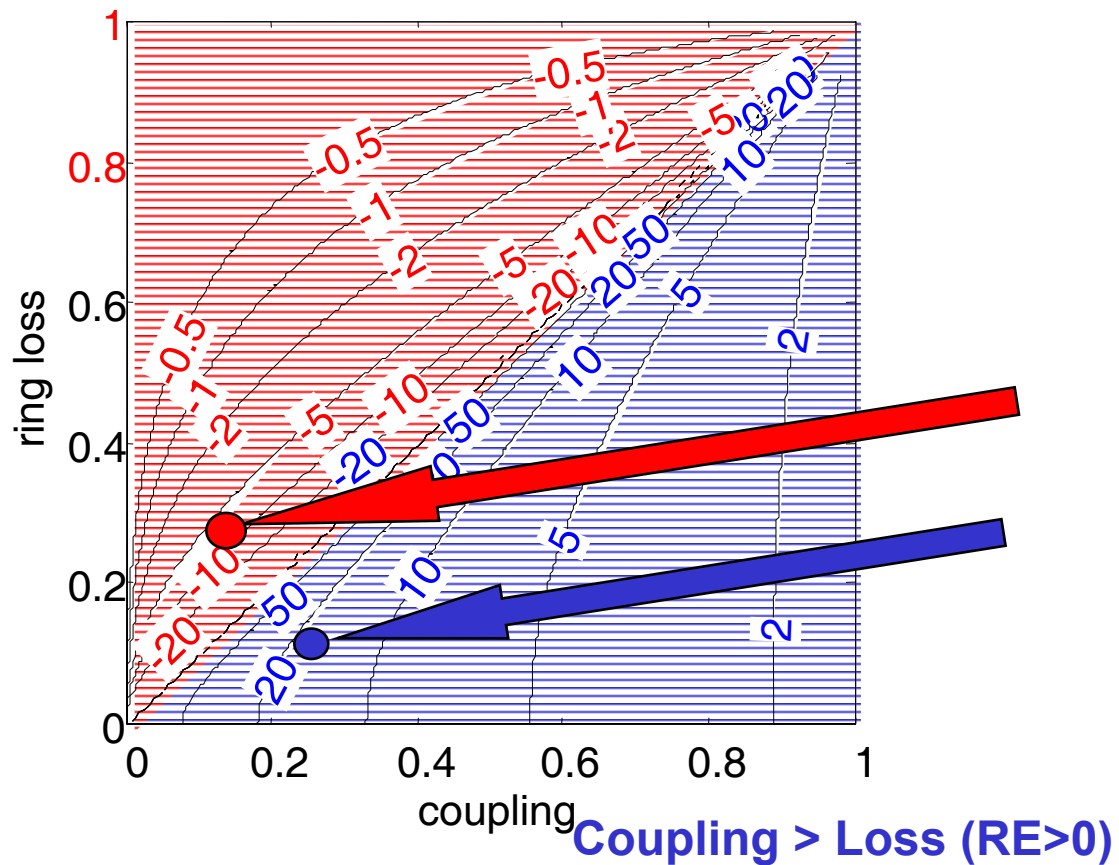
Ring Enhancement



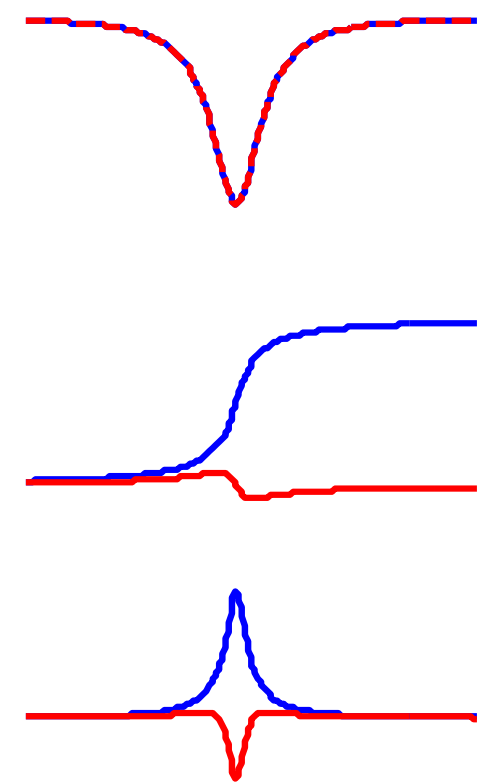
Ring enhancement =

Phase sensitivity of the ring.
Phase sensitivity of straight waveguide
of equal length.

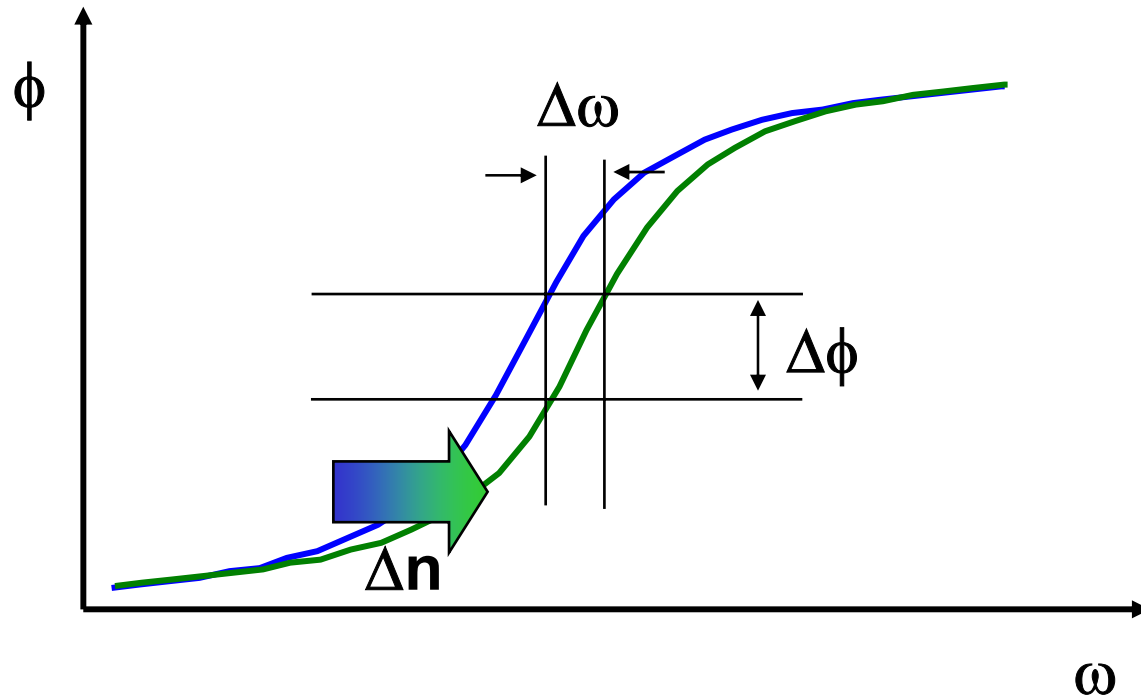
Coupling < Loss (RE<0)



Amplitude
Phase
Group delay

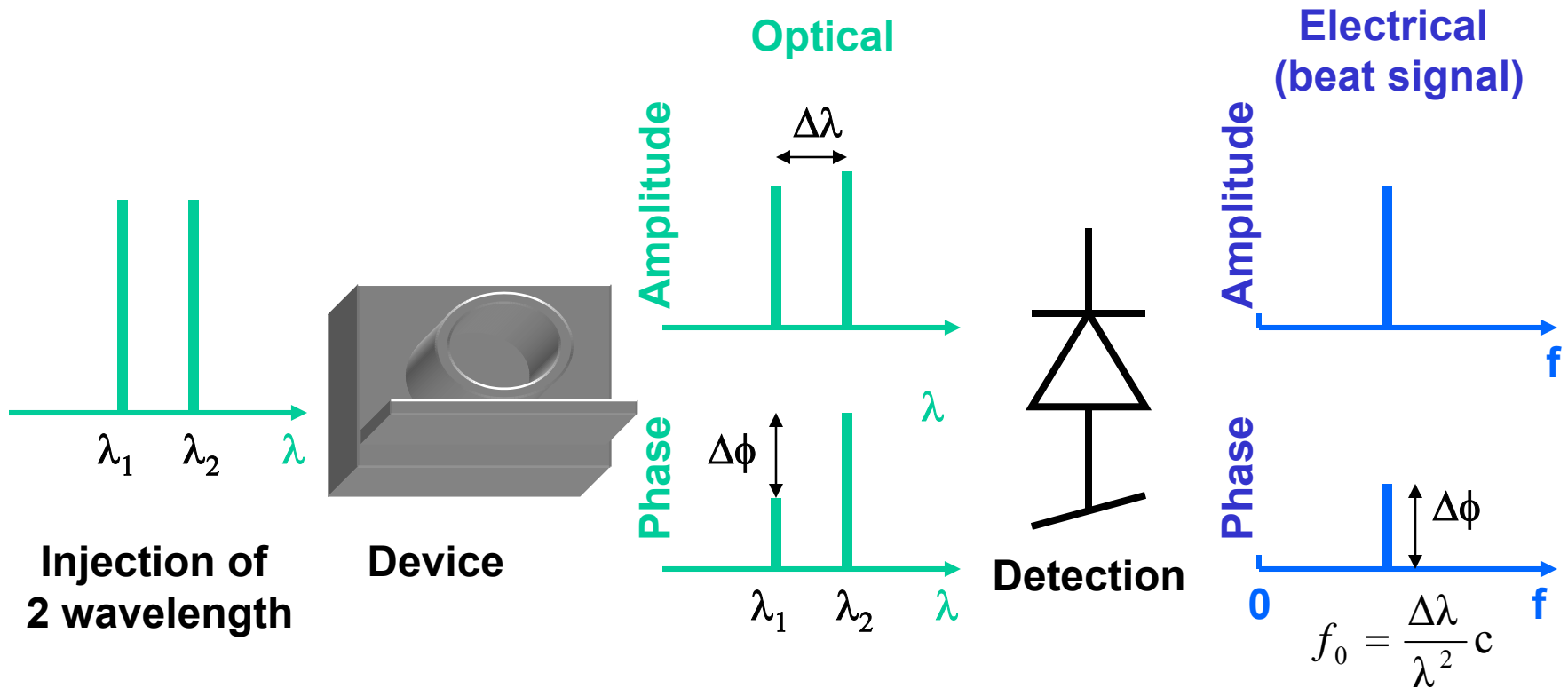


Group Delay Determines V_π



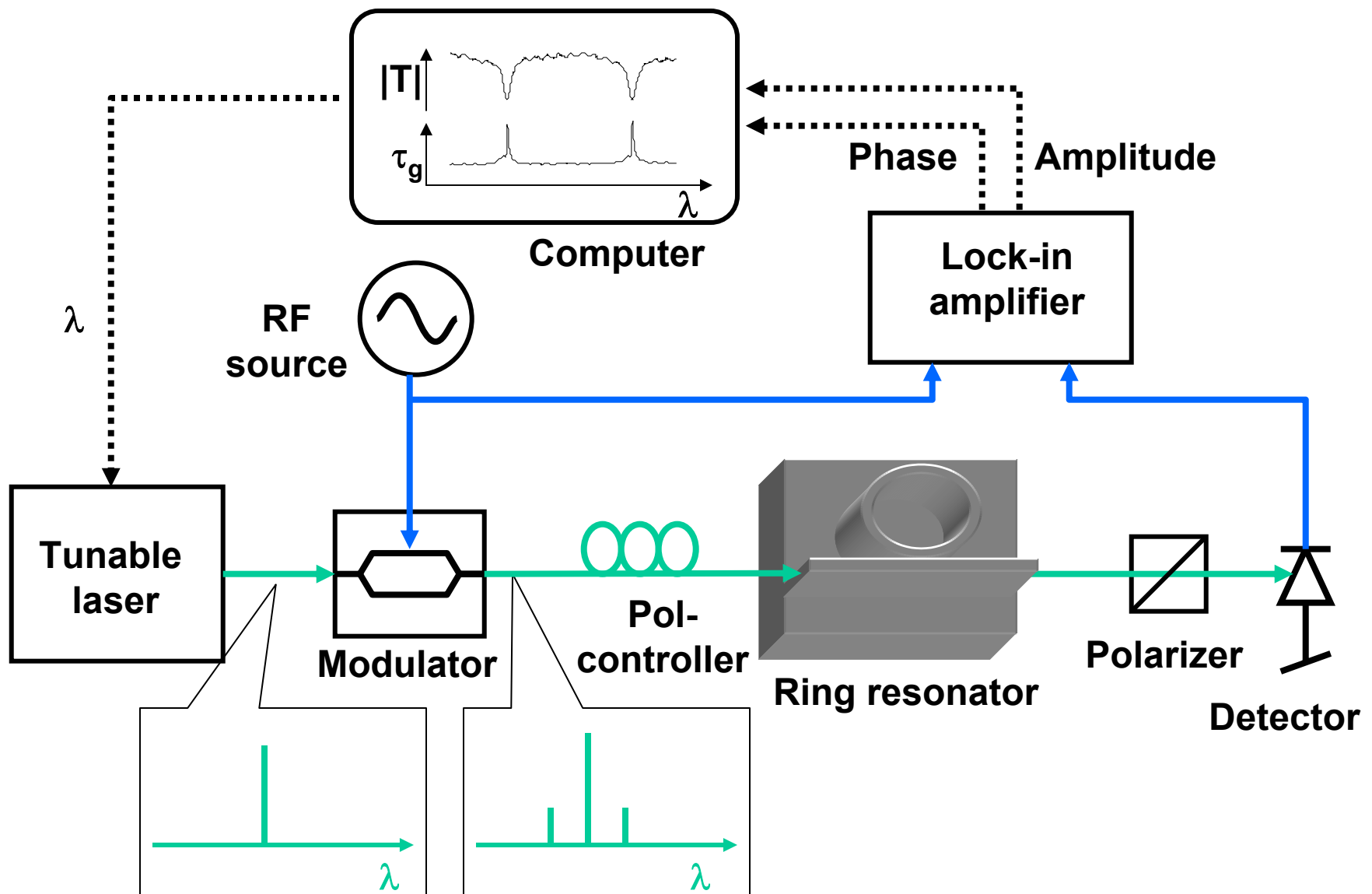
$$\phi = \frac{n\omega l}{c} \quad \longrightarrow \quad \frac{\partial \phi}{\partial n} = \frac{\partial \phi}{\partial \omega} \frac{\omega}{n} = \tau_g \frac{\omega}{n}.$$

Measurement of the Group Delay



Group delay:
$$\tau_g = \frac{1}{2\pi} \frac{d\phi}{df} \approx \frac{\Delta\phi}{2\pi f_0}.$$

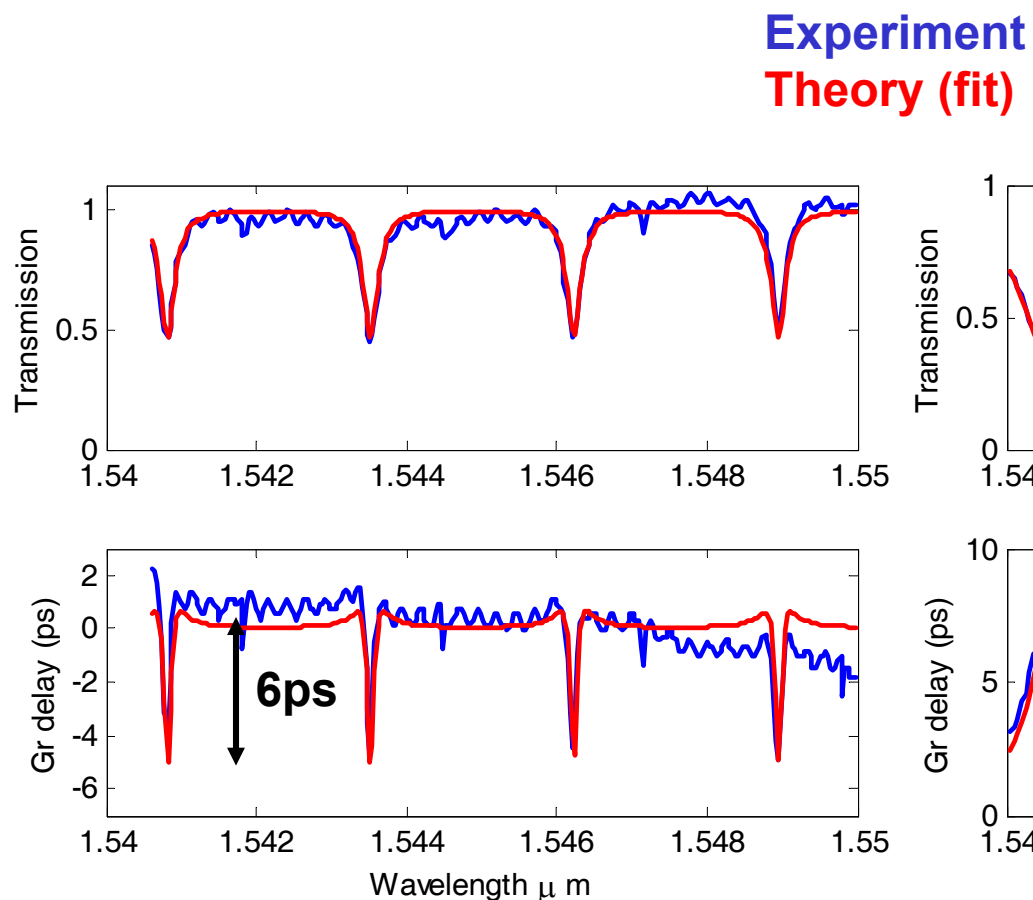
Experimental Setup



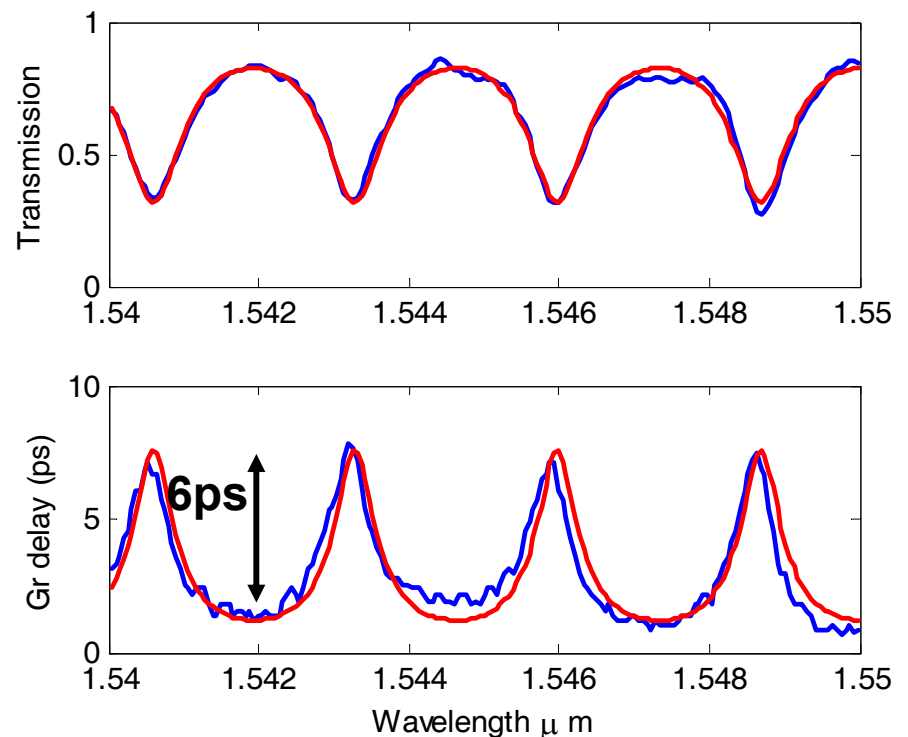
Examples



Coupling < Loss

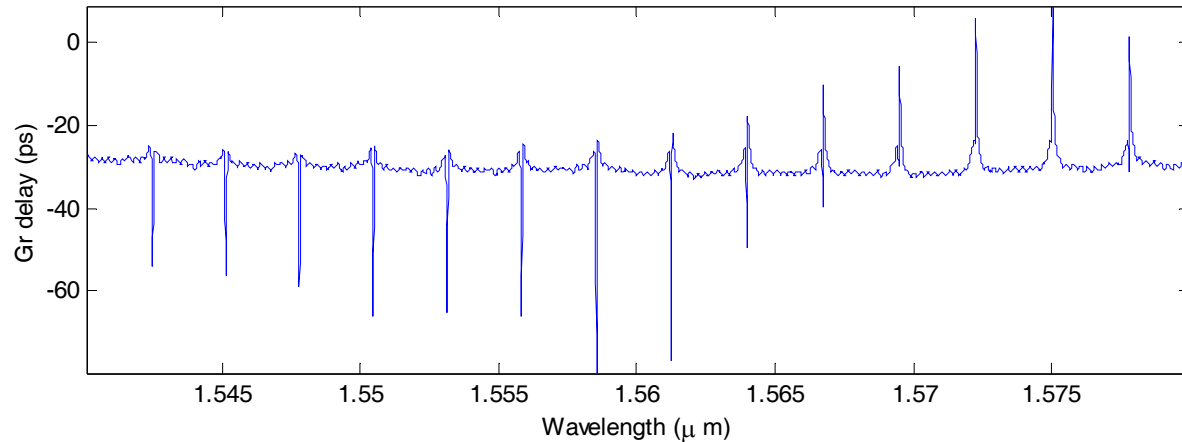
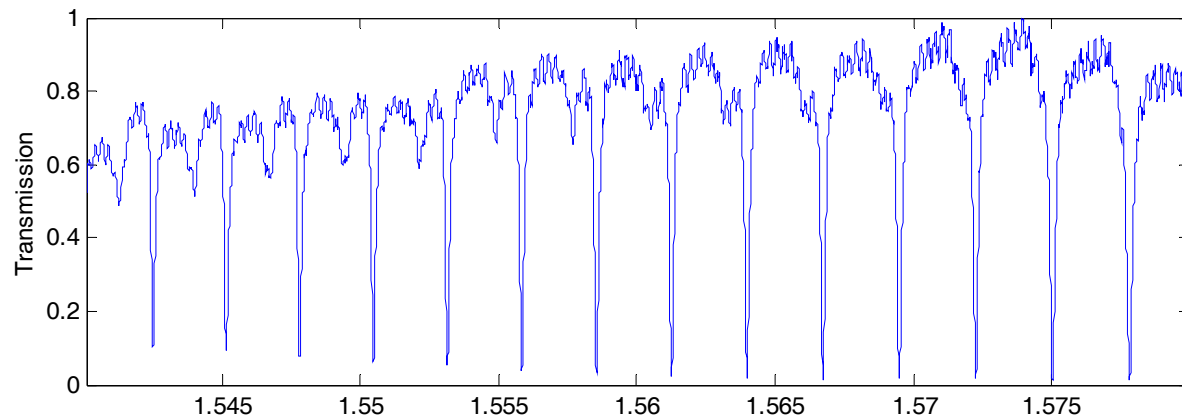


Coupling > Loss



Both Cases in One Sample

Coupling \approx Loss



Bandwidth Considerations



- **Electrical constraints**
 - Maximum ring-size limited by maximum capacitance to satisfy modulation speed requirements (RC-limit): $\sim 200\text{-}300\text{ }\mu\text{m}$ for 10 GHz modulator (0.5 μm waveguides).
- **Optical constraints:**
 - Optical bandwidth of the ring resonator (fsr/finesse): $B=20\text{ GHz}$ for 10 GHz modulator.

Limits lifetime & effective travel length in one ring.

$$\tau_{g \max} = \frac{1}{\pi \cdot B} \approx 32\text{ ps}$$

$$l_{eff \ max} = \frac{c}{n} \frac{1}{\pi \cdot B} \approx 3\text{ mm}$$

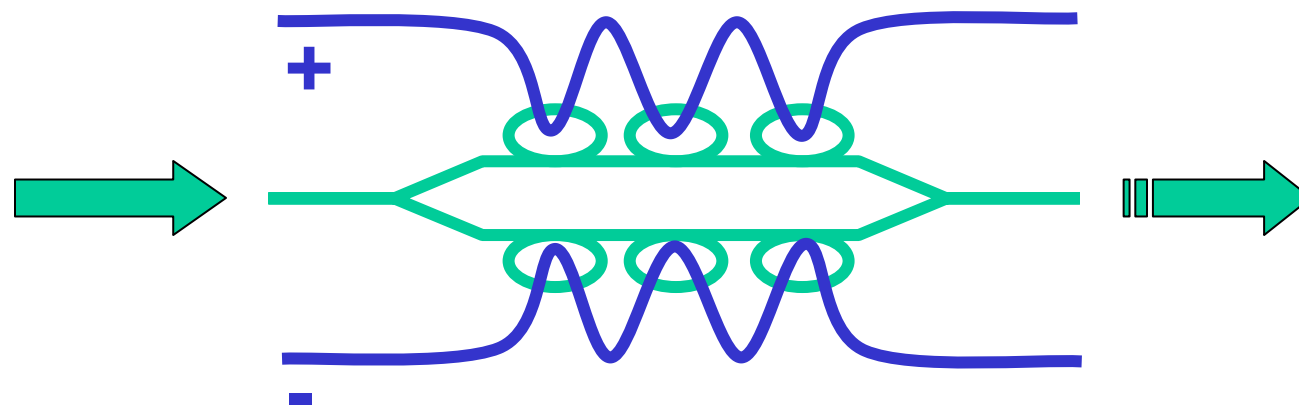
Loss Requirements



- **Goal** $v\pi = 100 \text{ mV.}$
- **Index change:** $\frac{\Delta n}{V} \approx 2 \cdot 10^{-4} \text{ V}^{-1}$ **current layer design.**
 $6 \cdot 10^{-3} \text{ V}^{-1}$ **coupled QW's.**
- **Required effective travel length:**
current layer design $l = \frac{\lambda}{\Delta n} = 2 \cdot 3.75 \text{ cm.}$
coupled QW's $2 \cdot 1.25 \text{ cm.}$
- **Loss requirements:** $\sim 1 \text{ cm}^{-1}.$

Updated Design

- Use rings size and bandwidth to match the 10GHz requirements.
- Further decrease V_π by cascading rings.
- Ensure that the coupling is larger than the loss in a ring.
- Design structure to minimize loss.
 - Simpler with larger rings



Coupler Physics & Performance

M. Kwakernaak

Coupler Physics and Performance

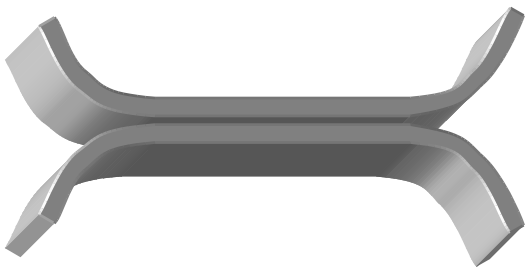


- **Comparison of couplers.**
- **Ring design with couplers.**
- **MMI design.**
- **MMI coupled ring results.**

MMI's vs. Coupled Waveguides

Coupled waveguides

- Requires extremely narrow gap ($0.3\text{-}0.4\mu\text{m}$).
- Depends critically on gap width.
- Arbitrary coupling ratios.
- Size scales with coupling ratio; high coupling is difficult if small devices are required.
- Excess loss at waveguide-coupler transitions.



Multi-mode interference couplers

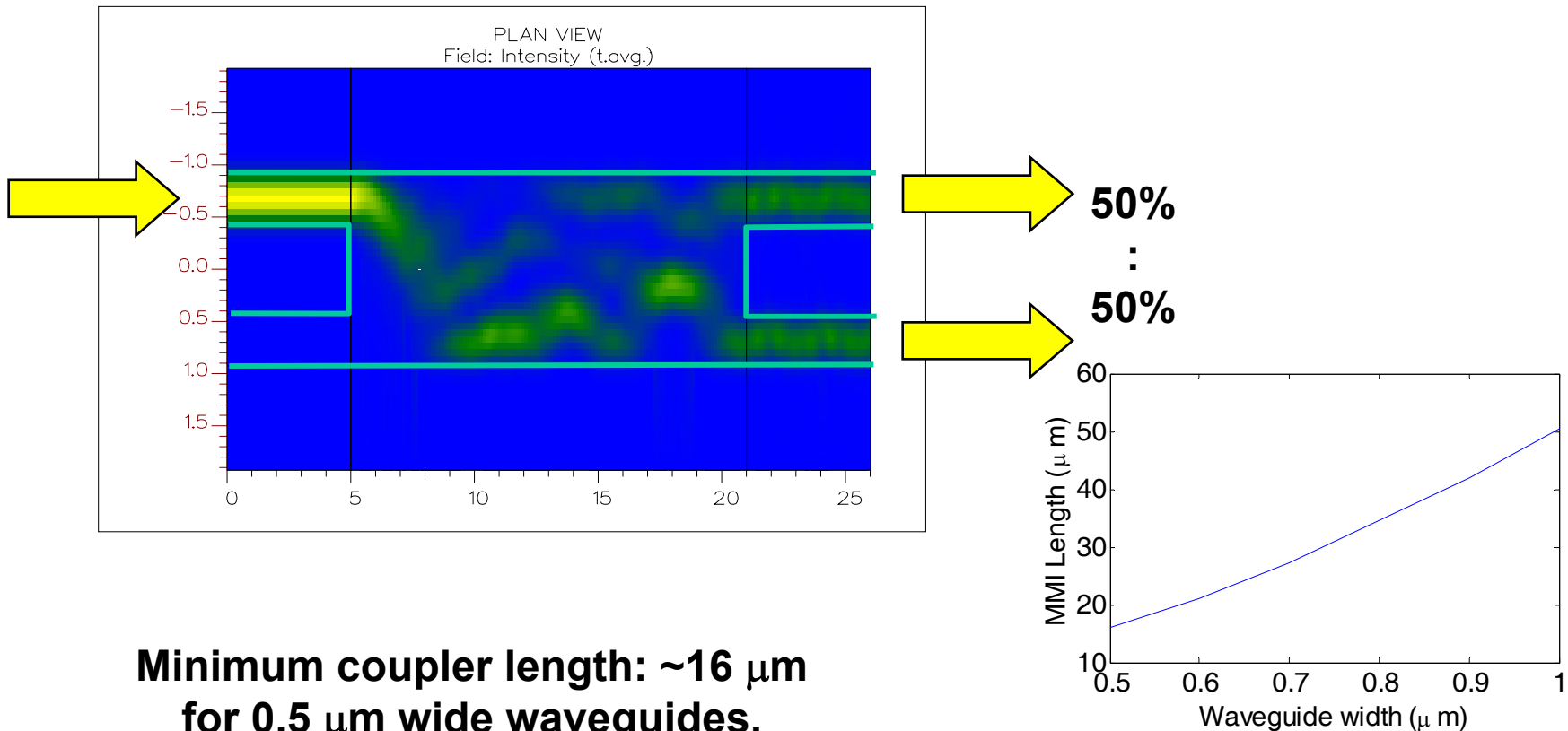
- No small features.
- Tolerant to fabrication.
- 50:50 coupling, other ratios are difficult.
- Minimum size is limited.
- Excess loss due to modal mismatch of MMI region and waveguides.



Ring design with MMI couplers

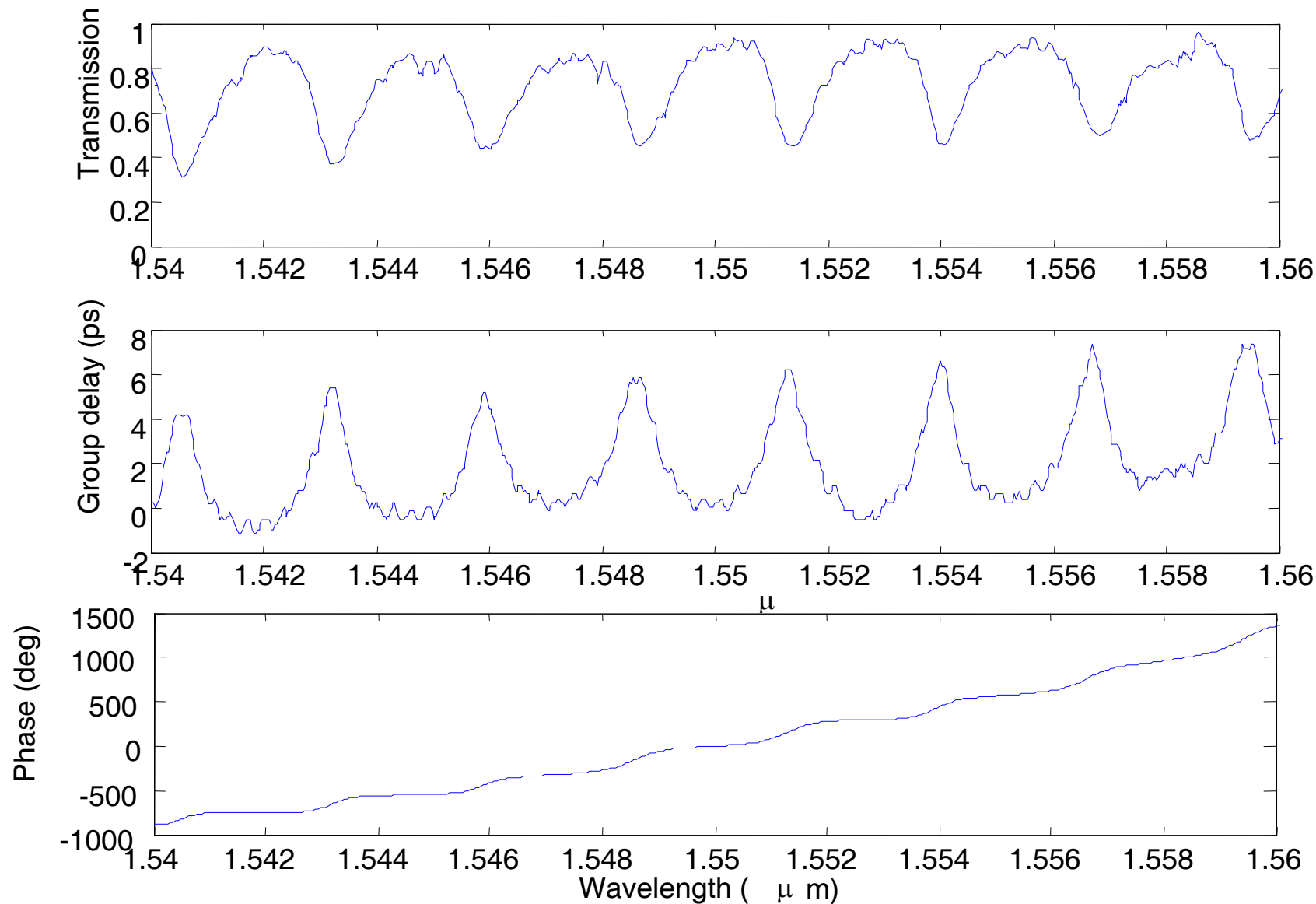
- **MMI's have 50:50 coupling ratio.**
- **Ring resonators with 50%50 coupler -> enhancement of ~6.**
- **Capacitance limit -> $300\mu\text{m}$ circumvent.
-> 1.8mm effective travel length.**

2x2 Multimode Interference (MMI) Coupler



--> compact solution if 50% coupling is required.

MMI Coupled Ring Resonator



Waveguide Loss

M. Kwakernaak

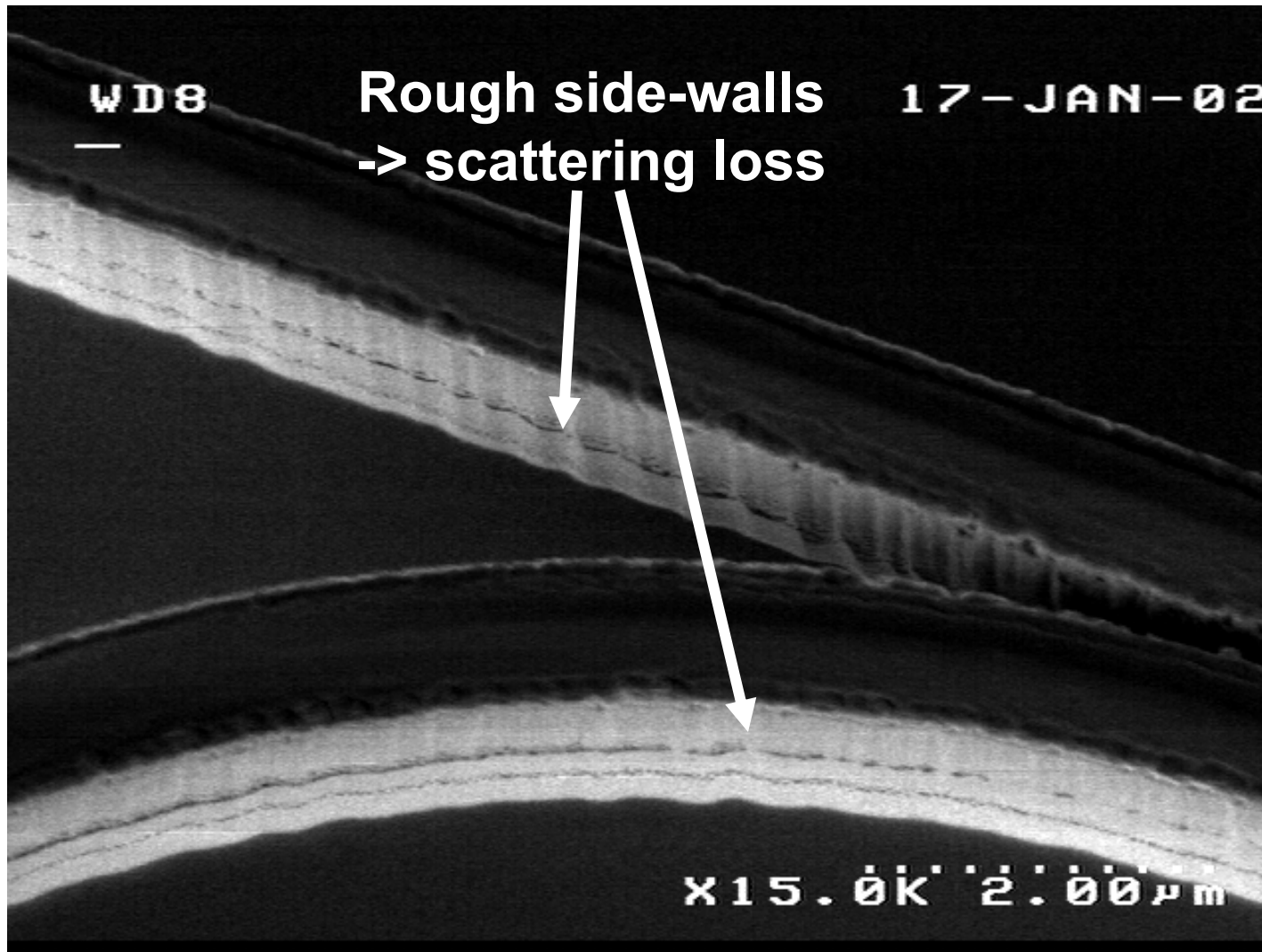
Waveguide Loss

- **Sources of loss.**
- **Roughness loss theory.**
- **Loss measurements.**

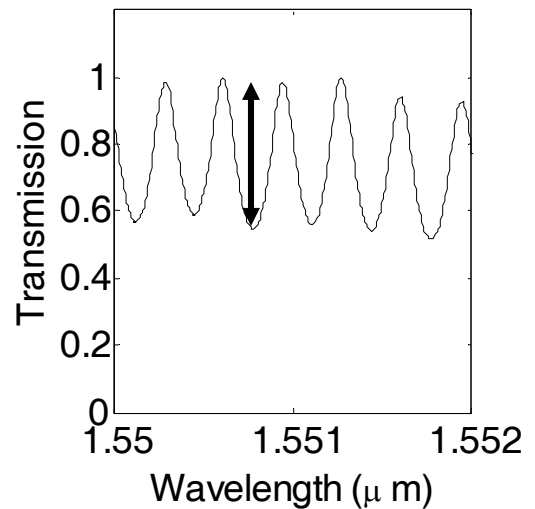
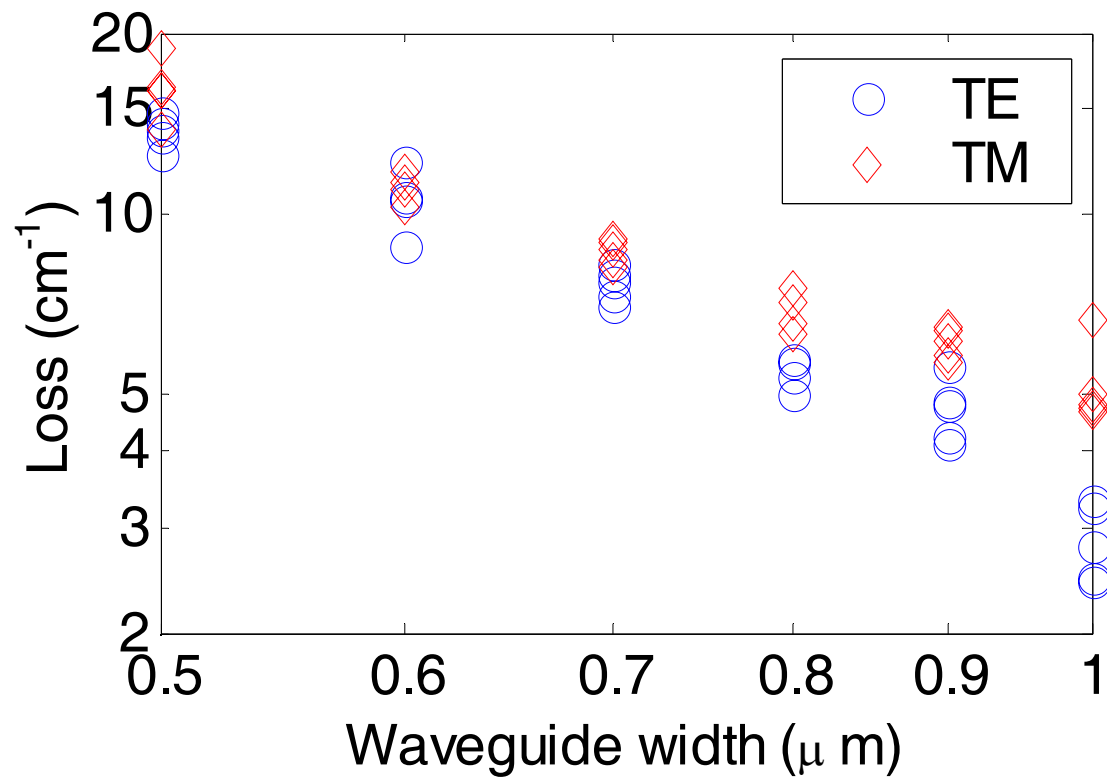
Sources of Loss

- **Straight waveguides**
 - **Material loss**
 - minimize modal overlap with p-doped region.
 - trade-off between electro-optic coefficient and loss.
 - 0.16 cm^{-1} have been demonstrated.
 - **Scattering loss.**
- **Bent waveguides**
 - **Bends enhance scattering loss.**
 - **Leakage**
 - minimized by deep etching.
- **Junctions**
 - **Mode mismatch.**
- **Coupler excess loss**
- **Multi-mode behavior**
 - coupling into other modes = loss.

Roughness Scattering



Loss measurements



Increase of loss with decreasing width -> scattering.

Conclusions



- **Taking advantage of the ring structure requires coupling > loss.**
- **Group-Delay measurements allow to unambiguously determine ring performance.**
- **MMI-couplers provide an alternative with potential advantages.**
- **Loss is the key to achieve the V_π -goal.**

Nanolithography

A. Lepore

Electron Beam Lithography: Tools



Issues with UIUC Tools (Cambridge, JEOL)

- **Delays (training of UIUC postdoc)**
- **Expertise**
- **Stitching errors with small fields (UIUC -- write time issue)**
- **Sample alignment (UIUC -- wafer chuck issue)**

Solution

- **Sarnoff now a second source for nanolithography expertise**
- **ARL now a second source for nanolithography tool**
 - Current: ARL system provides easy and accurate sample alignment and larger patterned area on wafer pieces
- **Sarnoff acquiring excessed ARL tool (formerly situated at LPS)**
 - Cambridge e-beam tool loaned/donated to SRI Int'l by ARL

Electron Beam Lithography: Processes



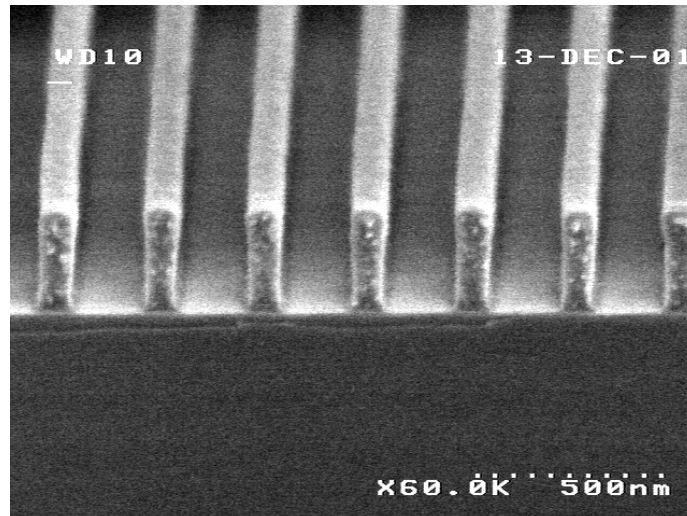
Resist

- **Negative resist**- edge acuity limitation
- **Positive resist**- difficult narrow gap formation
- **Resist erosion during dielectric etch**
 - affects deep etching ($\sim 5 \mu\text{m}$)

Mask

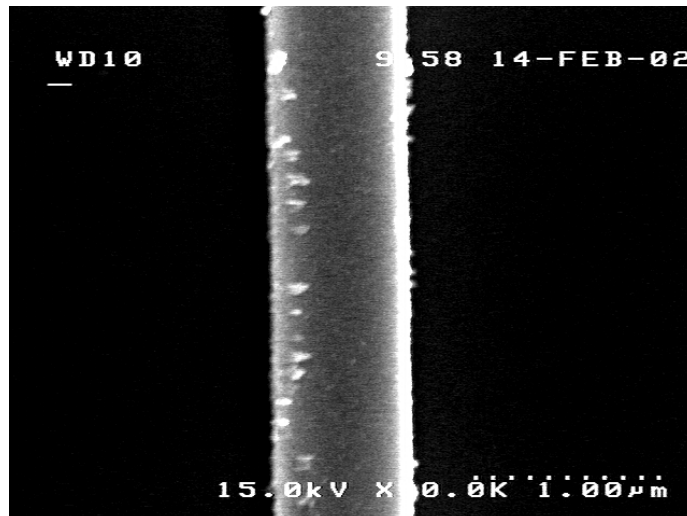
- **Mask erosion**
- **Evaluate direct metal mask on semiconductor and metal mask on dielectric-selectivity, grain size, contact resistance, adhesion, stress, sticking coefficient**

Calibration test of high-low molecular weight PMMA bilayer resist for metal liftoff

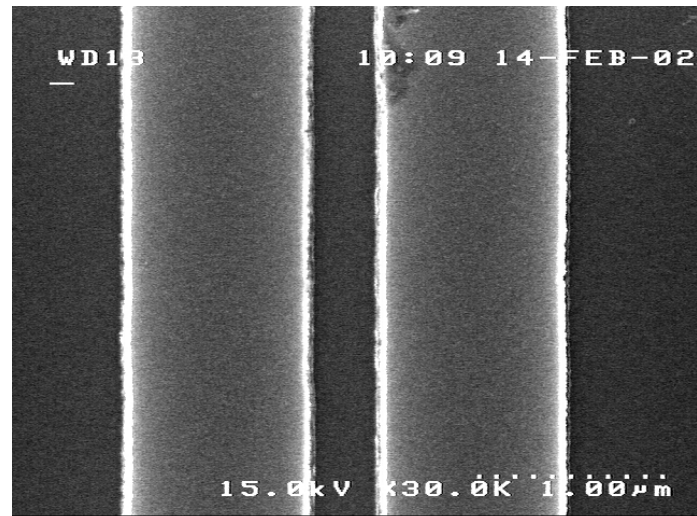


← PMMA 1
← PMMA 2

→ ← 20nm

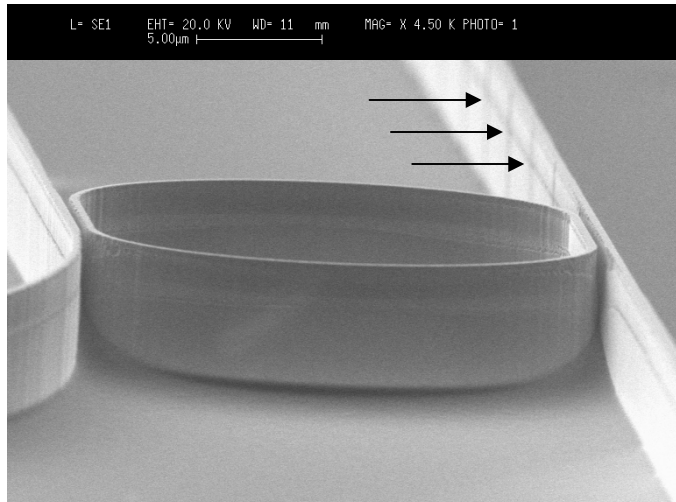


Ni etch mask as-deposited

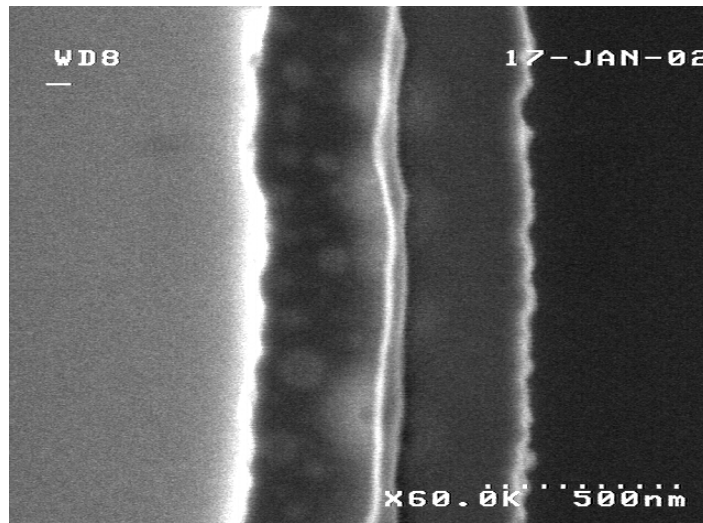


NiCr etch mask in gap coupler region

Electron Beam Lithography: Stitching Errors

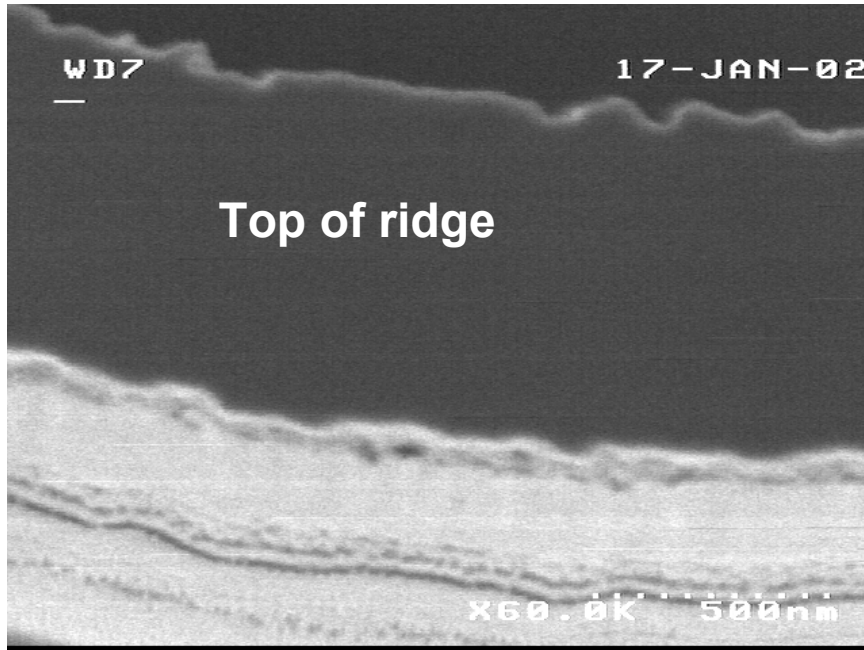


Previous: 70nm every 80μm (rings stitched)

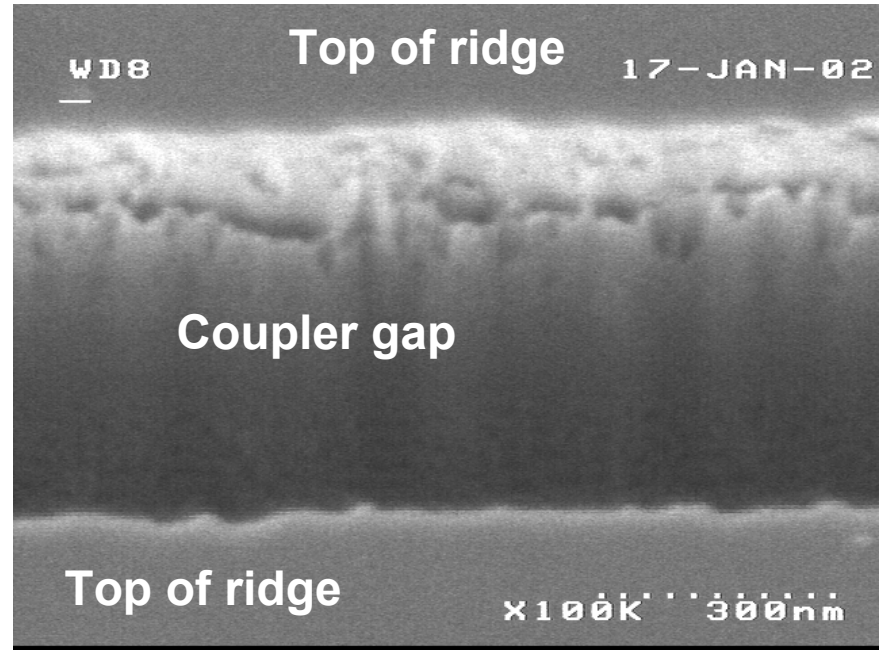


Now: 50nm every 500 μm (rings not stitched)

Electron Beam Lithography: Etch Mask Erosion



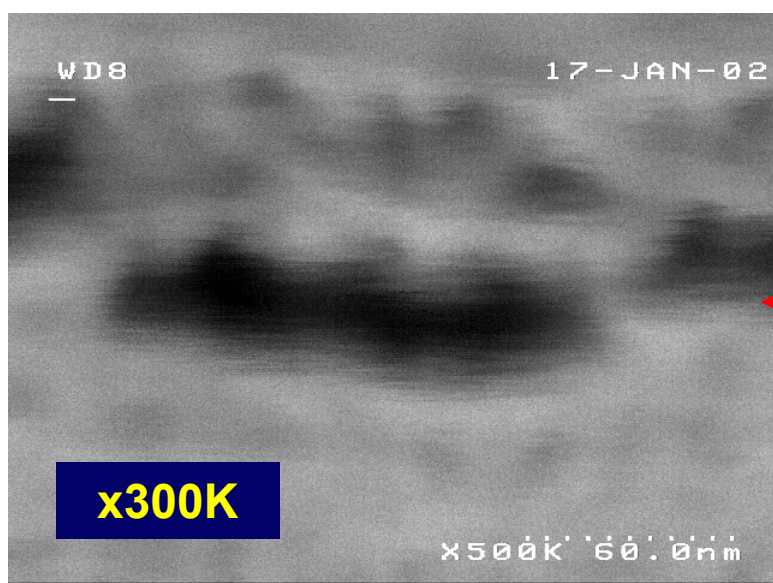
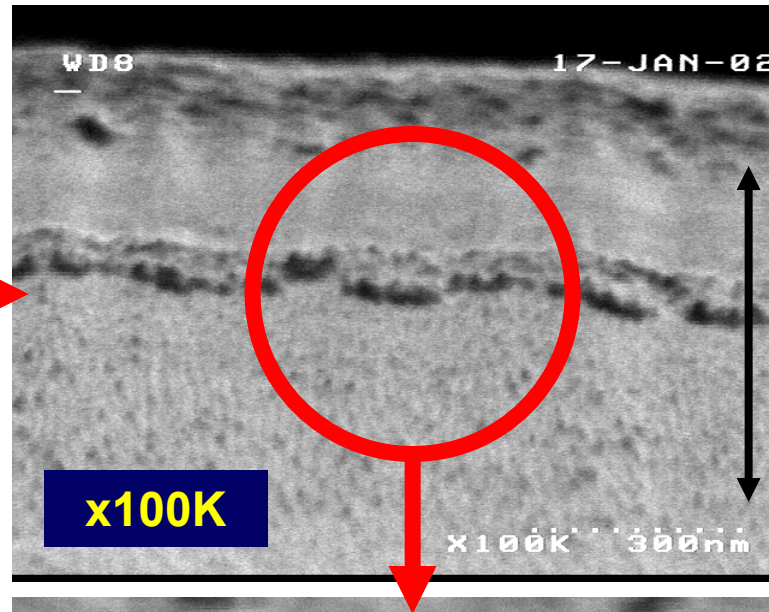
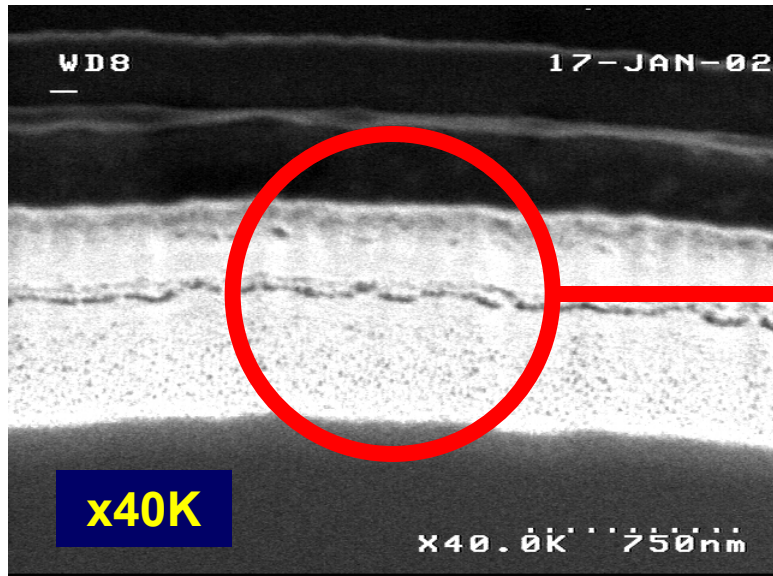
Early-stage erosion of dielectric mask, telegraphs to semiconductor through entire etch (shower curtain)



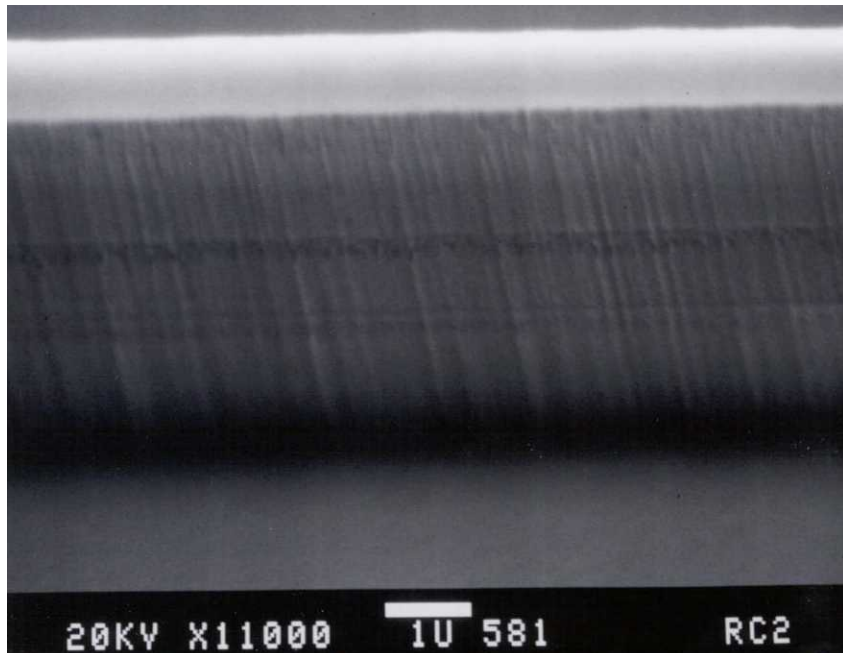
Later-stage dielectric mask erosion from deep etch, severe roughness transfers only to upper portion of semiconductor

Waveguide Fabrication: Edge Acuity

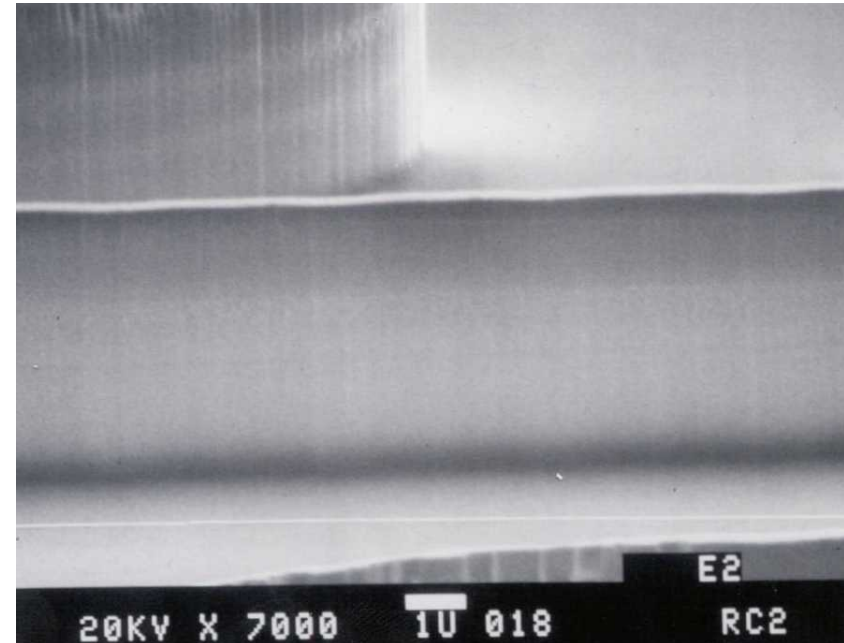
... shower curtain effect ...



Roughness Reduction



As etched via ICP



Reduced roughness using wet chemical etch after ICP etch

Pattern Transfer Issues



Waveguide requirements:

- Good edge acuity in mask and etched structure for low loss
- Low damage to epitaxial material structure for low loss
- Deep etching needed for confinement in tight bends (required for small ring circumference)
- Gap couplers require high anisotropy available with ICP etching

Etching requirements:

- Aggressive ICP etching requires durable mask
- CH_4/H_2 etching reduces mask durability requirements relative to ICP etching

Next step:

- MMI-couplers reduce anisotropy requirements and may allow less aggressive etch approaches such as CH_4/H_2
- Bulk of waveguide is straight and does not require deep etching

ECE·ILLINOIS

Electrical and Computer Engineering
University of Illinois at Urbana-Champaign

Advanced Processing and Circuits Group

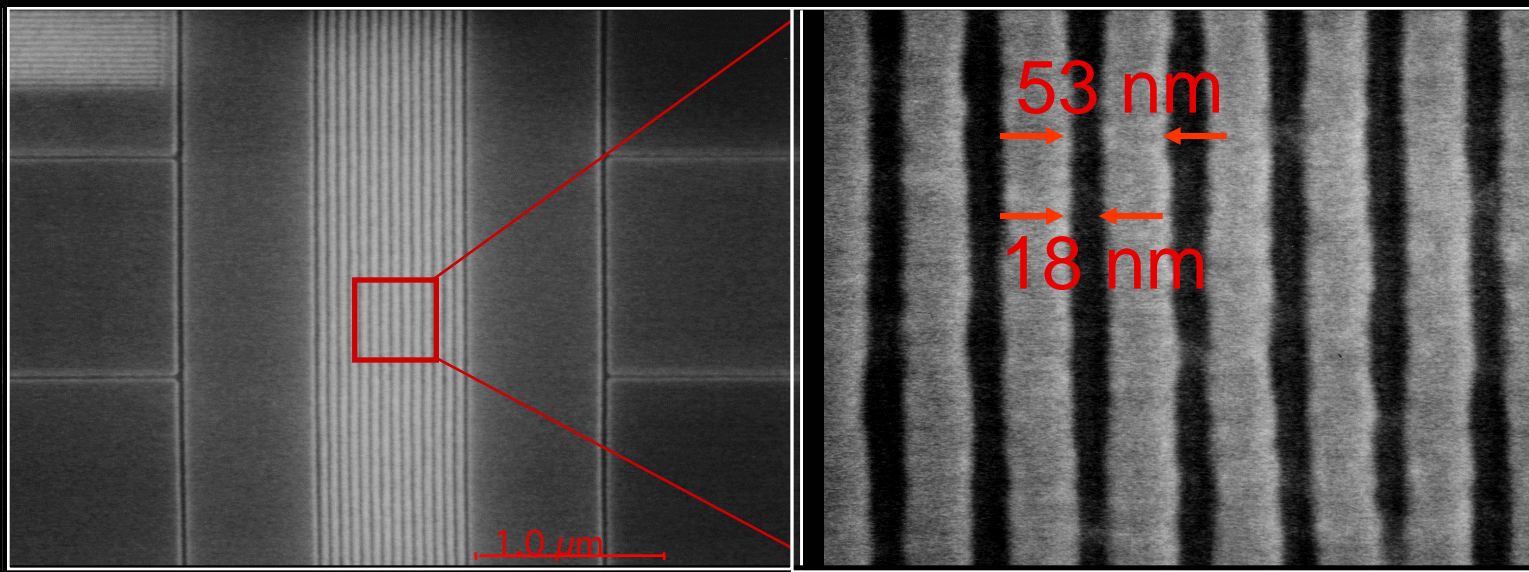
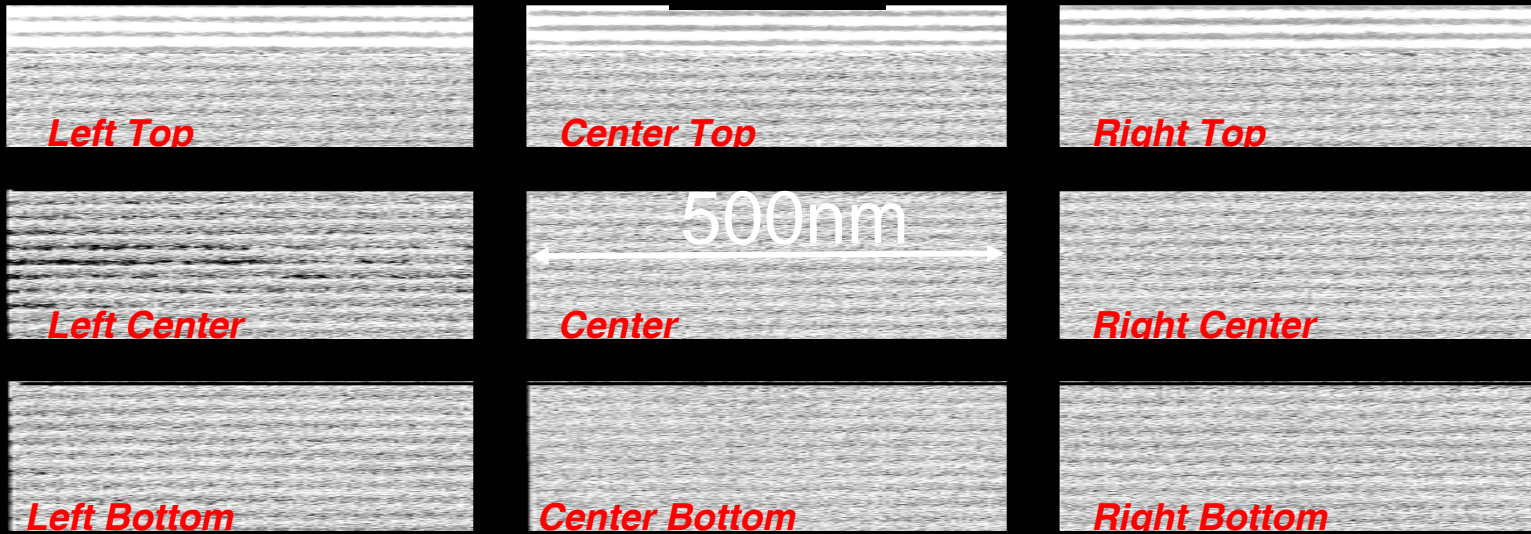
Nanoscience Review

I. Adesida (UIUC)

Nano-lithography

25 nm line/space pattern)

400 μm



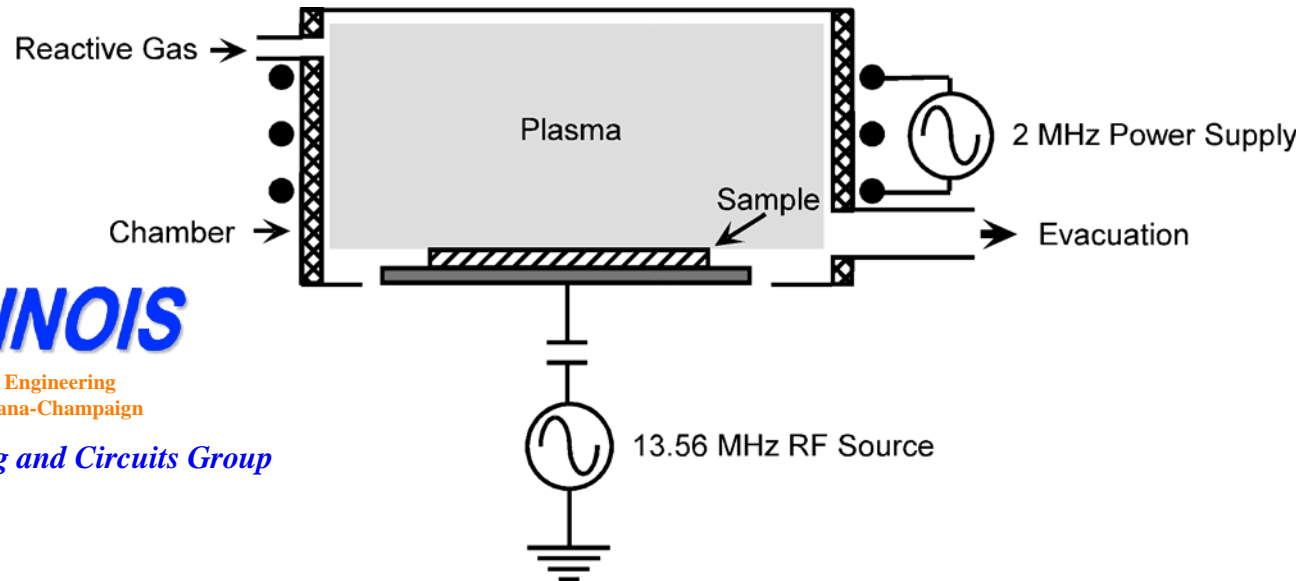
Inductively-Coupled-Plasma Reactive Ion Etching (ICP-RIE)



ECE·ILLINOIS

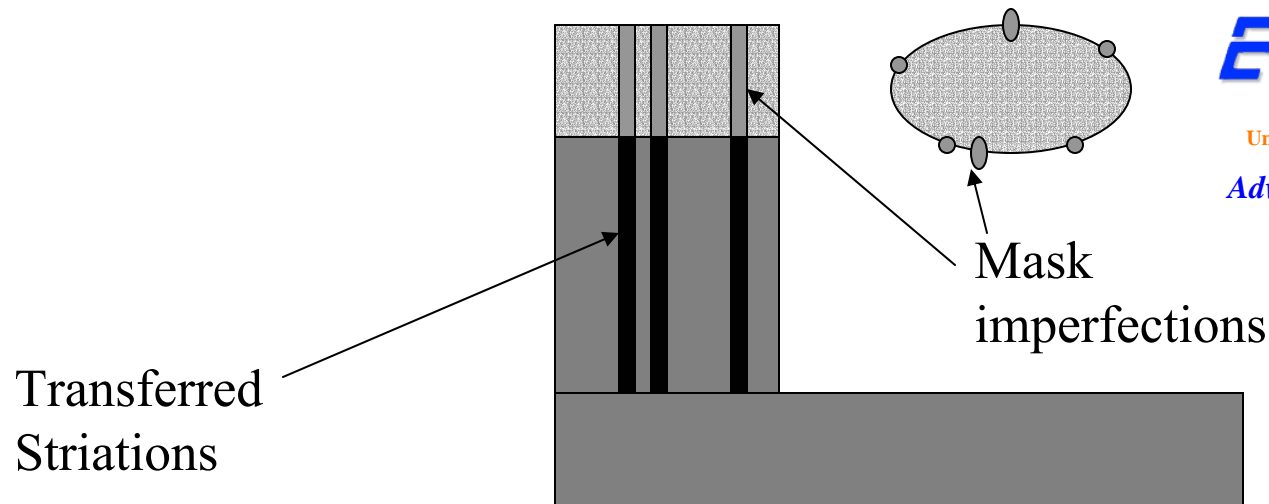
Electrical and Computer Engineering
University of Illinois at Urbana-Champaign

Advanced Processing and Circuits Group



- **Plasma density (1×10^{11} - 1×10^{12} ions/cm $^{-3}$) is 2-3 orders of magnitude higher than RIE.**
- **Ion energy independently varied by superimposing an RF Bias on substrate.**
- **Operation at lower pressures than RIE (<10 mT) leads to more directional etching (high anisotropy).**
- **High ion flux with low energies enables low etch damage while maintaining high etch rates.**

The “Shower Curtain” Effect



ECE·ILLINOIS

Electrical and Computer Engineering
University of Illinois at Urbana-Champaign

Advanced Processing and Circuits Group

Striations in the sidewall profile are often attributed to existing imperfections in the masking material. The transfer of these striations is known as the “shower curtain” effect.

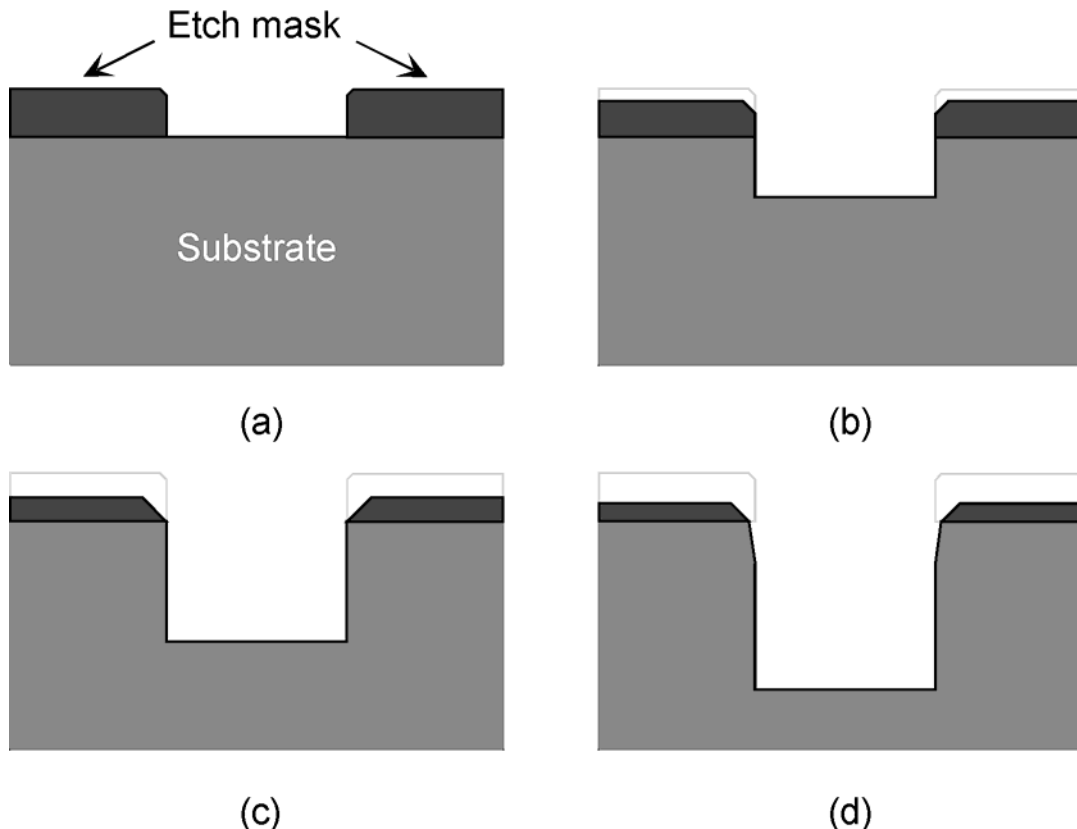
Mask Erosion



ECE·ILLINOIS

Electrical and Computer Engineering
University of Illinois at Urbana-Champaign

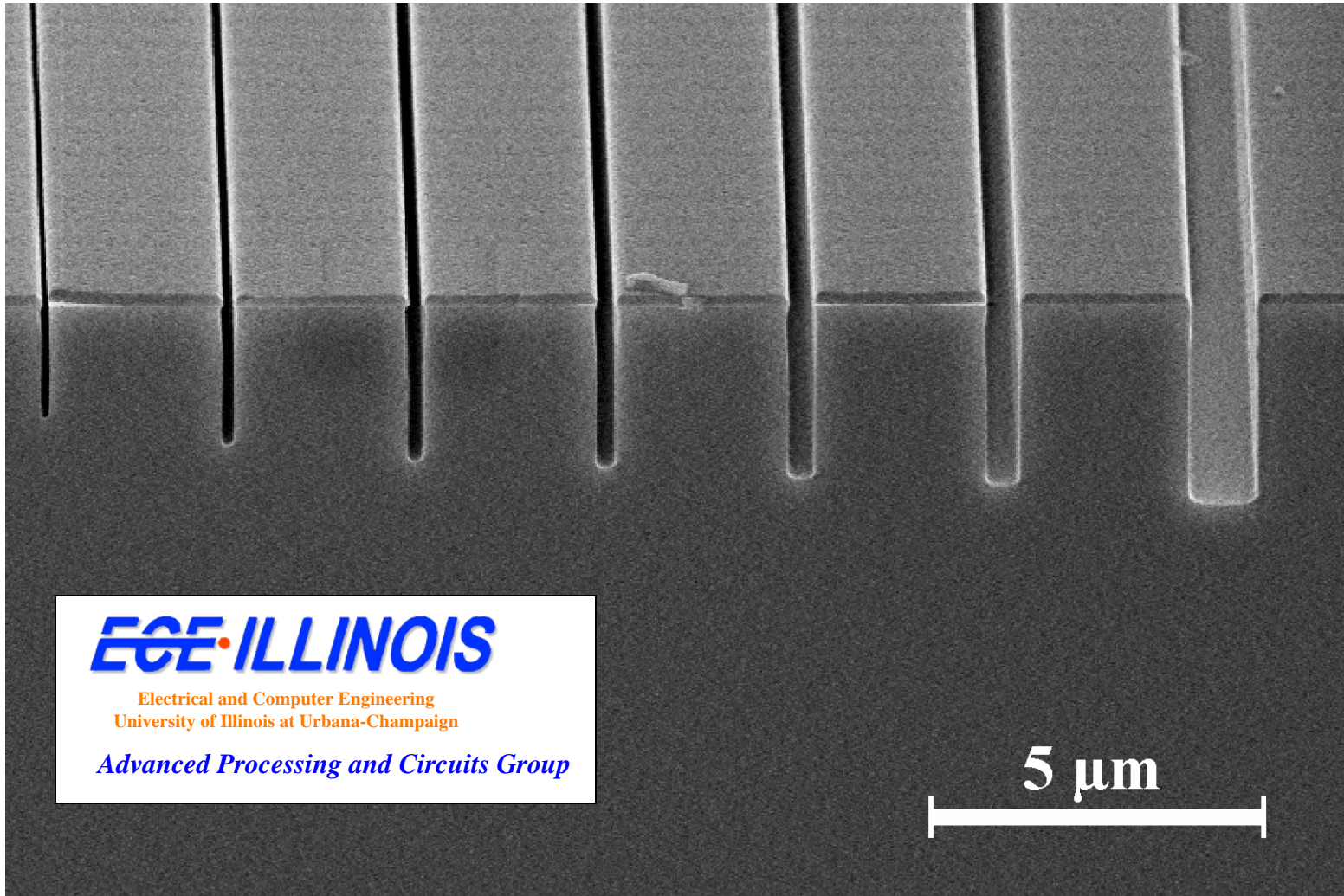
Advanced Processing and Circuits Group



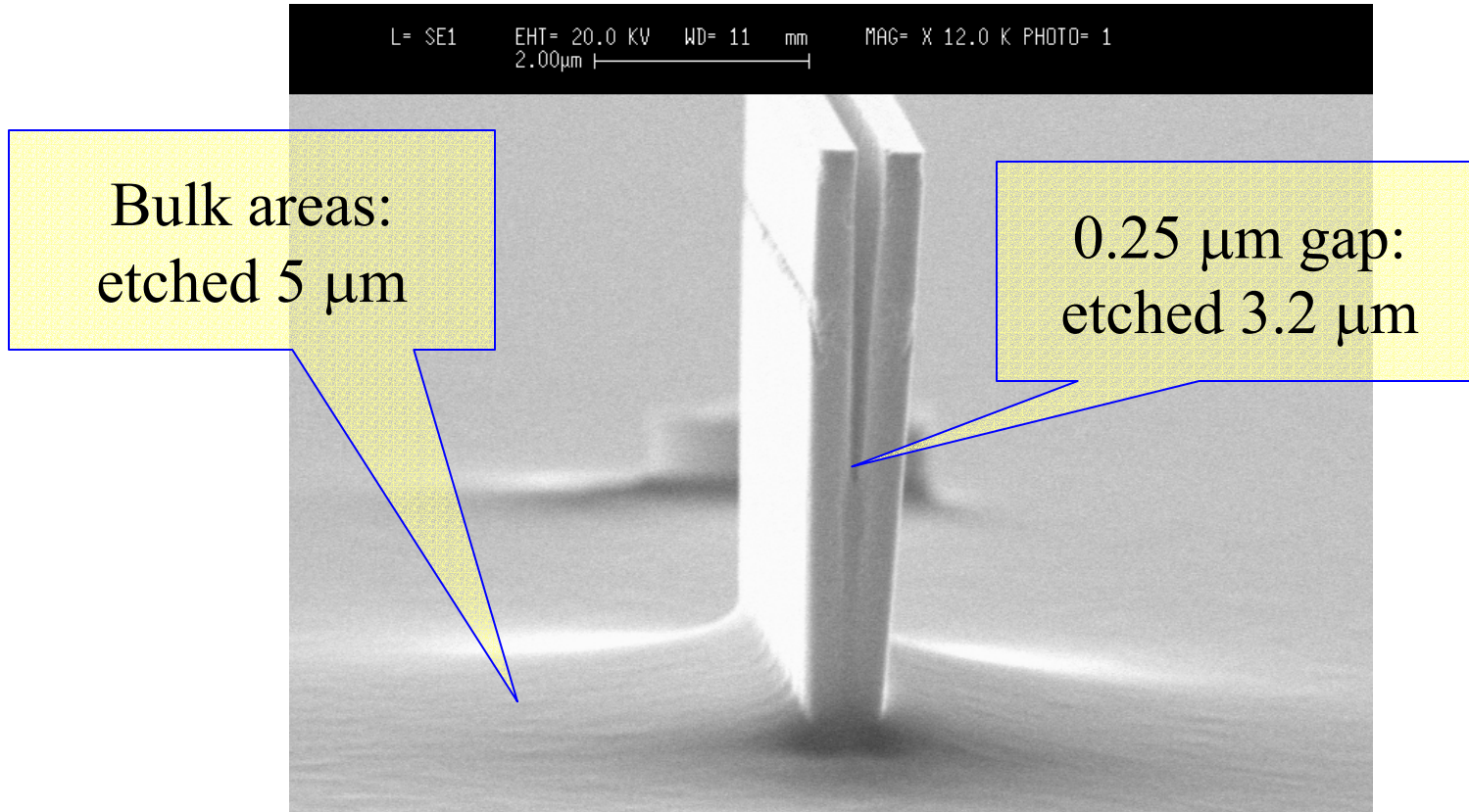
To avoid the effects of mask erosion there are two approaches:

- use of an alternate masking material with improved selectivity
- augmenting the thickness of the mask

Loading Effects



Aspect Ratio Dependence of the Etch: Isolation in the Gap

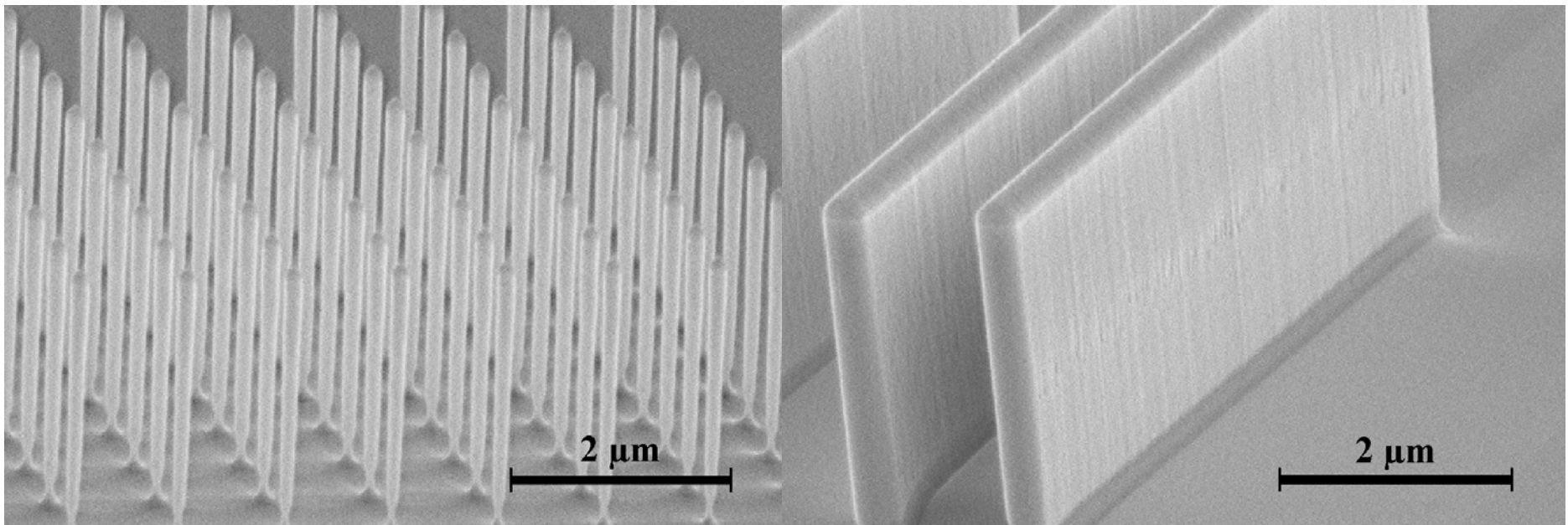


ECE • ILLINOIS

Electrical and Computer Engineering
University of Illinois at Urbana-Champaign

Advanced Processing and Circuits Group

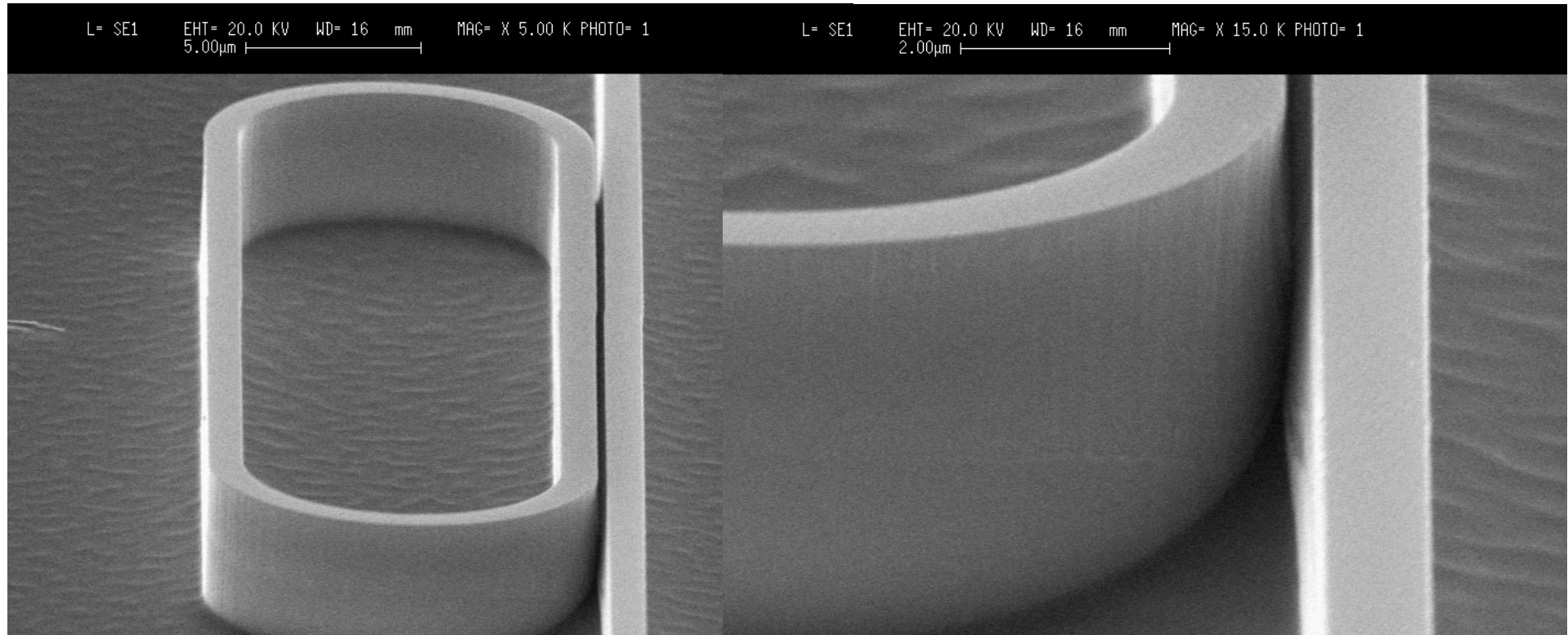
InP Etching



ECE·ILLINOIS

Electrical and Computer Engineering
University of Illinois at Urbana-Champaign

Advanced Processing and Circuits Group

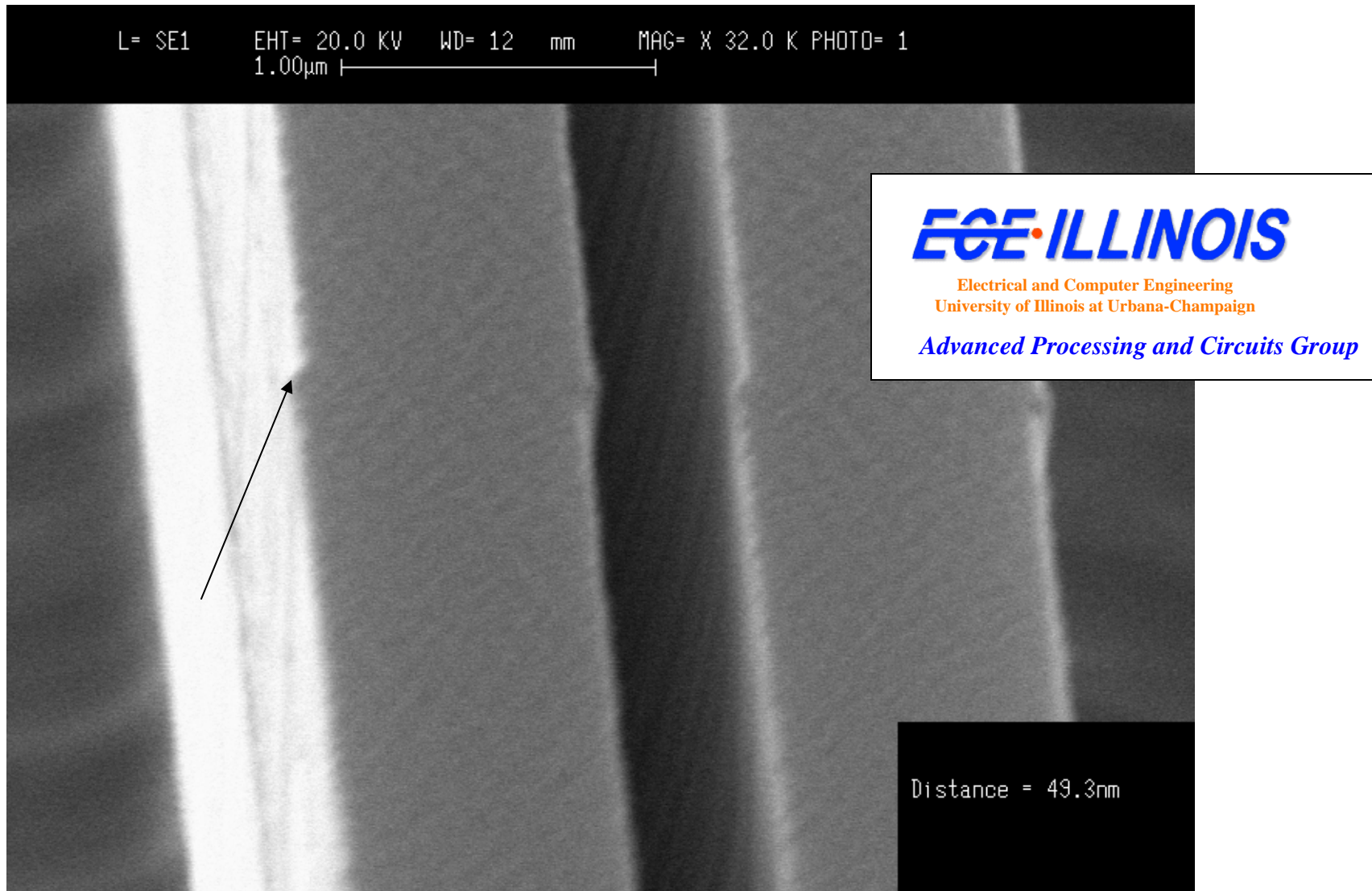


ECE·ILLINOIS

Electrical and Computer Engineering
University of Illinois at Urbana-Champaign

Advanced Processing and Circuits Group

Field Stitching With the JEOL 6000 FS



Approaches to Smoothing Sidewall Roughness



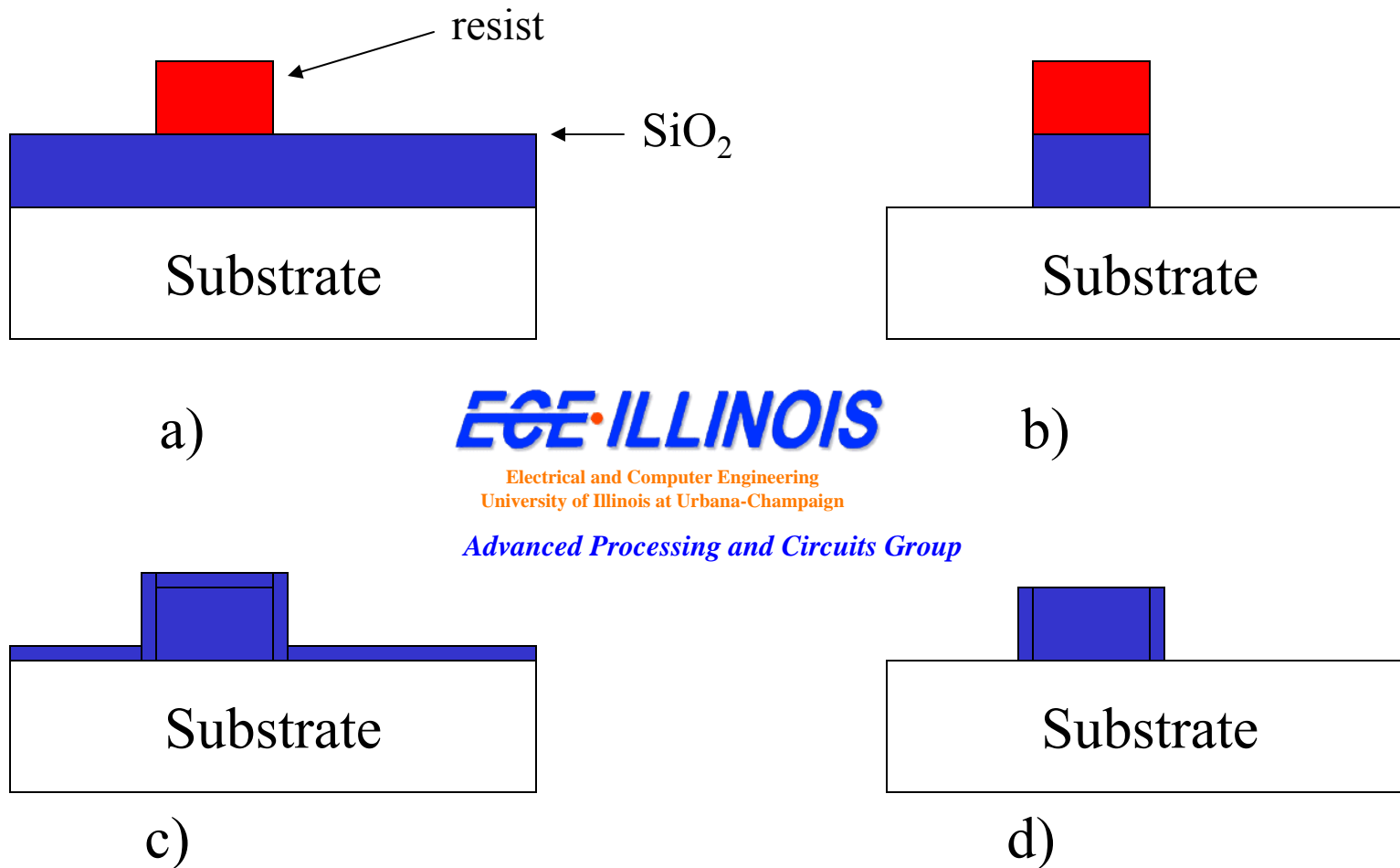
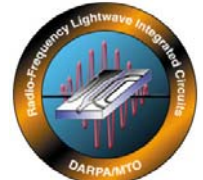
- Multipass Lithography
- Redeposition of Oxide Etch Mask
- Use of E-beam resist as etch mask to SiO_2 in RIE
- Use of NiCr as an etch mask to SiO_2 in RIE
- Use of metal as a direct etch mask

ECE·ILLINOIS

Electrical and Computer Engineering
University of Illinois at Urbana-Champaign

Advanced Processing and Circuits Group

Multipass Lithography/SiO₂ Redeposition



ECE·ILLINOIS

Electrical and Computer Engineering
University of Illinois at Urbana-Champaign

Advanced Processing and Circuits Group

ECE·ILLINOIS

Electrical and Computer Engineering
University of Illinois at Urbana-Champaign

Advanced Processing and Circuits Group

Anisotropic Etching

S. Rommel (UIUC)

S. Rommel: Outline

... Device Processing Development for REMs ...



I.) Summary of Work

II.) Processing Technology Development

- A.) InP/InGaAsP etching
- B.) Electron-Beam Lithography
- C.) Mask Transfer to SiO_2 ***
 - 1) Use of AZPN114 Resist
 - 2) Use of NEB-22 Resist

III.) Future Plans/Technology Transfer



Electrical and Computer Engineering
University of Illinois at Urbana-Champaign

Advanced Processing and Circuits Group



July-September 2000:

- Project Initiated
- Developed a Cl₂-based anisotropic ICP-RIE process to etch InP



Electrical and Computer Engineering
University of Illinois at Urbana-Champaign

Advanced Processing and Circuits Group

October 2000-March 2001:

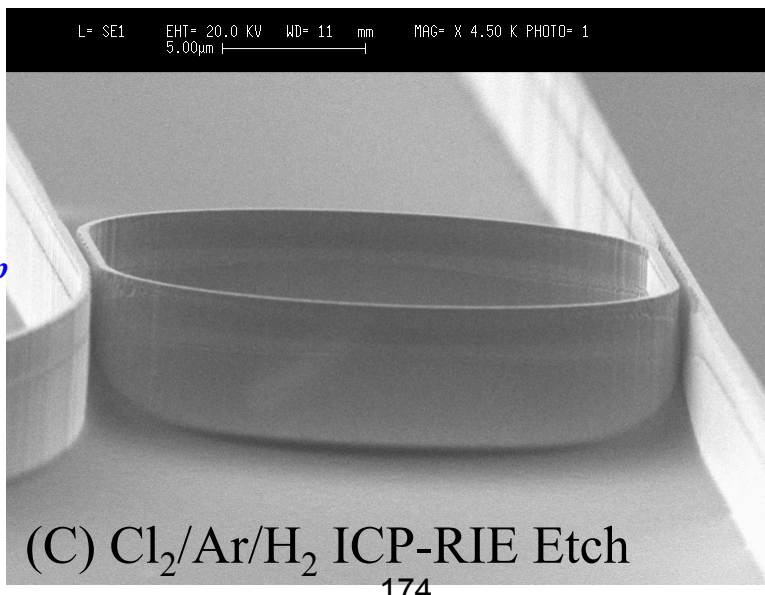
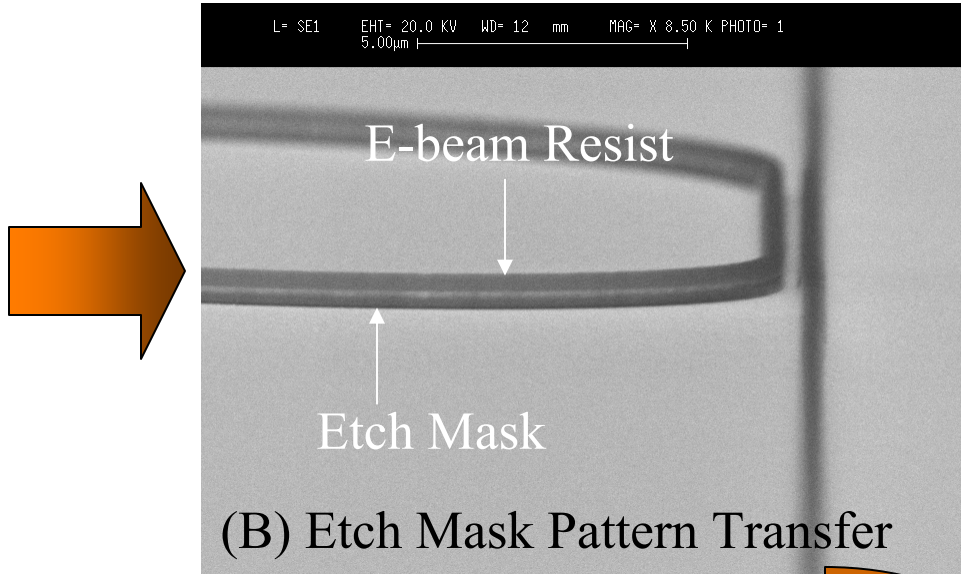
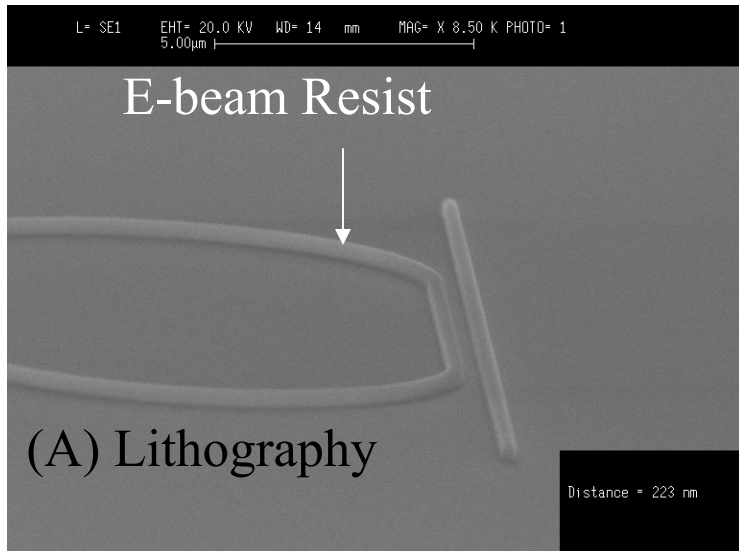
- Developed an e-beam lithography process on the Leica 10.5 EBMF e-beam to realize ring resonators
- Optimized etching for heterostructures with InGaAsP
- Delivered Sarnoff with initial device samples

April 2001-May 2001:

- Refined hard etch mask process
- Began routine deliveries to Sarnoff late April 2001

June 2001-present:

- Began process development on the JEOL 6000 FS e-beam; demonstrated superior devices; Researching methods for improving sidewall roughness of SiO₂ etch mask

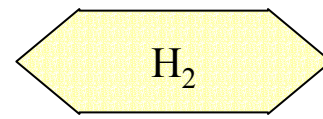
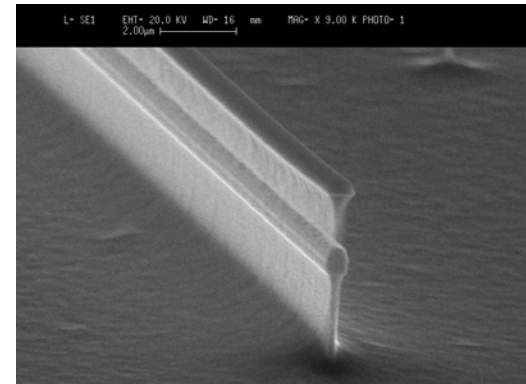
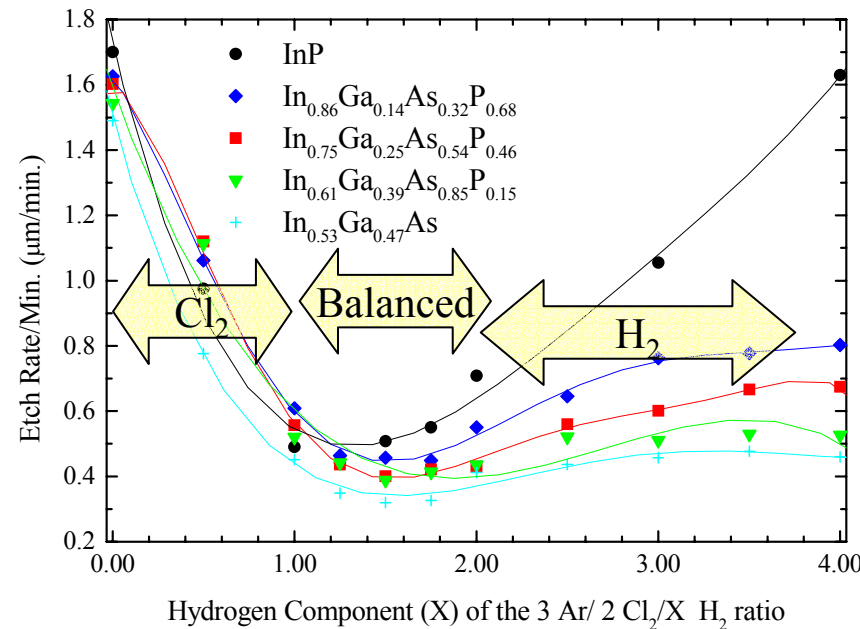
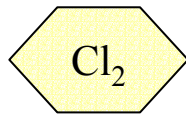
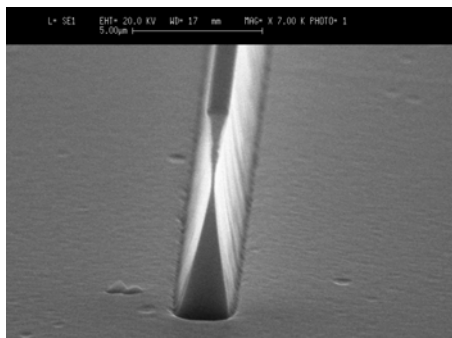


ECE•ILLINOIS

Electrical and Computer Engineering
University of Illinois at Urbana-Champaign

Advanced Processing and Circuits Group

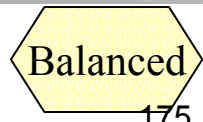
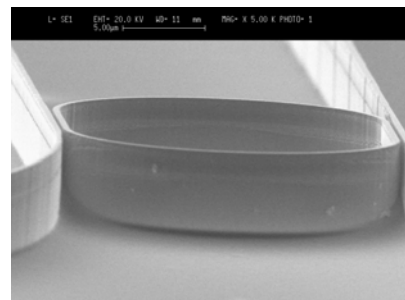
InP Etching Regimes



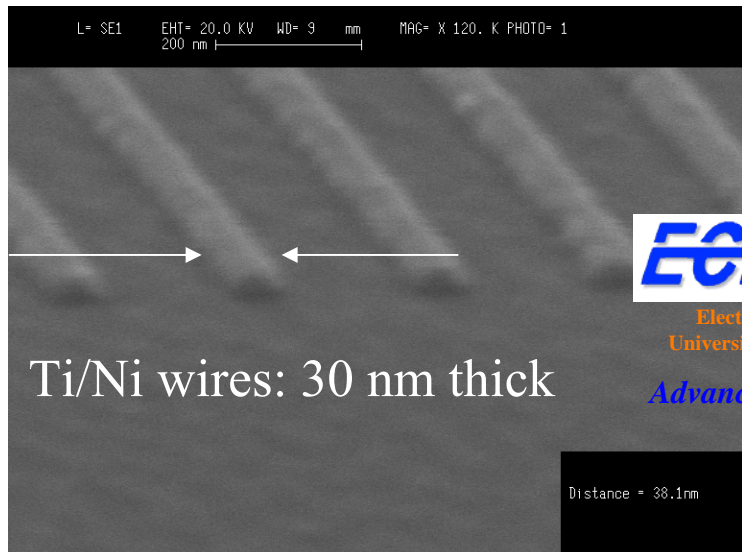
ECE·ILLINOIS

Electrical and Computer Engineering
University of Illinois at Urbana-Champaign

Advanced Processing and Circuits Group



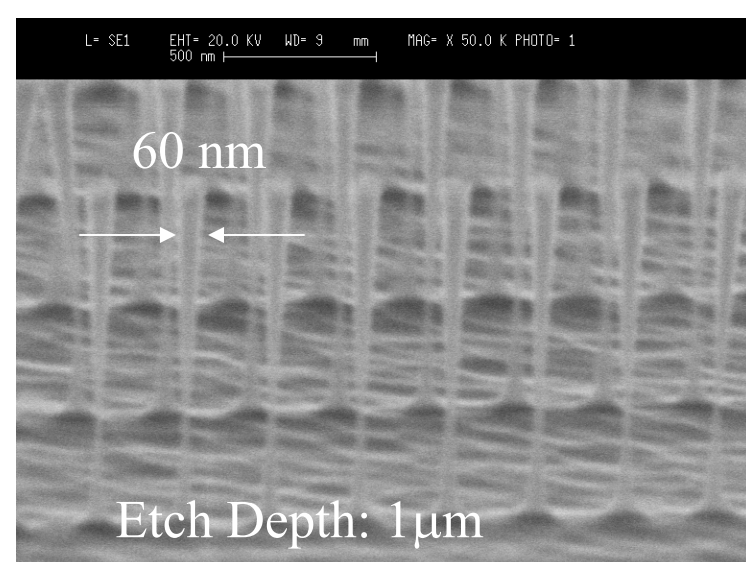
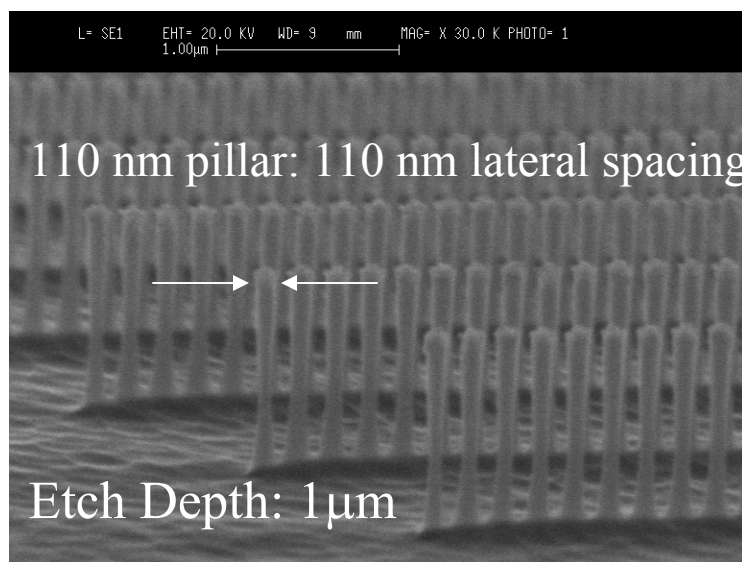
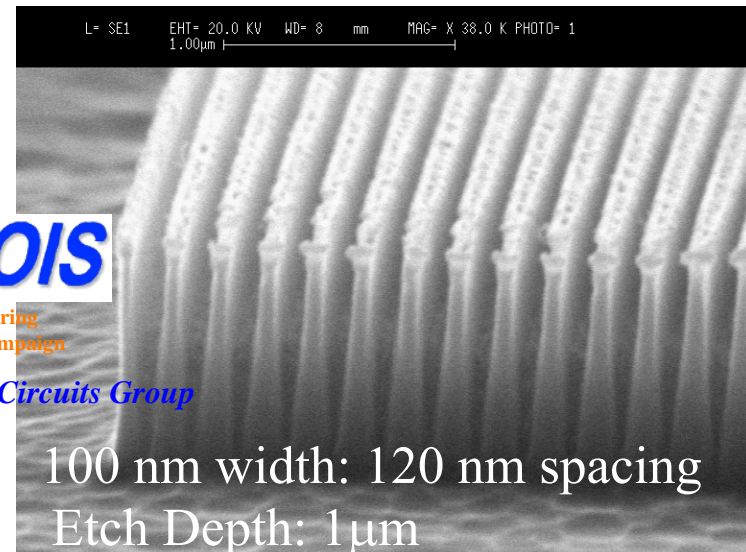
InP Nanofabrication



ECE·ILLINOIS

Electrical and Computer Engineering
University of Illinois at Urbana-Champaign

Advanced Processing and Circuits Group



Choices for Masking Materials



Three broad categories of masking materials:

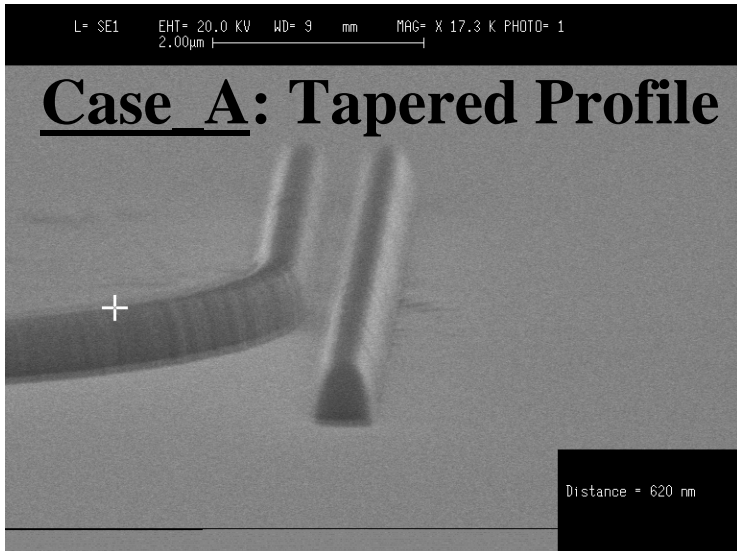
- **Metals**: Ni, Cr, NiCr, Ti, Al, W, Pt
- **Dielectrics**: SiO_x , SiN_x
- **Polymers**: Photoresist, E-beam resist

ECE·ILLINOIS

Electrical and Computer Engineering
University of Illinois at Urbana-Champaign

Advanced Processing and Circuits Group

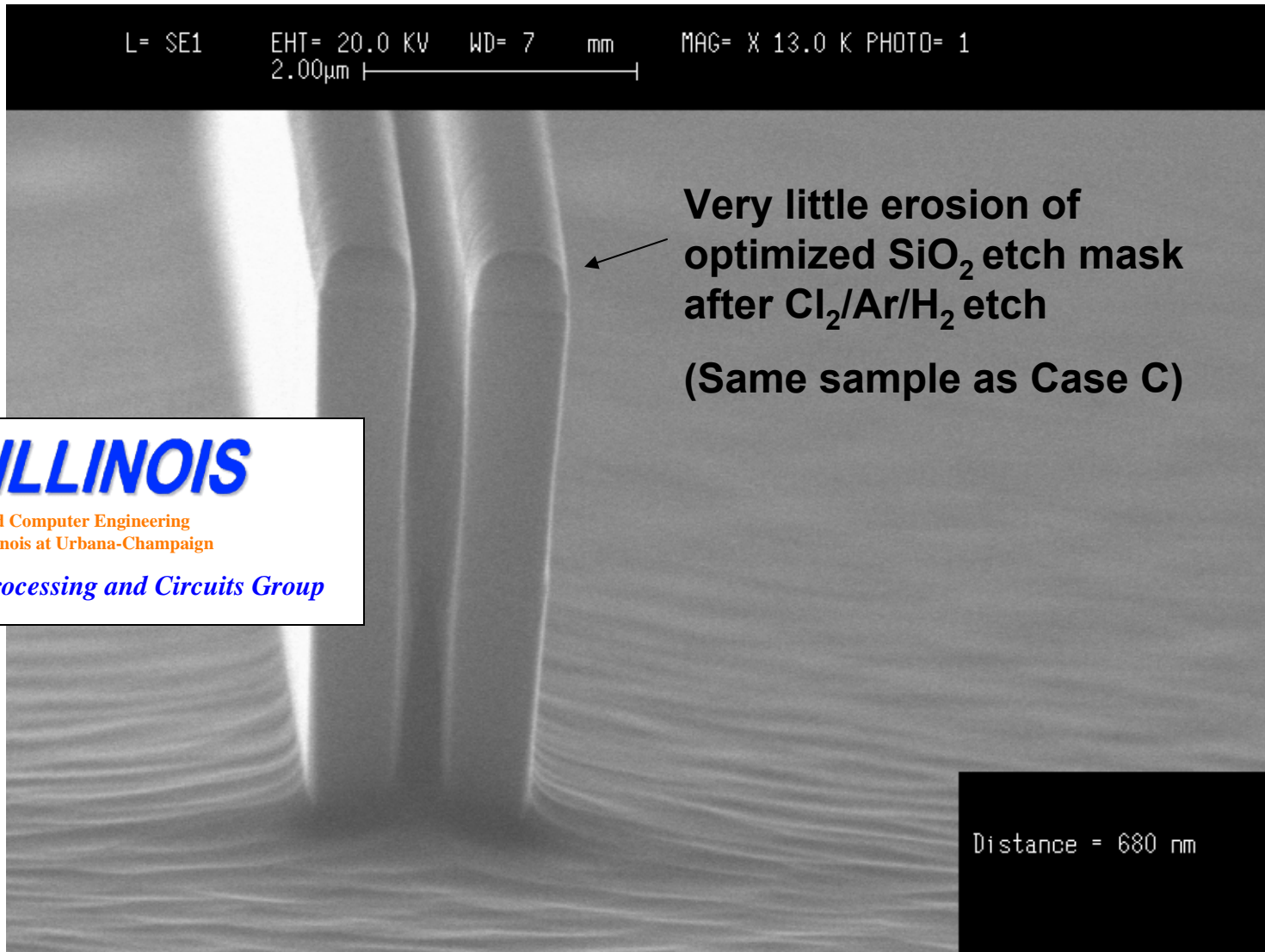
Profile of the SiO_2 etch mask depends on the process conditions



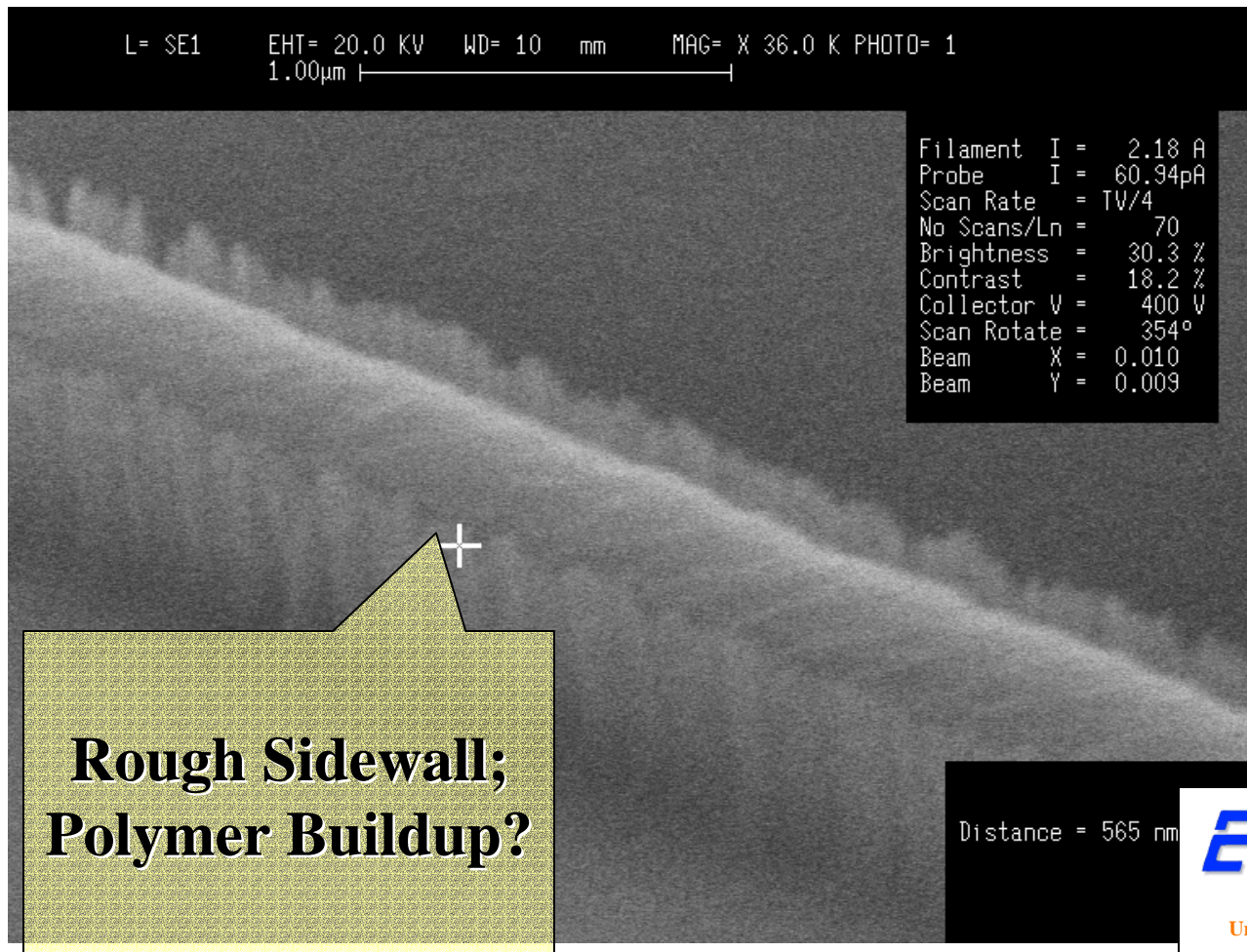
ECE·ILLINOIS

Electrical and Computer Engineering
University of Illinois at Urbana-Champaign

Advanced Processing and Circuits Group



SiO₂ Profile A, Etched Dec. 2001 with Identical CHF₃ etch conditions to Oct. 2001



- Baking: 5 min.
120°C, 2 min. 200°C,
hot plate

- CHF₃ RIE, 590 V,
60% CHF₃ flow, 60%
RF power, 35 mT, 17
min.

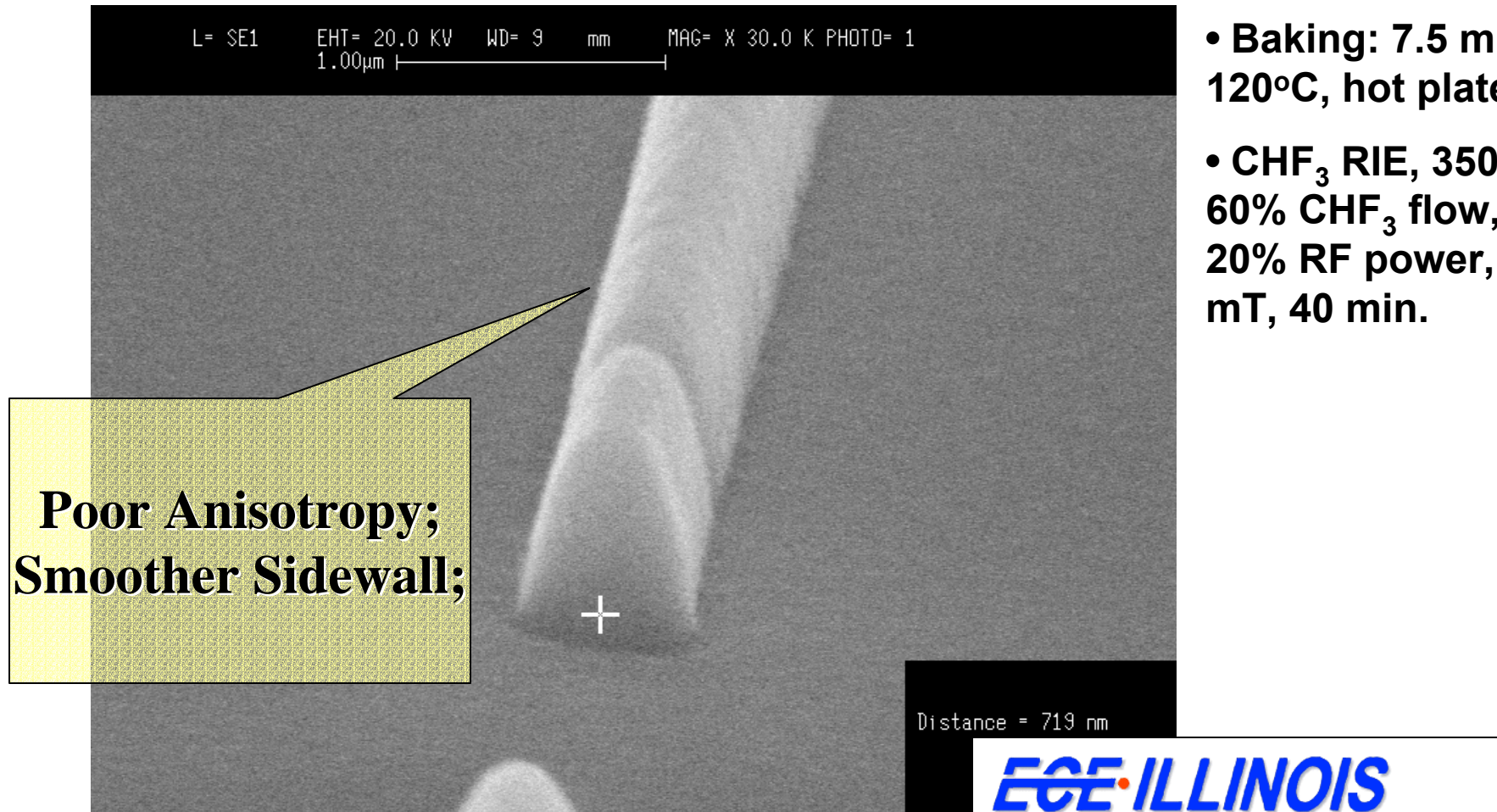
- Resist appears to
be sputtering during
etch.

ECE-ILLINOIS

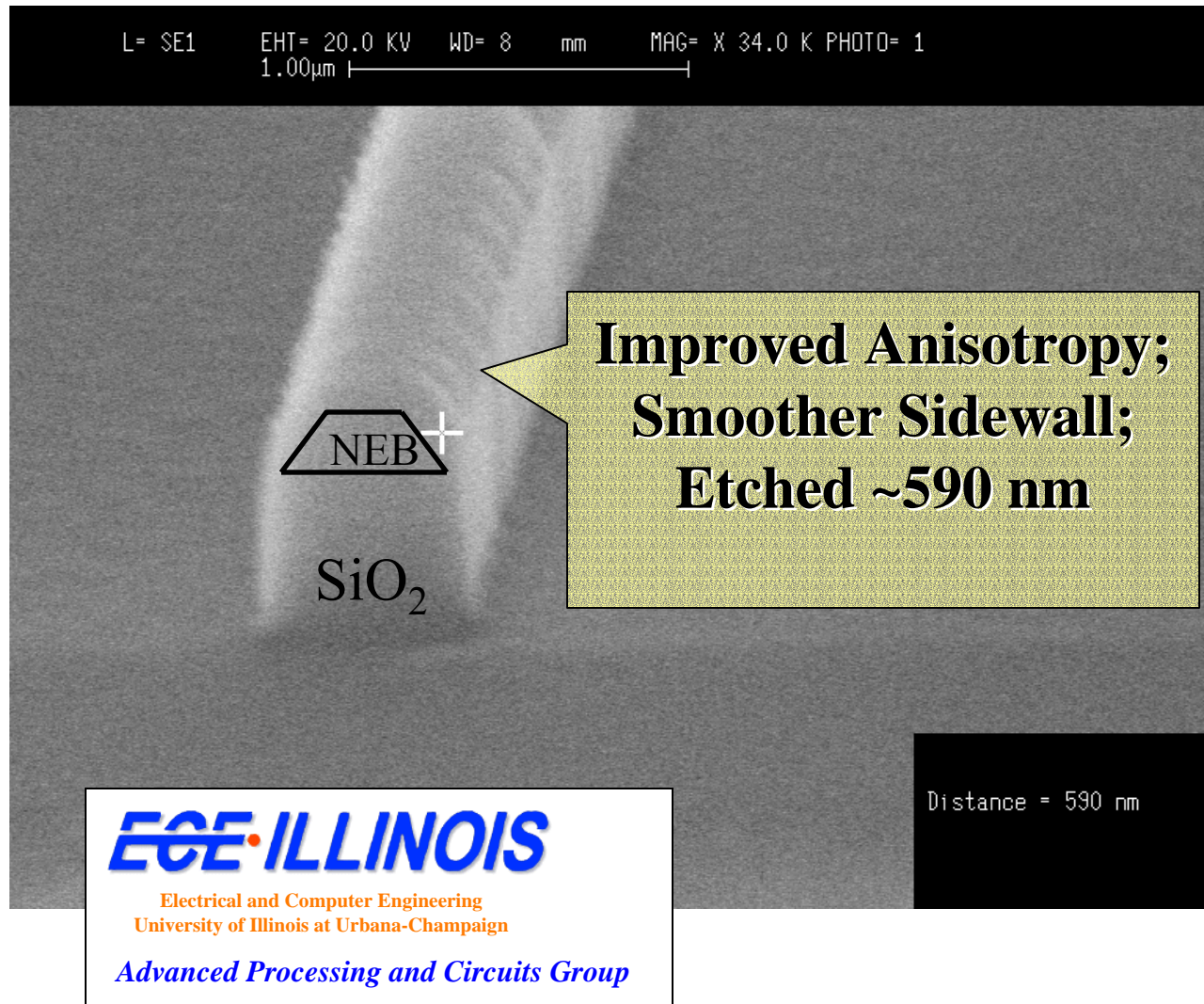
Electrical and Computer Engineering
University of Illinois at Urbana-Champaign

Advanced Processing and Circuits Group

NEB SiO₂ Profile B, Etched Dec. 2001



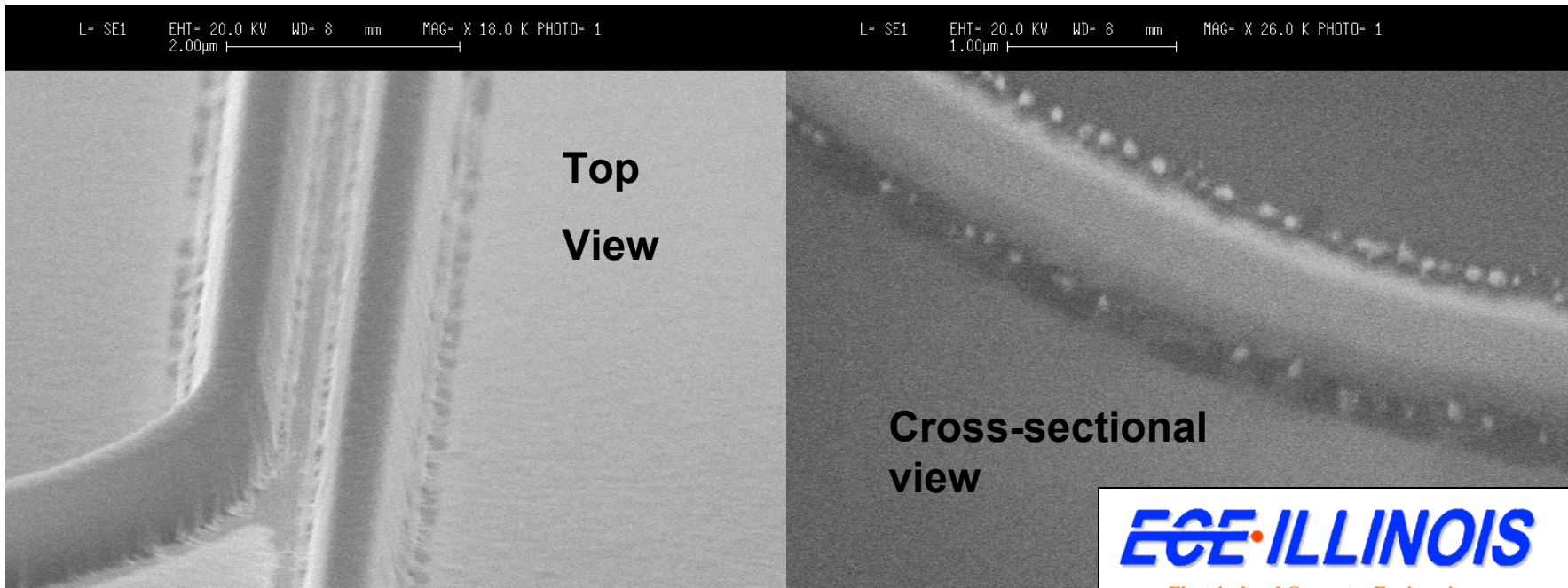
NEB SiO₂ Profile C, Etched Dec. 2001



- **Baking:** 10 min.
120°C, 10 min. 200°C,
hot plate
- CHF₃ RIE, 350 V,
60% CHF₃ flow, 20%
RF power, 35 mT, 40
min.
- Resist has begun to
taper.

Further etching will
deteriorate SiO₂
Profile/Smoothness

AZPN114 SiO₂ Profile D, Etched Feb. 2002, (Slightly Overetched)



ECE-ILLINOIS

Electrical and Computer Engineering
University of Illinois at Urbana-Champaign

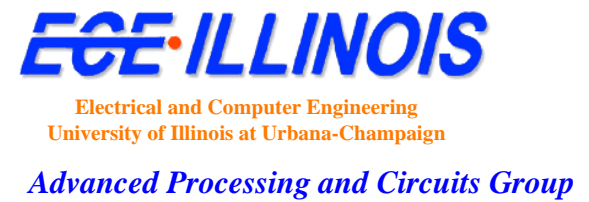
Advanced Processing and Circuits Group

- Baking: 5 min. 120°C, 2 min. 200°C, hot plate
- CHF₃ RIE, 350 V, 60% CHF₃ flow, 20% RF power, 35 mT, 70 min.
- Upper Sidewalls are very smooth; This almost worked!
- Resist residue has begun to buildup at the base=> roughness

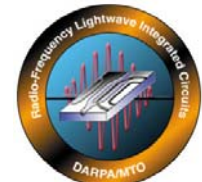
AZPN114 SiO₂ Profile E, Etched Feb. 2002



- Baking: 5 min. 120°C, 2 min. 200°C, hot plate
- CHF₃ RIE, 350 V, 60% CHF₃ flow, 20% RF power, 35 mT, 68 min.
- Upper Sidewalls are very smooth
- Little resist residue has begun to buildup at the base!
Roughness ~ e-beam exel spacing (25 nm)!



Alternate SiO_2 Etch Mask/ Direct Etch Mask Approaches



Ti/Pt/Au/Ni Direct Mask

Pros: Ni is strong etch mask; Etch mask serves dual purpose as electrical contact.

Cons: Grain size of Ni may result in striations; Liftoff with PMMA challenging due to reflow

NiCr-> SiO_2 Intermediate Etch Mask

Pros: NiCr has small grain size => smoothness; Profile will be consistently smoother than using e-beam resist (less sputtering)

Cons: NiCr is difficult to evaporate; Heating during evaporation leads to severe reflowing of PMMA impeding liftoff.

ECE·ILLINOIS

Electrical and Computer Engineering
University of Illinois at Urbana-Champaign

Advanced Processing and Circuits Group

Etching Design Rules



Gap Spacing (mm) Gap Etch Depth (mm) Bulk Depth (mm) Mask Thickness (nm)

0.25	3	5	>500 nm
0.3	3	>3.5	~500 nm
0.35	3	3.25	400 nm
0.4	3	3.8	350 nm

- Pushing the gap spacing below 0.3 mm makes the demands on the etch mask substantially more stringent
- Pushing the etch depth beyond 4 mm makes the demands on the etch mask substantially more stringent
- One possible compromise is to not strip e-beam resist prior to ICP etching; incorporate as part of the etch mask design.

ECE-ILLINOIS

Electrical and Computer Engineering
University of Illinois at Urbana-Champaign

Advanced Processing and Circuits Group

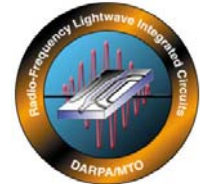
Conclusions

- A $\text{Cl}_2/\text{Ar}/\text{H}_2$ etch chemistry is required to etch anisotropic, submicron features deeper than 2 microns.
- Switching etch mask material from Si_3N_4 to SiO_2 has permitted us to etch substantially deeper without significant mask erosion.
- The choice of e-beam resist, baking conditions, and SiO_2 pattern transfer technique THE most critical design components to minimize sidewall roughness.
- Improved process control is expected by gradually writing all of the patterns on the new JEOL e-beam. The Cambridge tool will remain as a reserve.

Coupled QW Modulators

H. Mohseni

Outline



- 1- The Need**
- 2- Existing Technology**
- 3- Limitations of the Existing Technology**
- 4- Coupled Quantum Wells**
- 5- Modeling**
- 6- Results**

The Need

- Important parameters of an electrorefractive material are:

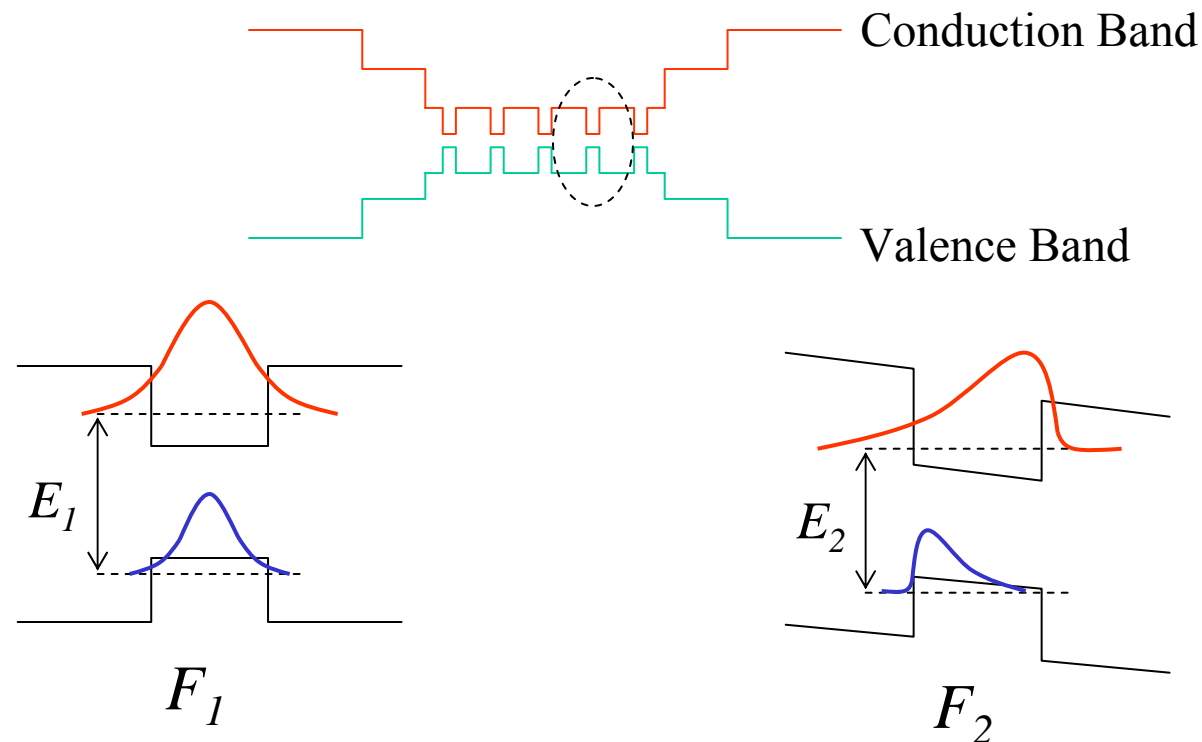
- 1- Sensitivity $\rho = \Delta n / \Delta E$
- 2- Optical absorption α

- Similar to any electrorefractive modulator, a high sensitivity is desirable since the operating voltage is inversely proportional to the sensitivity: $V_{\pi} \sim 1/\rho$

- However, REM requires a considerably low optical absorption due to the stringent loss requirements

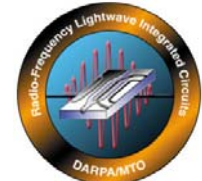
Existing Technology

- Existing technology is based on quantum confined Stark effect (QCSE) in multiple quantum wells (MQW)



$$F_2 > F_1 \Rightarrow E_2 < E_1$$

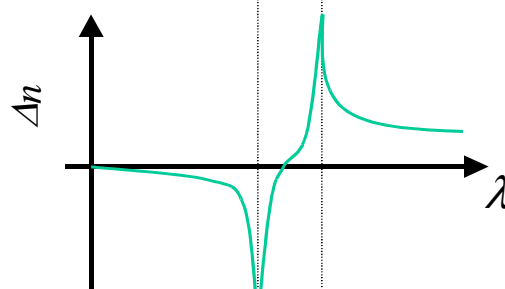
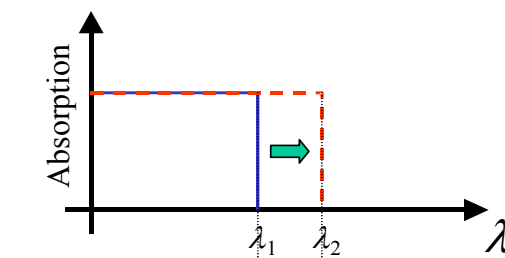
Kramers-Kronig Relation, Limitations of Existing Technology



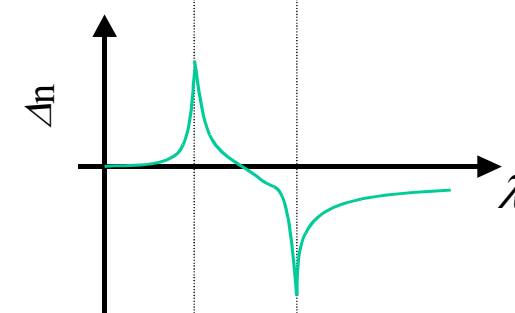
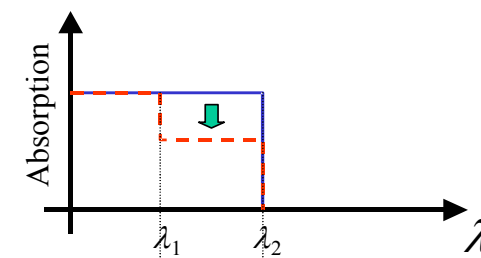
- Kramers-Kronig relation connects the change of absorption to the change of index:

$$\Delta n(\lambda) = \frac{\lambda^2}{2\pi^2} \int \frac{\Delta \alpha(\lambda')}{\lambda^2 - \lambda'^2} d\lambda'$$

- Two important cases are:



Case I

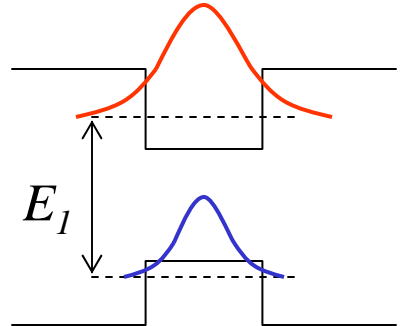


Case II

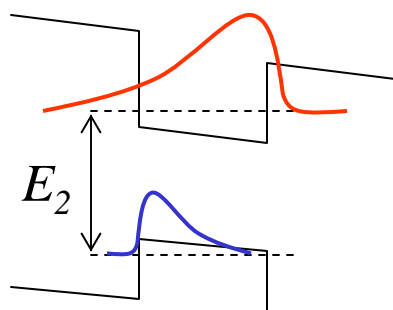
Kramers-Kronig Relation, Limitations of Existing Technology (cont'd)



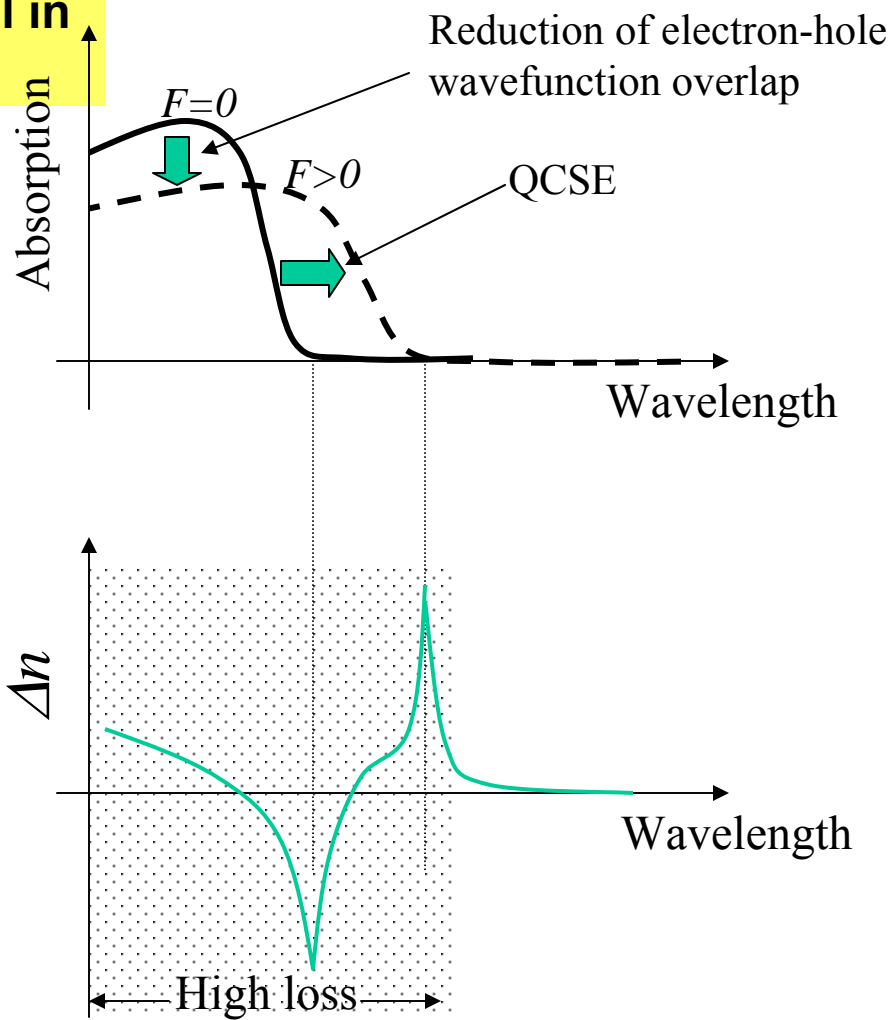
- MQW shows a mixture of case I and case II, and hence Δn is small in the low loss wavelenghts



$F=0$

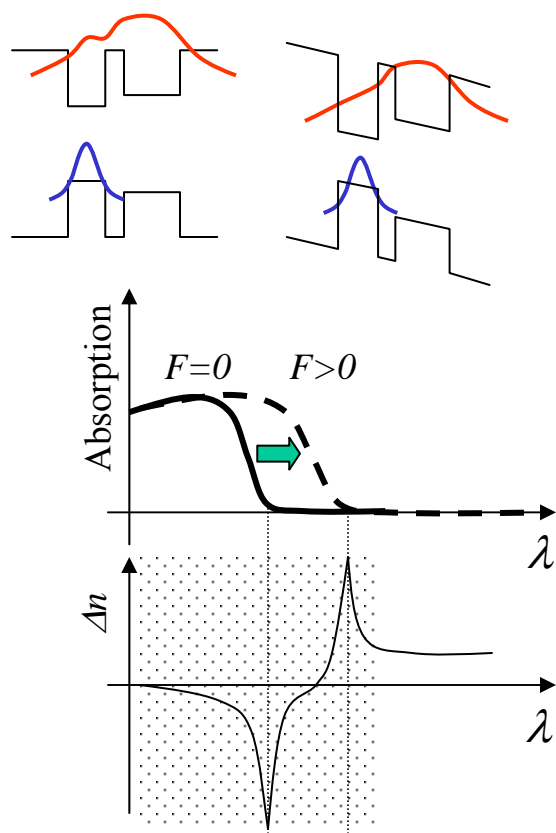


$F>0$

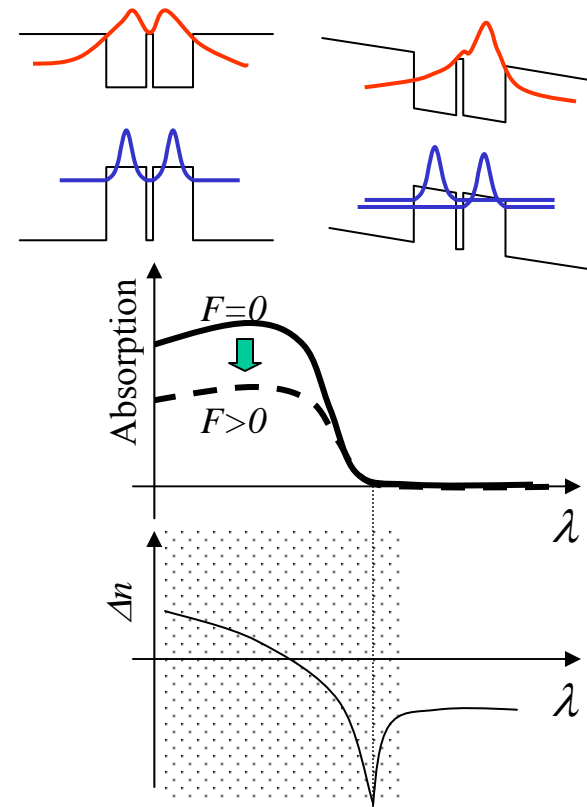


Coupled Quantum Wells

- Added degrees of freedom in the coupled quantum wells makes it possible to design structures which are close to either case I or case II. Therefore, high Δn can be achieved even far from the absorption edge.



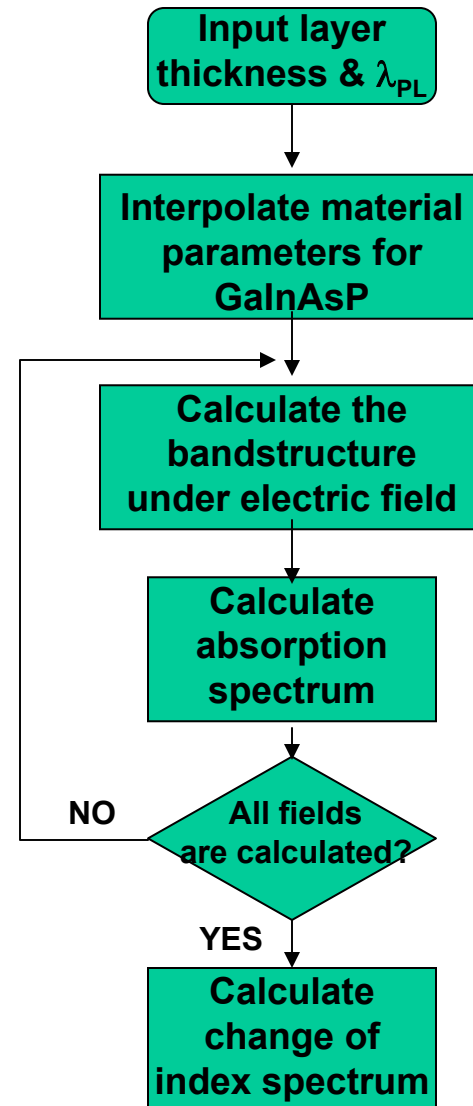
Similar to case I



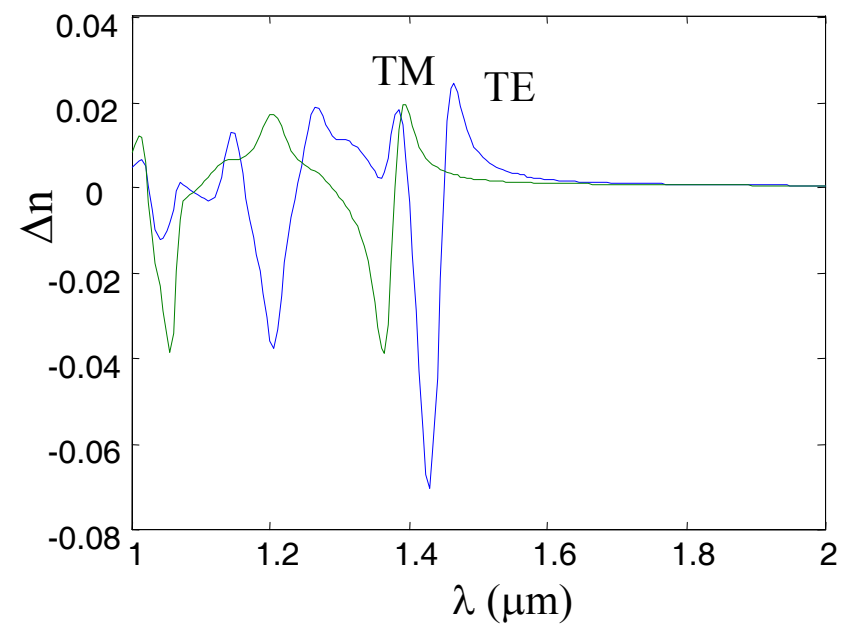
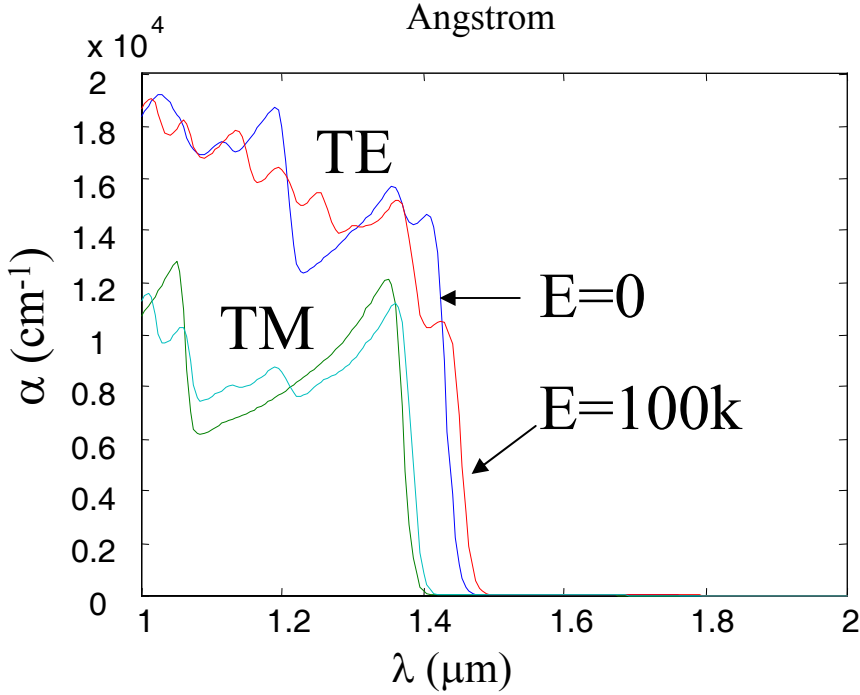
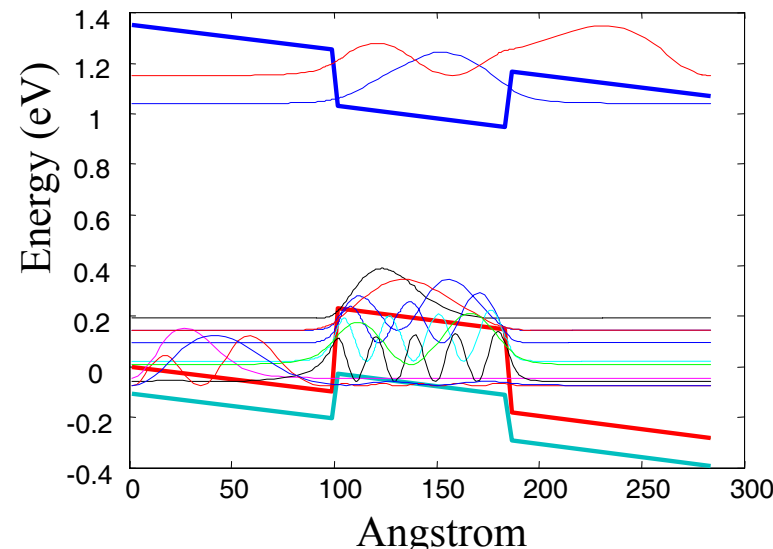
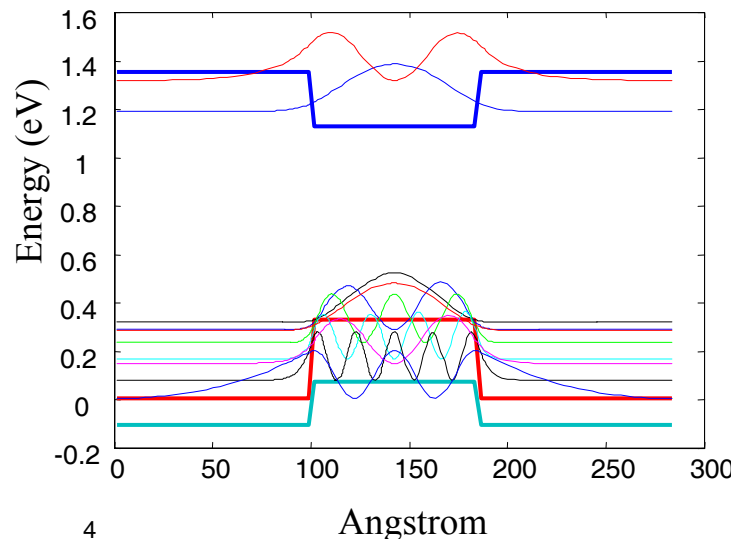
Similar to case II

Modeling

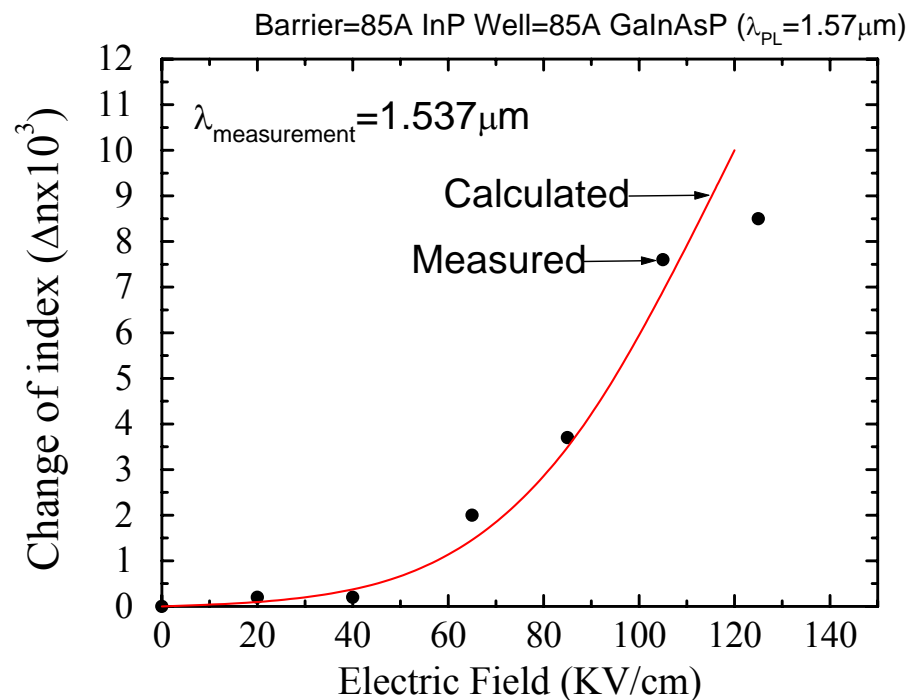
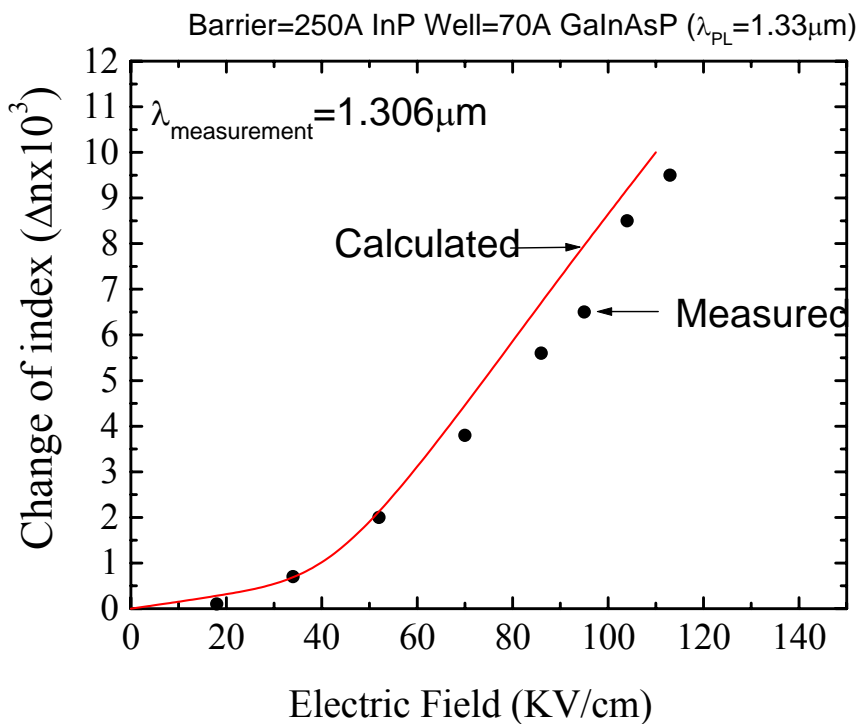
- Material parameters calculated using interpolation with bowing effects.
- Eigenvalues and eigenfunctions of electron, light-hole, heavy-hole, and spin-orbit calculated based on a 4x4 k.p model
- Optical absorption spectrum calculated for the bulk and quantum wells, considering excitonic effects.
- Kramers-Kronig relation used to calculate the change of index spectrum



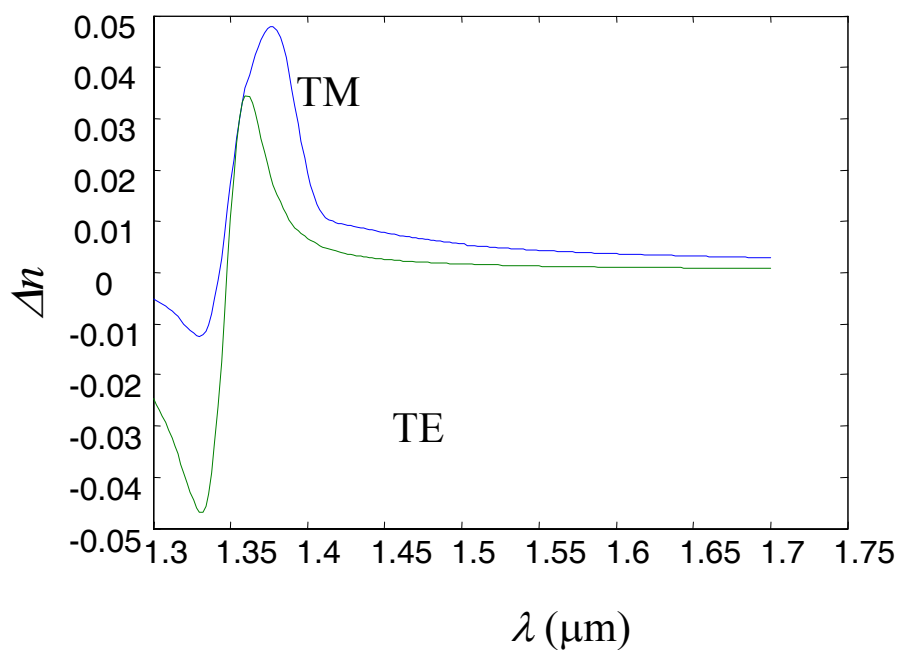
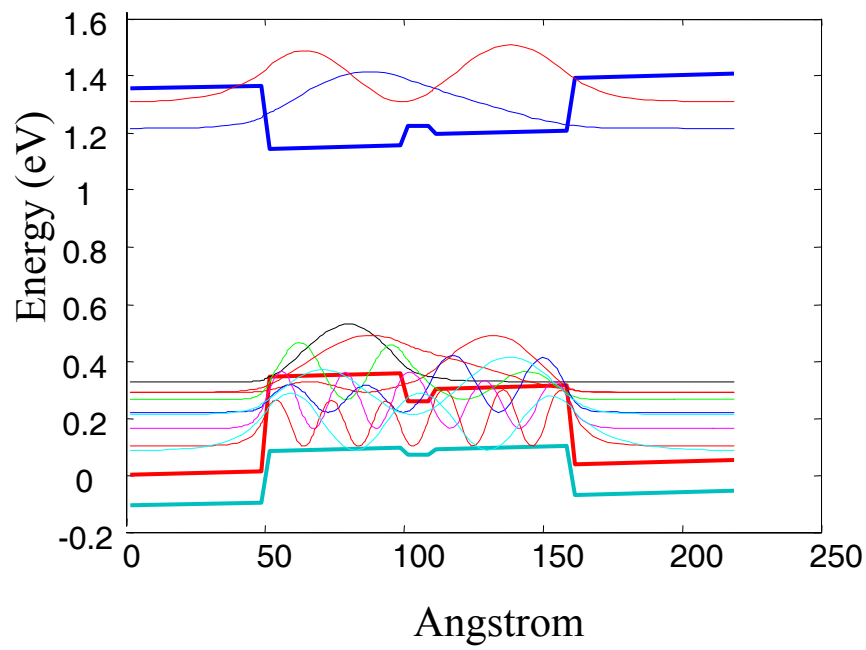
Simulation Results for a Single Quantum Well



Comparison with the Experimental Results at $\lambda \sim 1.3\mu\text{m}$ and $\text{I} \sim 1.5\mu\text{m}$

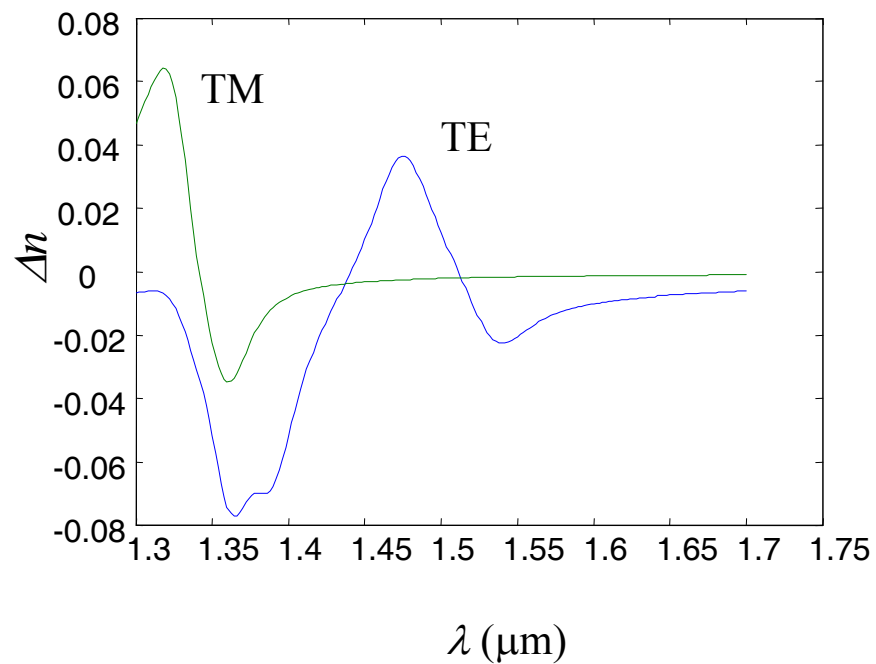
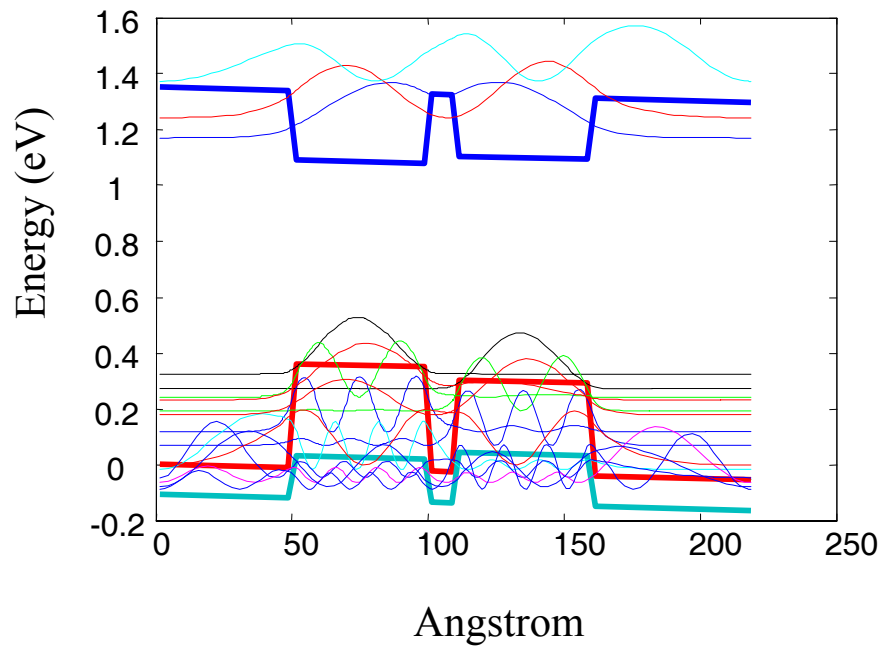


Optimized Asymmetric Coupled QW (Case I)



- 2.3 times more sensitive than the conventional MQW design for a similar loss of 1cm^{-1}

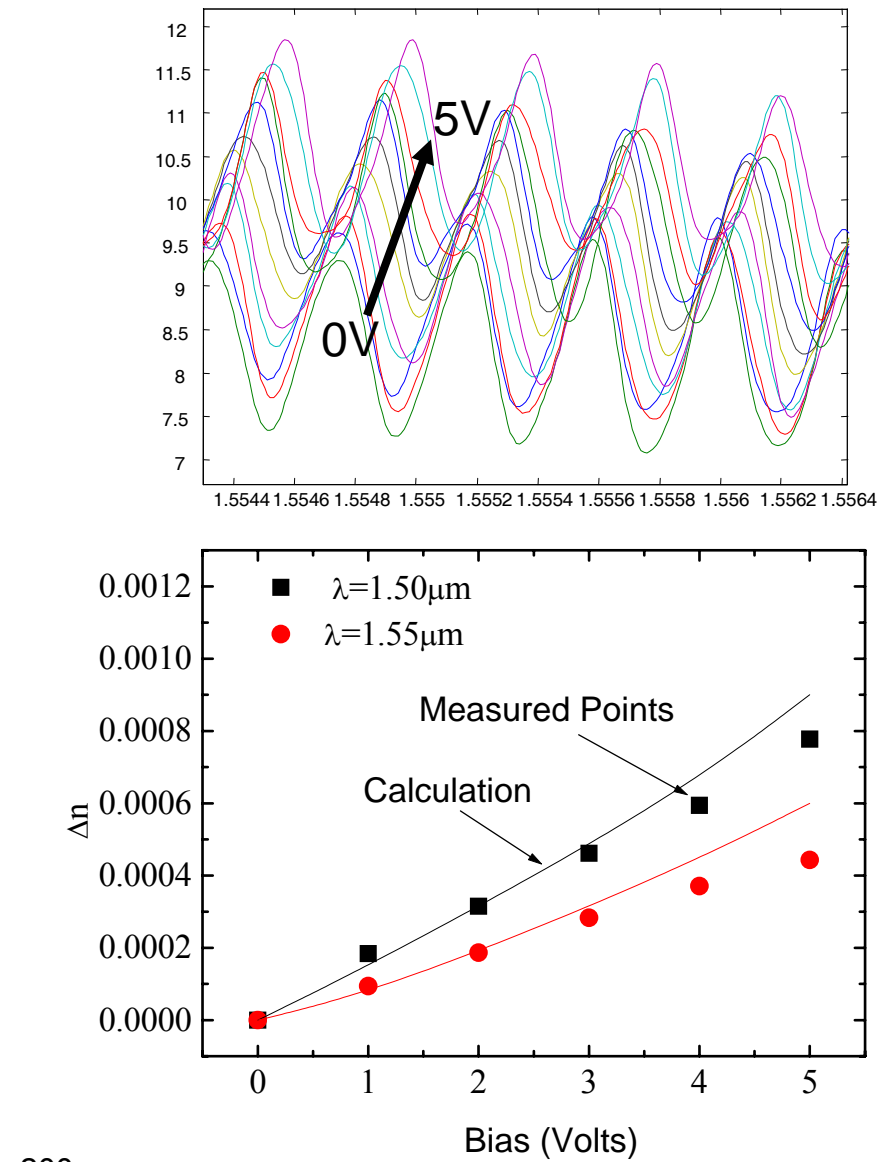
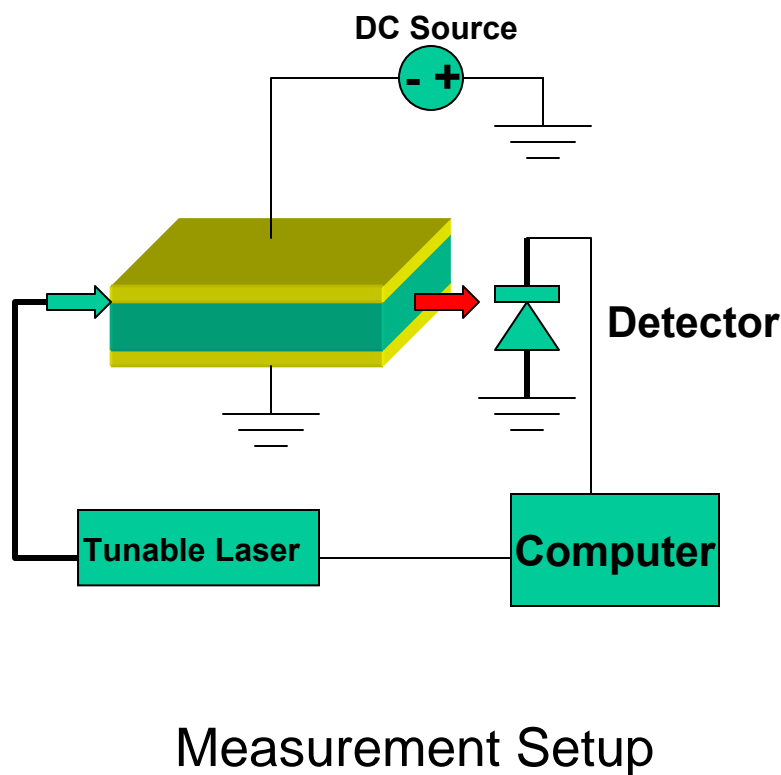
Optimized Asymmetric Coupled QW (Case II)



- 3.3 times more sensitive than the conventional MQW design for a similar loss of 1cm^{-1}

Slab Waveguide Measurements

Experiment vs. Theory



Q & A, followed by Tour & Lunch

J. Abeles

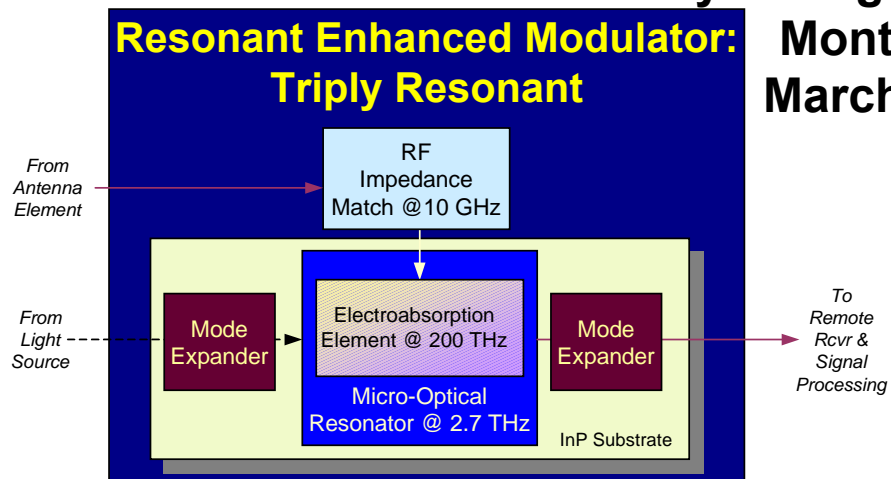
Resonant Enhanced Modulator Development

A. Lepore, M. Kwakernaak, H. Mohseni, D. Bechtle, J.H. Abeles
Sarnoff Corporation, Princeton NJ

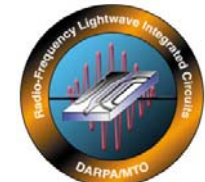
I. Adesida, S. Rommel
University of Illinois, Urbana-Champaign

GOMAC: DARPA RFLICS I

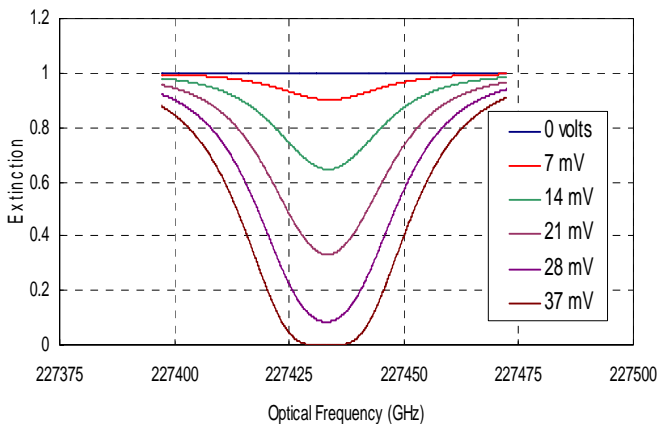
Hyatt Regency Monterey
Monterey, CA
March 11, 2002



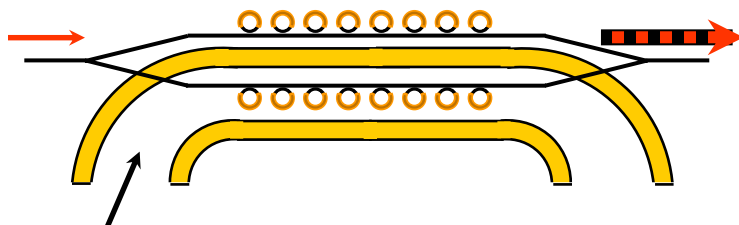
Resonant Enhanced Modulator Concept



- **Push-Pull Config'n**
- **$37 \text{ mV} = V_p$**
- **10 GHz Operation**



- Microresonators do not enhance sensitivity
 - Commensurate decrease in bandwidth.
- Ganging multiple resonators,
 - Lower capacitance per resonator
 - Compared to traveling wave design
- Ganging demands electrorefractive modulation
 - Avoids narrowing modulation bandwidth
- Traveling wave structure is created
 - Correct phase at each microresonator



Need:
 $\sim 1 \text{ cm}^{-1}$ losses

DARPA-Requested Status 2-20-02



1. Most significant accomplishments

- **World record low-loss waveguides**
- **Characterization of group delays in rings**
- **Design of high-coupling REM**
- **Demonstration of MMI coupler**
- **Electrically modulated structure**

2. Most recent experimental data (prototype hardware) or when will the first prototype will be tested:

- **September 2002**

3. What is the plan to meet the program objectives in the final half of the program with hardware fabrication schedules.

- *not presented at GOMAC*

4. Upcoming challenges.

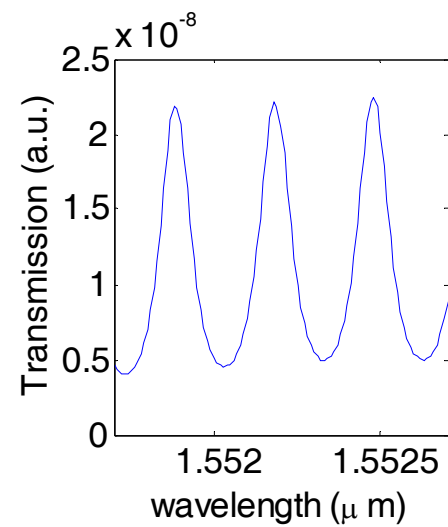
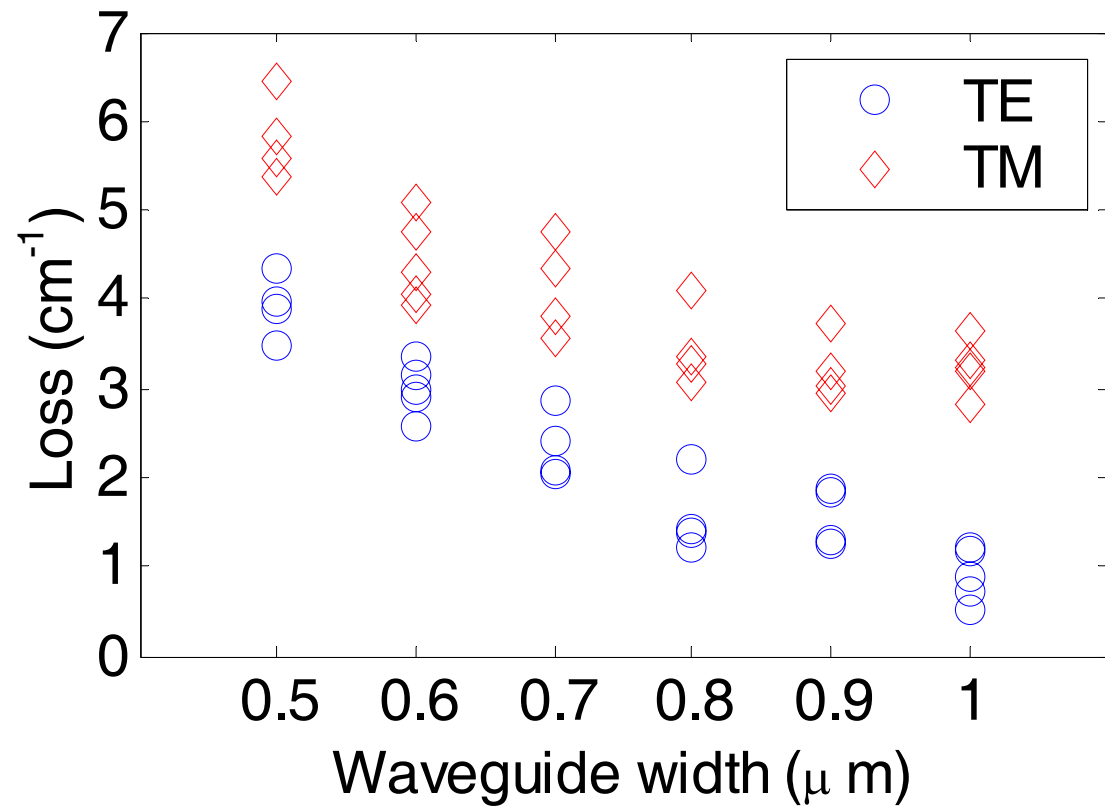
- **Waveguide loss of 1 cm⁻¹ (April '02)**
- **Low loss rings (April '02)**

5. Financial status

- *not presented at GOMAC*

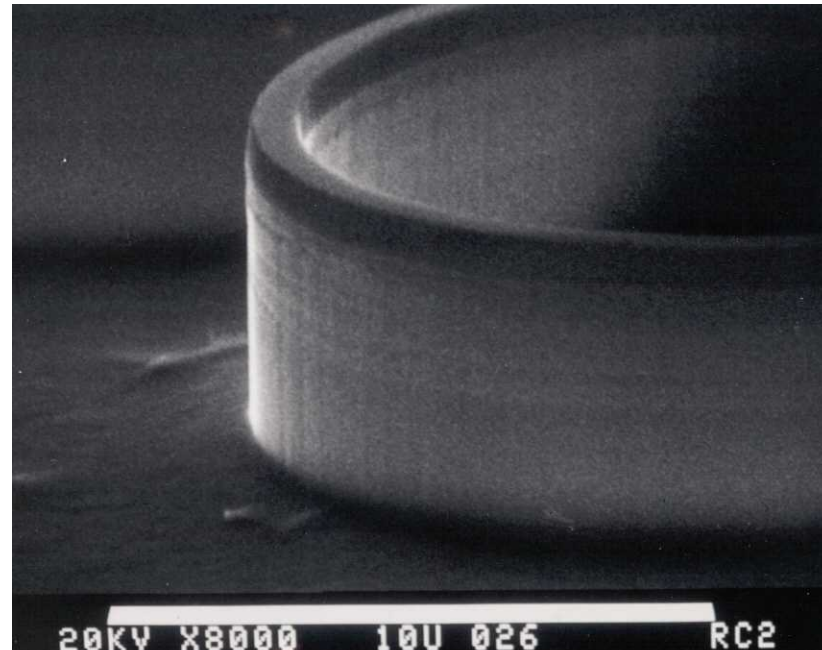
Goal: 100 mV modulator

World Record Low Loss Waveguides



4 cm^{-1} for 0.5 μm width x 4 μm depth waveguide!

Low-Loss Deeply-Etched Waveguide



REM Fabrication Activities (7-31-01 Review)

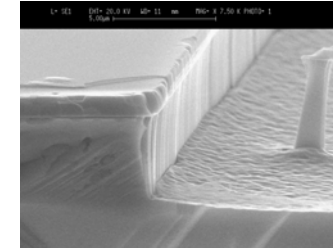
Fabrication:

June, 2000

Program Start

ICP Characterization

Leica/Cambridge e-beam initial use



October, 2000

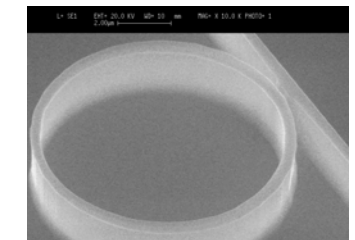
Ring nanostructures reported by UIUC

Resist development

Etching condition studies

Leica/Cambridge e-beam dosage studies

Etching of coupling region



February, 2000

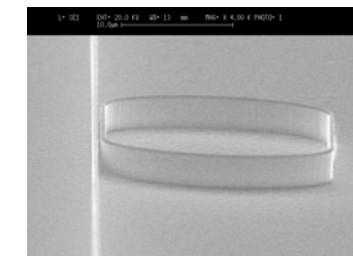
Sample microrings delivered to Sarnoff

Resist quality development (cont'd)

Pattern interchange (Sarnoff-UIUC)

Sample handling

Stitching issues



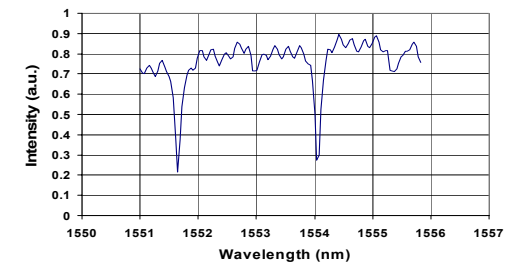
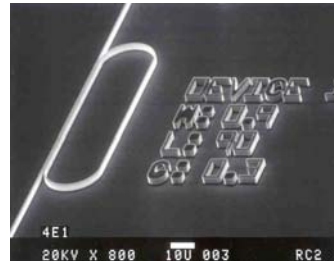
May, 2000

Routine characterization of microrings structures at Sarnoff

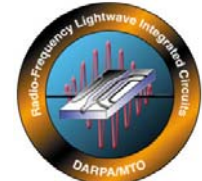
Resist development (cont'd)

Switch to new JEOL e-beam tool

Switch to larger rings for diagnostics



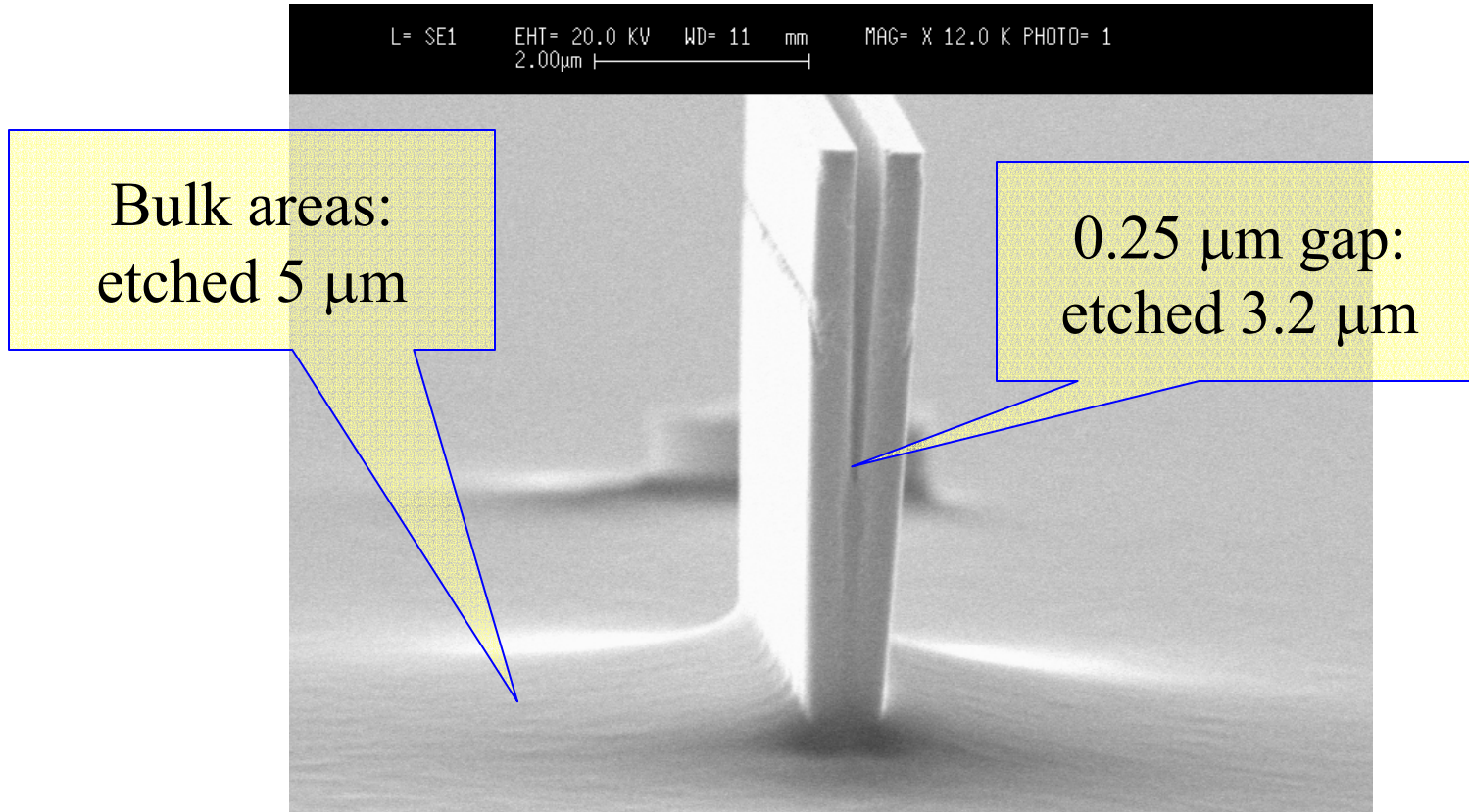
Key Technical Accomplishments



- **Demonstrated world record low-loss waveguides using improved process**
- **Demonstrated metal mask patterns w/ 100kV positive-tone resist**
- **Demonstrated MMI-coupled rings**
- **Developed understanding of coupler design space and phase issues**
- **Configured testbed for phase measurement (group delay)**
- **Established and verified modeling software for layer structure design**
- **Electron-beam lithography: established redundant patterning capability, increased throughput, reduced stitch impact***
- **Established high-resolution imaging (500k magnification)***
- **Substantial increase of processing throughput and yield**

* Army Research Laboratory, Sensors and Electronic Devices Directorate

Aspect Ratio Dependence of the Etch: Isolation in the Gap

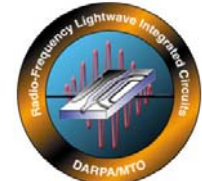


ECE • ILLINOIS

Electrical and Computer Engineering
University of Illinois at Urbana-Champaign

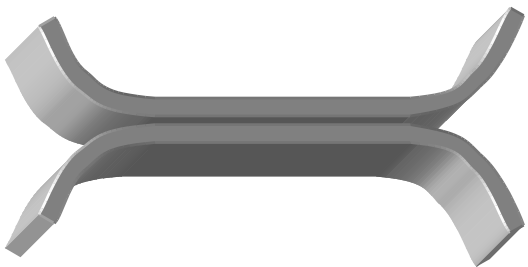
Advanced Processing and Circuits Group

MMI vs. Air Gap Couplers



Air gap coupled waveguides

- Requires extremely narrow gap ($0.3\text{-}0.4\mu\text{m}$).
- Depends critically on gap width.
- Arbitrary coupling ratios.
- Size scales with coupling ratio; high coupling is difficult if small devices are required.
- Excess loss at waveguide-coupler transitions.
- Multiple rings electrically isolated

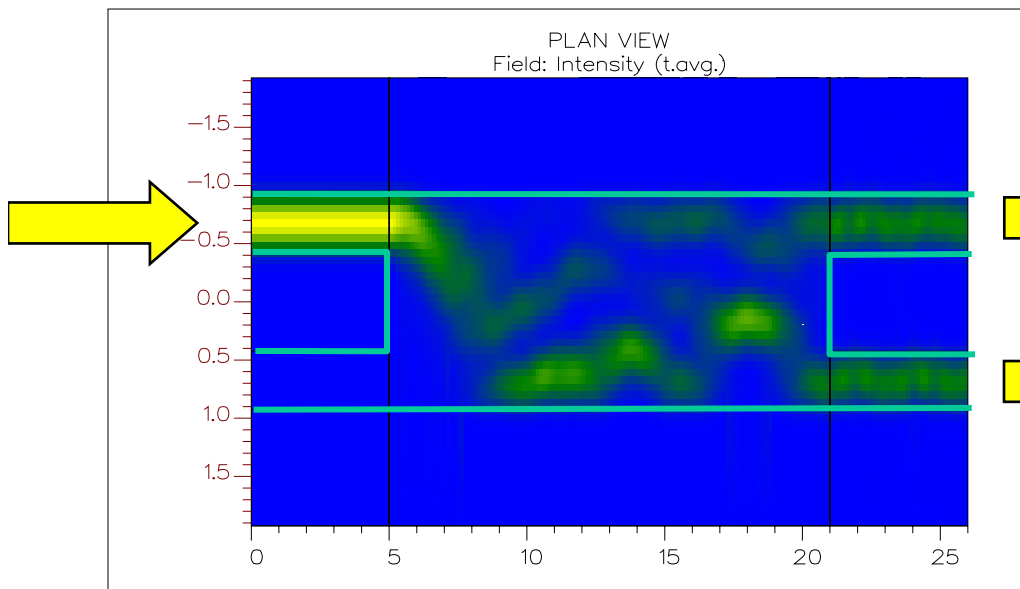


Multi-mode interference couplers

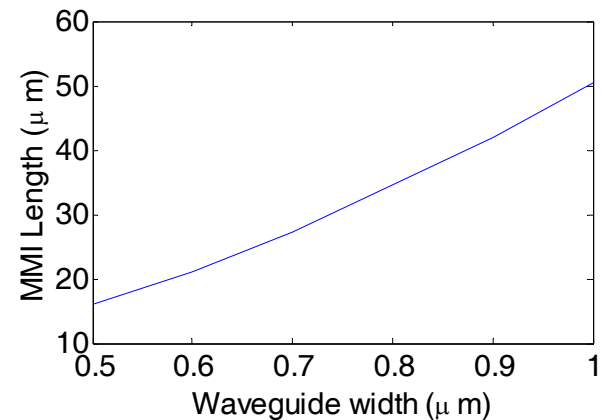
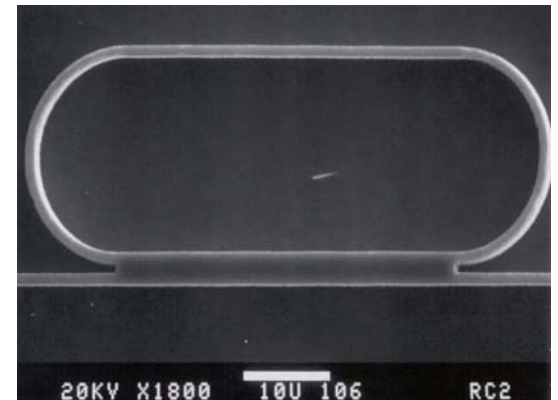
- No small features.
- Tolerant to fabrication.
- 50:50 coupling, other ratios are difficult.
- Minimum size is limited.
- Excess loss due to modal mismatch of MMI region and waveguides.
- Multiple rings electrically connected



2x2 Multimode Interference (MMI) Coupler



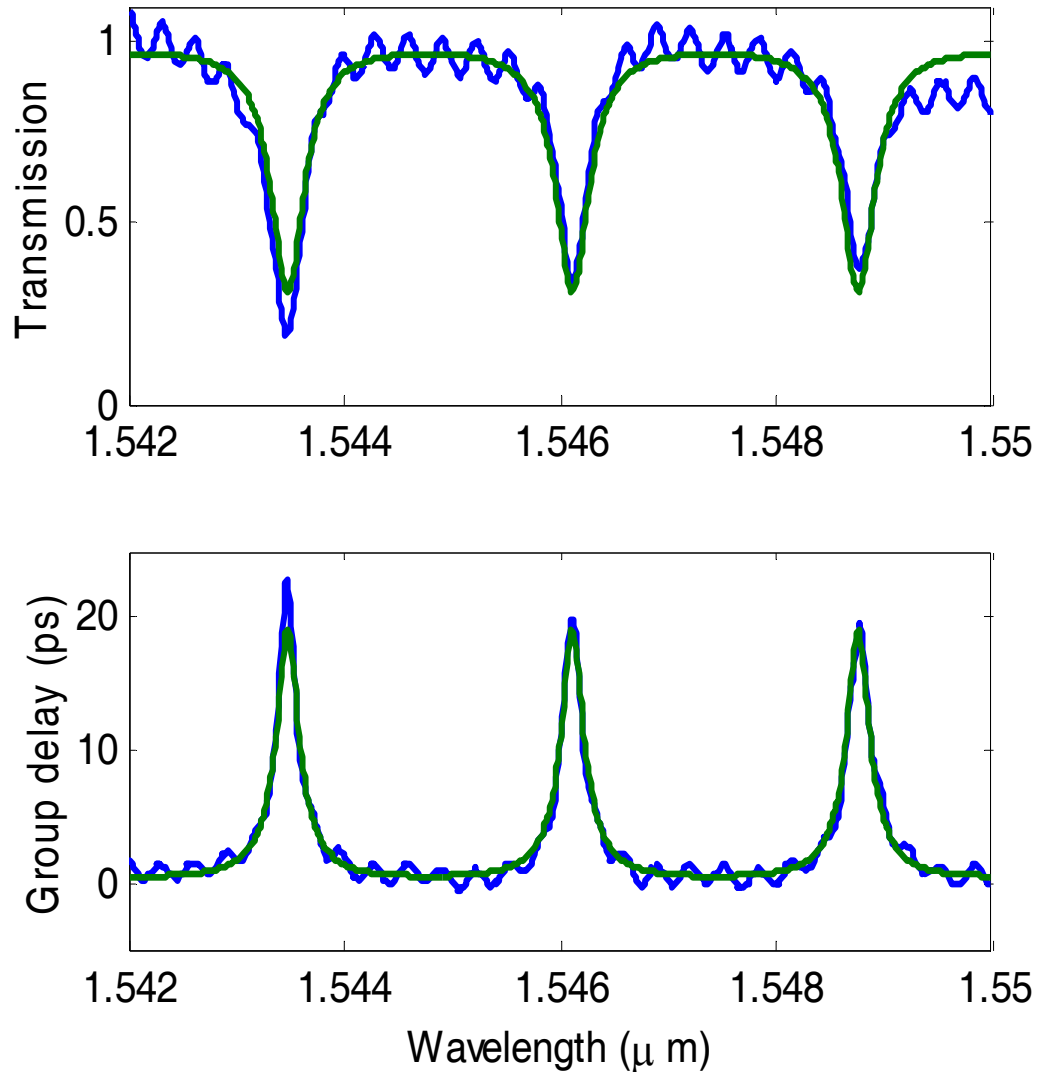
50%
:
50%



**Minimum coupler length: $\sim 16 \mu\text{m}$
for $0.5 \mu\text{m}$ wide waveguides.**

--> compact solution if 50% coupling is required.

MMI Coupled Ring Resonator



Waveguide width: $0.9\mu\text{m}$.

Circumference: $250\mu\text{m}$.

MMI length: $42\mu\text{m}$.

Loss: 17% ($\rightarrow 7\text{cm}^{-1}$).

Coupling: 50%.

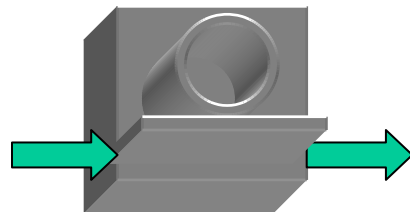
20ps group delay.

\rightarrow 6 roundtrips.

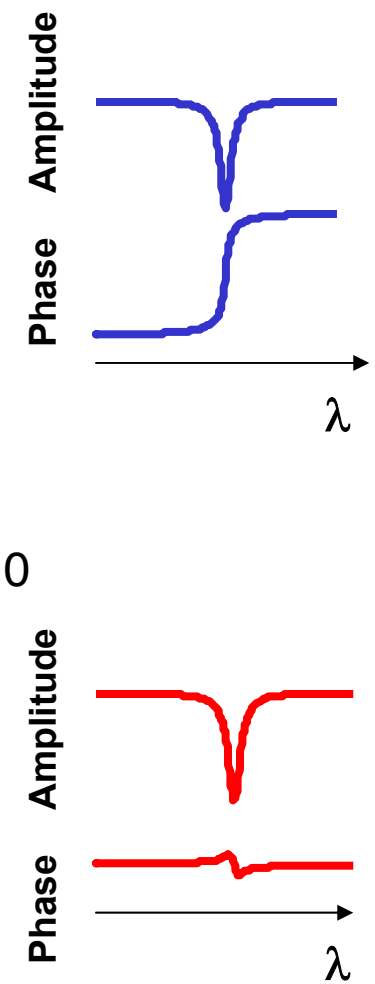
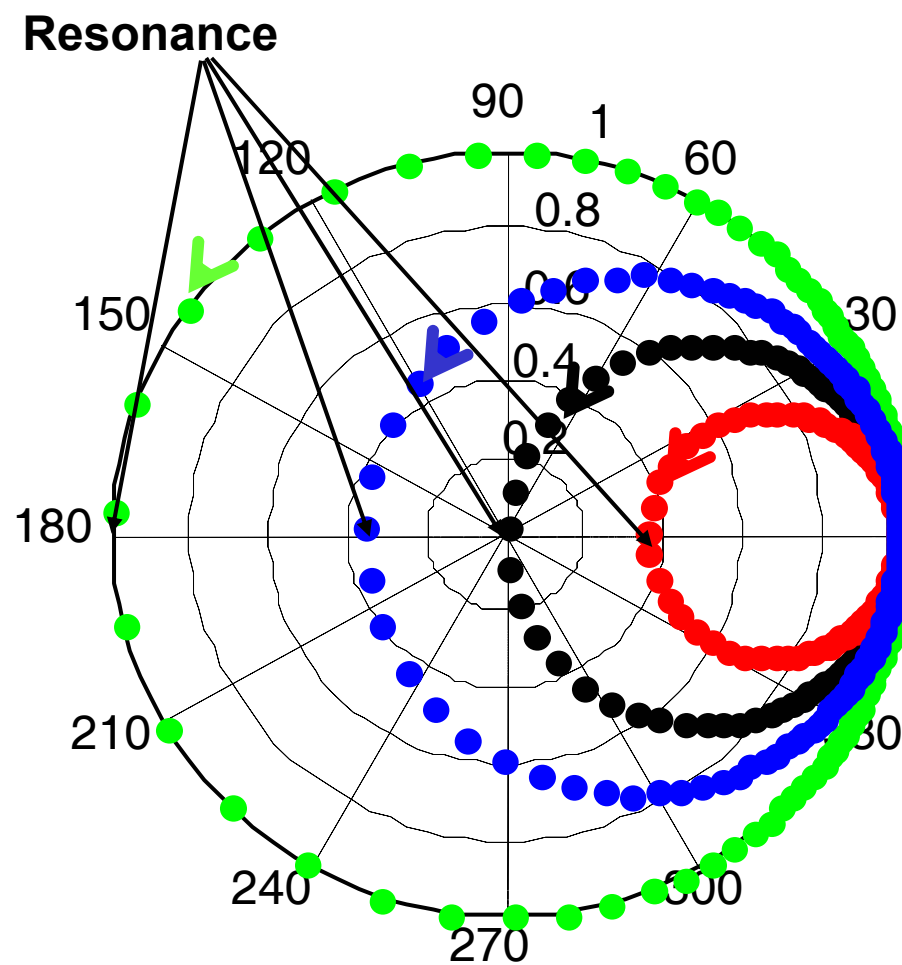
Optical bandwidth: 44 GHz.

(\rightarrow 22 GHz modulator bandwidth) .

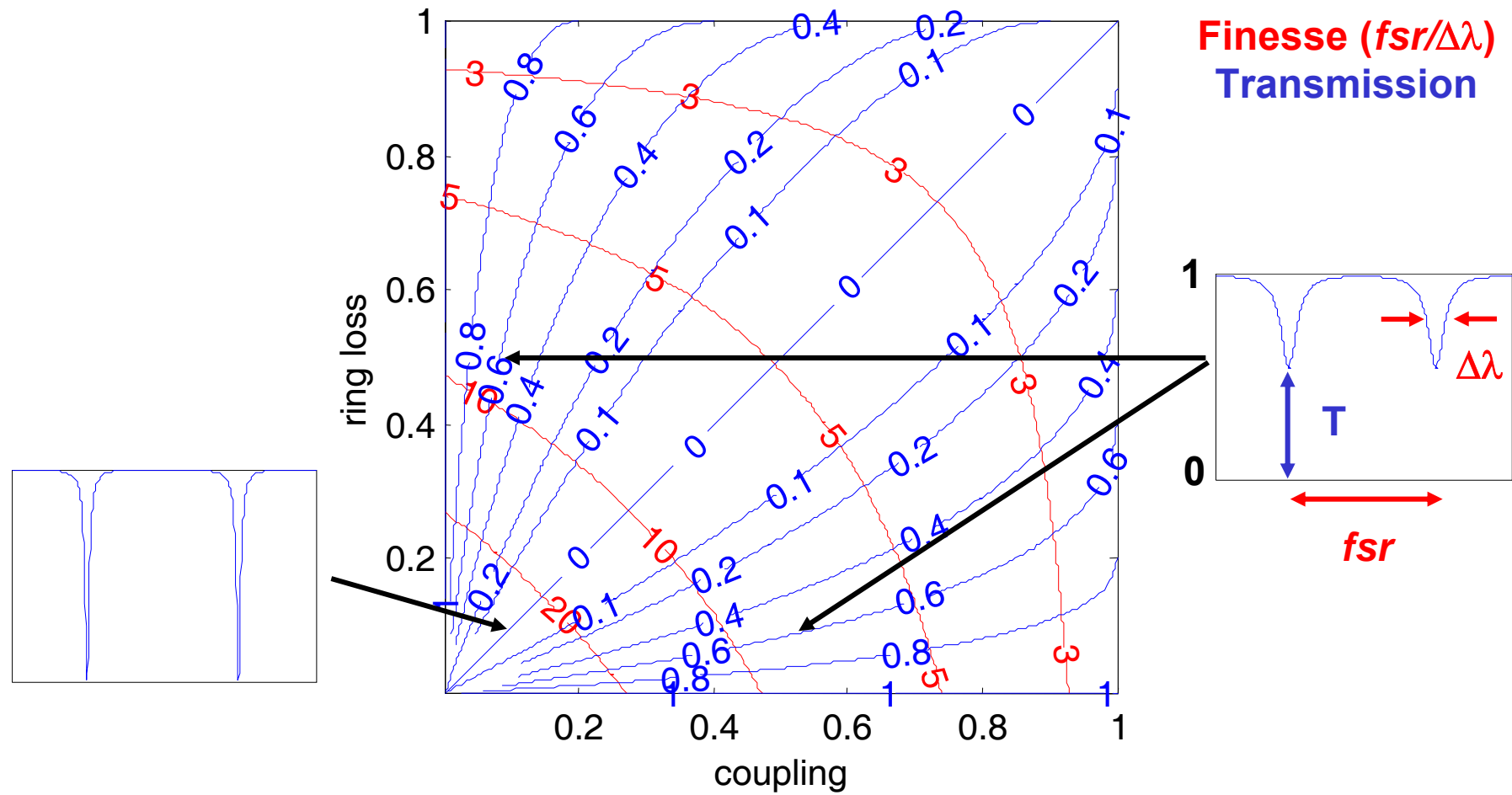
Ring Transmission, Complex Space



- No Loss
- Coupling > Loss
- Coupling = Loss
- Coupling < Loss



Phase Diagram



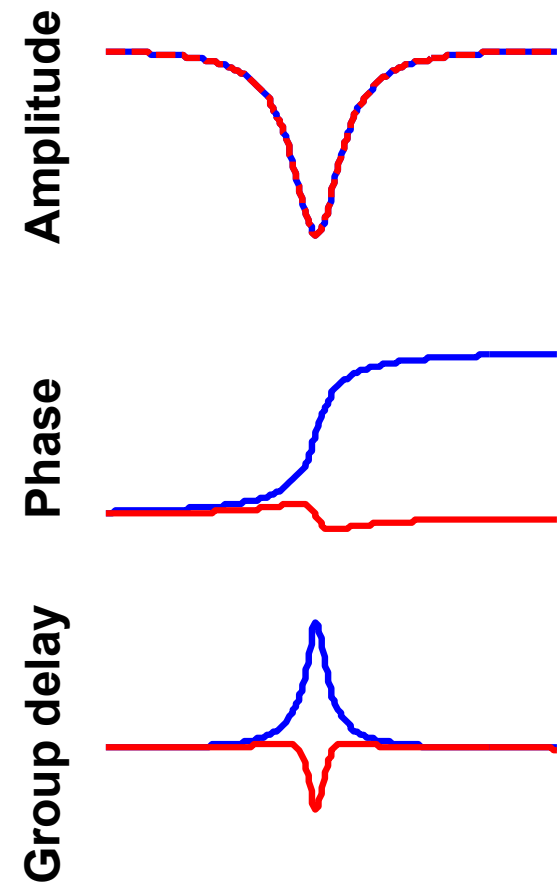
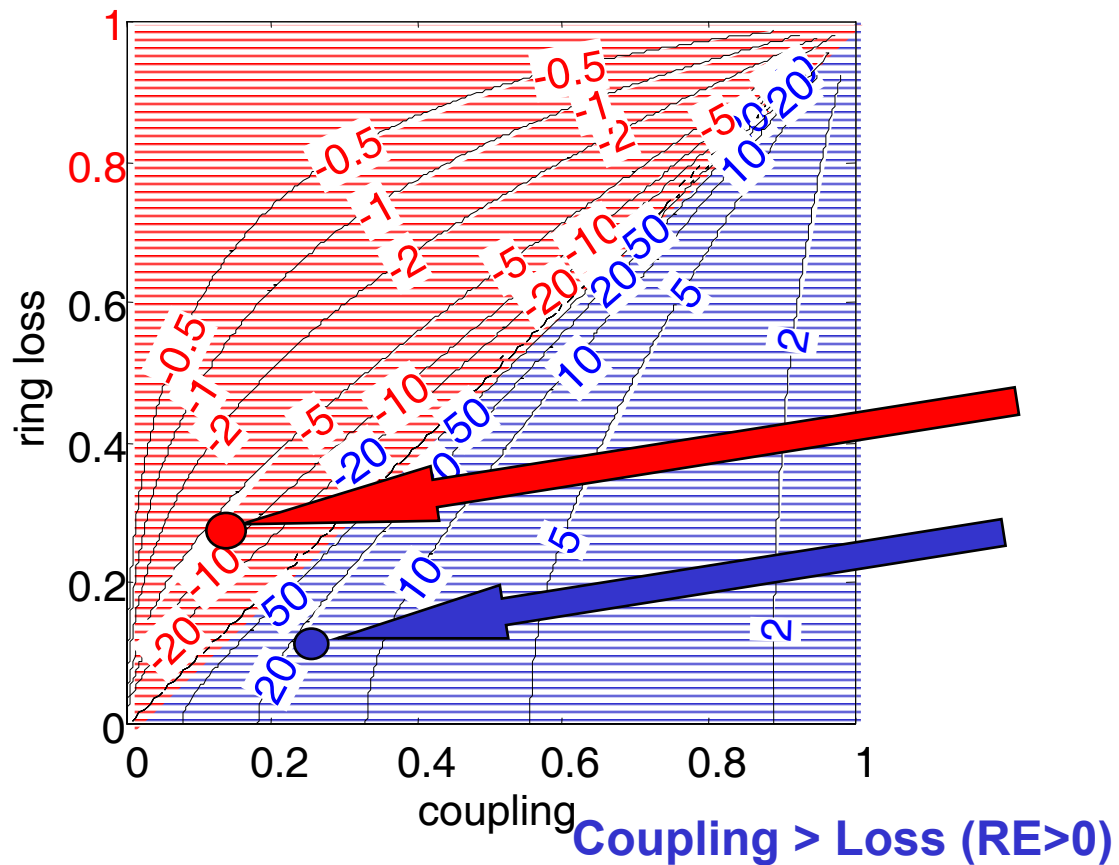
Ring Enhancement



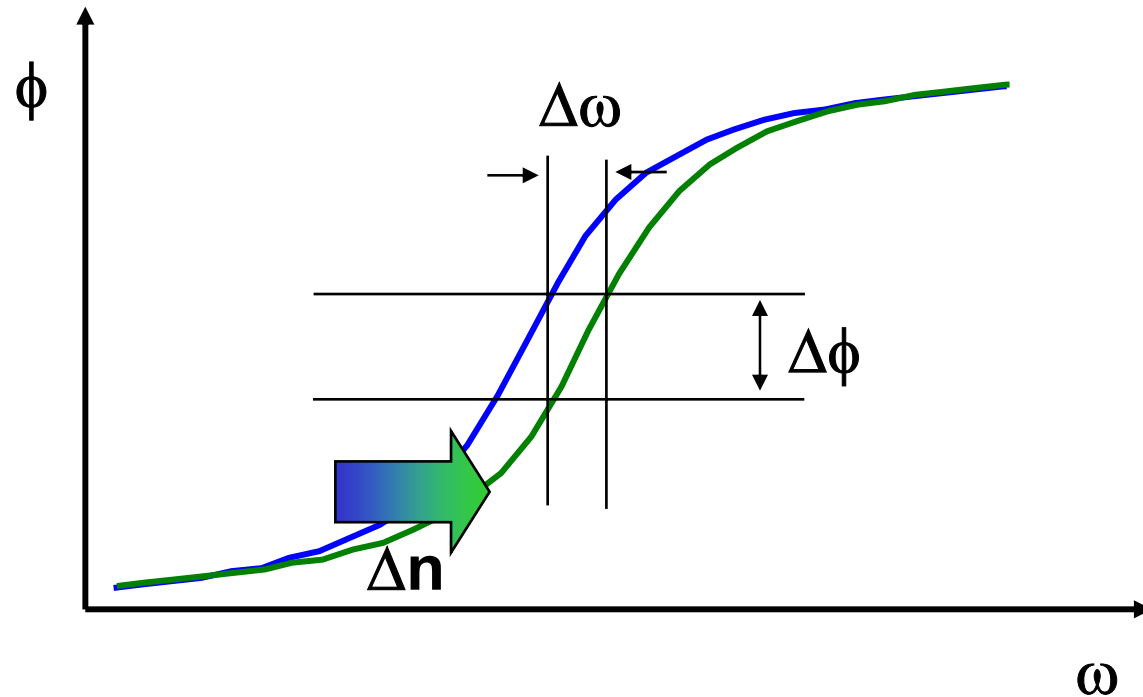
Ring enhancement =

Phase sensitivity of the ring.
Phase sensitivity of straight waveguide
of equal length.

Coupling < Loss (RE<0)

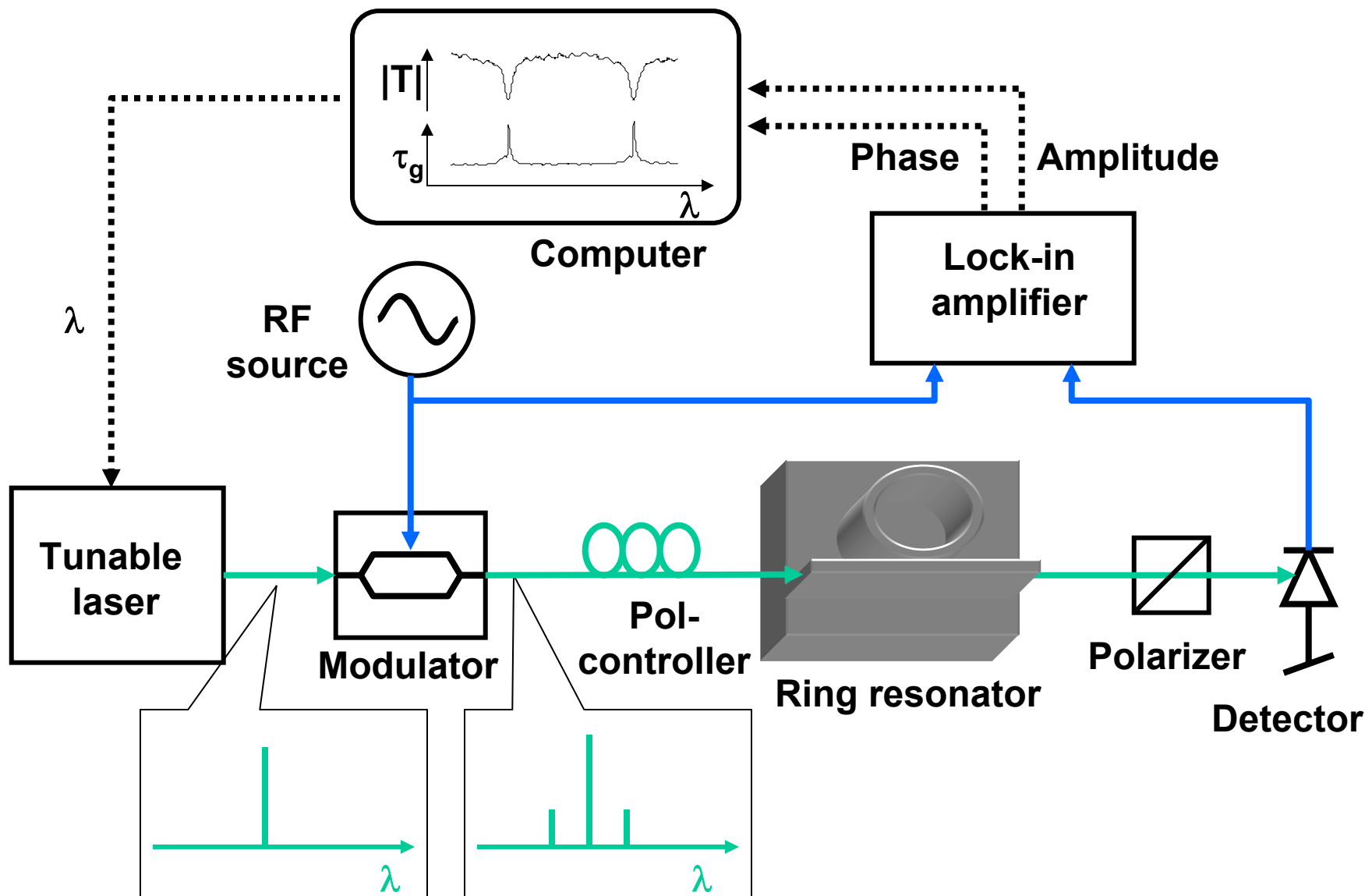


Group Delay Determines V_π



$$\phi = \frac{n\omega l}{c} \longrightarrow \frac{\partial \phi}{\partial n} = \frac{\partial \phi}{\partial \omega} \frac{\omega}{n} = \tau_g \frac{\omega}{n}.$$

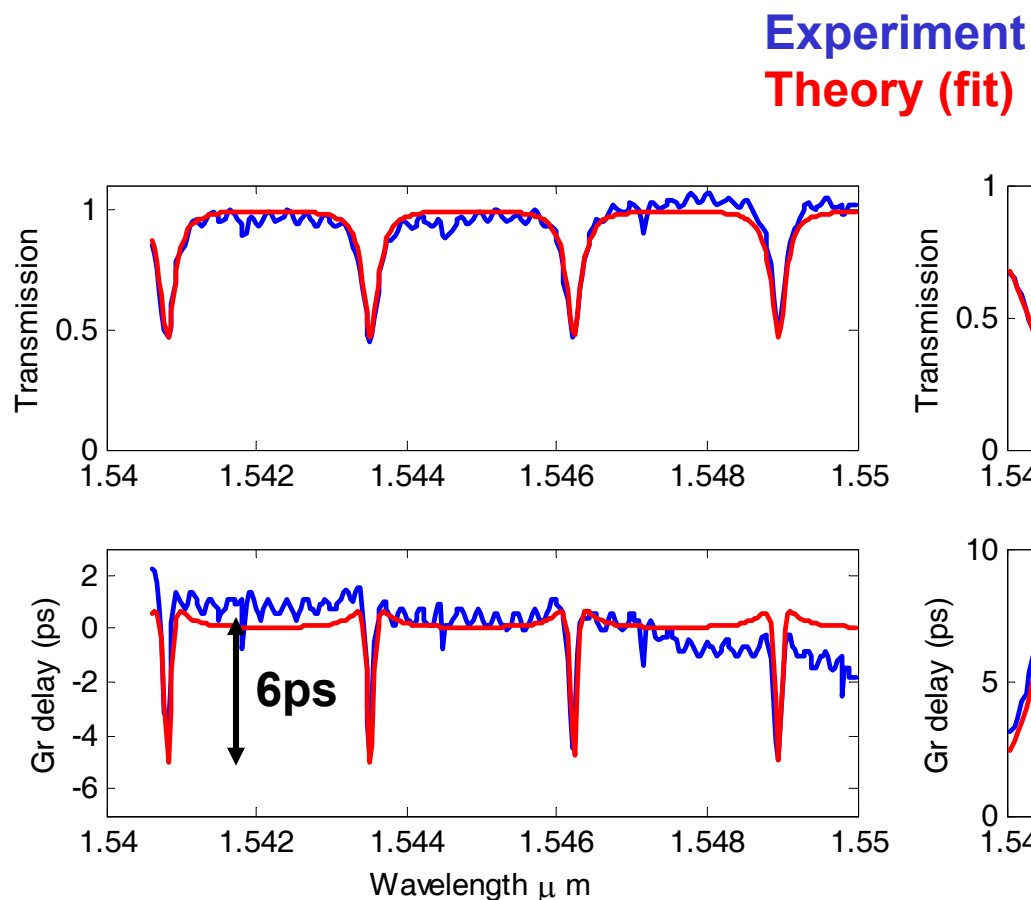
Experimental Setup



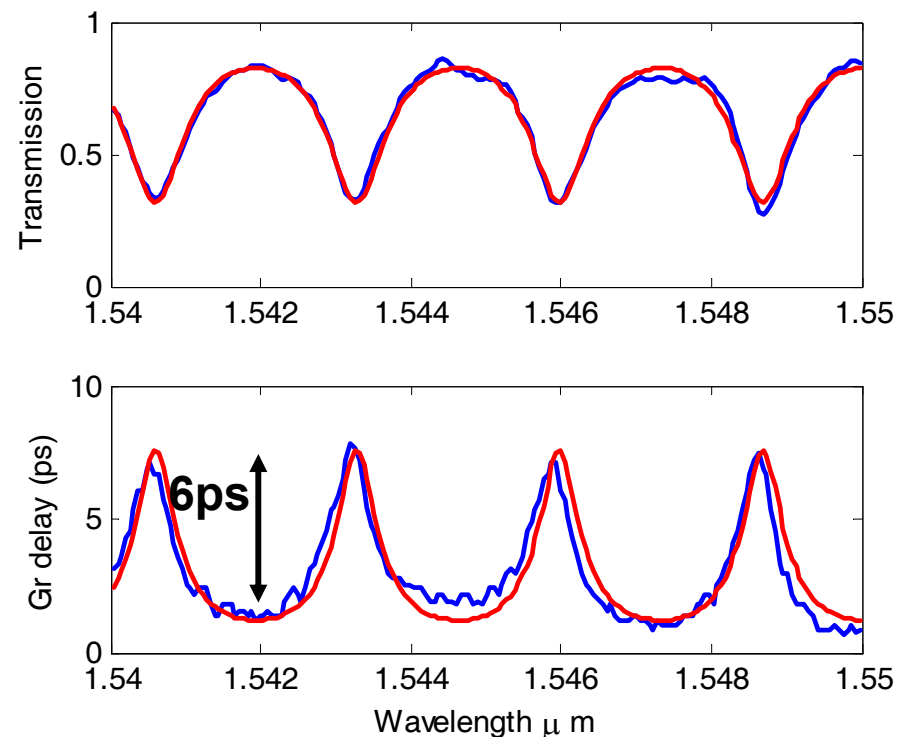
Examples



Coupling < Loss

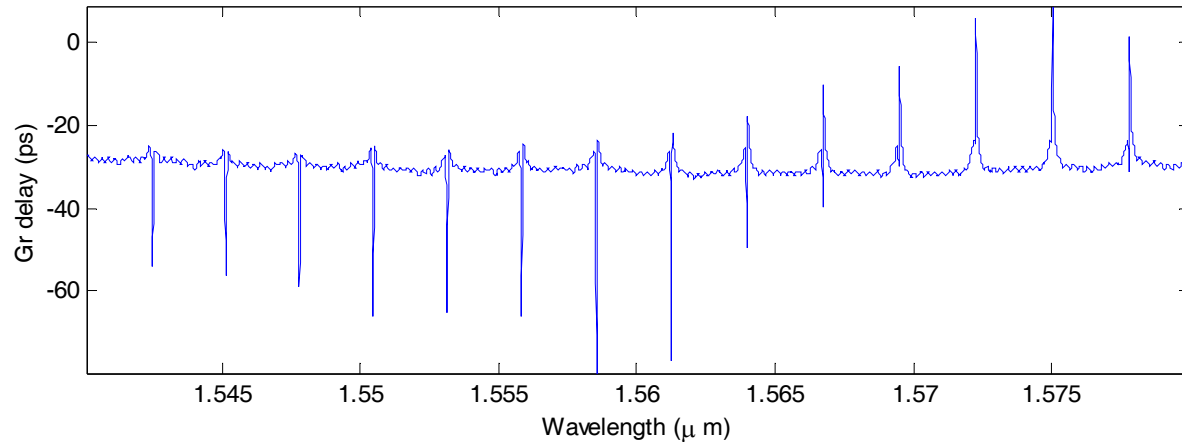
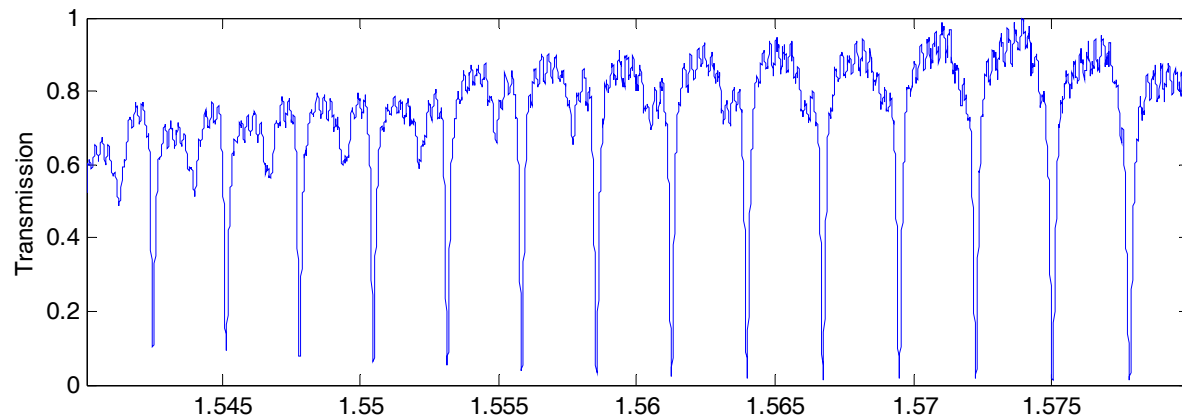


Coupling > Loss



Both Cases in One Sample

Coupling \approx Loss



Sources of Loss



- **Straight waveguides**
 - **Material loss**
 - minimize modal overlap with p-doped region.
 - trade-off between electro-optic coefficient and loss.
 - 0.16 cm^{-1} have been demonstrated.
 - **Scattering loss.**
- **Bent waveguides**
 - **Bends enhance scattering loss.**
 - **Leakage**
 - minimized by deep etching.
- **Junctions**
 - **Mode mismatch.**
- **Coupler excess loss**
- **Multi-mode behavior**
 - **coupling into other modes = loss.**

Approaches to Smoothing Sidewall Roughness



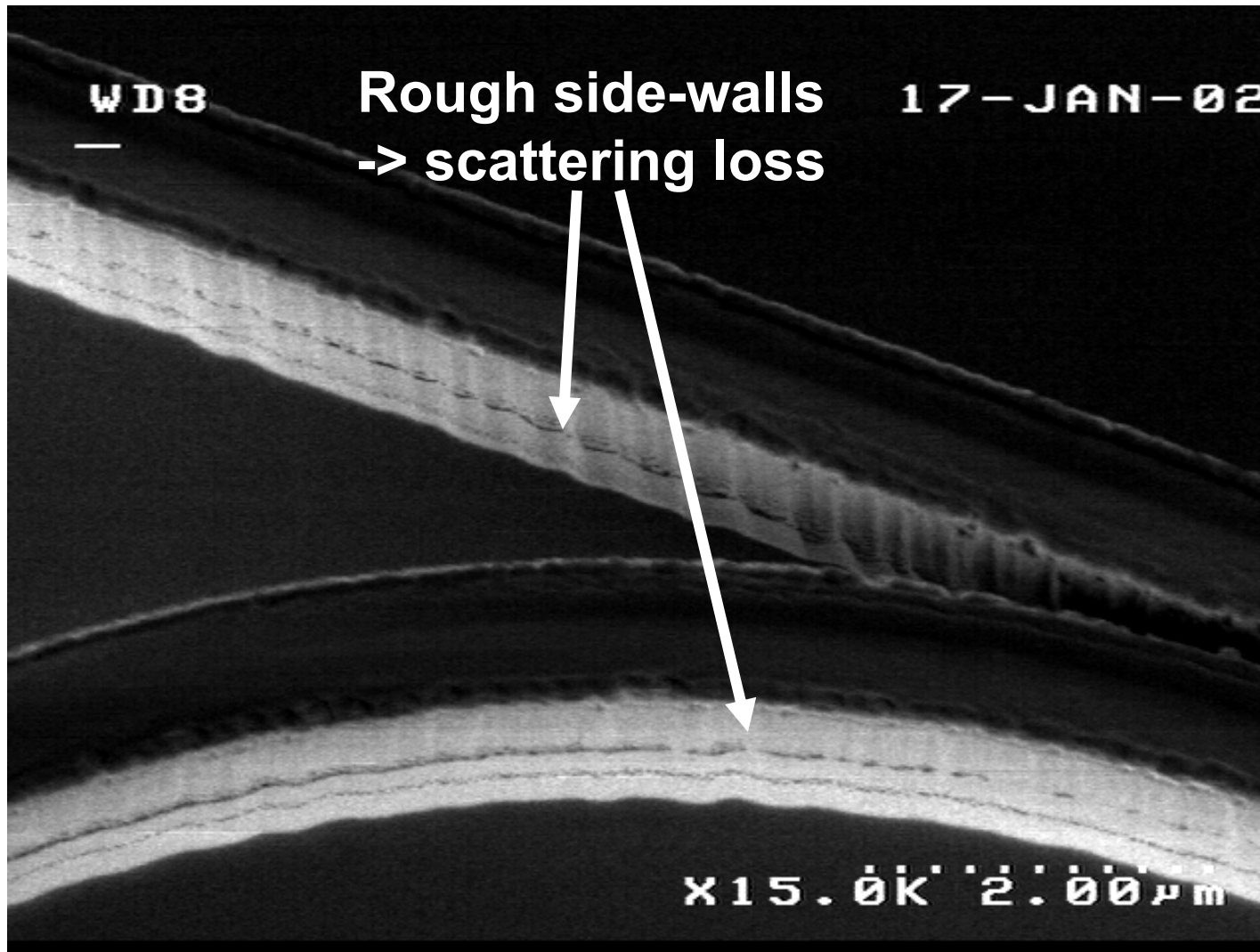
- Multipass Lithography
- Redeposition of Oxide Etch Mask
- Use of E-beam resist as etch mask to SiO_2 in RIE
- Use of NiCr as an etch mask to SiO_2 in RIE
- Use of metal as a direct etch mask

ECE·ILLINOIS

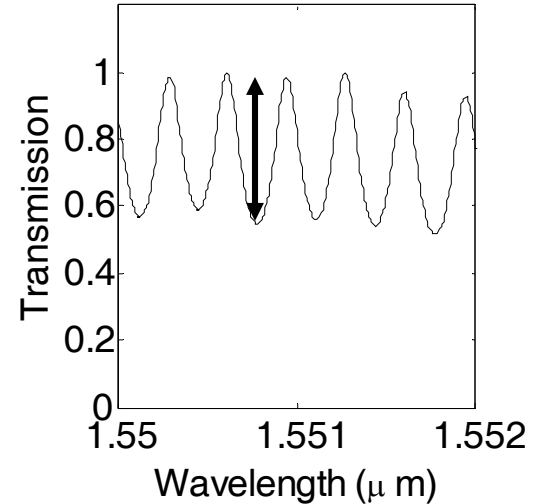
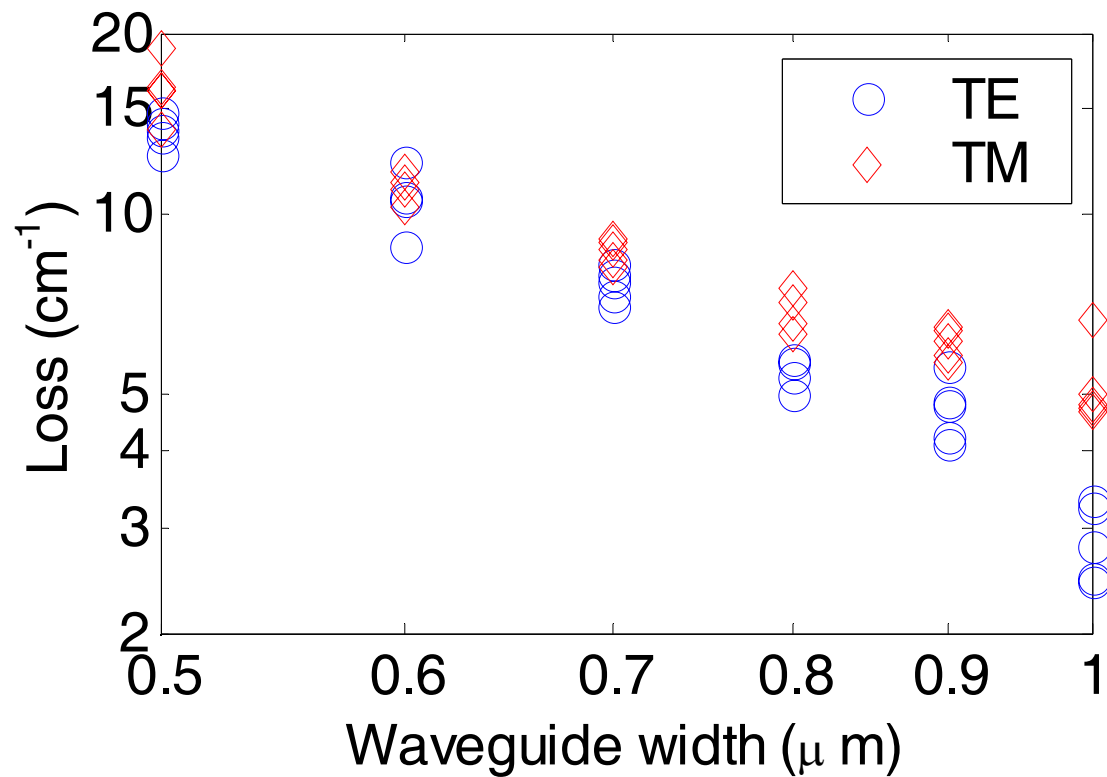
Electrical and Computer Engineering
University of Illinois at Urbana-Champaign

Advanced Processing and Circuits Group

Roughness Scattering



Earlier Loss Measurements (Compare Slide 4)



Increase of loss with decreasing width -> scattering.

Electron Beam Lithography: Processes



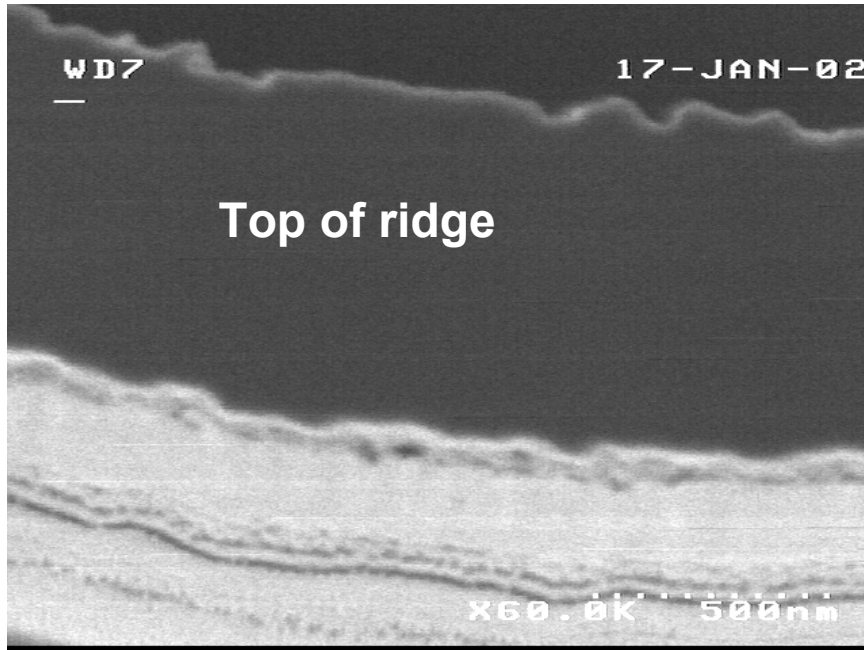
Resist

- **Negative resist**- possible edge acuity limitation
- **Positive resist**- difficult narrow gap formation
- **Resist erosion during dielectric etch**
 - affects deep etching ($\sim 5 \mu\text{m}$)

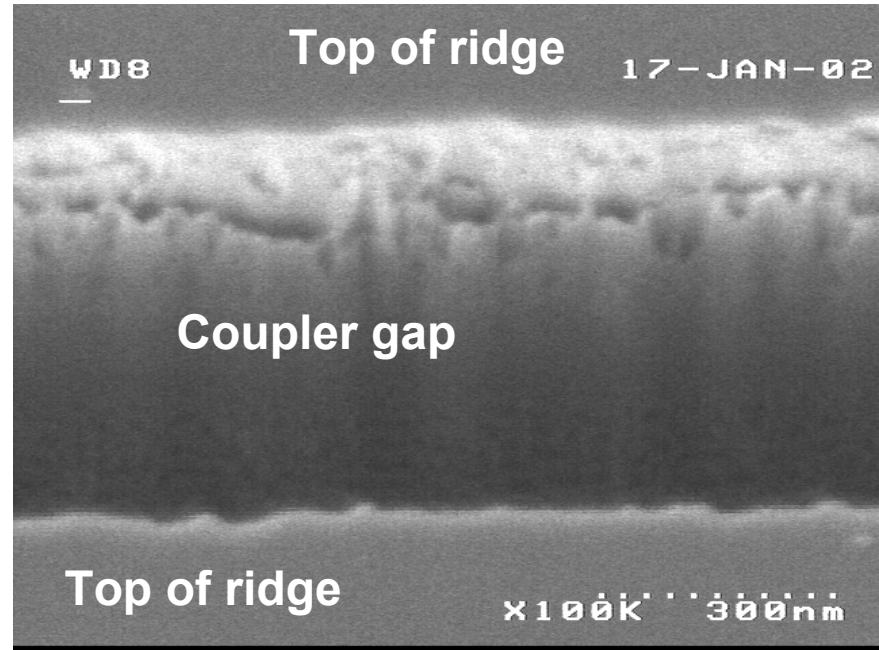
Mask

- **Mask edge erosion**
- **Evaluate direct metal mask on semiconductor and metal mask on dielectric- Issues: selectivity, grain size, contact resistance, adhesion, stress, sticking coefficient**

Electron Beam Lithography: Etch Mask Erosion



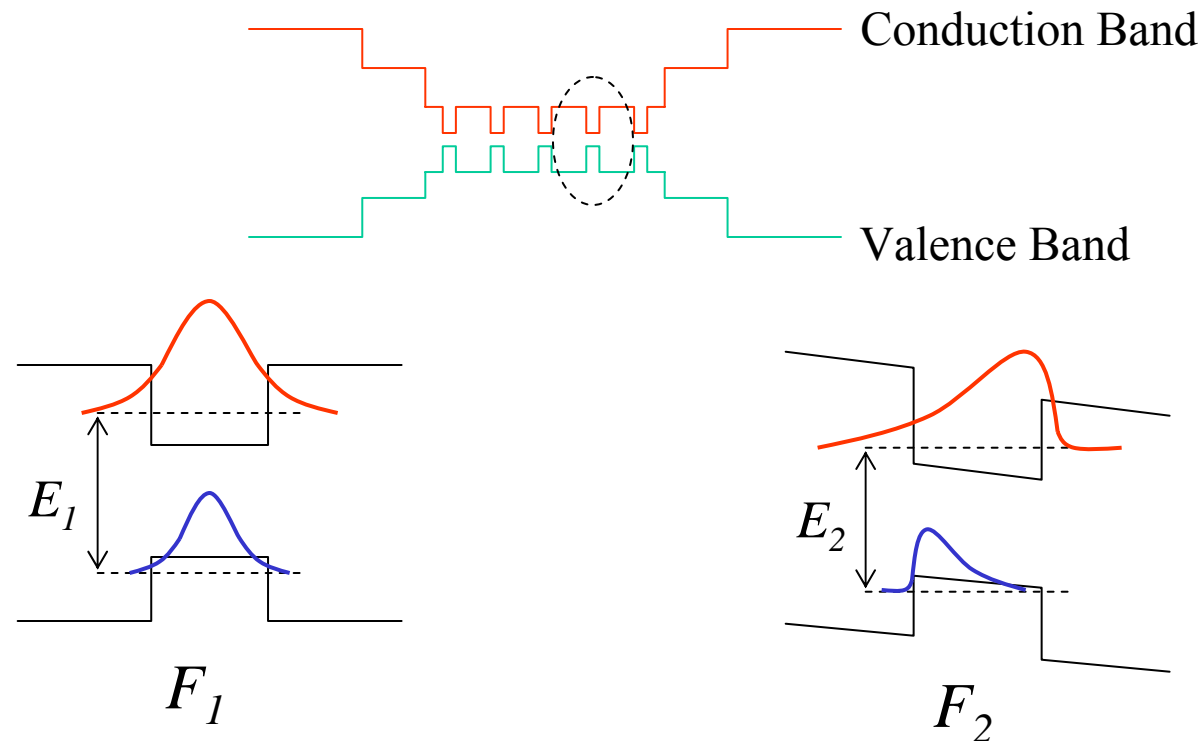
Early-stage erosion of dielectric mask, telegraphs to semiconductor through entire etch (shower curtain)



Later-stage dielectric mask erosion from deep etch, severe roughness transfers only to upper portion of semiconductor

Existing Technology

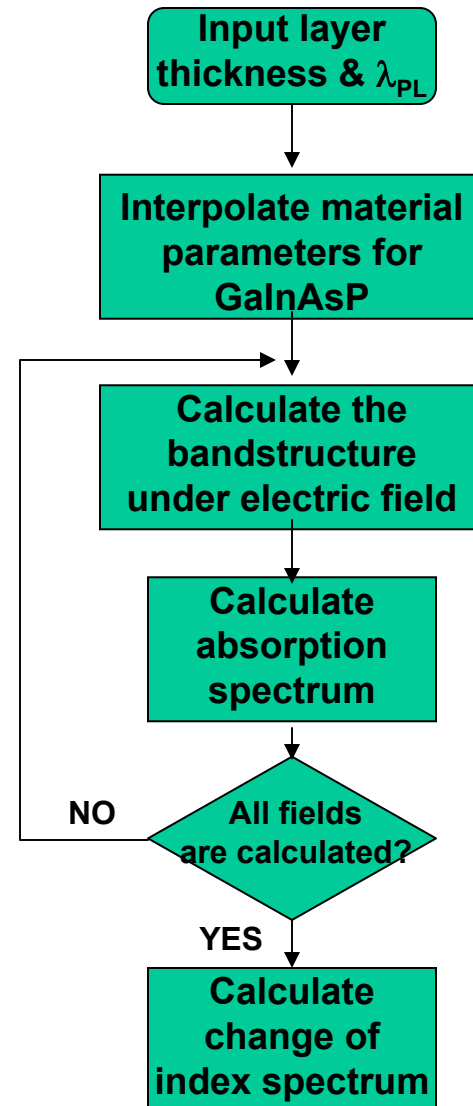
- Existing technology is based on quantum confined Stark effect (QCSE) in multiple quantum wells (MQW)



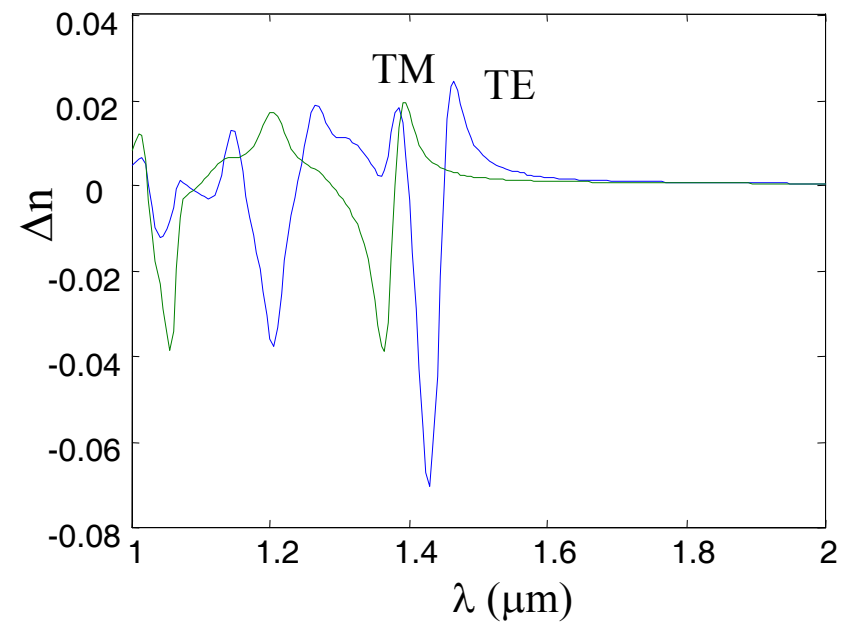
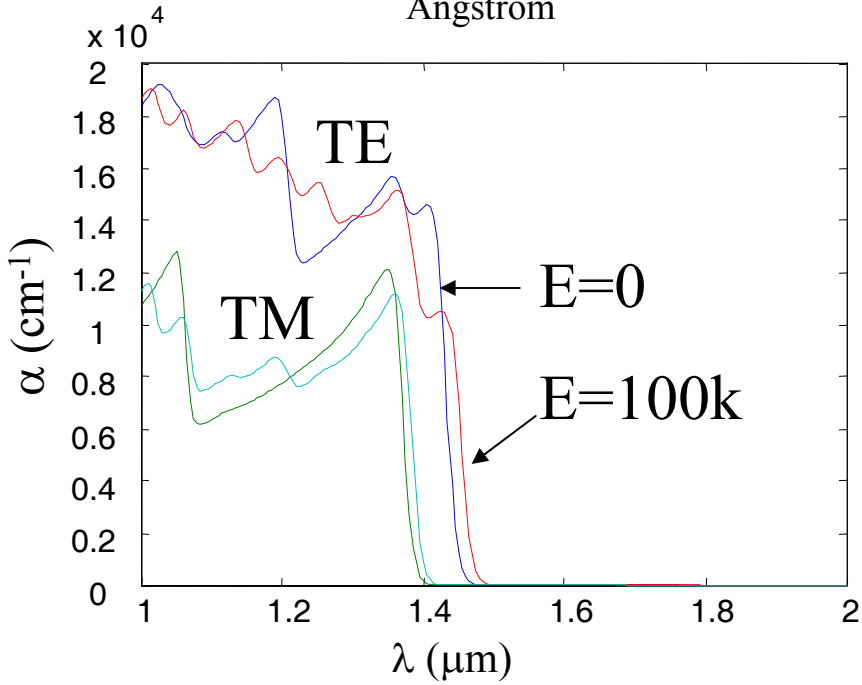
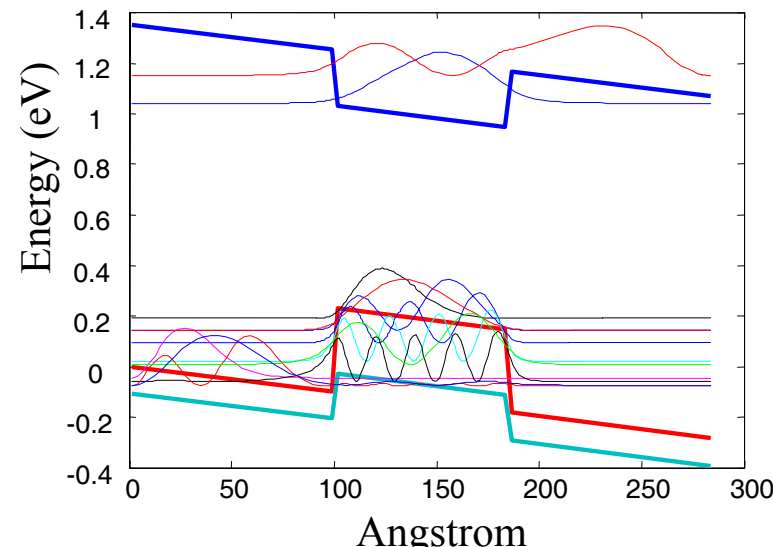
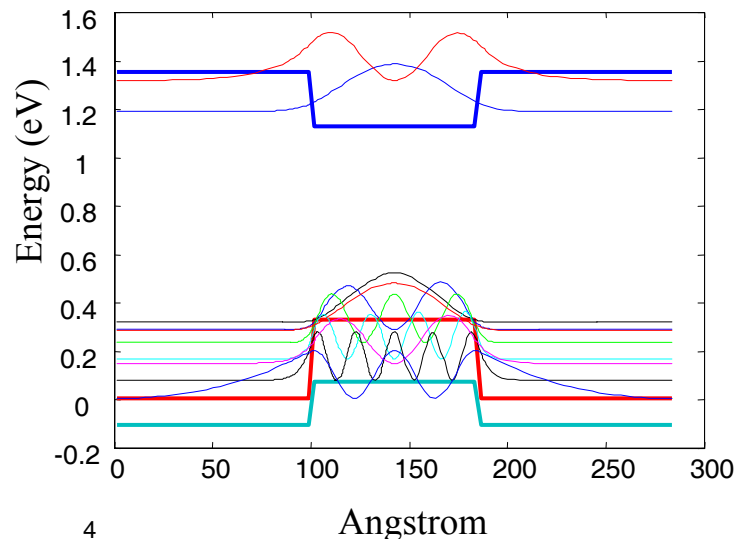
$$F_2 > F_1 \Rightarrow E_2 < E_1$$

Modeling

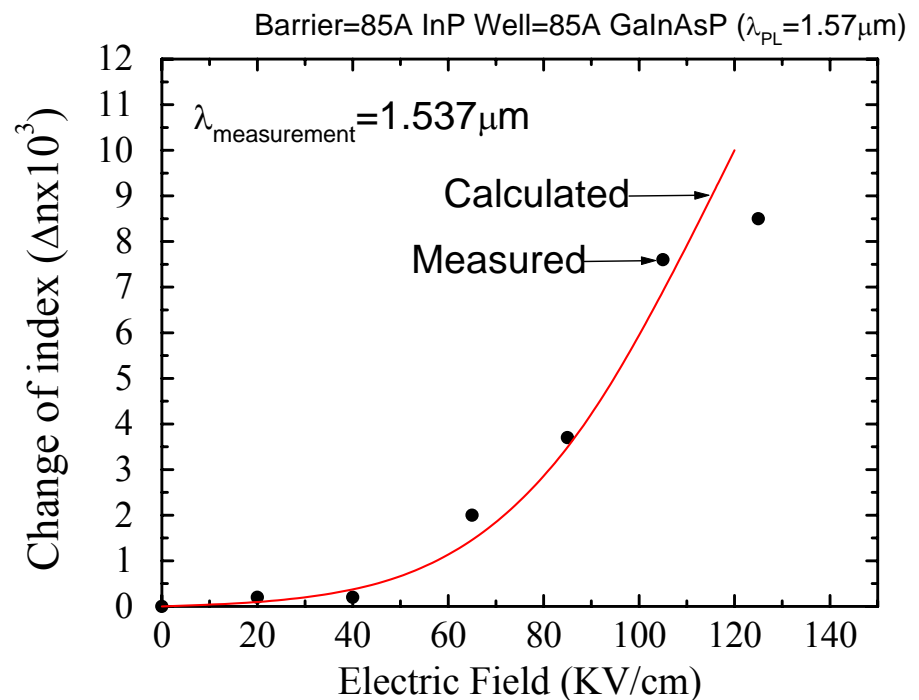
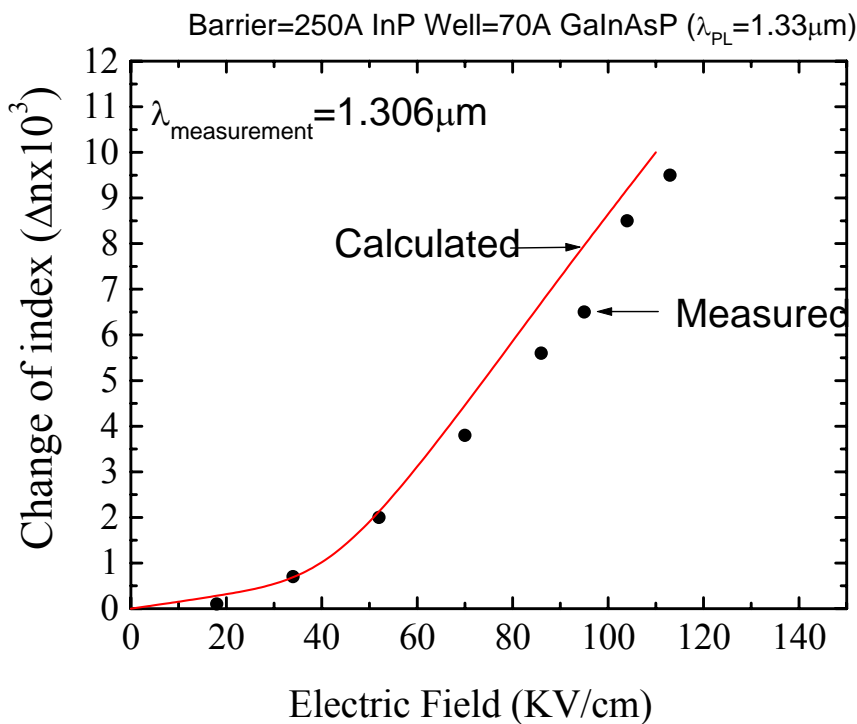
- Material parameters calculated using interpolation with bowing effects.
- Eigenvalues and eigenfunctions of electron, light-hole, heavy-hole, and spin-orbit calculated based on a 4x4 k.p model
- Optical absorption spectrum calculated for the bulk and quantum wells, considering excitonic effects.
- Kramers-Kronig relation used to calculate the change of index spectrum



Simulation Results for a Single Quantum Well

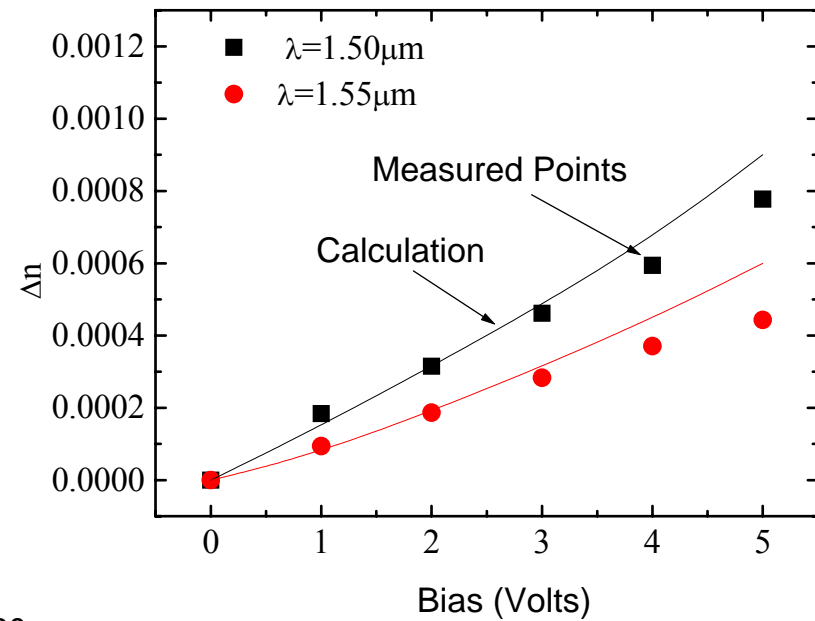
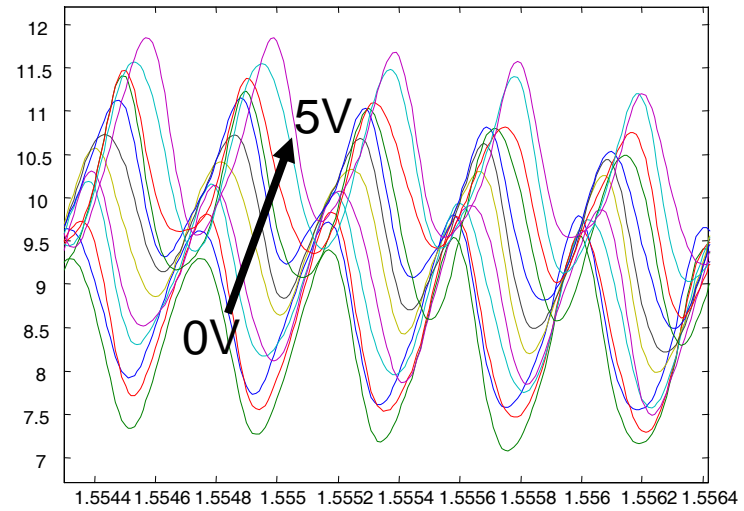
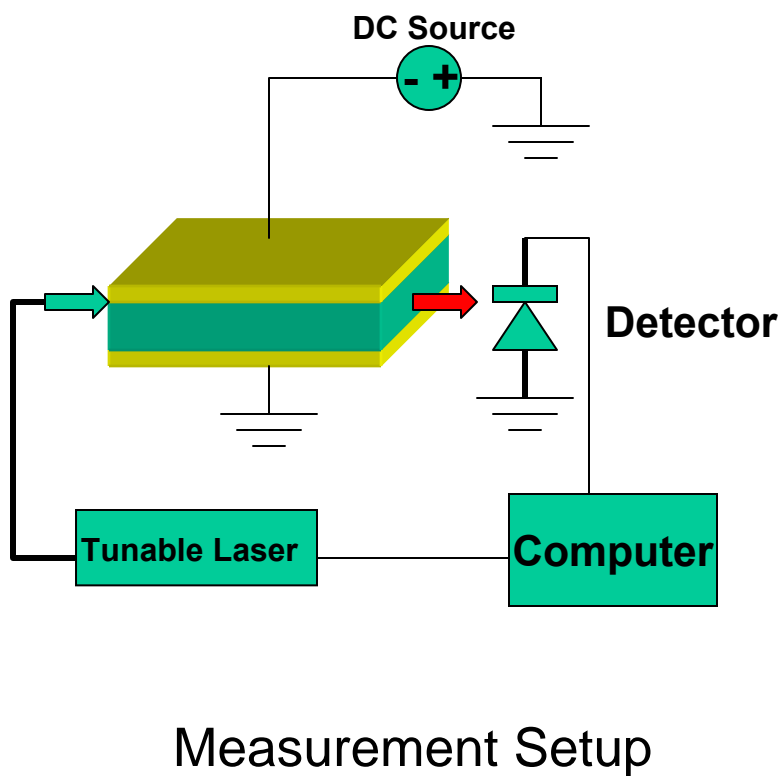


Comparison with the Experimental Results at $\lambda \sim 1.3\mu\text{m}$ and $\text{I} \sim 1.5\mu\text{m}$



Slab Waveguide Measurements

Experiment vs. Theory



Conclusions



- The key focus at this time is optical loss of deeply etched InP-based waveguides
 - Demonstrated state-of-the-art waveguide loss at submicron waveguide widths
- Demonstrated strongly-coupling rings with desirable phase response
- Improved electrorefractive material structures designed using newly developed in-house model
- Impact of MMI-couplers in multi-ring device to be evaluated relative to air-gap couplers

Site Visit: Resonant Enhanced Modulator Program

**Under the DARPA/MTO Radio Frequency
Lightwave Integrated Circuits Program**

**A.N. Lepore, M.H. Kwakernaak, H. Mohseni, Z.A.
Shellenbarger, D. Bechtle, & J.H. Abeles (PI)**

**Sarnoff Corporation
Princeton, NJ 08543-5300**

Wednesday October 9, 2002

RFLICS/REM Site Visit Agenda



8:00-8:15	Introduction	Joe Abeles
8:15-8:30	Program Overview	Allen Lepore
8:30-9:00	Process Development	Allen Lepore
9:00-9:30	UIUC Process Support	Ilesamni Adesida
9:30-9:40	Break	
9:40-10:10	Materials Development	Hooman Mohseni
10:10-10:40	Device Design & Test	Martin Kwakernaak
10:40-11:00	Resource & Financial Overview	Al Grupper
11:00-12:00	AOSP Planning*	<i>Ralph Whaley</i>
12:00-1:00	Lunch	

** Breakout Meeting*

Resonant Enhanced Modulator Introduction

Joseph H. Abeles

Most Significant Accomplishments

... since Feb, 2002 Site Review ...



- **Development of advanced processing methods:**
 - Low-loss deep-etched waveguides (1 cm^{-1} achieved at $1 \mu\text{m}$ width)
 - Planarization of anisotropic wafer using Cytop™ dielectric
 - Low-capacitance contact to waveguides
- **Implementation of MMI couplers in ring geometry**
 - Total ring loss equivalent of 3.5 cm^{-1} demonstrated including MMI
- **First demonstration of Mach-Zehnder Ring Modulator structure**
 - Electrical modulation to 3 GHz
 - 5 dB Ring Enhancement
- **Demonstration of enhanced modulator material**
 - 3 to 4× enhanced electrorefractive effect (compared to literature)
 - Special materials growth procedures

Most Recent Experimental Prototype



- **Single-ring Mach-Zehnder modulator**
 - Material not optimized
- **Discussed more extensively in Martin Kwakernaak's Presentation**

Plan to Meet Program Objectives



- **Iterate fabrication loop to get 1 GHz REM**
- **Introduce RF electrode structure to achieve 10 GHz REM by January, 2003**

Upcoming Challenges



- **Overcoming poor yield of adequate-quality-ICP-etching**
- **Reducing losses of MMI couplers**
- **Introducing phased RF electrode with adequately low loss**
- ***Packaging***

Financial Status

- **Funding is low for this point of the program**
- **Project January completion to project**
- **Discussed more fully in Albert Grupper's presentation**

Resonant Enhanced Modulator Program Overview

Allen N. Lepore

RFLICS/REM Program Overview



- **Significant accomplishments- operating prototype devices and improved materials demonstrated**
- **Recent experimental data- prototype devices currently under test up to 3GHz**
- **Plan to meet program objectives- revised program plan for 10GHz design with two fabrication iterations**
- **Challenges- yield, consistent low-loss sample generation, schedule**
- **Financial status- see Al Grupper presentation**

Key Technical Accomplishments



- **Prototype REM devices tested to 3 GHz**
 - Testbed configured for on-chip probing to 3 GHz
- **Novel materials developed with improved dn/dV (4 \times improvement)**
 - Experimental agreement with coupled quantum well model, allows for design optimization
- **5th-generation of RF device designs**

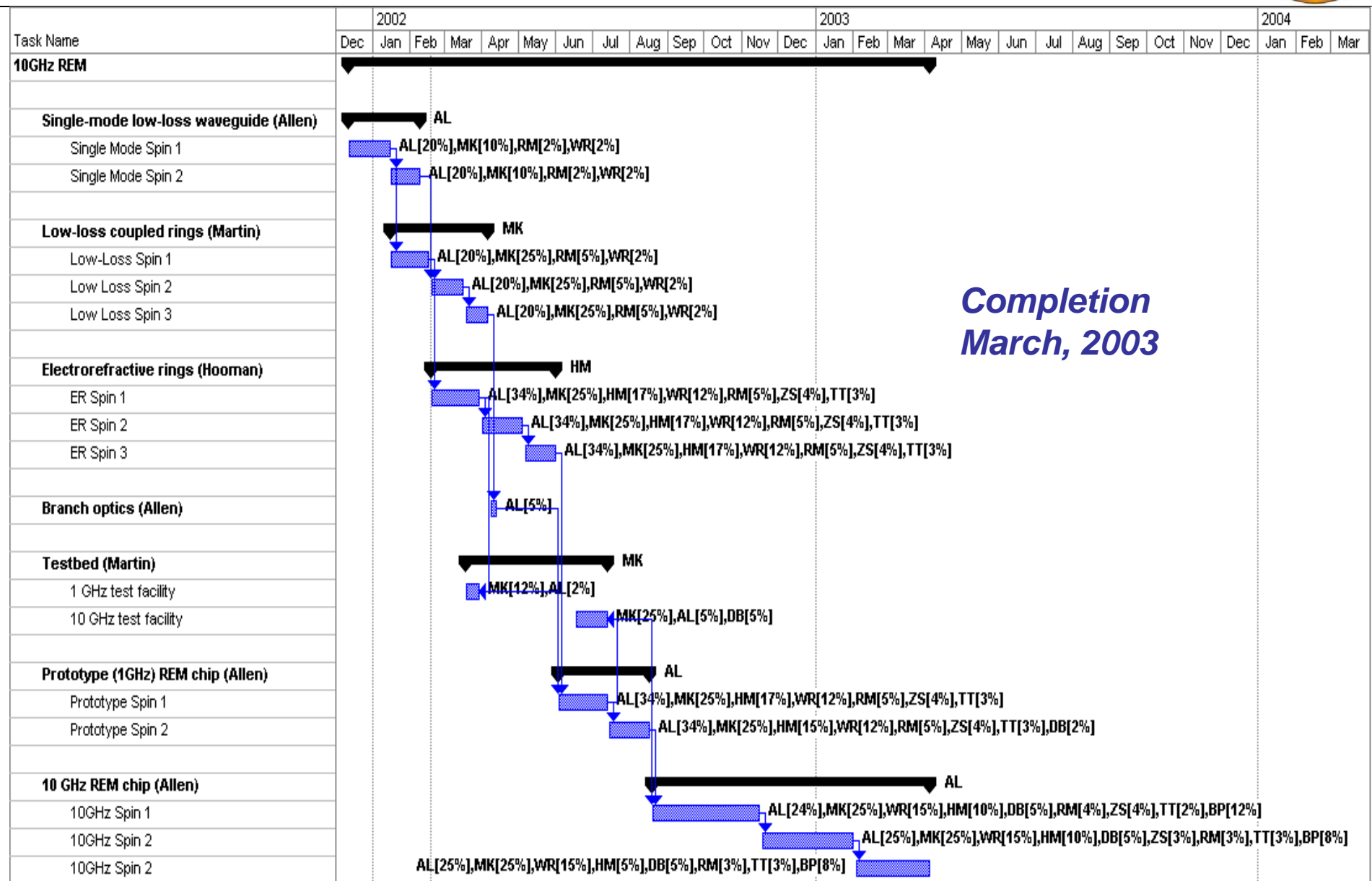
Resource Accomplishment



- **Electron-beam lithography:**
 - Draft CRADA now complete*

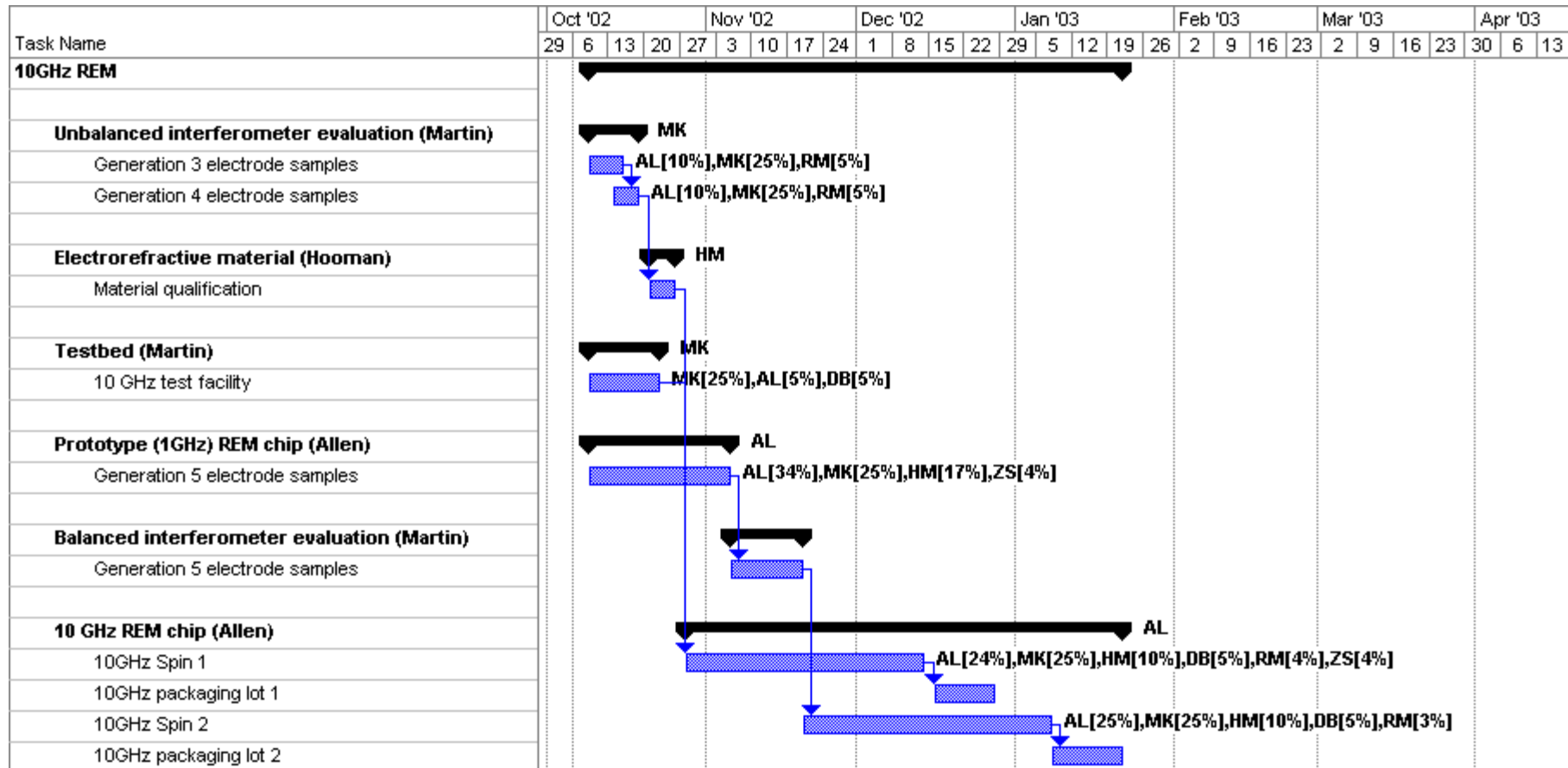
* Army Research Laboratory,
Sensors and Electronic Devices Directorate

Previous Program Plan



*Completion
March, 2003*

Program Plan for 10 GHz Devices



Key Issues Affecting Schedule

- **Processing at multiple sites: Sarnoff, UIUC, ARL**
- **Quality Control over ICP process at UIUC**
 - Transfer of responsibility to new post-doctoral student (Dr. Bae)
 - ICP etch evaluation loop too long
 - No in-batch feedback (AFM or FE-SEM) at UIUC
- **Downtime for electron-beam lithography and high-resolution SEM**
 - 1 month ebeam operation with non-optimal performance
 - 1 month ebeam unavailable due to maintenance/repair

Resonant Enhanced Modulator Process Development

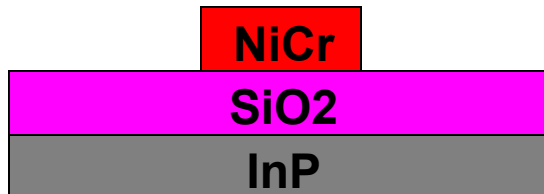
Allen N. Lepore

Process Development: Outline



- **Waveguide process overview**
- **Electrode process overview**
- **Device design/fabrication issues**
- **Process development for electrodes – planarization issues**
- **Good ideas to try...**

REM Waveguide Process



1. Metal mask liftoff using e-beam pattern



2. Transfer metal pattern to dielectric



3. Blanket redeposit thin (50nm) dielectric for sidewall smoothing



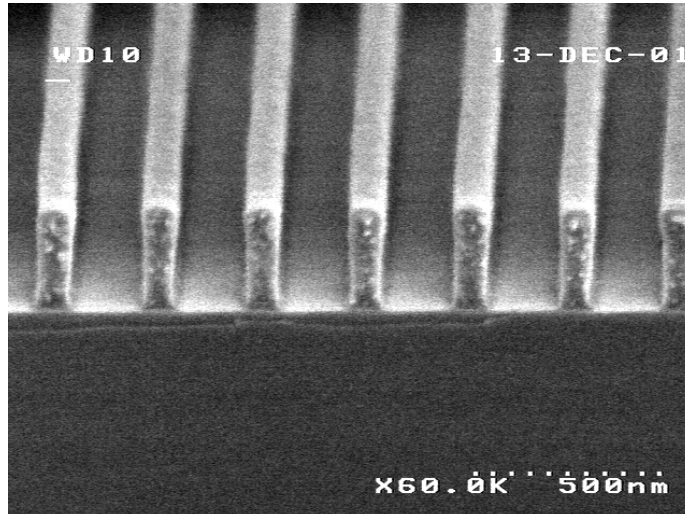
4. Anisotropic dielectric removal from planar surfaces



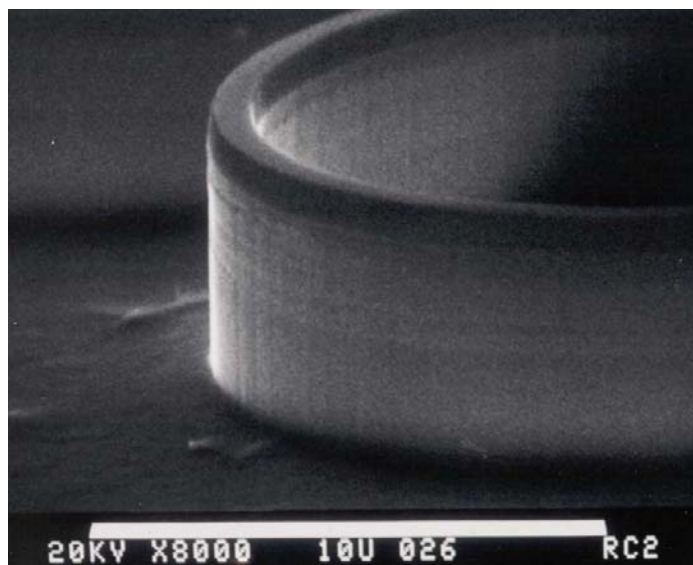
5. ICP anisotropic etch of waveguide

Benefits of Metal Etch Masks

**Bilayer ebeam resist
for metal mask liftoff**

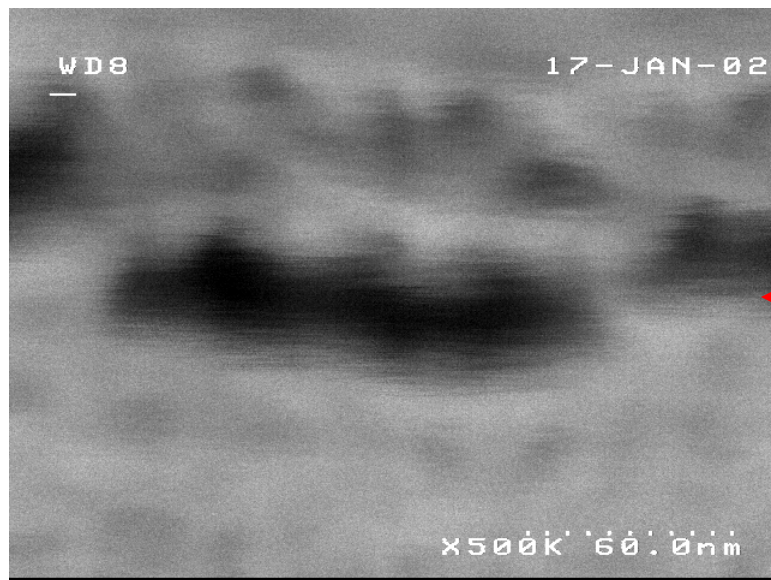
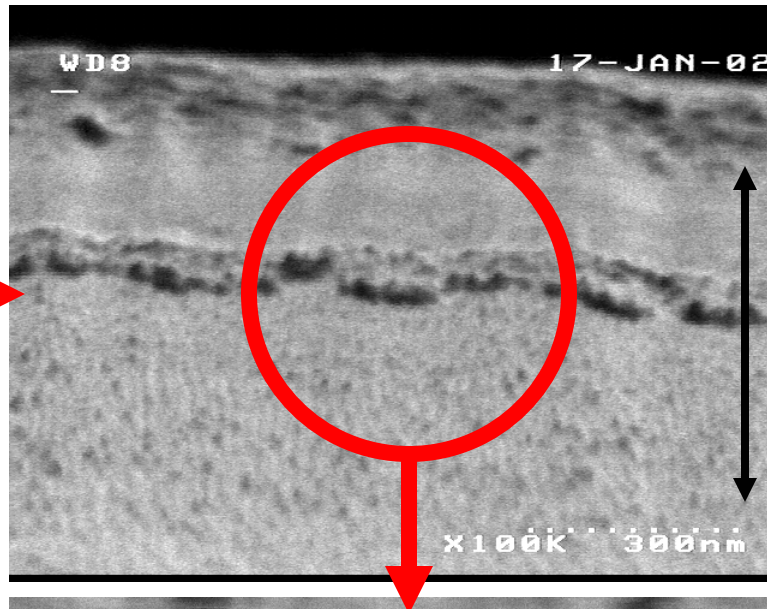
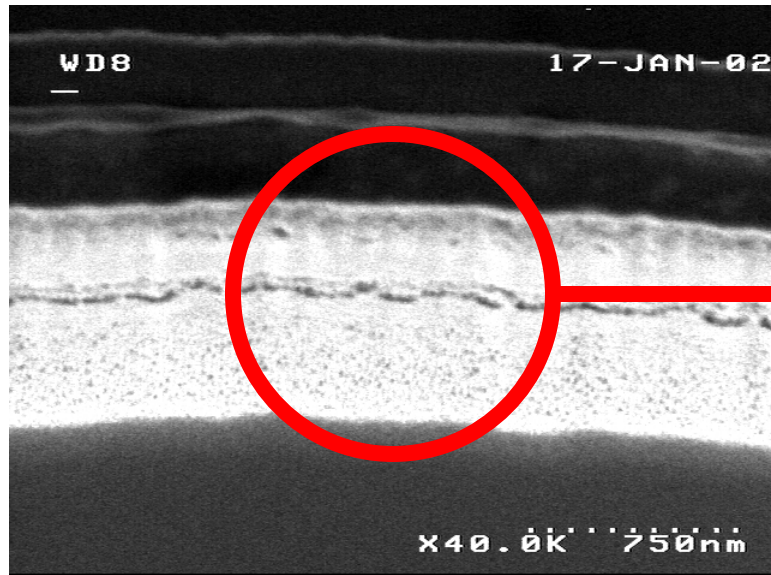


**NiCr/SiO₂-
masked ICP-
etched ring**



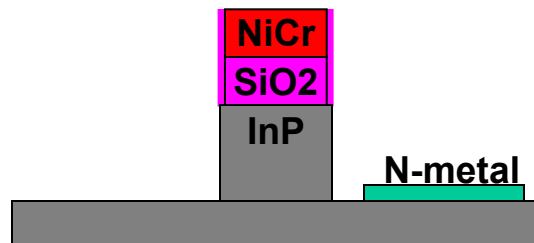
Without Metal Mask

... mask erosion - shower curtain effect ...

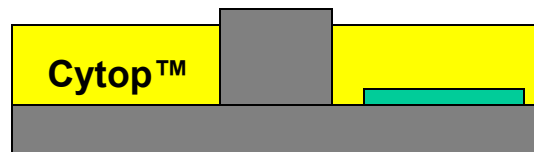


Layer/depth-dependent
sidewall
damage

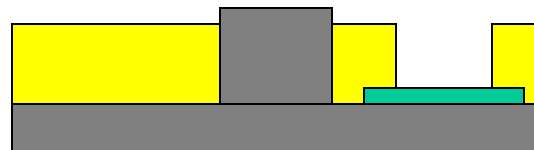
New Topside REM Device Process



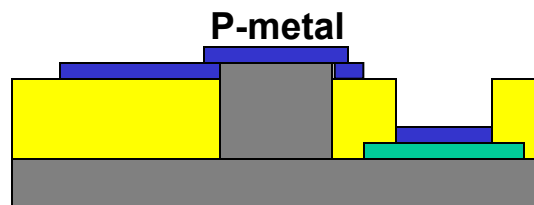
1. N-contact formation



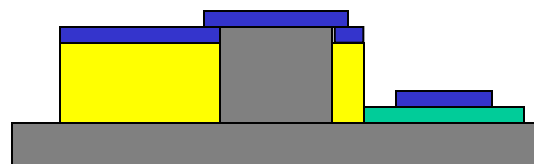
1. Strip ICP etch mask and planarize with Cytop™ polymer



2. Open N-contact via

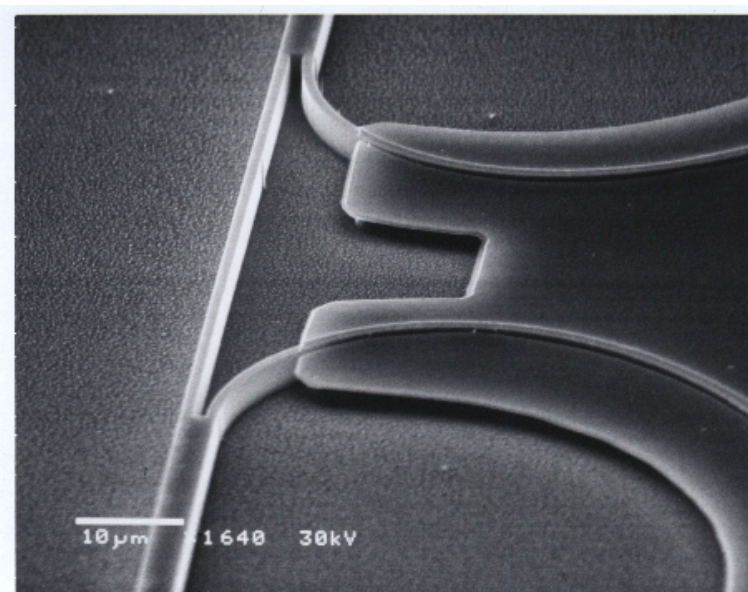
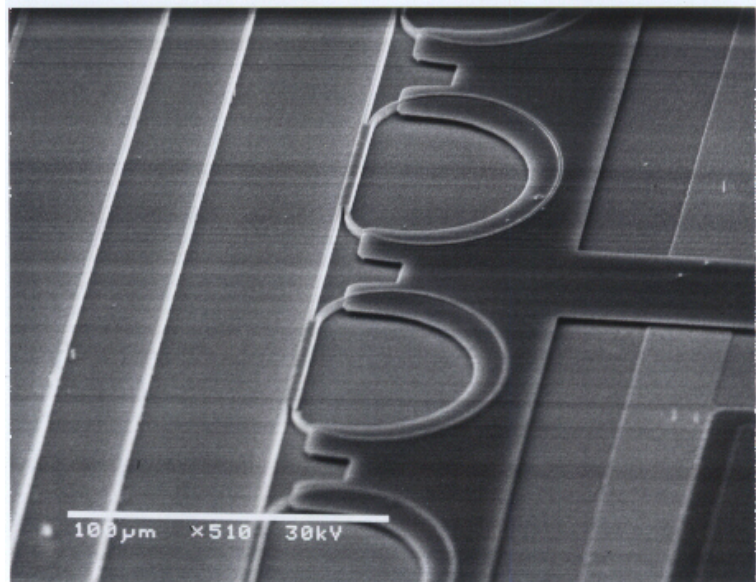
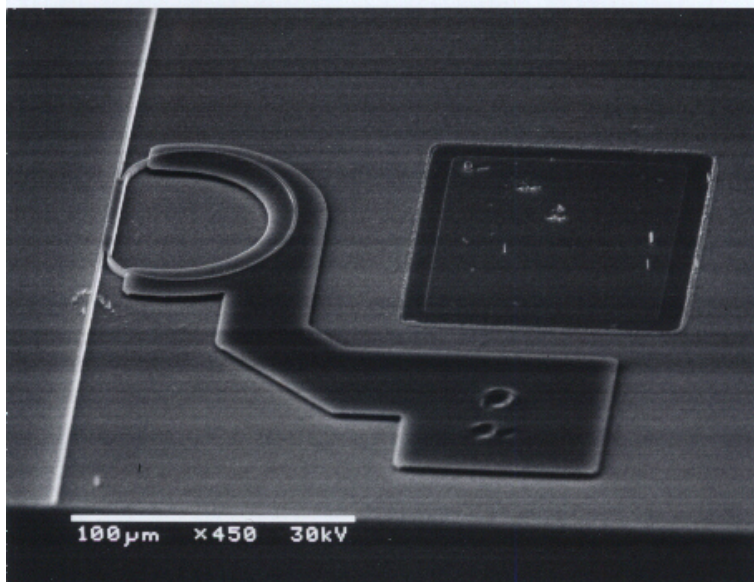


3. P-contact formation

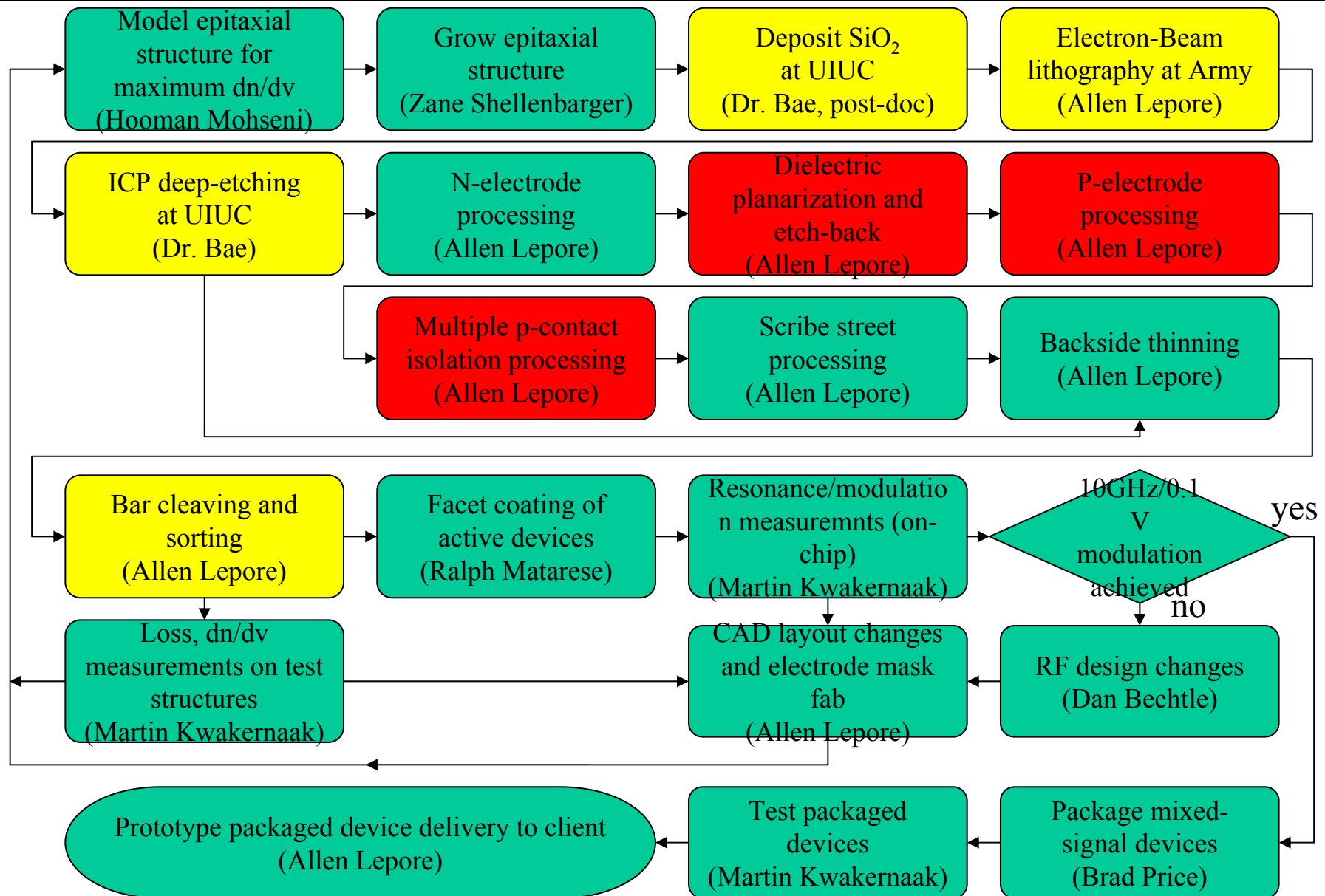


4. Excess dielectric removal

Completed & Functional Devices



RFLICS/REM Flowchart



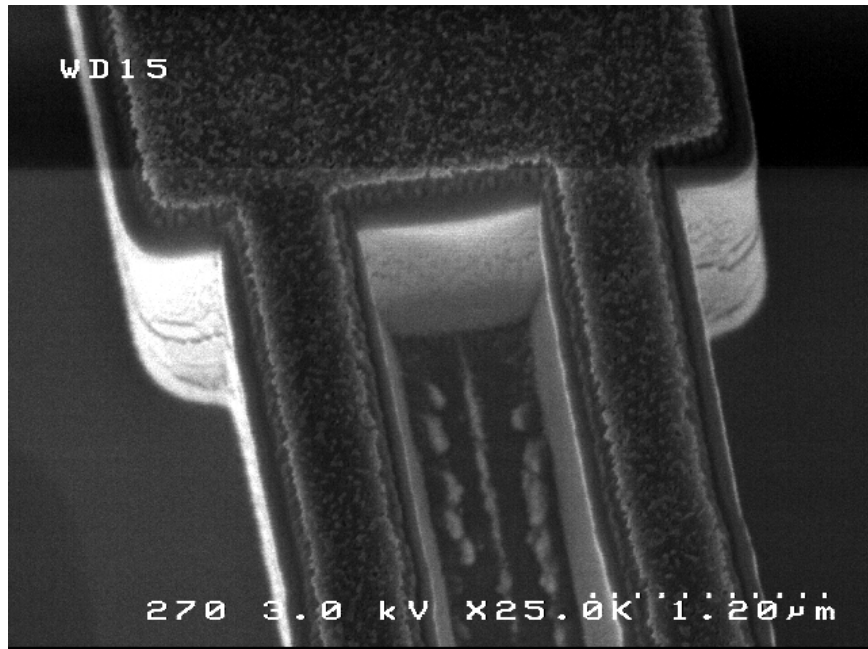
Detailed Update: Device Design & Fabrication



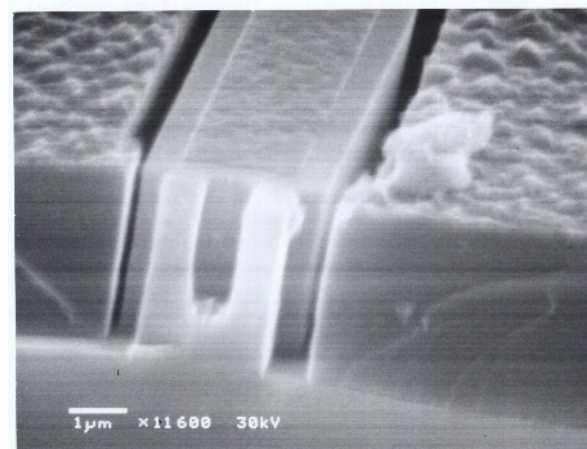
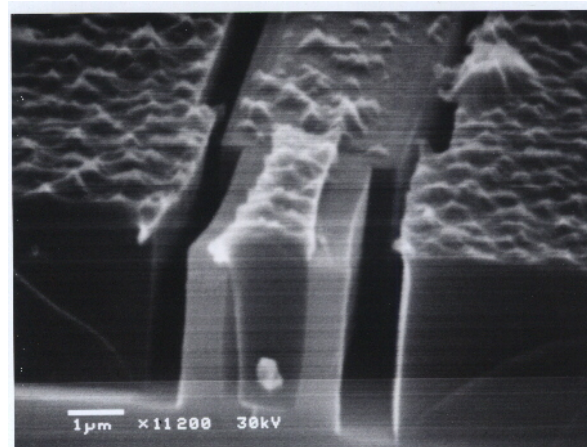
- Sidelined gap couplers and associated difficulties with narrow gap etching
- MMI coupler reproducibility sufficient (multi-ring device)
- Leakage and reverse breakdown acceptable
- MMI-coupled ring loss minimization:
 - accelerated bends replace racetrack design: continuous radius change to minimize mode shift
 - ring offset at MMI-junction compensates for mode
 - MMI size controlled precisely to minimize loss: ebeam dose modulation by feature size
- Poor reproducibility of ICP process (multi-user system)
- P-metal process improvements: loss not degraded
- Encapsulation removed after processing to permit facet coating

Gap Etching

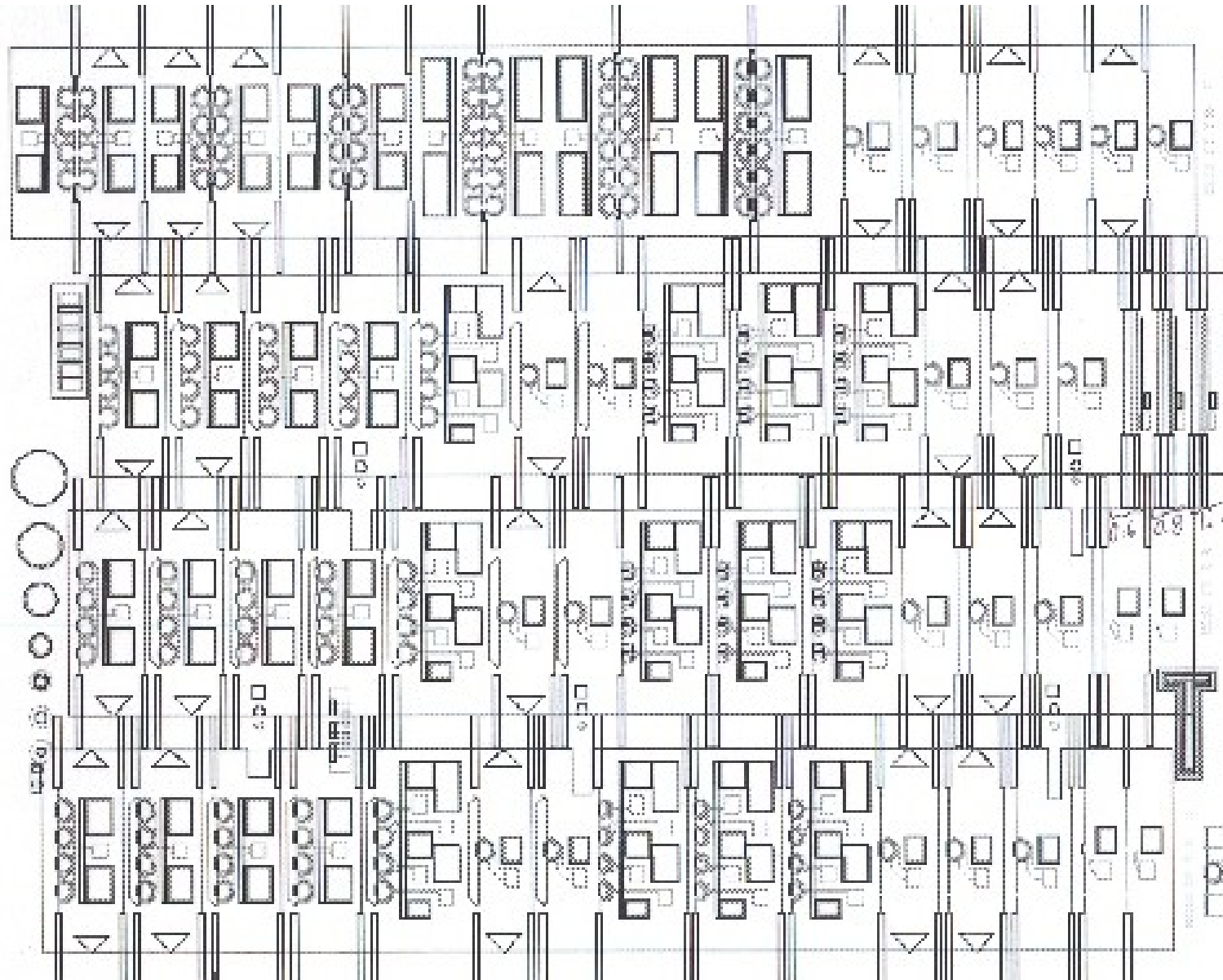
MMI coupler showing incomplete etching and residue in gap



Planarized MMI-branch showing etch depth variation with gap width

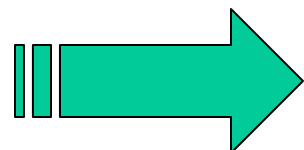
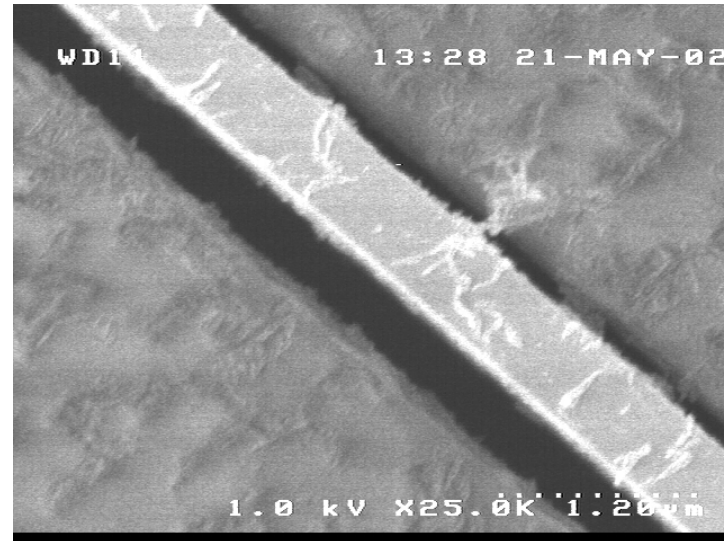


Prototype Device Layouts



Planarization Difficulties

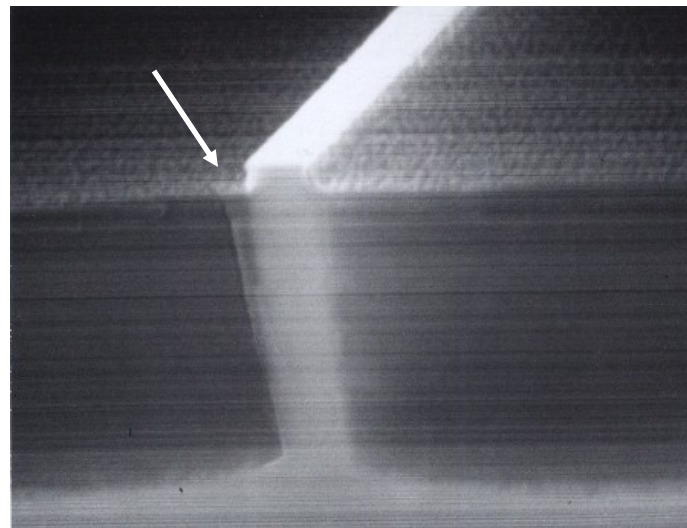
BCB Sidewall delamination after planarization etch



- Electrode short circuits active layers
- Excess loss if mode contacts metal

Planarization Attempts with BCB

- multiple coat, single cure
- multiple coat, multiple cure
- coat/cure, etch-back, recoat/cure
- oven vs. hotplate bake
- Temperature ramping to reduce stress
- baked adhesion promoter*
- gap filling with photoresist or Cytop- difficult to reproduce

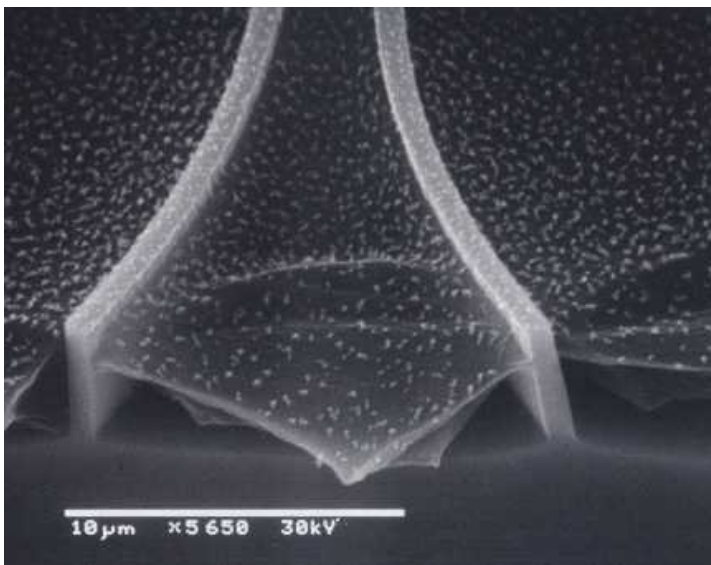


* Dan Schank @ Dow Chemical recommendation

Planarization Solution



Replace BCB with CYTOP™ polymer



- Greatly improved sidewall adhesion relative to BCB

PRO

- Etches readily in oxygen plasma
- Less post-etch residue than BCB

CON

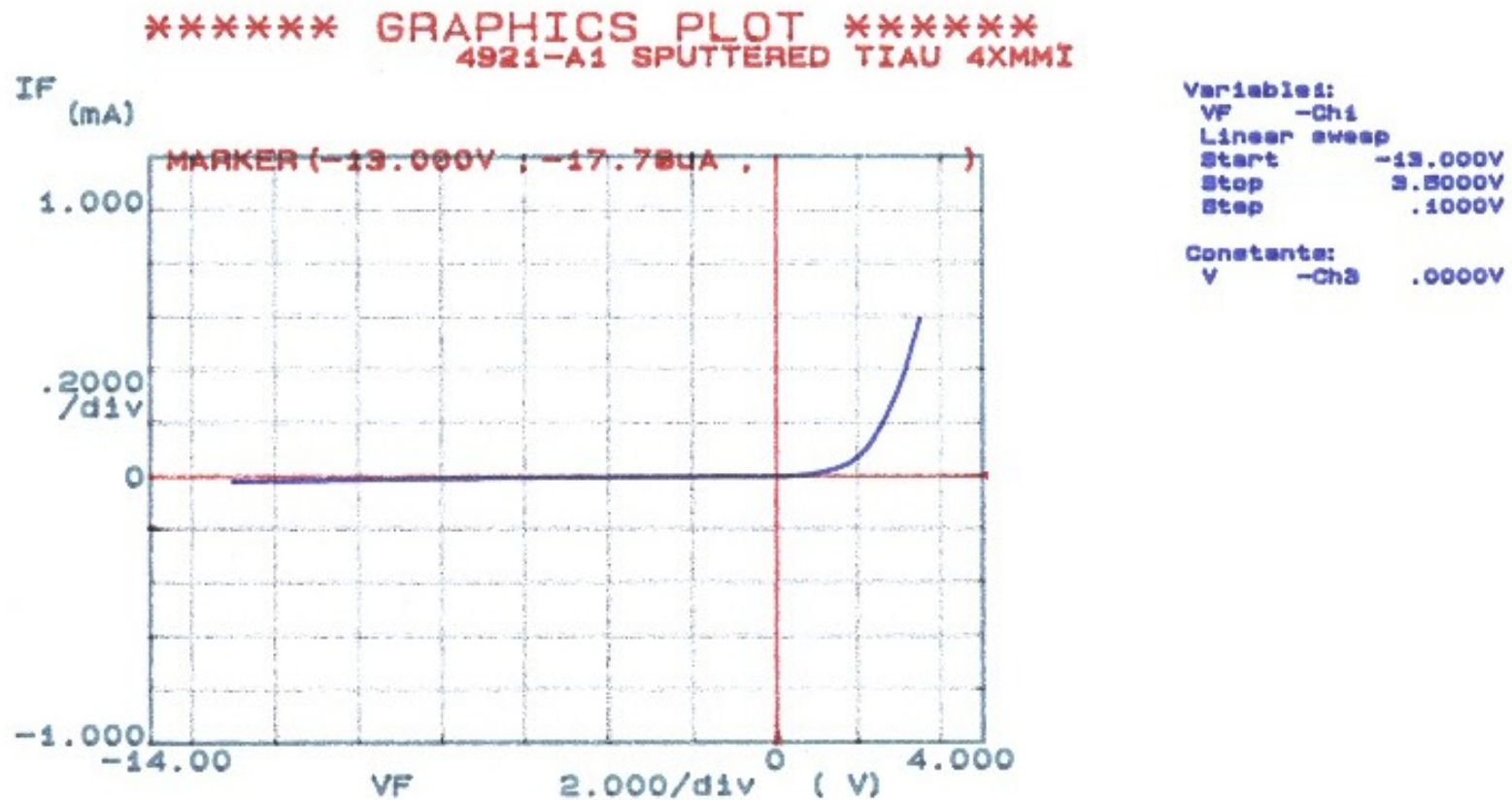
- Glass transition temperature much lower than BCB- impedes facet coating if excess material exposed

Good Ideas to Try...



- **MOCVD anneal/regrowth post-ICP for additional smoothing**
- **Encapsulation of Cytop with BCB or polyimide**
- **Tape-assisted liftoff, ultrasonic-assisted liftoff of metal etch mask to improve yield**

Excellent Leakage Characteristics



Sidewall Roughness of Optical Waveguides

Ilesanmi Adesida, J. W. Bae, W. Zhao, D. Selvanathan, J. H. Jang

**Micro and Nanotechnology Laboratory
Department of Electrical and Computer Engineering
University of Illinois at Urbana Champaign**

Losses of Ring Resonator Coupled Waveguide



Objective

- Analyze waveguide losses
- Locate critical loss component
- Quantify the fabrication requirement within maximum loss specification
- Development of fabrication process for low loss photonic devices

Waveguide loss has influence on :

- Finesse of resonator
- Extinction ratio and bandwidth of modulator
- Insertion loss of photonic devices

Sources of loss

- Substrate coupling loss
- Bending loss at ring resonator
- Coupling loss between waveguide and ring resonator
- Radiation loss at etched waveguide sidewalls

Losses of Ring Resonator Coupled Waveguide



How to reduce losses ?

- Deep ICP-RIE etching of waveguide structures ($\sim 5 \mu\text{m}$)
Negligible substrate coupling loss
- Strongly guided waveguide structure : $n_{\text{core}} (3.24) \gg n_{\text{cladding}} (1.0)$
Negligible bending loss
- Optical mode matching at ring resonator and waveguides
Careful design and tight control of waveguide etching are required
- Smooth sidewall
Development of etch mask technology and ICP-RIE process
to get smooth sidewall ($\sigma_{\text{RMS}} \sim \text{a few nm}$)

How to estimate sidewall roughness of waveguides ?

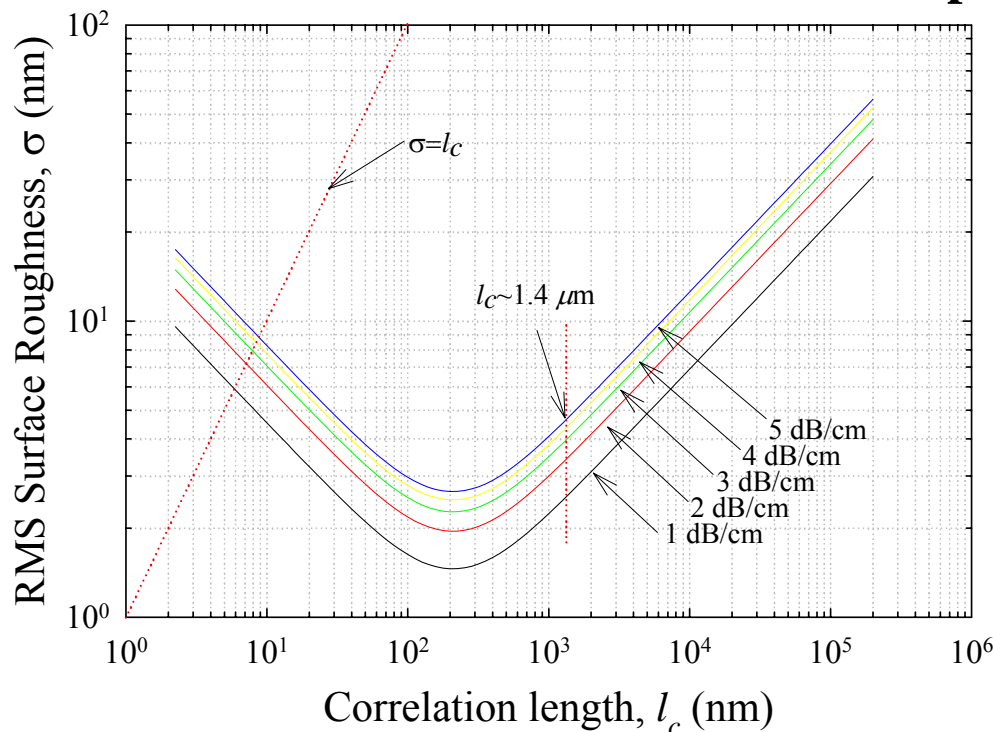
- AFM can be used to assess sidewall roughness
- Carbon Nanotube AFM tip better for 3-D imaging
- Carbon Nanotube AFM tip has same resolution as etched Si tip
(Tip diameter $\sim 10 \text{ nm}$ for both AFM tips)

Preliminary Calculation of Radiation Loss

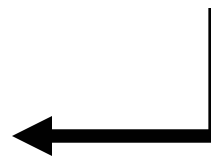
Perturbation method to calculate radiation modes from waveguides
 Statistical treatment of sidewall roughness (σ_{RMS} , l_c)

Radiation Loss

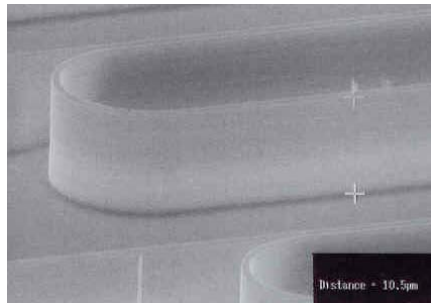
- RMS roughness, σ_{RMS}
- Correlation length l_c
- Guided mode profile of the waveguide



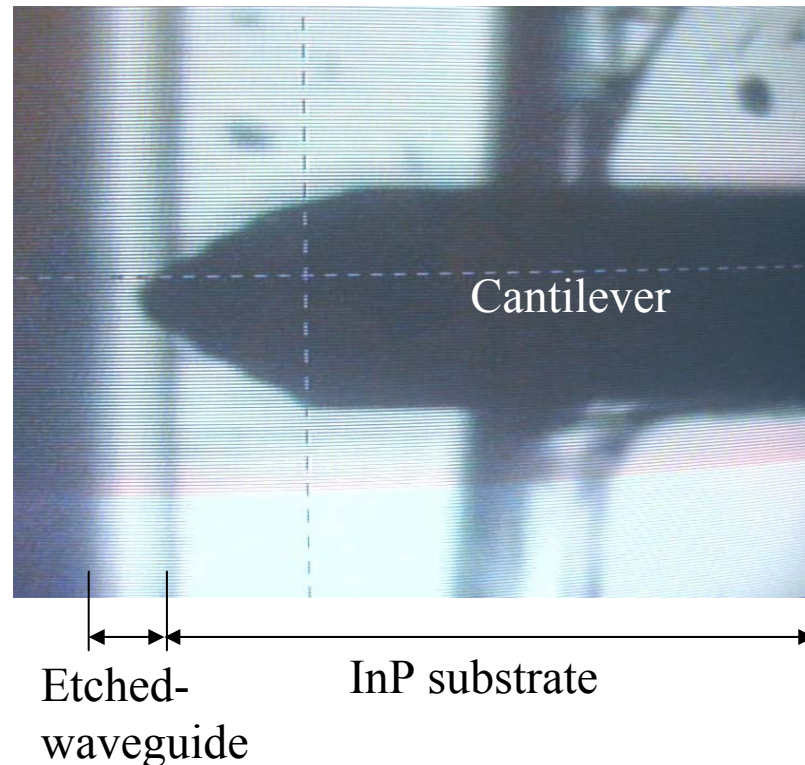
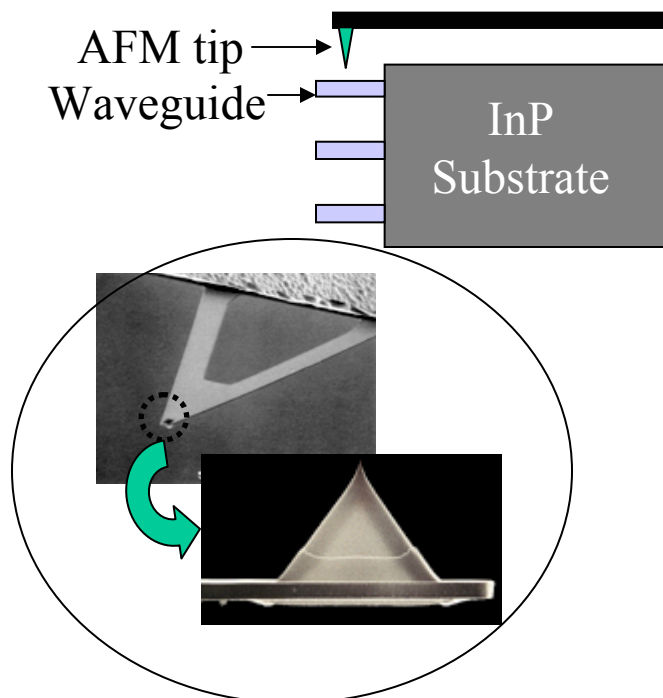
Radiation loss is strongly dependent upon correlation length (l_c) as well as RMS surface roughness (σ_{RMS})



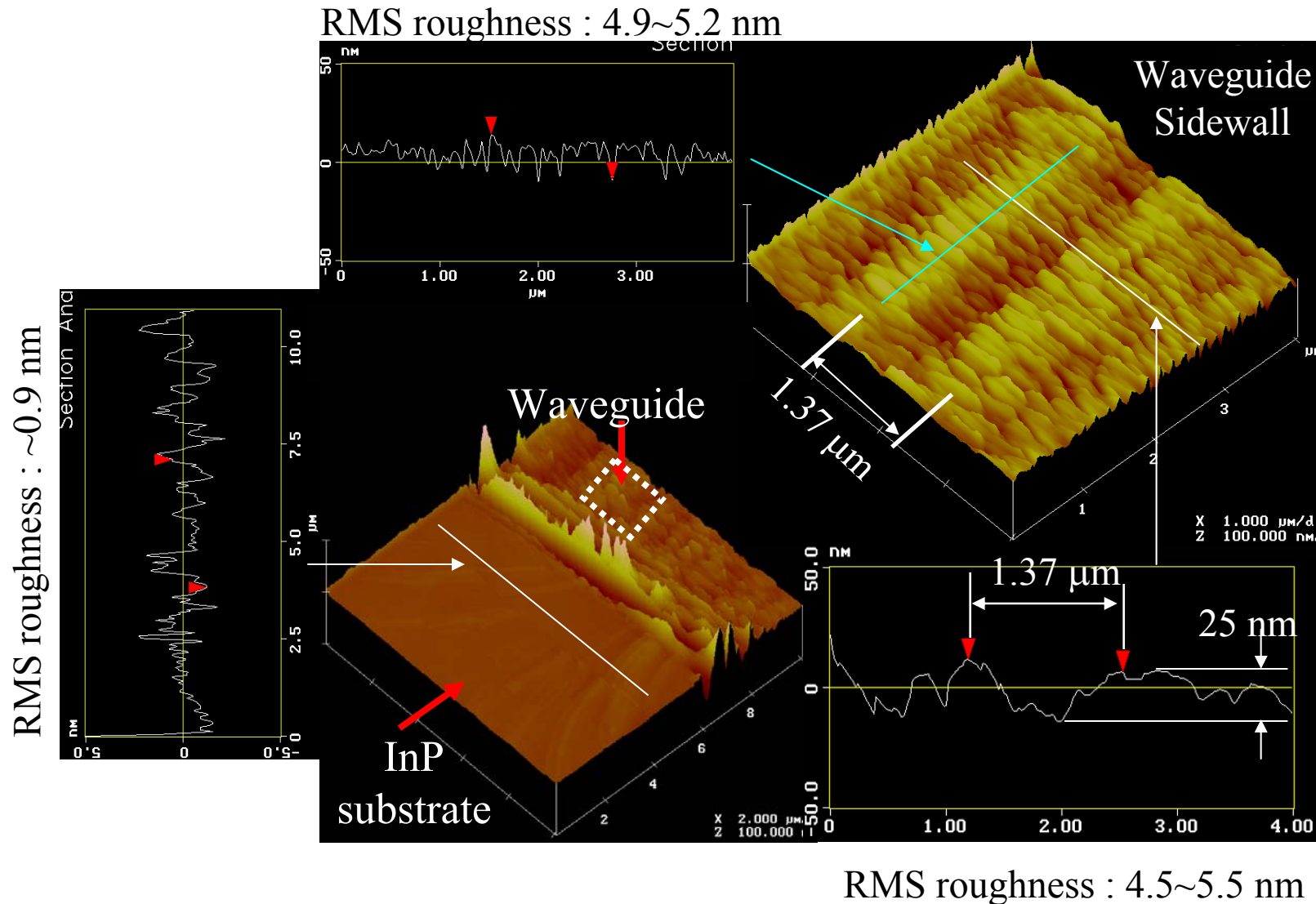
Strategy to Assess Sidewall Roughness with AFM



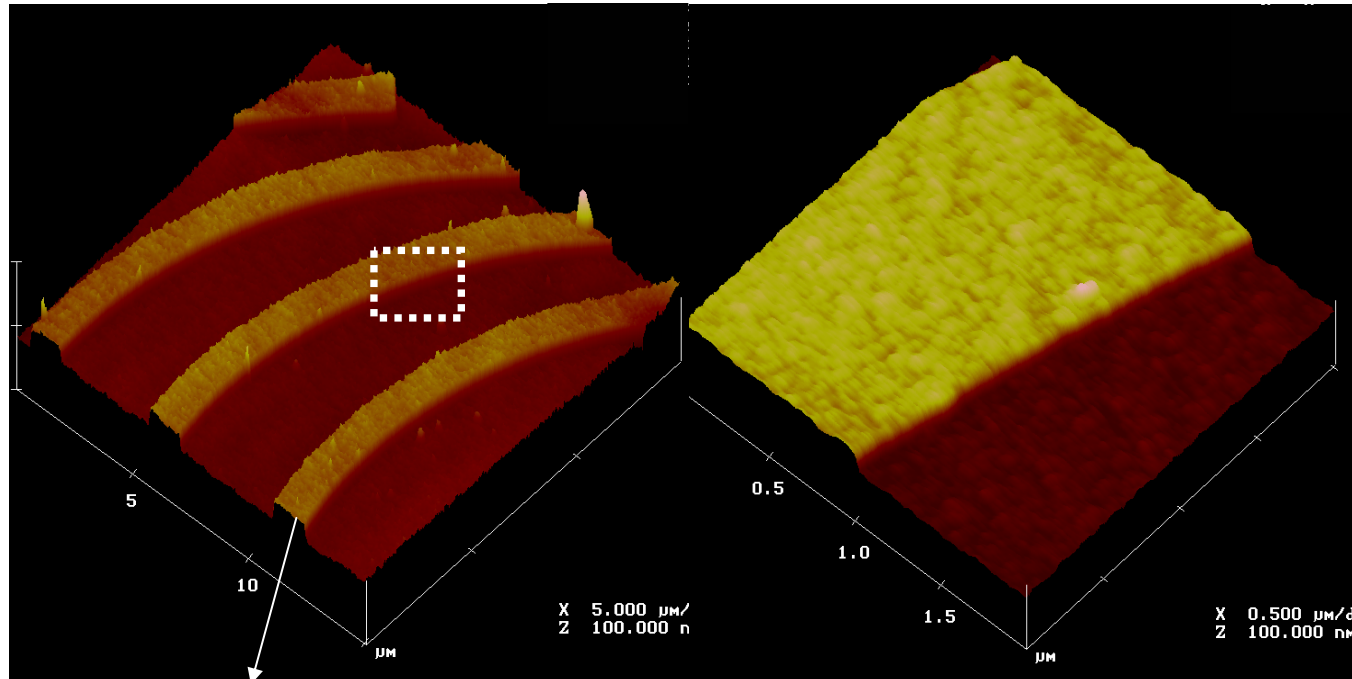
Deep etched (10 μm deep) ring resonator coupled waveguide



Assess the Surface Morphology using AFM



Test Pattern to assess pixellation of E-beam Lithography

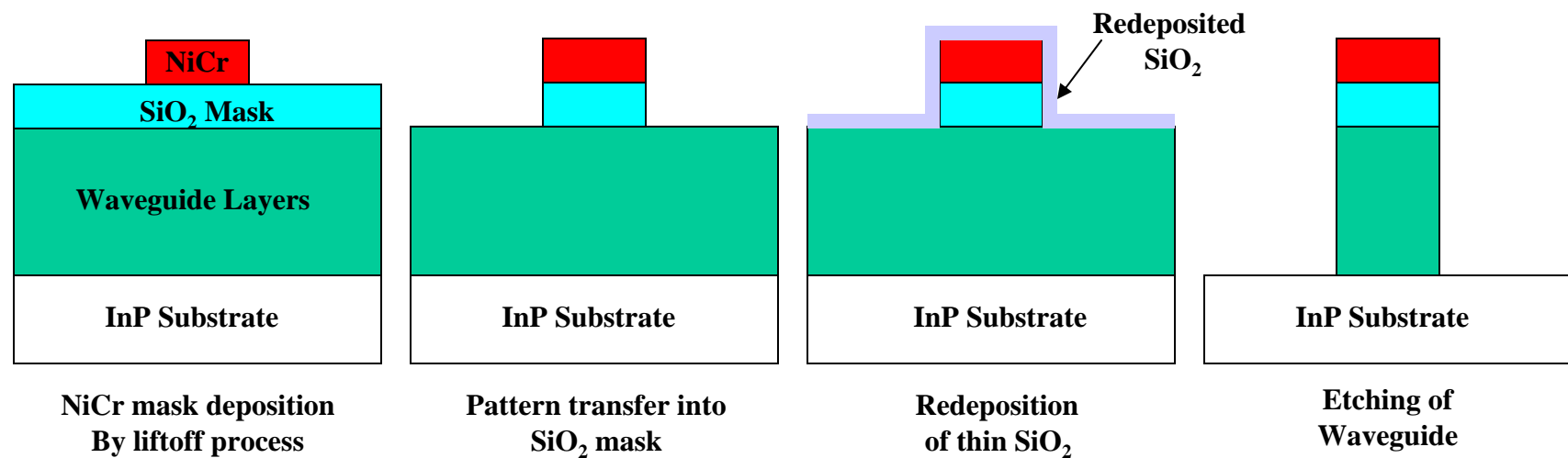


0.9 μm wide NiCr line
patterned by e-beam litho.

RMS roughness on mask : 2~3 nm

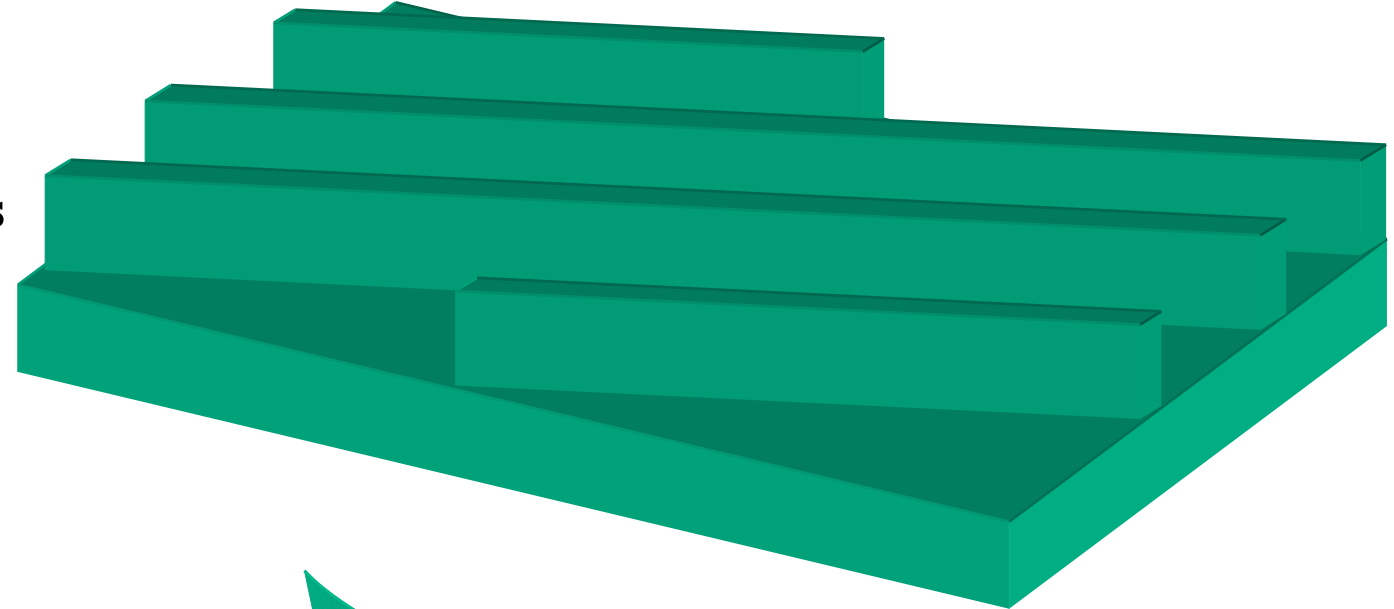
Methods to Reduce Sidewall Roughness of Waveguides

- Investigate e-beam resists and their thickness
 - In order to reduce line edge roughness of NiCr metal mask which is the first cause of sidewall roughness of waveguides
- Investigate the effect of re-deposited SiO_2 on top of NiCr metal mask after transferring patterns on the first SiO_2

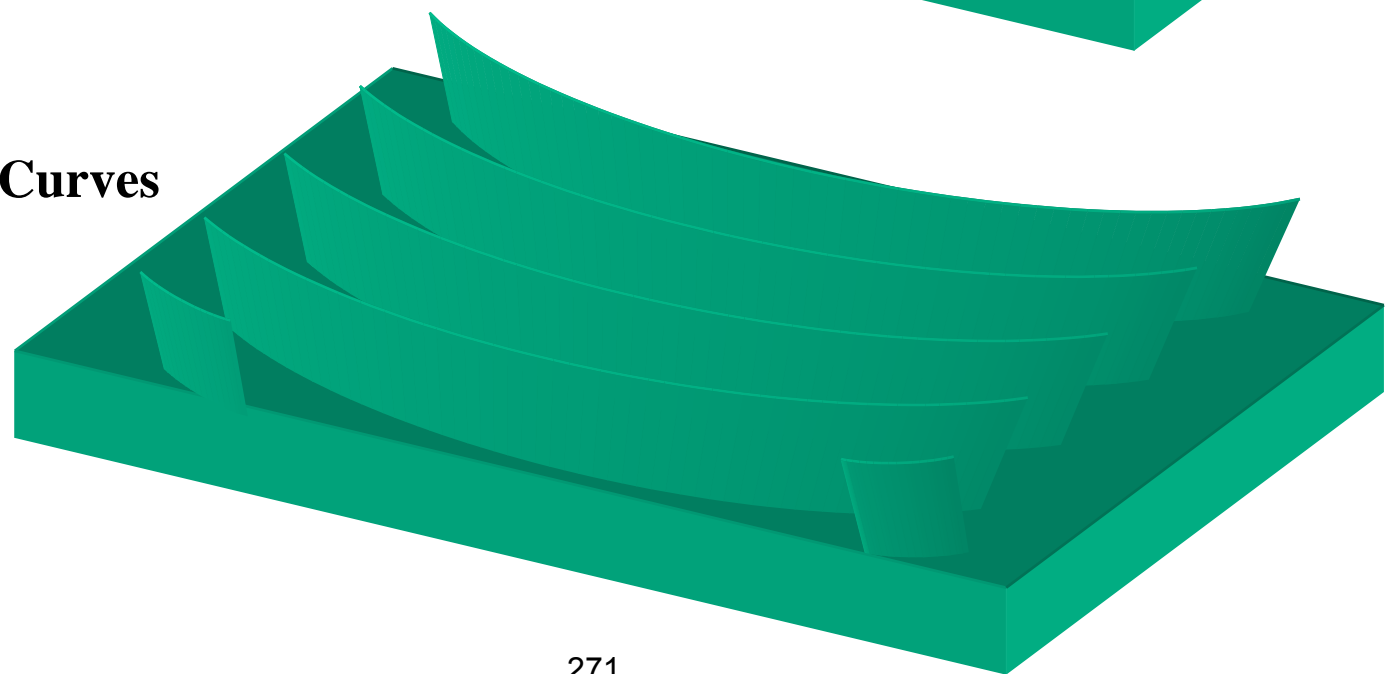


Test Pattern to assess pixellation of E-beam Lithography

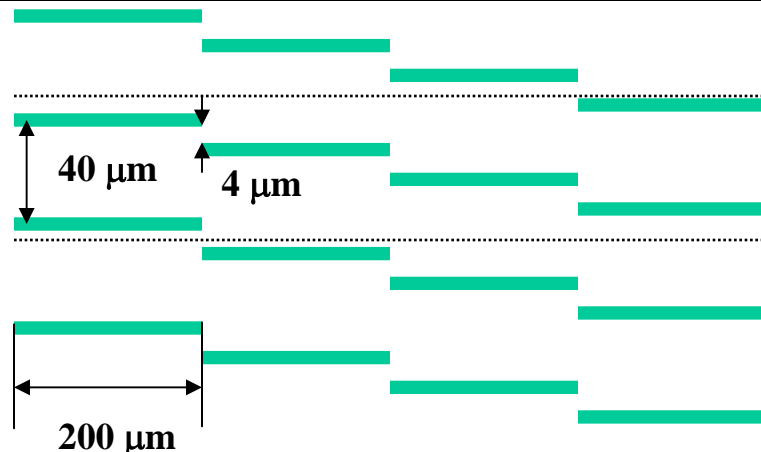
Angled Lines



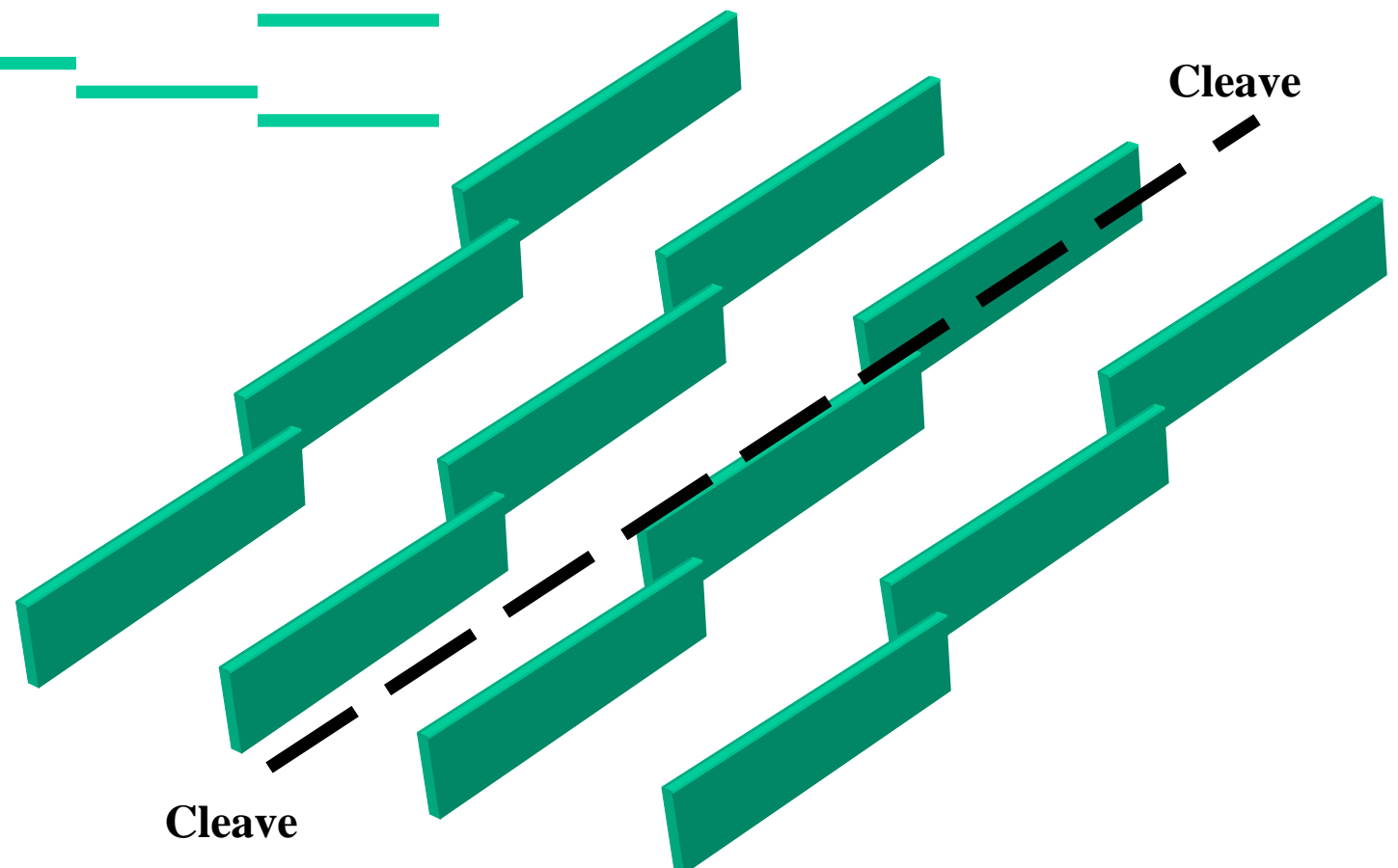
Nested Curves



AFM Test Structure for ICP-etched Sidewall Roughness Evaluation



Any cleavage results in a sample with a waveguide segment close to sample edge for easy access of AFM tip



Materials Development

Hooman Mohseni

Outline



- **Modeling**
 - QW Model
 - Device Model
- **Material Growth Characterization**
 - PL
 - X-ray
 - TEM
- **Modulator Characterization**
 - Planar Waveguides
 - Index-guided Waveguides
- **Agreement of Model and Measurement**
- **QW Optimization**
- **Growth Optimization**
- **Results**
- **Future Work**

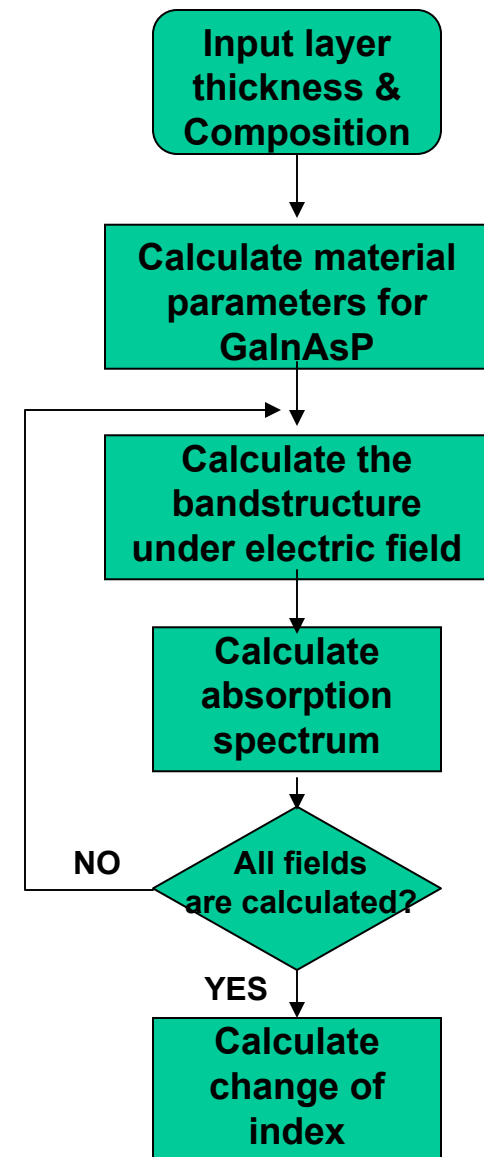
QW Model Overview



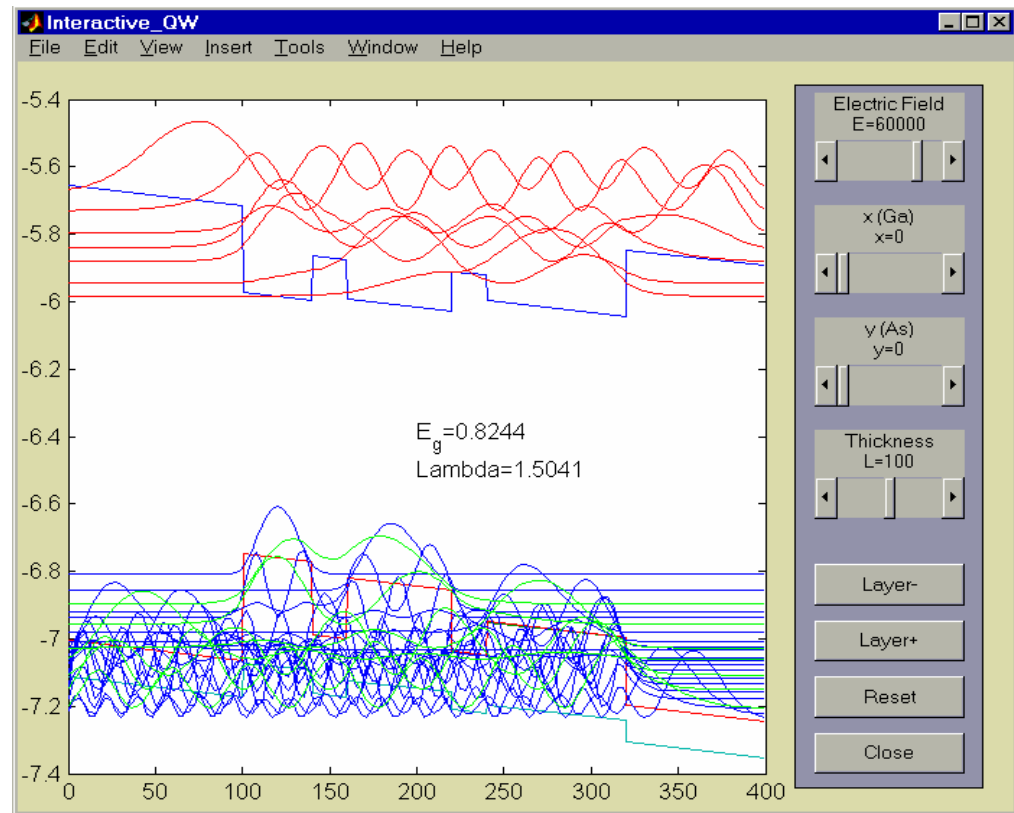
Existing Model's Capabilities:

- Calculates material parameters for GaInAsP layers (considers bowing and strain effects.)
- Calculates the band lineups* using Model Solid method (considers bowing and strain effect.)
- Calculates energy states and wavefunctions for electrons, light-holes, and heavy-holes using the effective mass method.
- Calculates optical absorption spectrum for the bulk and quantum wells (considers two-body and three-body effects*.)
- Calculates the change of index spectrum using Kramers-Kronig relation.

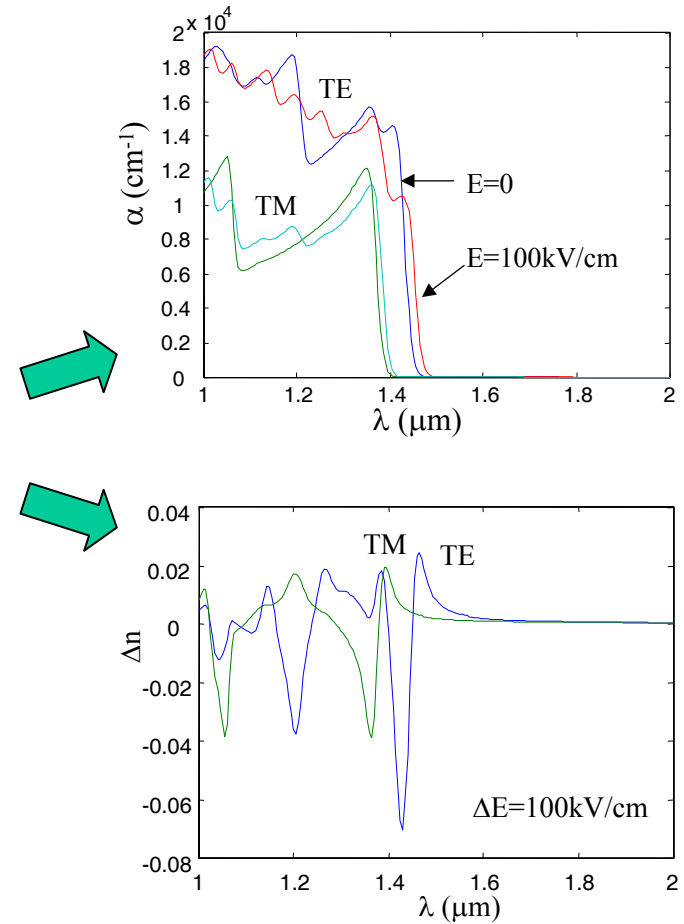
* Newly implemented



QW Model Examples



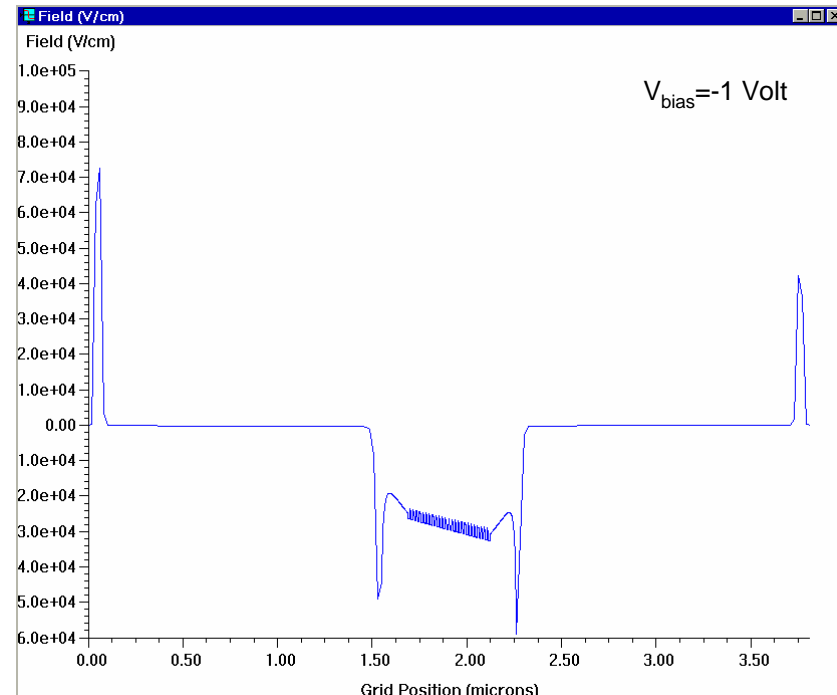
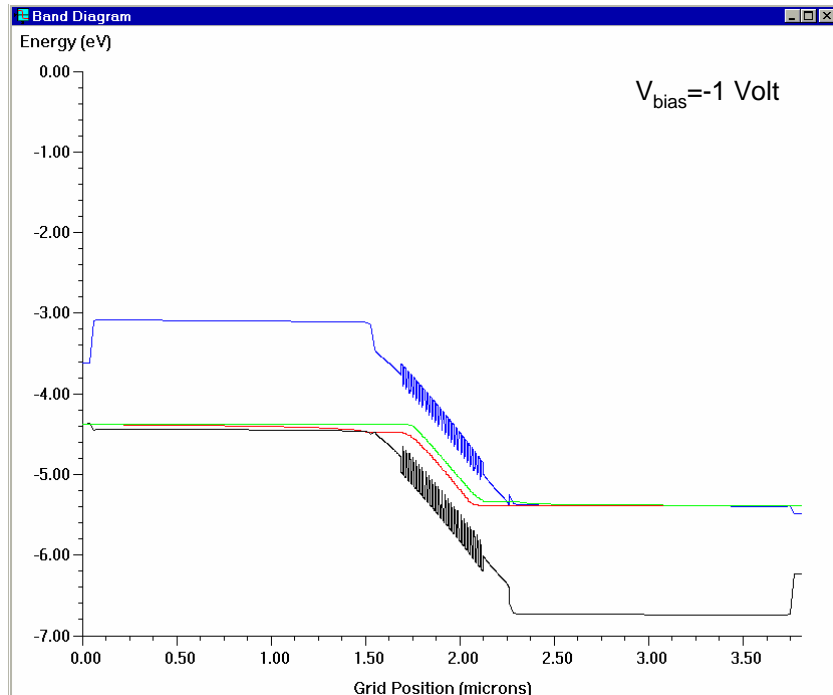
Wavefunction Calculation*



Index/Absorption Calculation

* Numerically optimized since last review: update time ~0.6 sec (typical)

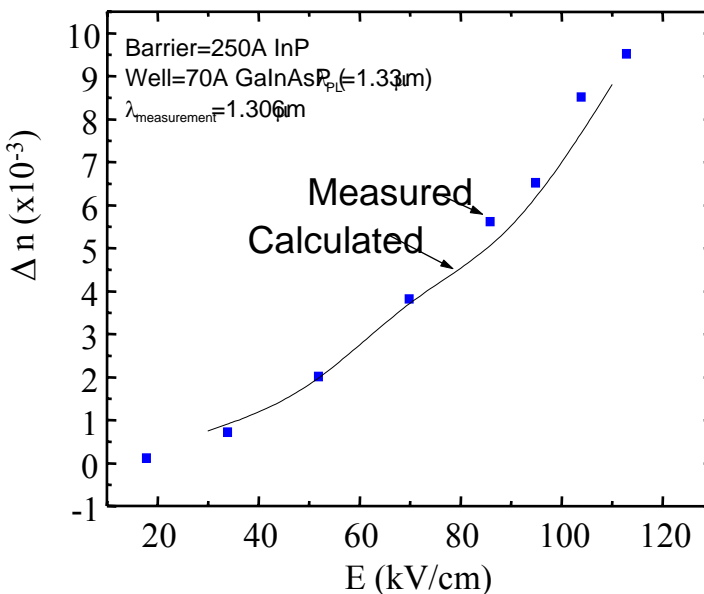
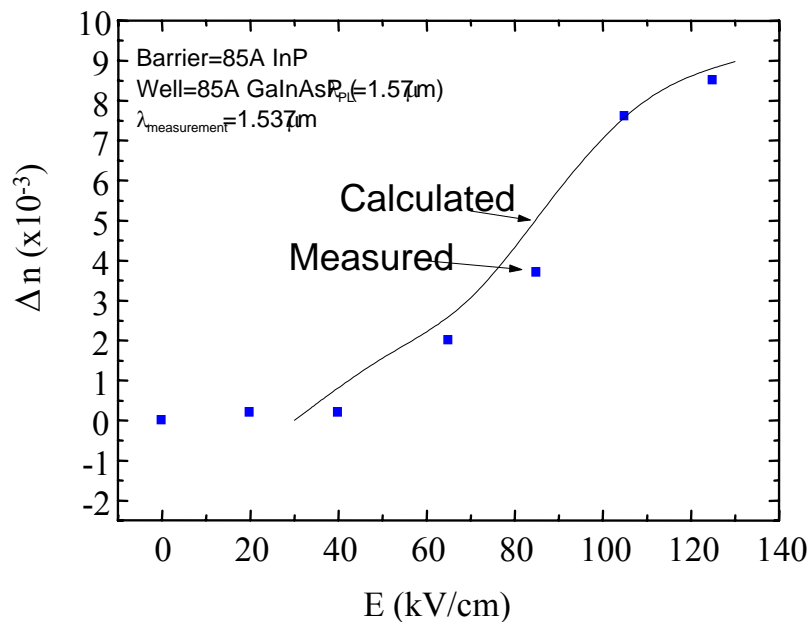
Device Model



- Energy Band Diagram of a sample device @ $V_{bias} = -1$ Volt

- Internal Electric Field of a sample device @ $V_{bias} = -1$ Volt

Comparison with the Published (Lucent) Results at $\lambda \sim 1.3 \mu\text{m}$ and $\lambda \sim 1.5 \mu\text{m}$



Calculated change of index versus measured change of index by Zucker et al^a around $1.3 \mu\text{m}$ and $1.5 \mu\text{m}$.

^a Appl. Phys. Lett. 54(1), p. 10 (1989)

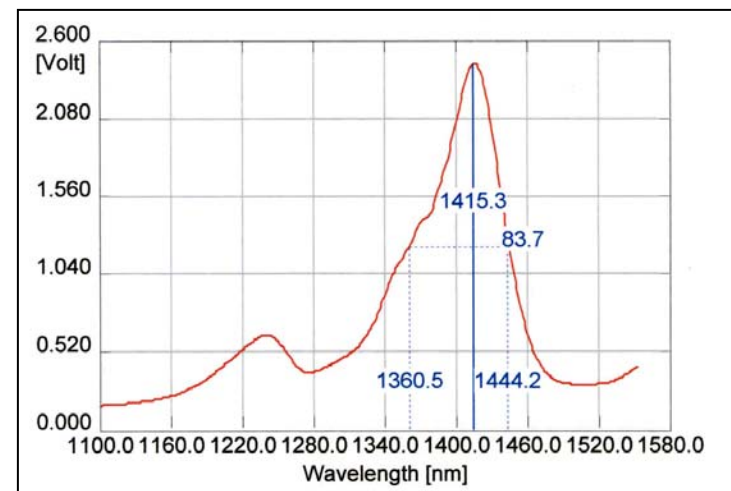
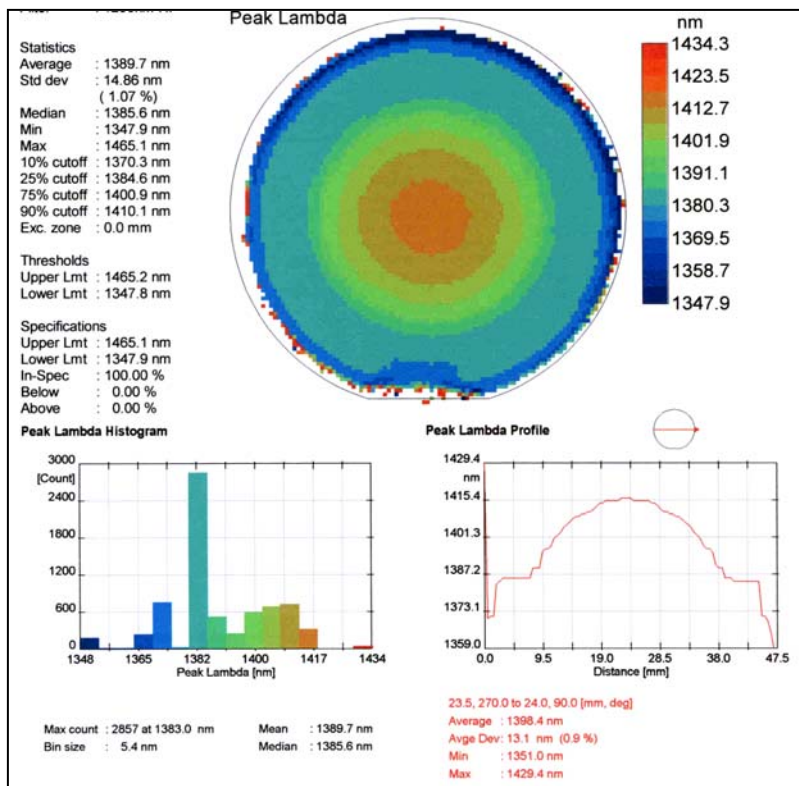
Material Characterization: Photoluminescence



As grown material can be “quite different” from the nominal structure!

Material characterization is essential for modeling and optimization

PL



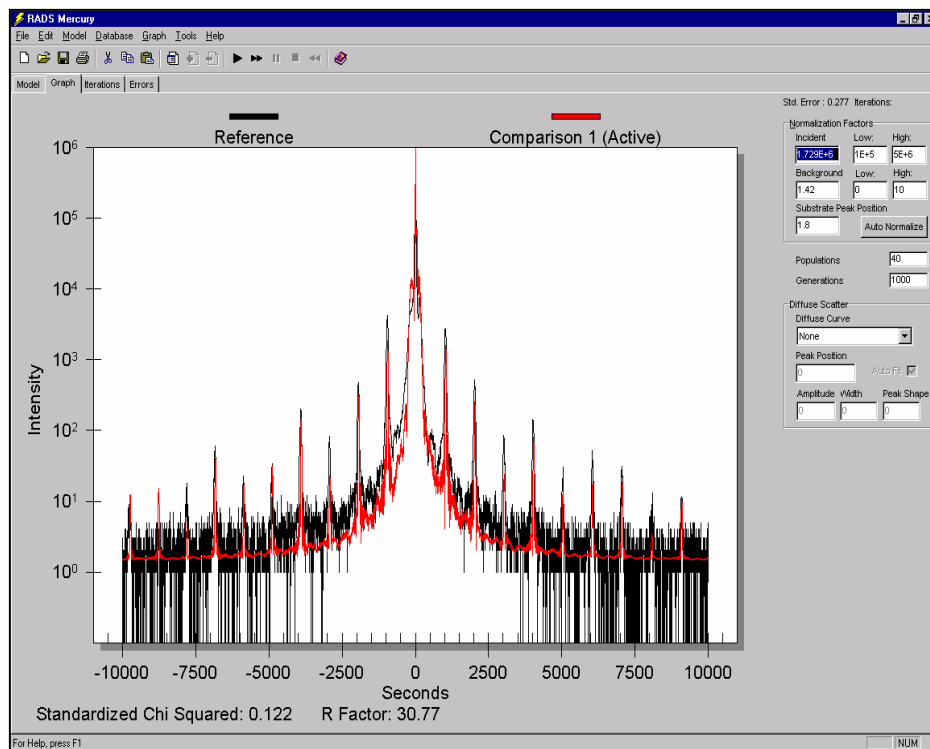
Photoluminescence (PL):

- Material quality (Intensity, FWHM)
- Effective Bandgap (Peak wavelength)
- Macroscopic uniformity (PL mapping)
- Growth calibration

Material Characterization: Double Crystal X-ray Diffraction



X-ray



	Thickness	Low	High	Material	X	Low	High	Y	Low	High	
107	500.00	500	500	In(x)Ga(1-x)As	▼	0.5320	0.532	0.532	0.0000	0	0
106	15000.00	15000	15000	InP	▼	0.0000	0	0	0.0000	0	0
105	1380.00	1380	1380	In(x)Ga(1-x)As(y)P(1-y)	▼	0.7507	0.7	0.8	0.5374	0.5	0.6
104	94.82	70	150	InP	▼	0.0000	0	0	0.0000	0	0
...	3.00	3	3	In(x)Ga(1-x)As(y)P(1-y)	▼	0.6116	0.1	0.95	0.4616	0.1	0.95
...	22.30	15	26	In(x)Ga(1-x)As	▼	0.5881	0.45	0.6	0.0000	0	0
5...	68.01	35	70	In(x)Ga(1-x)As(y)P(1-y)	▼	0.5800	0.56	0.7	0.8671	0.8	0.9
4	65.00	65	65	InP	▼	0.0000	0	0	0.0000	0	0
3	1380.00	1380	1380	In(x)Ga(1-x)As(y)P(1-y)	▼	0.7336	0.7	0.8	0.5973	0.5	0.6
2	15000.00	15000	15000	InP	▼	0.0000	0	0	0.0000	0	0
1	5000.00	5000	5000	In(x)Ga(1-x)As	▼	0.5320	0.532	0.532	0.0000	0	0
Sub.	00	00	0	InP	▼	0	0	0	0	0	0

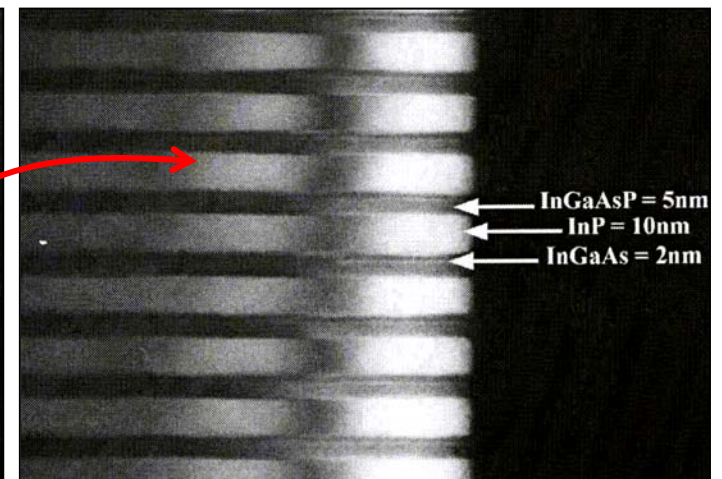
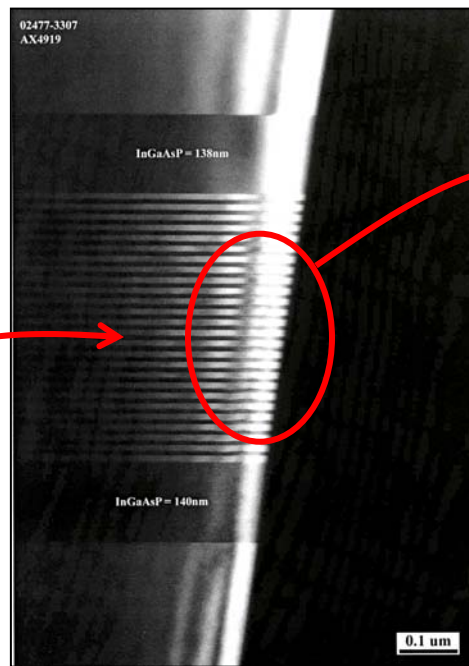
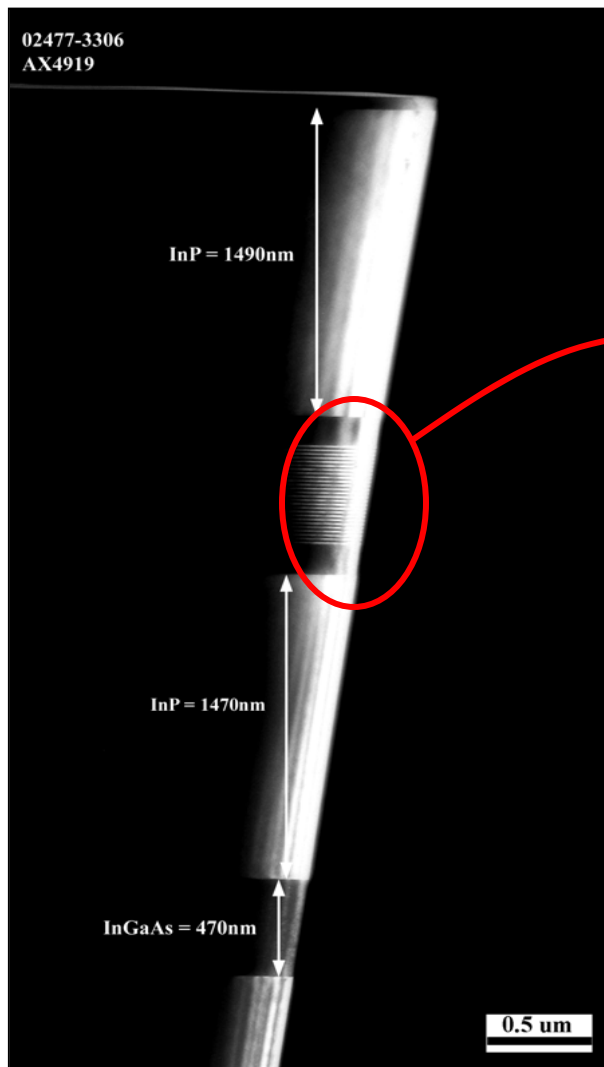
X-ray diffraction and simulation:

- Material quality (Intensity, FWHM)
- Strain (Relative peak position)
- Composition and thickness of the layers (Simulation, not always possible!)
- Growth calibration

Material Characterization: Transmission Electron Microscopy



TEM

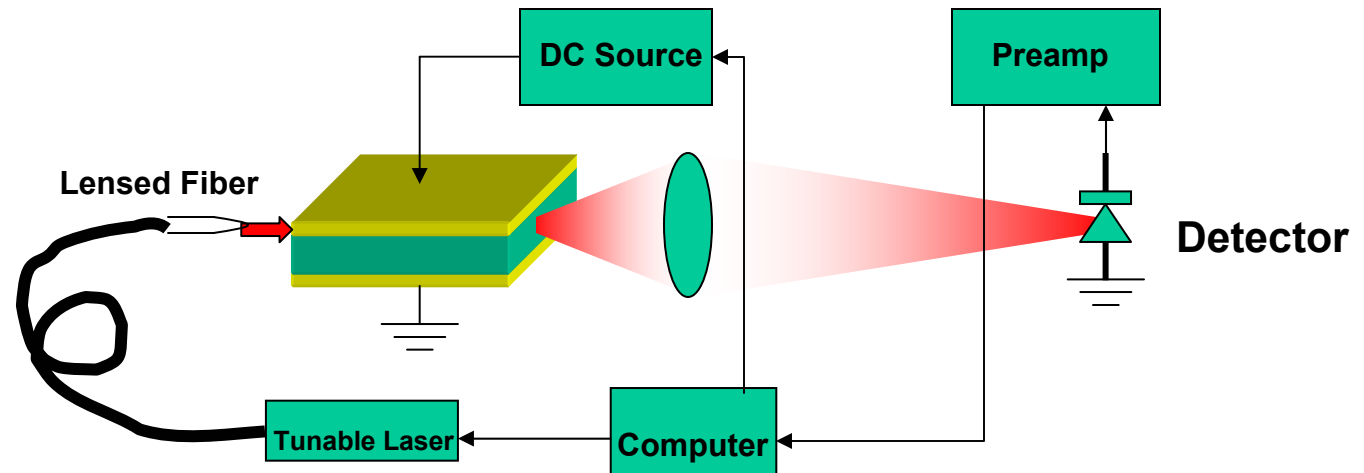


Transmission Electron Microscopy (TEM):

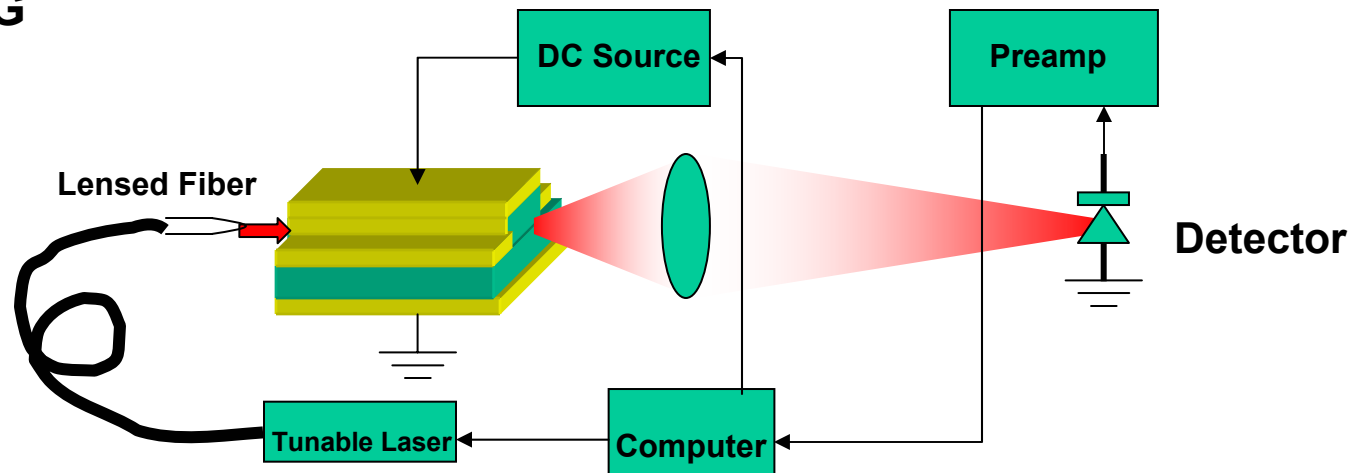
- Material thickness
- Microscopic uniformity
- Interface abruptness

Measurement Setup

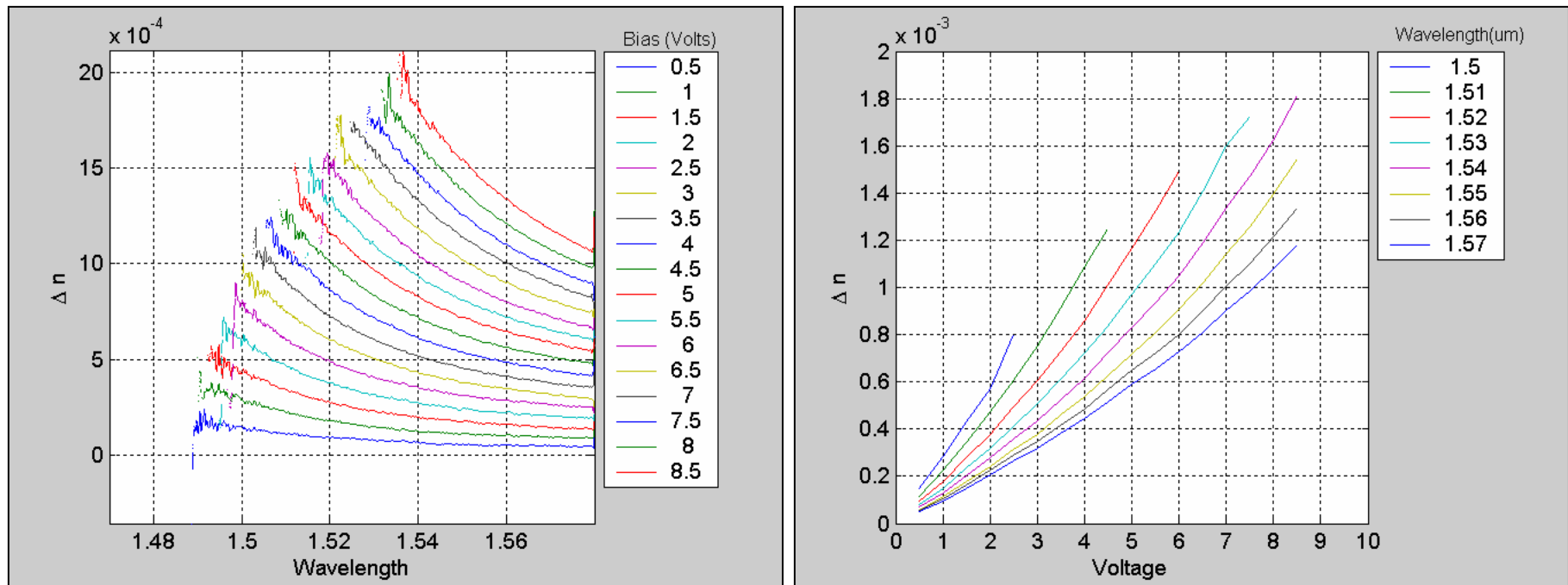
Planar WG



Index-Guided WG

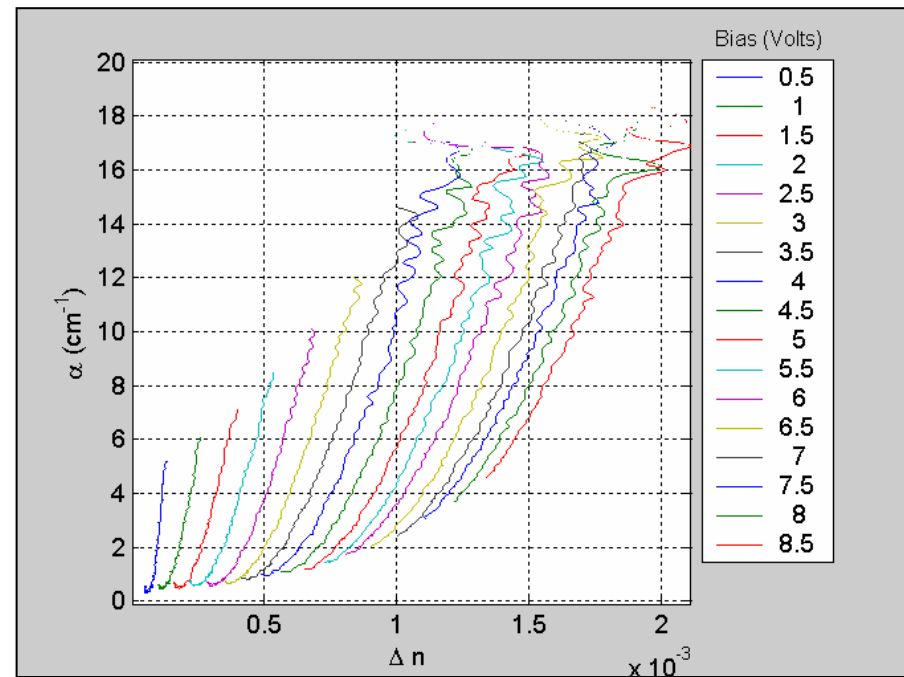
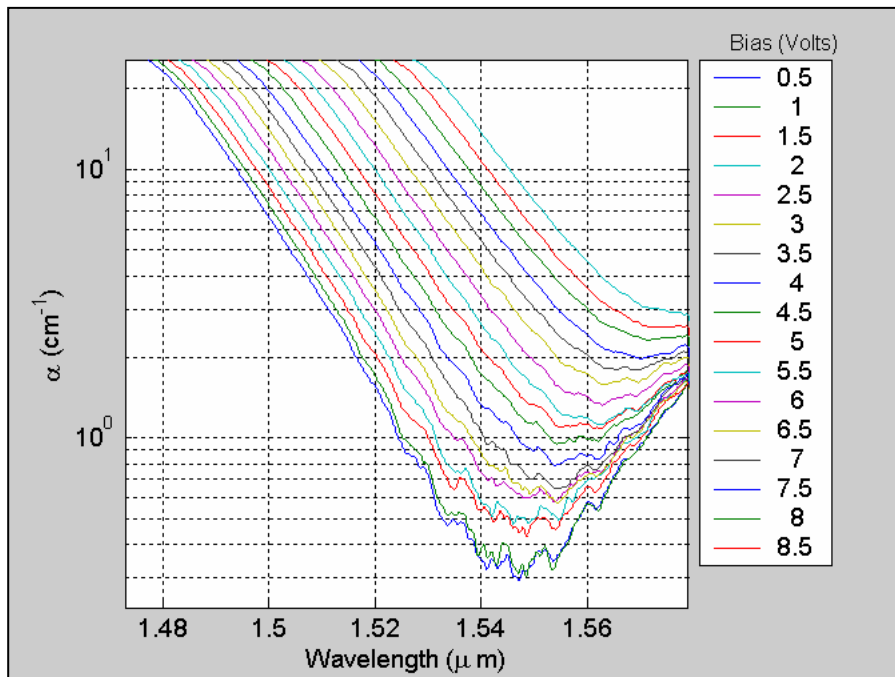
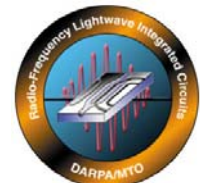


Typical Index vs. Voltage -or- vs. Wavelength



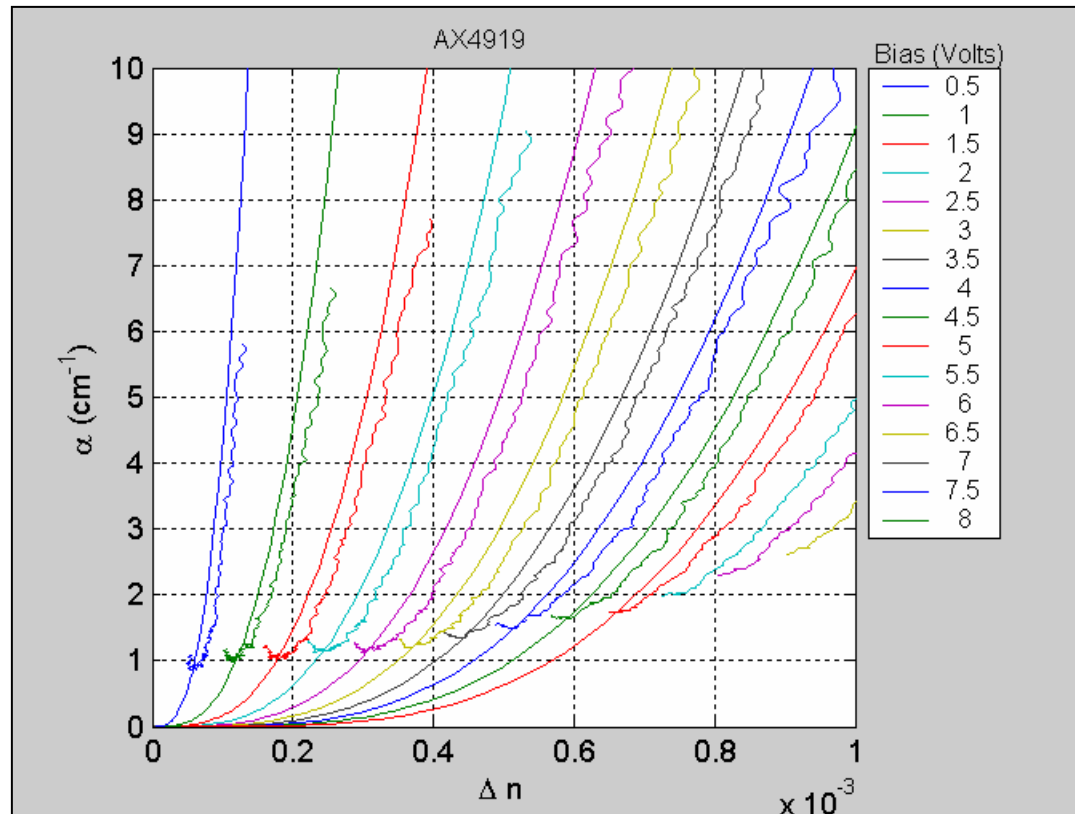
- Change of index versus wavelength for different voltage bias
- Change of index versus voltage bias for different wavelengths

Typical Absorption vs. Wavelength -or- vs. Index



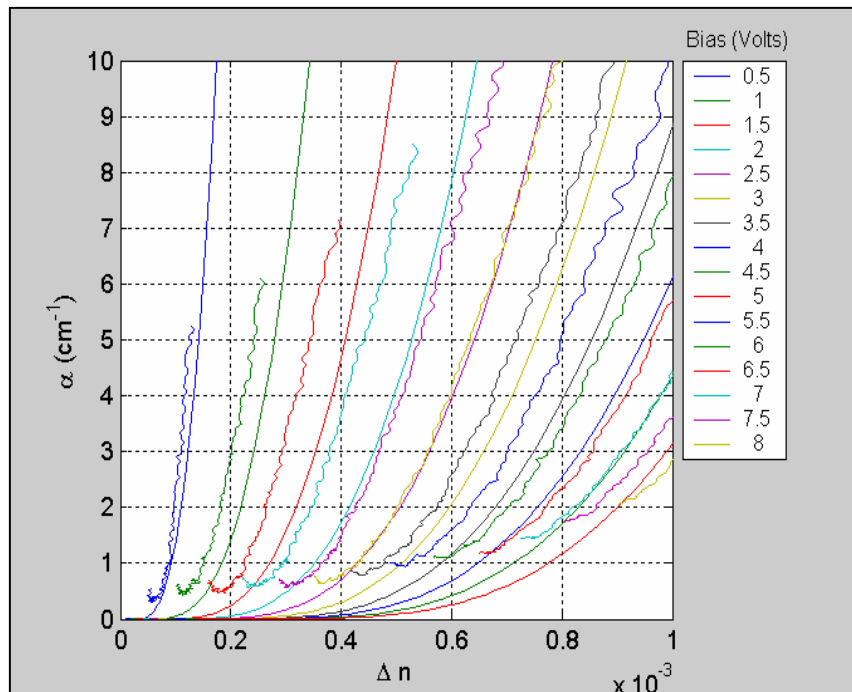
- Loss versus wavelength for different voltage bias
- Loss versus change of index for different voltage bias

Agreement of Modeling and Measurement

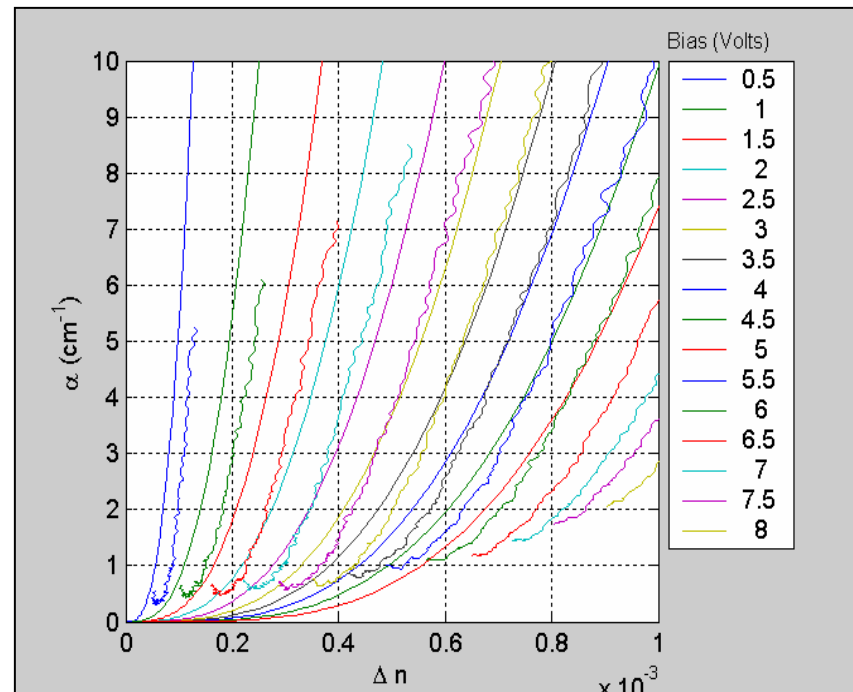


- **Adjustable parameters for the model:**
 - Structure (from x-ray simulation)
 - Linewidth broadening and band edge (from measured loss)
 - Internal field (from device modeling)
 - No other adjustable Parameter

Dependence of Modeled Parameters on Adjustable Parameters



- Modeled without x-ray simulation

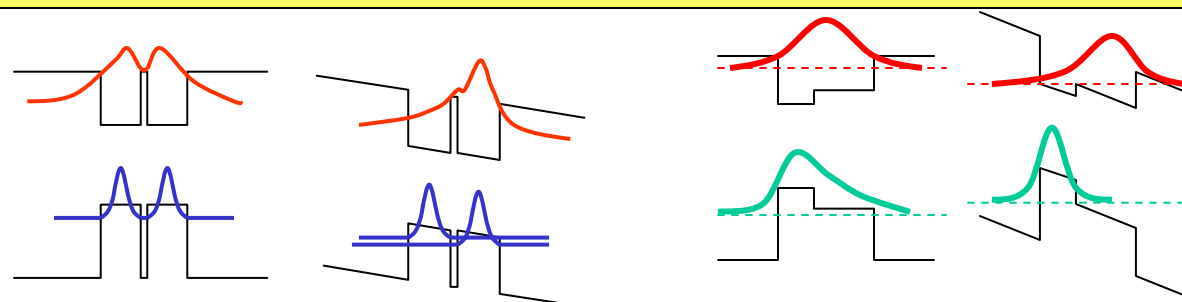


- Modeled without field-dependent exciton broadening

QW Optimization



- Theoretically, coupled quantum wells show significantly higher sensitivities than the regular quantum wells.
- However, we chose the new class of two and three-step quantum wells for practical reasons:

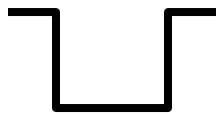
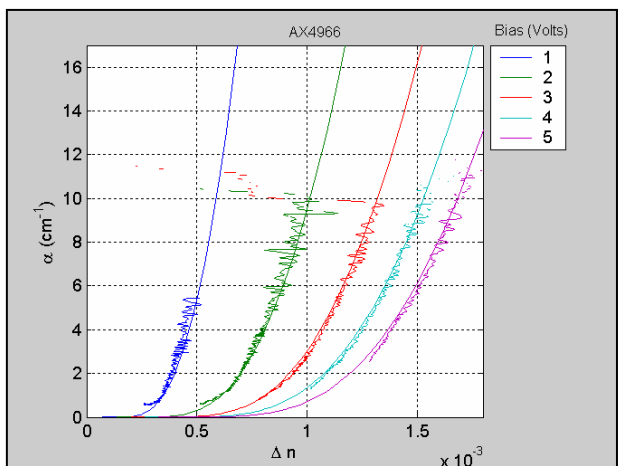
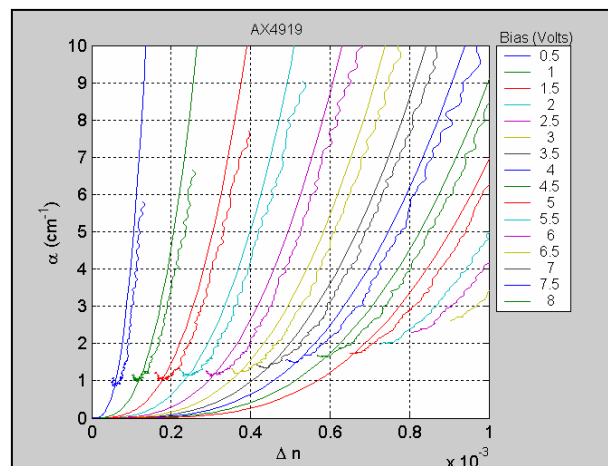
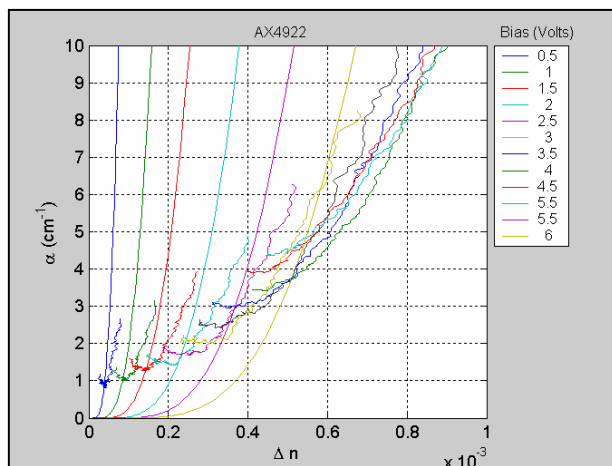


- Coupled QW without and with external electric field
- Enhancement due to the resonant tunneling of electrons
- Step QW without and with external electric field
- Enhancement due to the “bond” to “leaky” mode transition of holes

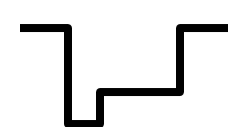
- **Advantages of Step QWs Over Coupled QWs**
 - Less sensitive to interface abruptness
 - Does not need very thin layers
 - Takes advantage of material systems with high valence band offset (e.g. GaInAsP)

QW Optimization

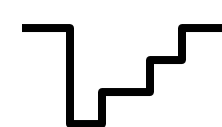
Measured and simulated results for two-step and three-step QWs compared to a sample with regular quantum well design.



Regular QW



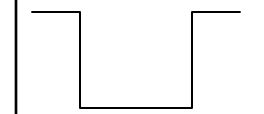
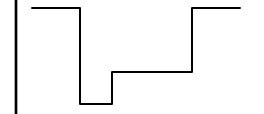
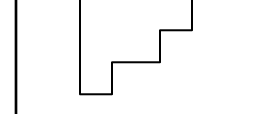
Two-step QW



Three-step QW

QW Optimization Summary



Sample #	$\Delta n/\Delta V @ \alpha=1 \text{ cm}^{-1}$	$V_\pi L$ (V.mm) (Push-Pull)	DC Bias (V)	Type	Potential Profile
AX4922	$\sim 1 \times 10^{-4}$	~ 3.8	1	Regular QW	
AX4919	$\sim 1.3 \times 10^{-4}$	~ 2.9	1	2-step Asym.	
AX4966	$\sim 3 \times 10^{-4}$	~ 1.29	1	3-step Asym.	

Note: Lincoln Lab showed $V_\pi L=5.8$ V.mm @ $\alpha=1 \text{ cm}^{-1}$ @ $V_{DC}=6$ Volts from regular QWs in the 2001 R-FLICS review.



Goals:

- Improve growth uniformity
- Reduce excitonic broadening

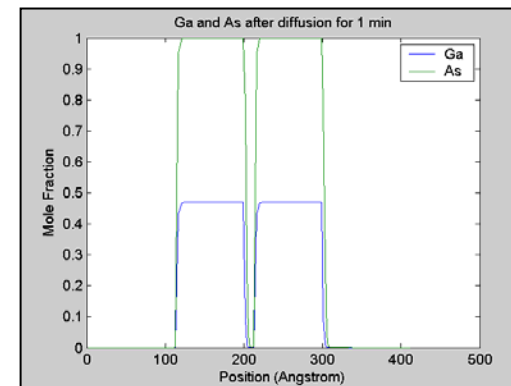
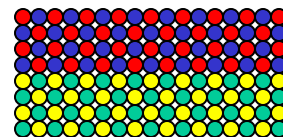
Approaches:

- Reduce growth temperature to reduce interdiffusion
- Use all-ternary material system to reduce inhomogenous broadening

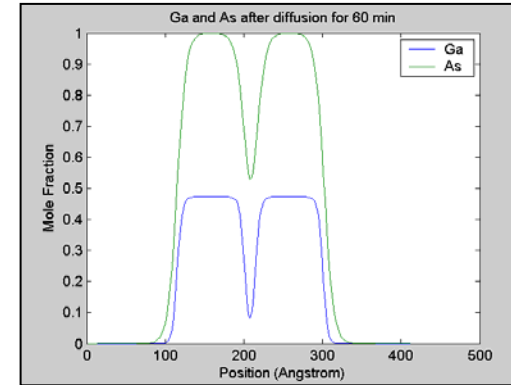
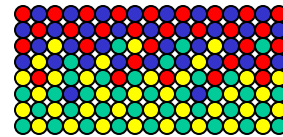
Interdiffusion Modeling

Our modeling^a shows that interdiffusion can severely deform the potential profile of the quantum wells at the usual growth temperature of $\sim 650^{\circ}\text{C}$

Crystal interface as grown



Crystal interface after interdiffusion for 60 min @ 650°C



Schematic

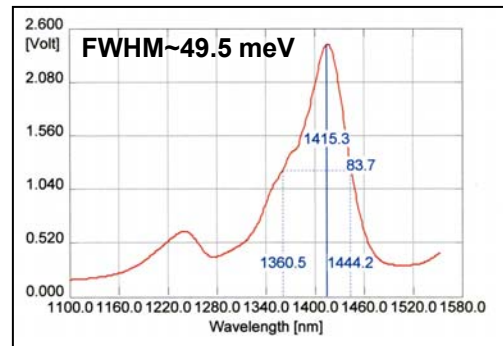
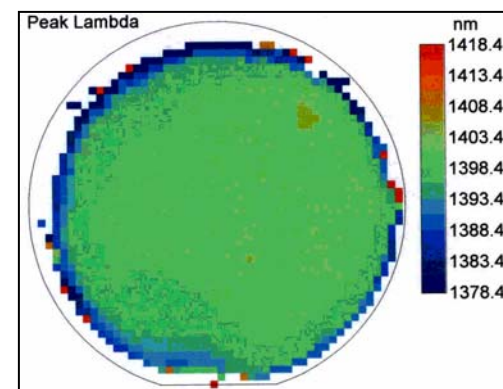
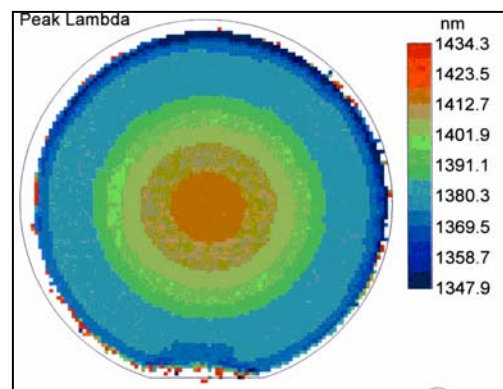
Composition

Band Diagram

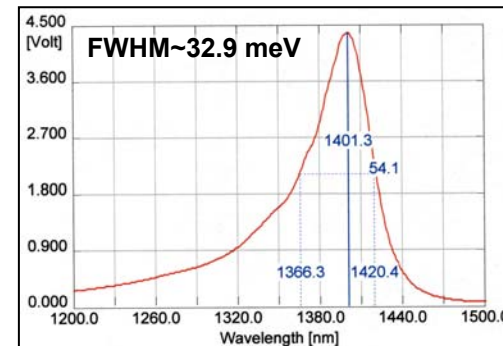
a) Based on the interdiffusion data from: Bursik et al, J. of Appl. Phys. **91**, 9613 (2002)

Low Temperature strain compensated InAsP/GaInP

Low temperature strain compensated InAsP/GaInP structures show excellent uniformity and narrow linewidth due to the reduce interdiffusion and elimination of quaternary layers.



PL of a regular MQW using quaternary layers grown at ~655°C



PL of a MQW structure using strain compensated ternary layers grown at ~550°C

Future Work



- **Further optimization of the step QWs**
- **Add program codes for local search of optimum layer composition and thickness**
- **Design structures based on all-ternary layers
(InAsP/GaInP)**

Device Design & Test

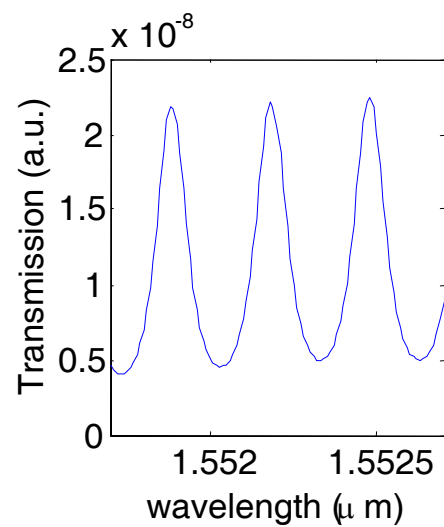
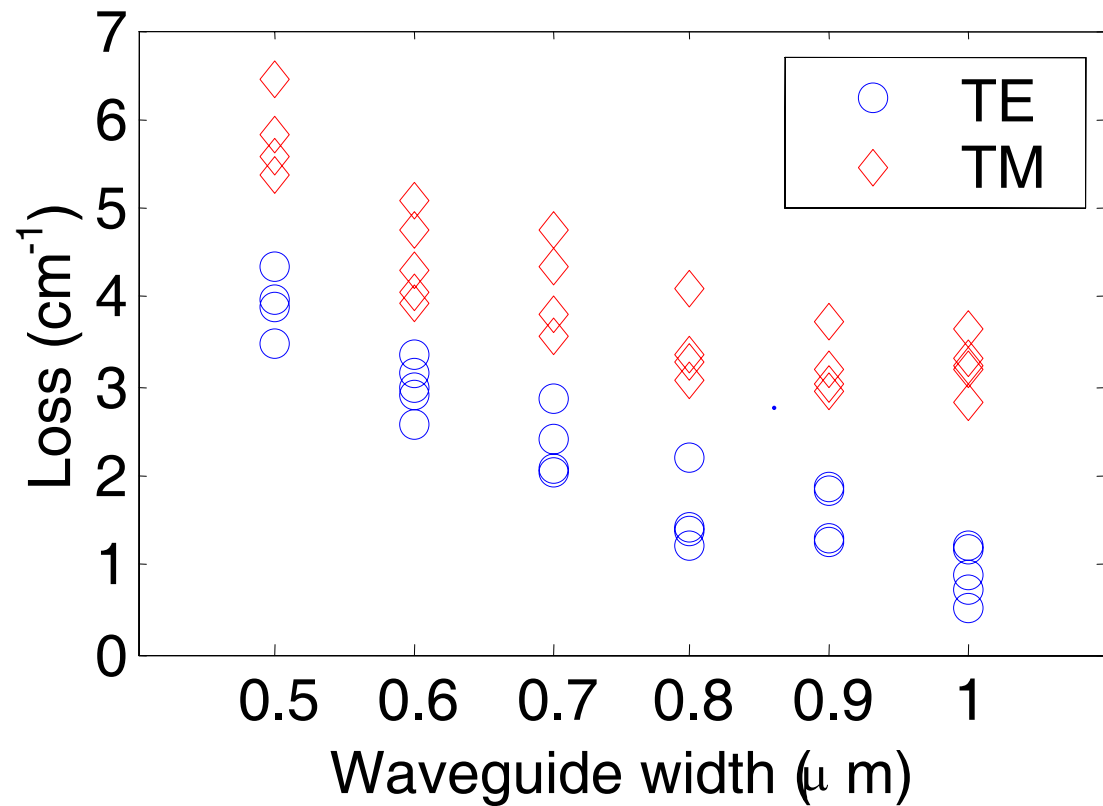
Martin Kwakernaak

Device Design & Test



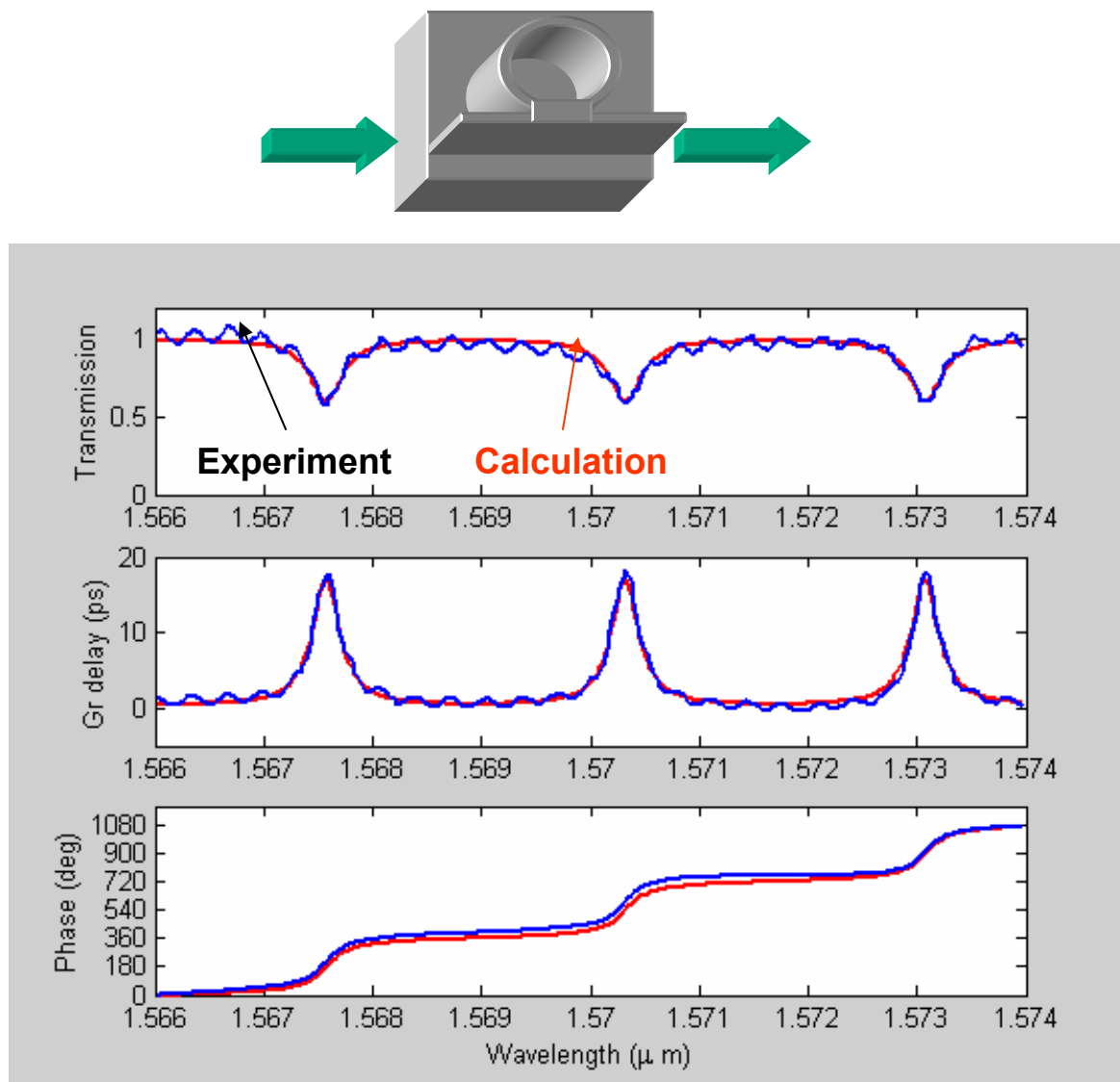
- **Passive device results**
 - Low loss waveguides
 - Low loss ring resonator
- **Advantage of ring resonator-modulator**
 - Modulation gain
 - Frequency Response of ring modulator
- **Interferometer with ring resonator**
- **Electro-optic measurements:**
 - DC-measurements
 - RF-measurements
- **Summary/Outlook**

Low Loss Waveguides



4 cm^{-1} for 0.5 μm width x 4 μm depth waveguide!

Low Loss Ring-Resonator



Waveguide width: 0.9mm.

Circumference: 250 mm.

MMI length: 42mm.

Loss: 8.5%

**$\rightarrow 3.5\text{cm}^{-1}$ effective loss
(includes coupler loss).**

Coupling: 50%.

18ps group delay.

$\rightarrow 6$ roundtrips.

**Optical bandwidth: 44
GHz.**

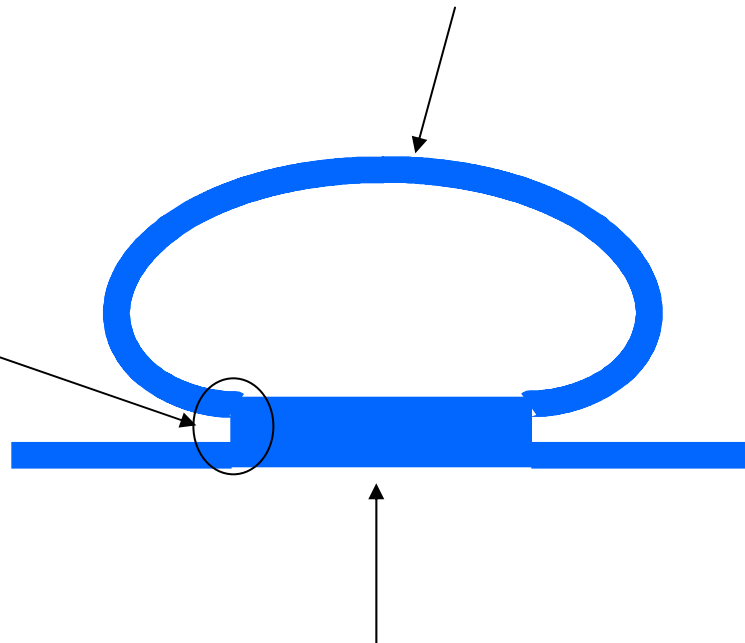
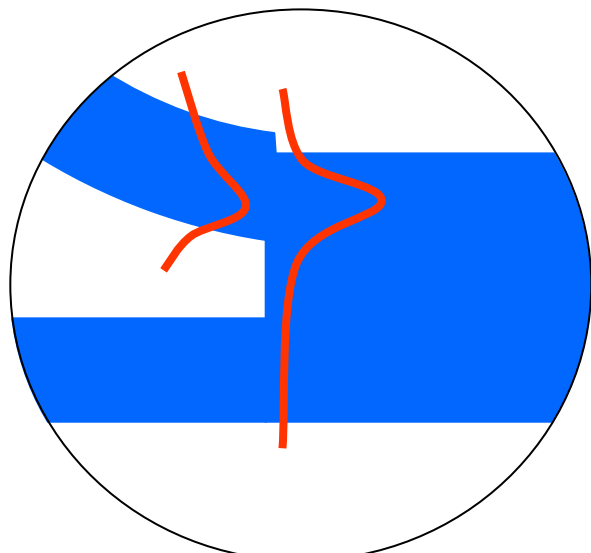
**($\rightarrow 22$ GHz modulator
bandwidth) .**

Ring Resonator Design

Offset at junction.

**Optimized matching of the field in the bend
and the MMI**

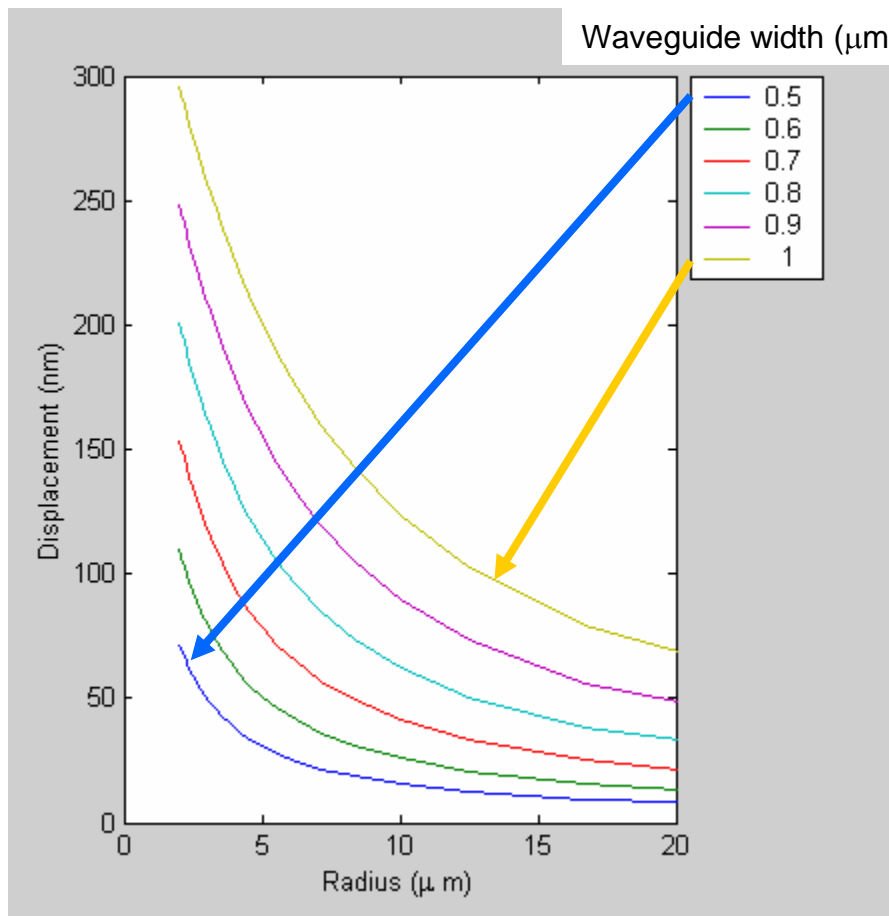
→ No mode conversion / loss



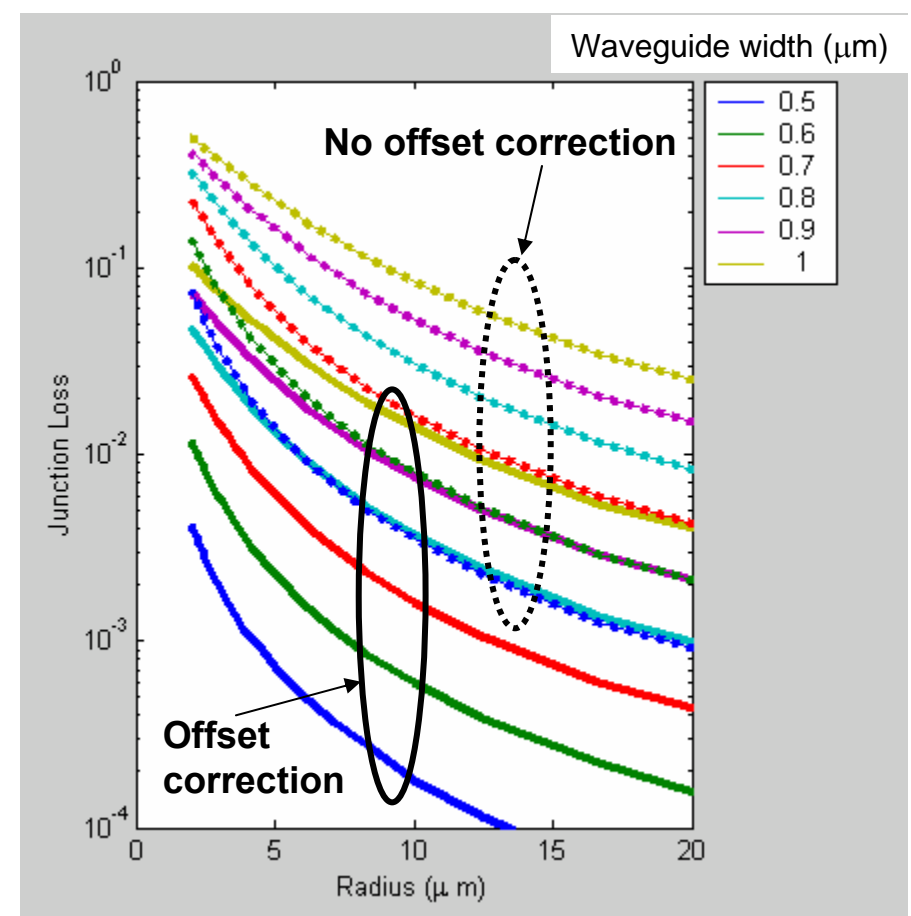
**MMI-coupler:
50% coupling (reproducible)**

Junction offset

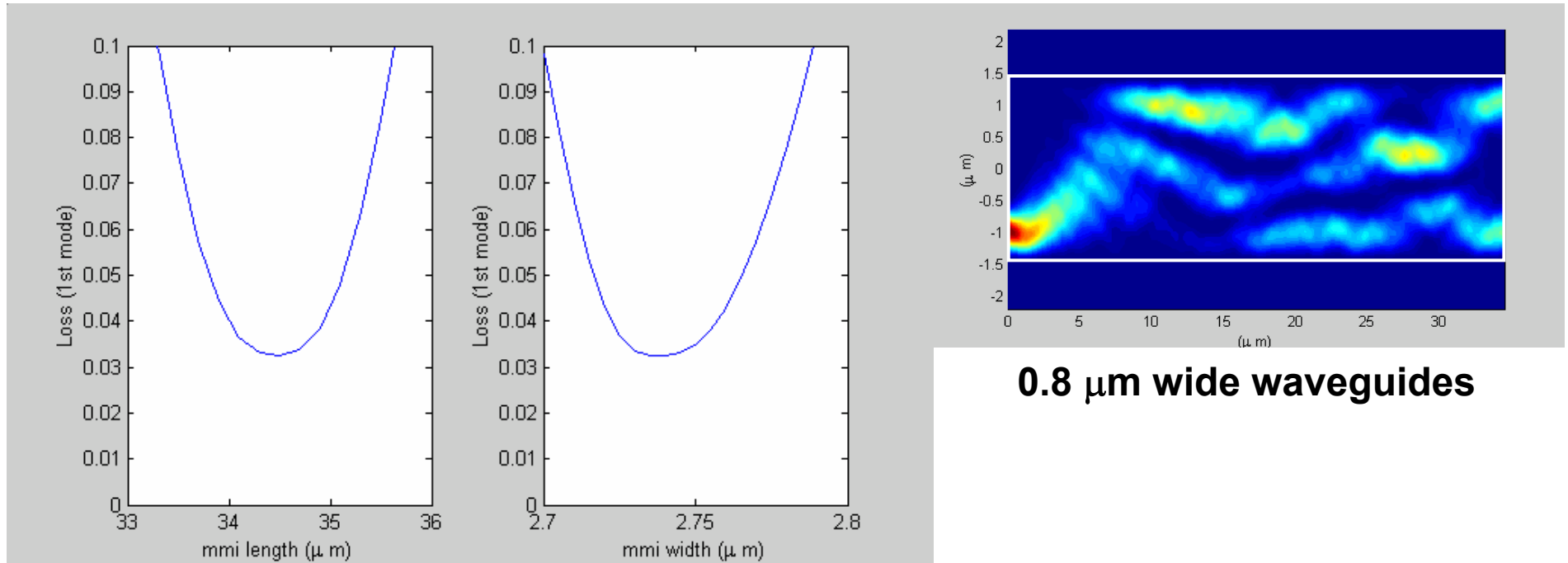
Mode displacement



Junction loss



MMI-Loss and Tolerances

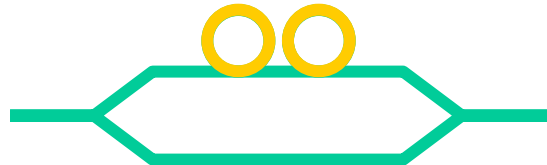


0.8 μm wide waveguides

Tight tolerances for low loss operation

→ ~30nm width tolerance

Modulator Gain of Ring Resonator Modulator



- **Gain =**
$$\frac{(\text{transmission}) / V_{\pi}^2 \text{ of the ring modulator}}{(\text{transmission}) / V_{\pi}^2 \text{ of a loss-less Mach-Zehnder modulator}}$$
 of equal electrode length



- **(transmission) / V_{π}^2** determines the noise figure of an analog link
- **Excess losses reduce the gain**
- **Qualifies the modulator structure (not the material)**

Frequency Response of a Ring Modulator (small signal)

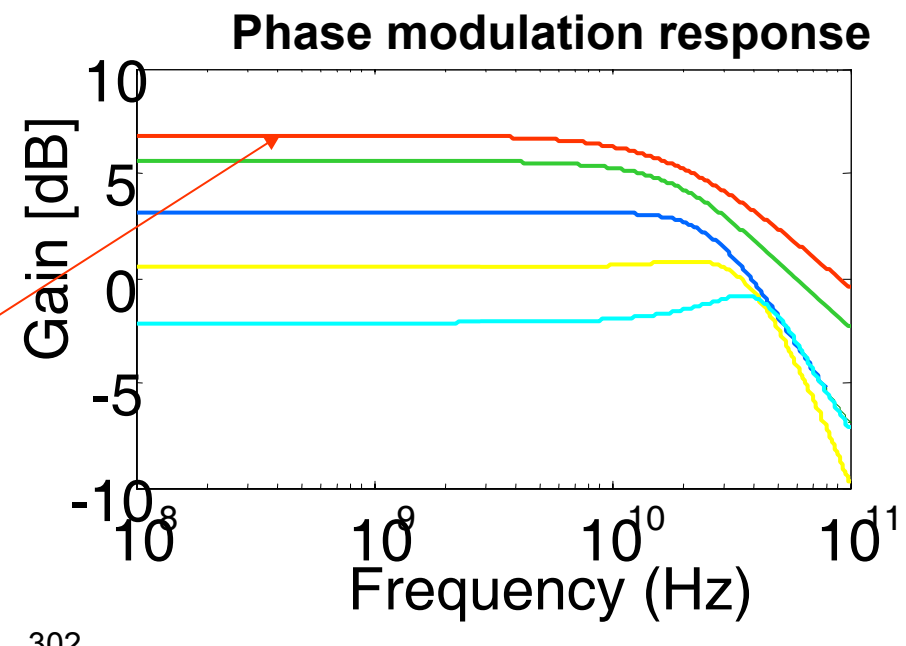
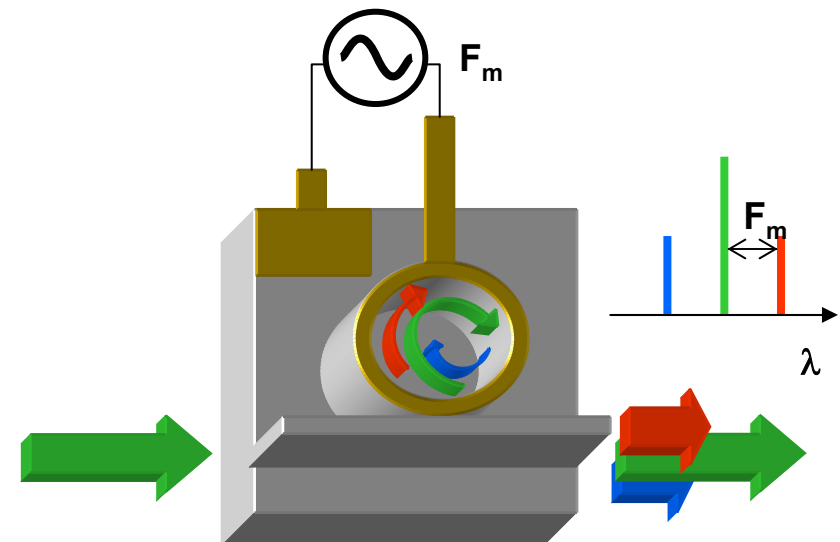
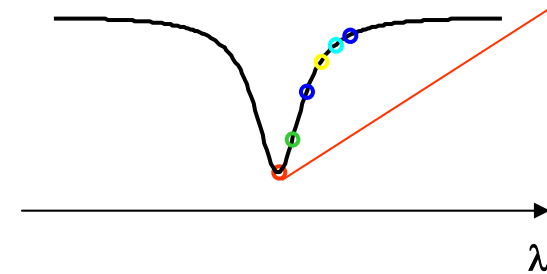


Calculation of modulation response:

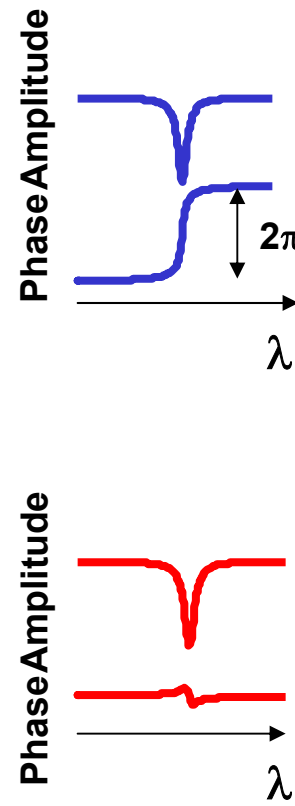
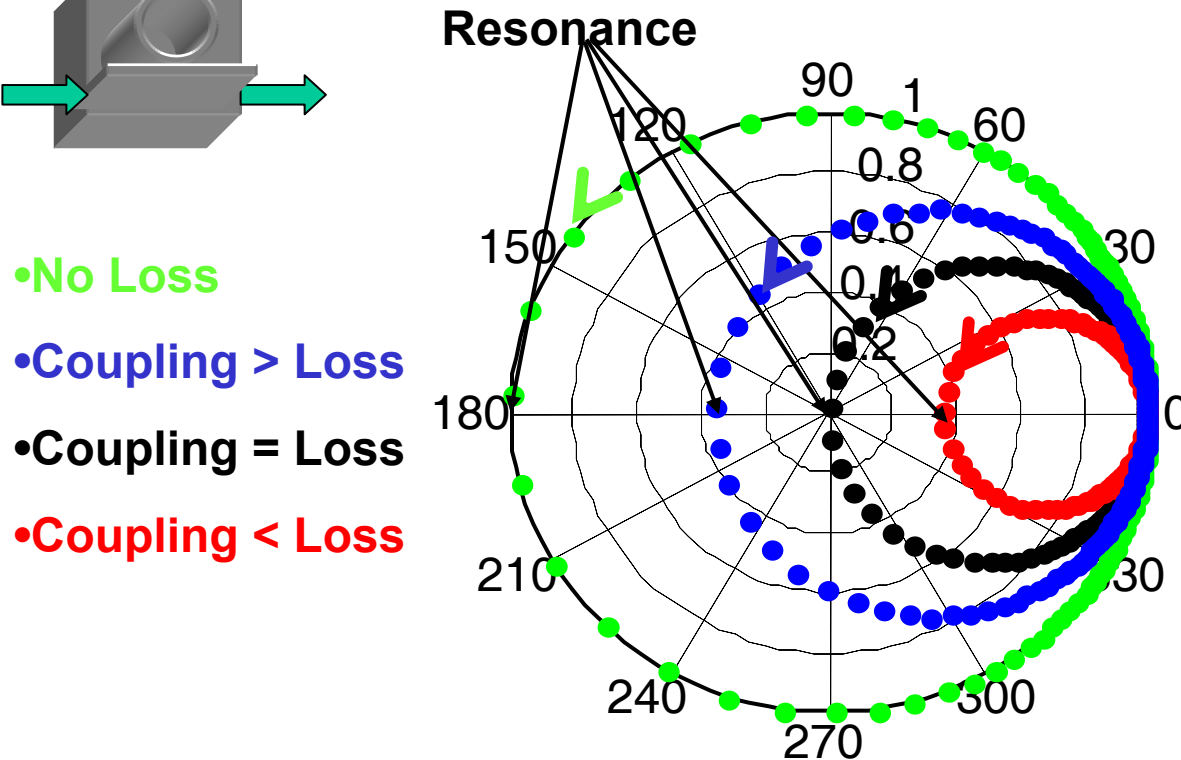
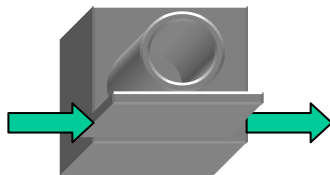
- **3 Wavelength:**
 - Input wavelength and
 - two closest sidebands
- **Cold cavity resonator equations** for each wavelength
- **Equations for the coupling of the 3 components in the phase modulated ring.**

→ **Output components:**
amplitude and phase

- **Calculation of Phase/Amplitude modulation**

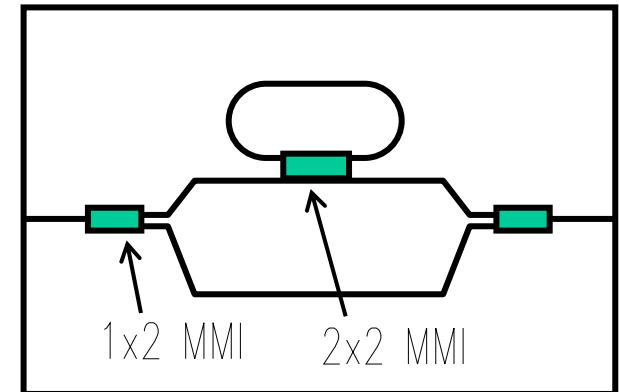
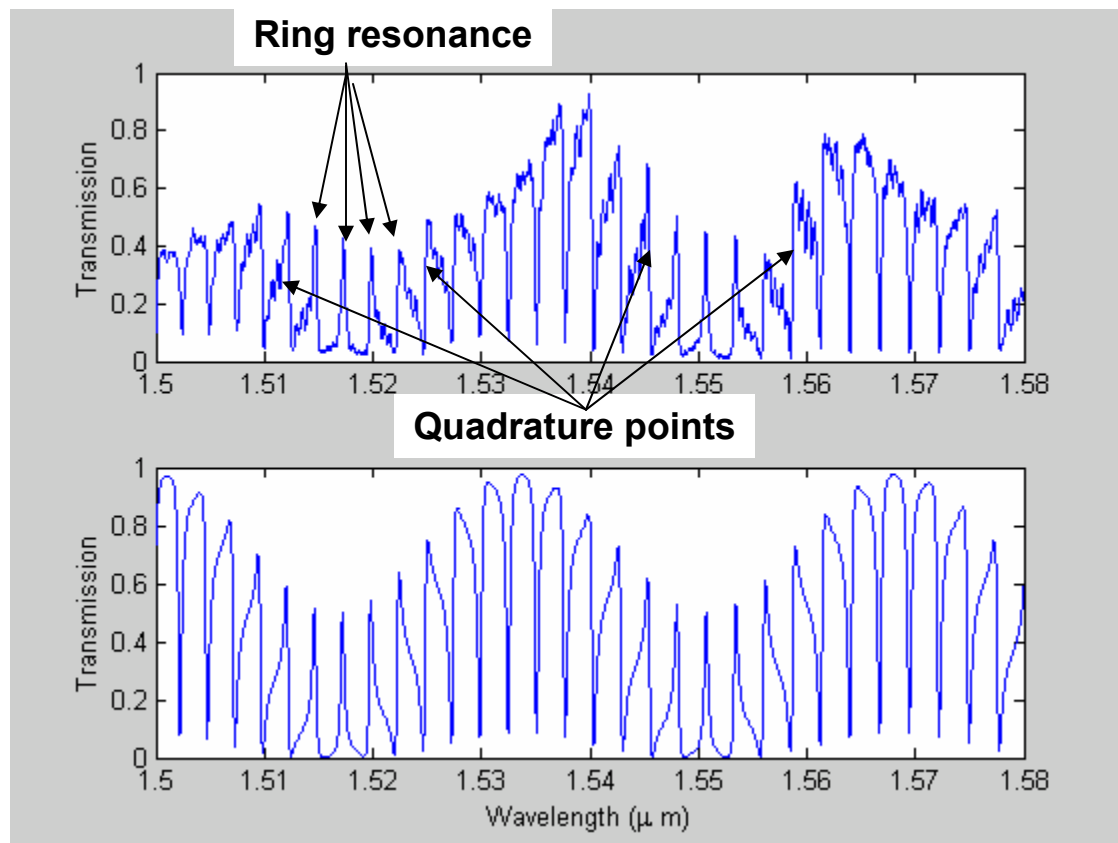


Ring Transmission, Complex Space



An interferometer with ring resonators needs to be in quadrature (90 deg phase) at the ring resonance.

Asymmetric MZI with MMI-Coupled Ring Resonator



Waveguide width: $0.8\mu\text{m}$

MMI-length: $34.5\mu\text{m}$

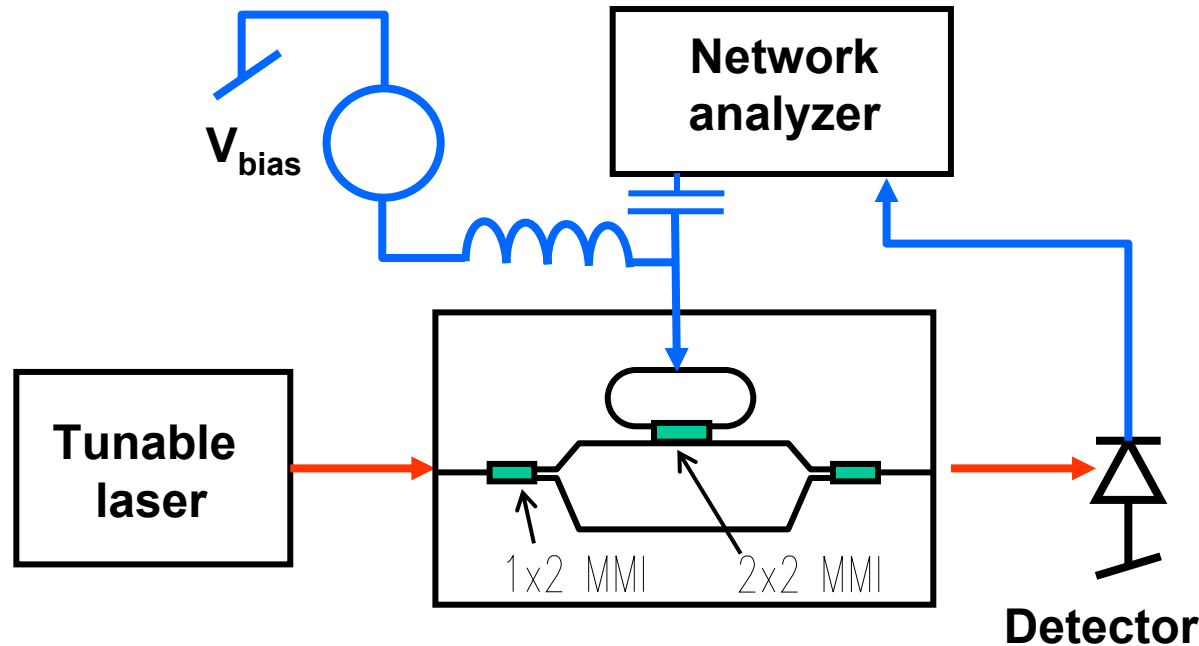
Ring circumference: $250\mu\text{m}$

Ring loss: 15%

Coupling 50%

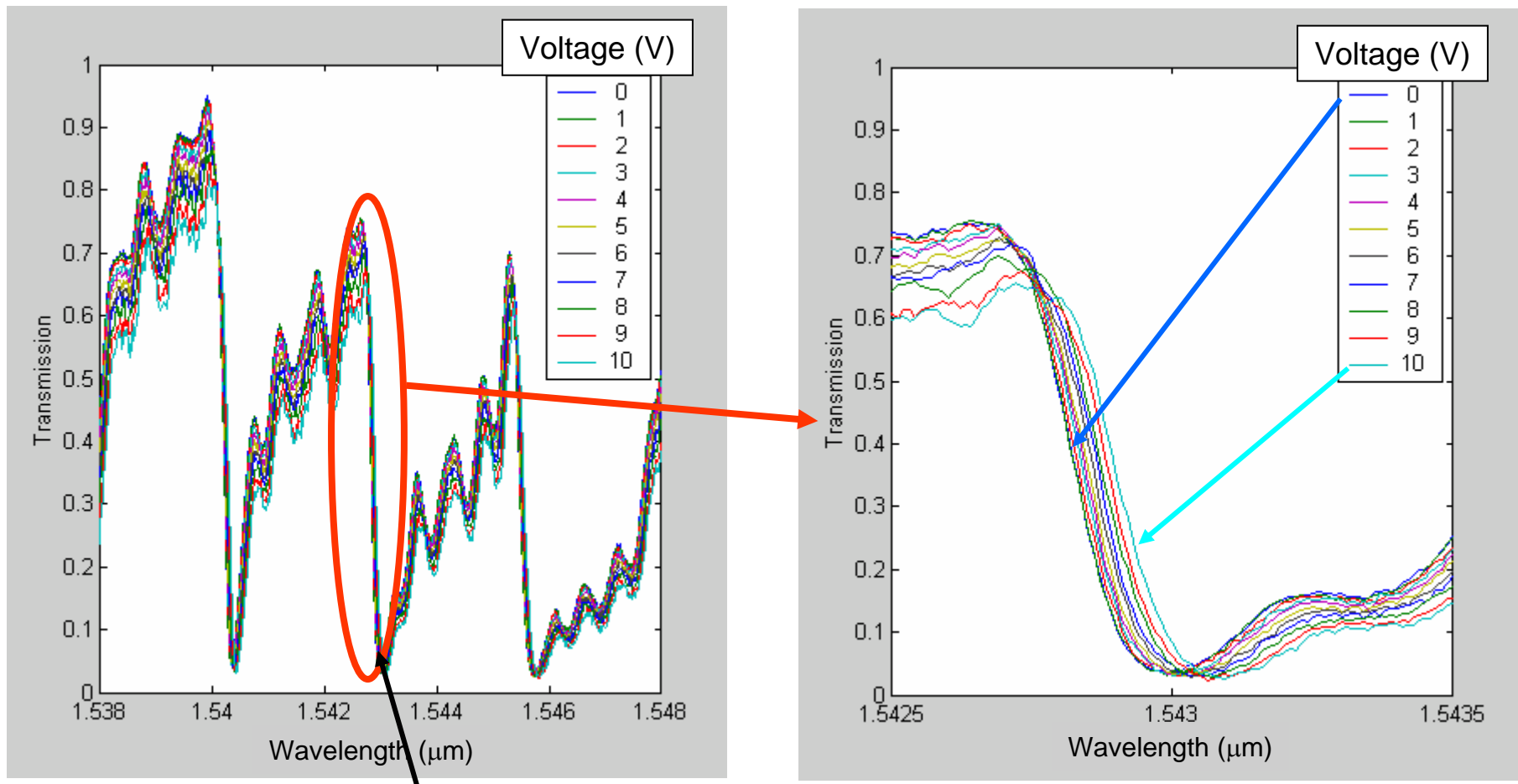
The asymmetric MZI makes sure that the quadrature condition can be selected by the wavelength

Electro-Optic Measurements



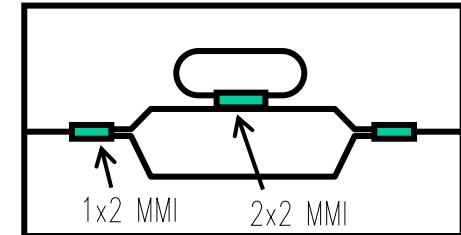
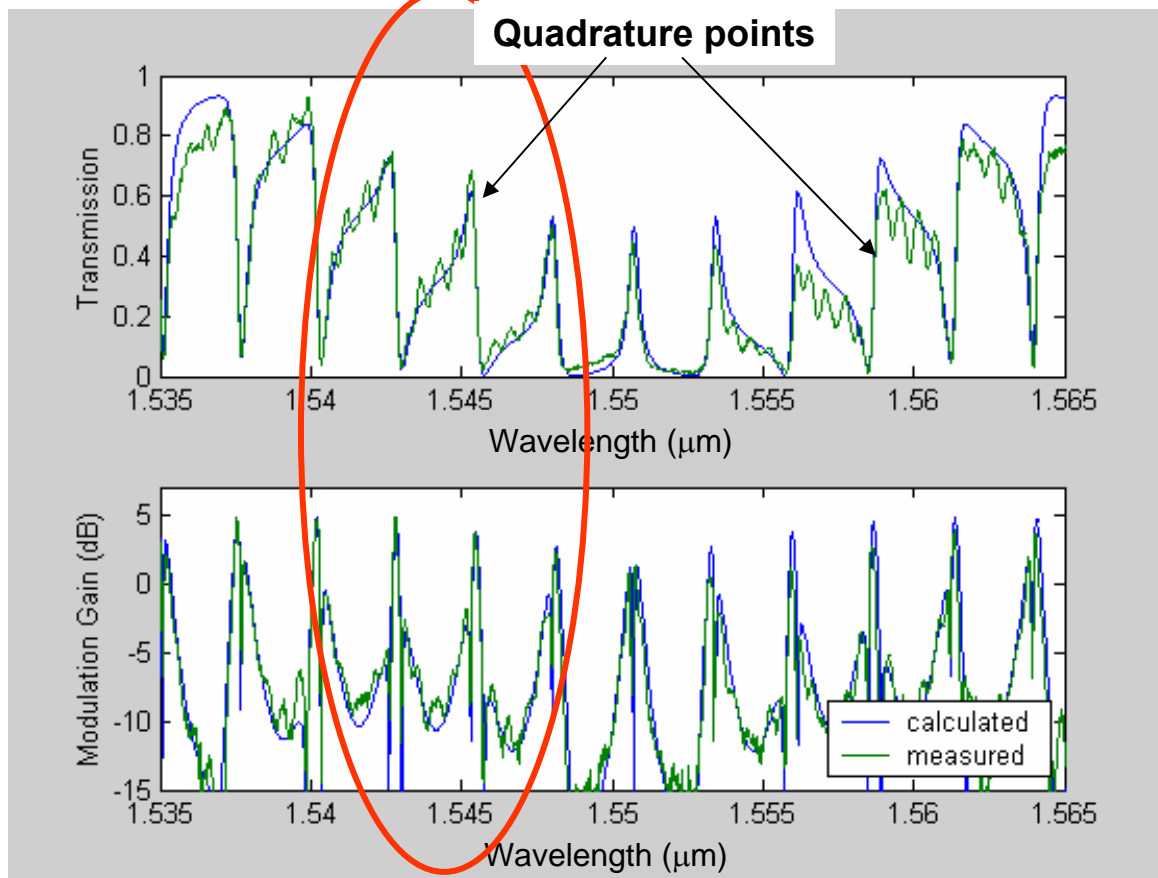
- **DC-measurement:**
 - no RF-modulation, wavelength scan, (variation of V_{bias}).
- **Modulation response:**
 - fixed wavelength, Frequency scan.
- **Wavelength response of modulation:**
 - fixed RF-frequency, wavelength scan.

DC-measurements



Quadrature condition \rightarrow steepest slope. $V\pi \sim 16V$ due to error in material growth

RF-measurements



Transmission measurement:

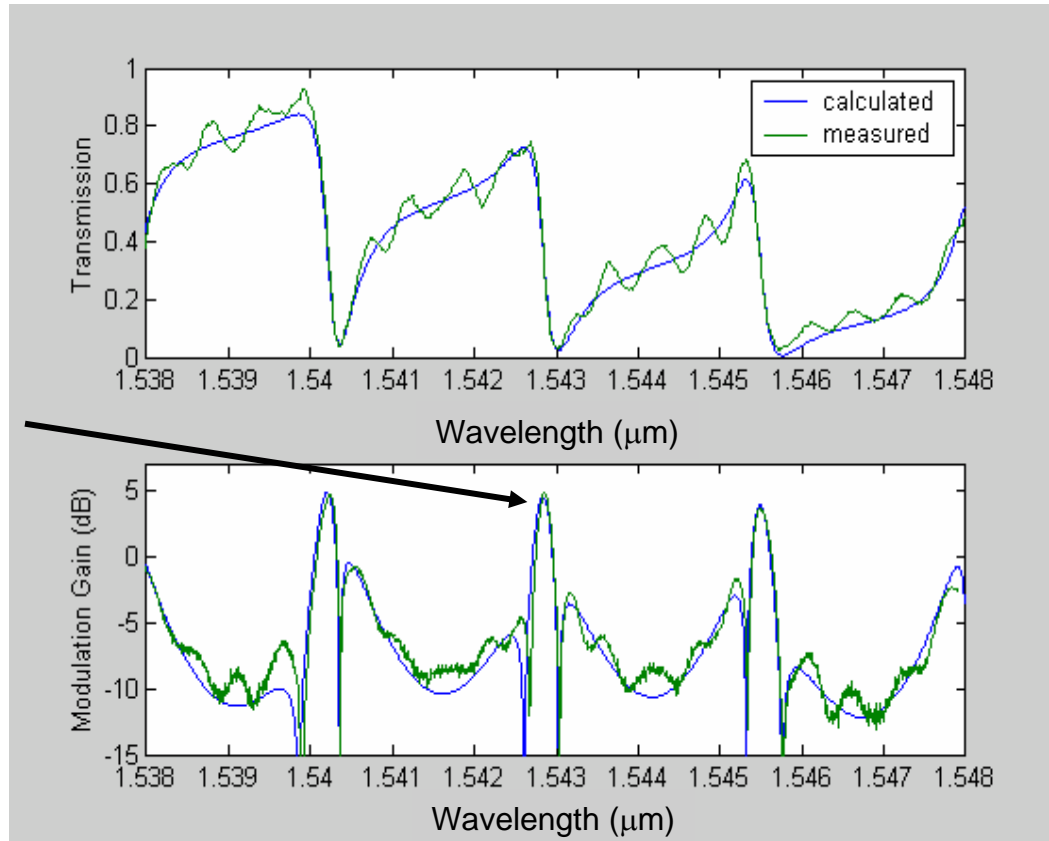
- no modulation.
- measurement of DC-transmission
- wavelength scan.

Wavelength response of modulation:

- fixed RF-frequency (1GHZ)
- Measurement of S21
- wavelength scan.

RF-measurements, cont'd

Max. 5dB ring enhancement



**Good fit of
calculation and
experiment**

**Modulator
enhancement
(due to ring
resonance):
confirmed**

Waveguide width: $0.8\mu\text{m}$

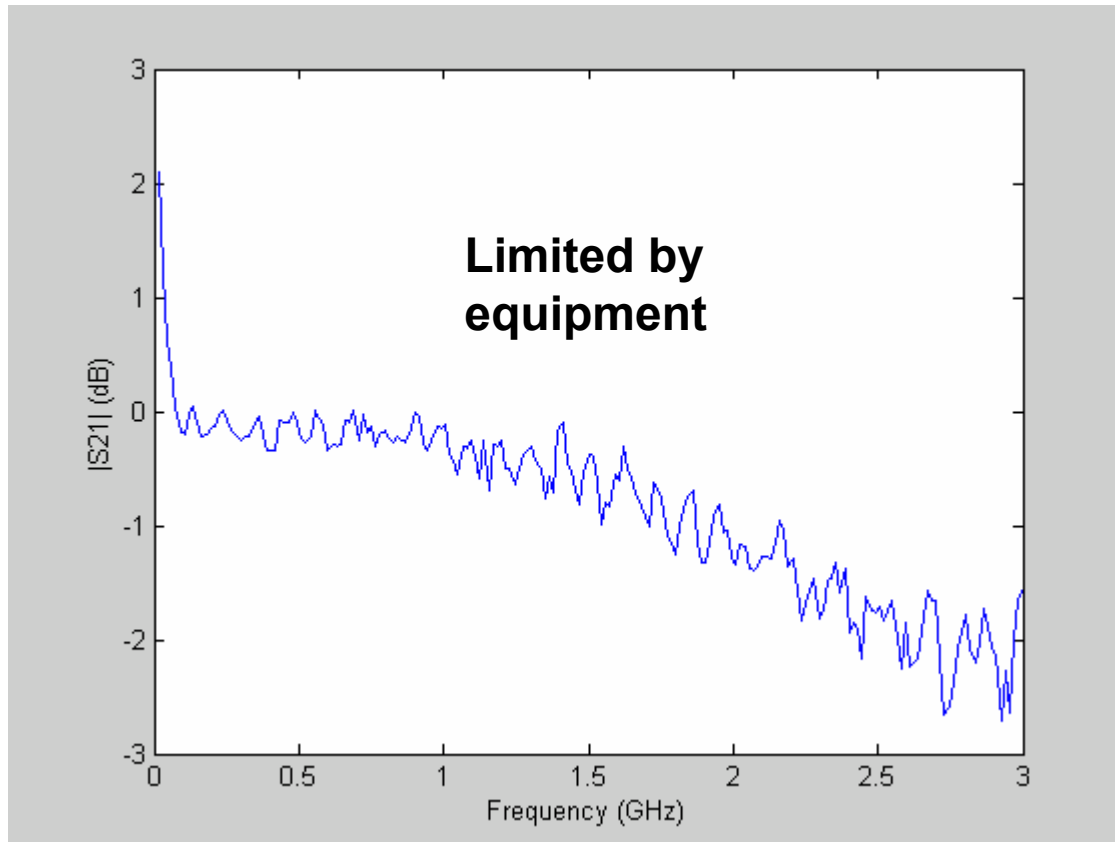
Ring loss: 15%

MMI-length: $34.5\mu\text{m}$

Coupling 50%

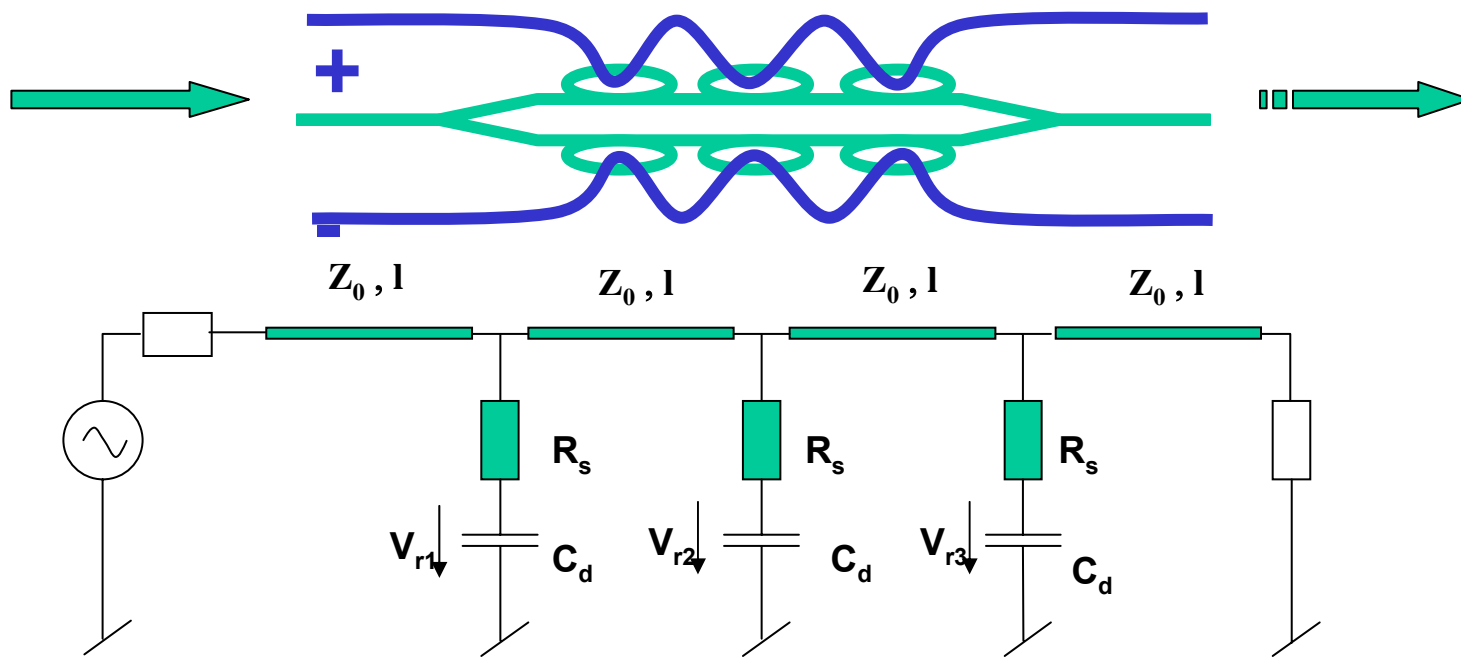
Ring circumference: $250\mu\text{m}$

First Measurement of Ring Modulator Frequency Response



**Frequency scan
(Wavelength fixed)**

Multi-ring resonator as a loaded transmission line



Multi-ring resonator acts like a loaded transmission line.

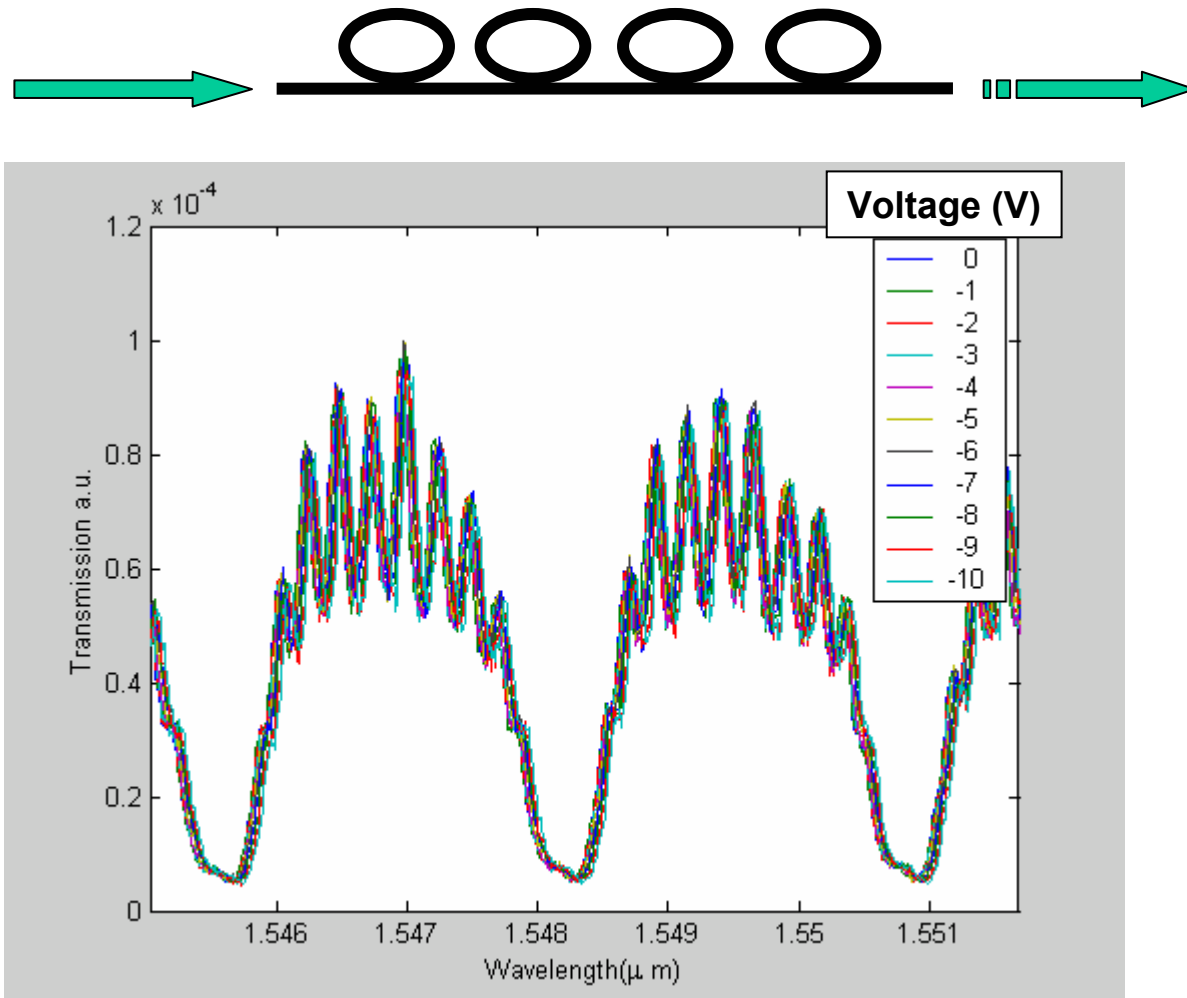
Loading is reduced due optical recycling of the rings.

Dwell time in the rings has to be determined and reproducible.

→Optical and Electrical delay from ring to ring can be matched

(Coupling of ring resonator determines optical delay!)

'Lithographic' alignment of ring-resonance's



Optimization of modulator

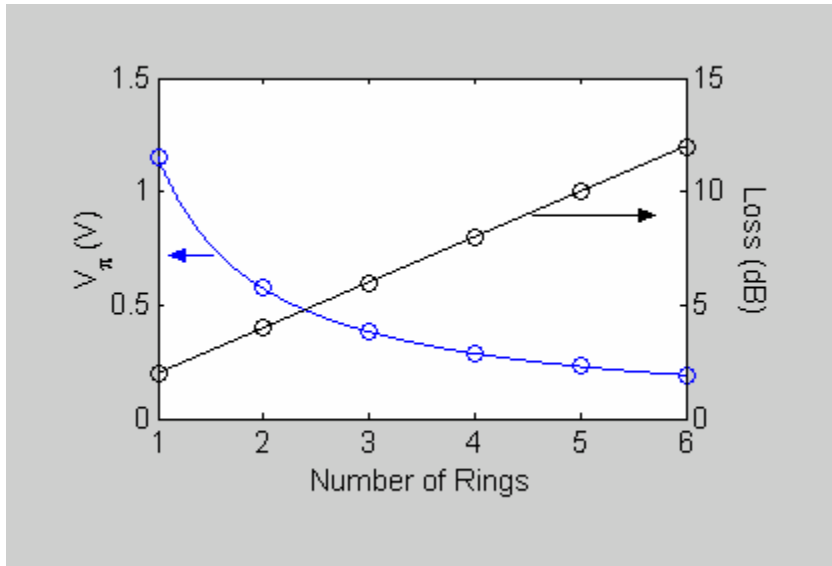
- Figure of merit = $(\text{transmission})/V_{\pi}^2 =$

$$\frac{L^2 e^{-\alpha L}}{(V\pi L)^2}$$

→ optimum length for optimum modulation performance → $L_{\text{opt}} = 2/\alpha$
Material dependent

- → maximized performance can be achieved with 3 – 4 rings (per arm) based on best achieved ring results (3.5cm⁻¹ effective loss).
- V_{π} of best ring result with best material →
 - one ring: 1.7V
 - With 3 rings in each arm: ~0.3V

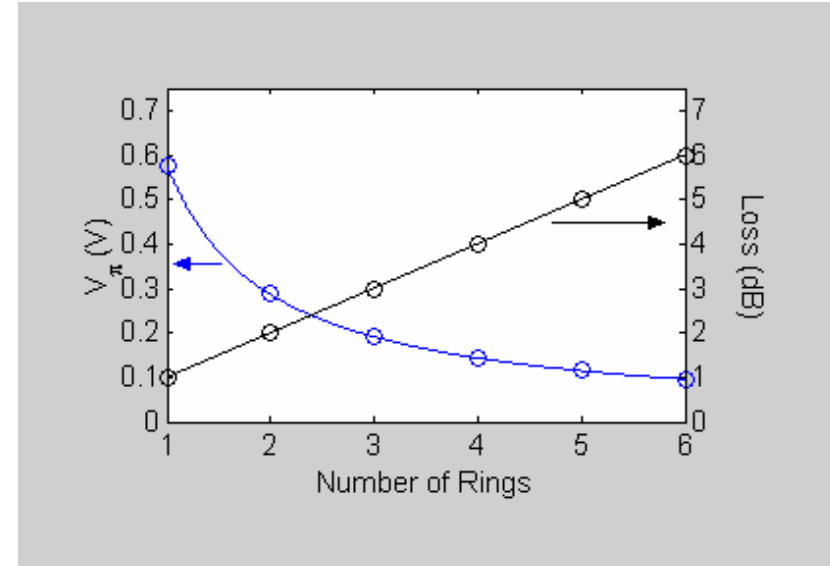
Estimation of V_{pi} and Loss of a balanced Mach-Zehnder Ring modulator.



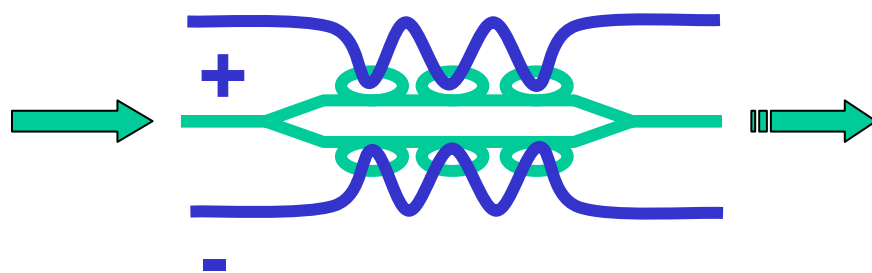
Internal loss and V_{pi} with current device components

Fiber-coupling loss not included

Number of rings per arm



Internal loss and V_{pi} anticipated at the end of the project



Summary



- **Low loss waveguides demonstrated.**
- **Low loss rings demonstrated.**
- **Reproducible coupling ratio's in MMI's achieved.**
- **Optimized MMI's and ring resonator design.**
- **Electro-optic ring-modulator at RF frequencies demonstrated.**
- **Need to combine**
 - **low loss waveguides**
 - **Accurate MMI fabrication**
 - **Highly sensitive material**
 - **Electrode process**
 - **Multi-ring devices**

→ **Multi ring resonator low V_π modulator**

Resource & Financial

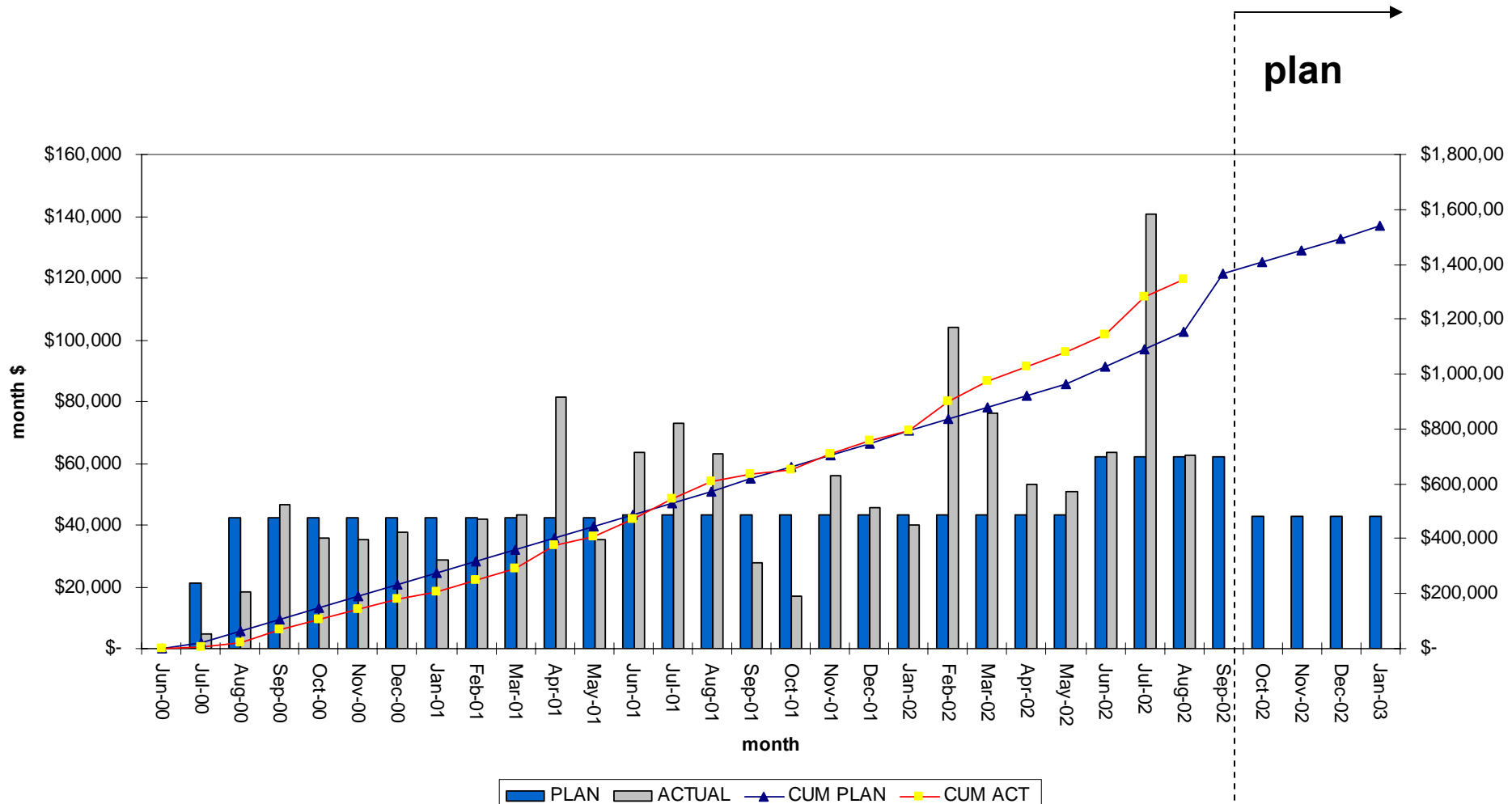
Albert P. Grupper, Col, AUS, Ret.

Summary of Financials



- Original \$1,607,000 proposal accepted by DARPA without modifications
- Negotiated to approx. \$1,590,874 by Army Research Lab
- Current authorized funds \$1,301,665
- Expecting increment of \$252,642 (according to DARPA guidance)
- Total funding: \$52,693 short of original proposal
- Deliverables will be affected

Resonant Enhanced Modulator: Spending Actuals & Plan



Contract Funds Status Report

CONTRACT FUNDS STATUS REPORT (DOLLARS IN <u>0</u>)											
1 CONTRACT NUMBER		3 CONTRACT FUNDING		5 PREVIOUS REPORT DATE		7 SARNOFF CORPORATION			9 INITIAL CONTRACT PRICE		
F30602-00-C-0116		INC		AS OF <u>8/31/02</u>		CN5300, PRINCETON NJ, 08543-5300			TARGET \$1,590,874		
MOD P00002		FOR FY 2000		AS OF <u>8/31/02</u>		CEILING N/A					
2 CONTRACT TYPE		4 APPROPRIATION		6 CURRENT REPORT DATE		8 PROGRAM			10 ADJUSTED CONTRACT PRICE		
CPFF				AS OF <u>9/30/02</u>		Resonant Enhanced Modulator (REM)			TARGET \$1,301,665		
11		FUNDING INFORMATION									
LINE ITEM/WBS ELEMENT	APPROPR.	FUNDING	ACCURRED EXPEND.	CONTRACT WORK AUTHORIZED			FORECAST			TOTAL	FUNDS CARRY
				DEFINITIZED	NOT DEFINITIZED	SUBTOTAL	NOT YET AUTHORIZED	ALL OTHER WORK	SUBTOTAL	REQUIREMENTS	FUNDS OVER
	IDENTIFICATION	AUTH TO DATE	PLUS OPEN COMMIT.								REQUIRED
			TOTAL								
	a	b	c	d	e	f	g	h	i	j	k
											l
											m
TOTAL		\$1,301,665	\$1,464,082	\$1,301,665	\$0	\$1,301,665	\$289,209	\$0	\$289,209	\$1,590,874	\$0
				FUNDING DECREMENT			\$36,567		\$36,567	\$36,567	
				ADJUSTED TOTAL			\$252,642		\$252,642	\$1,538,181	
											\$1,538,181
12		9/30/02 CONTRACT WORK AUTHORIZED (WITH FEE/PROFIT) ACTUAL OR PROJECTED									
		ACTUAL TO DATE	Oct-02	Nov-02	Dec-02	Jan-03	Feb-03	Mar-03	Apr-03	May-03	03Q4 AT COMPLETION
a.	OPEN COMMITMENTS	\$96,786	\$72,590	\$48,393	\$24,197	\$0	\$0	#REF!	#REF!	#REF!	#REF! \$0
b.	ACCRUED EXPENDITURES	\$1,367,296	\$1,410,017	\$1,452,739	\$1,495,460	\$1,538,181	\$0	\$0	\$0	\$0	\$0 \$1,538,181
c.	TOTAL	\$1,464,082	\$1,482,607	\$1,501,132	\$1,519,656	\$1,538,181	\$0	#REF!	#REF!	#REF!	#REF! \$1,538,181
13		FORECAST OF BILLINGS									
TO THE GOVERNMENT-Non Cumula		\$1,288,382	\$78,914	\$42,721	\$42,721	\$42,721	\$42,721	\$0	\$0	\$0	\$0
14		ESTIMATED TERMINATION COSTS									
Non Cumulative		\$202,055	\$132,607	\$104,781	\$76,955	\$49,129	\$0	\$0	\$0	\$0	\$0
REMARKS		MOD P00002 provides funding thru 11/1/2002									



- **Embarked upon contract relying on UIUC to provide nanofabrication services (including lithography and dry etching)**
- **UIUC relied exclusively on postdoc when professor was promoted to director of entire center**
 - **Entire 1st year devoted to calibration**
- **UIUC stopped providing e-beam services midway through 2nd program year**
- **Etching**
 - **quality inconsistent**
 - **harmed during 3rd program year by departure of postdoc, replacement with fresh postdoc**

Univ. of Illinois Spending



- **Subcontract negotiated at \$150,000 per annum**
- **First Program Year (6-14-00 through 6-13-01):**
 - **\$136,000**
- **Second Program Year (6-14-01 though 6-13-02):**
 - **\$140,000**
- **Total Program Spending to date (through 9-30-02)**
 - **\$293,500**

Cost impact to program is greater and lies in:

1. **Samples not arriving at Sarnoff until after 1st year**
2. **E-beam lithography not performed at UIUC as planned**
(partially compensated by A. Lepore
at ARL in mid-2nd year)

Lessons Learned from UIUC Experience



- **Sarnoff remains totally dependent on UIUC for ICP etching**
 - Equipment not available at Sarnoff or most other laboratories
 - \$500,000 price tag
 - Capital for purchase not currently available from Sarnoff
- **Need to address in order to carry out further development of microring-based (or similar) structures**
- **Need to explore program contribution to ICP etcher**
 - Eliminate \$150,000/year contract
 - Could mitigate cost of ICP reactor if distributed over several program years

Current Plan to Complete



- **Sept. 20th E-mail to DARPA**
 - Sarnoff plans to complete without overrun by delivering early
- **Status (October 9):**
 - Results reported today show that quality of etching still limits yield
 - 1 GHz REM devices not available for test
- **January completion required by funding limitations**
- **Plan to achieve program goals by January now entails high risks**
 - Etching issues must be resolved to complete
 - Number of deliverables to be reviewed
 - Packaging options fewer

Resonant Enhanced Modulator Program

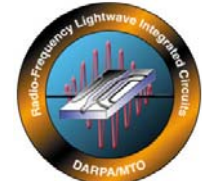
**Under the DARPA/MTO Radio Frequency
Lightwave Integrated Circuits Program**

H. Mohseni, M.H. Kwakernaak, Z.A. Shellenbarger, H. An, D. Bechtle, B. Price, A.N. Lepore, & J.H. Abeles (PI)

**Sarnoff Corporation
Princeton, NJ 08543-5300**

**Ilesanmi Adesida and J. W. Bae
Micro and Nanotechnology Laboratory
Department of Electrical and Computer Engineering
University of Illinois at Urbana Champaign**

Outline



- Program Goal and Significant Accomplishments
- Resonance Enhanced Modulator Concept
- Process Development
- Material Development
- Device Design and Test
- Summary
- Outlook

Program Goal and Significant Accomplishments



Program Goal:

- Deliver 12 packaged resonant enhanced modulators with $V_{\pi} < 0.25$ Volts

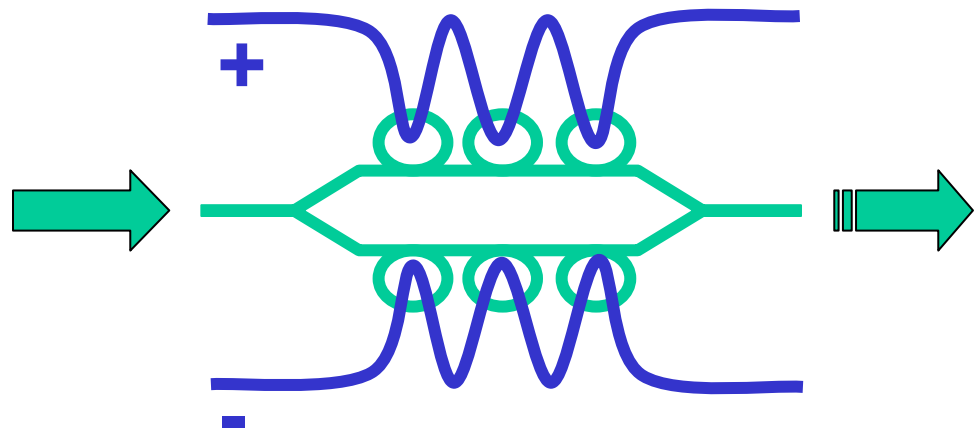
Accomplishments:

- Development of advanced processing methods:
 - Low-loss deep-etched waveguides (1 cm^{-1} achieved at $1 \mu\text{m}$ width)
 - Planarization of anisotropic wafer using Cytop™ dielectric
 - Low-capacitance contact to waveguides
- Implementation of MMI couplers in ring geometry
 - Total ring loss equivalent of 3.5 cm^{-1} demonstrated including MMI
- First demonstration of Ring Modulator structure
 - Electrical modulation to 6 GHz
 - 5 dB Ring Enhancement
- Demonstration of enhanced modulator material
 - 3× enhanced electrorefractive effect (compared to literature)
 - Controlled material growth

Resonance Enhanced Modulator Concept

Phase modulation with ring-resonators in interferometer arms.

→ Enhancement of the phase modulation due to ring resonance



Long group delay in ring resonator enhances modulation → reduction in V_π

$$\frac{\partial \phi}{\partial n} = \frac{\partial \phi}{\partial \omega} \frac{\omega}{n} = \tau_g \frac{\omega}{n}$$

Optical Bandwidth of $B=20$ GHz →

$$\left\{ \begin{array}{l} \tau_{g \max} = \frac{1}{\pi \cdot B} \approx 32 \text{ ps} \\ l_{eff \ max} = \frac{c}{n \pi \cdot B} \approx 3 \text{ mm} \end{array} \right.$$

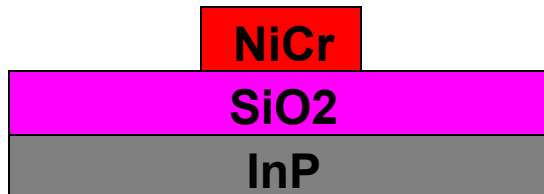
Resonant Enhanced Modulator Process Development

Process Development: Outline

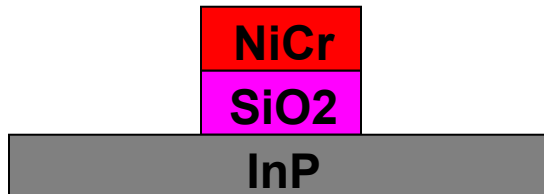


- Waveguide process overview
- Electrode process overview
- Device design/fabrication issues
- Process development for electrodes – planarization issues

REM Waveguide Process



1. Metal mask liftoff using e-beam pattern



2. Transfer metal pattern to dielectric



3. Blanket redeposit thin (50nm) dielectric for sidewall smoothing



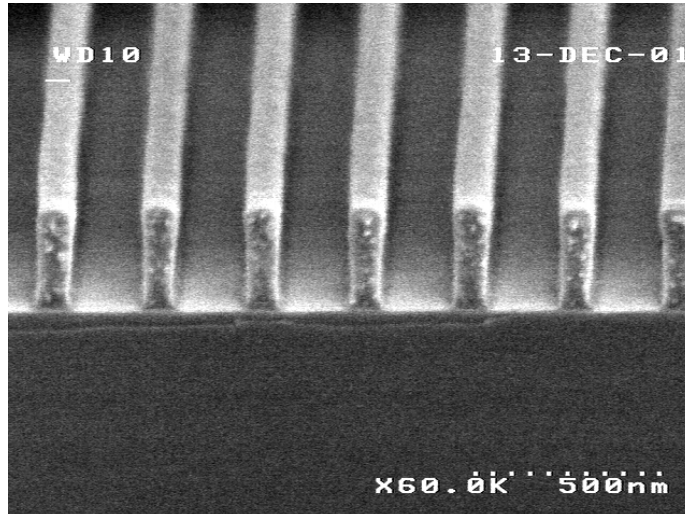
4. Anisotropic dielectric removal from planar surfaces



5. ICP anisotropic etch of waveguide

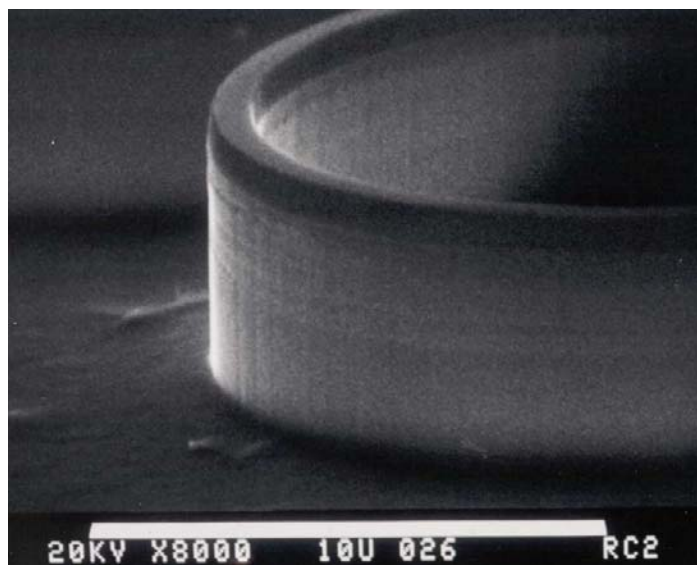
Benefits of Metal Etch Masks

**Bilayer ebeam resist
for metal mask liftoff**



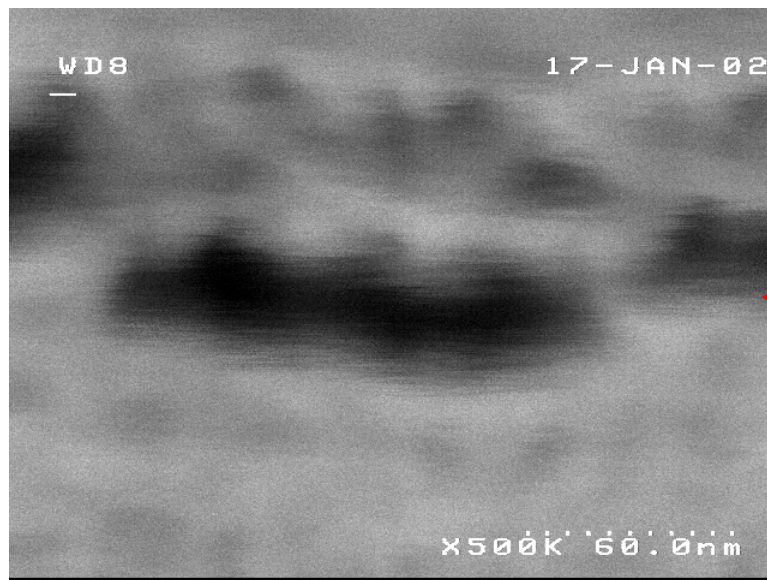
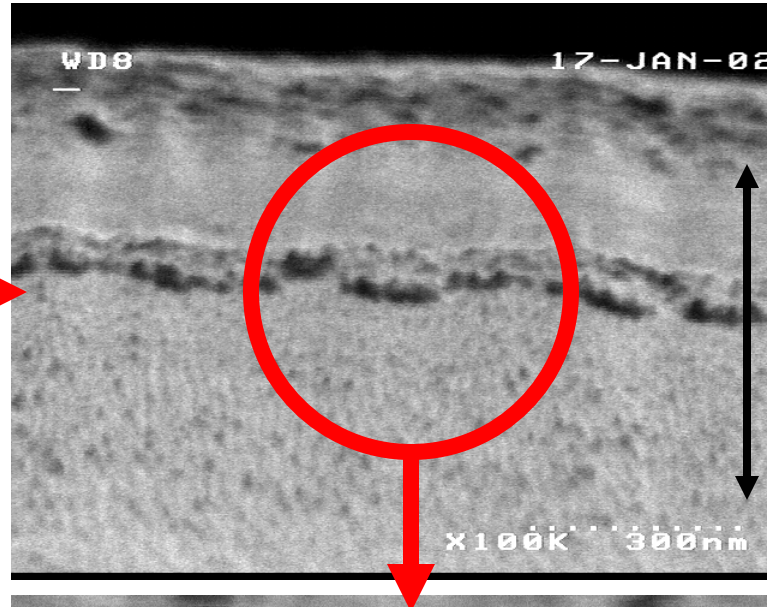
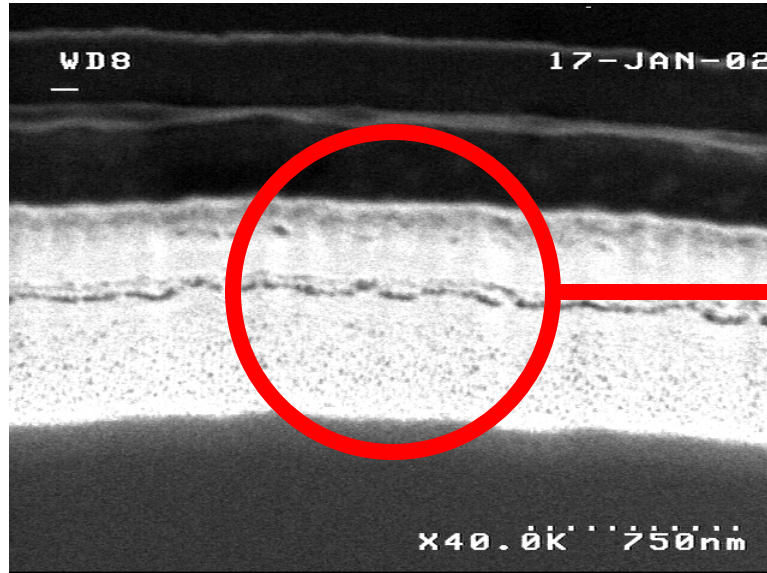
← PMMA 950k MW
← PMMA 496k MW

**NiCr/SiO₂-
masked ICP-
etched ring**



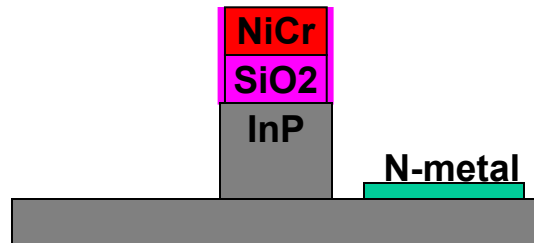
Without Metal Mask

... mask erosion - shower curtain effect ...

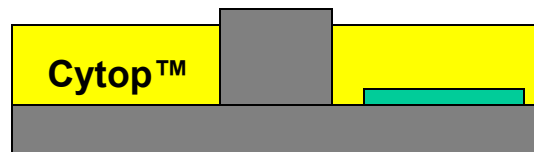


Layer/depth-
dependent
sidewall
damage

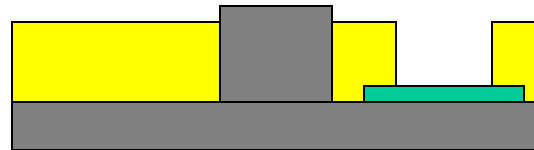
New Topside REM Device Process



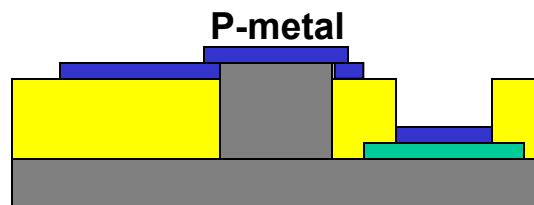
1. N-contact formation



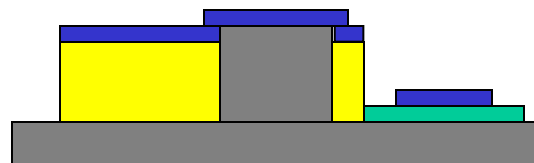
1. Strip ICP etch mask and planarize with Cytop™ polymer



2. Open N-contact via

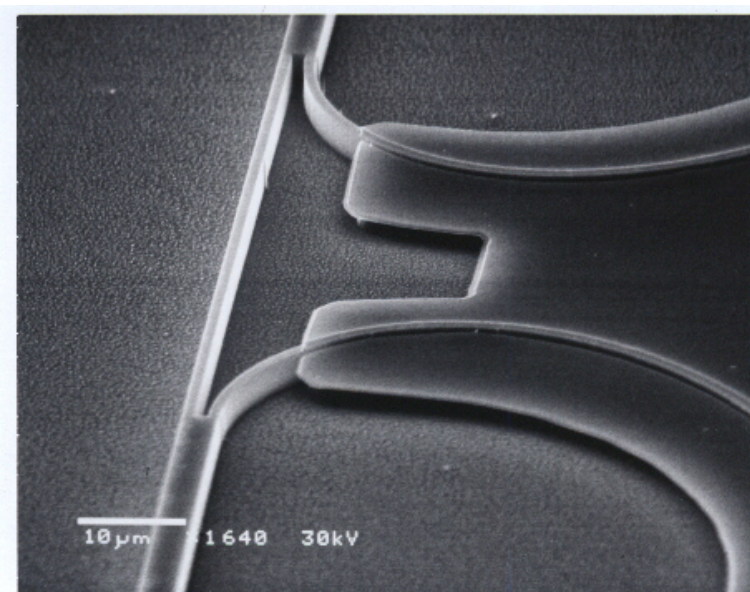
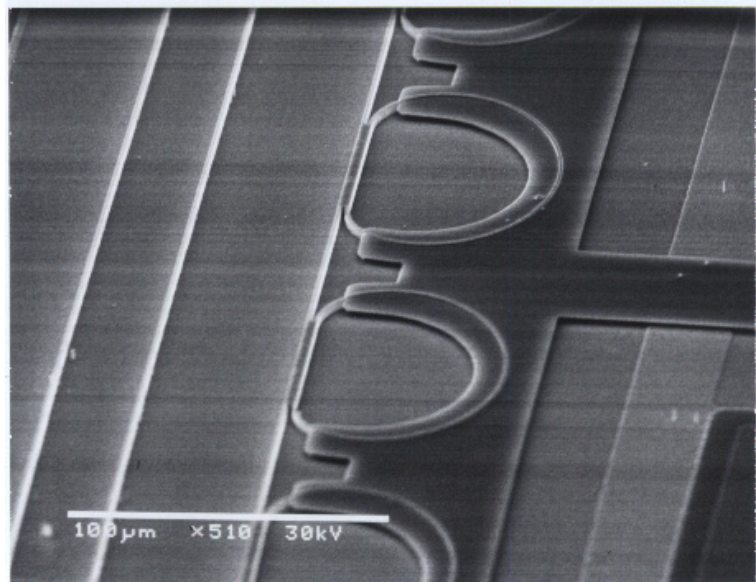
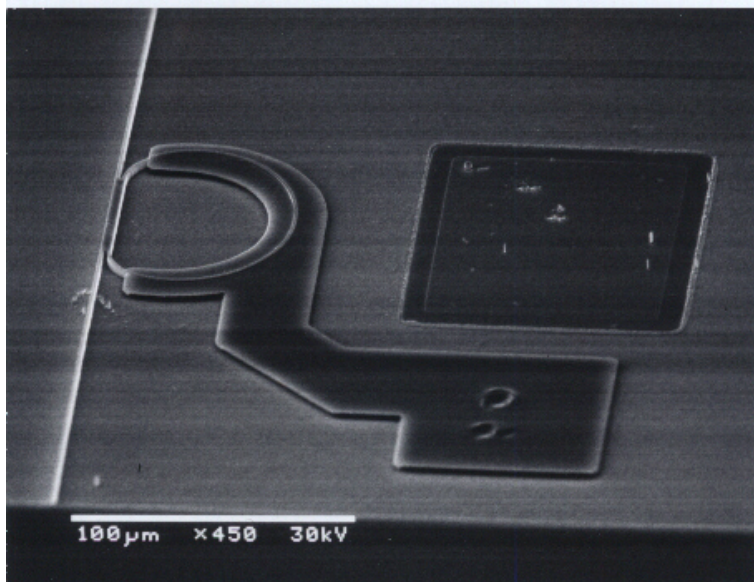


3. P-contact formation



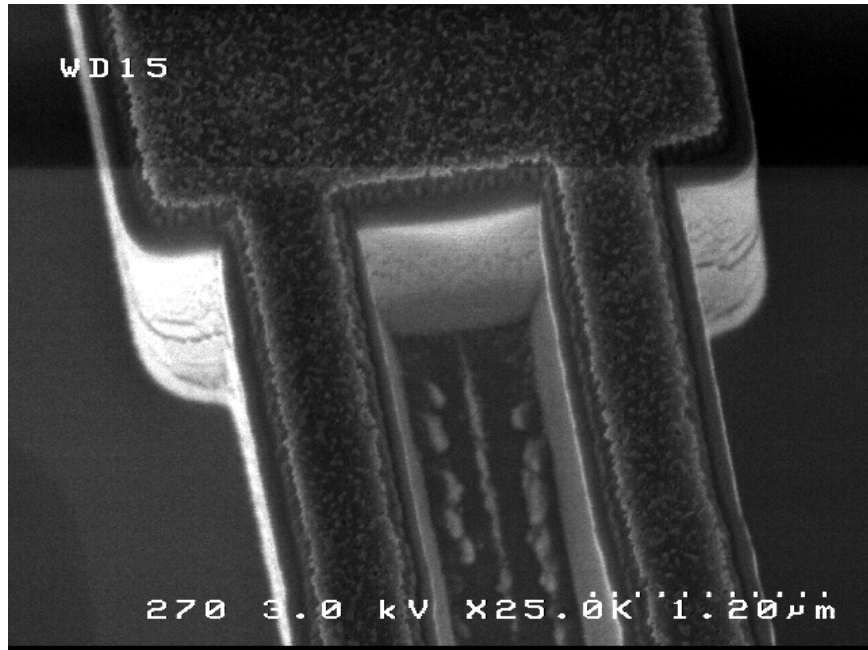
4. Excess dielectric removal

Completed & Functional Devices

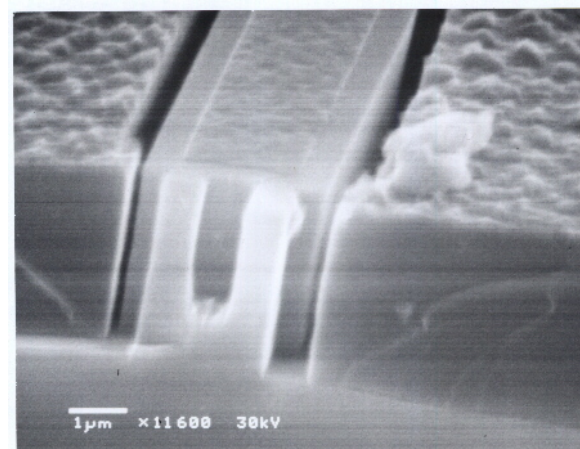
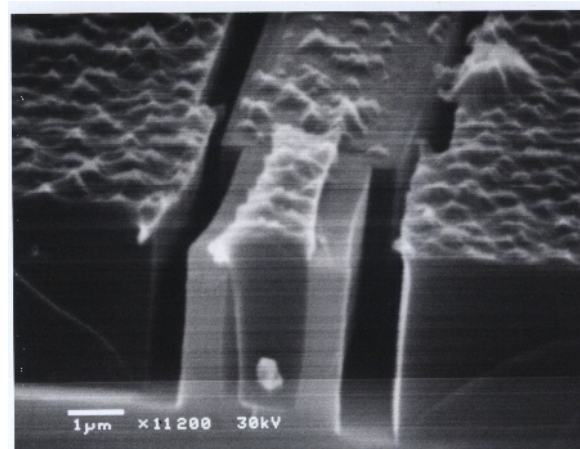


Gap Etching

MMI coupler showing incomplete etching and residue in gap

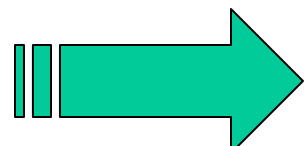
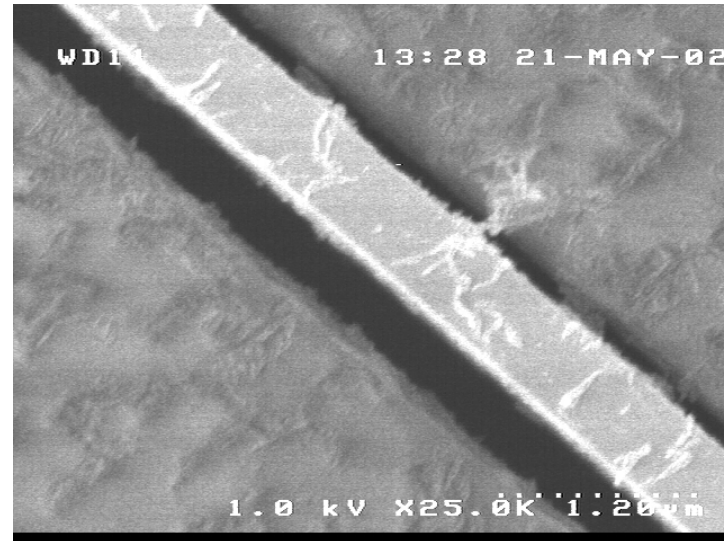


Planarized MMI-branch showing etch depth variation with gap width



Planarization Difficulties

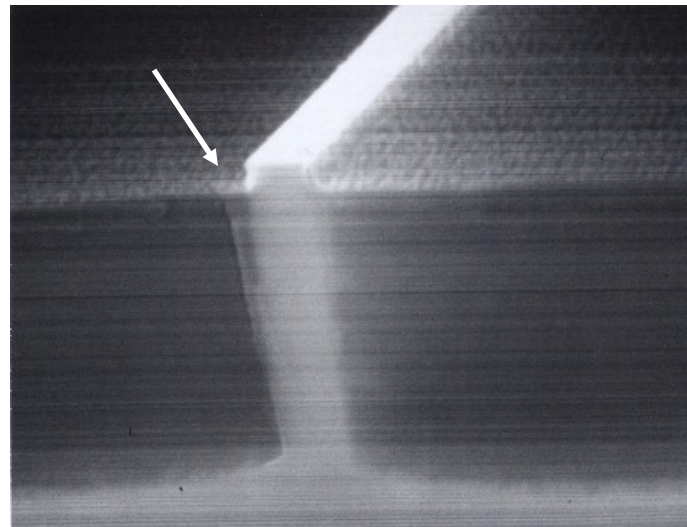
BCB Sidewall delamination after planarization etch



- Electrode short circuits active layers
- Excess loss if mode contacts metal

Planarization Attempts with BCB

- multiple coat, single cure
- multiple coat, multiple cure
- coat/cure, etch-back, recoat/cure
- oven vs. hotplate bake
- Temperature ramping to reduce stress
- baked adhesion promoter*
- gap filling with photoresist or Cytop- difficult to reproduce

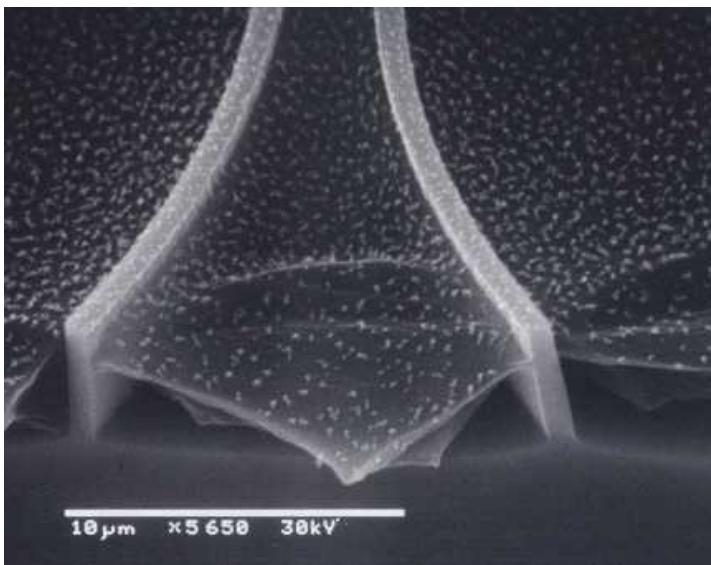


* Dan Schank @ Dow Chemical recommendation

Planarization Solution



Replace BCB with CYTOP™ polymer



- Greatly improved sidewall adhesion relative to BCB

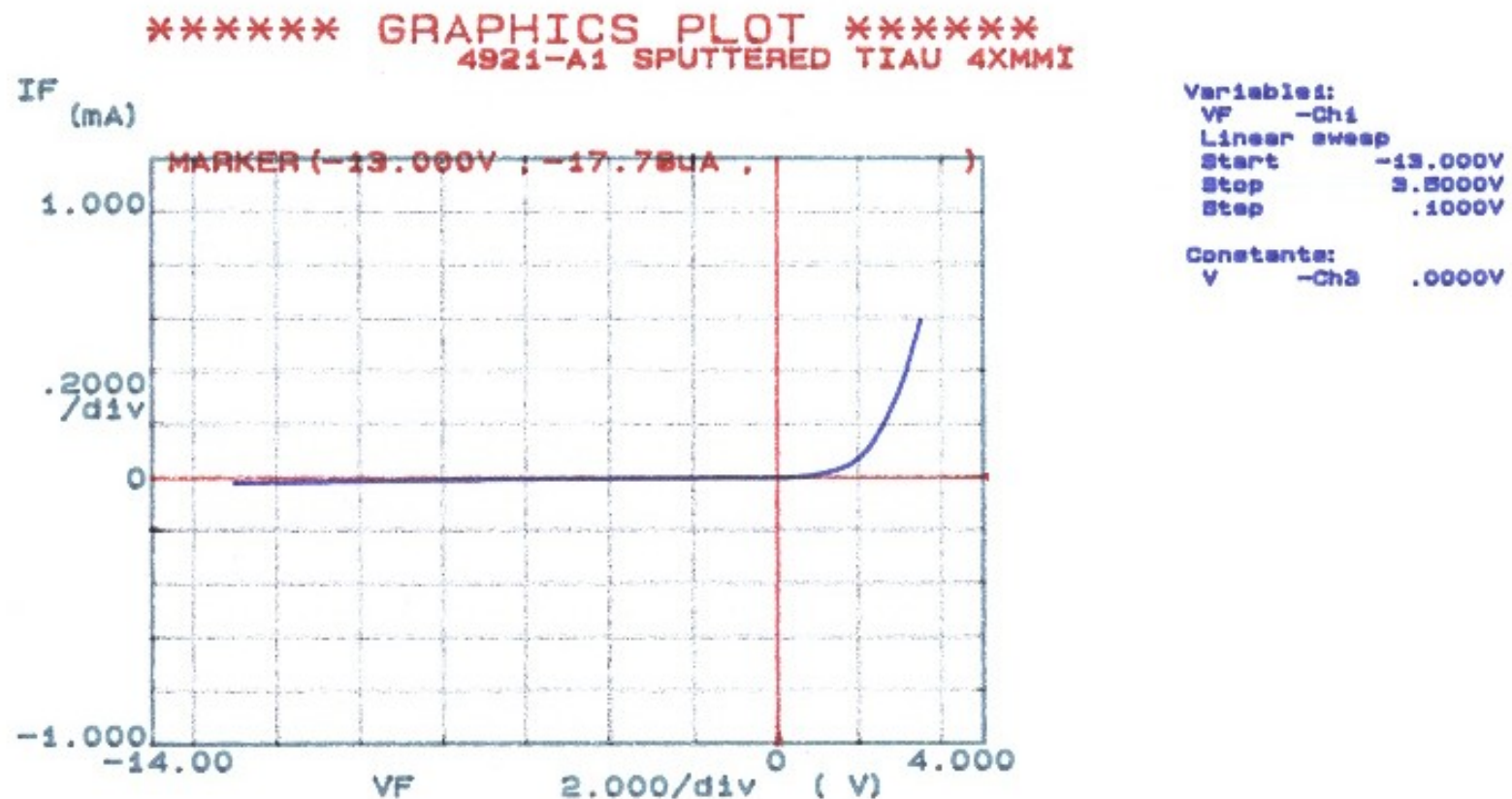
PRO

- Etches readily in oxygen plasma
- Less post-etch residue than BCB

CON

- Glass transition temperature much lower than BCB- impedes facet coating if excess material exposed

Leakage Characteristics



Materials Development

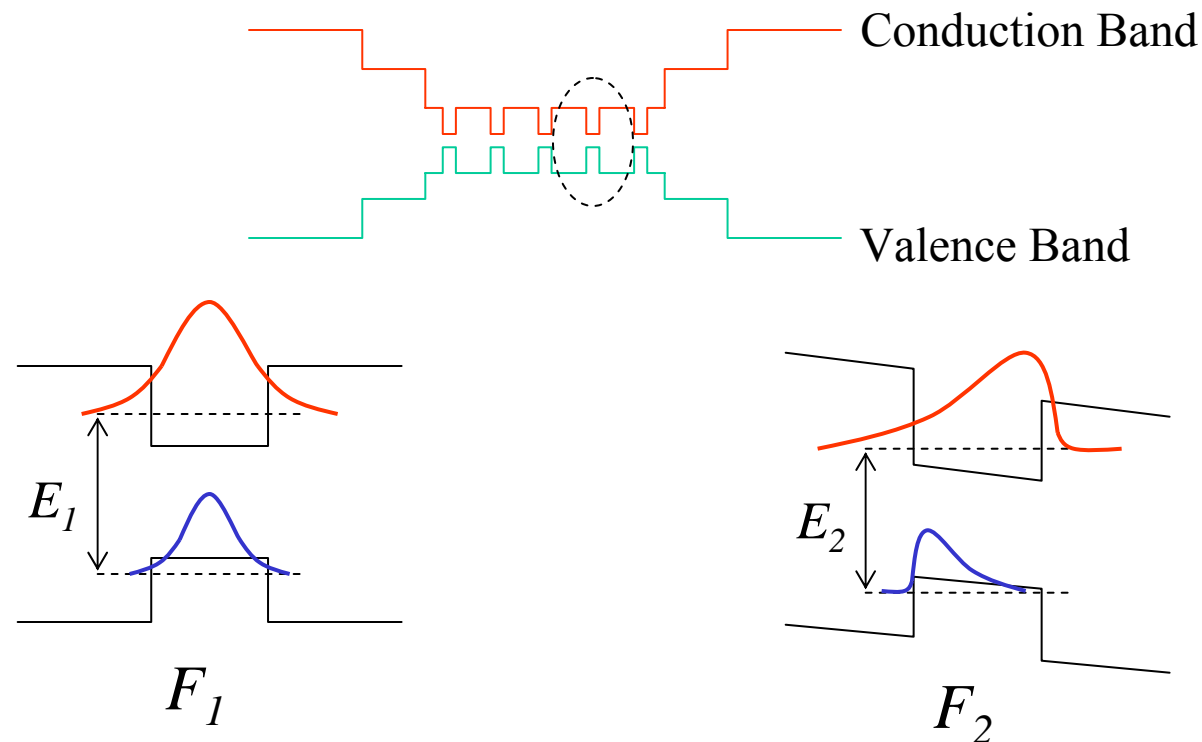
Outline



- **Modeling**
 - QW Model
 - Device Model
- **Material Growth Characterization**
 - PL
 - X-ray
 - TEM
- **Modulator Characterization**
 - Planar Waveguides
 - Index-guided Waveguides
- **Agreement of Model and Measurement**
- **Stepped Quantum Well Modulators**
- **Growth Optimization**
- **Summary**

Existing Technology

- Existing technology is based on quantum confined Stark effect (QCSE) in multiple quantum wells (MQW)



$$F_2 > F_1 \Rightarrow E_2 < E_1$$

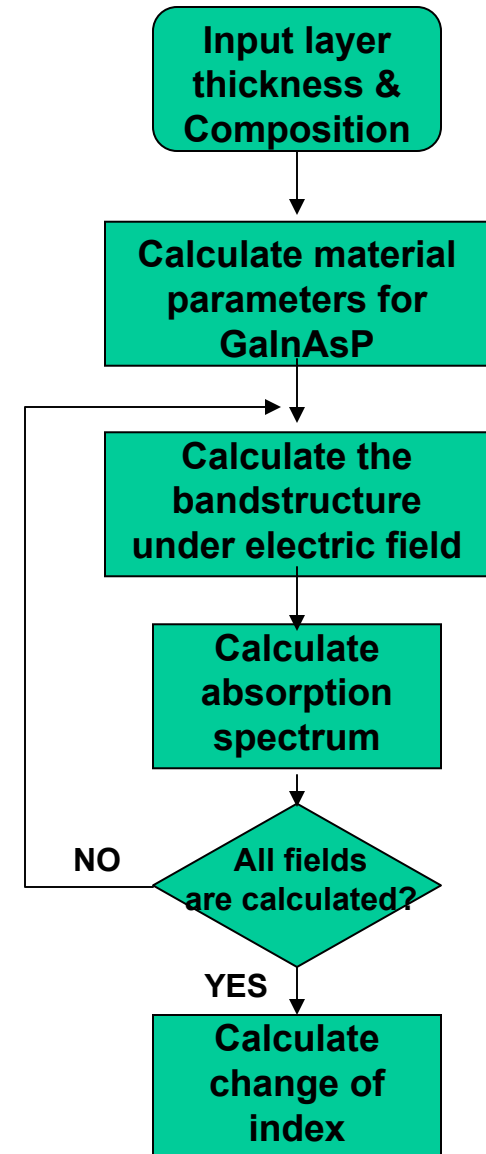
QW Model Overview



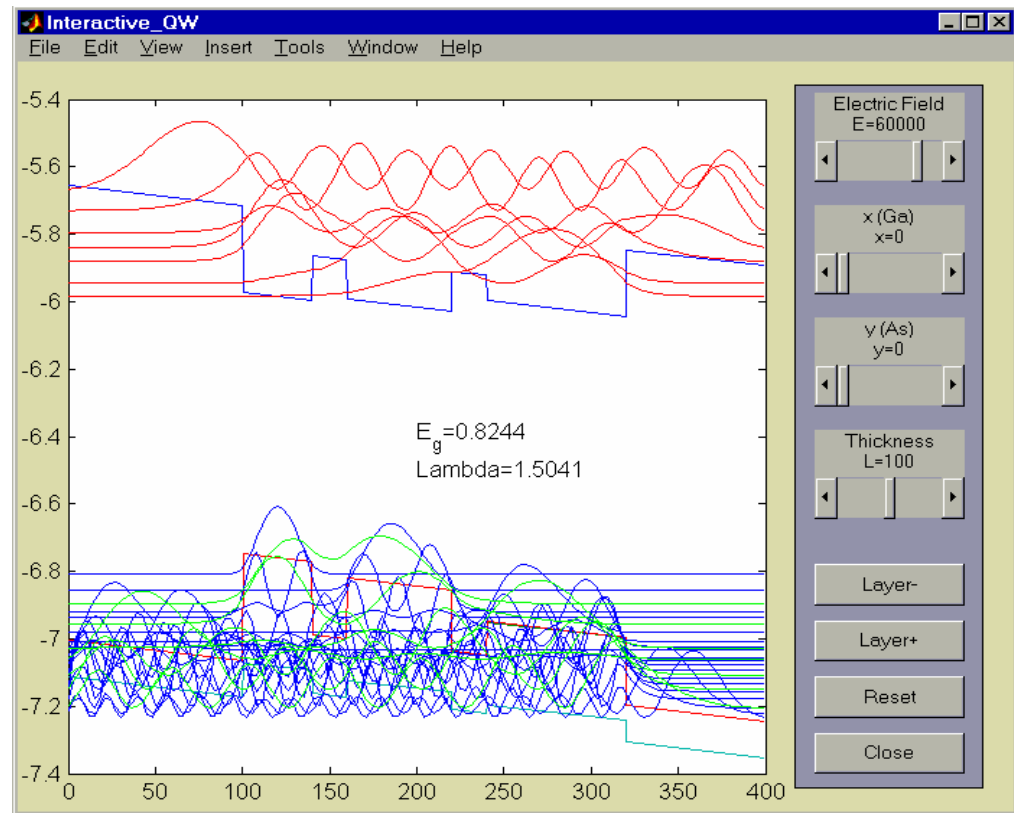
Existing Model's Capabilities:

- Calculates material parameters for GaInAsP layers (considers bowing and strain effects.)
- Calculates the band lineups* using Model Solid method (considers bowing and strain effect.)
- Calculates energy states and wavefunctions for electrons, light-holes, and heavy-holes using the effective mass method.
- Calculates optical absorption spectrum for the bulk and quantum wells (considers two-body and three-body effects*.)
- Calculates the change of index spectrum using Kramers-Kronig relation.

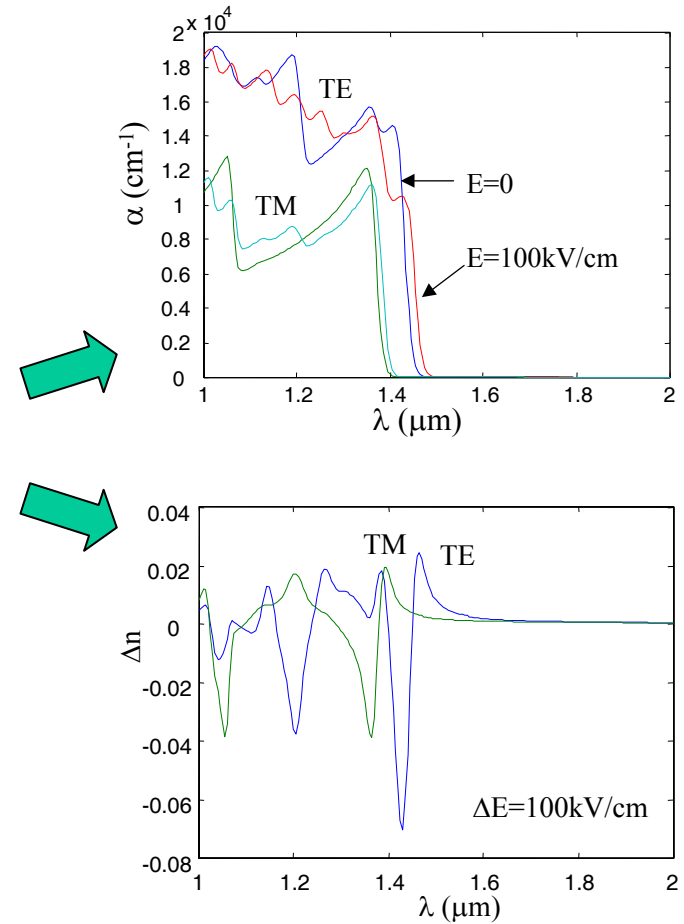
* Newly implemented



QW Model Examples



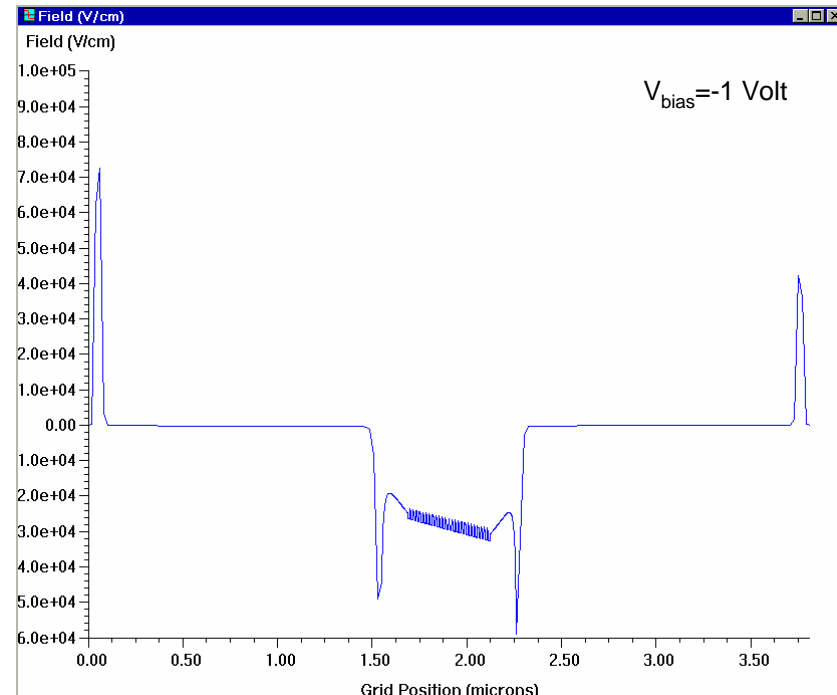
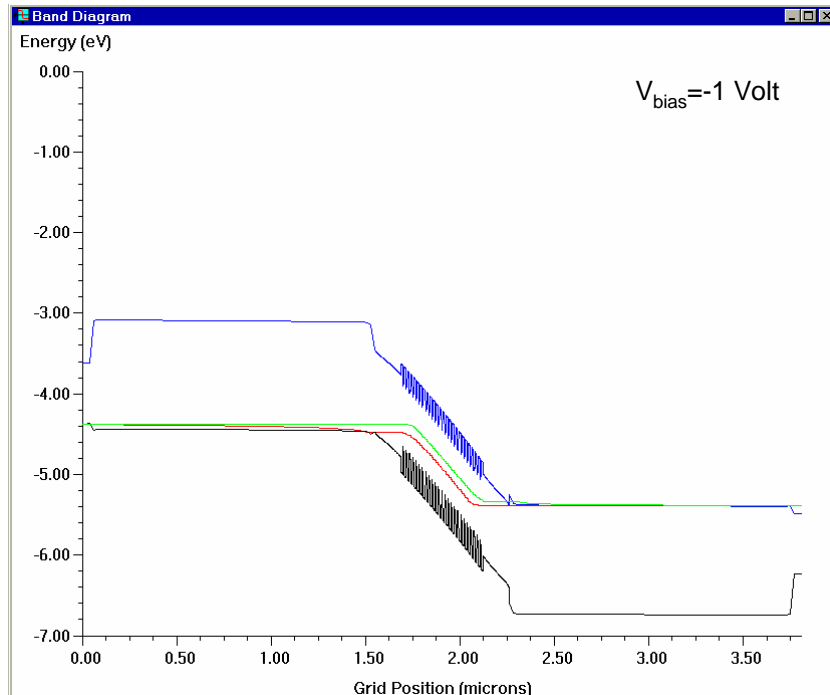
Wavefunction Calculation*



Index/Absorption Calculation

* Numerically optimized since last review: update time ~0.6 sec (typical)

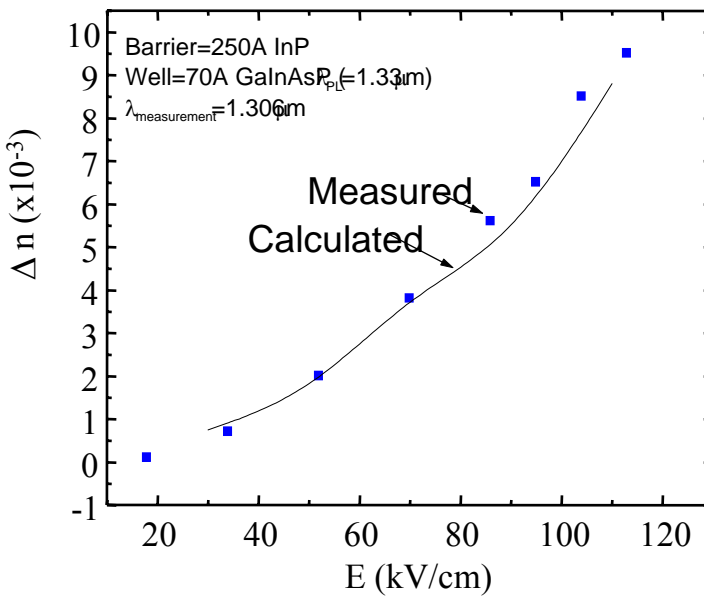
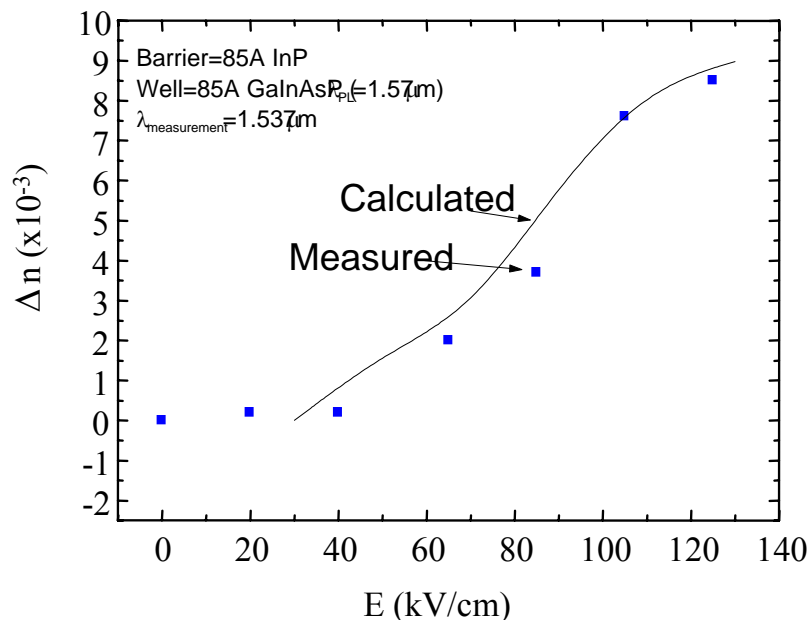
Device Model



- Energy Band Diagram of a sample device @ $V_{bias} = -1$ Volt

- Internal Electric Field of a sample device @ $V_{bias} = -1$ Volt

Comparison with the Published (Lucent) Results at $\lambda \sim 1.3 \mu\text{m}$ and $\lambda \sim 1.5 \mu\text{m}$



Calculated change of index versus measured change of index by Zucker et al^a around $1.3 \mu\text{m}$ and $1.5 \mu\text{m}$.

^a Appl. Phys. Lett. 54(1), p. 10 (1989)

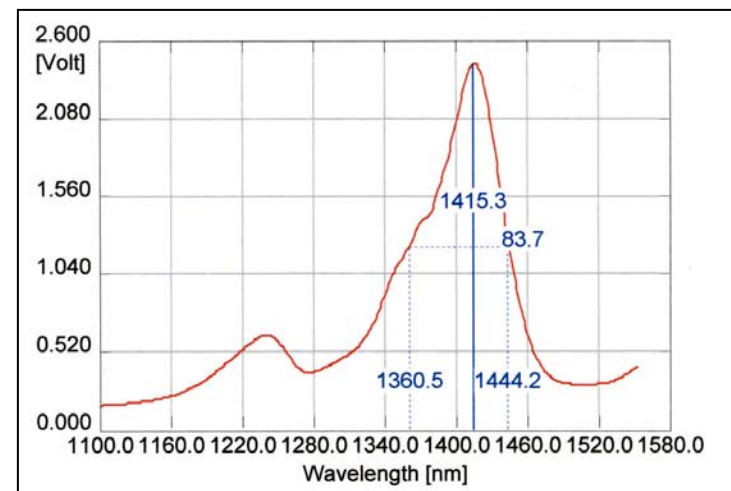
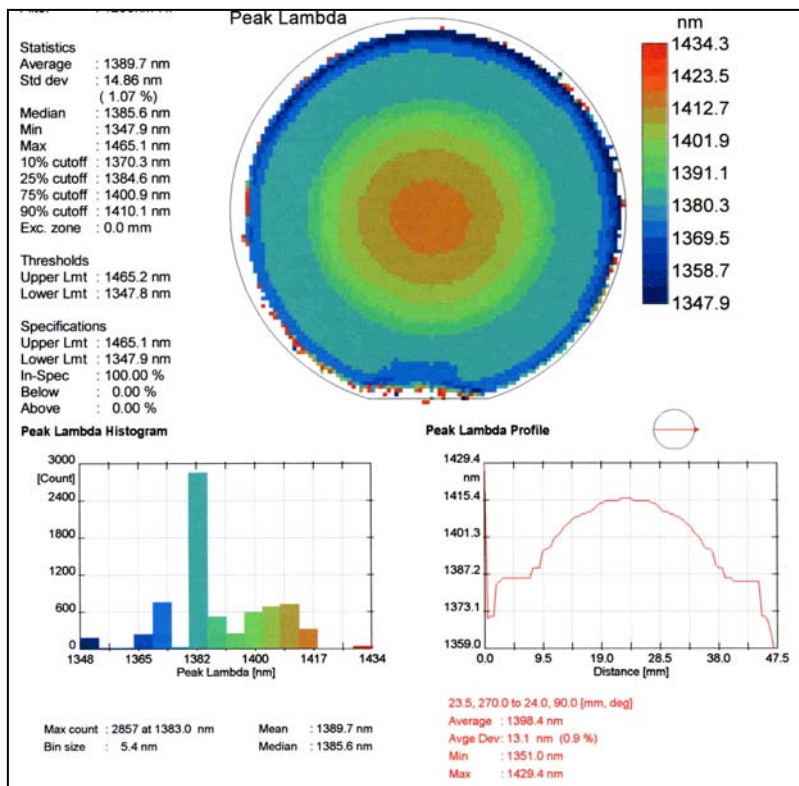
Material Characterization: Photoluminescence



As grown material can be “quite different” from the nominal structure!

Material characterization is essential for modeling and optimization

PL



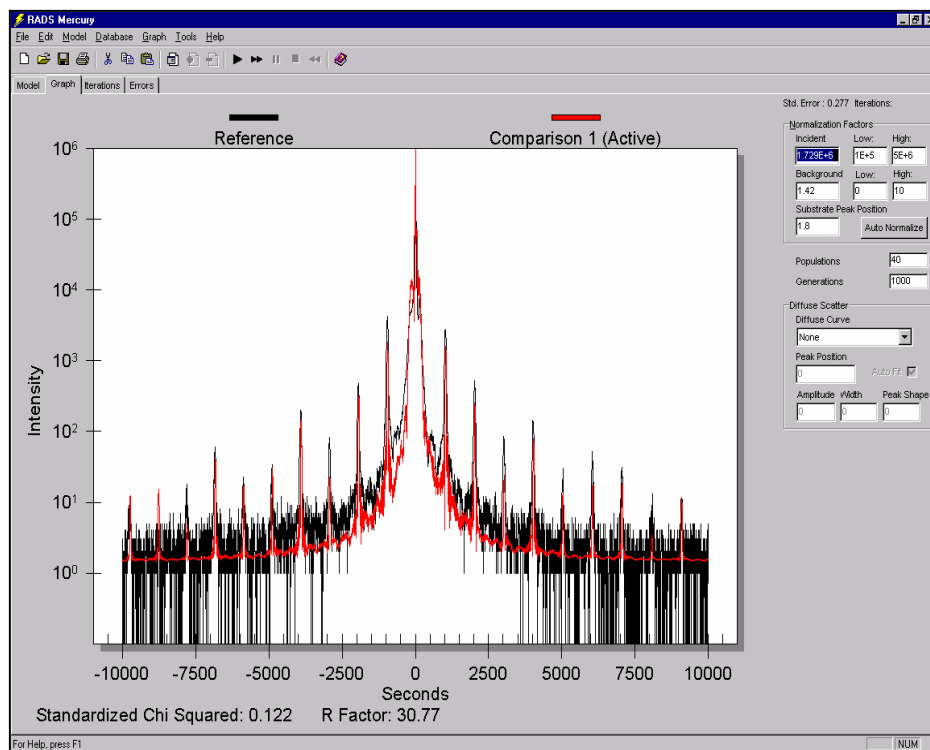
Photoluminescence (PL):

- Material quality (Intensity, FWHM)
- Effective Bandgap (Peak wavelength)
- Macroscopic uniformity (PL mapping)
- Growth calibration

Material Characterization: Double Crystal X-ray Diffraction



X-ray



	Thickness	Low	High	Material	X	Low	High	Y	Low	High	
107	500.00	500	500	In(x)Ga(1-x)As	▼	0.5320	0.532	0.532	0.0000	0	0
106	15000.00	15000	15000	InP	▼	0.0000	0	0	0.0000	0	0
105	1380.00	1380	1380	In(x)Ga(1-x)As(y)P(1-y)	▼	0.7507	0.7	0.8	0.5374	0.5	0.6
104	94.82	70	150	InP	▼	0.0000	0	0	0.0000	0	0
...	3.00	3	3	In(x)Ga(1-x)As(y)P(1-y)	▼	0.6116	0.1	0.95	0.4616	0.1	0.95
...	22.30	15	26	In(x)Ga(1-x)As	▼	0.5881	0.45	0.6	0.0000	0	0
5...	68.01	35	70	In(x)Ga(1-x)As(y)P(1-y)	▼	0.5800	0.56	0.7	0.8671	0.8	0.9
4	65.00	65	65	InP	▼	0.0000	0	0	0.0000	0	0
3	1380.00	1380	1380	In(x)Ga(1-x)As(y)P(1-y)	▼	0.7336	0.7	0.8	0.5973	0.5	0.6
2	15000.00	15000	15000	InP	▼	0.0000	0	0	0.0000	0	0
1	5000.00	5000	5000	In(x)Ga(1-x)As	▼	0.5320	0.532	0.532	0.0000	0	0
Sub.	00	00	0	InP	▼	0	0	0	0	0	0

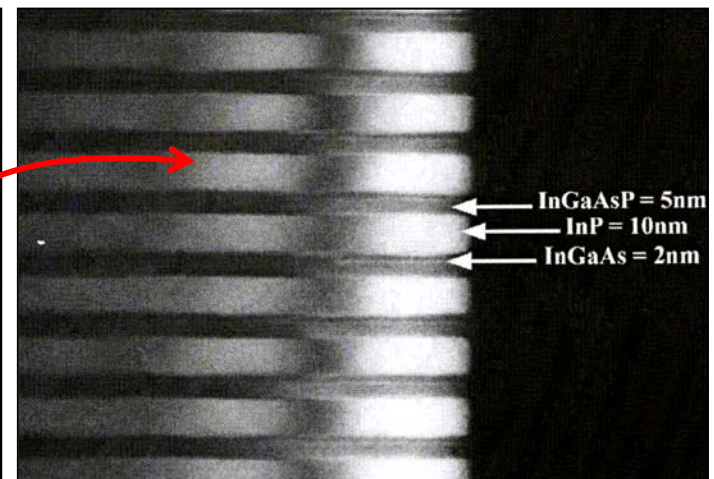
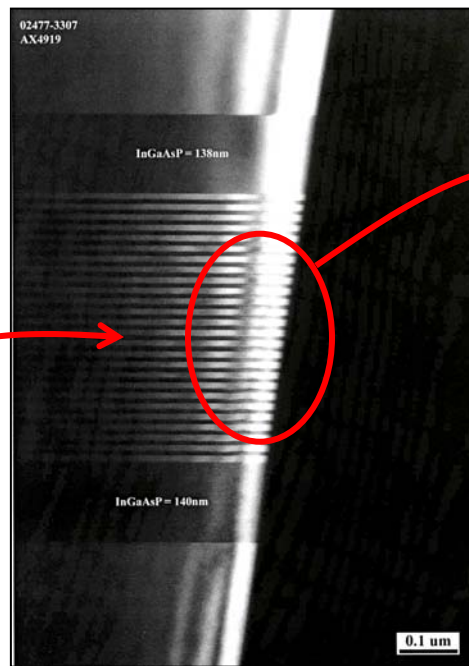
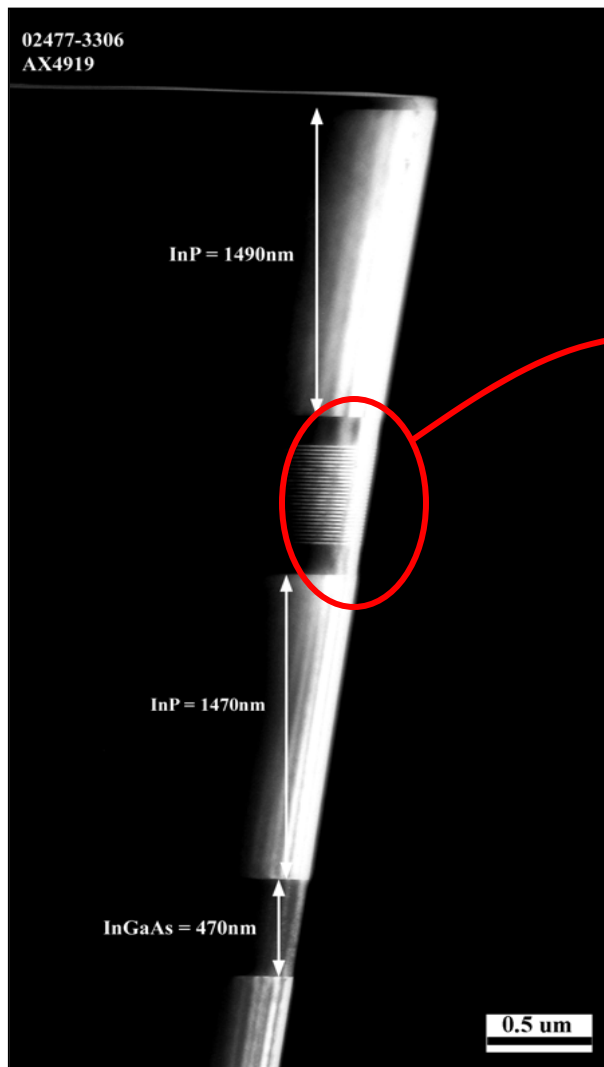
X-ray diffraction and simulation:

- Material quality (Intensity, FWHM)
- Strain (Relative peak position)
- Composition and thickness of the layers (Simulation, not always possible!)
- Growth calibration

Material Characterization: Transmission Electron Microscopy



TEM

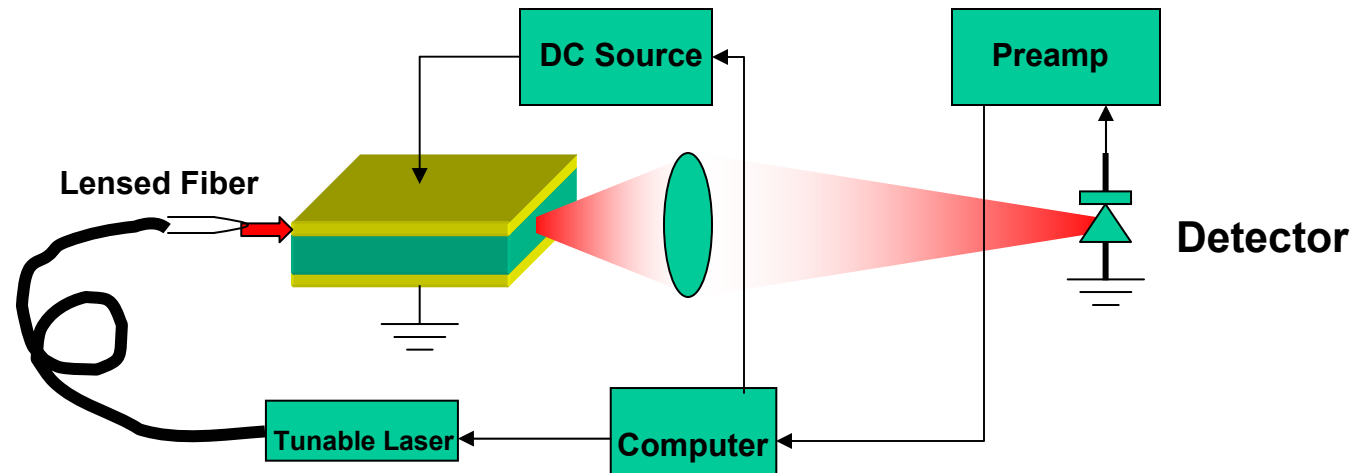


Transmission Electron Microscopy (TEM):

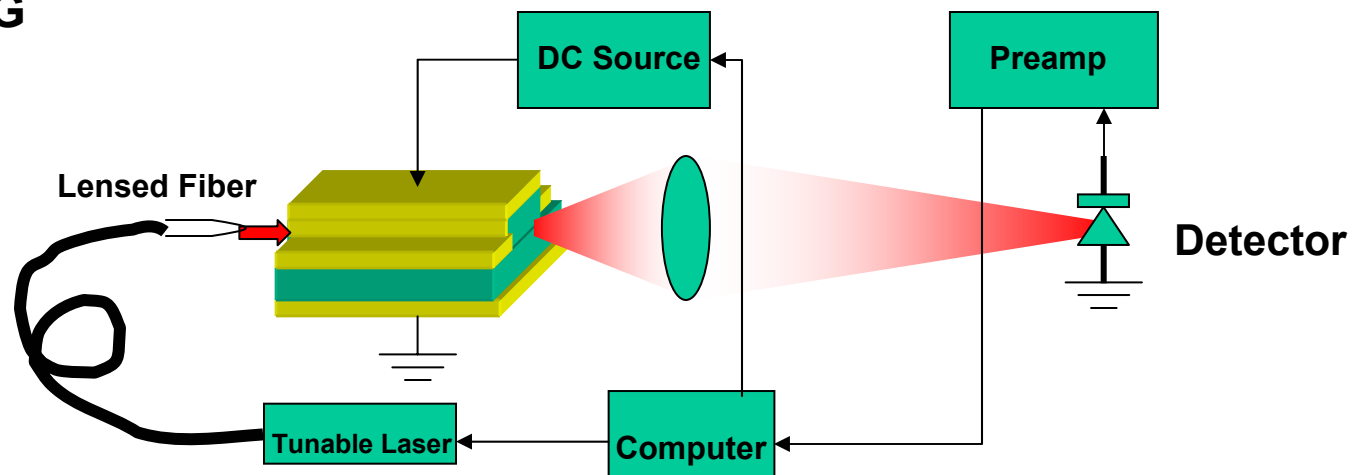
- Material thickness
- Microscopic uniformity
- Interface abruptness

Measurement Setup

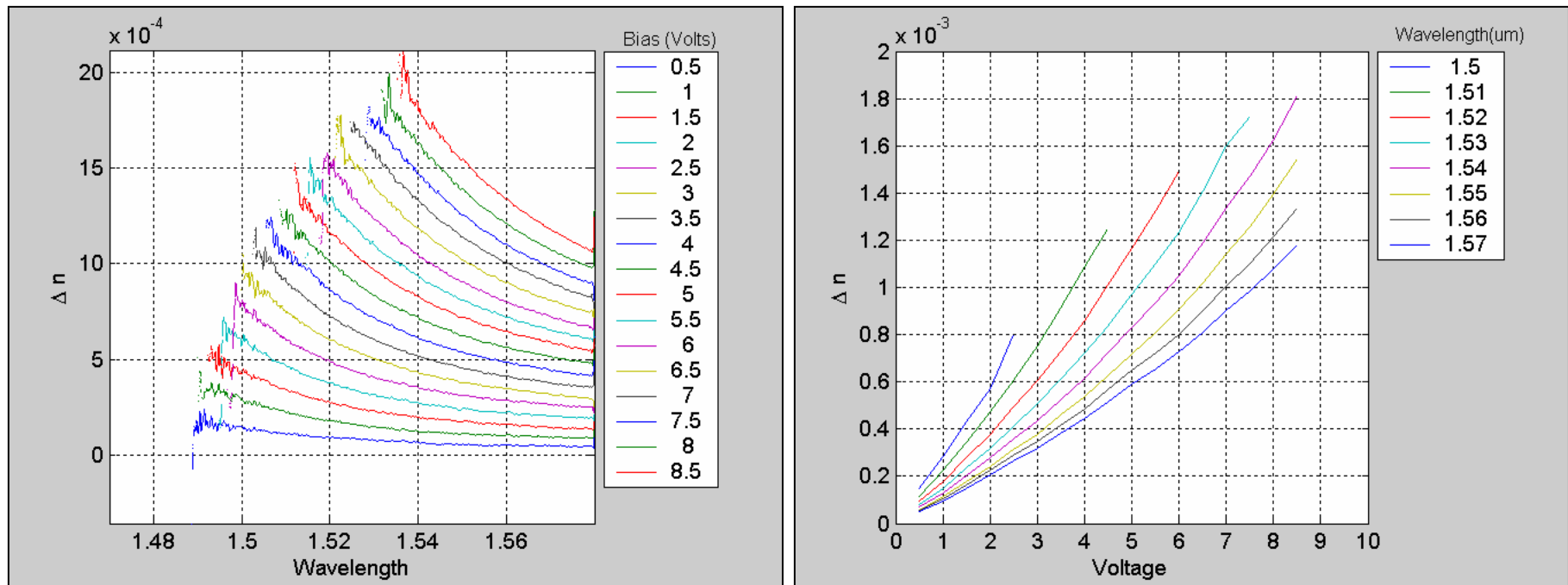
Planar WG



Index-Guided WG

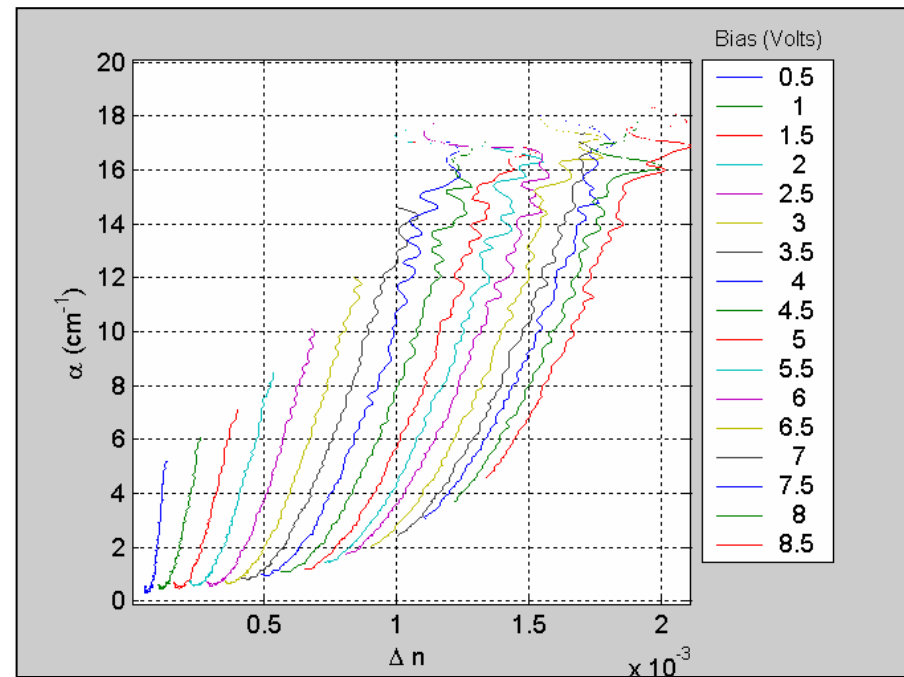
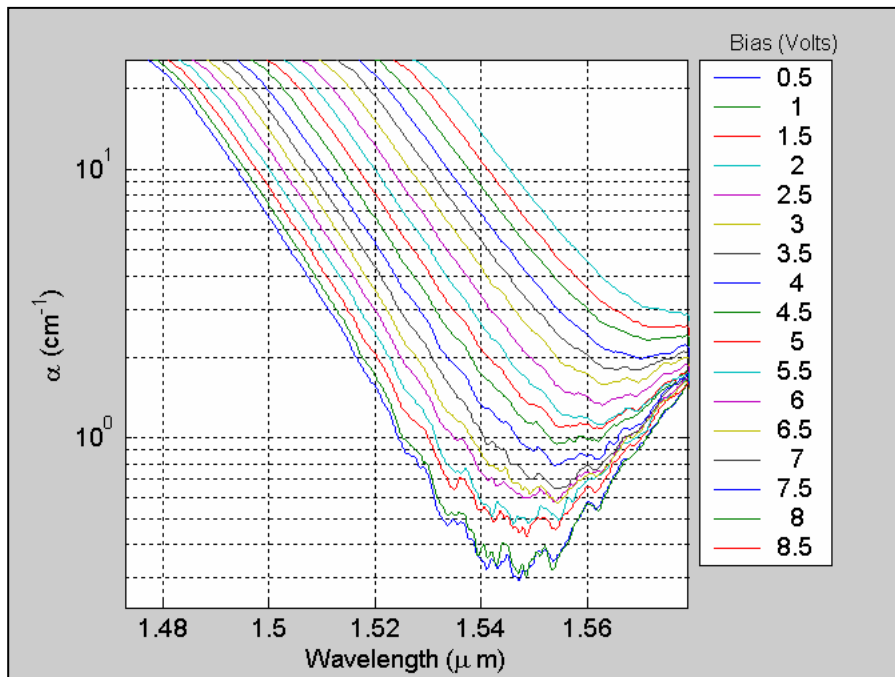


Typical Index vs. Voltage -or- vs. Wavelength



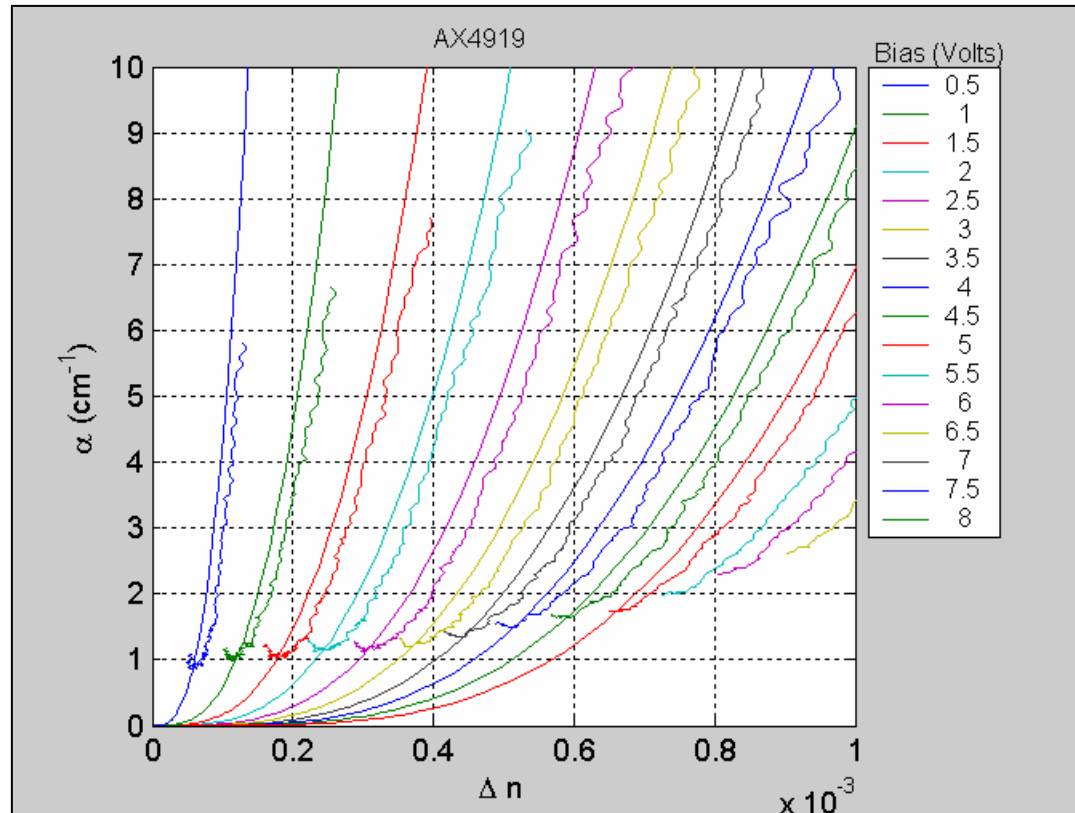
- Change of index versus wavelength for different voltage bias
- Change of index versus voltage bias for different wavelengths

Typical Absorption vs. Wavelength -or- vs. Index



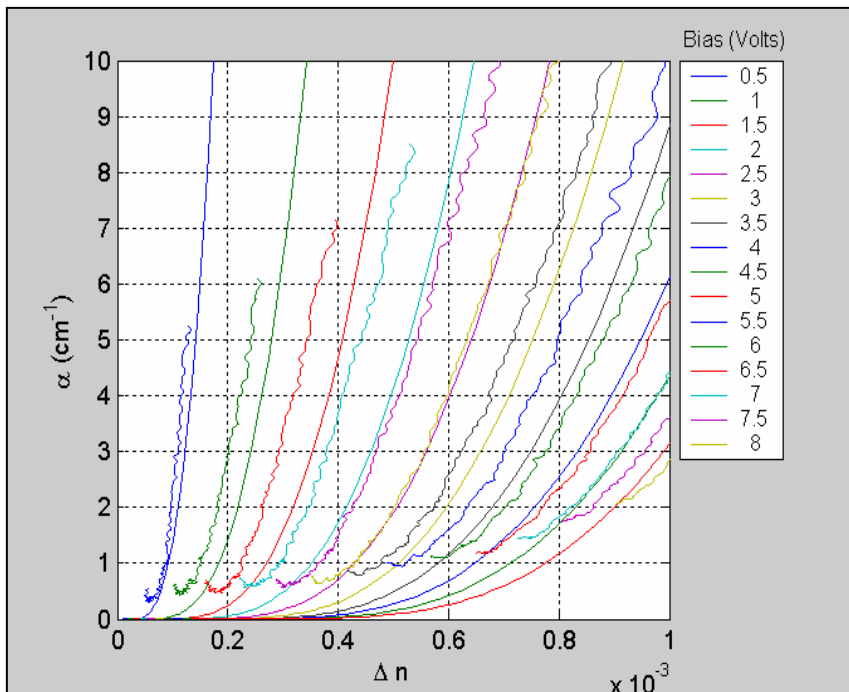
- Loss versus wavelength for different voltage bias
- Loss versus change of index for different voltage bias

Agreement of Modeling and Measurement

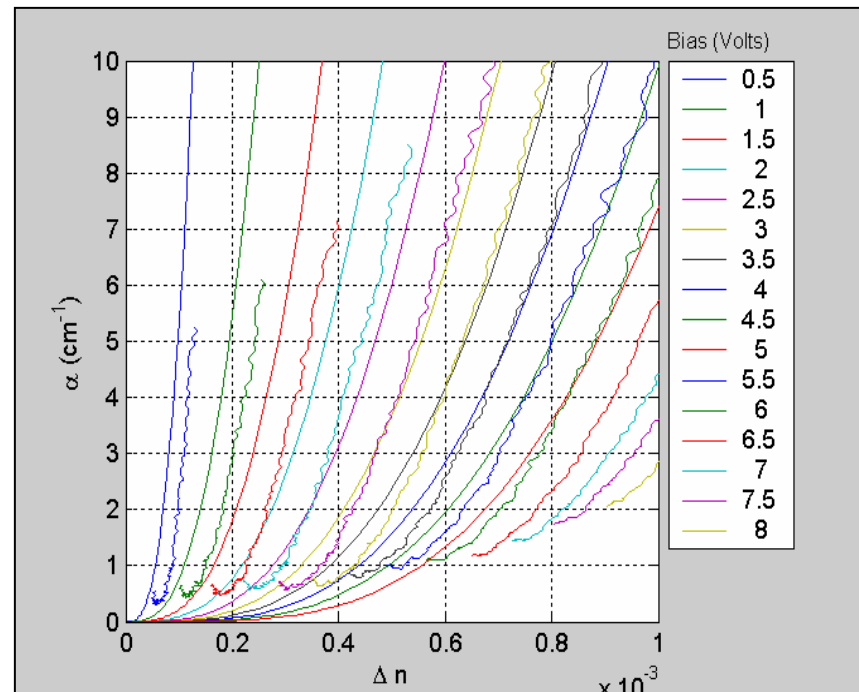


- **Adjustable parameters for the model:**
 - Structure (from x-ray simulation)
 - Linewidth broadening and band edge (from measured loss)
 - Internal field (from device modeling)
 - No other adjustable Parameter

Dependence of Modeled Parameters on Adjustable Parameters

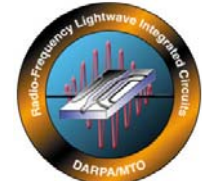


- Modeled without x-ray simulation



- Modeled without field-dependent exciton broadening

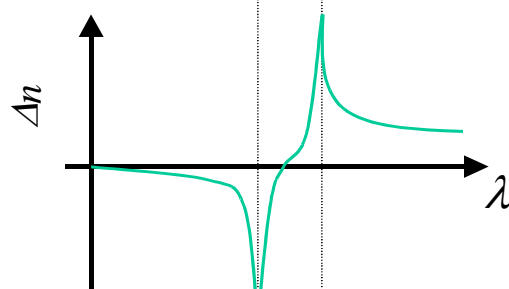
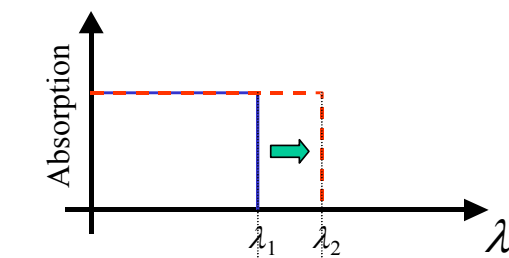
Kramers-Kronig Relation, Limitations of Existing Technology



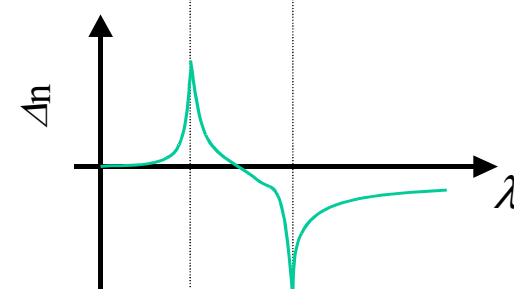
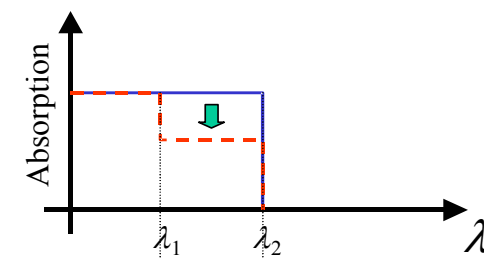
- Kramers-Kronig relation connects the change of absorption to the change of index:

$$\Delta n(\lambda) = \frac{\lambda^2}{2\pi^2} \int \frac{\Delta \alpha(\lambda')}{\lambda^2 - \lambda'^2} d\lambda'$$

- Two important cases are:



Case I

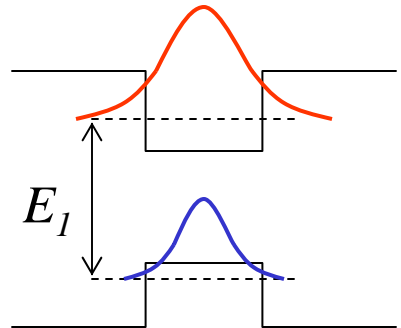


Case II

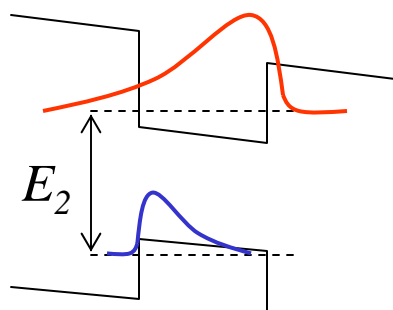
Kramers-Kronig Relation, Limitations of Existing Technology (cont'd)



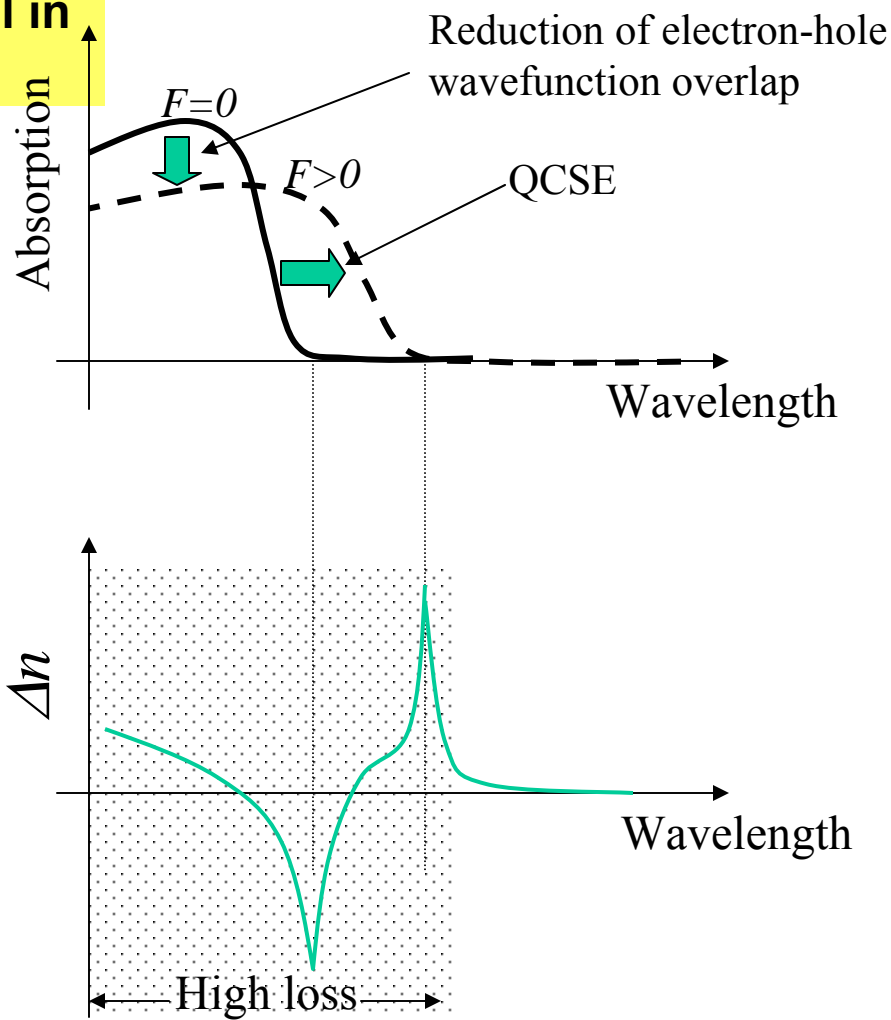
- MQW shows a mixture of case I and case II, and hence Δn is small in the low loss wavelenghts



$F=0$

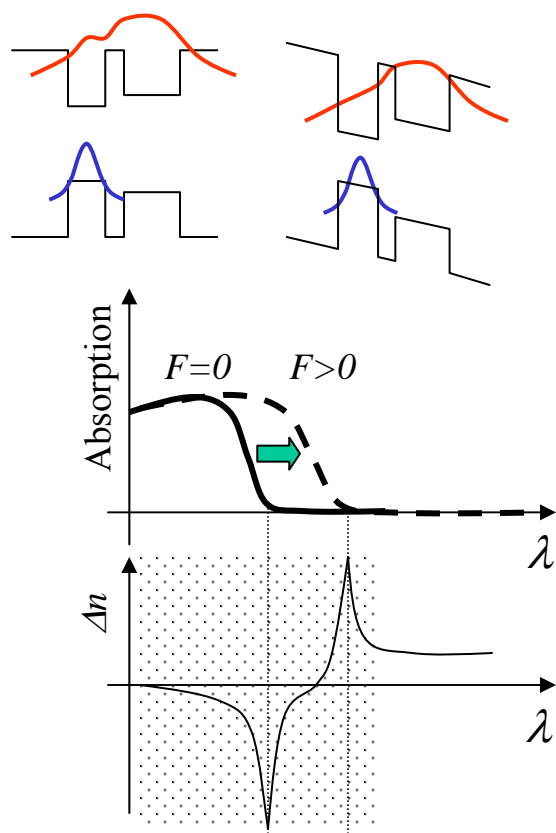


$F>0$

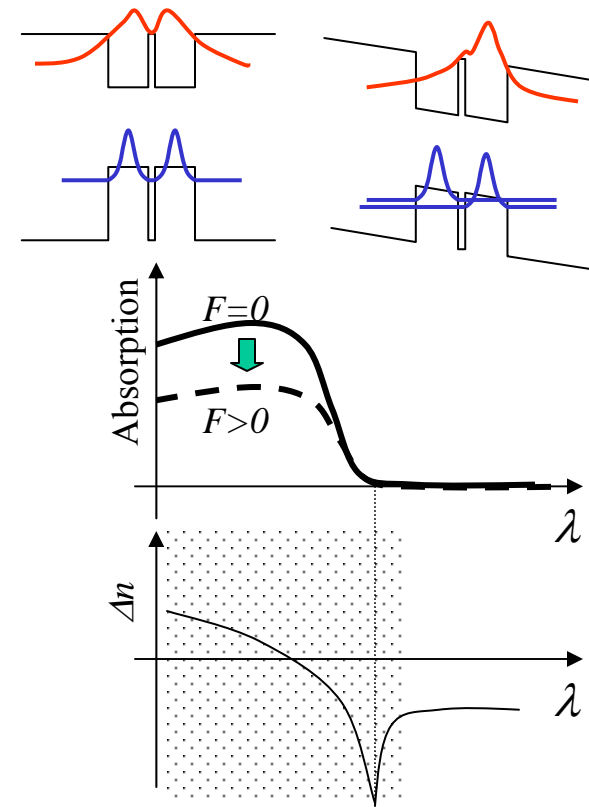


Coupled Quantum Wells

- Added degrees of freedom in the coupled quantum wells makes it possible to design structures which are close to either case I or case II. Therefore, high Δn can be achieved even far from the absorption edge.



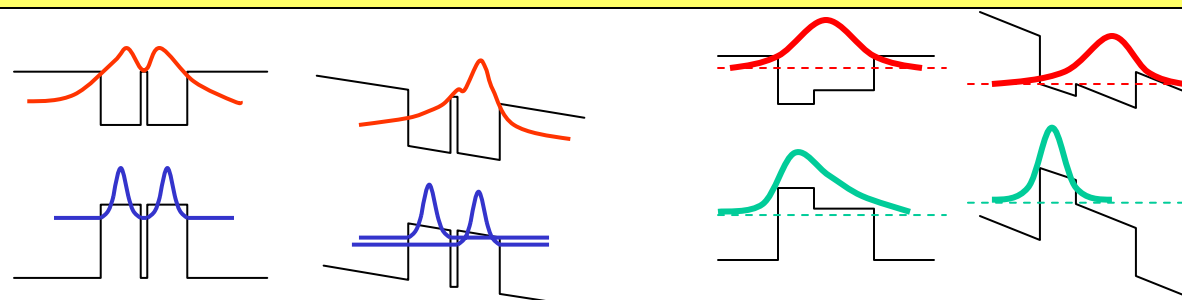
Similar to case I



Similar to case II

Stepped Quantum Wells

- Theoretically, coupled quantum wells show significantly higher sensitivities than the regular quantum wells.
- However, we chose the new class of two and three-step quantum wells for practical reasons:



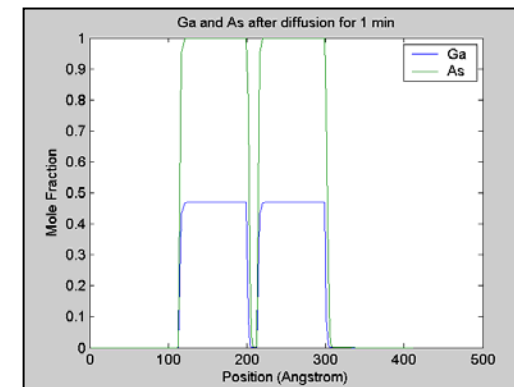
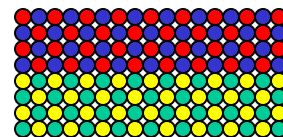
- Coupled QW without and with external electric field
- Enhancement due to the resonant tunneling of electrons
- Step QW without and with external electric field
- Enhancement due to the “bond” to “leaky” mode transition of holes

- **Advantages of Step QWs Over Coupled QWs**
 - Less sensitive to interface abruptness
 - Does not need very thin layers
 - Takes advantage of material systems with high valence band offset (e.g. GaInAsP)

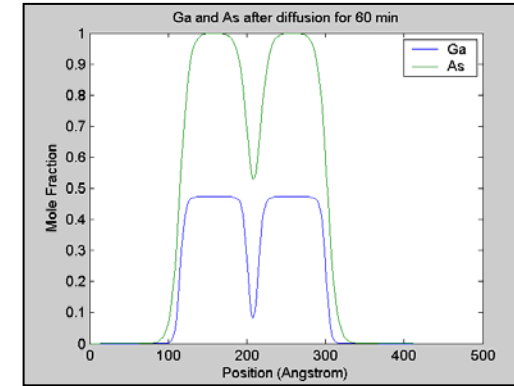
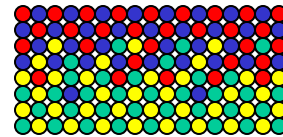
Interdiffusion Modeling

Our modeling^a shows that interdiffusion can severely deform the potential profile of the quantum wells at the usual growth temperature of $\sim 650^{\circ}\text{C}$

Crystal interface as grown



Crystal interface after interdiffusion for 60 min @ 650°C



Schematic

Composition

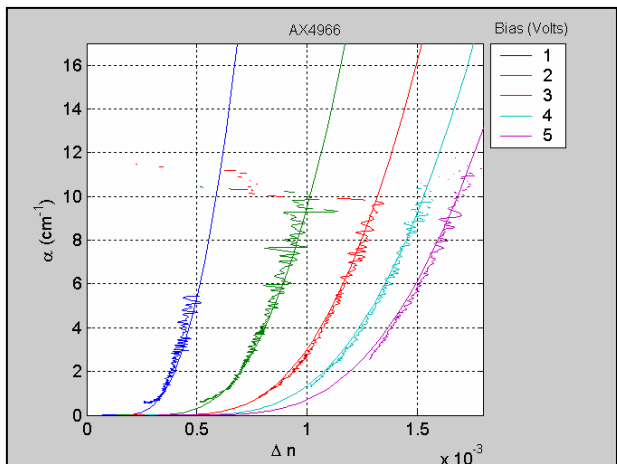
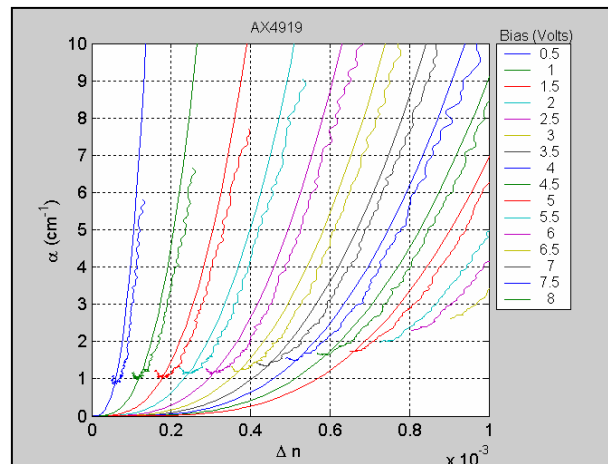
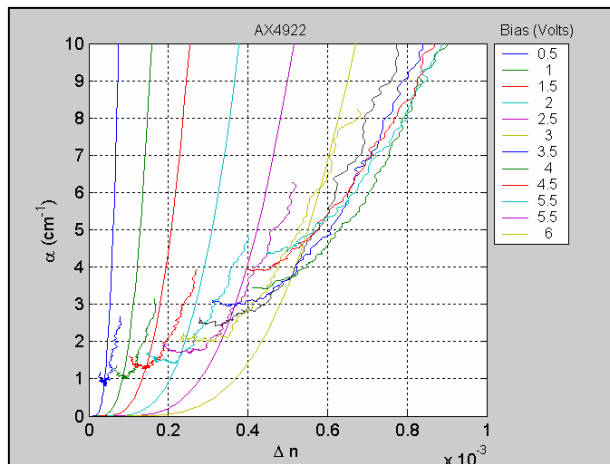
Band Diagram

a) Based on the interdiffusion data from: Bursik et al, J. of Appl. Phys. **91**, 9613 (2002)

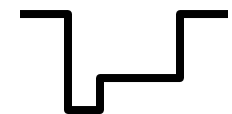
Realization of Stepped Quantum Well Modulators



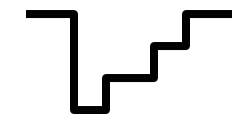
Measured and simulated results for two-step and three-step QWs compared to a sample with regular quantum well design.



Regular QW

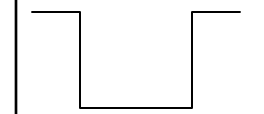
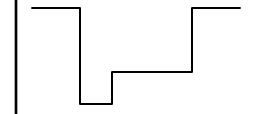
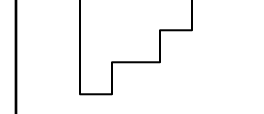


Two-step QW



Three-step QW

Stepped Quantum Well Summary

Sample #	$\Delta n/\Delta V @ \alpha=1 \text{ cm}^{-1}$	$V_\pi L (\text{V.mm})$ (Push-Pull)	DC Bias (V)	Type	Potential Profile
AX4922	$\sim 1 \times 10^{-4}$	~ 3.8	1	Regular QW	
AX4919	$\sim 1.3 \times 10^{-4}$	~ 2.9	1	2-step Asym.	
AX4966	$\sim 3 \times 10^{-4}$	~ 1.29	1	3-step Asym.	

Note: Lincoln Lab showed $V_\pi L=5.8 \text{ V.mm}$ @ $\alpha=1 \text{ cm}^{-1}$ @ $V_{DC}=6 \text{ Volts}$ from regular QWs in the 2001 R-FLICS review.

Growth Optimization



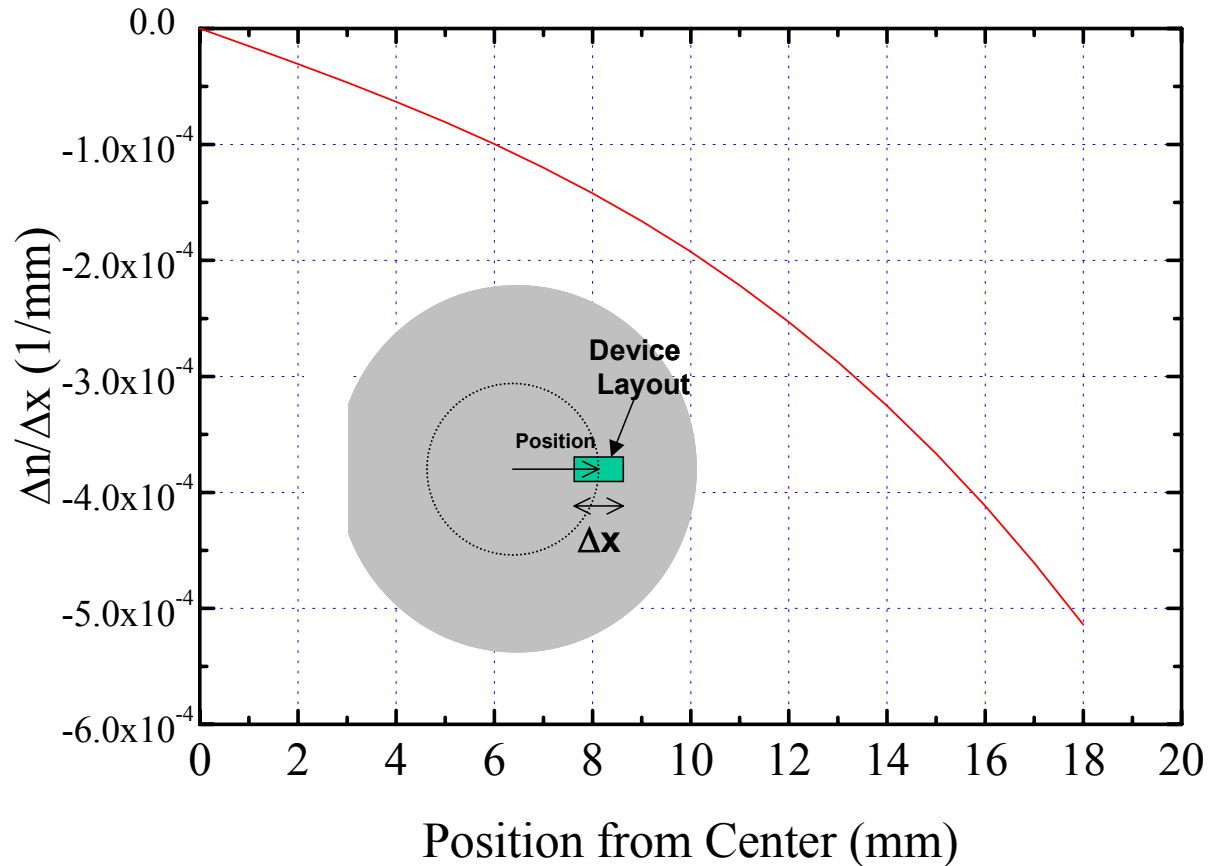
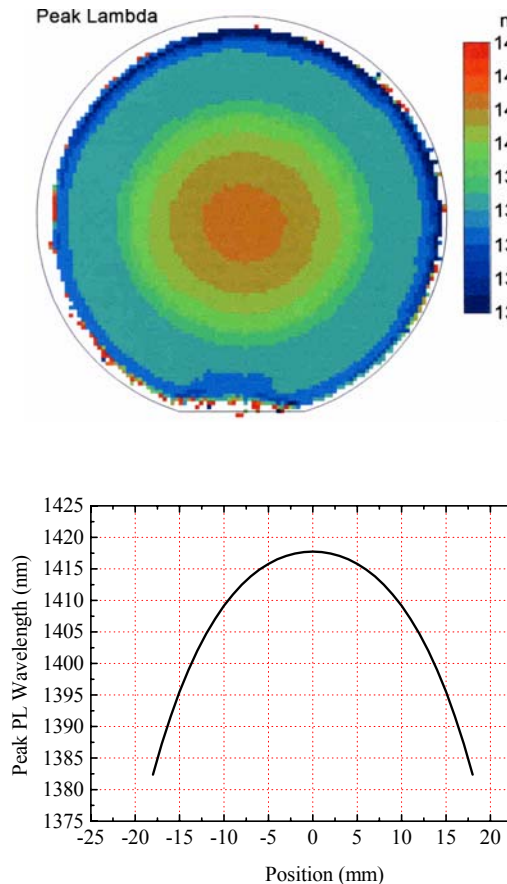
Goals:

- Improve growth uniformity
- Reduce excitonic broadening

Approaches:

- Optimize growth temperature
- Use all-ternary material system to reduce inhomogenous broadening

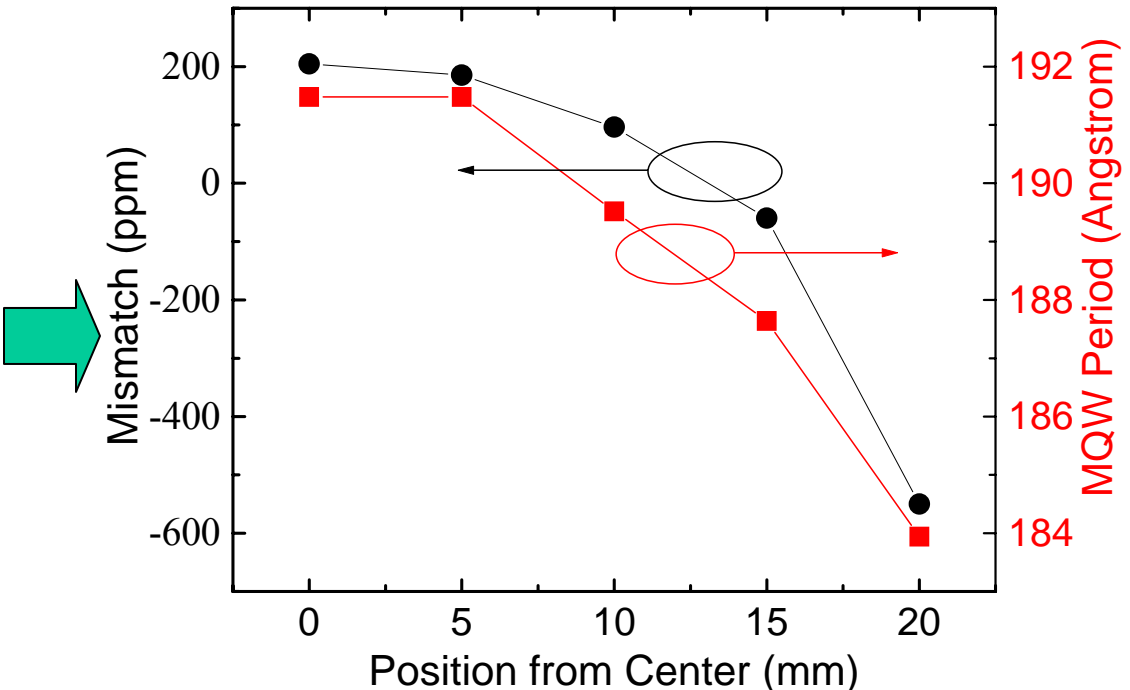
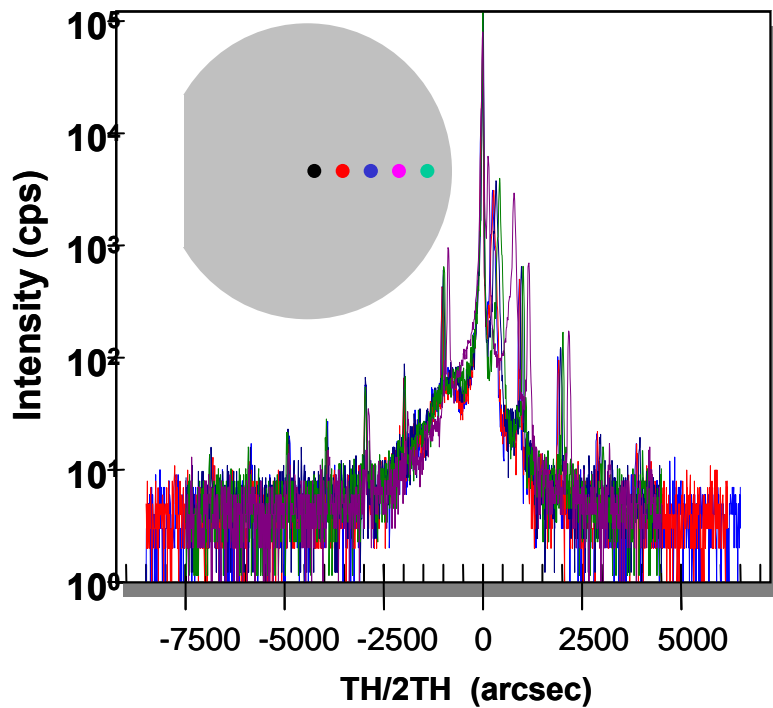
Material Bandgap Non-uniformity



PL mapping of a typical growth

Change of Index per mm versus
distance from the center

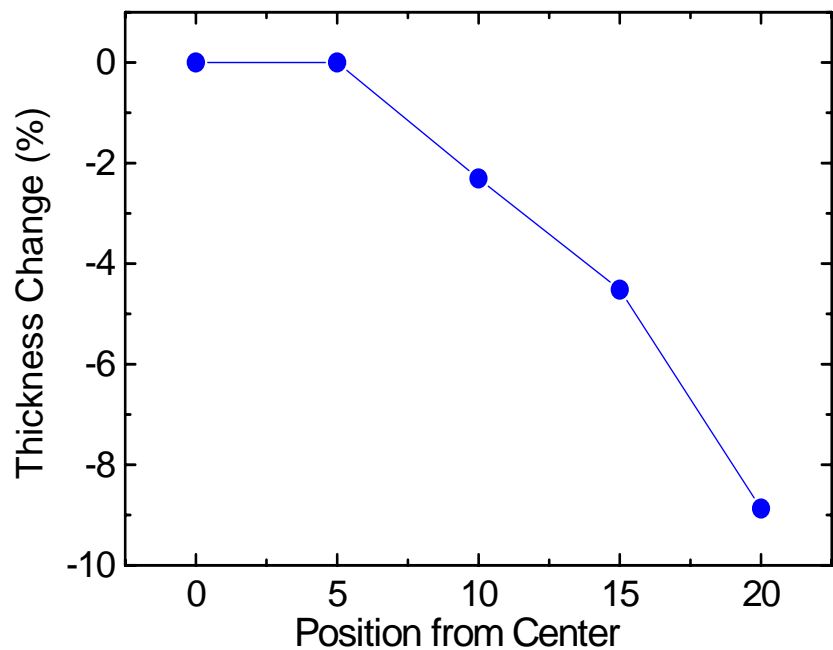
Material Structural Non-uniformity



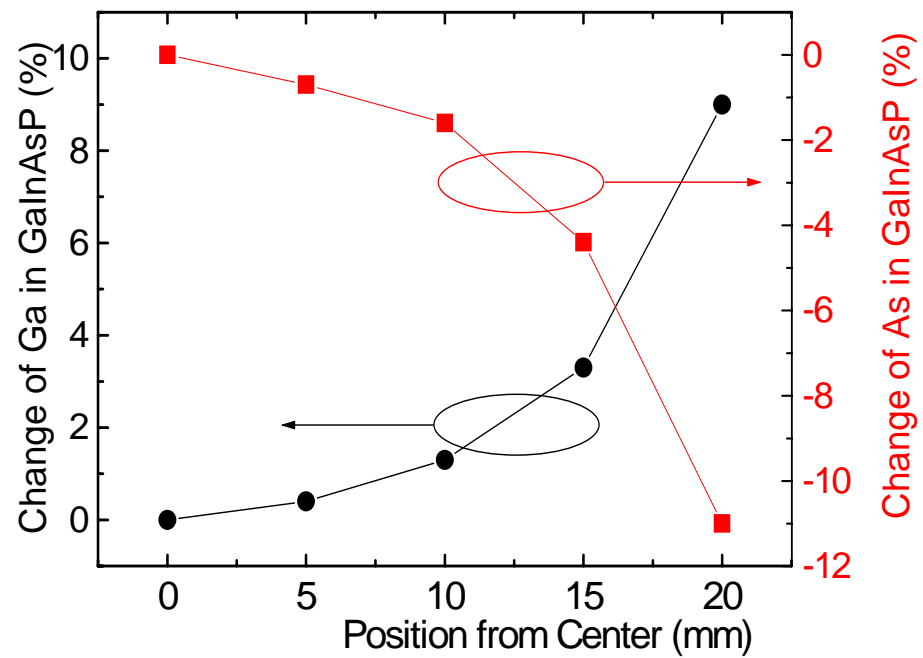
X-ray mapping of a typical growth

Average lattice mismatch and period of the MQW structure extracted from x-ray mapping

Material Composition and Thickness Non-uniformity

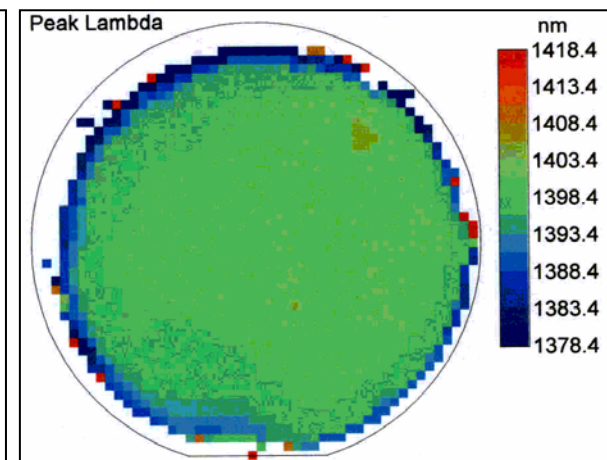
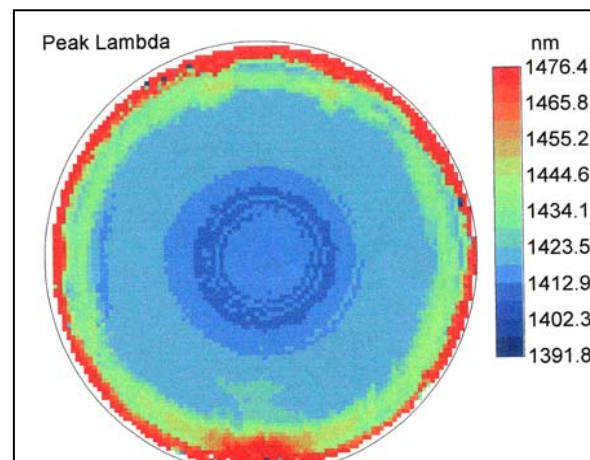
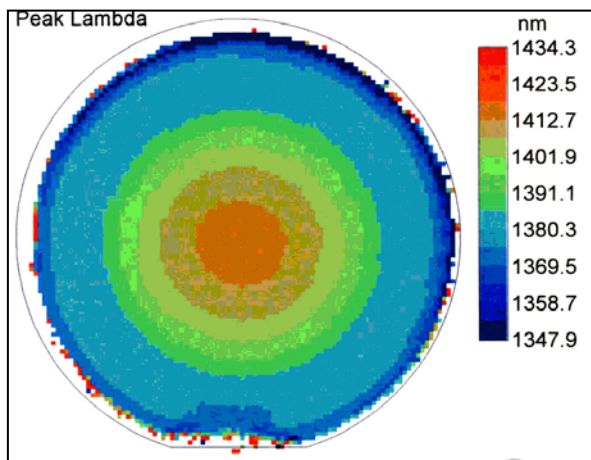
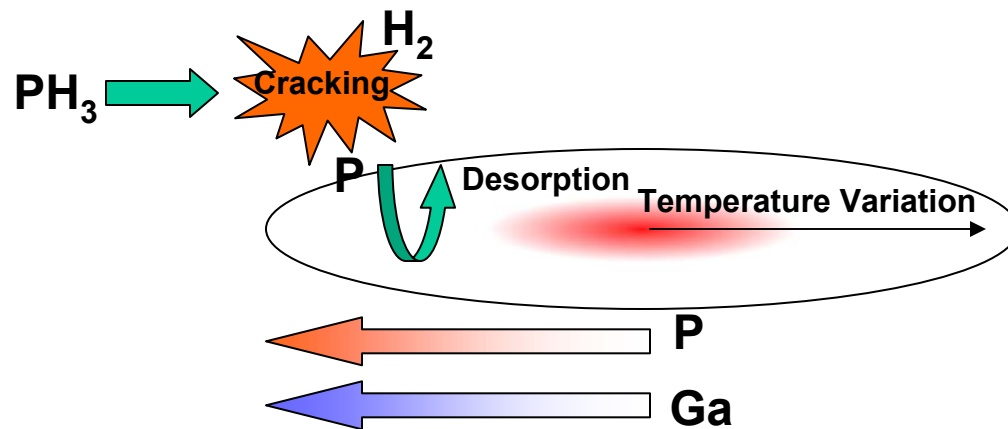


Thickness variation versus position (calculated from x-ray mapping)



Gallium and Arsenic composition variation versus position (calculated from x-ray and PL mapping)

Low Temperature and All-Ternary Growth Methods

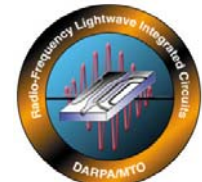


Conventional Growth:
 $\Delta\lambda_{\text{PL}} \approx 30 \text{ nm}$ for
 $0 < R < 20 \text{ mm}$

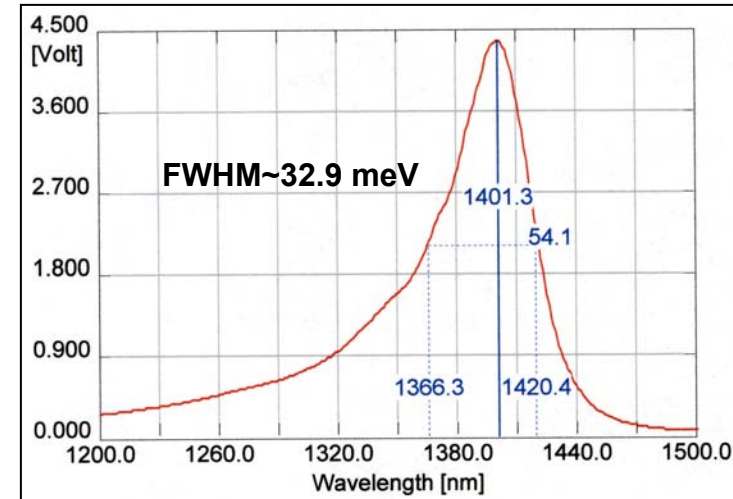
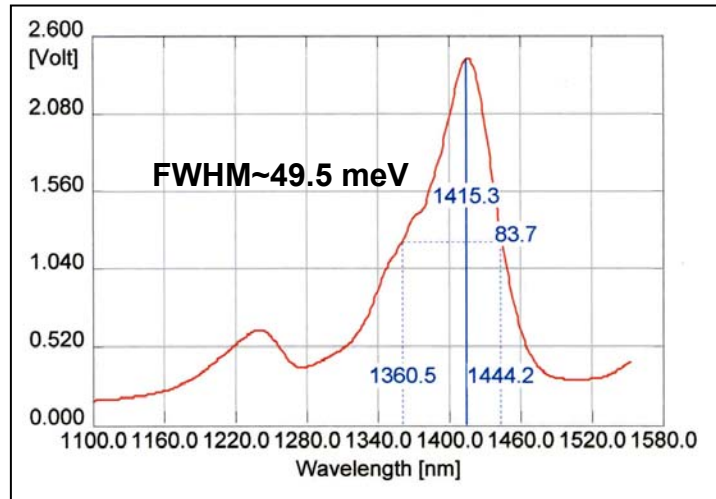
Low Temperature Growth:
 $\Delta\lambda_{\text{PL}} \approx 10 \text{ nm}$ for
 $0 < R < 20 \text{ mm}$

Low Temperature All-ternary (InAsP/GaInP) Growth:
 $\Delta\lambda_{\text{PL}} \approx 2 \text{ nm}$ for
 $0 < R < 20 \text{ mm}$

Low Temperature strain compensated InAsP/GaInP



Low temperature strain compensated InAsP/GaInP structures show narrow linewidth due to the reduce interdiffusion and elimination of quaternary layers.



PL of a regular MQW using quaternary layers grown at ~655°C

PL of a MQW structure using strain compensated ternary layers grown at ~550°C

Summary



- Developed an accurate modeling toll for quantum well modulators
- Developed excellent material growth control using systematic characterization methods
- Demonstrated stepped quantum well modulators with three times lower V_π than the existing modulators
- Demonstrated enhanced material uniformity and excitonic linewidth

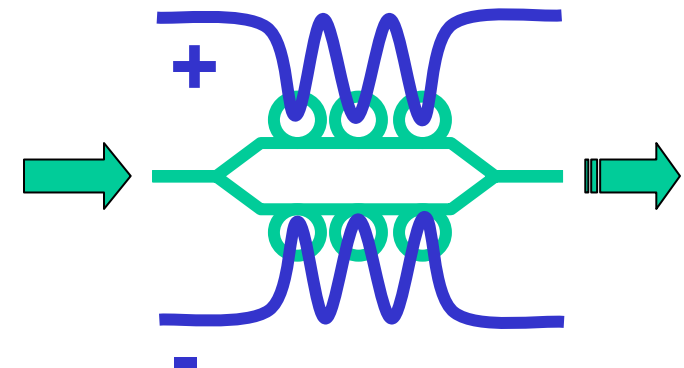
Device Design & Test

Resonance enhanced modulator concept



Phase modulation with ring-resonators in interferometer arms.

Low optical loss in the rings is essential for this concept (requirement: loss < coupling).



**Ring-resonator Q limits the E/O bandwidth.
→ Fundamental Bandwidth*Sensitivity limitation.**

**Multiple ring-resonators with RF delay lines
→ Further reduction of $V\pi$ without additional bandwidth penalty.**

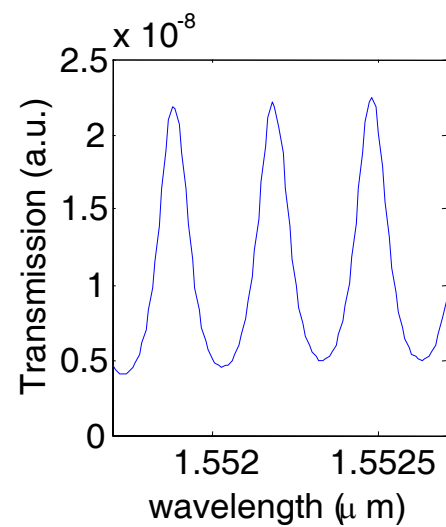
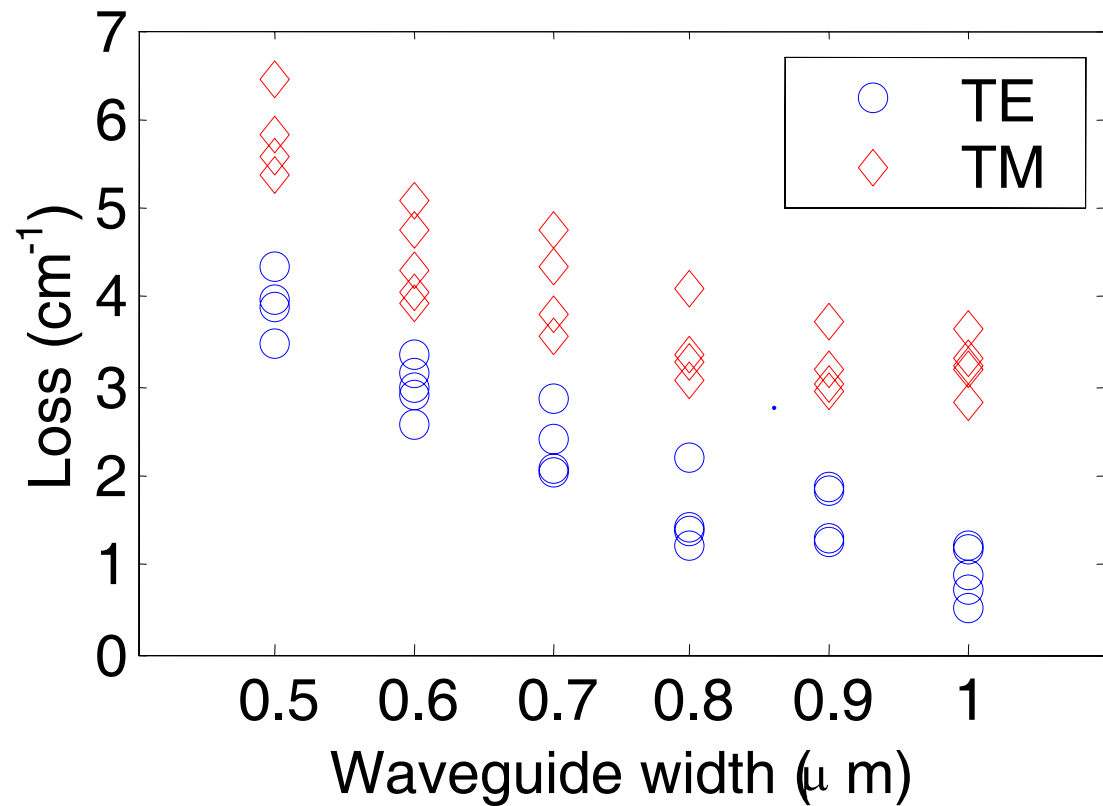
**Group delay in the ring resonators must match the RF-delay
→ Known coupling coefficient is essential.**

Device Design & Test



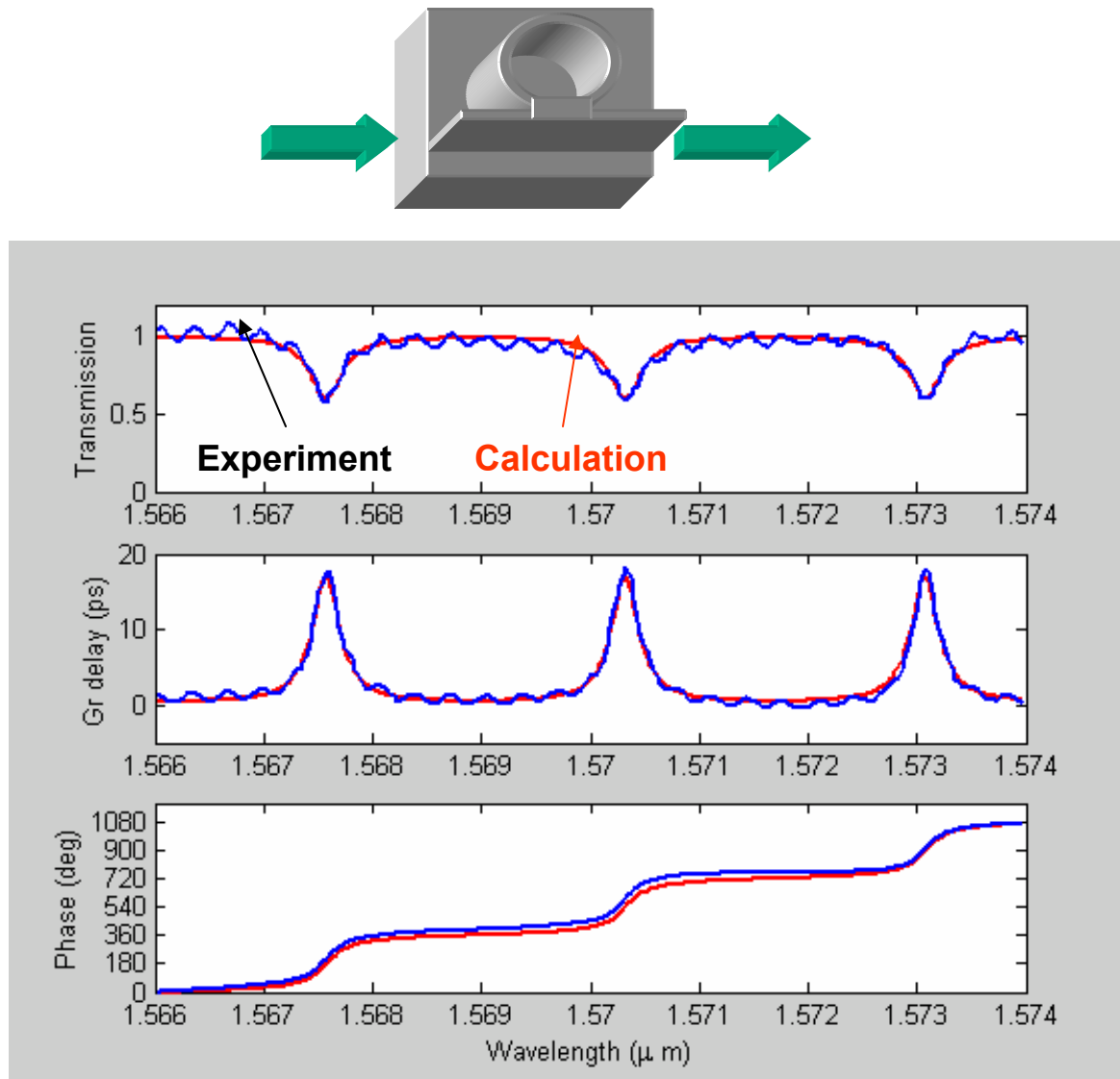
- **Passive device results**
 - Low loss waveguides
 - Low loss ring resonator
- **Advantage of ring resonator-modulator**
 - Modulation gain
 - Frequency Response of ring modulator
- **Interferometer with ring resonator**
- **Electro-optic measurements:**
 - DC-measurements
 - RF-measurements
- **Summary/Outlook**

Low Loss Waveguides



4 cm^{-1} for 0.5 μm width x 4 μm depth waveguide!

Low Loss Ring-Resonator



Waveguide width: 0.9mm.

Circumference: 250 mm.

MMI length: 42mm.

Loss: 8.5%

**$\rightarrow 3.5\text{cm}^{-1}$ effective loss
(includes coupler loss).**

Coupling: 50%.

18ps group delay.

$\rightarrow 6$ roundtrips.

**Optical bandwidth: 44
GHz.**

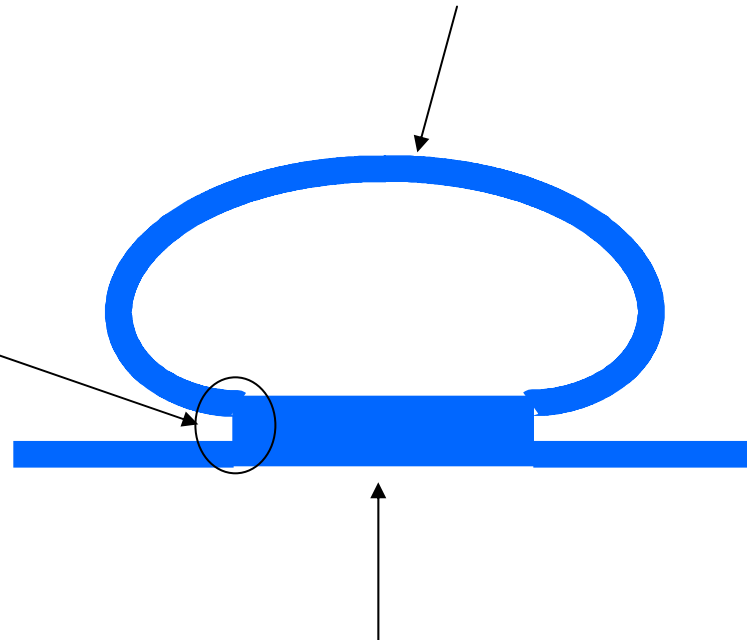
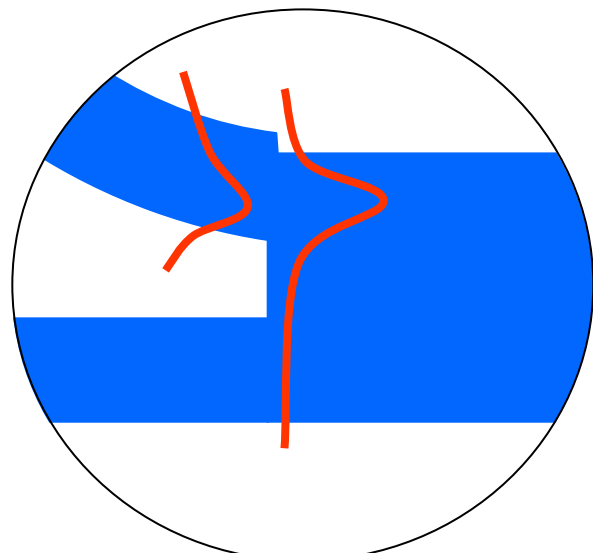
**($\rightarrow 22$ GHz modulator
bandwidth) .**

Ring Resonator Design

Offset at junction.

**Optimized matching of the field in the bend
and the MMI**

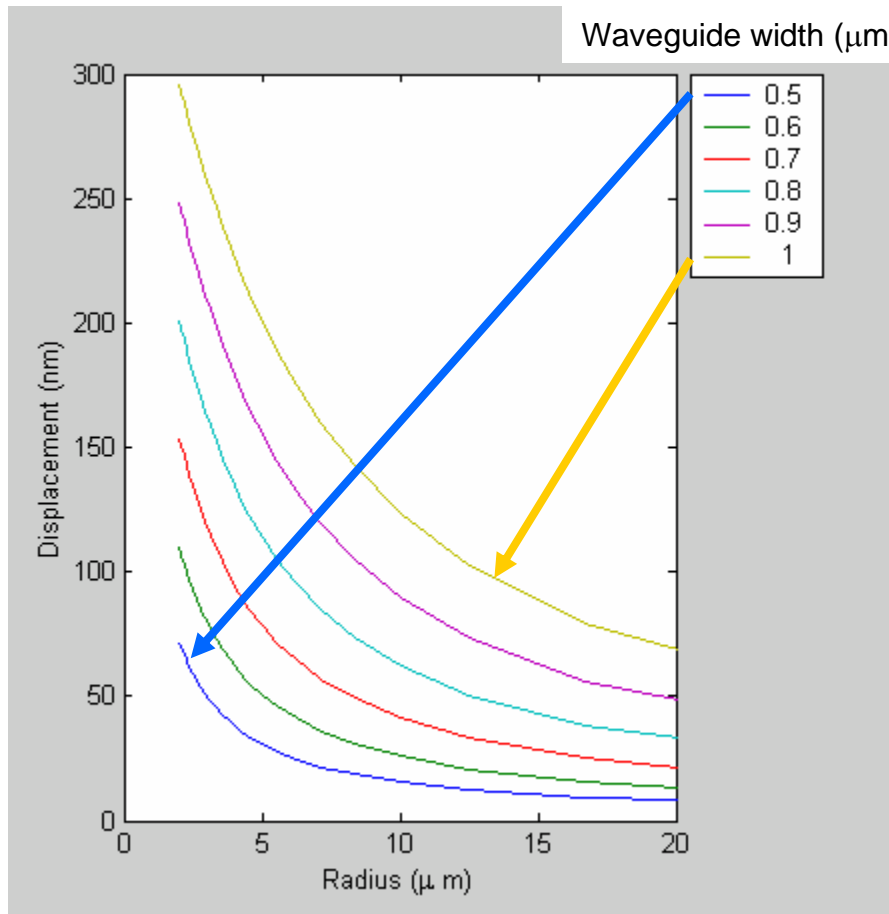
→ No mode conversion / loss



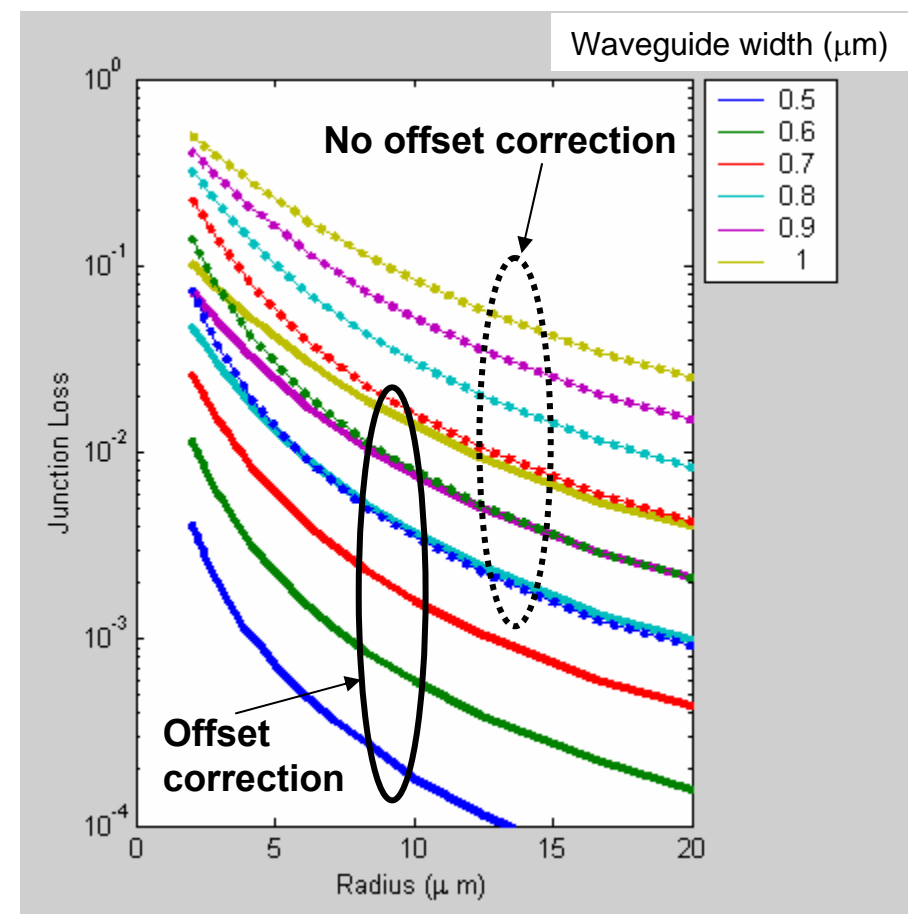
**MMI-coupler:
50% coupling (reproducible)**

Junction offset

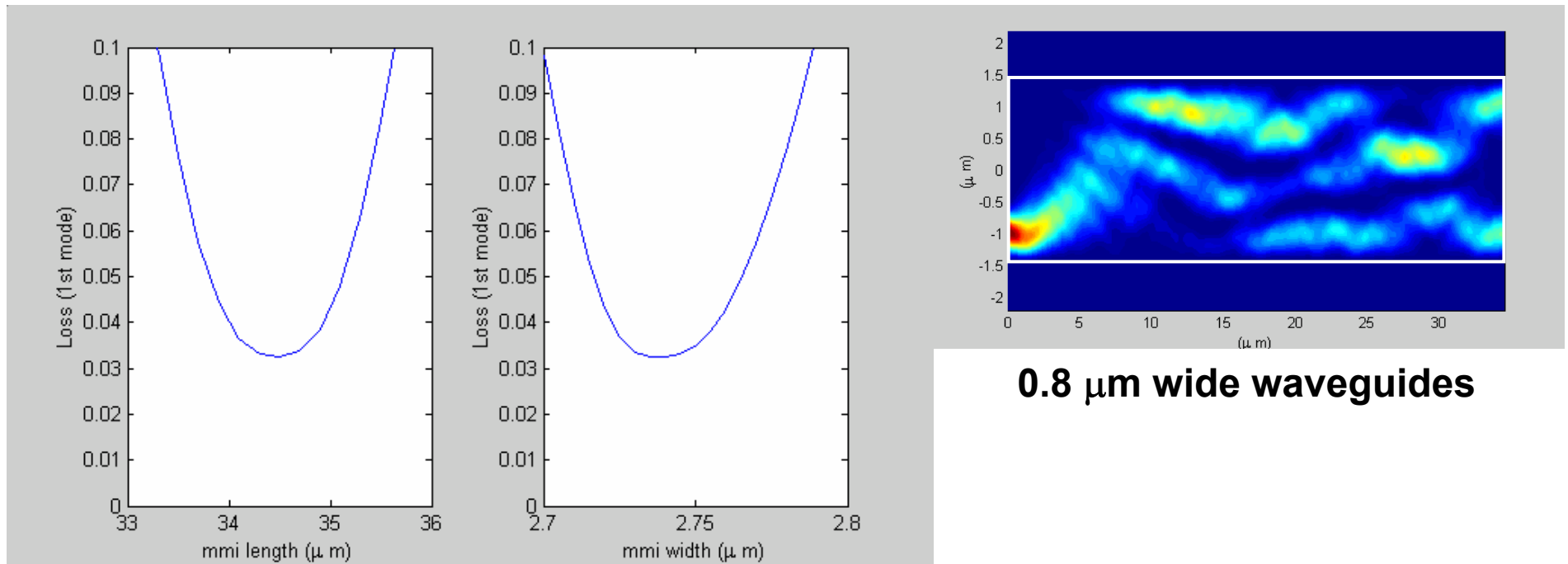
Mode displacement



Junction loss



MMI-Loss and Tolerances

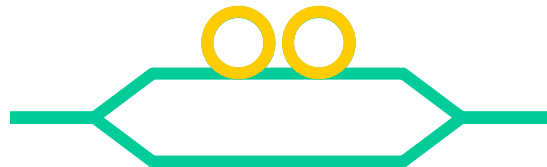


0.8 $\mu\text{ m}$ wide waveguides

Tight tolerances for low loss operation

→ ~30nm width tolerance

Modulator Gain of Ring Resonator Modulator

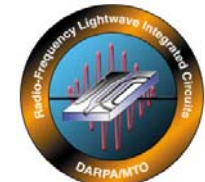


- **Gain =**
$$\frac{(\text{transmission}) / V_{\pi}^2 \text{ of the ring modulator}}{(\text{transmission}) / V_{\pi}^2 \text{ of a loss-less Mach-Zehnder modulator}}$$
 of equal electrode length



- **(transmission) / V_{π}^2** determines the noise figure of an analog link
- **Excess losses reduce the gain**
- **Qualifies the modulator structure (not the material)**

Frequency Response of a Ring Modulator (small signal)

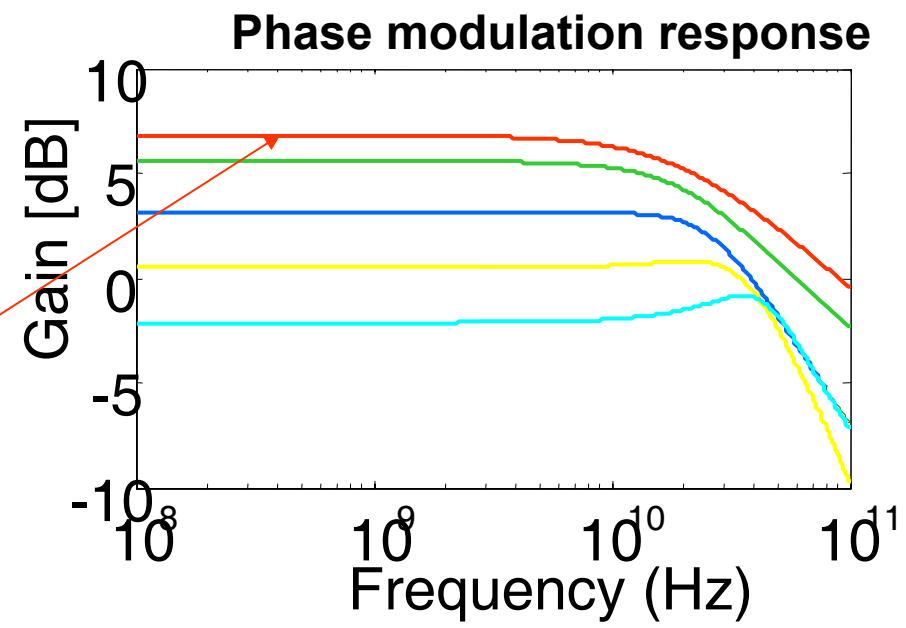
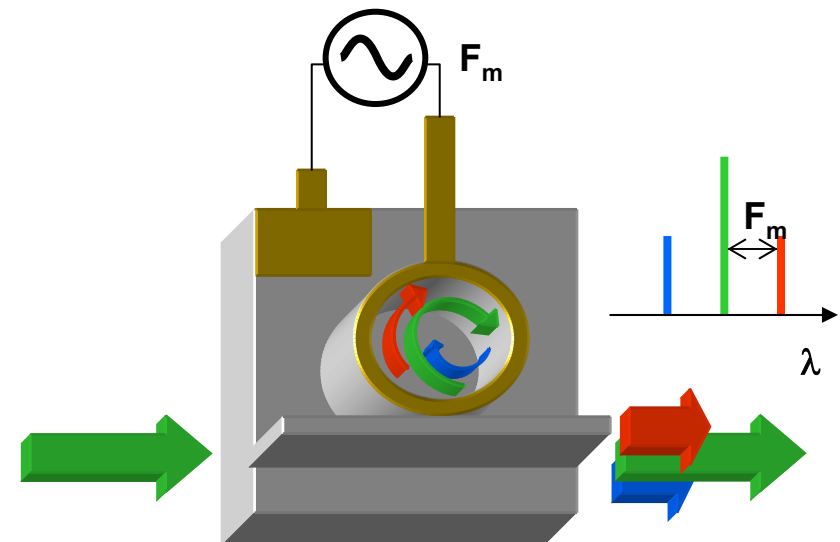
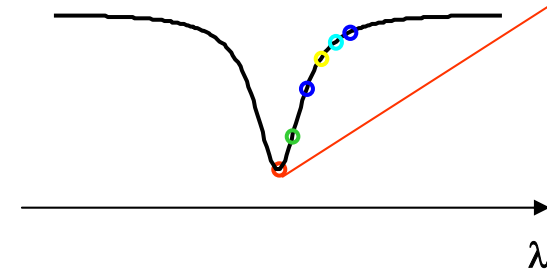


Calculation of modulation response:

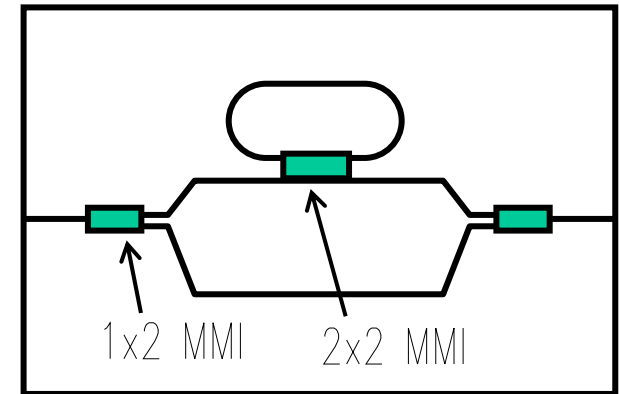
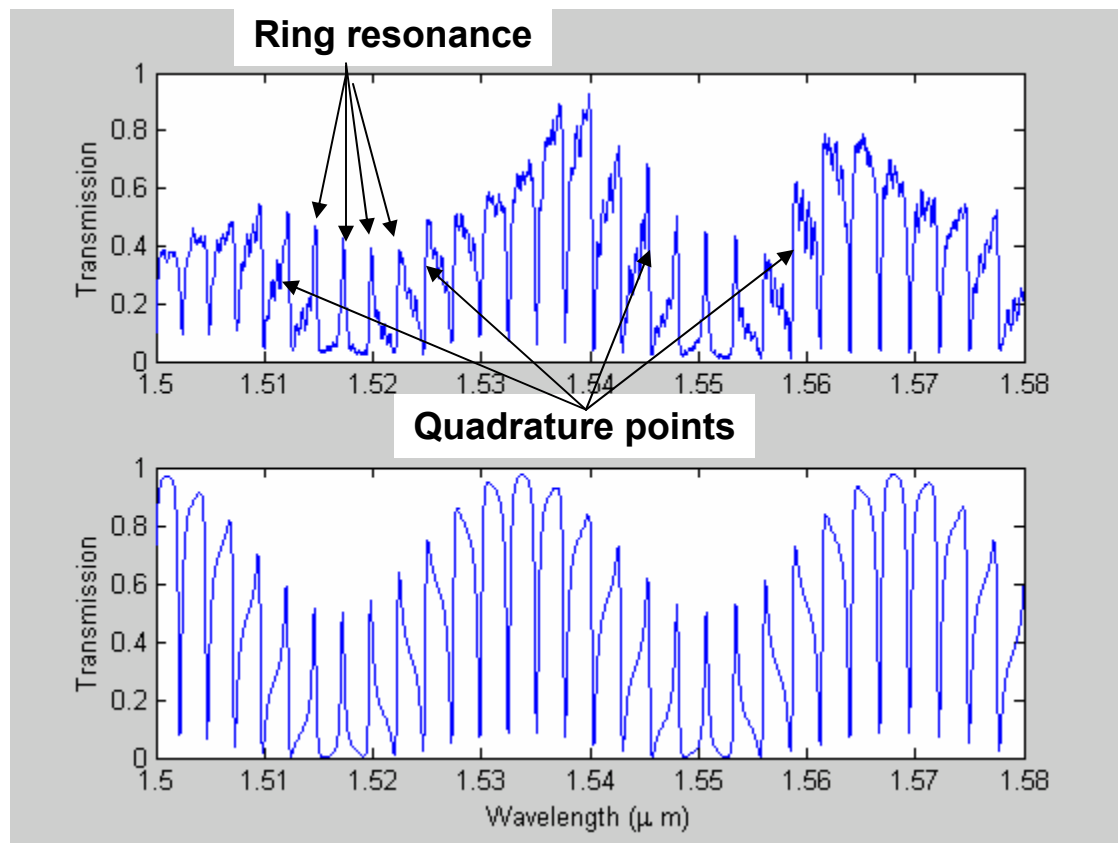
- **3 Wavelength:**
 - Input wavelength and
 - two closest sidebands
- **Cold cavity resonator equations** for each wavelength
- **Equations for the coupling of the 3 components in the phase modulated ring.**

→ **Output components:**
amplitude and phase

- **Calculation of Phase/Amplitude modulation**



Asymmetric MZI with MMI-Coupled Ring Resonator



Waveguide width: $0.8\mu\text{m}$

MMI-length: $34.5\mu\text{m}$

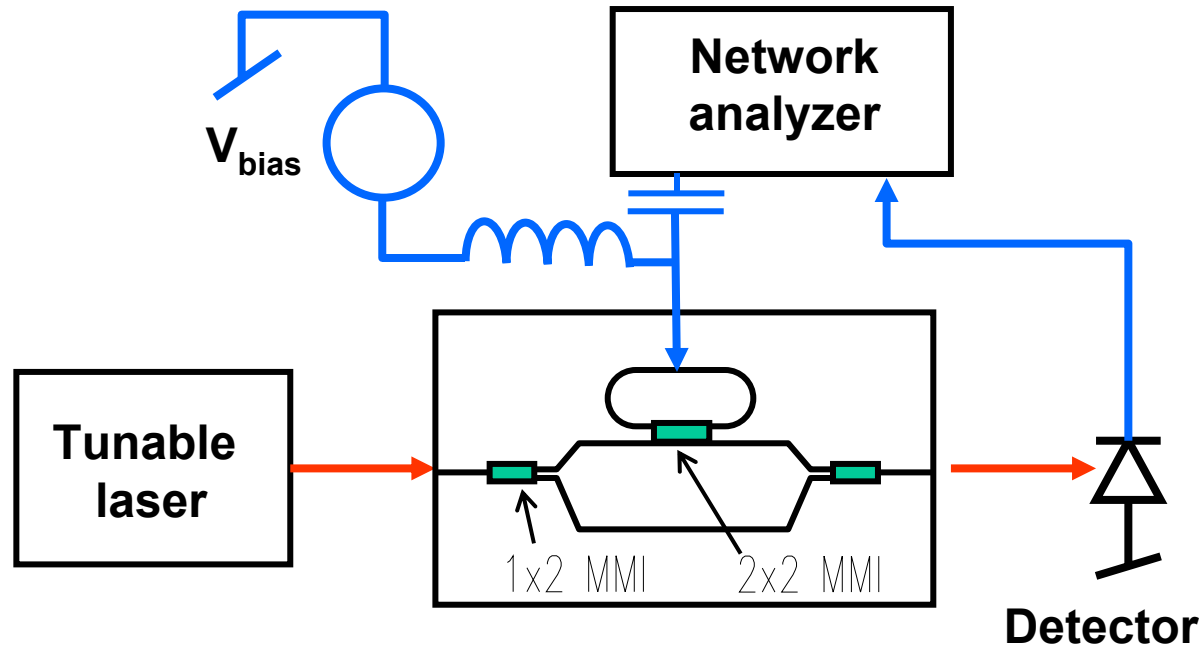
Ring circumference: $250\mu\text{m}$

Ring loss: 15%

Coupling 50%

The asymmetric MZI makes sure that the quadrature condition can be selected by the wavelength

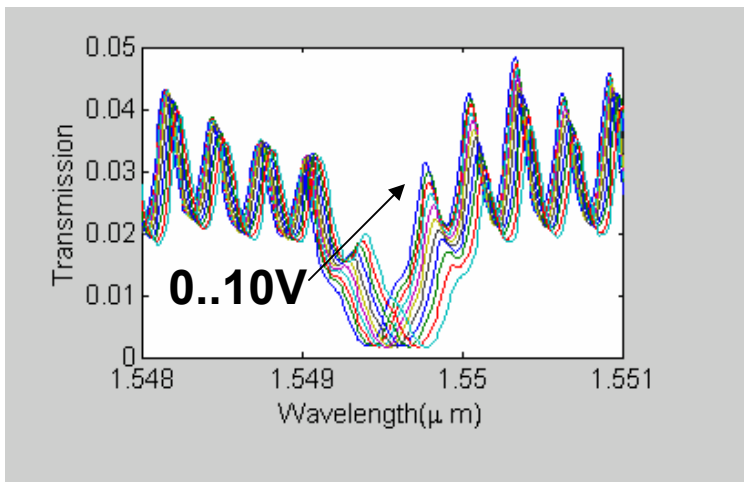
Electro-Optic Measurements



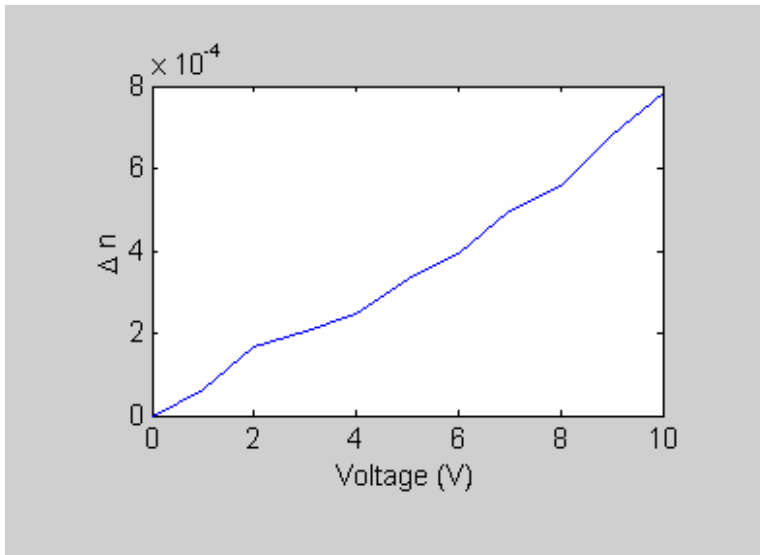
- **DC-measurement:**
 - no RF-modulation, wavelength scan, (variation of V_{bias}).
- **Modulation response:**
 - fixed wavelength, Frequency scan.
- **Wavelength response of modulation:**
 - fixed RF-frequency, wavelength scan.

Modulation Results

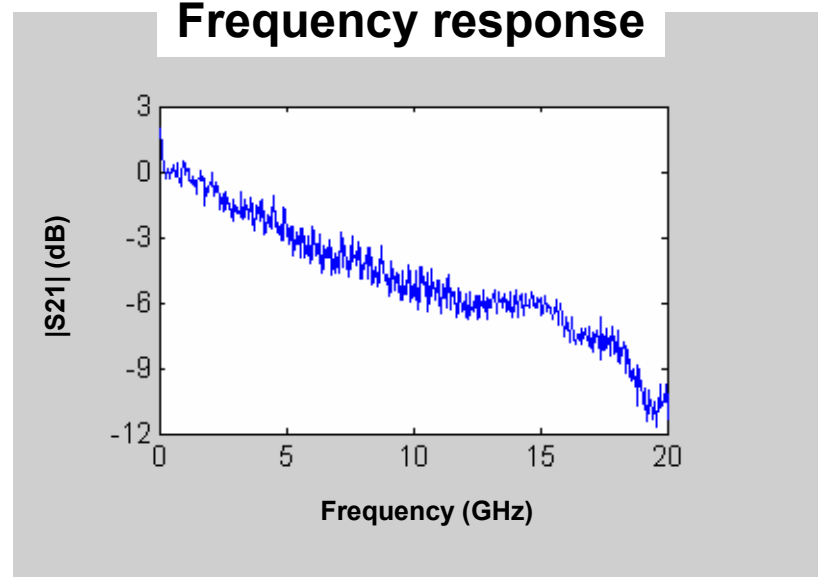
Transmission at various bias voltages



Index change in the ring-resonator



Frequency response

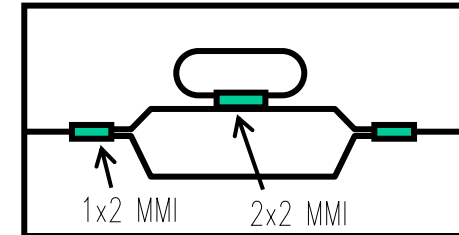
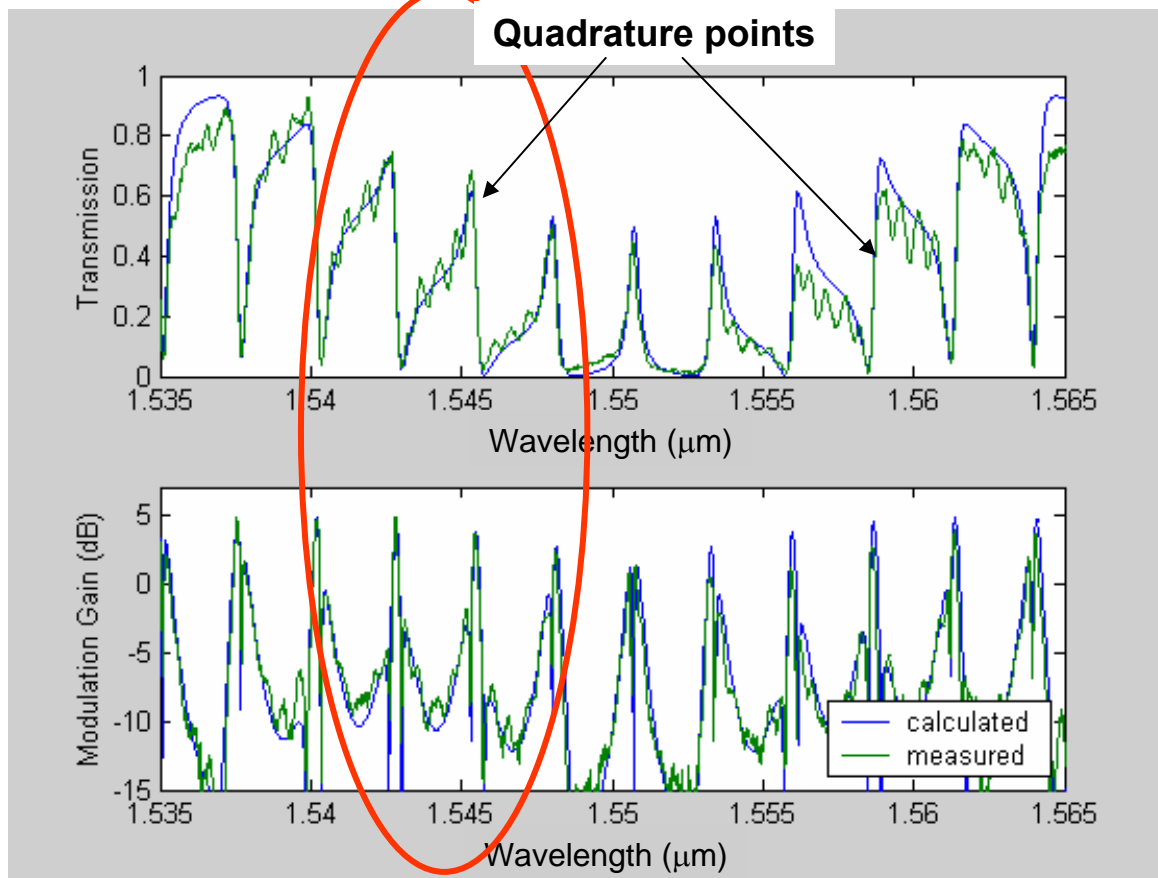


- Reduced index change in deep etched ring-resonators
- Frequency response rolls off too quickly

→ contact/surface leakage problem

RF-measurements

Asymmetric Mach-Zehnder with E/O ring resonator



Transmission measurement:

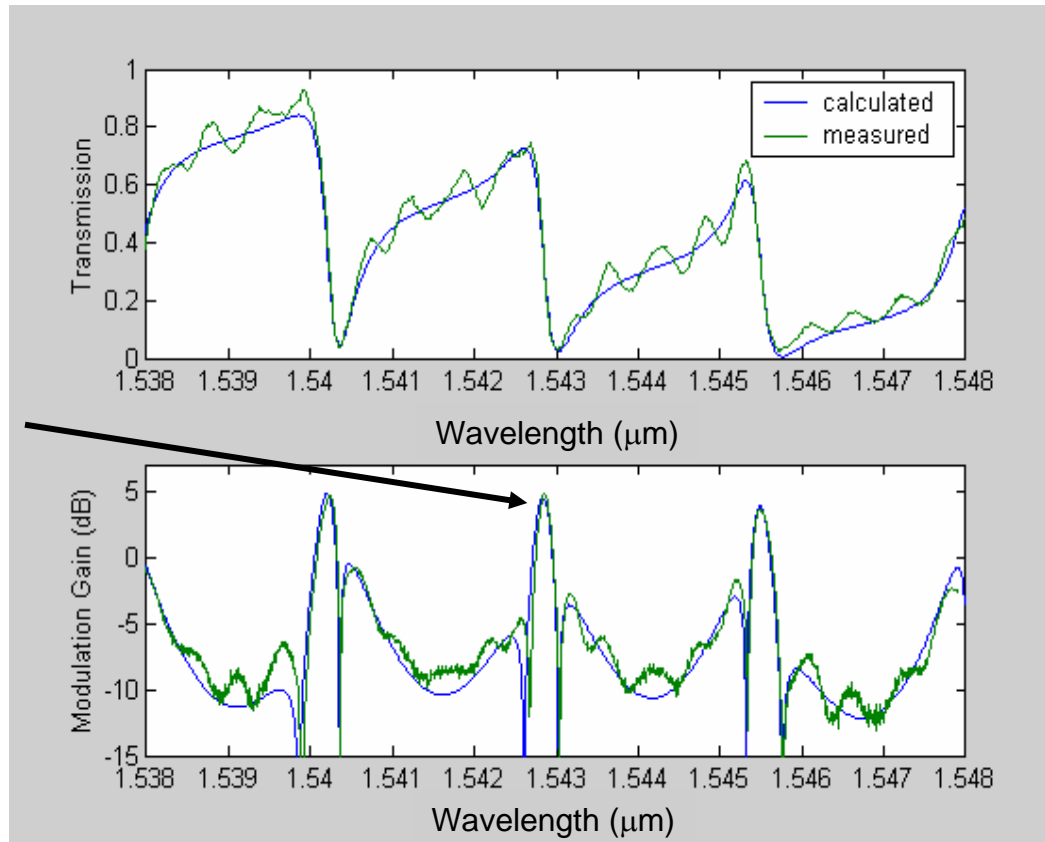
- no modulation.
- measurement of DC-transmission
- wavelength scan.

Wavelength response of modulation:

- fixed RF-frequency (1GHZ)
- Measurement of S21
- wavelength scan.

RF-measurements, cont'd

Max. 5dB ring enhancement



**Good fit of
calculation and
experiment**

**Modulator
enhancement
(due to ring
resonance):
confirmed**

Waveguide width: $0.8\mu\text{m}$

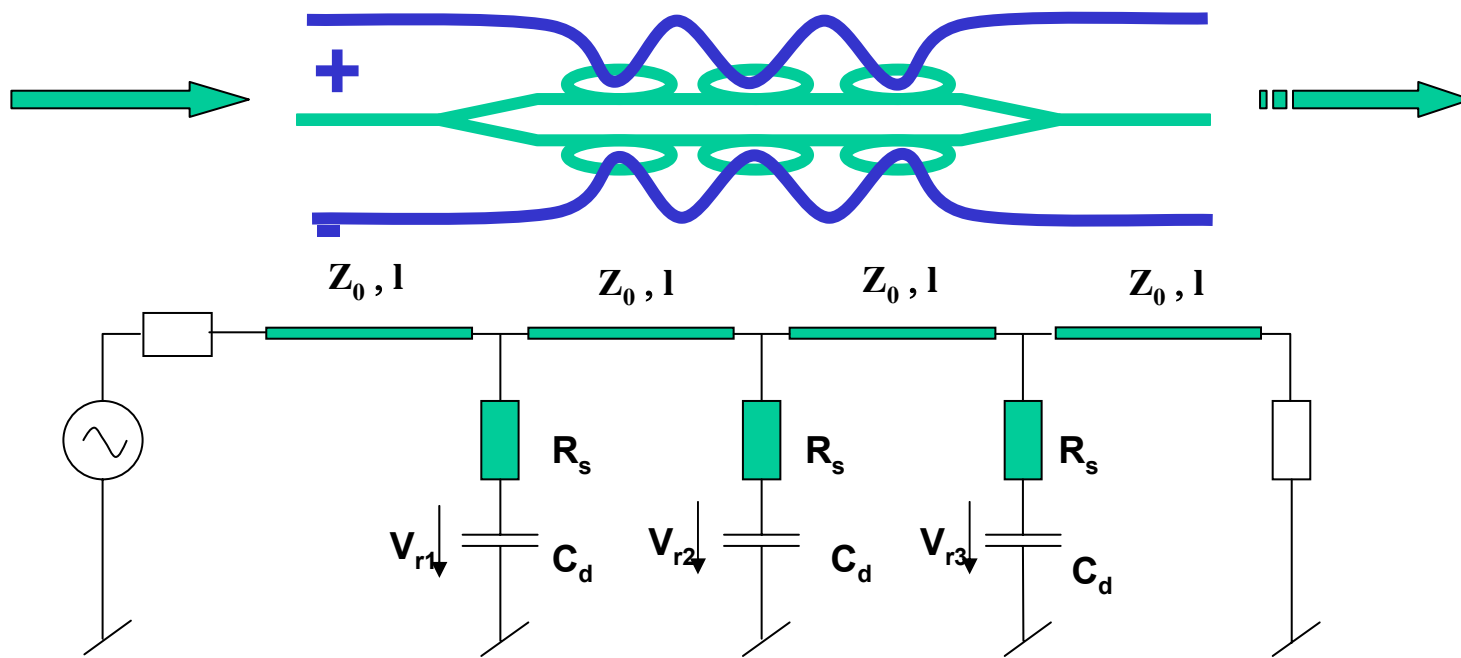
Ring loss: 15%

MMI-length: $34.5\mu\text{m}$

Coupling 50%

Ring circumference: $250\mu\text{m}$

Multi-ring resonator as a loaded transmission line



Multi-ring resonator acts like a loaded transmission line.

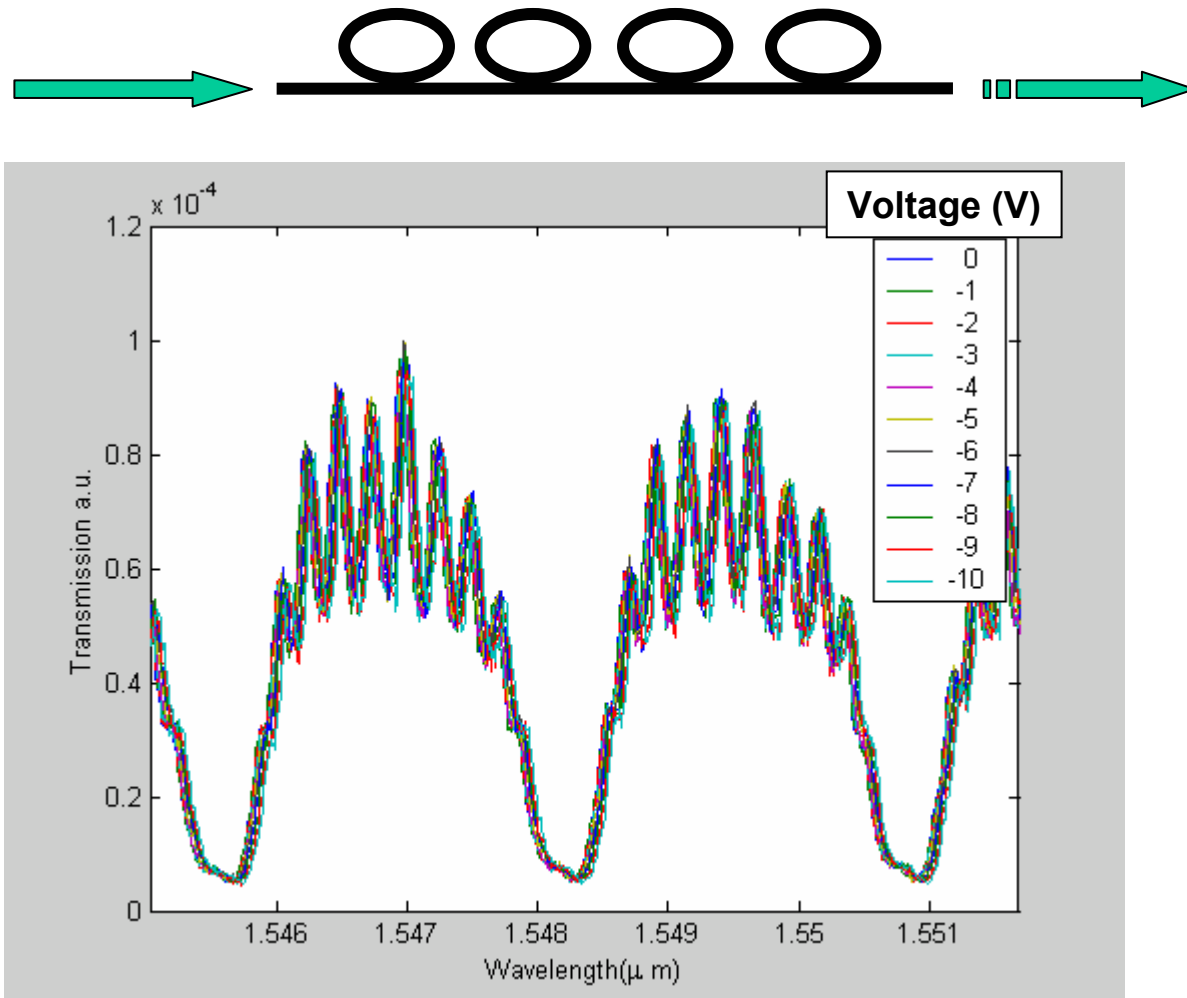
Loading is reduced due optical recycling of the rings.

Dwell time in the rings has to be determined and reproducible.

→Optical and Electrical delay from ring to ring can be matched

(Coupling of ring resonator determines optical delay!)

'Lithographic' alignment of ring-resonance's



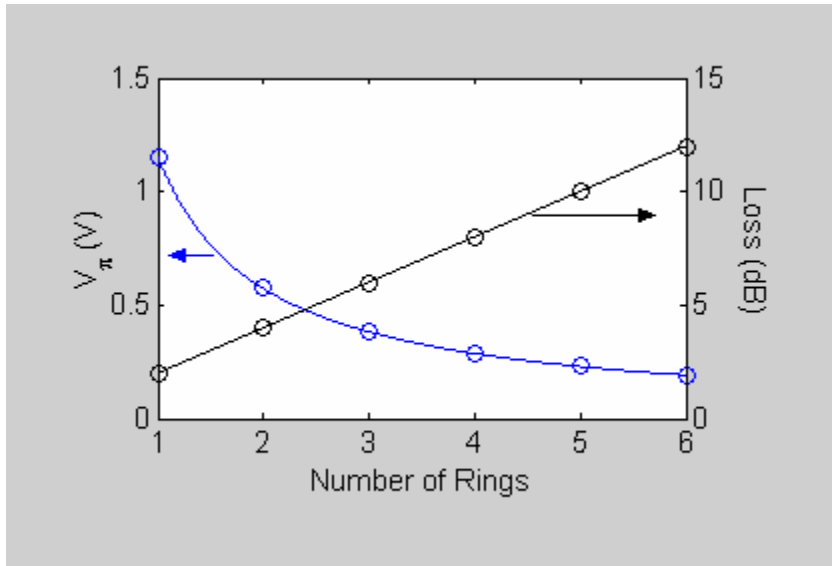
Optimization of modulator

- Figure of merit = $(\text{transmission})/V_{\pi}^2 = \frac{L^2 e^{-\alpha L}}{(V\pi L)^2}$ ← Material dependent

→ optimum length for optimum modulation performance → $L_{\text{opt}} = 2/\alpha$

- maximized performance can be achieved with 3 – 4 rings (per arm) based on best achieved ring results (3.5cm⁻¹ effective loss).
- V_{π} of best ring result with best material →
 - one ring: 1.7V
 - With 3 rings in each arm: ~0.3V

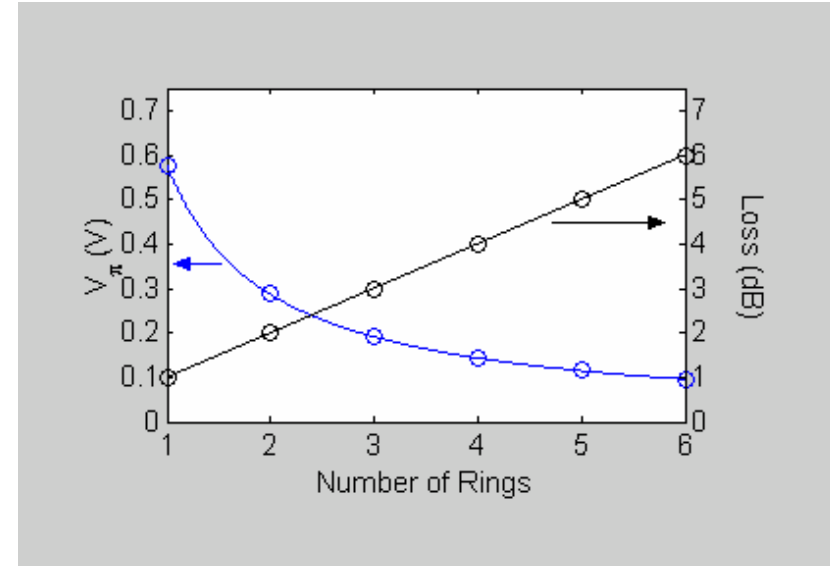
Estimation of V_{pi} and Loss of a balanced Mach-Zehnder Ring modulator.



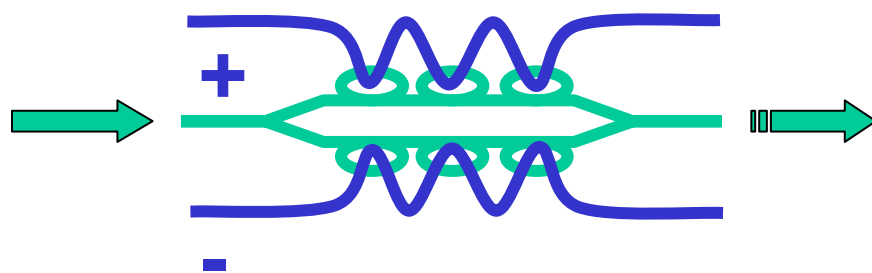
Internal loss and V_{pi} with current device components

Fiber-coupling loss not included

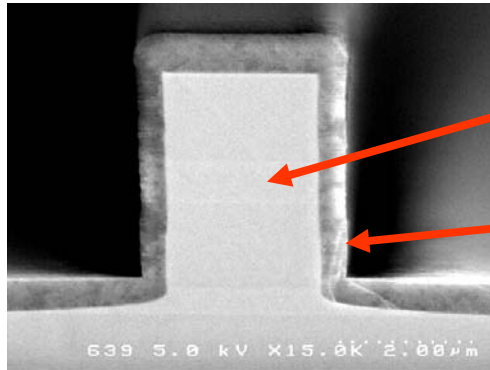
Number of rings per arm



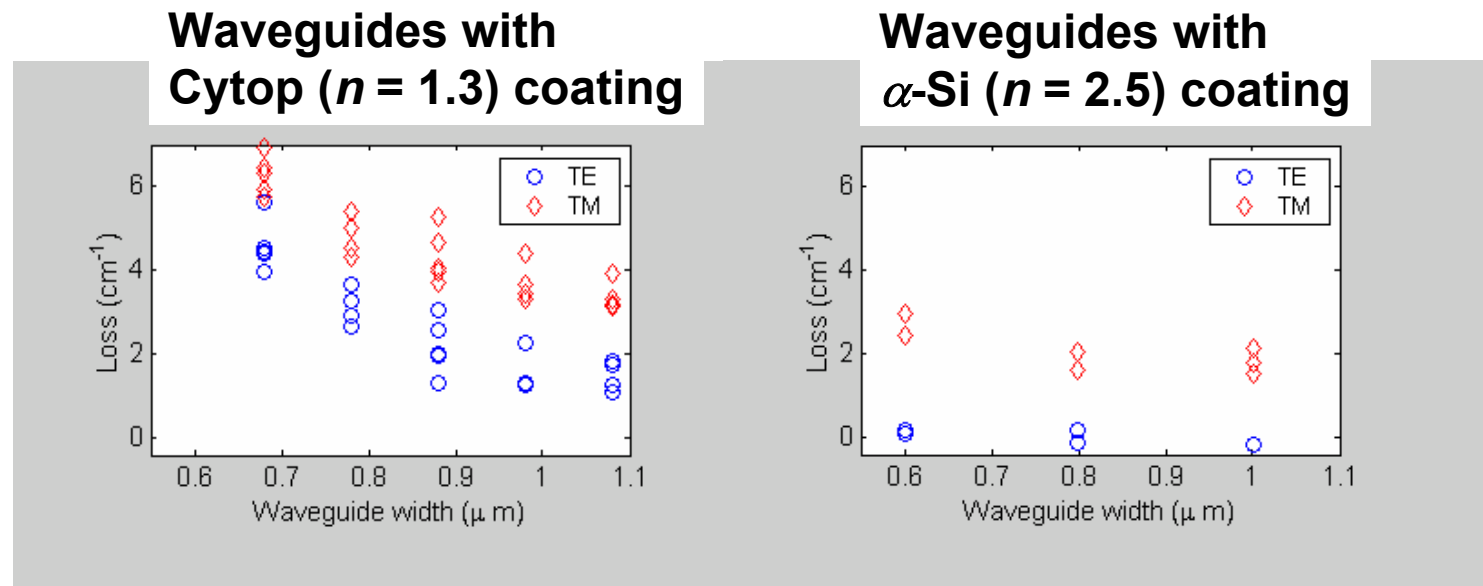
Internal loss and V_{pi} anticipated at the end of the project



Loss reduction with α Si encapsulation

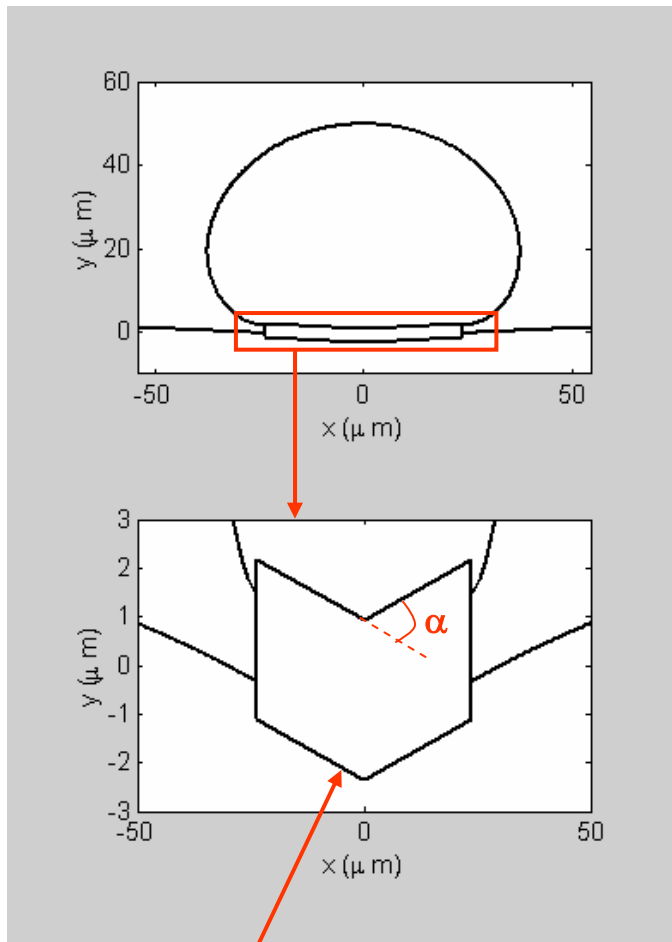


- + Lower scattering loss
- + Lower loss MMI-couplers
- Larger minimum radius

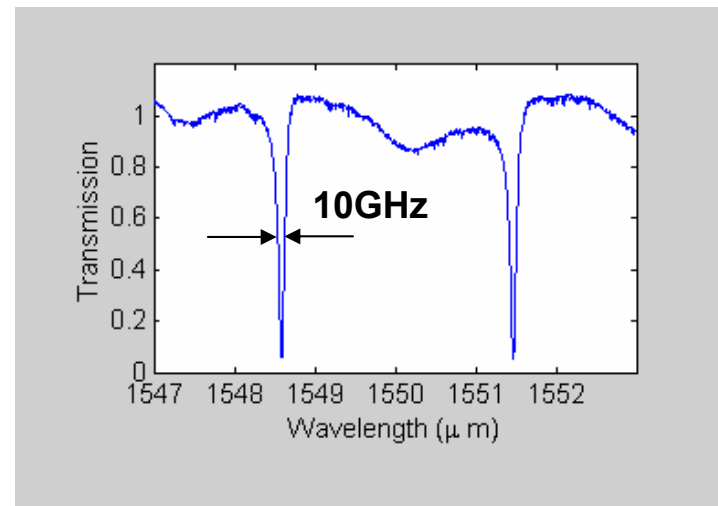


Losses $< 0.5 \text{ cm}^{-1}$ with α -Si coating

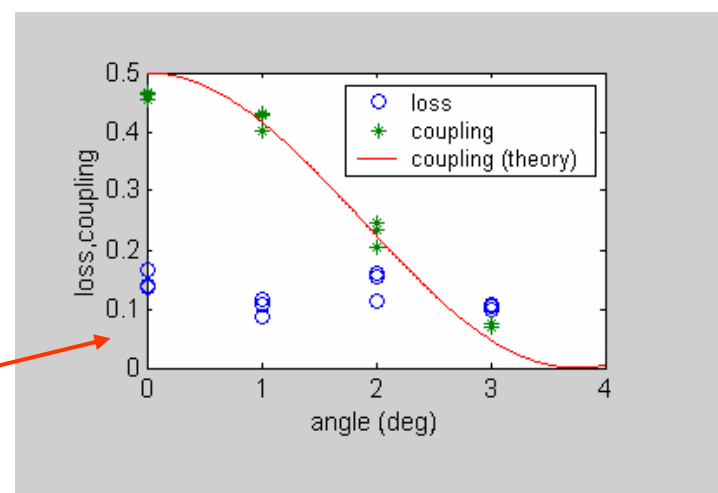
High Q Ring-Resonators



Angled MMI-coupler
→ Coupling coefficient can be selected



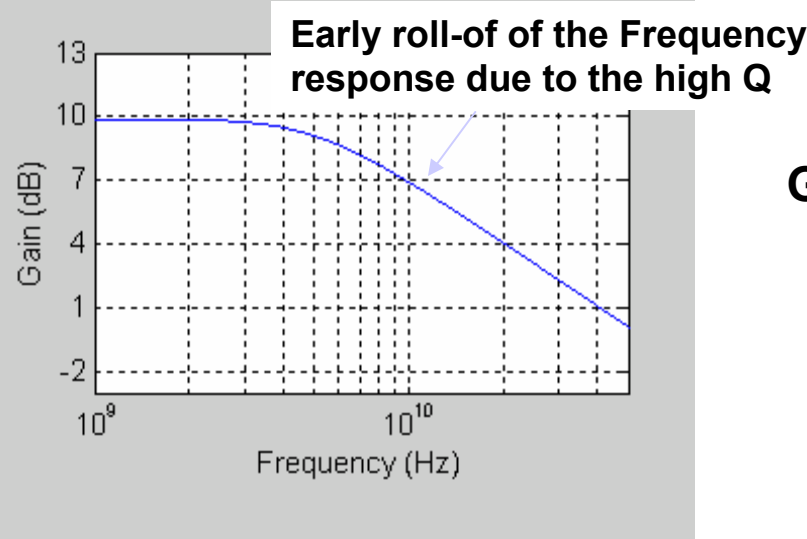
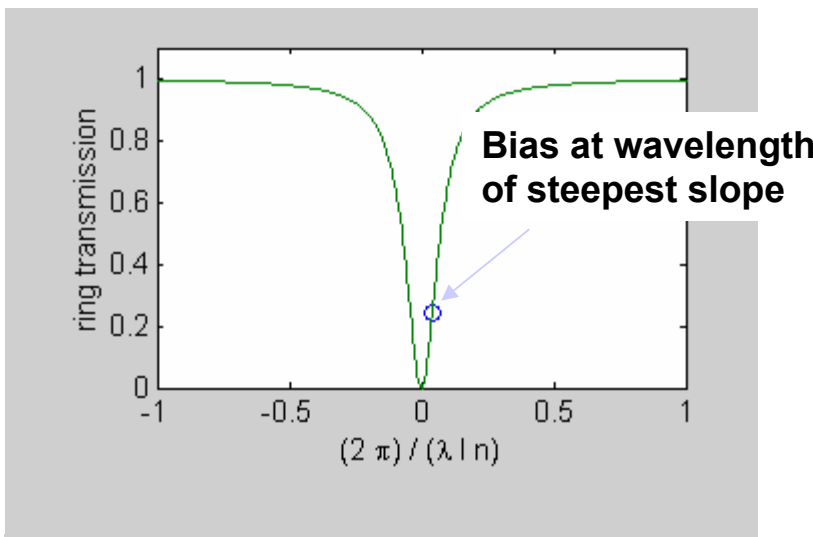
$\alpha=3 \text{ deg} \rightarrow Q=20'000$
 $\rightarrow \text{finesse}=36$
 $\rightarrow 10\text{GHz} \text{ optical bandwidth}$



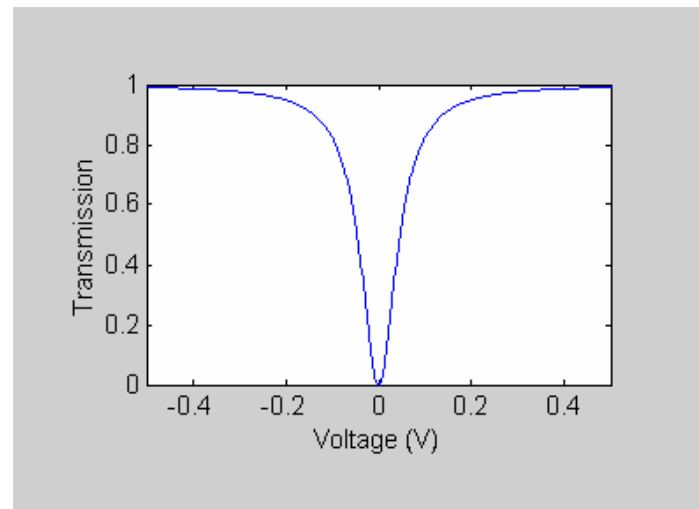
Alternate Modulator Design with High-Q Ring



Calculated E/O response of a single $Q=20'000$ ring resonator



DC-response with $dn/dV=10^{-4}$



$(\text{transmission}) / V_\pi^2$ of the ring
Gain = modulator
 $(\text{transmission}) / V_\pi^2$ of a lossless Mach-Zehnder modulator



Summary



- **Low loss waveguides demonstrated.**
- **Low loss rings demonstrated.**
- **Reproducible coupling ratio's in MMI's achieved.**
- **Optimized MMI's and ring resonator design.**
- **Electro-optic ring-modulator at RF frequencies demonstrated.**
- **Need to combine**
 - **low loss waveguides**
 - **Accurate MMI fabrication**
 - **Highly sensitive material**
 - **Electrode process**
 - **Multi-ring devices**

→ **Multi ring resonator low V_π modulator**

Program Goal and Significant Accomplishments



Program Goal:

- Deliver 12 packaged resonant enhanced modulators with low V_{π}

Accomplishments:

- Development of advanced processing methods:
 - Low-loss deep-etched waveguides (1 cm^{-1} achieved at $1 \mu\text{m}$ width)
 - Planarization of anisotropic wafer using Cytop™ dielectric
 - Low-capacitance contact to waveguides
- Implementation of MMI couplers in ring geometry
 - Total ring loss equivalent of 3.5 cm^{-1} demonstrated including MMI
- First demonstration of Ring Modulator structure
 - Electrical modulation to 6 GHz
 - 5 dB Ring Enhancement
- Demonstration of enhanced modulator material
 - 3× enhanced electrorefractive effect (compared to literature)
 - Controlled material growth

Outlook



- Improve leakage current of deeply etched waveguides
- Introducing phased RF electrode with adequately low loss
- Packaging

RFLICS/REM Site Visit Agenda

26 MAR 03



9:00-9:10	Introduction	Joe Abeles
9:10-9:30	Program Status and Plan	Allen Lepore
9:30-9:45	Design and Fabrication Issues	Allen Lepore
9:45-10:00	Materials Development	Hooman Mohseni
10:00-10:30	Device Results & Concepts	Martin Kwakernaak
10:30-10:35	Break	
10:35-10:45	Packaging	Brad Price
10:45-11:00	Technical Q&A	
11:00-11:20	Contract Review	AI Grupper
11:20-12:00	Lab Tour	Martin Kwakernaak
12:00-1:00	Lunch	
1:00	Departure1	

Program Status and Plan

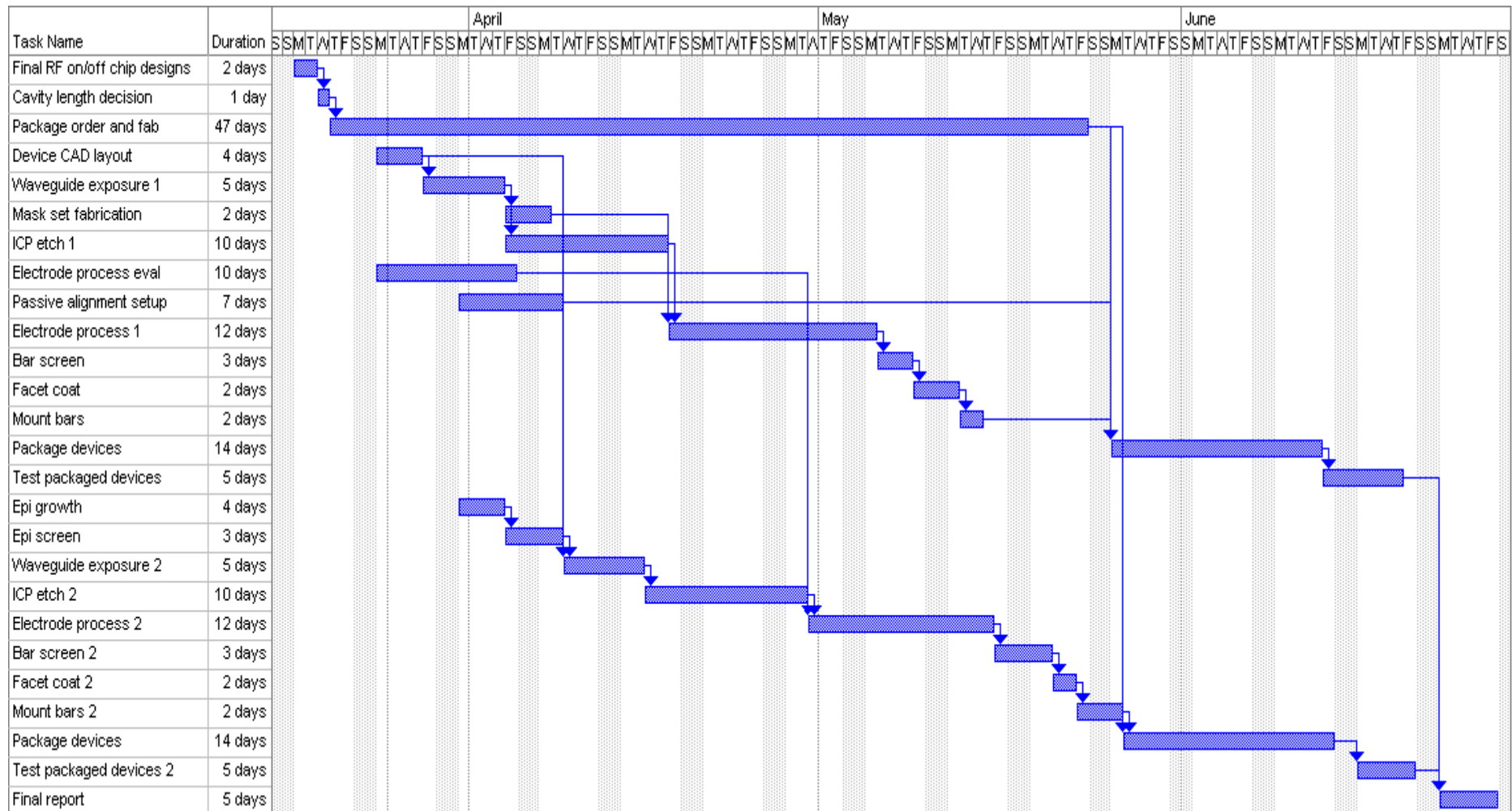


Allen Lepore



- **Plan to meet program objectives**
 - Program plan for 10GHz design
 - Scheduling issues
- **Technical issues:**
 - P-contact
 - 10 GHz design
 - Passive device packaging
 - Material uniformity
- **Latest device results**
- **New device concepts**

Program Plan for 10GHz Devices



Scheduling Issues

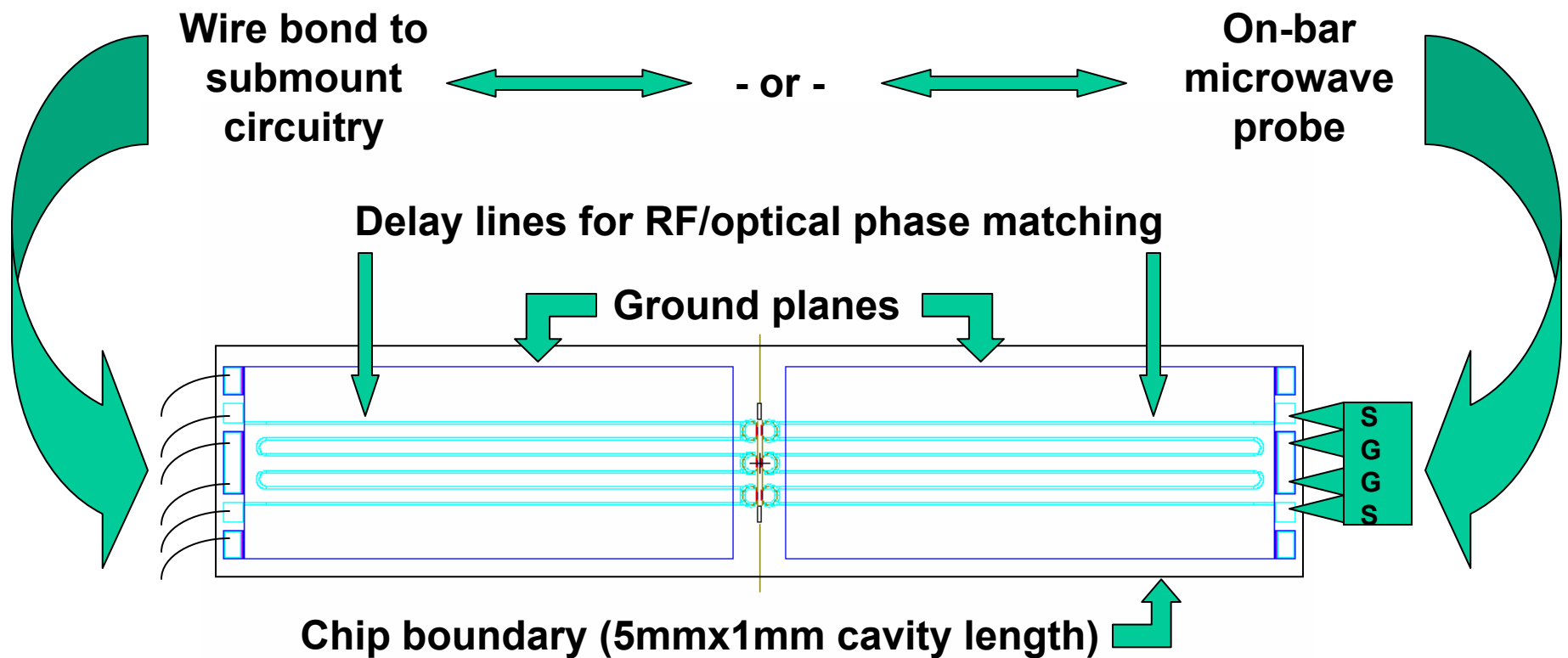
- Continue to process devices at multiple sites: Sarnoff, UIUC, ARL
- Average UIUC cycle time 12 days
- Custom package procurement
- ARL ebeam availability:
 - Internal ARL usage increased
 - Equipment downtime, service contract restored
 - Last REM exposures Nov 02
 - A. Lepore switching to 2 days/week at ARL

Design and Fabrication Issues



- **Final device design**
 - Based upon current electrode process parameters and materials
- **Review of electrode process**
- **P-contact improvements**
- **Alternative electrode processing**

10GHz Device Layout

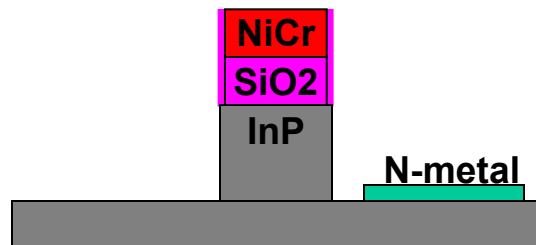


Device Fabrication

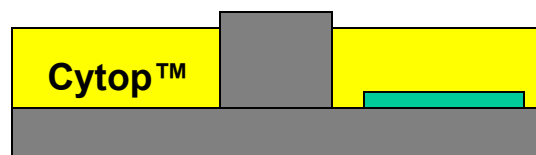


- Yield issues
 - ICP yield improving
 - UIUC continuing AFM characterization of etched sidewall
- P-contact limiting modulation
 - Leakage
 - Junction exposed and unpassivated
 - Etch damage leaves undesirable surface states
- P-metal process improvements
- Encapsulation variations

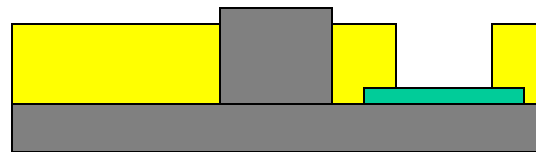
REM Electrode Process



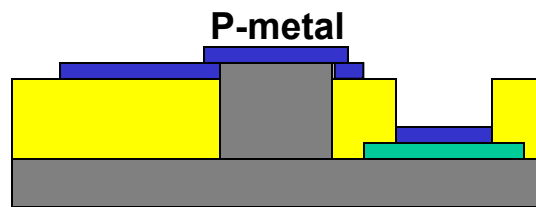
1. N-contact formation



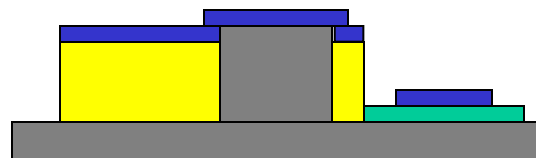
2. Strip ICP etch mask and planarize with Cytop™ polymer



3. Open N-contact via

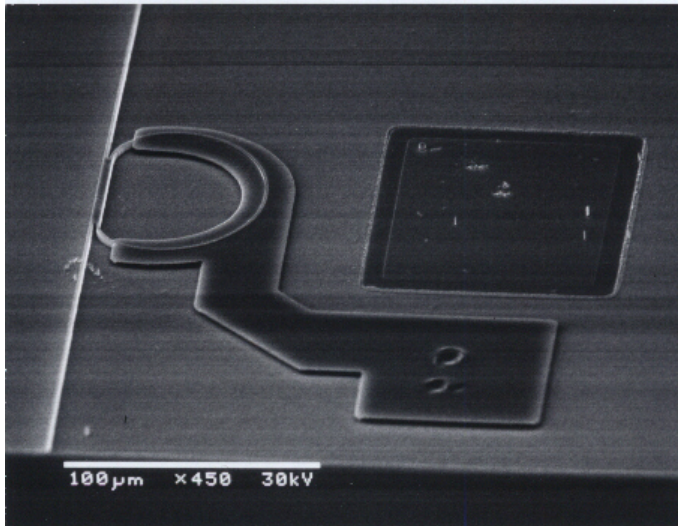


4. P-contact formation

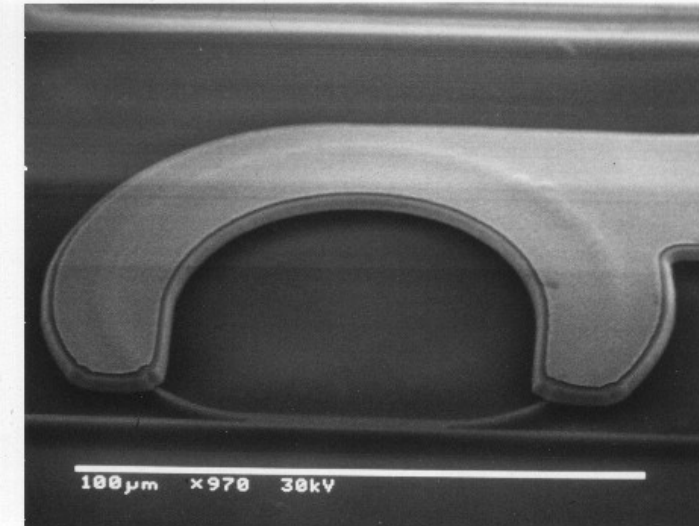
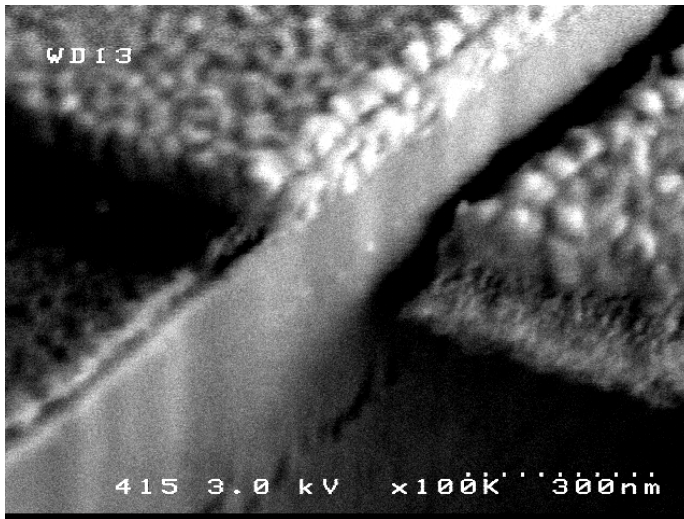


5. Excess dielectric removal

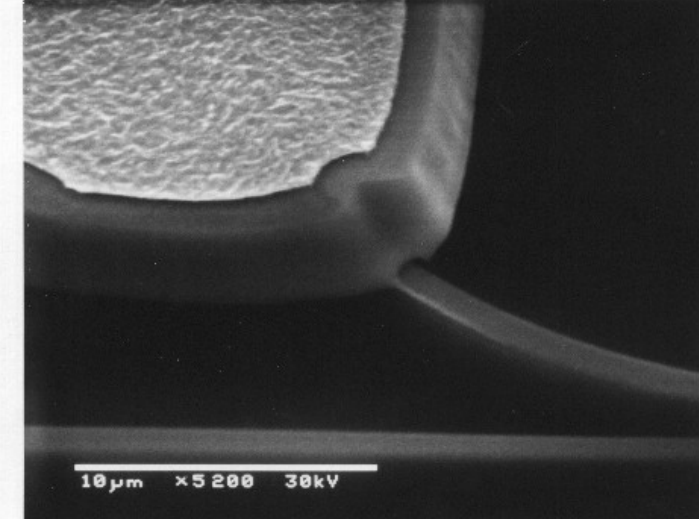
P-Contact Improvements



↳ Contacts without plating ↳

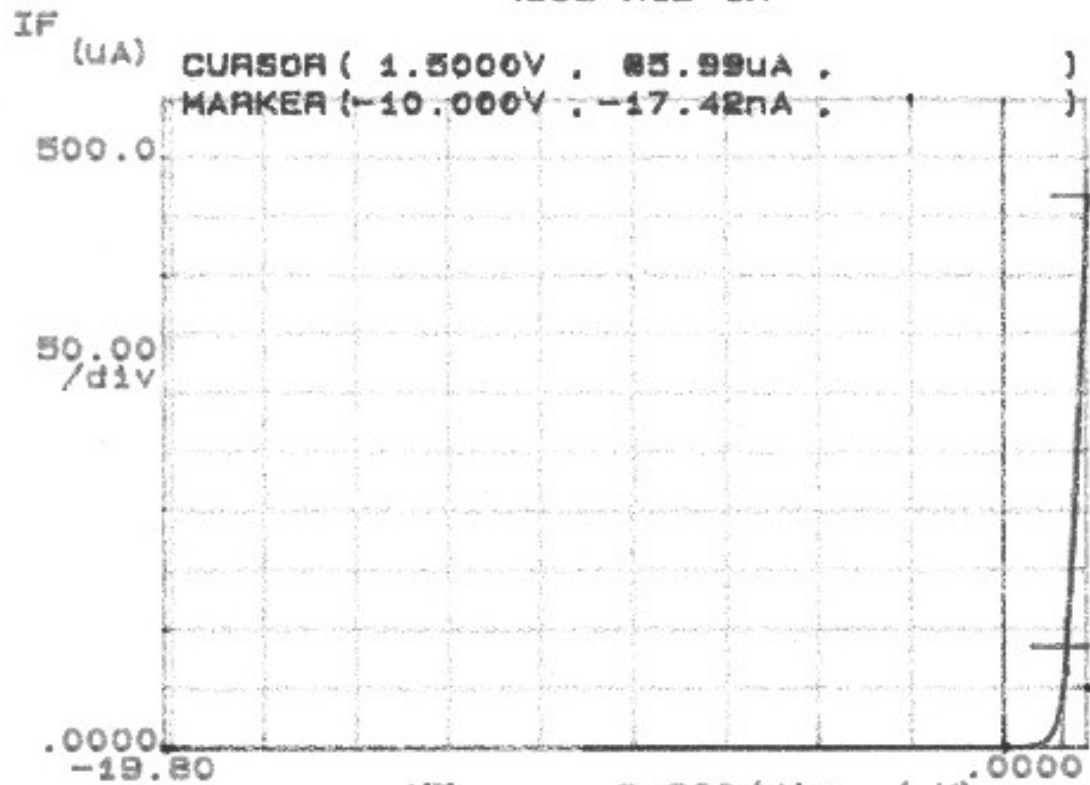


↳ Electroplated contacts ↳



Improved I-V Characteristics

***** GRAPHICS PLOT *****
4965-A1B 1R

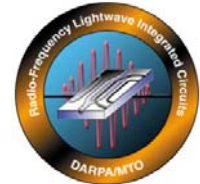


Variables:
VF -Ch1
Linear sweep
Start 2.0000V
Stop -10.000V
Step -.1000V

Constants:
V -Ch3 .0000V

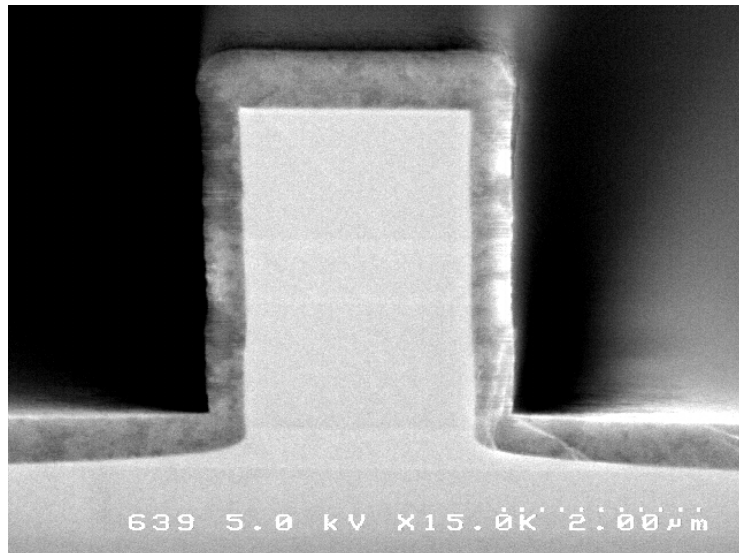
	GRAD	1/GRAD	Xintercept	Yintercept
LINE1	784E-08	1.31E+03	1.39E+00	-1.06E-03
LINE2				

Further Process Improvements

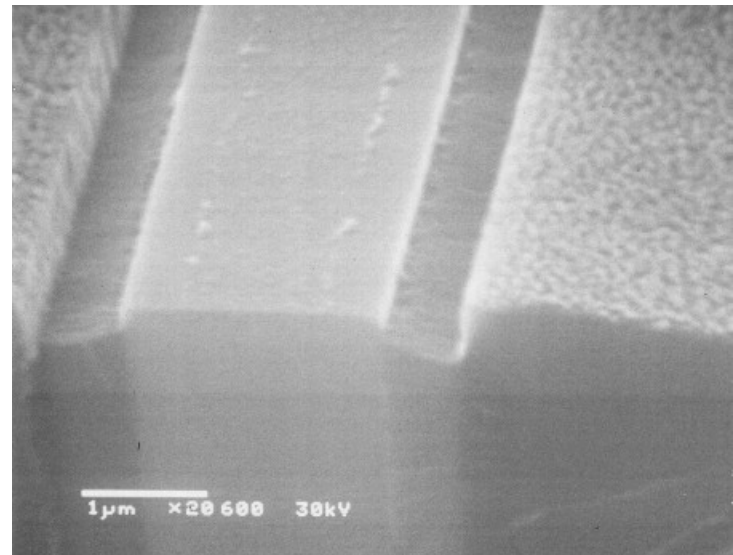


- **Chemical treatment of semiconductor surface**
- **Thin epitaxial overgrowth of InP**
- **Silicon nitride encapsulation before polymer planarization**
- **Amorphous Si encapsulation**

Amorphous Silicon Encapsulation



Amorphous Si encapsulation-cross-section



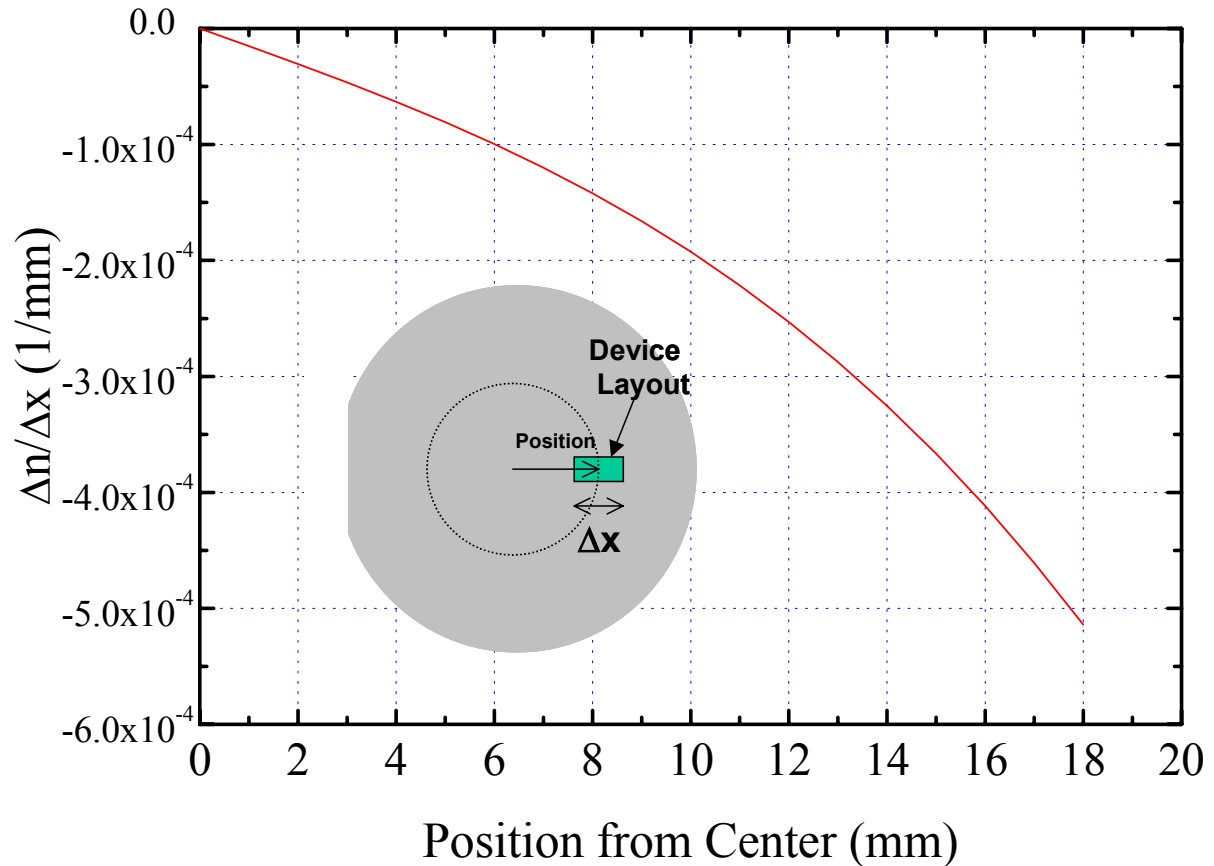
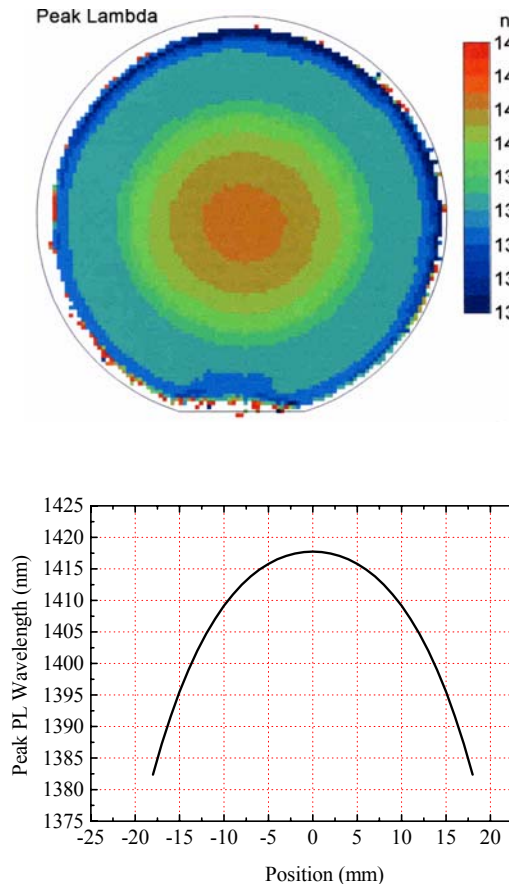
Selective removal of encapsulation from top of waveguide

Materials Development



Hooman Mohseni

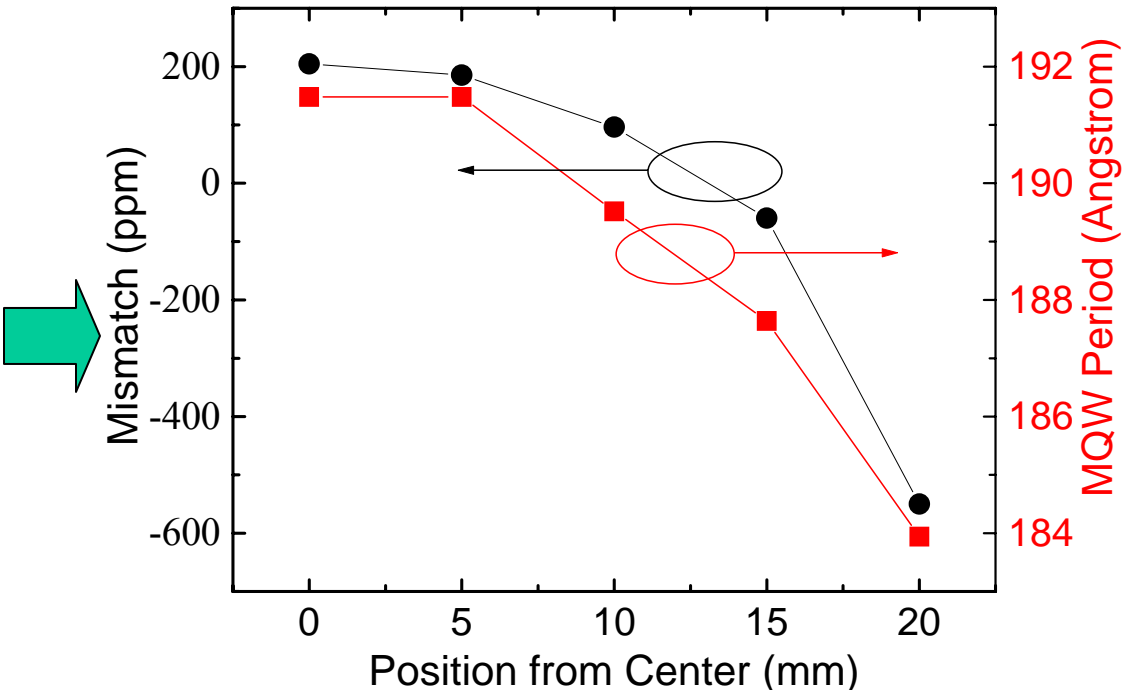
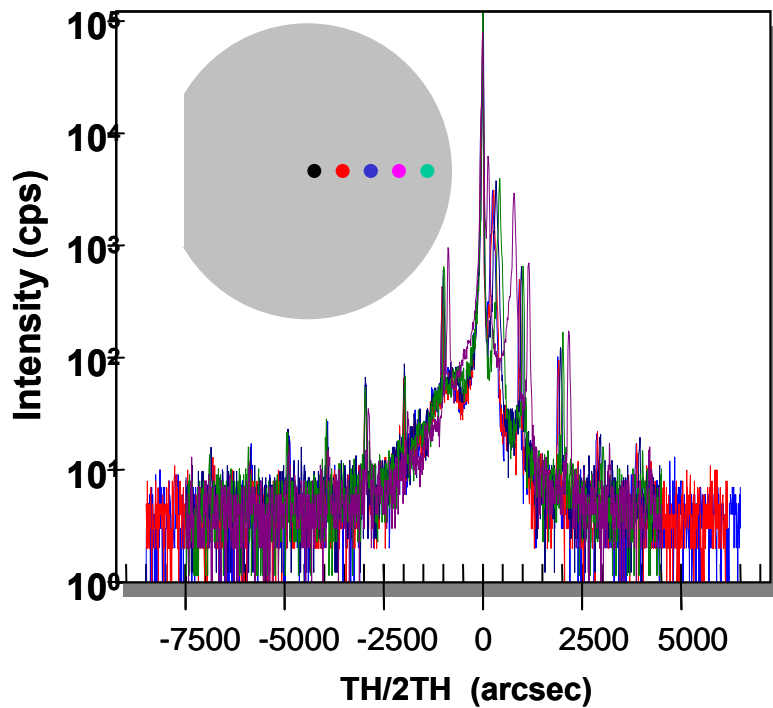
Material Bandgap Non-uniformity



PL mapping of a typical growth

Change of Index per mm versus
distance from the center

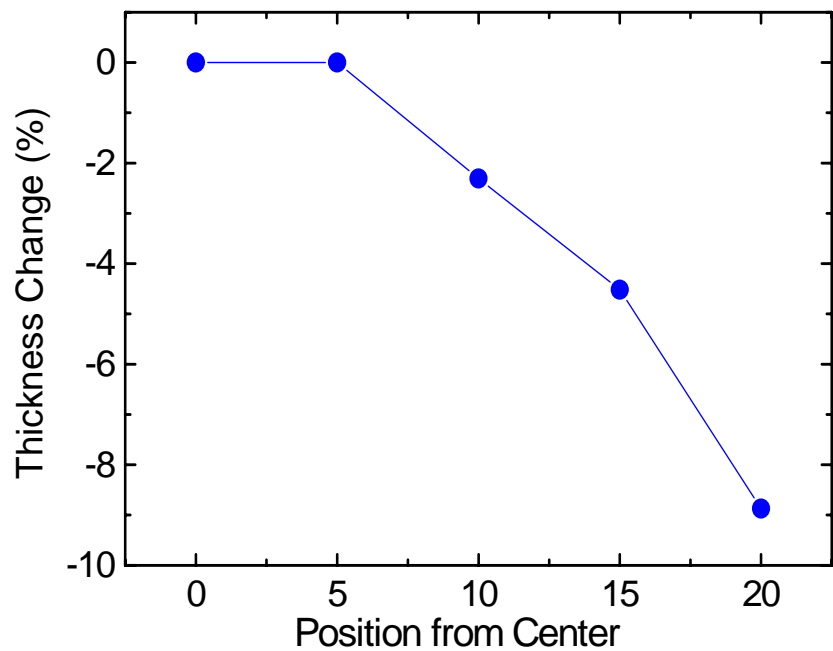
Material Structural Non-uniformity



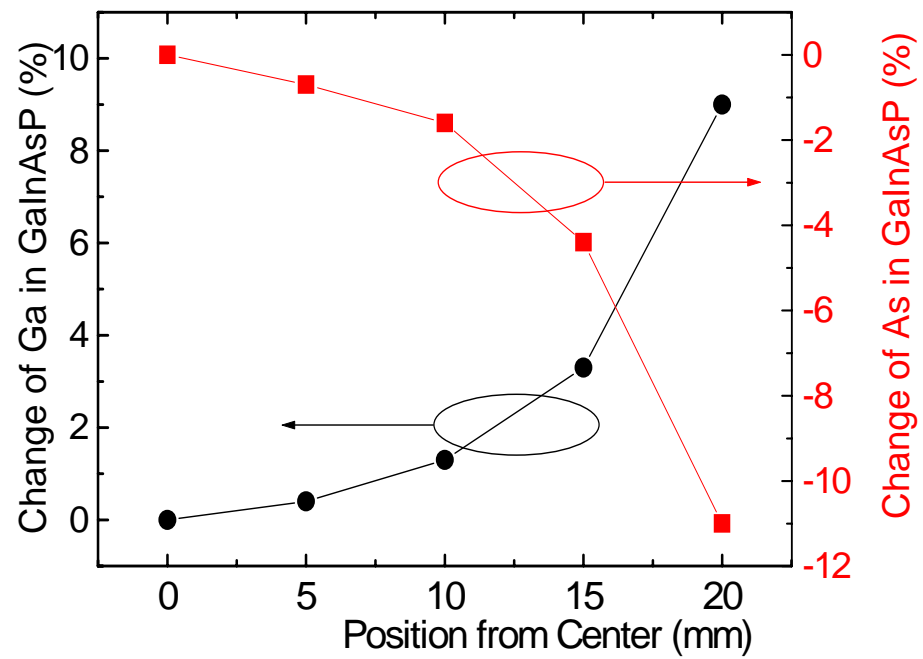
X-ray mapping of a typical growth

Average lattice mismatch and period of the MQW structure extracted from x-ray mapping

Material Composition and Thickness Non-uniformity

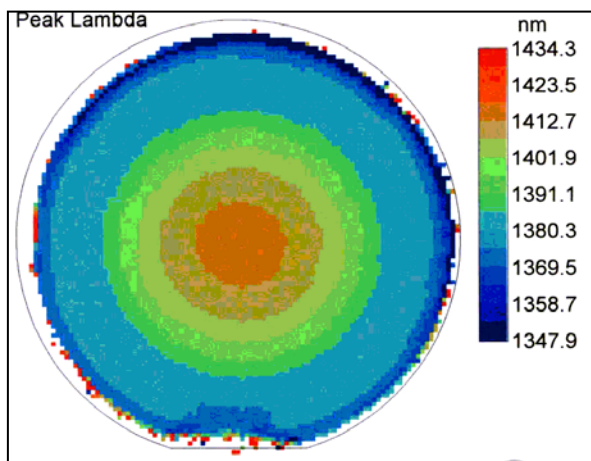
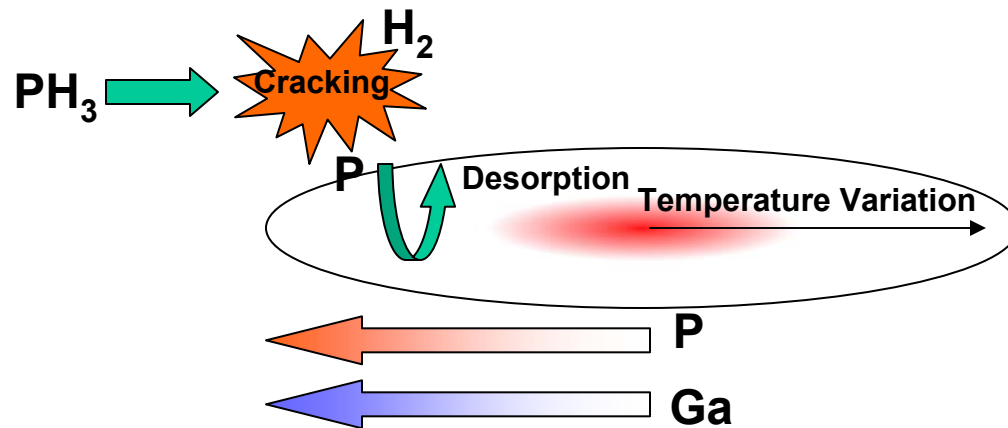


**Thickness variation versus position
(calculated from x-ray mapping)**

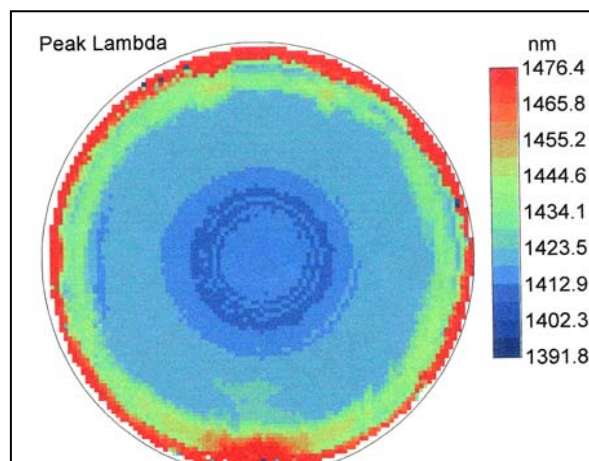


**Gallium and Arsenic composition
variation versus position (calculated
from x-ray and PL mapping)**

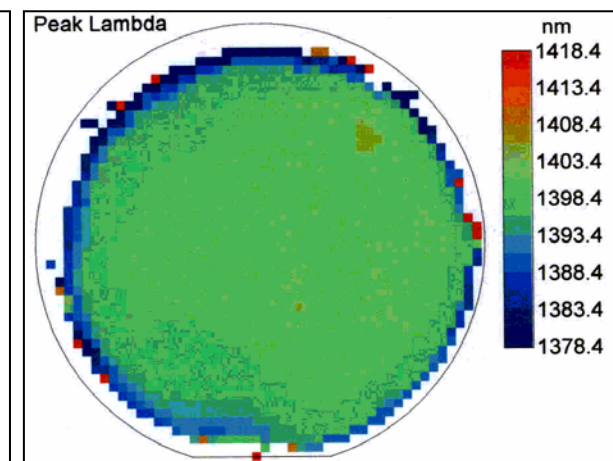
Low Temperature and All-Ternary Growth Methods



Conventional Growth:
 $\Delta\lambda_{PL} \approx 30 \text{ nm}$ for
 $0 < R < 20 \text{ mm}$

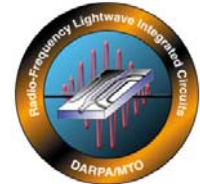


Low Temperature Growth:
 $\Delta\lambda_{PL} \approx 10 \text{ nm}$ for
 $0 < R < 20 \text{ mm}$



Low Temperature All-ternary (InAsP/GaInP) Growth:
 $\Delta\lambda_{PL} \approx 2 \text{ nm}$ for
 $0 < R < 20 \text{ mm}$

Device Results and Concepts

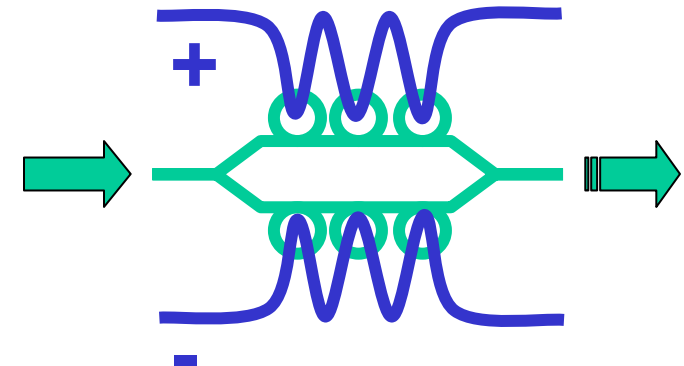


Martin Kwakernaak

Resonance enhanced modulator concept

Phase modulation with ring-resonators in interferometer arms.

Low optical loss in the rings is essential for this concept (requirement: loss < coupling).



**Ring-resonator Q limits the E/O bandwidth.
→ Fundamental Bandwidth*Sensitivity limitation.**

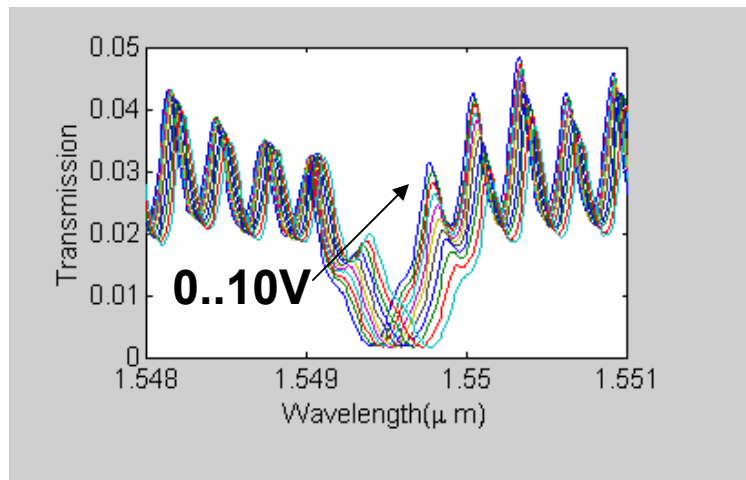
**Multiple ring-resonators with RF delay lines
→ Further reduction of $V\pi$ without additional bandwidth penalty.**

**Group delay in the ring resonators must match the RF-delay
→ Known coupling coefficient is essential.**

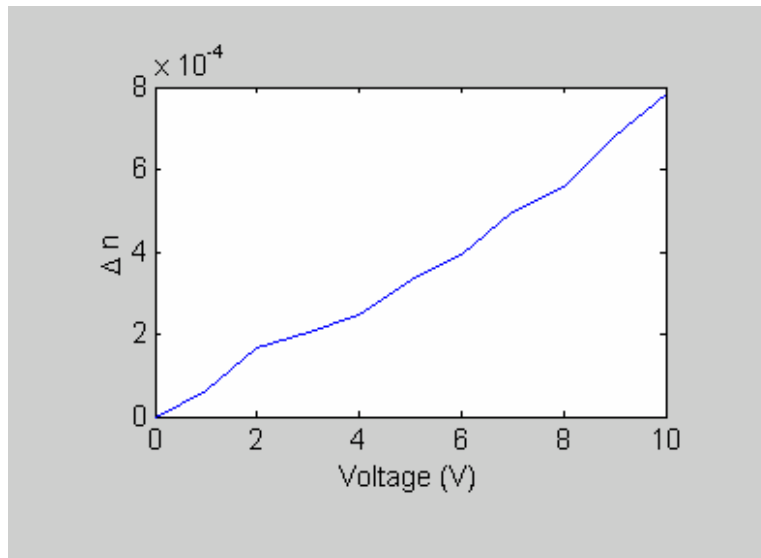
modulation results



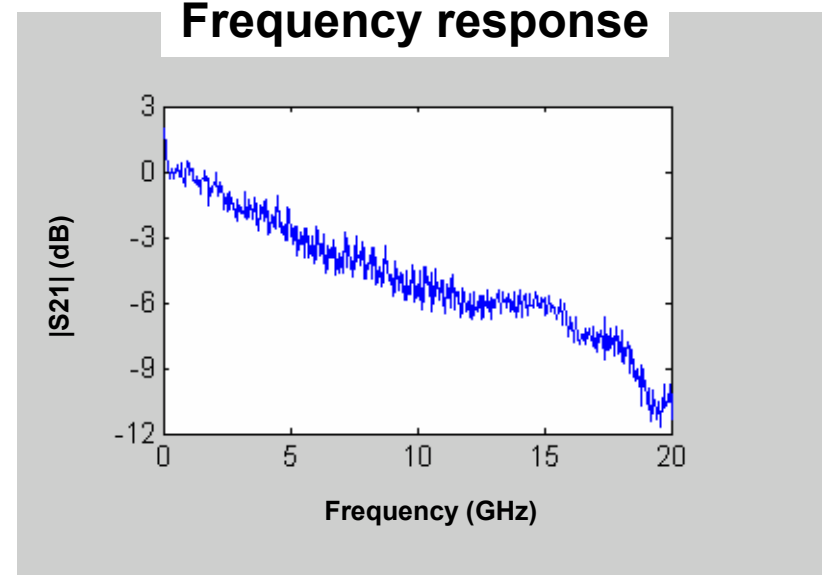
Transmission at various bias voltages



Index change in the ring-resonator

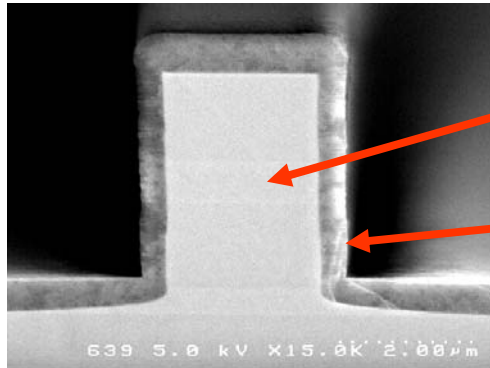


Frequency response



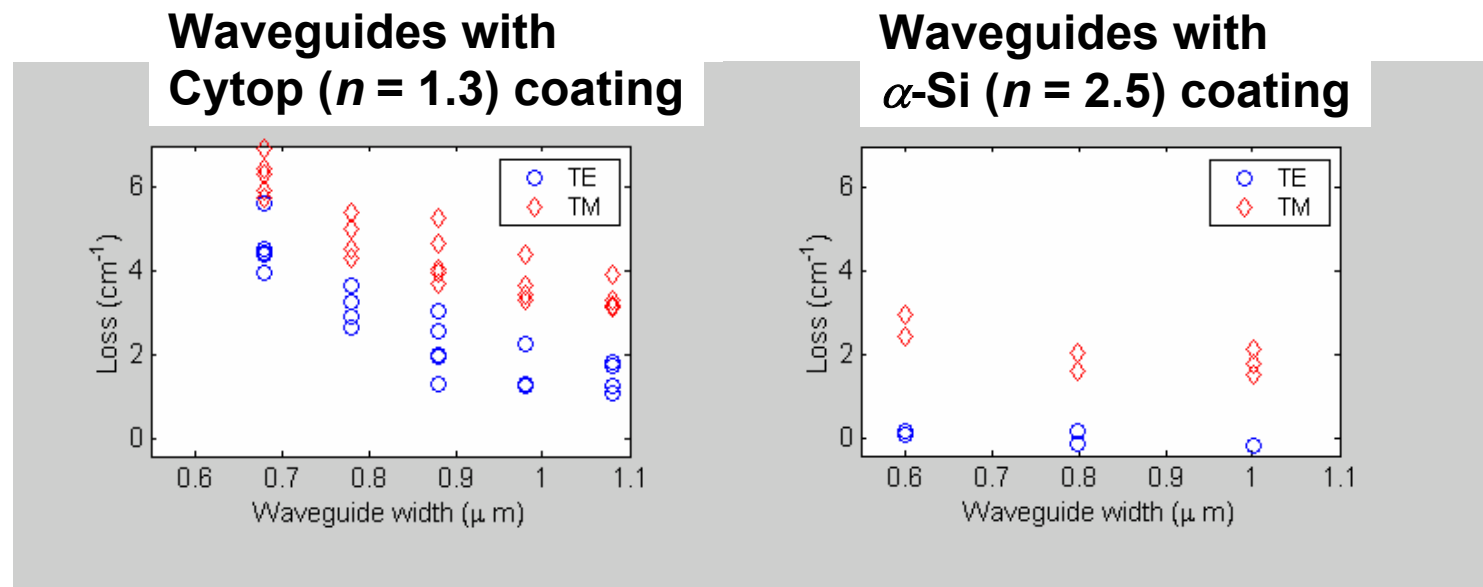
- Index change in deep etched ring-resonators is close to un-etched material
- Frequency response still rolls off, but is significantly improved

Loss reduction with α Si encapsulation



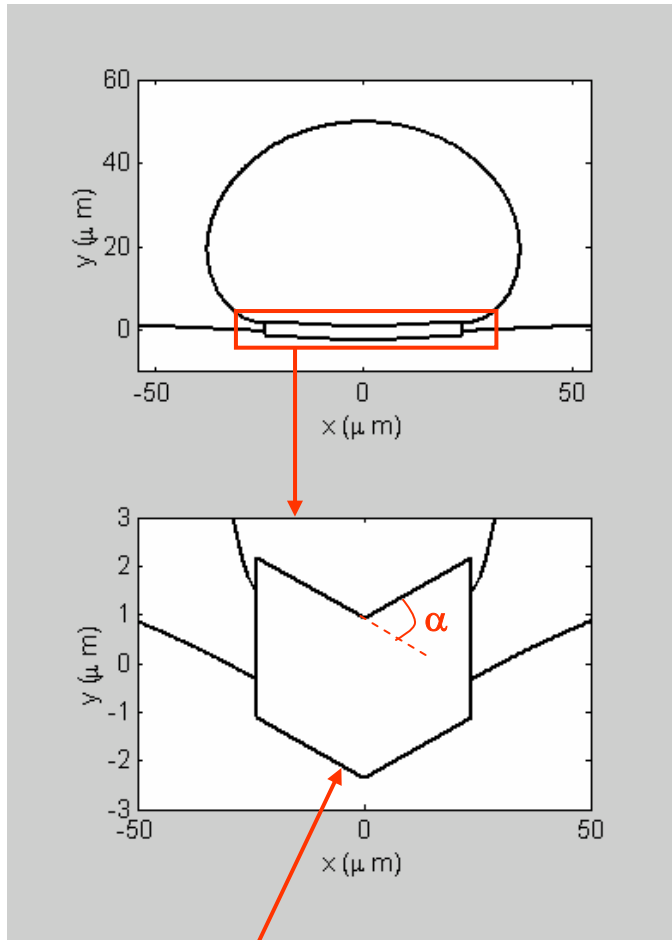
InGaAsP/InP
waveguide
 α -Si
encapsulation
($n = 2.5$)

- + Lower scattering loss
- + Lower loss MMI-couplers
- Larger minimum radius

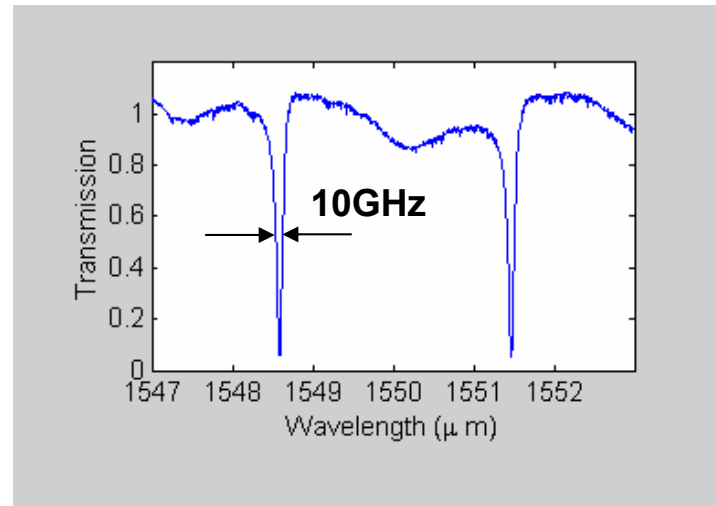


Losses $< 0.5 \text{ cm}^{-1}$ with α -Si coating

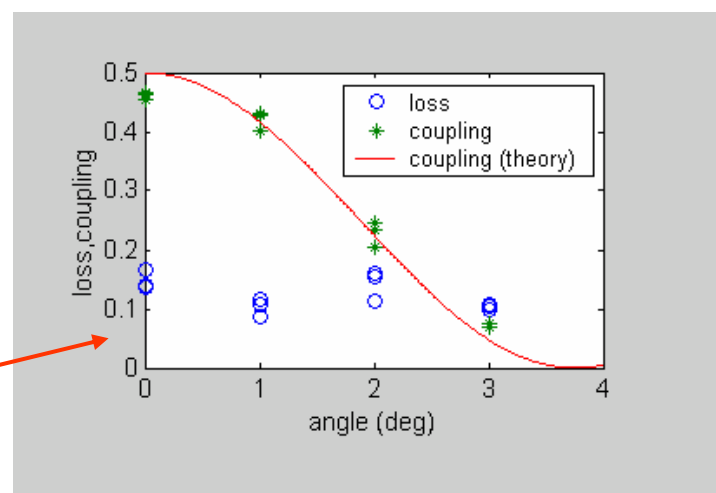
High Q Ring-Resonators



Angled MMI-coupler
→ Coupling coefficient can be selected



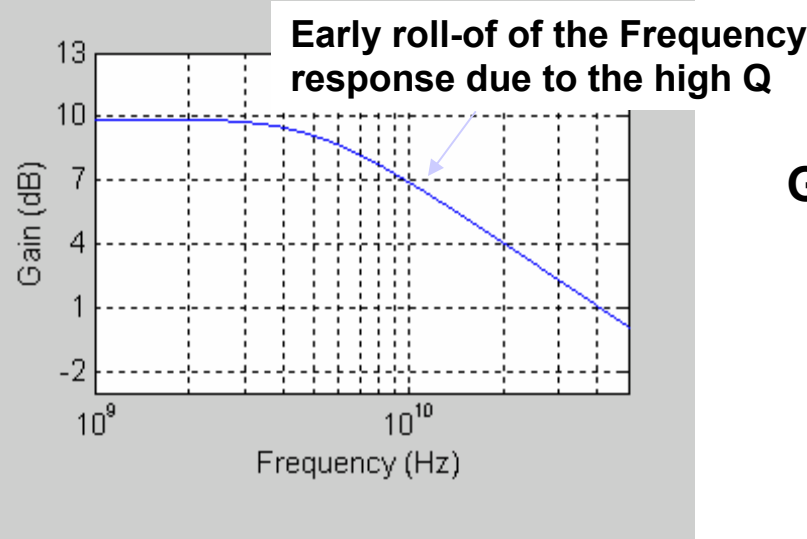
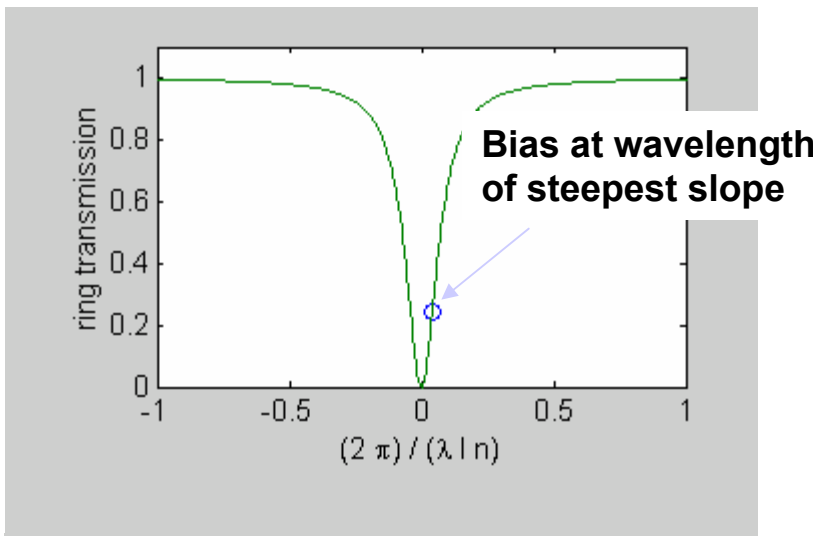
$\alpha=3 \text{ deg} \rightarrow Q=20'000$
 $\rightarrow \text{finesse}=36$
 $\rightarrow 10\text{GHz} \text{ optical bandwidth}$



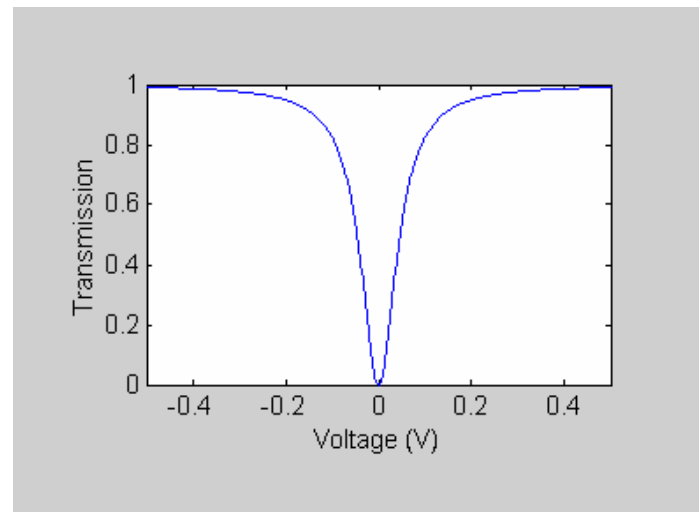
Alternate Modulator Design with High-Q Ring



Calculated E/O response of a single $Q=20'000$ ring resonator



DC-response with $dn/dV=10^{-4}$



$(\text{transmission}) / V_\pi^2$ of the ring
Gain = modulator
 $(\text{transmission}) / V_\pi^2$ of a lossless Mach-Zehnder modulator



Packaging



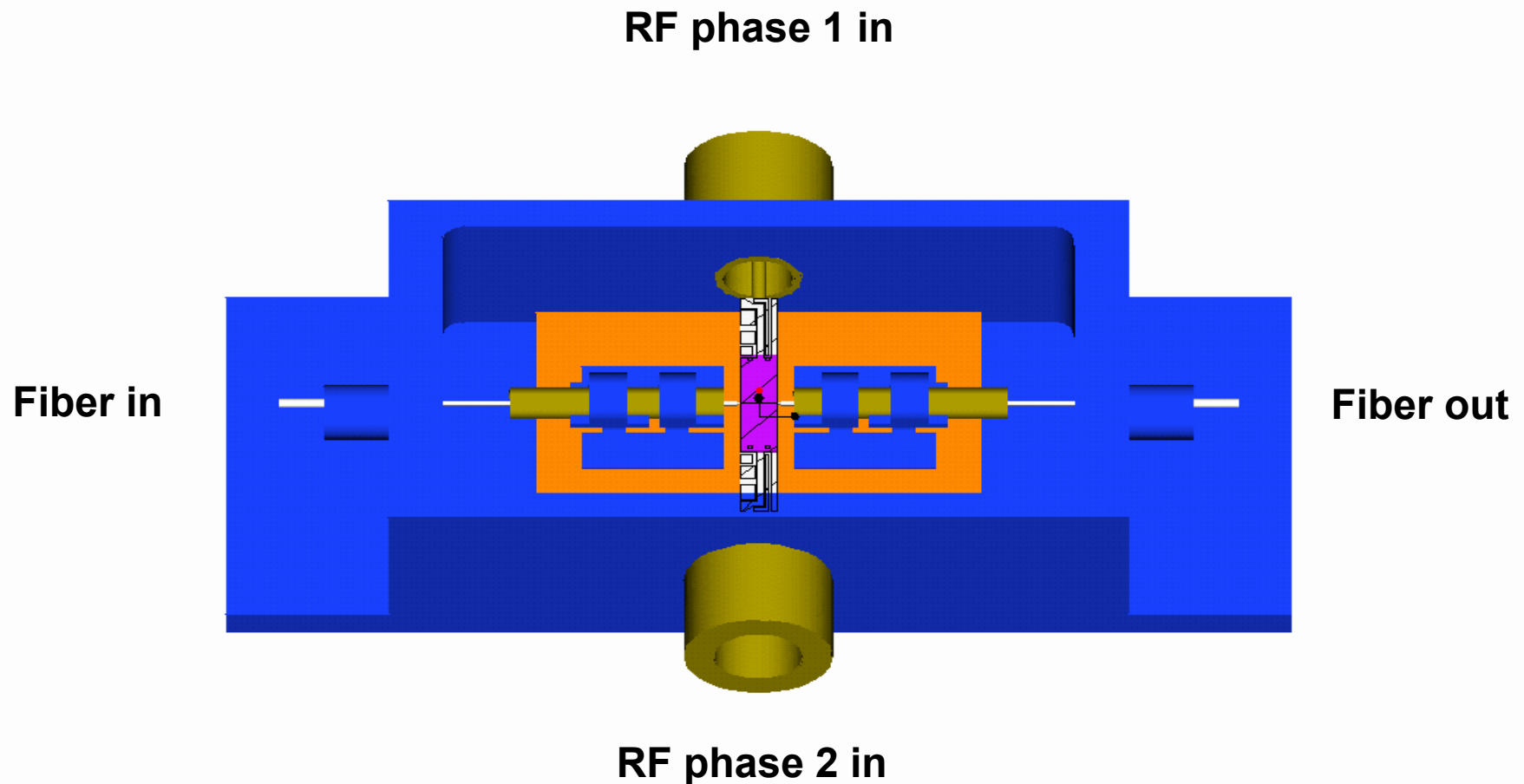
Brad Price

Packaging Design Issues



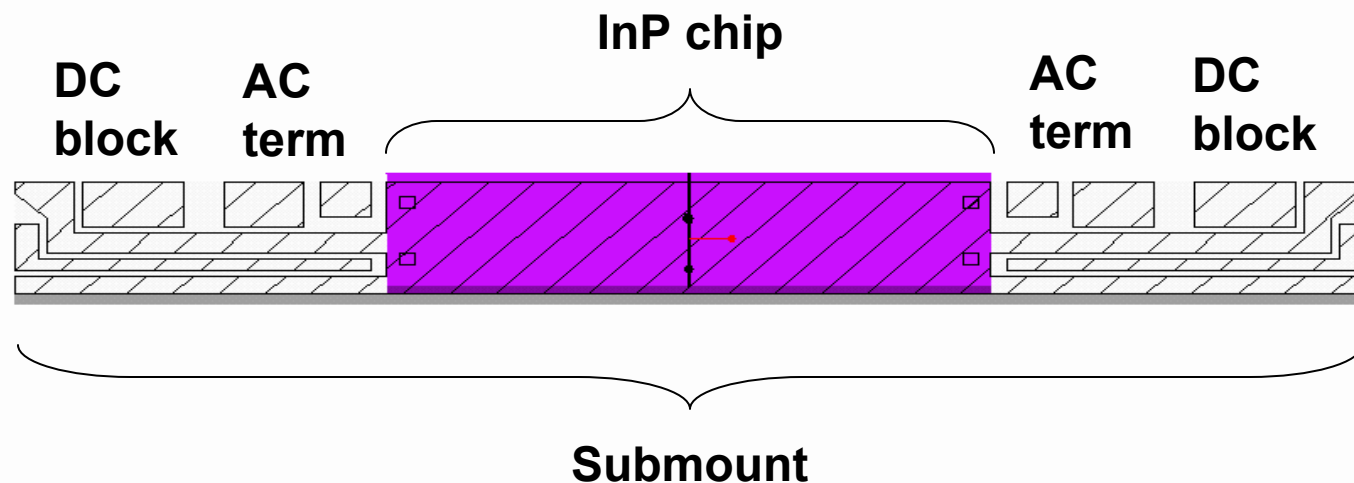
- Simplify package to reduce lead time for procurement
- Passive device, low DC and RF power dissipation
 - Eliminate internal TEC
 - Low thermal resistance path from device to package base
 - Use external TEC as needed
 - Simplified package assembly
- RF blocking capacitor and termination included in submount circuit
 - Only 2 RF feedthroughs required for opposing phases
 - No DC feedthroughs, DC bias external using bias tees
- Passive device alignment
 - Laser welder currently configured for active device alignment
 - Add modulated source to fiber, measure device AC photocurrent
 - May need to improve microscope for initial alignment to high-aspect-ratio waveguides

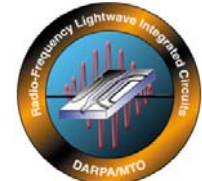
Package Design



Submount

- Limit width to 1mm to match existing cavity length
- Blocking capacitor for external DC biasing through RF lines
- Device pad pitch to match on-wafer probe pad configuration





Effect of H₂ on the etch profile of InP/InGaAsP alloys in Cl₂/Ar/H₂ inductively coupled plasma reactive ion etching chemistries for photonic device fabrication

Sean L. Rommel,^{a)} Jae-Hyung Jang, Wu Lu, Gabriel Cueva, Ling Zhou, and Ilesanmi Adesida

Department of Electrical and Computer Engineering and Micro and Nano Technology Laboratory, University of Illinois at Urbana-Champaign, Urbana, Illinois 61801

Gary Pajer, Ralph Whaley, Allen Lepore, Zane Schellnberger, and Joseph H. Abeles
Sarnoff Corporation, Princeton, New Jersey 08543-5300

(Received 29 January 2002; accepted 22 April 2002)

This study demonstrates etch profile engineering of InP, In_{1-x}Ga_xAs_{1-y}P_y, and In_{0.53}Ga_{0.47}As heterostructures results from adding H₂ to standard Cl₂/Ar inductively coupled plasma-reactive ion etching chemistries. Etch rate curves of bulk InP, In_{1-x}Ga_xAs_{1-y}P_y, and In_{0.53}Ga_{0.47}As show a general parabolic trend as a function of the H₂ component of the Cl₂/Ar/H₂ ratio. Three distinct etching profiles of InP/InGaAsP layers were realized by varying the Cl₂/Ar/H₂ ratio. Highly anisotropic profiles result for Cl₂/Ar/H₂ ratios between 2/3/1 and 2/3/2. Waveguiding structures fabricated using this technology are presented with a loss as low as 2 dB/cm. An InP racetrack resonator with a quality factor (*Q*)>8000 is also presented. © 2002 American Vacuum Society. [DOI: 10.1116/1.1486232]

I. INTRODUCTION

A fundamental building block of planar lightwave integrated circuits, known as a ring resonator, consists of a straight waveguide segment adjacent to a ring waveguide separated by a narrow air gap. An input signal launched into the straight waveguide segment couples into the ring resonator via the air gap if it is narrow enough to allow a wavefunction overlap (i.e., a spacing <300 nm). It is desirable to make the ridge waveguide narrow so that the structure supports only a single transverse mode and the tail of the eigenmode “leaks out” of the ridge to ensure coupling to the resonator. This basic structure acts as a notch filter. When the wavelength is on-resonance, the signal ideally propagates only in the ring; when the transmission is off-resonance, the signal is only transmitted through the straight waveguide.

The key to realizing these structures is the development of dry-etching processes that can produce highly anisotropic structures with high edge acuity and smooth surface morphology. Striations on the edge of the waveguides may cause scattering loss, and should be minimized. Recently, such structures have been realized primarily in AlGaAs/GaAs systems.¹⁻³ InGaAsP microdisk resonators formed by polymer wafer bonding⁴ and cascaded InGaAsP/InP resonators have also been demonstrated.⁵ However, loss in the structures grown directly on InP substrates has not been studied extensively.

Dry-etching studies of InP have pursued two general chemistries: methane-based etching and Cl₂-based etching. Reactive ion etching studies typically pursued a CH₄/H₂ etch in conjunction with a cyclical O₂ clean to etch highly anisotropic structures.⁶ However, this chemistry suffers from

a low etch rate of ~60 nm/min, and is undesirable for practical device fabrication. An alternative approach using Cl₂/Ar in a chemically assisted ion-beam etching chamber was established by Youtsey *et al.*⁷ In this study, etch rates as high as 2 μm/min were reported for substrate temperatures of 225 °C.

Recently, inductively coupled plasma-reactive ion etching (ICP-RIE) has been used to etch InP.⁸⁻¹⁰ Due to its high plasma density, ICP-RIE results in a high ion flux with low ion energies. Thus, ICP-RIE chemistries may be developed that simultaneously maintain high etch rates while minimizing damage from high energy bombardment.

This study presents a Cl₂/Ar/H₂ chemistry that was used to etch InP-based waveguides. The composition of Cl₂/Ar/H₂ was found to have a strong influence on the degree of undercut in the profile. Under appropriate conditions, a nearly perfect anisotropic profile was achieved. Low-loss characteristics of racetrack resonators etched using the process developed are presented.

II. ETCH RATES AND PROFILES

The samples discussed in this study were etched in a PlasmaTherm SLR 770 ICP-RIE system. Samples were transferred into the etching chamber via a load lock. A rf bias (13.56 MHz) between 0 and 500 W is supplied to the chuck during etching. An inductive coil power (2 MHz) between 0 and 1000 W is supplied to the chamber via a primary coil in the upper electrode. The chamber pressure is maintained by a feedback-controlled throttle valve. Process gases are introduced into the chamber via a series of mass flow controllers calibrated to flow rates as low as 0.1 sccm.

An initial process optimization was performed on InP substrates patterned via a bilayer photoresist mask technology

^{a)}Electronic mail: rommel@uiuc.edu

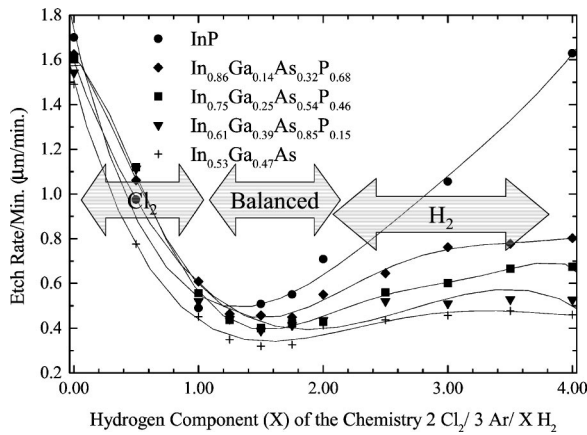


FIG. 1. Etch rate of InP/InGaAsP alloys as a function of the H₂ concentration in ICP-RIE Cl₂/Ar/H₂ chemistries. The etch conditions were 900 W inductive power, 110 W rf power, -215 V dc bias, 1.5 mT, 225 °C, and a Cl₂/Ar/H₂ ratio of 2/3/x. The graph is observed to have three regions: Cl₂ dominated, anisotropic (balanced etch), and H₂ dominated.

described elsewhere.⁷ Rf power was varied between 50 and 250 W, and the inductive coil power was varied between 300 and 900 W. In accordance with a recent study,^{8,9} the chamber pressure was restricted to less than 2 mT to enhance anisotropy. Initially, only Cl₂ was supplied to the chamber. Other than slightly increasing the etch rate, variations to the coil power were found to have little influence on the profile or surface morphology. Therefore, a coil power of 900 W was selected as the optimal operating point, as it resulted in the highest etch rate. In contrast, the profile was strongly influenced by the rf power. An undercut of 0.75 μm was observed for rf powers between 50 and 75 W. As the rf power was increased to 90–120 W, the undercut decreased to 0.45 μm. While etching at higher powers (>150 W) improved anisotropy, the etch mask began to deteriorate, resulting in sidewall erosion of the etched structures. Therefore, despite the undercut, the optimal rf power for a Cl₂ etch was determined to be ~110 W. This undercut was slightly mitigated by the addition of an Ar physical component. A Cl₂/Ar ratio of 2/3 reduced the undercut to 0.25 μm for the present operating conditions. An elevated substrate temperature of 225 °C was introduced to smoothen the etch surfaces, and also to accelerate the etch rate.⁷ These conditions (110 W rf power, 900 W coil power, 1.5 mT, Cl₂/Ar ratio of 2/3, substrate temperature of 225 °C) were then used to study the role of H₂ on the etch profile. The dc bias resulting from these conditions was -215 V.

A series of five samples with 1-μm-thick epitaxial layers were grown to determine bulk etch rates. The compositions of these layers were InP, In_{0.86}Ga_{0.14}As_{0.32}P_{0.68}, In_{0.75}Ga_{0.25}As_{0.54}P_{0.46}, In_{0.61}Ga_{0.39}As_{0.85}P_{0.15}, and In_{0.53}Ga_{0.47}As. The samples were then patterned by contact lithography, and the etch rate was determined by extracting the slope of four etch depth measurements acquired via a stylus profilometer. Figure 1 presents the etch rates obtained for these layers as a function of the H₂ concentration. A

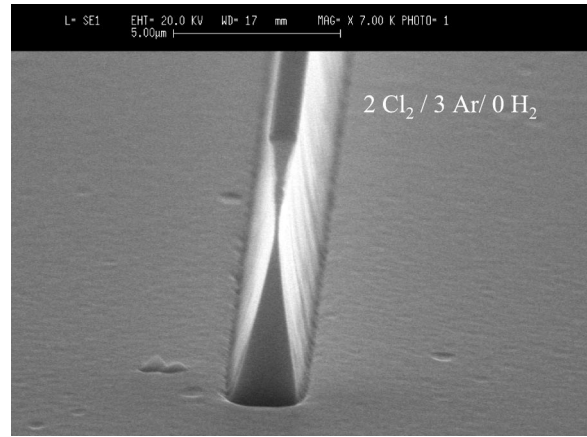


FIG. 2. Scanning electron micrograph of an InP/InGaAsP epitaxial layer etched with 110 W rf power, 900 W inductive power, -215 V dc bias, Cl₂/Ar/H₂ = 6/9/0 sccm, 1.5 mT, and 225 °C. These layers exhibit a large undercut of the etch mask, which is still in place.

fourth-order polynomial was then used to fit the experimental data.

The curves in Fig. 1 can be divided into three regions. In the first region with H₂ ratios between 0 and 1, the etch rates of all of the epitaxial layers decreased with increased H₂ concentration. These data suggest that gaseous H₂ reacts with Cl₂ in the chamber, resulting in a reduction in the number of available radicals responsible for chemical etching. Thus, the etch rate reduces with increased H₂. However, in this region, the amount of Cl₂ exceeded the H₂ and the etch was dominated by Cl₂-chemical etching.

A second region of the graph occurs between H₂ concentrations of 1 and 2. Over this region, the percentages of Cl₂ and H₂ are nearly equal. A slight difference in etch rate is observed as a function of material composition. This region contains the smallest amount of available chemically active species. It is, therefore, believed that in this region etching is dominated by a Cl₂/H₂ chemical etch balanced by an Ar physical component. As data will show later, this region results in the structures with the highest degree of anisotropy.

In the third region of the graph (H₂ concentrations >2), the flow of H₂ begins to dominate the flow of Cl₂. The etching in this region, therefore, is primarily attributed to a H₂ chemical etch. It is observed that the etch rate for all of the epitaxial layers begins to increase above this threshold. However, the degree of increase in the etch rate depends on the material composition. InP clearly shows the highest etch rate whereas In_{0.53}Ga_{0.47}As etches the slowest. The etch rates of the In_{1-x}Ga_xAs_{1-y}P_y quaternary layers increase as the As concentration is decreased. Thus, as the As concentration approaches 0, the layer has an etch rate curve similar to InP, and as the As concentration approaches 100%, the layer has an etch rate curve similar to In_{0.53}Ga_{0.47}As. For a Cl₂/Ar/H₂ ratio of 2/3/4, it is observed that a selectivity of 4 exists for InP against In_{0.53}Ga_{0.47}As.

This information was then used to determine the optimal point for etching device samples. A heterostructure designed for waveguiding was then grown. This layer consisted of

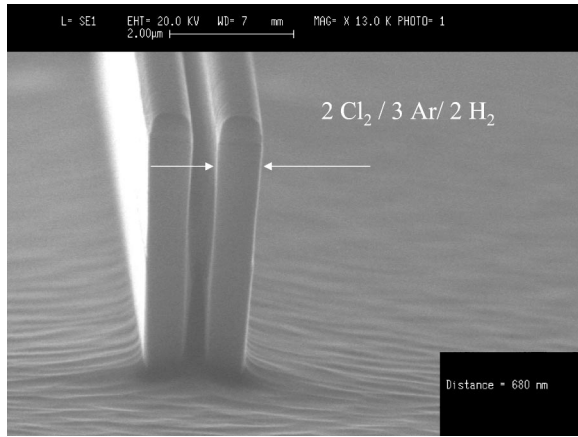


FIG. 3. Scanning electron micrograph of an InP/InGaAsP epitaxial layer etched with 110 W rf power, 900 W inductive power, -215 V dc bias, $\text{Cl}_2/\text{Ar}/\text{H}_2 = 6/9/6$ sccm, 1.5 mT, and 225 °C. The width of the etched segments is 0.7 μm , and the gap is 0.275 μm . The etch depth is 4 μm .

0.051 μm $\text{In}_{0.53}\text{Ga}_{0.47}\text{As}$, 1.41 μm InP, 0.3 μm $\text{In}_{0.86}\text{Ga}_{0.14}\text{As}_{0.32}\text{P}_{0.68}$, 0.09 μm $\text{In}_{0.75}\text{Ga}_{0.25}\text{As}_{0.54}\text{P}_{0.46}$, 0.3 μm $\text{In}_{0.86}\text{Ga}_{0.14}\text{As}_{0.32}\text{P}_{0.68}$, and 1.5 μm of InP on a semi-insulating InP substrate. A 500-nm-thick SiO_2 mask was deposited on the surface of the sample by plasma-enhanced chemical-vapor deposition. Submicron waveguides were then patterned by electron-beam lithography in a 0.35 - μm -thick AZPN114 negative resist. Subsequently, the patterns were transferred to the underlying SiO_2 mask via RIE in a CHF_3 plasma.

This heterostructure was then etched to determine the resulting profile as a function of H_2 concentration. The profile in the Cl_2 -dominated region exhibits a large undercut. Figure 2 shows a scanning electron microscope micrograph for the extreme case of $\text{Cl}_2/\text{Ar}/\text{H}_2$ ratios of $2/3/0$. As the percentage of H_2 was increased it was observed that the undercut simultaneously decreased. The transition between InP and the InGaAsP layers is not evident in the micrograph, in agreement

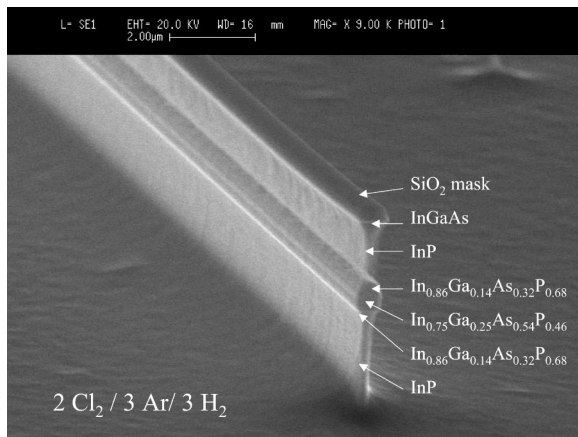


FIG. 4. Scanning electron micrograph of an InP/InGaAsP epitaxial layer etched with 110 W rf power, 900 W inductive power, -215 V dc bias, $\text{Cl}_2/\text{Ar}/\text{H}_2 = 6/9/9$ sccm, 1.5 mT, and 225 °C. InP layers show large undercuts whereas InGaAsP layers show little lateral etching.

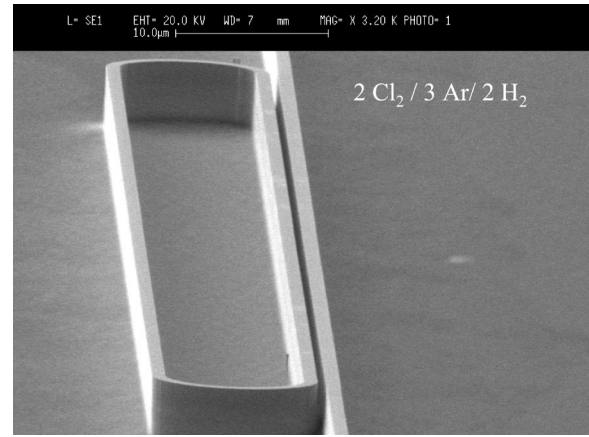


FIG. 5. Scanning electron micrograph of an InP/InGaAsP racetrack resonator fabricated with the process shown in Fig. 3. The ridge is etched to a depth of 5 μm , and has a width of 0.9 μm and gap of 0.275 μm .

with the data in Fig. 1. This clearly indicates that the epitaxial layers are etched at approximately the same rates.

Highly anisotropic etching occurs for a $\text{Cl}_2/\text{Ar}/\text{H}_2$ ratio of $2/3/2$, in the balanced etching regime. Figure 3 illustrates a section of a racetrack resonator-type structure etched under these conditions. The structure has a linewidth of 0.7 μm , and a gap of 0.275 μm between the line and racetrack. The sidewalls of the structure are very smooth, and show little surface roughness. Note that the gap appears completely etched. Again, it is difficult to discern the positions of the various epitaxial layers in the micrograph, suggesting that the layers have etched at nearly the same rate. Clearly, this chemistry is optimal for fabricating highly anisotropic waveguides.

In the third region (H_2 dominated), the etch profiles show a distinct behavior, which is illustrated in Fig. 4. Once again, InP layers suffer from a 0.15 μm undercut. However, it is evident that the addition of H_2 causes InP and InGaAsP/InGaAs epitaxial layers to etch at different rates. Furthermore, InGaAsP epitaxial layers of varying compositions are observed to etch at different rates as the etch rate data suggested. Three distinct stripes, corresponding to the 0.3 μm $\text{In}_{0.543}\text{Ga}_{0.457}\text{As}_{0.33}\text{P}_{0.67}$, 0.09 μm $\text{In}_{0.539}\text{Ga}_{0.461}\text{As}_{0.55}\text{P}_{0.45}$, and 0.3 μm $\text{In}_{0.543}\text{Ga}_{0.457}\text{As}_{0.33}\text{P}_{0.67}$ waveguiding region are evident in the center of the micrograph. This unique processing condition provides an enabling technology for InP-based nanofabrication. For example, by carefully tailoring the composition of InGaAsP epitaxial layers and the H_2 flow, quantum wires, quantum dots, and cantilever structures may be fabricated.

III. DEVICE FABRICATION AND RESULTS

A series of straight waveguides with widths between 0.7 and 1.0 μm were patterned on the heterostructure layer, and etched with the $\text{Cl}_2/\text{Ar}/\text{H}_2$ ratio fixed at $2/3/2$. The samples were etched to a depth of 4 μm to ensure that the waveguiding region was optically isolated from the substrate. The samples were then cleaved to expose an input and output facet. Light was then coupled into the waveguide via a series

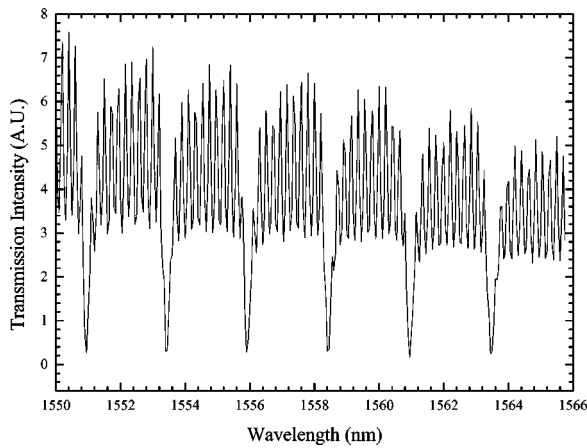


FIG. 6. Resonance data obtained from the device shown in Fig. 5. The quality factor of the device is 8000.

of lenses coupled into a tapered optical fiber. The output signal was coupled into a second fiber. The waveguides were found to have a loss as low as 2 dB/cm.

A racetrack resonator was then fabricated on the same wafer (see Fig. 5). In this design, a straight segment length of 90 μm is used to enhance the coupling between the straight guide and the ring. The ridge width was $\sim 0.9 \mu\text{m}$, and the air gap had a width of 0.275 μm . A radius of 15 μm was used in the curved regions. Again, the structure was etched with the optimized Cl₂/Ar/H₂ etch to a depth of 4 μm .

Clear resonance data are presented in Fig. 6. Because the ends of the facets were not antireflection coated, Fabry-Pérot resonances are also observed. The structure shows a quality factor of 8000, and a free-spectral range of 2.41 nm. Obtaining a larger free-spectral range can be achieved by reducing the circumference of the racetrack.

IV. CONCLUSION

The positive impact of the addition of H₂ to a Cl₂/Ar process for the etching of InP-based heterostructures was demonstrated. The addition of H₂ balances the physical and

chemical components, resulting in three distinct etch profiles. The Cl₂-dominated region (Cl₂/Ar/H₂ ratios between 2/3/0 and 2/3/1.5), is typified by high etch rates (1.8 $\mu\text{m}/\text{min}$) and large undercuts of InP and InGaAsP layers. The second region (Cl₂/Ar/H₂ ratios between 2/3/1.5 and 2/3/2.5) has balanced chemistry typified by low but uniform etch rates (0.5–0.6 $\mu\text{m}/\text{min}$) and highly anisotropic InP/InGaAsP profiles. A H₂-dominated region occurred for Cl₂/Ar/H₂ ratios above 2/3/2.5. In this region, InP layers exhibited large undercuts, whereas InGaAsP layers showed little lateral etching. Experimental evidence also suggests that the selectivity of InGaAsP layers relative to InP may be increased by increasing the As concentration. Waveguides fabricated with a Cl₂/Ar/H₂ ratio of 2/3/2 exhibited an insertion loss as low as 2 dB/cm. A racetrack resonator with a quality factor of 8000 was also demonstrated.

ACKNOWLEDGMENTS

The authors wish to thank J. S. Hughes of the University of Illinois at Urbana-Champaign for assistance with the electron-beam lithography. This project was supported by the DARPA/R-FLICs program managed by W. Schneider (DARPA) and monitored by Dr. J. Nicther (United States Air Force Research Laboratory) [Contact No. AF S(490000084) and by NSF-ITR (ANI 01-21662 ITR)].

- ¹M. K. Chin, C. Youtsey, W. Zhao, T. Pierson, Z. Ren, S. L. Wu, L. Wang, Y. G. Zhao, and S. T. Ho, *IEEE Photonics Technol. Lett.* **11**, 1620 (1999).
- ²J. V. Hryniewicz, P. P. Absil, B. E. Little, R. A. Wilson, and P. T. Ho, *IEEE Photonics Technol. Lett.* **12**, 320 (2000).
- ³P. P. Absil, J. V. Hryniewicz, B. E. Little, R. A. Wilson, and P. T. Ho, *IEEE Photonics Technol. Lett.* **12**, 398 (2000).
- ⁴Y. Ma, G. Chang, S. Park, L. Wang, and S. T. Ho, *IEEE Photonics Technol. Lett.* **12**, 1495 (2000).
- ⁵Y. Ma, S. H. Chang, S. S. Chang, and S. T. Ho, *Electron. Lett.* **37**, 564 (2001).
- ⁶I. Adesida, K. Nummila, E. Andideh, J. Hughes, C. Caneau, R. Bhat, and R. Holmstrom, *J. Vac. Sci. Technol. B* **8**, 1357 (1990).
- ⁷C. Youtsey, R. Grundbacher, R. Panepucci, I. Adesida, and C. Caneau, *J. Vac. Sci. Technol. B* **12**, 3317 (1994).
- ⁸E. W. Berg and S. W. Pang, *J. Vac. Sci. Technol. B* **16**, 3359 (1998).
- ⁹E. W. Berg and S. W. Pang, *J. Electrochem. Soc.* **146**, 775 (1999).
- ¹⁰J. Hong, J. W. Lee, C. R. Abernathy, E. S. Lambers, S. J. Pearton, R. J. Shul, and W. S. Hobson, *J. Vac. Sci. Technol. A* **16**, 1497 (1998).

Electro-Refractive Low Loss MMI-Coupled Ring Resonators

M.H. Kwakernaak, A.N. Lepore, H. Mohseni, H. An, Z.A. Shellenbarger, J.H. Abeles

Sarnoff Corporation, 201 Washington Road, Princeton NJ 08543, USA; e-mail: mkwakernaak@sarnoff.com

J.-O. Bae, S. L. Rommel, I. Adesida

Department of Electrical and Computer Engineering, University of Illinois at Urbana-Champaign, Urbana, IL 61801 USA

Abstract: MMI-coupled electro-refractive ring resonators have been fabricated using deeply etched InGaAsP/InP waveguides. RF-modulation with the ring resonator is demonstrated. The modulation efficiency is 5dB enhanced by modulating the ring compared to a straight waveguide.

Micro-optic ring resonators are attractive for active and passive micro-optical circuits. Rings and discs with directional couplers have been realized in lateral and vertical geometries [1,2,3]. Coupling of ring resonators with MMI couplers has been demonstrated with ridge-type waveguides on InP [4]. Switching has been demonstrated in active discs using electro-absorption [2]. We report the first demonstration of electro-refractive modulation in ring resonators. MMI couplers are used to provide reproducible coupling ratios, which are particularly important in electro-optic applications or when the resonators are part of an optical filter.

The ring resonators were fabricated in InGaAsP/InP using 25 quantum wells with a photoluminescence wavelength of 1415 nm. Deeply etched waveguides (4 μm) with widths of 0.8 μm and MMI couplers have been defined with a direct e-beam patterning and ICP etching [5]. MMI couplers with dimensions 2.7 μm x 34.5 μm are designed to provide a 50% coupling to the rings with circumference of 250 μm . The samples are coated with CytopTM dielectric. Electrical contacts are formed on top of the ring-waveguide and to the n-substrate to enable modulation. Optical losses of these straight waveguides are $\sim 1 \text{ cm}^{-1}$; these are the lowest loss waveguides of their kind ever reported.

Figure 2 shows the measured transmission and group delay of a ring resonator. Transmission has been measured with a tunable laser and the group delay extracted with a modulation phase shift method [6]. Dashed curves are calculations fit to the measured data. The resonator quality factor Q is 4500. The transmission and group-delay data allows unambiguous determination of coupling and loss, which are 51% and 8.5% (0.4 dB) per ring revolution, respectively. In this (over-coupled) regime the ring resonator Q is determined by the coupling coefficient rather than the loss, and is thus defined by the design.

Figure 3a shows the transmission of an interferometer with a ring resonator in one arm. Index modulation of the ring resonator results in an enhanced phase modulation of one interferometer arm. The measured modulation response of the configuration is displayed in Figure 3b. In this measurement the ring resonator is reverse biased, and a 1 GHz sine-signal is applied. The modulation depth of the signal is retrieved with a network analyzer, while the wavelength is scanned.

Support by DARPA/MTO under contract number F30602-00-C-0116 is acknowledged.

1. V. Van, P.P. Absil, J.V. Hryniewicz, P.-T. Ho, "Propagation loss in single-mode GaAs-AlGaAs microring resonators: measurement and model", *IEEE J. Lightwave Technol.* 19, 1734 (2001).
2. K. Djordjev, C. Seung-June, C. Sang-Jun, P.D. Dapkus, "Vertically coupled InP microdisk switching devices with electroabsorptive active regions", *IEEE Photon Technol. Lett.* 14, 1115 (2002).
3. G. Griffel, J.H Abeles R.J. Menna, A.M. Braun, J.C. Connolly, M. King "Low-threshold InGaAsP ring lasers fabricated using bi-level dry etching", *IEEE Photon Technol. Lett.* 12, 146 (2000).
4. D.G. Rabus, M. Harnacher, "MMI-coupled ring resonators in GaInAsP-InP", *IEEE Photon Technol. Lett.* 13, 812 (2001).
5. S. L. Rommel, J-H Jang, W. Lu, G. Cueva, L. Zhou, I. Adesida , G. Pajer, R. Whaley, A. Lepore, Z. Shellenbarger,, J. Abeles, "The effect of H₂ on the etch profile of InP/InGaAsP alloys in Cl₂/Ar/H₂ inductively coupled plasma-reactive ion etching chemistries for photonic device fabrication.", *J. of Vacuum Science and Technology B*, 20, 1327 (2002).
6. P. Hernday, " Dispersion measurements", in "Fiber optic test and measurement," D. Derickson. Ed., Prentice-Hall 1998.

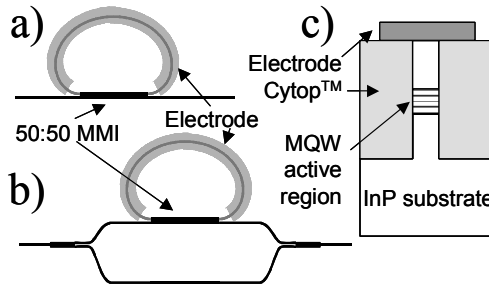


Fig. 1. a) Ring resonator. b) Mach-Zehnder interferometer with a ring resonator in one arm. c) Deeply etched waveguide structure.

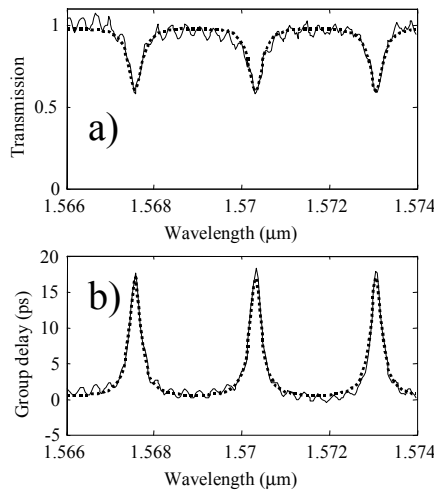


Fig. 2. Transmission a) and group delay b) of a single ring resonator (see figure 1a). Solid: measured data; Dotted: calculation.

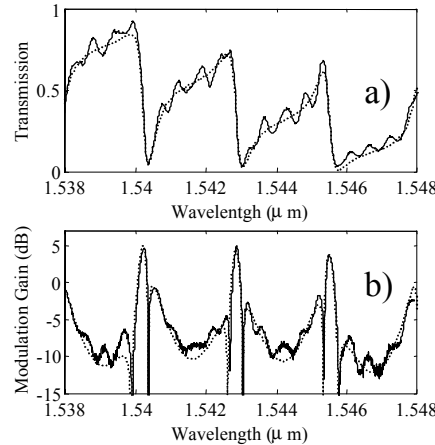


Fig.3. a) Transmission of a Mach-Zehnder interferometer with a ring-resonator in one arm (see figure 1b). b) Modulation gain (i.e. modulation efficiency as compared to that of a straight waveguide of length equal to the ring circumference). Solid: measured data; Dotted: calculation.

Characterization of sidewall roughness of InP/InGaAsP etched using inductively coupled plasma for low loss optical waveguide applications

J. W. Bae, W. Zhao, J. H. Jang, and I. Adesida

Micro and Nanotechnology Laboratory and Department of Electrical and Computer Engineering, University of Illinois at Urbana Champaign, Urbana, IL 61801 USA

Allen Lepore, Martin Kwakernaak and Joseph H. Abeles

Sarnoff Corporation, Princeton, NJ 08543, USA

Photonic devices and circuits based on InP/InGaAsP materials require optical waveguides with highly anisotropic and smooth sidewall profile to achieve good optical mode quality and low loss performance. In the fabrication of optical waveguides, critical factors include lithography, masking, and etching. Each factor introduces various degrees of sidewall roughness (SWR). The rough sidewall of waveguides causes scattering loss, which is the one of the major sources of optical loss in deep etched waveguides. Therefore, the characterization of sidewall roughness for the various processes is required.

In this study, the SWR of InP/InGaAsP heterostructures fabricated using inductively-coupled-plasma reactive-ion-etching was investigated as a function of the masking strategy and the etched depth of waveguides. Atomic force microscope (AFM) was utilized to directly measure the SWR of waveguides. The effect of masking strategies on SWR was investigated using two types of masks including NiCr/SiO₂ and SiO₂/NiCr/SiO₂. The evolution of SWR during ICP etching was investigated by varying the etch depth from 4 μm to 10 μm. Electron beam lithography was used to delineate specially designed line patterns that permit AFM tip to directly measure the SWR. The root-mean-square sidewall roughness was measured to be less than 2 nm, which is currently the lowest published SWR for InP-based optical waveguide devices. The effect of thin SiO₂ remasking layer on top of NiCr metal mask on the SWR, and the process development for the low loss optical waveguide fabrication will also be presented.

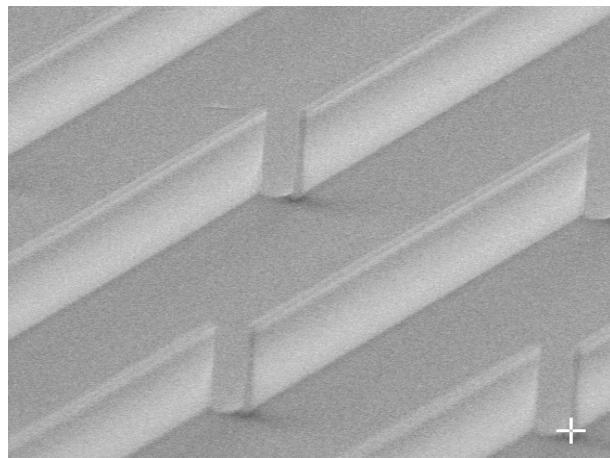


Fig 1 : A scanning electron micrograph of InP/InGaAsP heterostructure ridge waveguides etched using inductively coupled plasma system. 1- μ m wide lines were etched to a depth of 10.7 μ m.

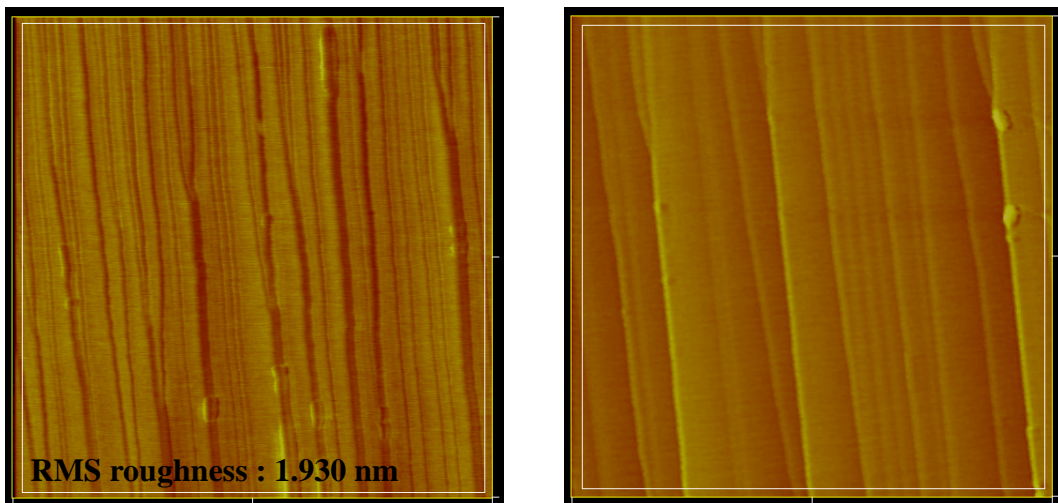


Fig 2 : Atomic force microscope (AFM) images of sidewall of InP/InGaAsP heterostructure ridge waveguides etched using NiCr/SiO₂ mask (a) and SiO₂/NiCr/SiO₂ (b), respectively. Etch conditions are Cl₂/H₂/Ar = 6 sccm/6 sccm/9 sccm, 3 mTorr of working pressure, -210 V of bias voltage, 900W of inductive power, and 250 °C.

Direct measurement of nanoscale sidewall roughness of optical waveguides using an atomic force microscope

J. H. Jang, W. Zhao, J. W. Bae, D. Selvanathan, S. L. Rommel, and I. Adesida^{a)}

Micro and Nanotechnology Laboratory and Department of Electrical and Computer Engineering, University of Illinois at Urbana Champaign, Urbana, Illinois 61801

A. Lepore, M. Kwakernaak, and J. H. Abeles

Sarnoff Corporation, Princeton, New Jersey 08543

(Received 8 April 2003; accepted 22 September 2003)

An atomic force microscope (AFM) with an ultrasharp tip was used to directly measure the sidewall profile of InP/InGaAsP waveguide structures etched using an inductively coupled plasma reactive ion etching (ICP-RIE) in Cl₂-based plasma. A special staircase pattern was devised to allow AFM tip to access the etched sidewall of the waveguides in the normal direction. Statistical information such as correlation length and rms roughness of the sidewall profile obtained through three-dimensional imaging by AFM has been presented. rms roughness as low as 3.45 nm was measured on the sidewall of 4-μm-deep etched InP/InGaAsP heterostructures. © 2003 American Institute of Physics. [DOI: 10.1063/1.1627480]

Recent progress in dry etching technologies has enabled the realization of microphotonic devices based on optical waveguides.^{1–3} Deep-etched optical waveguides with high refractive index contrast between the core and the cladding layers ($\Delta n^2 = n_{\text{core}}^2 - n_{\text{cladding}}^2$) are of interest because of their advantages in miniaturizing photonic devices utilizing sharp bends and compact ring resonators. However, they suffer more from deleterious optical scattering loss than waveguides with low index contrast because scattering loss at the imperfect sidewall is proportional to Δn^2 .⁴ Theoretical studies on waveguide loss have shown that detailed statistical information on the sidewall profile, such as auto-correlation function or spectral distribution of sidewall roughness (SWR), is required for accurate estimation of scattering loss.^{4–6} With the same rms roughness, scattering loss can vary depending upon the correlation length of SWR. Thus, to achieve low-loss optical waveguides, an appropriate characterization tool to measure SWR, as well as etching technologies producing highly vertical and smooth sidewalls, are required. Various etching techniques have been investigated, but quantitative studies on the resulting SWR have been quite limited.

Scanning electron microscopy (SEM) and atomic force microscopy (AFM) are commonly utilized to measure planar surface morphology or texture. However, a SEM-based measurement technique (electron probe roughness analyzer) has been utilized to obtain the roughness of an etched sidewall profile.⁷ The method has an advantage as a noncontact measurement technique, but its resolution was limited to 1 nm.⁷ An AFM has better sensitivity in characterizing planar surface morphology than SEM, but it is difficult to use in measuring the vertical surface of three-dimensional (3-D) structures. This is especially true where the 3-D structures consist of small geometries. Attempts have been made to overcome this limitation. For example, a specially prepared high aspect ratio boot-shaped AFM tip that was mounted in an AFM

system with two-dimensional (2-D) servo control system has been demonstrated for this purpose.⁸ The AFM system was utilized to characterize the sidewall profile of a photoresist line, but its scanning area was limited by the length of the AFM tip. The resolution of the scanned image was limited by that of the positional stage controlling the lateral motion of the AFM tips. Another approach to obtain the sidewall profile of ridge waveguide structures using AFM was carried out with a sample mounted at a tilted angle.⁹ This method requires a complex calibration routine to obtain the correct results from the scan of the tilted specimen.¹⁰ It is very difficult to apply this technique to profile deep-etched optical waveguides with highly vertical sidewalls.

Transmission electron microscopy has also been employed to measure the interface line-edge roughness (LER) between the core and the cladding layers of Si/SiO₂ optical waveguides.¹¹ The auto-correlation function as well as rms roughness of LER were obtained. It should be noted that the authors assumed that the SWR was identical to the LER of the top surface; however, this may not be true in the case of deep-etched waveguides.

It is evident that there are still limitations in directly obtaining the roughness of waveguide sidewalls. Recent advances in AFM technologies, especially in the engineering of tips, have improved the potential of utilizing AFM for directly characterizing the vertical sidewalls of small geometrical structures such as semiconductor optical waveguides.

In this letter, an InGaAsP/InP heterostructure was etched utilizing inductively coupled plasma reactive ion etching (ICP-RIE) to obtain high-mesa optical waveguide structures. Large areas of the sidewalls of the deep-etched high-mesa structures were directly characterized with AFM for quantitative studies of SWR.

The fabrication procedure for high-mesa optical waveguides has been described elsewhere.¹² Briefly, PMMA-P(MMA-MAA) bilayer electron-beam resist system was used for the lift-off of NiCr metal mask, which was subsequently utilized for transferring patterns into a SiO₂ layer deposited on the waveguide heterostructures. The re-

^{a)}Electronic mail: iadesida@uiuc.edu

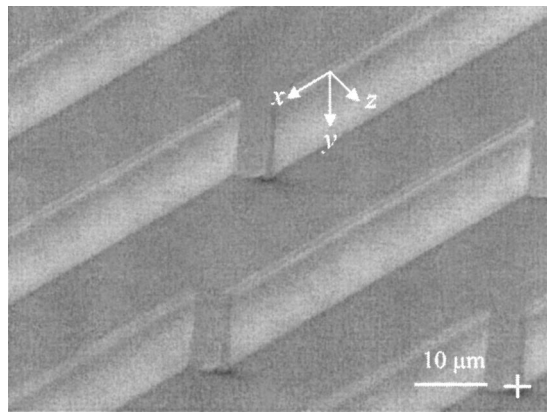


FIG. 1. A scanning electron micrograph of deep-etched InP/InGaAsP waveguide heterostructures using ICP-RIE system. Lines 1- μ m-wide were etched to a depth of 10.7 μ m. Waveguide sidewall is on x - y plane, where x is in light propagation direction. Z axis is normal to the waveguide sidewall.

sulting NiCr/SiO₂ was used as a mask to etch waveguide heterostructures using a Cl₂/Ar/H₂ gas mixture. The difference between the etch rates of InGaAsP and InP was minimum under the etching conditions of Cl₂/H₂/Ar=6 sccm/6 sccm/9 sccm, 3 mTorr of working pressure, -210 V bias voltage, 900 W inductive power, and 250 °C substrate temperature. This etching resulted in line patterns with rectangular cross sections and aspect ratios of up to 10, as shown in Fig. 1.

An AFM was used to characterize the sidewall profiles of the etched optical waveguides. A specially designed line pattern shown in Fig. 1 was delineated in parallel with the crystal orientation of InP by electron-beam lithography. The staircase patterns allowed the cleavage of the sample to result in at least one segment of the waveguides being very close to the cleaved wafer edges so that an AFM tip can easily access the sidewalls of the waveguides in the direction perpendicular to the sidewall. With the AFM tip normal to the etched sidewall, the feedback loop of the z -directional movement of the AFM tip is still effective, and no modification in the control loop is needed. The resolution of the AFM is highest in the direction of the surface normal. Therefore, this configuration allows an AFM tip full access to the sidewall, resulting in the full imaging of the sidewall in high resolution.

A cone-shaped ultrasharp AFM tip (typical diameter of curvature was \sim 10 nm) was utilized to achieve high-fidelity sidewall profiling. Figures 2(a) and 2(b) show typical SEM and AFM images of the sidewalls of waveguides etched up to 4 μ m deep, and Fig. 2(c) shows an AFM image of the sidewall of the InP substrate cleaved along the (100) crystal orientation. In the AFM images of the waveguide sidewalls, vertical striations on the sidewall are clearly visible. The striations begin at the top of SiO₂ mask layer and are transferred down to the bottom of the scanned sidewall. The origin of the vertical striations is ascribed to the line edge roughness (LER) of the etch mask. It is expected that mask erosion caused by ion bombardment during ICP-RIE etching adds to the LER of an etch mask. The SEM image in Fig. 2(a) shows the eroded mask at the top. Two sampled sidewall profiles in the x and y directions are also illustrated at the bottom and the left-hand sides of the AFM micrograph in

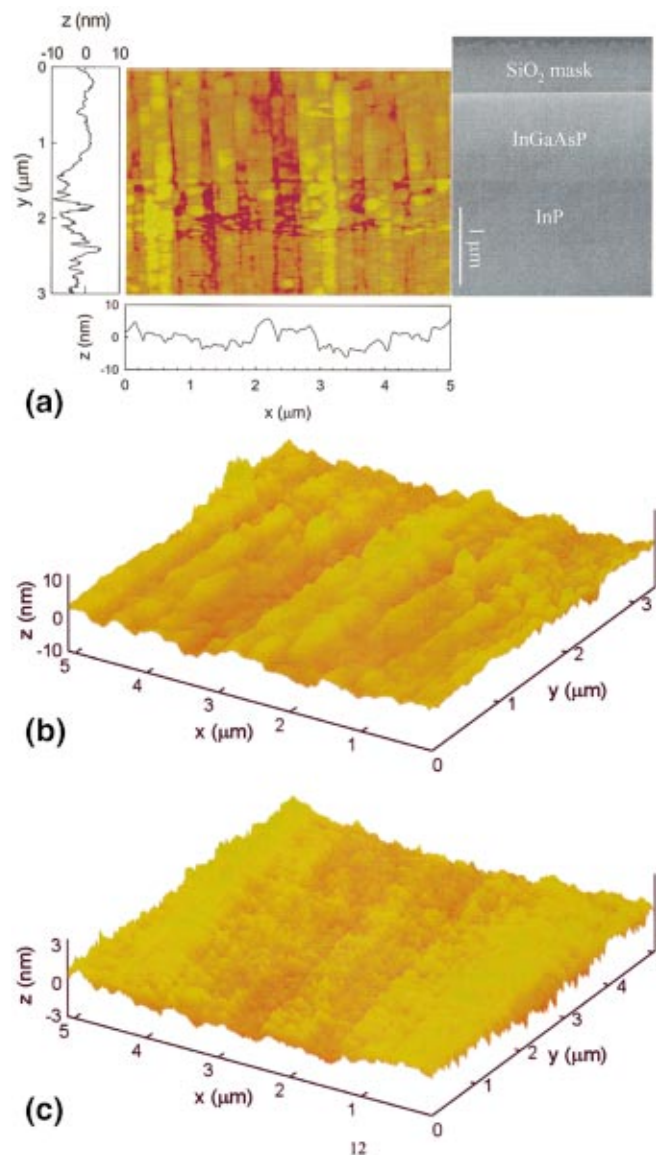


FIG. 2. (Color) (a) AFM and SEM micrographs of waveguide sidewall etched up to 4 μ m. Sampled profile in x and y direction was displayed. (b) Three-D view of sidewall profile measured with AFM.

Fig. 2(a). The rms roughness values in the x and y directions are displayed in Fig. 3. The rms roughness ranged from 2 to 6 nm. The rms roughness in the y direction (SWR_y) is highest in the InP region beneath the InGaAsP waveguiding layer, and is shown in Figs. 2(a) and 2(b), and Fig. 3(b). As the etching process proceeds from the top downwards, the material difference gives rise to additional roughness when it crosses the heterointerface between InGaAsP and InP. The etch rate of InGaAsP was about half the etch rate of InP for the etching conditions used in this work. The different etch rates of these distinct materials resulted in the different textures on the etched sidewall, as shown in Figs. 2(a) and 2(b). For reference, the sidewall of the cleaved InP substrate was also scanned in the same configuration. The AFM scan image is shown in Fig. 2(c). No significant striations were detected for the cleaved sidewall of InP substrate. The rms roughness measured on the cleaved sidewall of InP substrate was 0.75 nm and the peak-to-valley height difference was \sim 4.5 nm. Two-D and averaged one-dimensional autocovariance functions $C_z(x, y)$, $C_z(x)$, and $C_z(y)$ of SWR are shown in Figs.

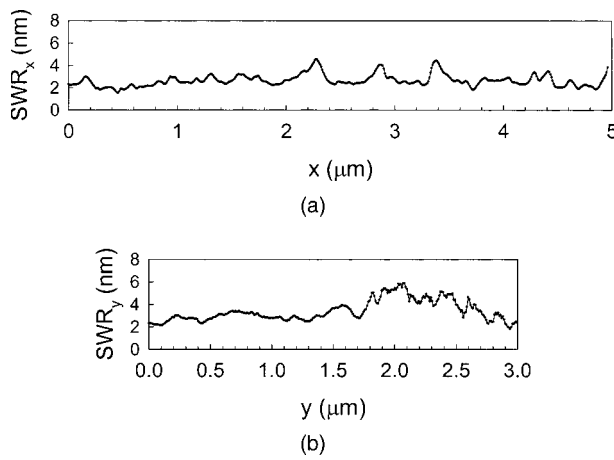


FIG. 3. Distribution of SWR of etched sidewall (a) $\text{SWR}(x)$ and (b) $\text{SWR}(y)$.

4(a) and 4(b). The power spectra of SWR shown in the inset of Fig. 4(b) were obtained from Fourier transform of autocovariance functions.

The rms surface roughness of the entire scanned area of the sidewall was calculated to be 3.45 nm, which is the square root of the peak value of the 2-D autocovariance function in Fig. 4(a). The peak values of autocovariance functions shown in Fig. 4(b) correspond to the square of rms roughness values in x and y directions. The rms roughness values were 3.4 and 2.7 nm in x and y directions, respectively. Correlation lengths (B_x and B_y) were extracted from the fitted curves in Fig. 4(b). The best fits were achieved with Gaussian and exponential functions for $C_z(x)$ and $C_z(y)$, respectively. The correlation length in the y direction (B_y) is much larger than that in the x -direction (B_x), as shown in Figs. 4(a) and 4(b). It implies that ion bombardment during ICP-RIE etching is highly directional in the vertical direction resulting in the randomness of the surface profile being much less in this direction. We have measured optical loss of waveguides fabricated using the same technique described in this letter. Two measurement techniques, cutback method and Fabry-Perot method, produced optical loss coefficient of $1/\text{cm}$,¹³ which agrees satisfactorily with the calculated loss obtained using the information obtained with SWR measurements.

In conclusion, the SWR of deep-etched InP/InGaAsP waveguides has been directly characterized using specially designed staircase patterns that made the waveguide's sidewalls accessible for large area scanning with AFM tips. ICP-RIE using NiCr/SiO₂ composite masking layer resulted in very smooth and highly vertical sidewall profiles. Autocovariance function and power spectrum of SWR were obtained, and were used to estimate optical loss performance of waveguides. For 4-μm-deep etched waveguides, SWR and correlation length along the light propagation direction were 3.4 nm and 0.16 μm, respectively.

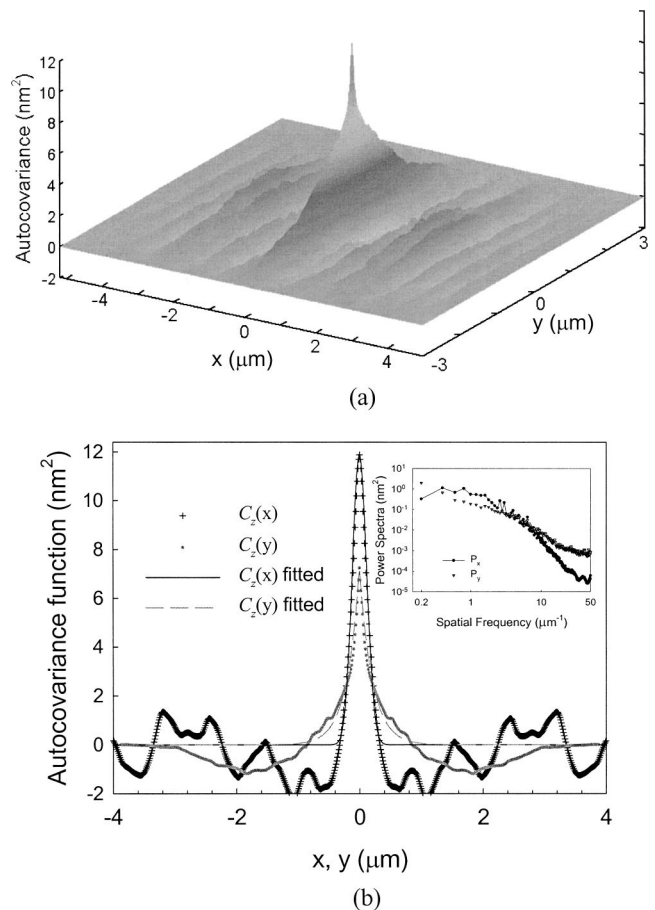


FIG. 4. Calculated autocovariance functions from the measured AFM data. (a) Two-D autocovariance function. (b) Averaged autocovariance functions, $C_z(x)$, and $C_z(y)$ in x and y direction, respectively. $C_z(x)$ is well-fit with the Gaussian function $C_z(x) = \text{SWR}_x^2 \exp(-|x/B_x|^2)$ and $C_z(y)$ is found to be fit better with the exponential function $C_z(y) = \text{SWR}_y^2 \exp(-|y/B_y|)$. The inset shows calculated power spectra. P_x is power spectrum in the x direction (horizontal), and P_y is power spectrum in the y direction.

This work was supported under the DARPA RFLICS Program Grant F30602-00-C-0116 (Monitor: James Nichter) and NSF Grant ANI 01-21662 ITR.

- ¹V. Van, P. P. Absil, J. V. Hrynewicz, and P.-T. Ho, *J. Lightwave Technol.* **19**, 1734 (2001).
- ²D. R. Zadeh, J. P. Zhang, R. C. Tiberio, and S. T. Ho, *J. Lightwave Technol.* **16**, 1308 (1998).
- ³S. J. Choi, K. Djordjev, S. J. Choi, and P. D. Dapkus, *J. Vac. Sci. Technol. B* **20**, 301 (2002).
- ⁴P. K. Tien, *Appl. Opt.* **10**, 2395 (1971).
- ⁵D. Marcuse, *Bell Syst. Tech. J.* **48**, 3187 (1969).
- ⁶J. P. R. Lacey and F. P. Payne, *IEE Proc. Part J* **137**, 282 (1990).
- ⁷A. Matsutani, F. Koyama, and K. Iga, *Appl. Phys. Lett.* **66**, 64 (1995).
- ⁸Y. Martin and H. K. Wickramasinghe, *Appl. Phys. Lett.* **64**, 2498 (1994).
- ⁹K. Hosomi, M. Shirai, K. Hiruma, J. Shigeta, and T. Katsuyama, *IEICE Trans. Electron.* **E79-C**, 1579 (1996).
- ¹⁰G. W. Reynolds and J. W. Taylor, *J. Vac. Sci. Technol. B* **17**, 2723 (1999).
- ¹¹K. K. Lee, D. R. Lim, H. C. Luan, A. Agarwal, J. Foresi, and L. C. Kimerling, *Appl. Phys. Lett.* **77**, 1617 (2000).
- ¹²S. L. Rommel, J. H. Jang, W. Lu, G. Cuevas, L. Zhou, I. Adesida, G. Pajer, R. Whaley, A. Lepore, Z. Schellenbarger, and J. H. Abeles, *J. Vac. Sci. Technol. B* **20**, 1327 (2002).
- ¹³M. H. Kwakernaak, A. N. Lepore, H. Mohseni, H. An, Z. A. Shellenbarger, J. H. Abeles, J.-O. Bae, S. L. Rommel, and I. Adesida, *Technical Digest of CLEO, 2003*, Baltimore, MD.

Characterization of sidewall roughness of InP/InGaAsP etched using inductively coupled plasma for low loss optical waveguide applications

J. W. Bae,^{a)} W. Zhao, J. H. Jang, and I. Adesida

Micro and Nanotechnology Laboratory and Department of Electrical and Computer Engineering,
University of Illinois at Urbana Champaign, Urbana, Illinois 61801

A. Lepore, M. Kwakernaak, and J. H. Abeles

Sarnoff Corporation, Princeton, New Jersey 08543

(Received 8 July 2003; accepted 21 September 2003; published 9 December 2003)

The effects of etch depth on the sidewall roughness (SWR) of InGaAsP/InP waveguides fabricated utilizing two types of masks, NiCr/SiO₂ and SiO₂/NiCr/SiO₂, were investigated with an atomic force microscopy. All the waveguides were etched in an inductively coupled plasma–reactive ion etching to depths ranging from 4 to 8 μm . The root-mean-square (rms) sidewall roughness values of the waveguides etched to depths of 4, 6, and 8 μm with SiO₂ remasking layer were measured to be 2.97, 3.45, and 3.64 nm, respectively. Also the rms SWR values of the waveguides etched without the remasking layer were 3.2, 3.65, and 3.89 nm, respectively. The SiO₂ thin remasking layer deposited on NiCr/SiO₂ mask structure reduced the SWR of the waveguides. Measurements indicated that SWR increased with etch time, which is ascribed to an increase in mask erosion during etching. © 2003 American Vacuum Society. [DOI: 10.1116/1.1625956]

I. INTRODUCTION

Photonic devices and circuits based on InP/InGaAsP materials require optical waveguides with highly anisotropic and smooth sidewall profiles to achieve excellent optical mode quality and low loss performance. Critical processes in the fabrication of the optical waveguides include lithography, masking, and etching. Each process induces various amount of roughness. A nonideal sidewall profile with roughness causes scattering loss in waveguides, and this is a source of optical loss in deep-etched waveguides.¹ Deep-etched waveguide structures allow strong lateral optical confinement. In this type of waveguide, curvature-induced bending loss and leakage loss to the substrate are negligible, or can be significantly reduced.^{1,2} Therefore, total optical loss is dominantly determined by scattering loss from the etched sidewalls.^{1–3}

Optical waveguides based on InP technologies mostly utilize quaternary InGaAsP materials for their core and cladding layers. For etched InP/InGaAsP waveguides, the refractive index change in the vertical direction is much smaller than that in the horizontal direction. The waveguides are usually realized by using dry etching techniques such as reactive ion beam etching (RIBE),⁴ reactive ion etching (RIE),^{5,6} and inductively coupled plasma–reactive ion etching (ICP–RIE).⁷ Whaley *et al.* reported the sidewall roughness (SWR) of InGaAsP/InP waveguides etched using RIE in CH₄/H₂/Ar gas mixture, and the roughness calculated from scanning electron micrographs (SEMs) was in the range from 12 to 31 nm.⁶ Although there have been several reports on the line edge or sidewall roughness of deep-etched waveguides based on either SEMs^{6,8,9} or electron probe analyzer,⁴ investigations using atomic force microscopy (AFM) have not been extensively discussed because of the

difficulty in performing measurements directly on the sidewall of waveguides.

In this study, the SWR of InP/InGaAsP waveguides fabricated using an ICP–RIE with Cl₂/H₂/Ar gas mixture was investigated as a function of masking strategies and the etch depths of the fabricated waveguides. In order to obtain the SWR of deep-etched waveguides, an AFM with a carbon nanotube tip was utilized.

II. EXPERIMENT

A. Patterning and measurement

Heterostructures consisting of InP/InGaAsP were grown on InP substrates using metalorganic chemical vapor deposition. Electron-beam lithography was utilized to generate waveguide test patterns using poly(methylmethacrylate) (PMMA)–P(MMA–MAA) bilayer resists. 40-nm-thick NiCr mask was then deposited using thermal evaporation. The lifted off NiCr metal layer was used as a mask for the reactive ion etching of 600 nm thick SiO₂ in CHF₃ plasma. The composite mask structure, NiCr (40 nm)/SiO₂ (600 nm), was then used as one of two mask structures to etch InP/InGaAsP heterostructures. In order to investigate the effect of a remasking layer on SWR of waveguides, a 50 nm thick SiO₂ layer was blanket deposited on the NiCr/SiO₂ using plasma enhanced chemical vapor deposition after the reactive ion etching of the initial 600-nm-thick SiO₂ in CHF₃ plasma. The sample with the composite mask of SiO₂/NiCr/SiO₂ is then etched in the ICP–RIE system using Cl₂/H₂/Ar. The 50-nm-thick SiO₂ on the surface of InP is etched (sputtered off) during the process. The resulting heterostructure and its performance were compared with that of NiCr/SiO₂ masked samples.

An atomic force microscopy (Digital Instruments Dimension 3100) was utilized to directly measure the SWR of

^{a)}Electronic mail: jwbae70@uiuc.edu

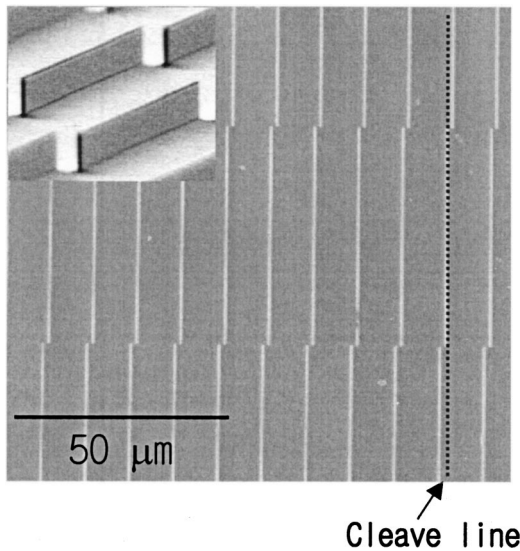


FIG. 1. SEM micrographs of specially designed patterns and deep etched waveguides. $1.2 \mu\text{m}$ wide waveguides were etched using ICP-RIE with $\text{Cl}_2/\text{H}_2/\text{Ar}$ chemistry.

waveguides. A specially designed test pattern for AFM study is shown in Fig. 1. The staircase patterns allow cleavage of the sample to result in at least one segment of waveguides being close to the cleaved edge so that an AFM tip can easily access the waveguide sidewall in the direction perpendicular to the sidewall. Measurements of SWR were performed using an AFM in the tapping mode with a carbon nanotube tip (diameter: 20 nm). All SWR measurement results obtained from AFM are rms roughness. High resolution SEM was utilized to observe the etched profiles of the waveguides and the mask erosion, and to aid in calculating the line edge roughness of NiCr line.

B. Etching

The highly optimized etch conditions used for the deep-etched InP/InGaAsP optical waveguides in this work have been described in detail elsewhere.¹⁰ The samples were etched in a Unaxis SLR 770 ICP-RIE system. The etching conditions were: a gas chemistry of $\text{Cl}_2/\text{H}_2/\text{Ar} = 6 \text{ sccm}/6 \text{ sccm}/9 \text{ sccm}$, 2 MHz rf coil power of 900 W, 13.56 MHz rf bias voltage of -210 V , working pressure of 2 mTorr, and a substrate temperature of 250°C . In order to investigate the effects of etch depth on the SWR of waveguides, the waveguides were etched to depths of 4, 6, and $8 \mu\text{m}$ utilizing two types of masks consisting of NiCr/SiO₂ and SiO₂/NiCr/SiO₂ structures. With our experimental conditions, the etch rate of the waveguide materials was $\sim 1 \mu\text{m}/\text{min}$.

III. RESULTS AND DISCUSSION

Several factors contribute to the SWR of etched waveguides. For this work, these factors include the line edge roughness (LER) of the NiCr layer patterned using lift-off technique and the SWR of the main etch mask layer (thick silicon dioxide) which was etched using CHF₃ RIE.

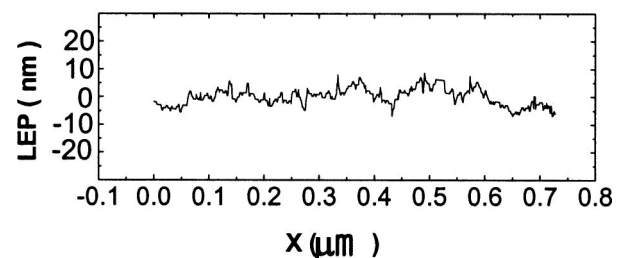
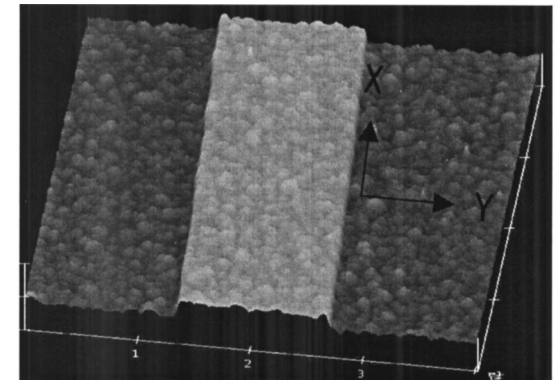


FIG. 2. AFM image and line edge profile of as-patterned 40-nm-thick NiCr line patterned using bilayer e-beam resists and then subsequent evaporation on SiO₂ layer. LER is 2.9 nm.

Figure 2 shows a three-dimensional (3D) AFM image ($4 \mu\text{m} \times 4 \mu\text{m}$) of as-patterned NiCr line. The $1.2\text{-}\mu\text{m}$ -wide NiCr line has a very smooth edge with the LER of the NiCr line calculated to be 2.9 nm from the line edge profile. The metal line with LER as small as 2.9 nm was used as a mask to transfer line patterns into the 600-nm-thick SiO₂ layer deposited on the waveguide heterostructures.

SEM images of waveguides etched without and with SiO₂ remasking layer are shown in Figs. 3(a) and 3(b), respectively. Both samples were etched to a depth of $4 \mu\text{m}$. The deep-etched waveguides have an excellent vertical sidewall profile, and no erosion was observed at the interface between the mask and the waveguide material. In the case of waveguides etched without the remasking layer, however, there is some erosion of the top and edges of the mask while no mask erosion was observed for waveguides etched with the remasking layer. It should be expected that mask structures with the SiO₂ remasking layer would exhibit lower mask erosion during etching. From these SEM images of etched samples, the variations in the SWR of waveguides etched using masks with and without a remasking layer appear similar. In order to accurately quantify the variations and to obtain clearer profile images, AFM with carbon nanotube tips was utilized for SWR measurements. Figures 4(a) and 4(b) show 3D AFM images ($2 \mu\text{m} \times 2 \mu\text{m}$) of waveguide sidewalls etched to a depth of $6 \mu\text{m}$ without and with the remasking layer, respectively. The SWRs were calculated from AFM data for each sample. The measurement arrangement allowed the AFM tip to easily access the waveguide sidewalls by using the specially designed pattern of Fig. 1. This facilitated the direct measurements of the SWRs of waveguides. The waveguide etched with a 50-nm-thick SiO₂

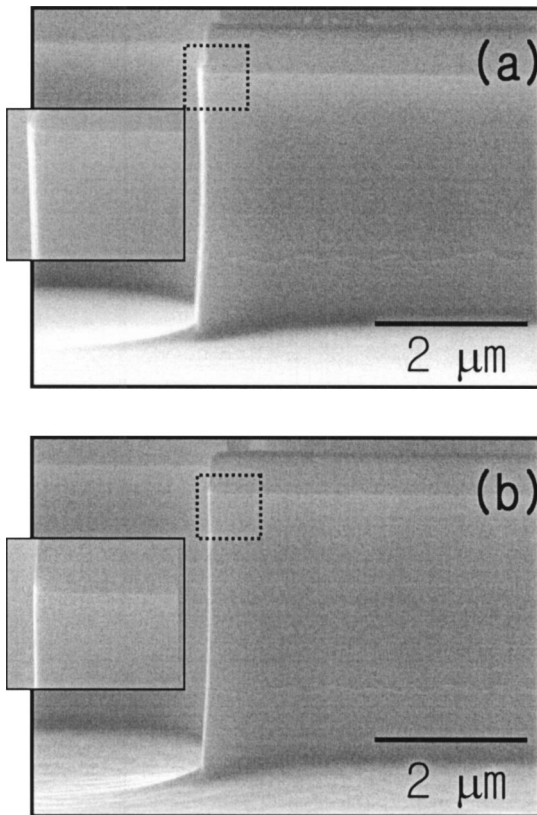


FIG. 3. SEM micrographs of waveguides etched to a depth of $4 \mu\text{m}$ using ICP-RIE with: (a) NiCr/SiO₂ and (b) 50-nm-thick SiO₂/NiCr/SiO₂ masks, respectively.

remasking layer shown in Fig. 4(b) has a smaller SWR than that of the waveguide etched without a remasking layer shown in Fig. 4(a). It is noteworthy that a thin silicon dioxide remasking layer deposited on the deep-etch-mask layer helps in reducing the erosion of the mask during etching, and it resulted in a lower SWR for the waveguide.

In order to investigate the variations of SWR of deep etched waveguides as a function of etch depth, waveguides were etched to the depths of 4, 6, and $8 \mu\text{m}$ using NiCr/SiO₂ and SiO₂/NiCr/SiO₂ masks, respectively. Etch depths were varied through etch time while the etch rate was kept constant. To investigate the dependence of SWR on the etch depth, we divided calculation areas into several regions. SWRs were calculated from AFM data, and its scan area was $10 \mu\text{m} \times 2 \mu\text{m}$ for etch data points. Scan region No. 1 from the top of waveguide is in the range from 0 to $2 \mu\text{m}$, and Nos. 2, 3, and 4 are 2–4, 4–6, and 6–8 μm , respectively. The calculated results are shown in Fig. 5. The variations in SWRs were small except that of scan area No. 2. The higher SWR at scan region No. 2 is due to the increased roughness at the interface between InP and InGaAsP layer induced by the difference in their etch characteristics such as etch rate. From the results obtained, SWRs were 2.97, 3.45, and 3.64 nm for the waveguides etched to depths of 4, 6, and $8 \mu\text{m}$ with the remasking layer, respectively. The SWRs without the remasking layer were 3.2, 3.65, and 3.89 nm, respectively. We have measured the sidewall roughness values over

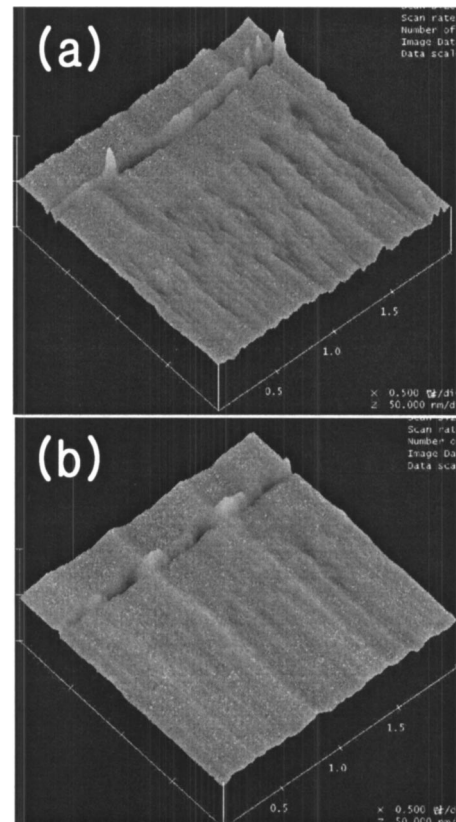


FIG. 4. AFM images of sidewalls of waveguides etched to a depth of $6 \mu\text{m}$ using: (a) NiCr/SiO₂ and (b) 50-nm-thick SiO₂/NiCr/SiO₂ masks, respectively.

at least three different areas, and the error ranges for the results were $6.5\% \pm 0.6\%$. We observed that SWRs increased with an increase in etch depth (or etch time). Also, the SWRs of the waveguides etched with the remasking layer were less than those of the waveguides etched without the

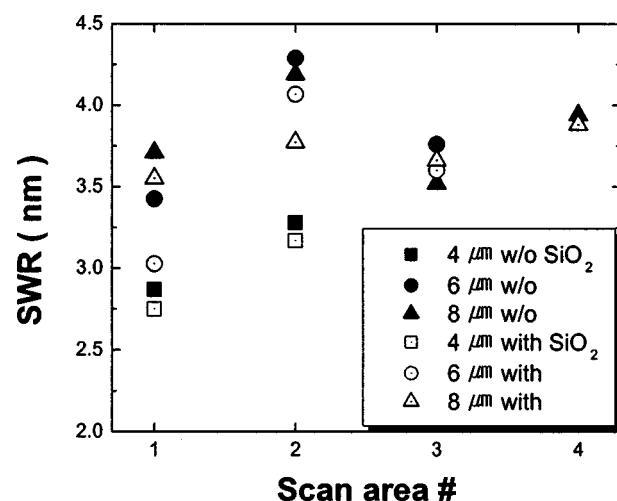


FIG. 5. Variations in the SWRs of waveguides etched to the depths of 4, 6, and $8 \mu\text{m}$ using NiCr/SiO₂ and SiO₂/NiCr/SiO₂ masks, respectively. The SWRs were calculated with AFM data.

remasking layer. Therefore, the use of the remasking layer helped in reducing the SWRs of the waveguides.

According to Marcuse,¹¹ optical radiation loss, P_{loss} , is proportional to the square of rms SWR (σ), i.e., $P_{\text{loss}} \propto \sigma^2$. Therefore, it is expected that waveguides etched with remasking layers would have lower losses. For example, for the waveguides etched to a depth of 4 μm , the SWRs are 2.97 and 3.2 nm for waveguides etched with and without the remasking layer, respectively. The scattering loss is expected to be significantly lower (by $\sim 14\%$) for the waveguides etched using the remasking layer.

IV. CONCLUSIONS

In this study, the effects of remasking layer and etch depth on the sidewall roughness of deep-etched InP/InGaAsP waveguides were presented. The use of a thin remasking layer reduced the erosion of deep-etch mask, and the reduction of mask erosion resulted in lower SWRs. The SWRs of waveguides etched to depths of 4, 6, and 8 μm with 50-nm-thick SiO_2 remasking layers were 2.97, 3.45, and 3.64 nm, respectively. The SWRs of waveguides etched for corresponding etch depths without the remasking layer were 3.20, 3.65, and 3.89 nm, respectively. It was noted that SWRs

increased with etch depths due to mask erosion. This work shows that optimized processing using remasking layers reduces sidewall roughness which in turn is expected to reduce optical losses significantly.

ACKNOWLEDGMENT

This work was supported under the DARPA R-FLICS program (Program Monitor: J. Nicther).

- ¹D. Ra zadeh, J. P. Zhang, R. C. Tiberio, and S. T. Ho, *J. Lightwave Technol.* **16**, 1308 (1998).
- ²M. K. Chin and S. T. Ho, *J. Lightwave Technol.* **16**, 1433 (1998).
- ³M. V. Bazyleko, M. Gross, and M. Faith, *Appl. Phys. Lett.* **69**, 2178 (1996).
- ⁴A. Matsutani, F. Koyama, and K. Iga, *Appl. Phys. Lett.* **66**, 64 (1995).
- ⁵R. Grover, J. V. Hryniwicz, O. S. King, and V. Van, *J. Vac. Sci. Technol. B* **19**, 1694 (2001).
- ⁶R. D. Whaley, B. Gopalan, M. Dagenais, R. D. Gomez, F. G. Johnson, S. Agarwala, O. King, and D. R. Stone, *J. Vac. Sci. Technol. B* **16**, 1007 (1998).
- ⁷M. Ariga, Y. Sekido, A. Sakai, T. Baba, A. Matsutani, F. Koyama, and K. Iga, *Jpn. J. Appl. Phys., Part 1* **39**, 3406 (2001).
- ⁸S. J. Pearson, *Mater. Sci. Eng., B* **10**, 187 (1991).
- ⁹J. R. Lothian, F. Ren, and S. J. Pearson, *Semicond. Sci. Technol.* **7**, 1199 (1992).
- ¹⁰S. Rommel *et al.*, *J. Vac. Sci. Technol. B* **20**, 1327 (2002).
- ¹¹D. Marcuse, *Bell Syst. Tech. J.* **48**, 3187 (1969).

Enhanced electro-optic effect in GaInAsP-InP three-step quantum wells

H. Mohseni,^{a)} H. An, Z. A. Shellenbarger, M. H. Kwakernaak, and J. H. Abeles
Sarnoff Corporation, Princeton, New Jersey 08543-5300

(Received 3 November 2003; accepted 21 January 2004)

We report on the enhanced electro-optic coefficient of GaInAsP three-step quantum wells (3SQW) for high power electrorefraction modulator applications. Measured electro-optic coefficient of the 3SQW is nearly three times higher than the conventional rectangular quantum well (RQW) at $\lambda=1.55 \mu\text{m}$. The enhanced electro-optic effect, combined with a low optical absorption coefficient $\alpha<1 \text{ cm}^{-1}$ in the 3SQW increases a modulator figure of merit by nearly 36 times, and decreases the power consumption by nearly one order of magnitude compared with a conventional RQW design.

© 2004 American Institute of Physics. [DOI: 10.1063/1.1682699]

InP-based electrorefraction modulators are attractive for analog rf applications such as photonic fiber optic links, because of their high saturation power and suitability to monolithic integration. A material with simultaneously high electro-optic coefficient and low optical absorption is desirable for modulators with low switching voltage and low optical insertion loss. In particular, the gain of an analog rf photonic link is proportional to the square of the electro-optic coefficient and inversely proportional to the optical absorption coefficient.

There have been extensive efforts to enhance the electro-optic coefficient with a low optical absorption in the III-V material. The most promising structures are symmetric¹ and asymmetric² coupled quantum wells, with theoretical enhancements approaching a factor of 10.² Experimentally, a factor of 5 higher electrorefraction has been obtained in an AlGaAs/GaAs asymmetric coupled quantum well.³ However, similar improvements have not been demonstrated in the InP-based materials.

This letter reports phase modulators employing InGaAsP/InP three-step quantum wells (3SQW) exhibiting nearly three times higher electro-optic coefficient compared to conventional rectangular quantum wells (RQW) at very low optical loss values. Stepped quantum wells, unlike coupled quantum wells, do not require very thin epitaxial layers or large change of material composition. Recent data⁴ indicate that even at the conventional growth temperature and duration, material interdiffusion can severely deform thin potential barriers. A high degree of interdiffusion in the GaInAsP material system may complicate the attainment of enhanced electrorefraction in the coupled quantum well approach.

An enhanced change of index in stepped quantum wells has been predicted theoretically,⁵ and measured experimentally.⁶ However, optical absorption, and hence modulator performance, of these structures was not demonstrated. Later detailed experimental studies on GaAs/AlGaAs stepped quantum wells revealed negligible improvement of modulation performance due to the enhanced optical absorption.⁷

We calculated optical absorption spectrum of the quantum wells using an effective mass approach. The excitonic

effect was calculated based on a variational method,² and change of index was calculated from the Kramers-Kronig relationship. The electric field inside the active region was calculated using diffusion-drift and Poisson's equation. We optimized the thickness and composition of the layers of the quantum well to maximize change of index per change of voltage $\Delta n/\Delta V$, while keeping the absorption coefficient below $\alpha=1 \text{ cm}^{-1}$ at $\lambda \sim 1550 \text{ nm}$. Figure 1 shows the conduction and valence bands of an optimized 3SQW under an external electric field of $E=40 \text{ kV/cm}$. The barrier layers are InP and the composition and thickness of the layers in the quantum well from left to right are $\text{In}_{0.54}\text{Ga}_{0.46}\text{As}$ (21 Å), $\text{In}_{0.59}\text{Ga}_{0.41}\text{As}_{0.89}\text{P}_{0.11}$ (21 Å), and $\text{In}_{0.70}\text{Ga}_{0.30}\text{As}_{0.64}\text{P}_{0.36}$ (38 Å). Energy level of the first and second electronic states E_{e1} and E_{e2} , as well as first heavy- and light-hole states E_{hh1} and E_{lh1} with their corresponding squared wave functions are overlapped with the band structures.

Optimized quantum well structures were then grown by low-pressure metalorganic vapor phase epitaxy on *n*-type InP substrates. The thickness of the active region in all of the designs is kept at $\sim 0.4 \mu\text{m}$ by adjusting the number of quantum wells. This region is sandwiched between 1.5- μm -thick *n*- and *p*-type InP cladding layers, and the device is terminated with a 50-nm-thick, highly doped InGaAs cap layer. Structural and optical properties of the epitaxial layers were characterized with high-resolution x-ray diffraction and photo-

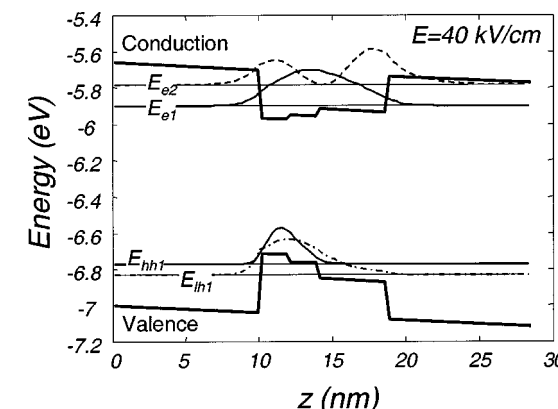


FIG. 1. Energy band structure of an optimized 3SQW at an external electric field of 40 kV/cm. Calculated first and second electron wave functions as well as the heavy- and light-hole wave functions are shown.

^{a)}Electronic mail: hmohseni@sarnoff.com

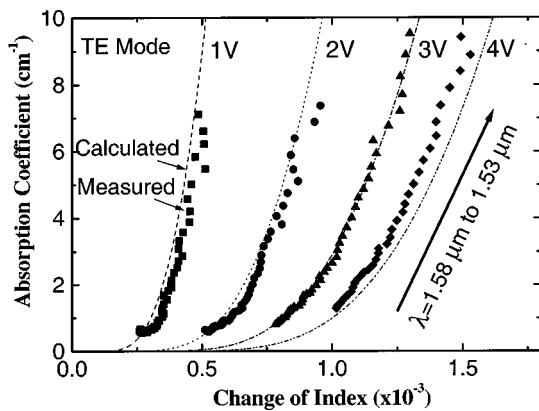


FIG. 2. Measured and calculated optical absorption coefficient vs change of index for a 3SQW modulator over $\lambda=1530-1580$ nm and bias values of $V=1, 2, 3$, and 4 V.

toluminescence techniques. The material is then processed into single mode ridge waveguides through standard photolithography and CH_4/H_2 based reactive ion etching. We measured optical absorption coefficient and change of index of the modulators by measuring Fabry-Perot oscillation,⁸ optical transmission, and the modulator photoresponse. Leakage currents were significantly lower than values that could cause heat-induced change of index. Figure 2 compares the measured and calculated optical absorption coefficient versus change of index for a modulator with 3SQW active region. The data points are collected from $\lambda=1.53$ to $1.58 \mu\text{m}$ with 10 nm increments, and for bias values of $1-4$ V. Calculated change of index and optical absorption coefficient show good agreement to the measured data for bias values up to nearly 3 V. We believe that field-dependent excitonic broadening is the main reason for the gradual deviation between the measured and modeled data at higher bias values. We compared the performance of 3SQW and RQW systematically. Since the detuning from the energy gap of the devices has a significant effect on the measurement, we only compared devices with similar band gap energies. Also, plotting α versus $\Delta n/\Delta V$, and eliminating their wavelength dependency reduced the detuning effect in our comparison. Figure 3 compares the performance of a modulator with 3SQW active region to a modulator with a conventional RQW at $\lambda=1.550 \mu\text{m}$ and TE polarization. The layer thick-

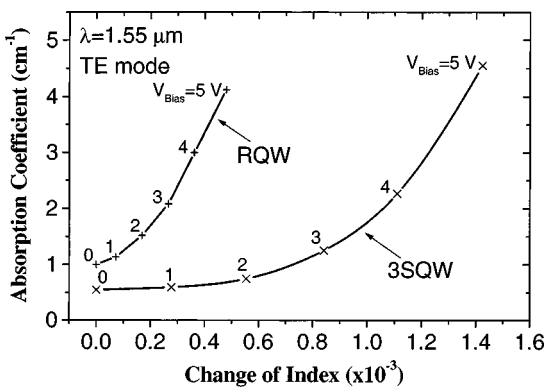


FIG. 3. Performance of a modulator with 3SQW active region compared to a modulator with a conventional RQW active region at $\lambda=1.550 \mu\text{m}$ and TE polarization. 3SQW shows nearly three times higher change of index per voltage and lower optical loss compared to the RQW.

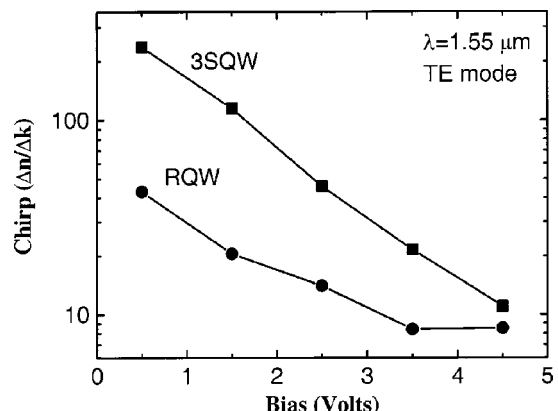
ness and composition of the RQW were optimized for maximum $\Delta n/\Delta V$ using our modeling approach. The barrier of the RQW is InP (85 Å) and the quantum well is $\text{In}_{0.58}\text{Ga}_{0.42}\text{As}_{0.90}\text{P}_{0.10}$ (85 Å). The peak photoluminescence energies of the 3SQW and RQW were 0.877 and 0.875 eV, respectively. Variation in the growth quality was negligible, since the samples were a few growth runs apart. The measured change of index of the RQW at $\alpha \sim 1 \text{ cm}^{-1}$ is about $1 \times 10^{-4}/\text{V}$, similar to the reported values in the literature,⁹ while it is about $2.8 \times 10^{-4}/\text{V}$ for 3SQW. Also, note that both α and $\Delta n/\Delta V$ are smaller in the 3SQW for bias values below ~ 4 V. The importance of a low optical loss can be better understood by considering the gain of an impedance matched analog rf photonic link:¹⁰

$$G = \left(\frac{e^{-\alpha L}}{V_\pi} \frac{\pi 10^{-l/10} R r_d P}{4} \right)^2, \quad (1)$$

where α is the optical absorption coefficient, L is the length of the modulator, and V_π is the voltage required for a π phase shift, R is the detector responsivity, r_d is the detector resistance, P is the laser power, and l is the total loss from the interconnects and fiber optics in decibels. Retaining the relevant parameter to the modulator, one can define modulator figure of merit as $M = (\exp(-\alpha L)/V_\pi)^2$. Assuming a small change of index, the value of V_π can be calculated as $V_\pi = \lambda/[2L(\Delta n/\Delta V)]$. Here λ is the laser wavelength and $\Delta n/\Delta V$ is the change of index versus change of bias in the modulator. Therefore, the optimum length of the modulator required to maximize M can be calculated as $L_{\text{opt}} = 1/\alpha$ and the figure of merit of a modulator with the optimum length becomes

$$M_{\text{opt}} = 4e^{-2} \left(\frac{\Delta n/\Delta V}{\alpha \lambda} \right)^2. \quad (2)$$

Inserting the measured values of optical absorption coefficient and change of index for bias values of 2 V into Eq. (2), one obtains $M_{\text{opt}} \sim 0.10 \text{ V}^{-2}$ for the RQW and $M_{\text{opt}} \sim 3.60 \text{ V}^{-2}$ for 3SQW. This means that replacing the conventional RQW with the 3SQW can improve the gain of an analog rf link by 15.5 dB. Low electroabsorption is also crucial for other applications such as resonant-enhanced micro-ring modulators,¹¹ where the ring quality factor Q is inversely proportional to the absorption coefficient α . Another important parameter for an electrorefractive modulator



is a high chirp factor $\Delta n/\Delta k = (4\pi/\lambda)(\Delta n/\Delta \alpha)$, since it ensures a high contrast ratio in Mach-Zehnder (MZ) modulators.¹² Figure 4 illustrates the measured chirp factor of modulators with 3SQW and RQW active regions at different bias values. The higher value of chirp in the 3SQW is due to both a higher change of index and lower change of absorption.

In conclusion, we demonstrated InP-based phase modulators based on 3SQW with nearly three times higher $\Delta n/\Delta V$ compared with conventional RQW. Enhanced $\Delta n/\Delta V$ combined with an optical absorption coefficient below 1 cm^{-1} lead to ~ 36 times higher figure of merit, and nearly one order of magnitude lower power consumption in the modulator. These properties make 3SQW an excellent candidate for high-power, low-drive voltage MZ modulators required for high performance analog rf link applications.

- ¹ Y. Chan and K. Tada, IEEE J. Quantum Electron. **27**, 702 (1991).
- ² C. Thirstrup, IEEE J. Quantum Electron. **31**, 988 (1995).
- ³ H. Feng, J. Pang, M. Sugiyama, K. Tada, and Y. Nakano, IEEE J. Quantum Electron. **34**, 1197 (1998).
- ⁴ J. Bursik, D. Malakhov, Y. Wang, G. Weatherly, and G. Purdy, J. Appl. Phys. **91**, 9613 (2002).
- ⁵ D. Dave, J. Appl. Phys. **74**, 6872 (1993).
- ⁶ Y. Suzuki, S. Arai, S. Baba, and M. Kohtoka, IEEE Photonics Technol. Lett. **3**, 1110 (1991).
- ⁷ T. Woodward, J. Cunningham, and W. Jan, J. Appl. Phys. **78**, 1411 (1995).
- ⁸ T. R. Walker, Electron. Lett. **21**, 581 (1985).
- ⁹ J. Zucker, K. Jones, B. Miller, and U. Koren, IEEE Photonics Technol. Lett. **2**, 32 (1990).
- ¹⁰ See, for example, S. Hamilton, D. Yankelevich, A. Knuesen, R. Weverka, and R. Hill, IEEE Trans. Microwave Theory Tech. **47**, 1184 (1999).
- ¹¹ M. Kwakernaak, A. Lepore, H. Mohseni, H. An, Z. Shellenbarger, and J. Abeles, presented at Conference on Lasers and Electro Optics, Baltimore, MD, 2003 (unpublished).
- ¹² M. K. Chin, IEEE Photonics Technol. Lett. **4**, 583 (1992).